MUNI
FACULTY
OF SCIENCE

MASARYK UNIVERSITY

Faculty of Science

Ondřej Caha

Thin films of topological insulators

Habilitation thesis

Brno 2023

© Ondřej Caha, Masaryk University (Brno, Czech Republic), 2023.

Contents

1 Introduction **2**

2 Topological insulators **3**
- 2.1 Topological invariant in quantum Hall state . . . 4
- 2.2 $\mathbb{Z}_2$ topological invariant of two-dimensional topological insulators . . . 6
- 2.3 Three-dimensional topological insulators . . . 11
- 2.4 Properties of strong topological insulators . . . 12
- 2.5 Bi_2Te_3, Bi_2Se_3 and Sb_2Te_3 family of topological insulators . . . 13
- 2.6 Topological crystalline insulators . . . 16

3 Experimental methods **19**
- 3.1 Structural analysis of thin films by X-ray scattering . . . 19
  - 3.1.1 Basics of x-ray scattering from thin films . . . 19
  - 3.1.2 X-ray scattering from the thin film with randomly alternating motifs . 22
  - 3.1.3 Substitutional and anti-site defects . . . 25
  - 3.1.4 Reciprocal space mapping: lattice parameters and domain size . . . 27
  - 3.1.5 Temperature dependent XRD experiments . . . 29
- 3.2 Other methods of structural analysis . . . 32
  - 3.2.1 X-ray absorption spectroscopy . . . 32
  - 3.2.2 Transmission electron microscopy . . . 37
- 3.3 Angle-resolved photoemission spectroscopy . . . 40
- 3.4 Electrical transport measurements . . . 42

4 Reprinted papers **44**
- 4.1 Properties of thin films of topological insulators Bi_2Te_3 and BiTe . . . 48
- 4.2 Structure of Bi_xTe_y thin films with general stoichiometry . . . 62
- 4.3 Optical and structural properties of $Bi_2(Se_xTe_{1-x})_3$ alloy . . . 75
- 4.4 Manganese doping of Bi_2Se_3 topological insulator . . . 86
- 4.5 Manganese doping of Bi_2Te_3 topological insulator . . . 107
- 4.6 Band gap in manganese doped topological insulators Bi_2Te_3 and Bi_2Se_3 . . . 119
- 4.7 Ferromagnetic transition in magnetic topological insulators $MnSb_2Te_4$ . . . 139
- 4.8 Doping induced topological phase transition of (Pb,Sn)Se . . . 184
- 4.9 Giant Rashba effect in (Pb,Sn)Te . . . 210

5 Conclusion and outlook **226**

6 List of publications **232**

Preface

My research activities during the last 15 years concentrated at the x-ray laboratory at the Department of condensed matter physics and later also CEITEC Nano core facility (since 2012, I have been responsible for a universal x-ray diffractometer with the rotating anode). As a person responsible for running an x-ray laboratory at the Faculty of Science and partially in CEITEC Nano, I have participated in an extensive range of various research topics emphasizing the x-ray scattering methods as a primary research tool. I have studied the structural properties of various epitaxial and polycrystalline thin films: III-V semiconductors, especially GaN, transition metal oxides, and magnetic metallic films, among others. The x-ray scattering experiments were primarily performed at standard laboratory conditions and high and low temperatures to study structural phase transitions in ferroelectric materials. The research also included structural characterization of bulk semiconductor crystals (Si, SiC), semiconductor nanostructures, and real devices (transistors, diodes). The principal method is laboratory-based x-ray scattering: x-ray diffraction, x-ray reflectivity, and small angle-x-ray scattering. Also, my research included more advanced synchrotron methods such as x-ray absorption spectroscopy, anomalous x-ray diffraction, or x-ray magnetic circular dichroism. The bulk crystals were also studied using x-ray diffraction imaging techniques (x-ray diffraction topography), and we have adapted rocking curve imaging (RCI) to the laboratory-based diffractometer. In recent years we have also adapted the x-ray fluorescence detector to the diffractometer and performed standing wave x-ray fluorescence experiments to study atomic positions in thin films.

Apart from plenty of smaller projects, my research focuses on two main research topics: topological insulator materials and structural analysis of semiconductor materials. The first idea of the topic was applications of x-ray scattering methods, but that approach would lead to quite diverse work composed of several non-related topics. Instead, I have decided to focus this work solely on topological insulators. This way, it can be more compact and broader since I have participated in x-ray scattering and other experimental techniques such as x-ray spectroscopy, photoemission spectroscopy, electron microscopy, and transport measurements. The research activities in this field started ten years ago in close collaboration with the group of prof. Gunther Springholz at Johannes Kepler University in Linz and prof. Oliver Rader at Helmholtz Zentrum Berlin.

I want to thank all my collaborators mentioned above and many other collaborators whose name list would be too long. I will mention especially prof. Václav Holý and prof. Günther Bauer for their continuous support. Lastly, I want to thank my wife and family.

Chapter 1

Introduction

The thesis deals with the work performed with topological insulators thin films. In collaboration with coworkers, we started the growth and characterization of the topological insulators relatively soon after their discovery in 2011. Our research at first focused on topological insulator thin film growth optimization and physical properties of bismuth chalcogenide thin films. Later we started to include magnetic doping with manganese since ferromagnetic topological insulators have unusual physical properties such as quantum anomalous Hall effect. We have published one of the early works showing high-quality epitaxial thin films of bismuth telluride 4.1 and structural properties of natural heterostructures combining Bi_2Te_3 and Bi_2 layers 4.2. The most significant results deal with ferromagnetic topological insulators. Our paper has demonstrated for the first time the direct observation of band gap opening in topological surface states due to ferromagnetic order in $Bi_2Te_3/MnBi_2Te_4$ heterostructures 4.6. Later we have shown a high ferromagnetic ordering temperature of 50 K in $MnSb_2Te_4$ topological insulator 4.7. Last but not least, we have also worked with topological crystalline insulator layers. We have demonstrated a phase transition from a topological crystalline insulator to a strong topological insulator by doping-induced symmetry breaking 4.8. The author's contribution was mainly in the structural characterization of the prepared films using XRD and later HRTEM, but also to band structure measurements at synchrotron sources.

The first part of the thesis briefly introduces the topological insulator theory and physical properties of selected topological insulator materials. The second chapter presents experimental methods used in the thesis by the author. Special attention is devoted to x-ray scattering methods as a primary specialization. The last part of the thesis includes a series of research papers divided into three groups:

- Topological insulators thin films Bi_2Te_3, Bi_xTe_y, and $Bi_2(Se_xTe_{1-x})_3$ studied by x-ray scattering, and other methods.
- Magnetically doped topological insulator thin films Bi_2Te_3, Bi_2Se_3 and Sb_2Te_3.
- Topological crystalline insulators, i.e., (Pb,Sn)Se and (Pb,Sn)Te alloys.

Chapter 2

Topological insulators

Topological insulators are materials with unique electronic structure of surface states. The bulk electronic structure of the topological insulators is topologically non-trivial. The boundary between topologically trivial and non-trivial material hosts surface (interface) states with Dirac cone-like dispersion. The bulk states have an ordinary band gap; thus, the volume electronic properties are identical to an ordinary insulator or semiconductor. In an ordinary insulator or semiconductor, the surface states are susceptible to particular surface morphology, impurities, and other defects. The typical surface states are usually localized at surface defects and cannot serve as a transport channel in a device. On the contrary, the interface between topologically non-trivial and trivial material has unique boundary states with linear dispersion, which are robust against boundary shape or impurities. Thus they are called topologically protected, and electric transport via boundary states has interesting quantum properties.

For the two-dimensional materials the surface states are one-dimensional edge states, in case of three-dimensional materials the surface states are two-dimensional. From the topological point of view normal materials are called topologically trivial insulators. The basic reason for the topological nontrivial systems is peculiar behavior of the half-integer spin under symmetry operations. The momentum in quantum mechanics under rotation by an angle ϑ along z-axis transforms as $\hat{\mathcal{R}}(\vartheta) = \mathrm{e}^{-\mathrm{i}\vartheta s_z}$. Interestingly, full rotation by $\vartheta = 2\pi$ of an electron with half-integer spin of $s_z = \pm 1/2$ does not produce identical state but leads to inversion of the wave function $\hat{\mathcal{R}}(2\pi) = \mathrm{e}^{\mp\mathrm{i}\pi} = -1$. Similar behavior has wave function of spin one-half particles under mirror symmetry $\hat{\mathcal{M}}$ or time reversal symmetry $\hat{\Theta}$. Two subsequent applications of mirror or time-reversal operations invert sign of the wave function $\hat{\mathcal{M}}^2 = \hat{\Theta}^2 = -1$ in any half-integer spin system. This property of half-integer spin is counter-intuitive; one would naively expect two subsequent mirror operations to project back to the original state as is valid for integer spin particles $\hat{\mathcal{M}}^2 = 1$. This transformation is related to the Pauli spin-statistics theorem and Pauli exclusion principle for fermions. The central statement of spin-statistics theorem is that many particle wave function is antisymmetric upon exchange of pair of half integer spin particles $\psi(x, y) = -\psi(y, x)$. All of these antisymmetric transformations can be seen as various projections of a single general symmetry. The topological insulators have certain topology of the electronic states protected by one of the above symmetries. Three-dimensional topological insulators are protected by a time-reversal symmetry; topological crystalline insulators by real space symmetry such as mirror symmetry, space-inversion or rotational axis.

The most prominent properties of the topological insulators are the quantum Hall effect (QHE), quantum spin Hall effect (QSHE), and quantum anomalous Hall effect (QAHE). Three-dimensional topological insulators possess other properties such as topological magneto-electric effect (TME), Majorana fermions at the topological insulator-superconductor interface, and others. There are also higher-order topological phases [1]; there can be topologically protected one-dimensional states (at sample edges) in 3D material. For practical purposes, 2D and 3D topological insulators have attracted the most interest.

Several review papers were published describing the theoretical and experimental progress of the topological insulator field [2–5]. The theory of topological insulators divides into two main groups: Topological field theory (TFT) based on more general topological concepts and topological band theory (TBT). Topological field theory [6] is more general and deals with interacting particles and disorders in the material. Topological band theory [7–11] is limited to the system with non-interacting particles but gives simple criteria of the non-trivial topology. In the limit of non-interacting particles, the TFT transforms into TBT; thus, both theories are consistent and equivalent.

The extensive search for topologically non-trivial materials has been recently performed by Vergniory et al. [12] and, in a limited case, by two other groups [13, 14]. These groups performed first-principle band structure calculations of many non-magnetic crystalline structures in the crystallographic database. They have found that 10–20% out of non-magnetic crystalline structures are topologically non-trivial materials.

This chapter briefly describes the theory of topological insulators. The first section is devoted to the quantum Hall effect, described using TFT. The following sections deal with quantum spin Hall insulators using TBT in two and three dimensions. The fourth section describes the fundamental properties of Bi_2X_3 family of topological insulators. The last section presents a short introduction to topological crystalline insulators.

2.1 Topological invariant in quantum Hall state

The first experimentally observed topologically non-trivial state was the quantum Hall effect state [15]. The quantum Hall effect is an unusual behavior of two-dimensional electron gas in a strong magnetic field. Two-dimensional electron gas can form at the interface of two semiconductors with a different band gap. In strong magnetic field and low temperatures the longitudinal electrical resistance drops to zero

$$\rho_{xx} = \frac{V_{xx}}{I} = 0, \tag{2.1}$$

while the transversal (i.e., Hall resistance) equals a value defined only by fundamental physical constants

$$\rho_{xy} = \frac{V_{xy}}{I} = \frac{1}{\nu}\frac{h}{e^2} = \frac{1}{\nu}25812.807\,\Omega, \tag{2.2}$$

and an integer number ν to very high precision. The resistivity and conductivity tensors are then

$$\hat{\rho} = \begin{pmatrix} 0 & -\rho_{xy} \\ \rho_{xy} & 0 \end{pmatrix}, \qquad \hat{\sigma} = \begin{pmatrix} 0 & \sigma_{xy} \\ -\sigma_{xy} & 0 \end{pmatrix}, \qquad \sigma_{xy} = \nu\frac{e^2}{h}. \tag{2.3}$$

Qualitative analysis of the problem has shown that electrons inside the material occupy Landau levels and do not contribute to the electrical conductivity of the sample. Edge states

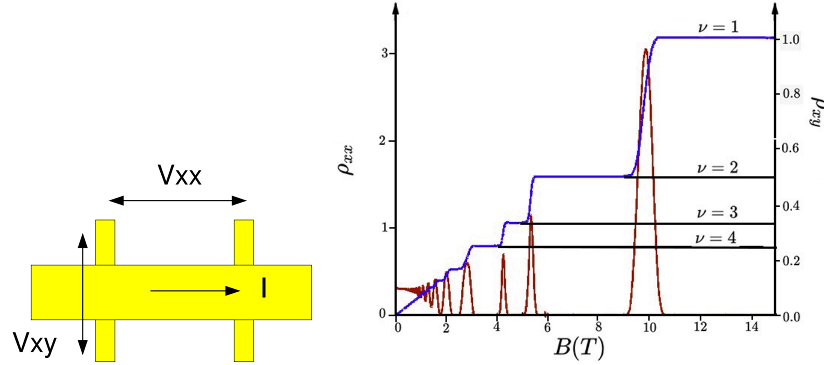

Figure 2.1: Schematic arrangement of quantum Hall effect and magnetic field dependence of transverse and longitudinal resistance. The right part of the figure is reprinted from [16]

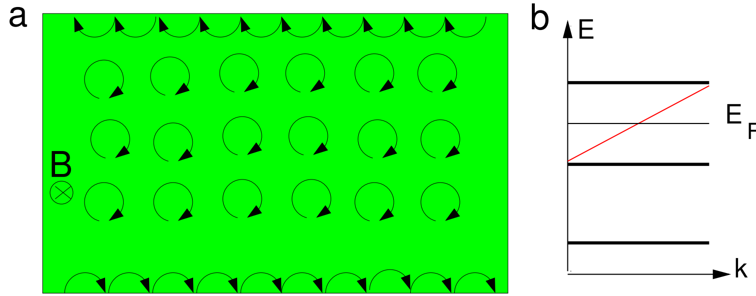

Figure 2.2: (a) Schematic representation of electrons' orbits in the quantum Hall effect. (b) Energy levels of bulk states (Landau levels and edge states in quantum Hall insulator).

dominate the transport properties [17]. The edge states at a particular edge can propagate only in one direction due to the strong magnetic field, as schematically shown in figure 2.2. Since no states with opposite propagation directions exist, electron backscattering is prohibited, and the longitudinal resistivity drops to zero. Moreover, the edge states are not affected by defects, impurities, sample shape, or other irregularities. Such topologically protected edge states are in considerable contrast to the ordinary edge and surface states which are extremely sensitive to defects. The schematic dispersion of the edge states is presented in figure 2.2(b).

A complete quantitative analysis has to consider the integer number ν. This number equals the first known topological invariant in solid state physics, called TKNN invariant after its definitions by Thouless, Kohmoto, Nightingale, and den Nijs [18] or Chern number. The TKNN invariant is defined using Berry's connection

$$A_m(\boldsymbol{k}) = \mathrm{i} \left\langle u_m(\boldsymbol{k}) \right| \nabla_{\boldsymbol{k}} \left| u_m(\boldsymbol{k}) \right\rangle, \tag{2.4}$$

where $u_m(\boldsymbol{k})$ is a periodic part of Bloch wavefunction $\psi_m(\boldsymbol{k})$

$$\hat{\mathcal{H}}|\psi(\boldsymbol{k})\rangle = E_m(\boldsymbol{k})|\psi_m(\boldsymbol{k})\rangle, \qquad |\psi_m(\boldsymbol{k})\rangle = \mathrm{e}^{\mathrm{i}\boldsymbol{k}\cdot\boldsymbol{r}}|u_m(\boldsymbol{k})\rangle. \tag{2.5}$$

Wavefunction $u_m(\boldsymbol{k})$ can be written as eigenfunction of Bloch Hamiltonian $\hat{H}(\boldsymbol{k})$ defined as

$$\hat{H}(\boldsymbol{k}) = \mathrm{e}^{-\mathrm{i}\boldsymbol{k}\cdot\boldsymbol{r}}\hat{\mathcal{H}}\mathrm{e}^{\mathrm{i}\boldsymbol{k}\cdot\boldsymbol{r}}, \qquad \hat{H}(\boldsymbol{k})|u_m(\boldsymbol{k})\rangle = E_m(\boldsymbol{k})|u_m(\boldsymbol{k})\rangle. \tag{2.6}$$

The integral of Berry's connection $A_m(\boldsymbol{k})$ over the closed line surrounding the two-dimensional Brillouin zone is called the first Chern number and could have only integer values

$$C_m = \frac{1}{2\pi}\oint_{\partial BZ} A_m(\boldsymbol{k})\mathrm{d}\boldsymbol{k} = \frac{1}{2\pi}\int_{BZ} F_m(\boldsymbol{k})\mathrm{d}^2\boldsymbol{k}. \tag{2.7}$$

The Chern number can be evaluated using Stokes theorem as surface integral of Berry curvature $F_m(\boldsymbol{k}) = \nabla \times A_m(\boldsymbol{k})$. The Hall conductivity can be evaluated as a sum of particular Chern numbers over occupied bands [18]

$$\sigma_{xy} = \frac{e^2}{h}\sum_m C_m = \frac{e^2}{h}C, \tag{2.8}$$

where total Chern number $C = \sum_m C_m$ called, in this case, TKNN invariant (Thouless, Kohmoto, Nightingale, den Nijs). One can rewrite the preceding formula into the real space coordinates

$$C = \frac{\mathrm{i}}{2\pi}\sum_m \int_{BZ} \mathrm{d}^2\boldsymbol{k}\int \mathrm{d}^2\boldsymbol{r}\left(\frac{\partial u^*}{\partial k_x}\frac{\partial u}{\partial k_y} - \frac{\partial u}{\partial k_x}\frac{\partial u^*}{\partial k_y}\right) = \frac{\mathrm{i}}{4\pi}\sum_m \oint_{\partial BZ} \mathrm{d}\boldsymbol{k}_i \int \mathrm{d}^2\boldsymbol{r}\left(u^*\frac{\partial u}{\partial k_j} - \frac{\partial u^*}{\partial k_j}u\right). \tag{2.9}$$

The quantum Hall state has a nonzero value of topological invariant inside the sample and zeroes outside. These edge states are then so-called topologically protected. The dispersion of the edge states is not sensitive to a particular sample shape, impurities, or other defects. The Chern number equals the number of filled Landau levels, and through the bulk-boundary correspondence, it corresponds to the number of chiral edge modes [19].

2.2 $\mathbb{Z}_2$ topological invariant of two-dimensional topological insulators

The following research focused on the possible topologically non-trivial materials without a high external magnetic field. Haldane predicted topologically non-trivial states in graphene[1] in a periodic magnetic field [20]. The subsequent theoretical works have suggested materials with large spin-orbit coupling leading to similar effects to the band structure as a magnetic field. The prediction by Kane and Mele [8] defines topological invariant in the time-reversal symmetry system. Let us define the time-reversal operator $\hat{\Theta}$. Time reversal invariant Hamiltonian commutes with time reversal operator $[\hat{\mathcal{H}}, \hat{\Theta}] = 0$. The Bloch Hamiltonian has to satisfy relation

$$\hat{\Theta}\hat{H}(\boldsymbol{k})\hat{\Theta}^{-1} = \hat{H}(-\boldsymbol{k}). \tag{2.10}$$

The time reversal operator in the spin 1/2 system also satisfies the relation

$$\hat{\Theta}^2 = -1. \tag{2.11}$$

This formula leads directly to Kramers theorem, i.e. each eigenstate of the time-reversal invariant Hamiltonian has to be at least two-fold degenerate. Using formula (2.11) one can show any eigenstate $|\psi\rangle$ and its time-reversal state are in fact orthogonal

$$\langle\Theta\psi|\psi\rangle = \langle\Theta\Theta\psi|\Theta\psi\rangle = -\langle\Theta\psi|\psi\rangle = 0. \tag{2.12}$$

[1] Haldane made his prediction years before the word "graphene" came into use. The original paper published in 1988 uses the term "2D graphite".

If no spin-orbit interaction is present, the Hamiltonian eigenstates are spin-degenerate for any Bloch wavevector $\boldsymbol{k}$ and any band m

$$E_{m\uparrow}(\boldsymbol{k}) = E_{m\downarrow}(\boldsymbol{k}) = E_{m\uparrow}(-\boldsymbol{k}) = E_{m\downarrow}(-\boldsymbol{k}), \tag{2.13}$$

where the degeneracy of states with inverted wavevector follows from the formula (2.10). The degeneracy of each state is then at least two-fold; the material is topologically trivial.

The spin-orbit interaction lifts spin degeneracy but keeps time-reversal symmetry. The time-reversal image of any state in the crystal is the state with an inverse value of Bloch wave vector $\boldsymbol{k} \to -\boldsymbol{k}$ and inverted spin. The Kramers theorem is satisfied when these pairs have the same energy eigenvalue

$$E_{m\uparrow}(\boldsymbol{k}) = E_{n\downarrow}(-\boldsymbol{k}), \tag{2.14}$$

where m, n are band indices. However, band indices m, n do not have to form pairs over the whole Brillouin zone; we discuss this topic in more detail at the end of this section as one of the topological criteria.

There exist number of possible methods to calculate $\mathbb{Z}_2$ topological invariant [8,10,21,22]. One method of evaluation $\mathbb{Z}_2$ invariant ν is using sewing matrix w [23]

$$w_{mn}(\boldsymbol{k}) = \langle u_m(-\boldsymbol{k})|\hat{\Theta}|u_n(\boldsymbol{k})\rangle. \tag{2.15}$$

From the properties of the time-reversal operator follows

$$w^{\mathrm{T}}(\boldsymbol{k}) = -w(-\boldsymbol{k}). \tag{2.16}$$

There are several high symmetry points in Brillouin zone where $\boldsymbol{k}$ is equivalent to $-\boldsymbol{k}$, which we will note as Γ_a – time-reversal invariant momenta (TRIM) points

$$\Gamma_a = -\Gamma_a + \boldsymbol{G}, \quad \Gamma_a = \frac{\boldsymbol{G}}{2}, \tag{2.17}$$

where $\boldsymbol{G}$ is a reciprocal lattice vector

$$\boldsymbol{G} = n_1\boldsymbol{b}_1 + n_2\boldsymbol{b}_2, \tag{2.18}$$

where n_1 and n_2 are arbitrary integer numbers. Only the lowest-order reciprocal lattice vectors count inside the first Brillouin zone. We can use the following notation

$$\Gamma_{n_1,n_2} = \frac{n_1}{2}\boldsymbol{b}_1 + \frac{n_2}{2}\boldsymbol{b}_2, \quad n_1, n_2 = 0, 1. \tag{2.19}$$

Negative values of n_1, $n_2 = -1$ can be omitted since they are equivalent to points with n_1, $n_2 = 1$. In general, there are four TRIM points in any 2D system; one is $\Gamma = (0, 0)$ point.

In TRIM points Γ_a, the matrix w is antisymmetric. The determinant of an antisymmetric matrix is the square of its Pfaffian. We can define the time-reversal parity of the antisymmetric matrix

$$\delta_a = \frac{\mathrm{Pf}[w(\Gamma_a)]}{\sqrt{\mathrm{Det}[w(\Gamma_a)]}} = \pm 1. \tag{2.20}$$

The total ν invariant is then the parity of the product of all individual values δ_a

$$(-1)^{\nu} = \prod_{a=1}^{4} \delta_a. \tag{2.21}$$

It is possible to choose the sign of the square root in the formula (2.20), and the sign of δ_a is arbitrary. However, the branch of the square root has to be chosen continuously over the Brillouin zone, and the product of an even number of δ_a is independent of branch selection. The invariant ν denotes two equivalence classes of the band structure, which can be continuously deformed, changing time-reversal symmetric Hamiltonian without closing a gap. The consequence leads to the existence of "topologically protected" surface states at the interface between material with $\nu = 1$ and $\nu = 0$. The topological surface states have to cross the band gap, and they have to be spin-polarized. The 2D topologically non-trivial system is known as a quantum spin Hall insulator. As in the quantum Hall state, the electron orbits inside the bulk are insulating with a band gap, and only the edge states contribute to the transport properties. Since the system is without an external magnetic field, the edge states have to differ from QHE edge states. The spin-up electrons propagate in a single direction, while opposite spin electrons propagate in the opposite direction.

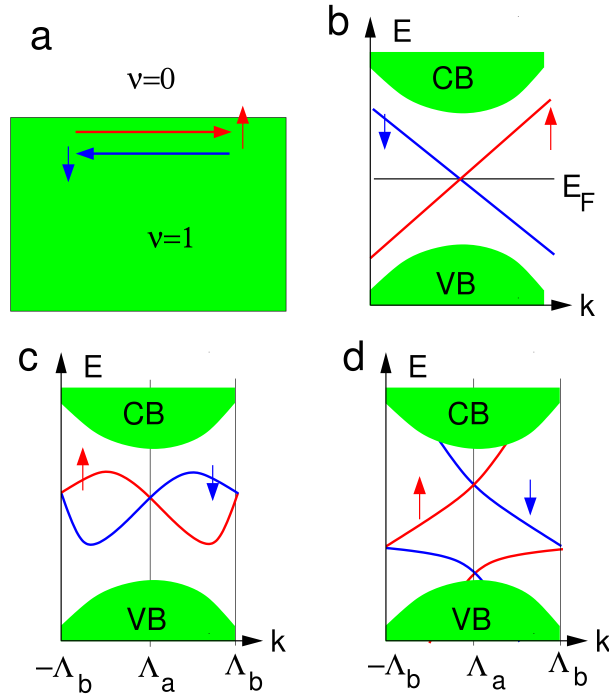

Figure 2.3: (a) Schematic representation of surface electronic orbits in the quantum spin Hall insulator. Red and blue lines correspond to spin-up and spin-down states, respectively. (b) Energy levels of bulk conduction and valence band states. The red and blue lines show the dispersion of spin-up and spin-down edge electron states. (c) and (d) Schematic energy levels of surface states in a topologically trivial and non-trivial case. The figure shows necessary Kramers degeneration in two nonequivalent time-reversal invariant momenta (TRIM) points Λ_a and Λ_b.

The dispersion of the surface states in this system was studied theoretically using an effective model by Bernevig, Hughes, and Zhang (BHZ) [24]. The effective model is developed for HgTe quantum well in a CdTe buffer. HgTe is a material with a large spin-orbit coupling

leading to an inverted band structure, while CdTe is an ordinary semiconductor. While CdTe is an ordinary semiconductor with p-type valence band Γ_8 (J=3/2) and s-type conduction band Γ_6 (J=1/2), HgTe has an inverted band structure due to strong spin-orbit splitting. Figure 2.4 shows the schematic band structure. The edge states of the BHZ Hamiltonian

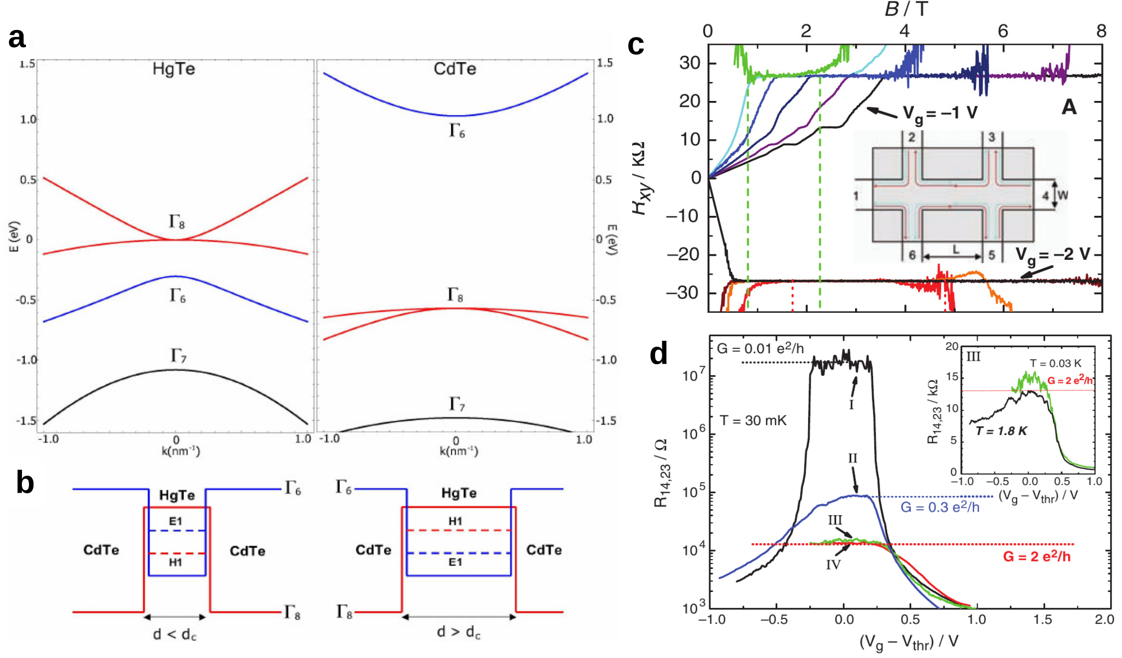

Figure 2.4: (a) Schematic band structure of HgTe and CdTe. (b) Schematic energy levels in the HgTe quantum well for the non-inverted case (left) and inverted case (right). Image reprinted from [24]. (c) Experimental Hall resistance and (d) longitudinal resistance concerning Fermi energy level tuning via gate voltage. Reprinted from [25]

have a simple form of its effective Hamiltonian [3] in the space defined by states $|\psi\uparrow\rangle$ and $|\psi\downarrow\rangle$

$$H_{\text{edge}} = Ak_y\sigma_z, \tag{2.22}$$

where A is a material parameter connected to a Dirac velocity $A = \hbar v$, σ_z Pauli spin matrix and edge is parallel with y axis. This is precisely the dispersion shown in figure 2.2(b) with two linear lines each for opposite spin polarization and Dirac point in its intersection. The defects or impurities can change the dispersion of the state. However, as long as time-reversal symmetry is conserved, the linear dispersion in the Dirac point is not changed; it only can be shifted upwards or downwards in the energy scale. Perturbation of the Hamiltonian without time-reversal symmetry opens a gap in the surface states.

Experimental demonstration of quantized electrical conductivity in this system was performed by König et al. [25]. They have observed quantized Hall conductivity $\sigma_{xy} = \frac{e^2}{h}$ and longitudinal conductivity $G = \frac{2e^2}{h}$. The factor of 2 in longitudinal conductivity is caused by two transport channels available – each edge has a contribution of $\frac{e^2}{h}$. The QSH effect was observed for HgTe quantum wells thicker than critical thickness $d_c \approx 6.5\,\text{nm}$. The interpreta-

tion of the critical thickness is straightforward – confinement energy has to be small enough to allow inversion of the quantum well states. Historically, the first theoretical prediction of quantized conductivity in HgTe quantum well was by Pankratov as early as 1987 [26].

There exists certain correspondence of $\mathbb{Z}_2$ invariant ν to Chern number. In a system with conserved S_z spin component, the solution splits for spin-up and spin-down with Chern number for each spin direction $n_\uparrow$ and $n_\downarrow$, respectively. The time-reversal symmetry leads to a result the total Chern number has to equal zero

$$n_{\text{total}} = n_\uparrow + n_\downarrow = 0, \quad n_\uparrow = -n_\downarrow. \tag{2.23}$$

Half of their difference evaluated modulo 2 is Kane-Mele $\mathbb{Z}_2$ topological invariant ν

$$\nu = \left(\frac{n_\uparrow - n_\downarrow}{2}\right) \mod 2. \tag{2.24}$$

$\mathbb{Z}_2$ topological invariant defines parity of the particular Chern number $n_\uparrow$ or $n_\downarrow$.

The above-presented definition of the topological invariant ν is not unique. Several alternative but equivalent definitions exist; see, for instance, [27]. Each of the equivalent definitions presents a different point of view on the concept of topological theory.

The first developed topological invariant concept was the Pfaffian invariant presented by Kane and Mele [28]. This concept historically preceded the above formulation with sewing matrix invariant. This invariant uses matrix m representing time-reversal operator in the basis of Bloch states

$$m_{mn}(\boldsymbol{k}) = \langle u_m(\boldsymbol{k})|\hat{\Theta}|u_n(\boldsymbol{k})\rangle. \tag{2.25}$$

The topological invariant is defined as an integral over a closed loop

$$\nu = \frac{1}{2\pi \mathrm{i}} \oint_{\partial EBZ} \frac{\mathrm{dPf}[m]}{\mathrm{Pf}[m]} \pmod 2, \tag{2.26}$$

where the integration goes over the boundaries of the effective Brillouin zone. The effective Brillouin zone is half of the whole Brillouin zone, where only one of each pair of time-reversal symmetric points $(k, -k)$ is present. The definition of the effective Brillouin zone is not unambiguous; the integration over the effective Brillouin zone boundaries has to omit vortices in the Pfaffian of m matrix. This invariant counts the number of the Pfaffian vortices pairs; vortices in Pfaffian come in pairs in k and $-k$. Two pairs of Pfaffian vortices can cancel with each other. The Pfaffian invariant is a parity of the number of vortices pairs. Thus invariant value $\nu = 1$ corresponds to an odd number of vortices pairs, and at least one pair of them must be present in the system as long as the time-reversal symmetry is preserved.

In this text, we will present one more definition of the topological invariant ν presented by Fu and Kane [29], so-called obstruction interpretation. The topological invariant ν is evaluated using the integral formula

$$\nu = \left\{\frac{1}{2\pi}\left[\oint_{\partial EBZ} A - \int_{EBZ} F\right]\right\} \pmod 2, \tag{2.27}$$

where $A = \sum_m A_m$ is the total Berry connection (sum of Berry connections over all occupied bands) constructed from Kramers pairs and $F = \nabla \times A$ is the Berry curvature. In a normal situation, the path integral of the Berry connection and the integral of the Berry curvature have the same value according to Stokes' theorem. The system is topologically trivial with the

invariant ν equals zero. In the topologically trivial system we can also choose a *c*ontinuous basis of the filled states $(e_i)_{i=1}^{2n}$ such that $\hat{\Theta} e_{2j-1}(\boldsymbol{k}) = e_{2j}(-\boldsymbol{k})$. Such a case corresponds to the example presented in figure 2.3(c), where the pair of Kramers states denoted by blue and red line degenerate with each other in all TRIM points. In the topologically non-trivial system, such a continuous basis definition is impossible. The situation is schematically shown in figure 2.3(d). Although the Kramers theorem is always satisfied, the pair of bands that degenerate at a certain TRIM point Λ_a do not necessarily degenerate at the other TRIM point Λ_b. Then we cannot construct a continuous basis as defined above, and the subsequent discontinuity obstructs Stokes theorem and leads to a nonzero integer value of the topological invariant ν. It is worth noting that a pair of such obstructions cancels out; this leads to the definition of $\mathbb{Z}_2$ invariant, which can be understood as a parity of the integer value.

2.3 Three-dimensional topological insulators

Generalizing 2D invariant to three dimensions, Fu, Kane, and Mele obtained four invariants [7] $(\nu_0; \nu_1\nu_2\nu_3)$. Instead of four high symmetry points in the 2D system, the 3D system has eight time-reversal invariant momentum points Λ_a. We will note them in a following way

$$\Gamma_{n_1 n_2 n_3} = \frac{1}{2}\left(n_1 \boldsymbol{b}_1 + n_2 \boldsymbol{b}_2 + n_3 \boldsymbol{b}_3\right), \qquad n_j = 0, 1, \tag{2.28}$$

where $\boldsymbol{b}_i$ are reciprocal lattice vectors. The strong invariant ν_0 is the parity of the product of all eight TRIM points as in formula (2.20)

$$(-1)^{\nu_0} = \prod_{a=1}^{8} \delta_a. \tag{2.29}$$

The other invariants are obtained as the product of only four TRIM points in the particular surface 2D Brillouin zone. Since three possible independent surface orientations exist, we can define three independent invariants. The invariant for surface perpendicular to x includes the product of TRIM points with $n_1 = 1$

$$(-1)^{\nu_1} = \prod_{n_{2,3}=0,1} \delta_{1 n_2 n_3}. \tag{2.30}$$

The definition of the other two invariants is straightforward

$$(-1)^{\nu_2} = \prod_{n_{1,3}=0,1} \delta_{n_1 1 n_3}, \qquad (-1)^{\nu_3} = \prod_{n_{1,2}=0,1} \delta_{n_1 n_2 1}. \tag{2.31}$$

The selection of the TRIM points for the invariants ν_1, ν_2, and ν_3 are shown in figure 2.5. The ordinary insulator has trivial values of these invariants (0;000). Non-trivial topological insulators are divided into the general class of *s*trong topological insulators with $\nu_0 = 1$ and *weak* topological insulator with $\nu_0 = 0$ but the nonzero value of at least one of the other invariants ν_1, ν_2, ν_3. The consequence of a topologically non-trivial state is the existence of topologically protected surface states with Dirac cone dispersion.

Strong topological insulators have an odd number of Dirac cones present at any surface orientation. Thus the strong topological insulator has topologically protected surface states

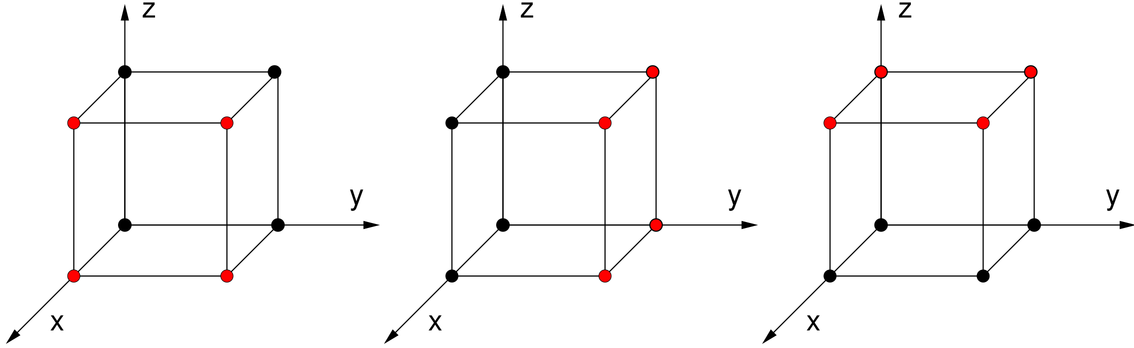

Figure 2.5: Schematic image one-eighth of Brillouin zone of the cubic lattice. Black and red circles denote all eight TRIM points. Left: Red circles denote TRIM points selected for invariant ν_1 – in a plane perpendicular to x-axis. Center and right: TRIM points selection for invariants ν_2 and ν_3, respectively.

insensitive to disorder as long as time-inversion symmetry is conserved. Breaking of time-reversal occurs with a magnetic field or magnetic order.

Weak topological insulators have an even number of Dirac points which can appear at particular surface orientations. At the same time, at the other surface orientations, there is only ordinary dispersion with a band gap. In a weak topological insulator, the Dirac cone-like dispersion is not robust to any time-reversal perturbation. Specific perturbations, such as coupling between two identical Dirac cones, can simultaneously open a band gap in a pair of Dirac cones. Weak topological insulators have topological surface states, but they are not as robust to impurities as strong topological insulators.

From the TFT point of view, the Chern number as a topological invariant exists in an even number of spatial dimensions. The systems in lower dimensions can be seen as a projection from higher dimension systems [6]. Then the Z topological invariant – Chern number transforms into a lower dimension only as parity, i.e., $\mathbb{Z}_2$ topological invariant. The quantum Hall effect exists in two dimensions, with the first Chern number as an integer topological invariant. The next lowest system is the four-dimensional system described by the second Chern number. Three-dimensional topological insulators and quantum spin Hall systems can be seen as their projection to three or two dimensions, respectively. The topological invariant is then just the parity of the second Chern number.

2.4 Properties of strong topological insulators

The surface states of the strong topological insulator can be evaluated with an effective Hamiltonian with the surface perpendicular to z-axis

$$\hat{H}_{\mathrm{surf}} = \hbar v_f(\sigma_x k_y - \sigma_y k_x), \tag{2.32}$$

up to the leading order in k [30, 31]. The dispersion of the surface states is linear Dirac cone with spin locked perpendicular to the momentum. The topological properties of such states are similar to edge states in QSH insulators; they resist perturbations, not breaking time-reversal symmetry.

Surface states in topological insulators are not localized and should have quantized longitudinal and Hall resistance. According [32], the Hall conductance of states with linear dispersion has half-integer quantum Hall effect

$$\sigma_{xy} = \left(N + \frac{1}{2}\right)\frac{e^2}{h}. \tag{2.33}$$

Since there are two surfaces of any imaginable sample expected total conductivity in the experiment is an integer product of e^2/h.

The spin-momentum locking directly leads to spin-related phenomena. For example, charge fluctuations lead to spin fluctuations; novel excitation is present in topological insulators. If a sample is irradiated by circularly polarized light, only electrons with specific spin and momentum are excited, leading to spin-polarized photocurrent [33].

The surface quantum Hall effect also can be observed via a magnetic field induced by surface currents. An electric field induces the magnetization, or a magnetic field electric polarization [6, 34]

$$\boldsymbol{M} = P_3\frac{e^2}{h}\boldsymbol{E} \qquad \boldsymbol{P} = -P_3\frac{e^2}{h}\boldsymbol{B}, \tag{2.34}$$

where $P_3 = \pm 1/2$ is the quantum of Hall conductance with sign according to the orientation of magnetic field with respect to the topological insulator surface. The consequences of this effect lead to a peculiar image magnetic monopole if a point charge is positioned close to a boundary of the topological insulator and trivial insulator [35]. Another related effect is Kerr and Faraday's rotation of incident light due to surface states [36, 37], which can be used to measure quantized value $P_3 e^2/h$.

The topological insulator with incorporated ferromagnetic ordered atoms have quantum anomalous Hall effect (QAHE), with quantized Hall conductivity and dissipation-less longitudinal transport with zero resistance without applying an external magnetic field [38, 39]. Magnetic atoms inside the topological insulator induce the magnetic field. The first experimental observation QAHE was done by Chang et al. [39] in vanadium doped $(Bi,Sb)_2Te_3$.

One of the most peculiar properties rises at the interface between a topological insulator and superconductor [40]. Such interfaces can host Majorana fermion excitations. Several proposed experimental configurations have several superconducting domains with different phases on top of a single topological insulator [41]. Other proposed concepts were based on the proximity of magnetic phase, and superconductor on topological insulator [42]. The topological insulator in Josephson junction has been recently reported to form a hybrid qubit as a promising structure for quantum computing [43].

2.5 Bi_2Te_3, Bi_2Se_3 and Sb_2Te_3 family of topological insulators

Bismuth and antimony chalcogenide materials Bi_2Te_3, Bi_2Se_3 and Sb_2Te_3 have been studied for many years as low band gap materials and especially as materials with the highest thermoelectric efficiency at room temperature [44]. They all have very similar hexagonal crystal structures consisting of five atomic layers (quintuple layer – QL), which are weakly bound at the so-called van der Waals gap. The crystal structure of Bi_2Te_3 is plotted in figure 2.6 (a). Crystal structure of Bi_2Se_3 and Sb_2Te_3 is almost identical to Bi_2Te_3 with only slightly different interplanar distances. The van der Waals gap has substantial consequences on the mechanical and structural properties. Crystal of bismuth chalcogenide very easily cleaves in

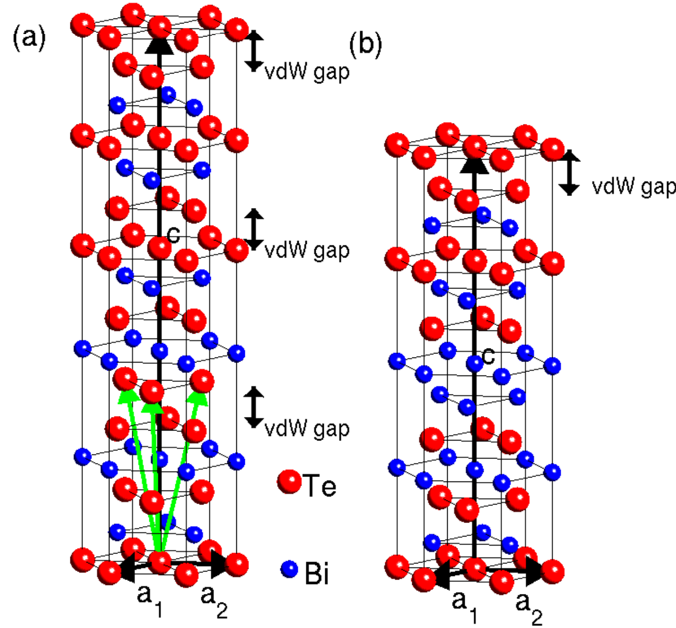

Figure 2.6: (a) Crystal structure of Bi_2Te_3. (b) Crystal structure of Bi_1Te_1 for comparison. Black and green arrows show unit vectors of the hexagonal and rhombohedral unit cells, respectively. Crystal structure of Bi_2Se_3 is very similar to Bi_2Te_3 structure with tellurium atoms replaced by selenium and minor changes in interatomic distances.

the van der Waals gap, and clean surfaces can be easily prepared via Scotch tape technique similar to the graphene preparation. The termination with anion (Se, Te) is also preferential if the clean layer surface is prepared evaporating protection capping layer [45]. The weak bonds also affect strain in the epitaxial layers; the van der Waals structure can release stress during the growth, and the critical thickness to grow relaxed film is small. In other words, even thin films grow as relaxed structures. The van der Waals gap is naturally strongly preferred surface termination; the surface of the Bi_2Te_3 films shows steps with the thickness of 1 nm, which is a thickness of a single QL motif [46].

The QL structure can be seen as a building block of compounds with different stoichiometry. The most prominent example is the BiTe structure (stoichiometry Bi_1Te_1), which is plotted in figure 2.6(b). It can be seen as a series of two QL and a bismuth bilayer – $2Bi_2Te_3$ + Bi_2. A theoretical description of x-ray diffraction in this random system is presented in section 3.1.2. More generally, with alternating changing such building blocks, it is possible to achieve any chemical composition between Bi_2Te_3 and Bi_4Te_3 (1 QL + Bi_2) [47, 48]. In the chapter 4, we present structural studies of Bi_2Te_3 and BiTe thin films [46] and homologous series of general Bi_xTe_y composition [49].

The structure of Bi_2X_3 is trigonal with fcc-type stacking of individual hexagonal layers (ABCABC. . .). The symmetry axis is only three-fold, and there is a high probability of forming inverted twin domains. The twin domain ratio depends on the mismatch to the substrate. While Bi_2Te_3 has a low mismatch (0.05 %) to the BaF_2 the probability of twin

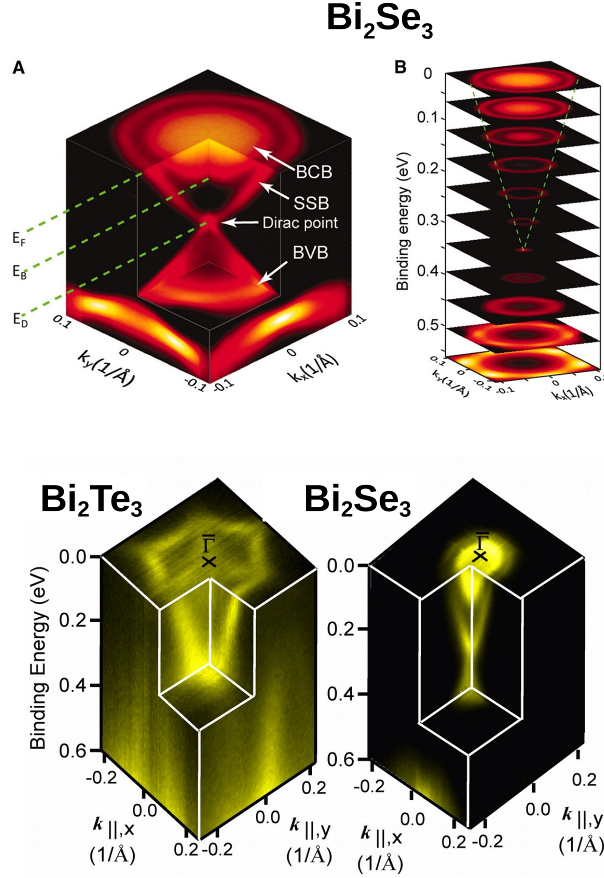

Figure 2.7: Experimental electronic structure of the Bi_2Se_3 and Bi_2Te_3 using ARPES.

domain formation is a couple of percents [46], for Bi_2Se_3 the mismatch reaches 2 % and the twin domains form approximately half of the film. The size of the domains is approx 100 nm as was shown by HRXRD [46] or low energy electron microscopy (LEEM) [45].

The non-trivial topology in Bi_2Se_3 was experimentally shown by Xia et al. [50]. All three materials are strong topological insulators with $\mathbb{Z}_2$ topological invariants (1;000) [2]. The experimental dispersions measured using ARPES are plotted in figure 2.7. From the bulk band structure point of view, Bi_2Se_3 is a narrow band gap semiconductor with a direct band gap in Γ point of 200 meV at 10 K. Topological surface states have excellent linear Dirac cone shape with Dirac cone positioned well inside the bulk band gap 2.7. Bulk band structure of Bi_2Te_3 is different; it has an indirect band gap with a conduction band minimum in Γ point and another local minimum close to Z-F line. The maximum of the valence band also lies close to Z-F line; it is an indirect band gap semiconductor with an indirect gap of 180 meV but the direct band gap transition is only 200 meV at 10 K temperature. The band gap has a maximum value for Se concentration of about 30 %.

Particular interest is given to magnetic doping with manganese to make a basis for the quantum anomalous Hall effect. Manganese atoms form septuple layer structures $MnBi_2X_4$ (SL). The crystal structure is composed of randomly alternating QL and SL blocks forming a natural heterostructure. The average number of the various blocks is determined by stoichiometry. Two reprinted works are devoted to manganese doping in Bi_2Se_3 and Bi_2Te_3.

Another paper presents direct evidence of the gap opening in the Dirac point correlating with out-of-plane magnetization in Mn-doped Bi_2Te_3. The last paper deals with the magnetic structure of $MnSb_2Te_4$, which shows an unusually high Curie temperature of about 50 K. These results are promising for possible observation of QAHE at temperatures above 10 K.

2.6 Topological crystalline insulators

Additional crystal symmetry can induce topologically protected states even in topologically trivial materials. These materials have to possess an even number of Dirac cones (or obstructions as defined in section 2.2) inside a Brillouin zone. In a specific case, the pair of Dirac cones is protected via crystal symmetry. We will briefly present the crystal with mirror symmetry, where a topological invariant mirror Chern number can be defined [51–53]. In a system with half-integer spin, mirror symmetry operator $\hat{\mathcal{M}}$ squares as $\hat{\mathcal{M}}^2 = -1$ and has two eigenvalues $\pm$i. In the three-dimensional system, let us note Σ a surface in the Brillouin zone which is invariant under mirror symmetry $\hat{\mathcal{M}}$. For example, if the mirror plane is xy-plane, mirror invariant reciprocal planes Σ are planes with $k_z = 0$, $k_z = \pi/c$. The electronic eigenstates at Σ plane decompose into two groups according to their mirror eigenvalue. Let us note them as $|u^+_{\boldsymbol{k},l}\rangle$ and $|u^-_{\boldsymbol{k},l}\rangle$ with eigenvalues +i and −i, respectively. We can evaluate the Chern number for each of the mirror subspace C_+, C_- using formula [53]

$$C_\pm = \frac{-\mathrm{i}}{2\pi}\int_\Sigma \mathrm{d}k_x \mathrm{d}k_y \mathrm{Tr}\left[\partial_x A^\pm_y(\boldsymbol{k}) - \partial_y A^\pm_x(\boldsymbol{k})\right], \tag{2.35}$$

where $A^\pm_{a;l,l'} = \langle u^\pm_{\boldsymbol{k},l}|\partial_a|u^\pm_{\boldsymbol{k},l'}\rangle$ is Berry connection in the mirror subspace. In time-reversal symmetric systems $C_+ + C_- = 0$ holds and the mirror Chern number C_m is defined analogous to formula (2.24) as

$$C_m = \frac{C_+ - C_-}{2}. \tag{2.36}$$

The mirror Chern number C_m can have odd or even values. When C_m is even, the surface Dirac cones exist only on mirror-symmetric surfaces. The Dirac cones are in pairs located not in the TRIM points but along mirror invariant lines in the surface Brillouin zone, which map onto itself under mirror symmetry. On the other hand, odd C_m implies an odd number of Dirac cones in any surface Brillouin zone. The material is a conventional topological insulator with Dirac cones positioned in TRIM points.

One of the most studied topological crystalline insulators is narrow band gap semiconductor (Pb,Sn)Se and (Pb,Sn)Te alloys. Lead compounds PbSe and PbTe are trivial insulators, while tin compounds SnTe and SnSe have inverted band structures [54, 55]. These materials crystallize in a cubic rock salt structure, and they have a direct band gap in L point. In PbTe, the valence band edge is formed by L_6^+ states and the conduction band edge by L_6^- states, while SnTe is inverted with L_6^- being valence edge states and L_6^+ conduction band edge states. At a certain concentration, the band gap closes, forming the Dirac cones. Band gap closing occurs at 20–25% of Sn in selenide and around 40–50% of Sn in telluride, according to figure 2.8. Band gap size is also temperature dependent, and a transition from trivial insulator to topological crystalline insulator can be induced by cooling. This effect was demonstrated by Tanaka et al. for (Pb,Sn)Te [57] and Dziawa et al. in (Pb,Sn)Se [58]. The particular dispersion of the surface states is surface orientation dependent. The rock salt structure has three possible mirror symmetric surface orientations (001), (111), and (110) [59]. Most studied

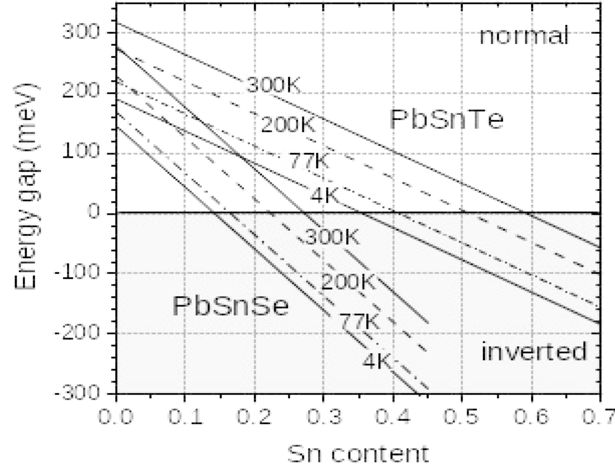

Figure 2.8: Band gap in (Pb,Sn)Se and (Pb,Sn)Te alloys as a function of composition. Figure reprinted from [56].

were (001) and (111) orientation; their surface Brillouin zones are plotted in figure 2.9. In (001) orientation, four Dirac cones are in the vicinity of $\bar{X}$ points. On the other hand, (111) surfaces have four Dirac cones in $\bar{\Gamma}$ and $\bar{M}$ points [60]. An example of the band gap in $\bar{\Gamma}$ point temperature dependence in (Pb,Sn)Se alloys is presented in figure 2.10. One can get a phase transition from topologically trivial into a topological crystalline insulator for a certain alloy composition.

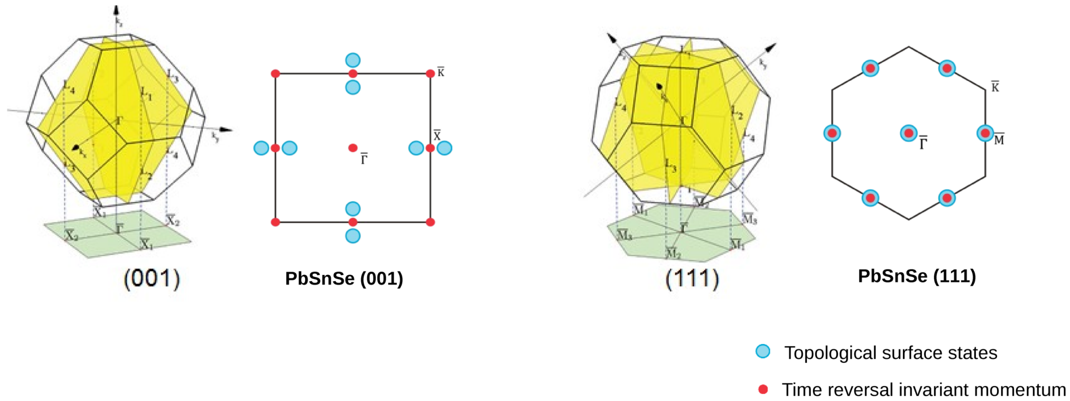

Figure 2.9: Surface Brillouin zones for (001) and (111) surface. Eight bulk L points project into the four $\bar{X}$ points in the case of (001) surface. At (111) surface the bulk L points project into $\bar{\Gamma}$ and three $\bar{M}$ points.

The strain in [111] direction lifts the degeneracy of the $\bar{\Gamma}$ and three $\bar{M}$ points. This leads to an odd number of Dirac cones with properties of a strong topological insulator [29]. Our experimental work has shown the degeneracy can be lifted by doping (Pb,Sn)Se with bismuth [61]. The experiments were performed for tin concentration $x = 28\,\%$. We have shown the band gap closes at $\approx 120\,\mathrm{K}$ without bismuth doping. If the bismuth concentration

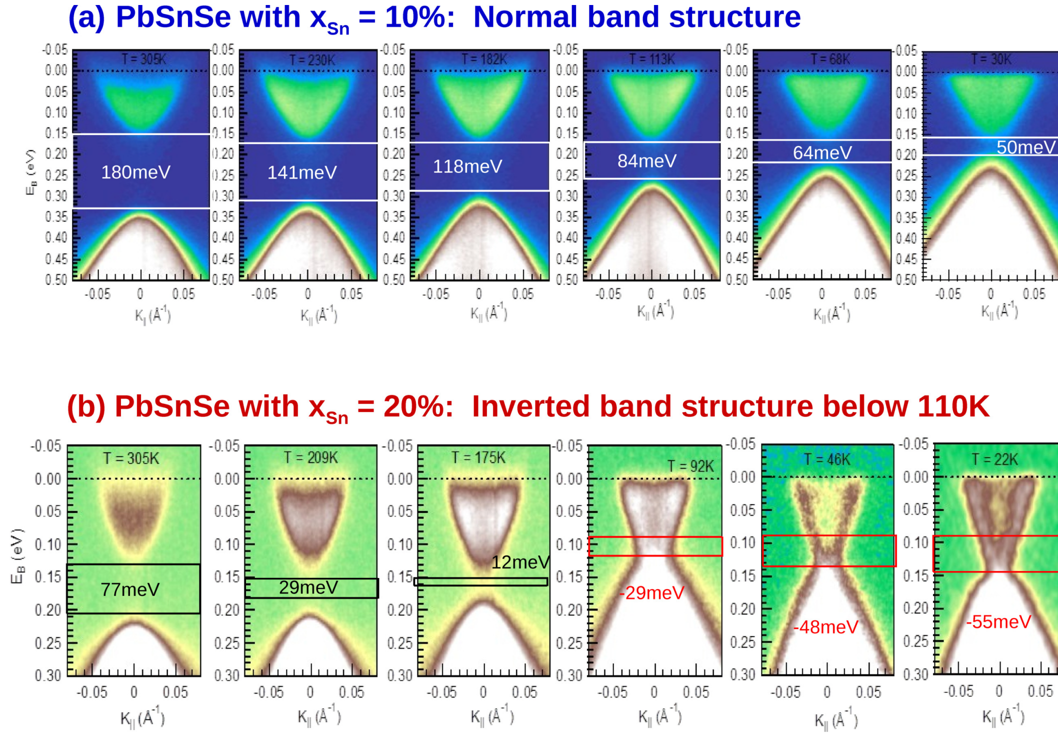

Figure 2.10: Experimental temperature dependence of the band gap in two (Pb,Sn)Se samples in topologically trivial (a) and transition to inverted band structure (b). The experiment was performed at end-station ARPES 1^2 at synchrotron BESSY II.

overcomes 0.5 % band gap in $\bar{M}$ points closes while in $\bar{\Gamma}$ remains opened. The resulting case has an odd number of Dirac cones which is $\mathbb{Z}_2$ topological insulator.

Chapter 3

Experimental methods

This chapter will briefly present several experimental methods in which the author has partially participated in the experiment or data analysis. Special attention is devoted to the x-ray diffraction analysis of thin films in the first section, which is the primary method used by the author. The second section describes several other methods: synchrotron-based x-ray absorption spectroscopy (XAFS), angle-resolved photoemission spectroscopy (ARPES), and two methods that are available in CEITEC Nano core facility – low-temperature transport measurement and high-resolution transmission electron microscopy (HR-TEM).

3.1 Structural analysis of thin films by X-ray scattering

In this chapter, we describe the primary method used for the structural characterization of epitaxial thin films. X-ray scattering provides beneficial information about the crystalline structure of samples. Another widely used method is electron microscopy, namely high-resolution transmission electron microscopy. The advantages of the x-ray diffraction are the following (i) non-destructive method, (ii) no need for surface preparation, even samples with protective cap layer can be studied, (iii) averaging the information over relatively large sample volume (tens of mm^2). On the other hand, x-ray diffraction is an indirect method, and the structure has to be modeled. The usage of an incorrect model leads to incorrect results. If an unknown structure is studied, selecting a proper model is critical. An example of such a case is presented in this work. First studies of manganese doped Bi_2Te_3 assumed manganese substitutional or interstitial incorporation of Mn atoms into Bi_2Te_3 lattice. The disordered structure of Bi_2Te_3 layers was attributed to the stacking of Bi_2Te_3 quintuple layers and Bi double layers. Nevertheless, it turned out the actual structure consists of alternating quintuple layers Bi_2Te_3 with septuple layer structure of $MnBi_2Te_4$ – i. e., Te-Bi-Te-Mn-Te-Bi-Te structure. The structure was confirmed by high-resolution TEM. A combination of several experimental methods achieves the best results in structural characterization. That is, of course, a general statement valid for all experimental science.

3.1.1 Basics of x-ray scattering from thin films

In this chapter, we will briefly describe the x-ray scattering theory with a focus on the model of randomly alternating structural motifs. More detailed descriptions can be found, for example, in the book by Pietsch et al. [62] The x-ray scattering from crystals can be described as a

quantum mechanical scattering model. In the following text, we will limit the description to elastic photon scattering. The x-ray photon propagation is described using Maxwell equations and derived wave equation

$$(\triangle + K^2)\boldsymbol{E}(\boldsymbol{r}) = \hat{V}(\boldsymbol{r})\boldsymbol{E}(\boldsymbol{r}), \tag{3.1}$$

where we have already evaluated the time-dependent part of the electromagnetic wave $\mathcal{E}(\boldsymbol{r}, t) = \boldsymbol{E}(\boldsymbol{r})\mathrm{e}^{-\mathrm{i}\omega t}$, $K = \frac{2\pi}{\lambda}$ is the magnitude of the vacuum wave vector, wavelength λ, frequency $\omega = Kc$, and $\hat{V}$ is the scattering potential

$$\hat{V}(\boldsymbol{r}) = -K^2\chi(\boldsymbol{r}) + \mathrm{grad}\,\mathrm{div}, \tag{3.2}$$

where $\chi(\boldsymbol{r})$ is electric susceptibility. Since x-ray wavelength is comparable with interatomic distance, spatial variation of electric susceptibility includes the atomic structure of matter. Here we have also neglected magnetic response, which is at x-ray frequencies very well satisfied. If the incident state is described with a state $|E_0\rangle$, total wave field $|E\rangle$ and the scattering potential as $\hat{V}$, scattering theory leads to the following formula

$$|E\rangle = |E_0\rangle + \hat{G}_0\hat{V}|E\rangle, \tag{3.3}$$

where $\hat{G}_0$ is Green's operator of the wave equation. This equation can be rewritten as

$$|E\rangle = |E_0\rangle + \hat{G}_0\hat{T}|E_0\rangle, \quad \hat{T} = \hat{V} + \hat{V}\hat{G}_0\hat{V} + \hat{V}\hat{G}_0\hat{V}\hat{G}_0\hat{V} + \cdots \tag{3.4}$$

The general solution to this formula is complicated. The simplest approximation is to take only the first term in the infinite series, the so-called first Born approximation, known as a kinematical approximation in the theory of x-ray scattering

$$|E\rangle \approx |E_0\rangle + \hat{G}_0\hat{V}|E_0\rangle. \tag{3.5}$$

In other words, the kinematical approximation describes the scattering process as a single scattering process. The kinematical approximation also assumes that the intensity of the incident wave is not affected by the scattering processes.

Thus the kinematical approximation can be used if the following conditions are satisfied

1. the intensity of the incident beam does not change within the scattering volume,
2. the scattered intensity is much lower than the incident beam intensity and
3. multiple scattering processes are negligible.

Those conditions are satisfied if

1. diffracting volume is small – comparable length-scale is coherence length of the x-ray radiation, or
2. sample consists of many small incoherent domains (sometimes the term "crystallite" is used instead of the more precise "coherently diffracting domain"), or
3. single crystal sample has very high defect density – effectively, it means the sample consists of many small domains bound by the defects (dislocations, stacking faults, among others).

In other cases (high-quality single crystals) dynamical theory of diffraction has to be used, which solves the whole equation (3.3) [63].

The studied thin film samples always consisted of many domains with size in the order of 100–300 nm, being much smaller than the coherence length of 2 μm in a typical high-resolution x-ray diffraction setup with Cu Kα source and Ge(220) two-bounce monochromator. Thus kinematical approximation is used in the following. The equation (3.5) can be rewritten in a space coordinates as

$$\boldsymbol{E}(\boldsymbol{r}) = \boldsymbol{E}_0 - \frac{1}{4\pi}\int \mathrm{d}^3\boldsymbol{r}' \frac{\mathrm{e}^{\mathrm{i}K|\boldsymbol{r}-\boldsymbol{r}'|}}{|\boldsymbol{r}-\boldsymbol{r}'|}\hat{V}(\boldsymbol{r}')\boldsymbol{E}_0(\boldsymbol{r}'). \tag{3.6}$$

The incident wave is usually in the form of the plane wave $\boldsymbol{E}(\boldsymbol{r}) = E_0\mathrm{e}^{\mathrm{i}\boldsymbol{K}_0\cdot\boldsymbol{r}}$. Usually, we observe the beam scatted into a direction far from the sample rather than intensity distribution in real space. The phase in Fraunhofer approximation equals

$$K|\boldsymbol{r}-\boldsymbol{r}'| \approx Kr - \boldsymbol{K}_s\cdot\boldsymbol{r}', \tag{3.7}$$

where scattered wave vector $\boldsymbol{K}_s = k\boldsymbol{r}/|\boldsymbol{r}|$ is pointing from scattering volume towards detector. The scattered wave field is then simply

$$\boldsymbol{E}_s(\boldsymbol{r}) = -\frac{1}{4\pi}\frac{\mathrm{e}^{\mathrm{i}Kr}}{r}E_0\int \mathrm{d}^3\boldsymbol{r}'\mathrm{e}^{-\mathrm{i}(\boldsymbol{K}_s-\boldsymbol{K}_0)\boldsymbol{r}'}\hat{V}(\boldsymbol{r}'), \tag{3.8}$$

which means the scattered amplitude is proportional to the Fourier transform of scattering potential. Usually scattering vector $\boldsymbol{Q}$ is defined as $\boldsymbol{Q} = \boldsymbol{K}_s - \boldsymbol{K}_0$ and the amplitude scatted to the direction $\boldsymbol{K}_s$ then equals

$$\boldsymbol{E}_s(\boldsymbol{Q}) = A\int \mathrm{d}^3\boldsymbol{r}'\mathrm{e}^{-\mathrm{i}\boldsymbol{Q}\cdot\boldsymbol{r}'}\hat{V}(\boldsymbol{r}'), \tag{3.9}$$

where A stands for a multiplication factor.

The susceptibility at x-ray frequencies is proportional to the electron density $\rho(\boldsymbol{r})$

$$\chi(\boldsymbol{r}) = -\frac{\lambda^2}{\pi}r_\mathrm{e}\rho(\boldsymbol{r}), \tag{3.10}$$

where $r_\mathrm{e} = \frac{e^2}{4\pi\epsilon_0 m_0 c^2}$ is the classical electron radius. It is worth noting that the formula is a high-frequency limit of classical Drude response of free electrons.

The electron density inside a crystalline sample is the sum of the electron density of each atom

$$\rho(\boldsymbol{r}) = \sum_{n=1}^{N}\sum_{j=1}^{M}\rho_j(\boldsymbol{r}-\boldsymbol{R}_n-\boldsymbol{r}_j), \tag{3.11}$$

where the first sum runs over all N unit cells, each positioned at $\boldsymbol{R}_n$ and the second sum over M atoms within the unit cell, r_j is position of j-th atom within unit cell. It is advantageous to evaluate Fourier transform of the electron density

$$\rho^{\mathrm{FT}}(\boldsymbol{Q}) = F(\boldsymbol{Q})\sum_n \mathrm{e}^{-\mathrm{i}\boldsymbol{Q}\cdot\boldsymbol{R}_n}, \tag{3.12}$$

where the structure factor of the unit cell F is evaluated as

$$F(\boldsymbol{Q}) = \int \mathrm{d}^3\boldsymbol{r}\rho_{\mathrm{cell}}(\boldsymbol{r})\mathrm{e}^{-\mathrm{i}\boldsymbol{Q}\cdot\boldsymbol{r}} = \sum_{j=1}^{M} f_j(\boldsymbol{Q})\mathrm{e}^{-\mathrm{i}\boldsymbol{Q}\cdot\boldsymbol{r}_j}, \tag{3.13}$$

where $f_j(\boldsymbol{Q})$ is the atomic form factor of j-th atom equal to the Fourier transform of electron density of the single atom.

The intensity of the scattered beam is proportional to the square of the magnitude of scattered wave amplitude

$$I(\boldsymbol{Q}) = |E(\boldsymbol{Q})|^2 = E^*(\boldsymbol{Q})E(\boldsymbol{Q}). \tag{3.14}$$

Putting formula (3.12) into the intensity we obtain

$$I(\boldsymbol{Q}) = A|F(\boldsymbol{Q})|^2 S(\boldsymbol{Q}), \qquad S(\boldsymbol{Q}) = \sum_{n,m} \mathrm{e}^{-\mathrm{i}\boldsymbol{Q}\cdot(\boldsymbol{R}_n-\boldsymbol{R}_m)}. \tag{3.15}$$

where $S(\boldsymbol{Q})$ is a geometric factor describing crystal structure and shape, and A is a multiplication factor including experimental geometry, incident intensity, and detector aperture. Usually, we measure only relative values, and the factor A is treated as an arbitrary fitting parameter.

The natural materials have non-negligible x-ray absorption. The usual way to account for absorption is to add photon energy-dependent dispersion corrections (Hönl corrections) to the atomic form factor

$$f(\boldsymbol{Q}, E) = f_0(\boldsymbol{Q}) + f'(E) + \mathrm{i}f''(E), \tag{3.16}$$

where $f'(E), f''(E)$ are real and imaginary dispersion correction, respectively. The absorption is proportional to the imaginary part. The real and imaginary parts of the form factor satisfy Kramers-Kronig relations. The susceptibility χ and refractive index $n = \sqrt{1+\chi}$ of any material is then complex.

The simplest way to account for absorption correction is to correct the wave vector $\boldsymbol{k}$ inside the material to match material refractive index n. The relationship is given by the simple optical formula

$$k^2 = n^2 K^2 = n^2 \left(\frac{\omega}{c}\right)^2, \tag{3.17}$$

by continuity of the in-plane component of vacuum wave vector $\boldsymbol{K}_\parallel$ and wave vector in material $\boldsymbol{k}_\parallel = \boldsymbol{K}_\parallel$. Instead of the scattering vector $\boldsymbol{Q} = \boldsymbol{K}_f - \boldsymbol{K}_i$, we will use the corrected scattering vector $\boldsymbol{q} = \boldsymbol{k}_f - \boldsymbol{k}_i$.

3.1.2 X-ray scattering from the thin film with randomly alternating motifs

In this section, we will present the theoretical description of the x-ray scattering on the sample with randomly alternating motifs. Non-stoichiometric crystals of van der Waals topological insulators of Bi_2X_3 family often form crystalline structures with random stacking of two or more building blocks. Systems with alternating structures were theoretically and experimentally studied previously by Holstein, Croset, Kopp et al. [64–67].

We have used a similar model also derived from Pukite's model of stepped surface [68]. Assume the layer consists of alternating motifs A and B. For example, it can be Bi_2Te_3

quintuple layer and bismuth bilayer [49] or Bi_2Te_3 quintuple layer and $MnBi_2Te_4$ septuple layer [69]. Assume the layer consists of P segments, each with n_j^A and n_j^B elements of type A and B, respectively. Here numbers n_j^A and n_j^B are random integer numbers different in every segment. In such a way, we can describe any sample with alternating A and B motifs.

In the following, we will limit to the symmetric scattering, where vector $\boldsymbol{Q}$ is parallel with surface normal axis z. Then only z component of the atomic positions plays a role.

Let us define the structure factor of motif A

$$F_A(q) = \sum_{t=1}^{M_A} f_t(q)\mathrm{e}^{-\mathrm{i}qz_t}, \tag{3.18}$$

where the sum runs over M_A atoms in motif A and the thickness of motif A is D_A. Correspondingly we define structure factor F_B and thickness D_B of motif B. The structure factor of the j-th segment is then

$$F_j(q) = \sum_{v=1}^{n_j^A} F_A(q)\mathrm{e}^{-\mathrm{i}qD_A v} + \mathrm{e}^{-\mathrm{i}qD_A n_j^A} \sum_{v=1}^{n_j^B} F_B(q)\mathrm{e}^{-\mathrm{i}qD_B v} \tag{3.19}$$

and its thickness

$$D_j = n_j^A D_A + n_j^B D_B. \tag{3.20}$$

The amplitude of the scattered radiation then equals to

$$E(q) = A\sum_{j=1}^{P} F_j(q)\mathrm{e}^{-\mathrm{i}qz_j}, \quad z_j = \sum_{k=1}^{j-1} D_k. \tag{3.21}$$

The scattered intensity is the sample average of the square of the amplitude

$$I(q) = \langle E^*(q)E(q)\rangle = |A|^2 \left\langle \sum_{i=1}^{P}\sum_{j=1}^{P} F_i^*(q)F_j(q)\mathrm{e}^{-\mathrm{i}(qz_j - q^* z_i)} \right\rangle. \tag{3.22}$$

The average can be divided into three terms: $j < i$, $j = i$ and $j > i$:

$$\begin{aligned} I(q) \;=\; & |A|^2 \left\{ \sum_{i=1}^{P} \left\langle |F_i(q)|^2 \mathrm{e}^{-2\,\mathrm{Im}\,(q) z_i} \right\rangle + \right. \qquad (3.23) \\ & \left. + \sum_{i=1}^{P}\sum_{j=1}^{i-1} \left\langle F_i^*(q)F_j(q)\mathrm{e}^{-\mathrm{i}(qz_j - q^* z_i)} \right\rangle + \sum_{i=1}^{P}\sum_{j=i+1}^{P} \left\langle F_i^*(q)F_j(q)\mathrm{e}^{-\mathrm{i}(qz_j - q^* z_i)} \right\rangle \right\}. \end{aligned}$$

Two later terms with $j > i$ and $j < i$ are complex conjugates of each other, so their sum is its real part multiplied by two

$$I(q) = |A|^2 \left\{ \sum_{i=1}^{P} \left\langle |F_i(q)|^2 \mathrm{e}^{-2\,\mathrm{Im}\,(q) z_i} \right\rangle + 2\,\mathrm{Re}\left[\sum_{i=1}^{P}\sum_{j=1}^{i-1} \left\langle F_i^*(q)F_j(q)\mathrm{e}^{-\mathrm{i}(qz_j - q^* z_i)} \right\rangle \right] \right\}. \tag{3.24}$$

To evaluate the averages, we have used a short-range order model – we assume the neighboring segments are statistically independent

$$\begin{aligned} I(q) &= |A|^2 \left\{ \sum_{i=1}^{P} \left\langle |F_i(q)|^2 \right\rangle \left\langle \mathrm{e}^{-2\,\mathrm{Im}\,(q)(D_1+\cdots+D_{i-1})} \right\rangle + \right. \\ &\left. +2\,\mathrm{Re}\left[\sum_{i=1}^{P} \langle F_i^*(q) \rangle \left\langle \mathrm{e}^{-2\,\mathrm{Im}\,(q)(D_1+\cdots+D_{i-1})} \right\rangle \sum_{j=1}^{i-1} \left\langle F_j(q) \mathrm{e}^{-\mathrm{i}q(D_j+\cdots+D_{i-1})} \right\rangle \right] \right\}. \end{aligned} \tag{3.25}$$

Moreover, any couple of $D_i, D_{j\neq i}$ are also statistically independent. On the other hand, j-th segment form factor F_j and its length D_j are strongly correlated. The averages can then simplify into the form

$$\begin{aligned} I(q) &= |A|^2 \left\{ \left\langle |F(q)|^2 \right\rangle \sum_{i=1}^{P} \left\langle \mathrm{e}^{-2\,\mathrm{Im}\,(q)D} \right\rangle^{i-1} + \right. \\ &\left. +2\,\mathrm{Re}\left[\langle F^*(q) \rangle \sum_{i=1}^{P} \left\langle \mathrm{e}^{-2\,\mathrm{Im}\,(q)D} \right\rangle^{i-1} \sum_{j=1}^{i-1} \left\langle F(q) \mathrm{e}^{-\mathrm{i}qD} \right\rangle \left\langle \mathrm{e}^{-\mathrm{i}qD} \right\rangle^{i-j-1} \right] \right\}. \end{aligned} \tag{3.26}$$

Let us define a couple of new quantities

$$\alpha = \langle F^*(q) \rangle, \quad \beta = \left\langle F(q)\mathrm{e}^{-\mathrm{i}qD} \right\rangle, \quad \gamma = \left\langle |F(q)|^2 \right\rangle, \quad \xi = \left\langle \mathrm{e}^{-\mathrm{i}qD} \right\rangle, \quad \zeta = \left\langle \mathrm{e}^{-2\,\mathrm{Im}\,(q)D} \right\rangle. \tag{3.27}$$

The formula for scattered intensity is evaluated using well-known formulas of geometric series summation

$$I(q) = |A|^2 \left\{ \gamma \frac{1-\zeta^P}{1-\zeta} + 2\,\mathrm{Re}\left[\frac{\alpha\beta}{\zeta-\xi} \left(\frac{1-\zeta^P}{1-\zeta} - \frac{1-\xi^P}{1-\xi} \right) \right] \right\}. \tag{3.28}$$

In the case of a very thick film, the sum can be calculated as a limit of $P \to \infty$

$$I(q) = |A|^2 \left\{ \gamma \frac{1}{1-\zeta} + 2\,\mathrm{Re}\left[\frac{\alpha\beta}{(1-\zeta)(1-\xi)} \right] \right\}. \tag{3.29}$$

An example of this model is presented in figure 3.1. The four figures show numerical simulation using the formula (3.28) for bismuth telluride and bismuth selenide doped with manganese. To simplify the simulation, each element consisted of just a single septuple layer $MnBi_2X_4$ and a random number of quintuple layers Bi_2X_3. The random distribution is described with its mean value $\langle N_{\mathrm{QL}} \rangle$ and its root mean square deviation (RMSD). The calculation was performed for the constant value of relative RMSD (RMSD/$\langle N_{\mathrm{QL}} \rangle$) (top panels) or constant mean length $\langle N_{\mathrm{QL}} \rangle$ (bottom panels). The limiting cases are straightforward to interpret.

The case of $\langle N_{\mathrm{QL}} \rangle = 50$ in the top panels corresponds to a vast number of quintuples (in average 50) with just one septuple layer structure. The system is then almost pure Bi_2X_3 system, and the peak positions correspond perfectly to a pure Bi_2X_3 system denoted by thin vertical black lines. On the other hand, the case of $\langle N_{\mathrm{QL}} \rangle = 1$ is in the average system with alternating septuple and quintuple layers. The peak positions correspond to the sum lattice parameter $c = D_{\mathrm{QL}} + D_{\mathrm{SL}}$.

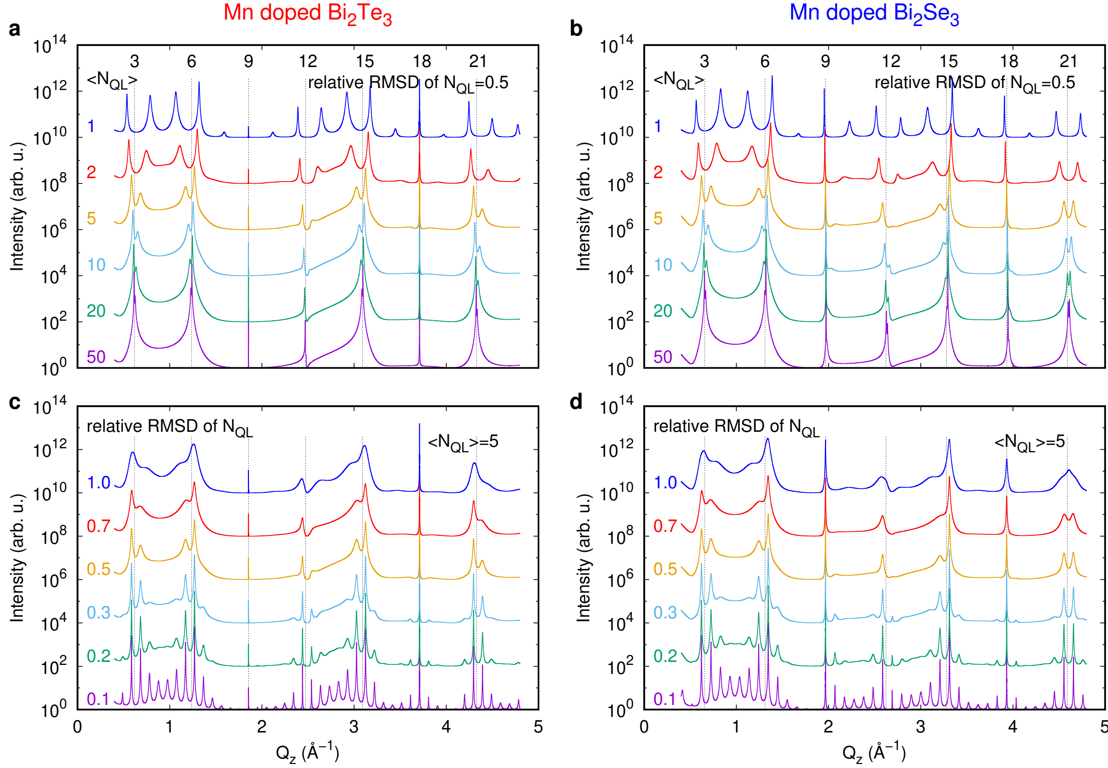

Figure 3.1: Simulation of XRD profile of in symmetric scans.

The bottom panels show the dependence of distribution width. The curve with relative RMSD 0.1 corresponds to an almost perfectly ordered multilayer of 5 quintuple layers and a single septuple layer. The peaks correspond to a real space period of $c = 5D_{\mathrm{QL}} + D_{\mathrm{SL}}$. Increasing RMSD, the peaks get smeared out to a broad diffraction curve. Interesting cases are peaks at $Q_z \approx 1.9\,\text{Å}^{-1}$ and its second order at $Q_z \approx 3.8\,\text{Å}^{-1}$ which stay sharp even in a case of very disordered structure. The reason is that the thickness of the septuple layer almost coincides with 4/3 of the quintuple layer thickness $D_{\mathrm{SL}} \approx 4/3 D_{\mathrm{QL}}$. The third order diffraction of quintuple layer structure (inter-planar distance $d = D_{\mathrm{QL}}/3$) thus corresponds to the fourth diffraction order of septuple layers (inter-planar distance $d = D_{\mathrm{SL}}/4$). In other words, both components share a mutual spatial frequency, and corresponding diffraction peaks do not vanish in any random QL/SL stacking.

3.1.3 Substitutional and anti-site defects

The x-ray diffraction also allows us to study substitutional point defects in the positions of the other atoms to a certain extent. The diffraction intensity is proportional to the square of the structure factor. However, the most substantial effect is caused by heavy atoms, and light atoms have only a minor contribution to the total scattering factor. For example, in the case of manganese doped Bi_2Te_3, Mn is a very light element to bismuth or tellurium, and it is generally not feasible to determine its position within the lattice.

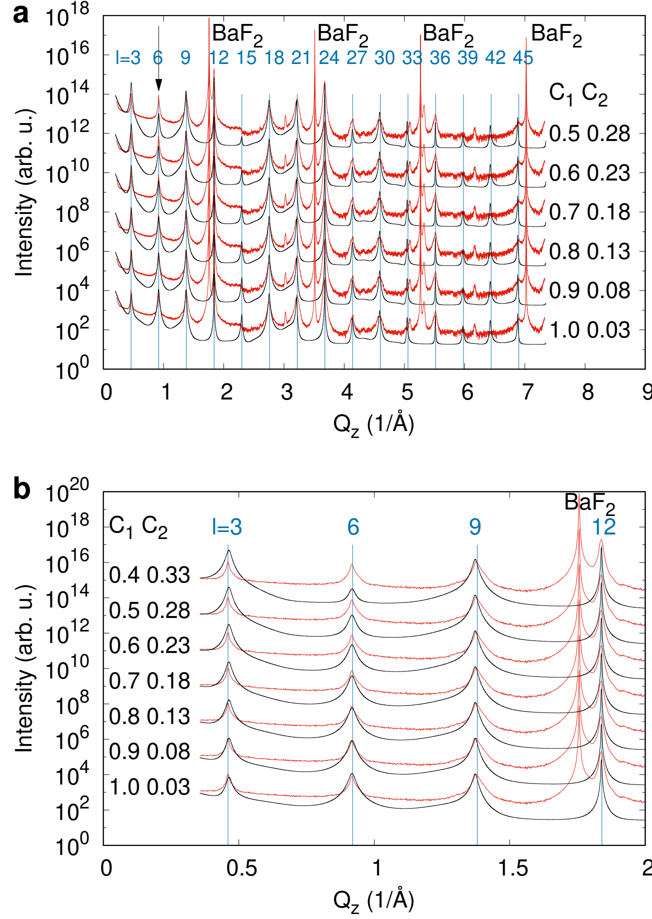

Figure 3.2: Experimental (red) and simulated (black) symmetric scans of $MnSb_2Te_4$ thin film grown on BaF_2 (111).

On the other hand, particular diffractions are sensitive to the positions of light atoms. We will present the example of $MnSb_2Te_4$ structure. The ideal structure of the septuple layer $MnSb_2Te_4$ is supposed to be Te-Sb-Te-Mn-Te-Sb-Te. In reality, the manganese and antimony atoms partially intermix, as is also confirmed by HRTEM in section 3.2.2. The structure factor of the diffractions is given by formula (3.13). Since the atomic form factor is proportional to the atomic number, the contribution of light elements is often negligible. Thus the determination of light atoms inside a structure composed of heavy elements is very uncertain and often almost impossible. However, in $MnSb_2Te_4$ diffraction 000 6 is sensitive to the intermixing of Sb/Mn atoms. This diffraction is relatively weak because form factors of Sb and Te atoms sum in structure factor with opposite phases; thus, their contribution to the total structure factor is tiny. In such case, even small changes in structure factors significantly impact the resulting intensity.

The simulation of $MnSb_2Te_4$ XRD profile with various intermixing values is plotted in figure 3.2. The simulation was performed for several values of C_1, which are the concentration of manganese in central position Mn(Mn) and C_2 manganese concentration in antimony position Mn(Sb). The SL has a single manganese position and two antimony positions. The

stoichiometry of the structure is $Mn_xSb_{2-x}Te_4$, where $x = C_1 + 2C_2$. The set of simulations was performed for the fixed total stoichiometry value $x = 1.06$, which was determined using the Rutherford backscattering (RBS) experiment [70]. The figure shows that the antimony and tellurium form factors do not cancel in the ideal structure; the simulated diffraction peak vanishes close to total Sb/Mn intermixing $C_1 \approx C_2 \approx 1/3$. Our experimental data shows the real intermixing is close to 10 % of the manganese position occupied by antimony ($C_1 = 0.9$).

3.1.4 Reciprocal space mapping: lattice parameters and domain size

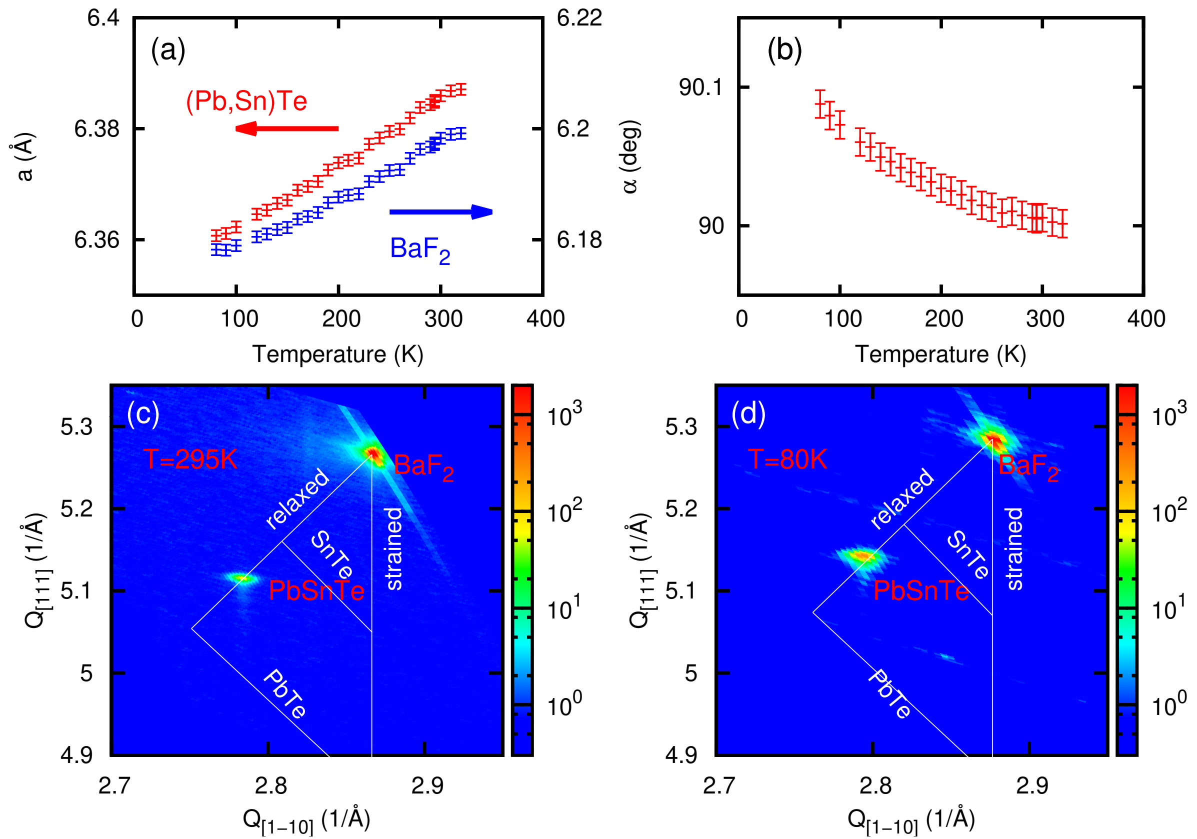

Figure 3.3: (a) Temperature dependence of (Pb,Sn)Te and BaF_2 lattice parameters. (b) Temperature dependence of (Pb,Sn)Te lattice angle. (c, d) Reciprocal space maps in the vicinity of 513 reciprocal lattice points at 80 K and room temperature, respectively.

Another essential property studied by x-ray diffraction is strain and lattice in the epitaxial layers. Most often, the epitaxial layer is grown on (001) or (111) surfaces of the cubic substrate. Without any other preferential in-plane direction induced, for example, by miscut, the symmetry along the out-plane axis is a four-fold or a three-fold rotational axis. For such a case, the in-plane strain in any in-plane direction has the same value. That dramatically simplifies the analysis since one needs to determine lattice parameters in arbitrary in-plane and out-of-plane directions.

The lattice parameters are determined by measuring XRD reciprocal space maps in the vicinity of two reciprocal lattice points. Usually, one symmetric diffraction is selected, and the other has to be asymmetric. We can achieve higher precision using the substrate peak as a reference. The symmetric diffraction is independent of the in-plane lattice parameter; its position is used to determine the tilt between the substrate and layer lattice. The asymmetric reciprocal space map is corrected for lattice tilt, and both in-plane and out-of-plane lattice parameters are determined. An example of (Pb,Sn) lattice parameter determination is presented in figure 3.3. Let us define the substrate lattice parameter a_{sub}, layer in-plane lattice parameter $a_{\|}$, out-of-plane $a_{\perp}$, and unstrained lattice parameter of the layer a_0. The reciprocal space maps in figure 3.3(c,d) show several essential lines, the so-called relaxation triangle. The vertical line parallel with Q_z axis denotes the position of fully strained lattice, also called pseudomorphic, when the in-plane lattice parameter matches the substrate one $a_{\|} = a_{\mathrm{sub}}$. The relaxed line corresponds to the case of the layer holding its free unstrained lattice parameter $a_{\perp} = a_{\|} = a_0$; this line connects the substrate peak position with the origin of coordinates. Two other lines correspond to the lattice of SnTe and PbTe. In general, the experimental peak should appear inside the relaxation triangle. The layer is fully relaxed at room temperature shown in panel (c). However, at a temperature of 80 K in panel (d), the layer peak is above the relaxation line, and the structure is over-relaxed. Differences in thermal expansion coefficients can easily explain such a case; (Pb,Sn)Te layer has a bigger thermal expansion coefficient than BaF_2 substrate. During cooling down, the layer lattice shrinks more than the substrate leading to an in-plane tensile strain in the layer.

The strain of cubic materials can be calculated from lattice parameters. For in-plane and out-of-plane strain it holds

$$\varepsilon_{\|} = \frac{a_{\|} - a_0}{a_0}, \quad \varepsilon_{\perp} = \frac{a_{\perp} - a_0}{a_0}. \tag{3.30}$$

Solving linear theory of elasticity for stress-free surface, we obtain the strain components constraint via Poisson's ratio ν

$$\varepsilon_{\perp} = -2\frac{\nu}{1-\nu}\varepsilon_{\|}. \tag{3.31}$$

Evaluating the preceding formula using lattice parameters, we obtain a formula for unstrained lattice parameter

$$a_0 = \frac{(1-\nu)a_{\perp} + 2\nu a_{\|}}{1+\nu}. \tag{3.32}$$

The formula is handy if we have to determine the composition of ternary alloy using Vegard's law. The Poisson's ratio for (001) and (111) orientation of cubic lattice can be evaluated using components of an elastic tensor as

$$\nu_{001} = \frac{C_{12}}{C_{11} + C_{12}}, \quad \nu_{111} = \frac{1}{2}\frac{C_{11} + 2C_{12} - 2C_{44}}{C_{11} + 2C_{12} + C_{44}}. \tag{3.33}$$

In the case of (111) surface, the cubic lattice is deformed along [111] direction. The lattice of the layer is not cubic anymore but rather rhombohedral. It can be helpful to evaluate not out-of-plane $a_{\perp}$ and in-plane $a_{\|}$ lattice parameters but rather to describe it using rhombohedral lattice parameter a_r and angle α_r. The transformation formulas follow from the geometrical correspondence

$$a_r = \sqrt{\frac{a_{\perp}^2 + 2a_{\|}^2}{3}}, \quad \cos\alpha_r = \frac{a_{\perp}^2 - a_{\|}^2}{a_{\perp}^2 + 2a_{\|}^2}. \tag{3.34}$$

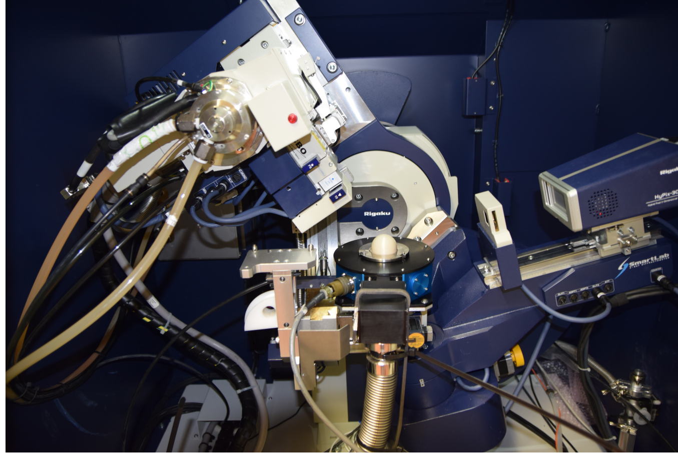

Figure 3.4: Inner view of Rigaku SmartLab diffractometer in CEITEC Nano core facility. A custom-built helium cryostat by ColdEdge company is mounted in the center of the goniometer. The cryostat allows for measurement down to liquid helium temperature.

If angle $\alpha = 90°$ the lattice is cubic without any strain and $a_{\perp} = a_{\parallel} = a_0$. That is the case of (Pb,Sn)Te/BaF_2 at room temperature, as shown in figure 3.3.

Not only peak positions carry helpful information. The shape of the diffraction peak itself can be fitted to obtain information about layer structure. The most common model is the so-called mosaic block model. The crystal is assumed to be composed of a vast number of small domains, each of them with random misorientation. The model parameters are average radii of the domains in the in-plane (horizontal) R_h and out-of-plane (vertical) R_v directions and average misorientation $\Delta\varphi$. The simulation procedure was described in several preceding works [62, 71].

3.1.5 Temperature dependent XRD experiments

The temperature dependence of the lattice parameters and strain can be essential for the interpretation of low-temperature experiments of the band structure. The structural analysis laboratory at CEITEC was equipped with a high-temperature chamber up to 1100 °C, and a liquid nitrogen cryostat. Later the low-temperature possibility was improved by purchasing a liquid helium dome cryostat shown in figure 3.4.

We present several examples of low-temperature measurements of the lattice parameters and strain. Figure 3.3 shows the temperature dependence of the lattice parameter of (Pb,Sn)Te and BaF_2 (111) substrate. The lattice angle of (Pb,Sn)Te increases with decreasing temperature. This dependence is a direct consequence of the (Pb,Sn)Te thermal expansion being larger than the expansion of BaF_2 substrate.

Another example of (Pb,Sn)Se layers grown on various substrates is presented in figure 3.5. The layers with 40 % Sn were grown on BaF_2 (111), InP (111), and KCl (001). The thermal expansion coefficient of InP is much smaller, the coefficient of BaF_2 is slightly smaller, and KCl is much bigger than the thermal expansion of (Pb,Sn)Se. The in-plane strain of the layer is then compressive on KCl and tensile on BaF_2 and InP. The BaF_2 substrate with the slightest difference in thermal expansion coefficient causes the smallest strain in the layer. On the other hand, the layer's electric field can be changed with the substrate choice due to

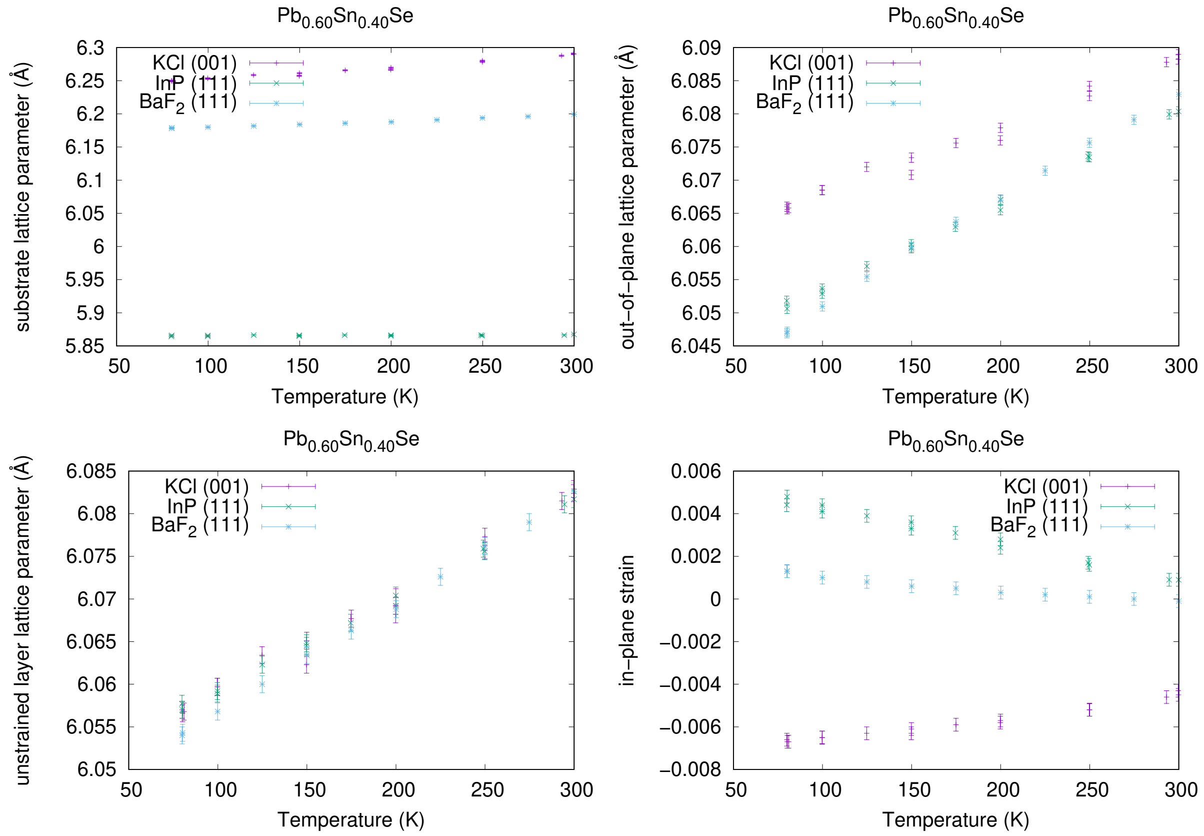

Figure 3.5: Temperature dependence of lattice parameters and strain of (Pb,Sn)Se layer with 40% Sn content. (a) Substrate lattice parameter, (b) out-of-plane lattice parameter of (Pb,Sn)Se, (c) unstrained bulk lattice parameter (Pb,Se)Se calculated from out-of-plane and in-plane lattice parameters, (d) in-plane strain of (Pb,Sn)Se.

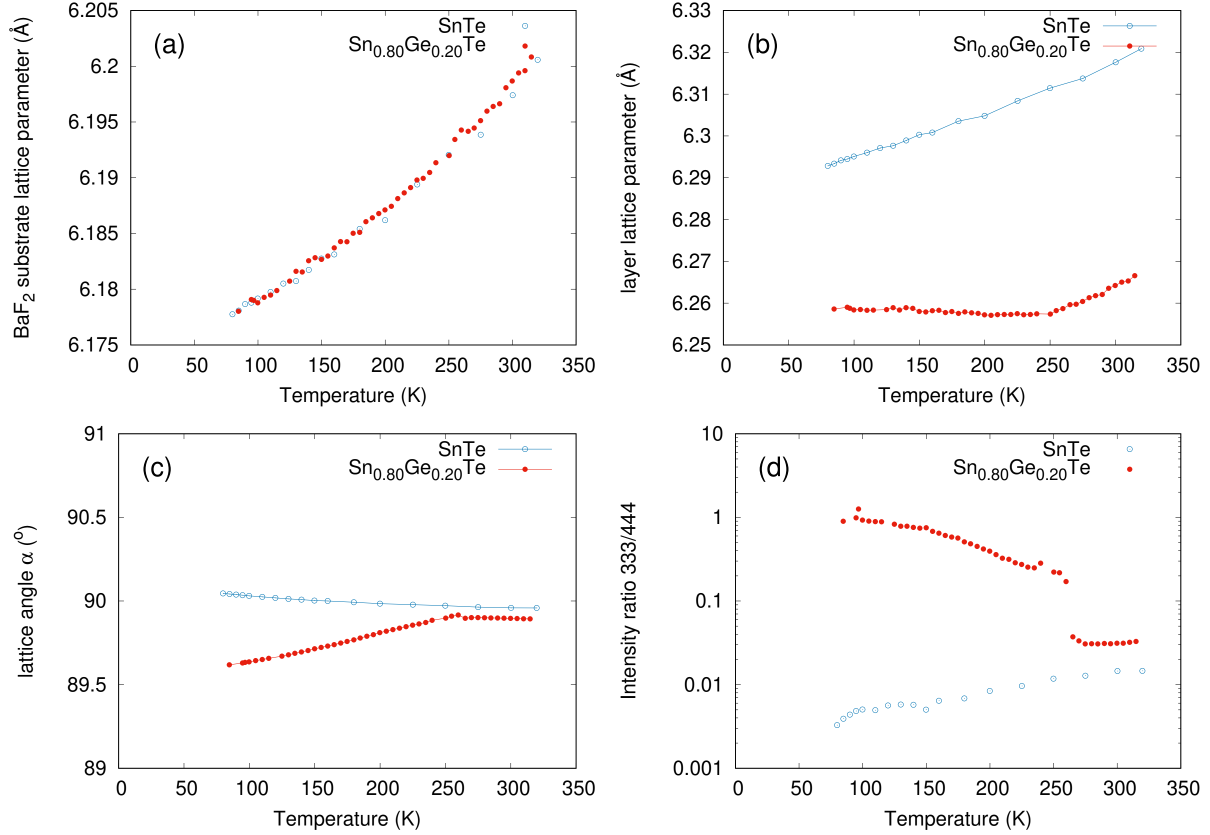

Figure 3.6: Temperature dependence of SnTe and (Sn,Ge)Te lattice parameters, lattice angle, and intensity ratio of 333 to 444 diffraction peaks.

the piezoelectric effect. The layers we have studied are conductive; the piezoelectric field is screened in the bulk of the material, and close to surface space charge region is formed with band bending.

Last we will present the phase transition observed in (Sn,Ge)Te layers. GeTe is ferroelectric with a transition temperature of 700 K, while SnTe has a low ferroelectric transition temperature below 100 K. Alloying SnTe with GeTe, one can tune the transition temperature. The experimental results of SnTe and $Sn_{0.80}Ge_{0.20}Te$ are presented in figure 3.6. The layer's lattice parameter shows a discontinuity in the thermal expansion and the lattice angle at a temperature of 260 K. However, the most prominent signature of the ferroelectric phase transition is the intensity change of 333 diffraction peaks. In the high-temperature rock-salt phase, the structure factor of the odd-parity diffraction is proportional to the difference between cationic (Sn,Ge) and anionic (Te) form factors. The form factor of Sn and Te are almost identical, and the intensity of 333 diffraction peak is very small. In the low-temperature ferroelectric rhombohedral phase, anions and cations shift with respect to ideal rock-salt positions. The structure factor of 333 diffraction peak drastically changes at the phase transition. This effect is very well seen in figure 3.6(d); the relative intensity of 333

diffraction with respect to 444 diffractions rises by approximately one order of magnitude at the phase transition temperature.

3.2 Other methods of structural analysis

In this section, we will briefly comment on two other methods we have used to characterize the structure of the topological insulator films.

3.2.1 X-ray absorption spectroscopy

The measurement of the particular element at its x-ray absorption edge is often called the x-ray absorption fine-structure (XAFS). It is an element-specific method that probes the optical transition of an electron from the localized core level state into the empty state above the Fermi level.

The XAFS spectra are usually divided into two regions: near vicinity of the absorption edge called x-ray absorption near-edge structure (XANES) or near-edge x-ray absorption fine structure (NEXAFS). In contrast, the spectra further above the edge are called Extended x-ray absorption fine structure (EXAFS).

The standard XAFS analysis procedure is extracting the contribution of the studied absorption edge. The absorption below the edge is subtracted, and the absorption coefficient is normalized to the height of the absorption edge. The normalized absorption μ_N equals zero below the edge, and its average above the edge equals one. This normalization is equivalent to normalizing by the concentration of the studied atom. The oscillatory part above the edge is usually denoted as $\chi = \mu_N - 1$.

The XANES part (spectral shape of absorption edge itself up to $\approx 20\,\mathrm{eV}$ above edge) probes electronic states just above Fermi level in the position of the particular element. It includes information on the particular element's chemical state. The proper interpretation is, however, quite complicated, and it is necessary to solve the material's electronic structure. Specialized computer programs are available; one of the most used is FDMNES code [72].

The EXAFS region further from edge $\geq 20\,\mathrm{eV}$ to $1\,\mathrm{keV}$ above the edge have a much more straightforward interpretation. The electronic states far above the Fermi level can be well approximated as free-electron states interacting with the neighboring atoms. Localized core level electron is excited into free-electron wave function spreading as a spherical wave. The spherical wave has a wave vector

$$k = \frac{1}{\hbar}\sqrt{2m_e(E - E_{\mathrm{edge}})}, \tag{3.35}$$

where E is photon energy, E_{edge} binding energy of the core level, and their difference is electron kinetic energy above the Fermi level. The spherical wave scatters on the neighbor atoms and interferes with an unscattered wave. The interference gives rise to the oscillatory behavior of the absorption probability $\chi(k)$ with a period of $\Delta k = \pi/R$, where R is the distance of the neighbor atom. The period of the oscillation can be used to determine the neighborhood of the particular atom. Often the simple analysis is performed as a Fourier transform of $\chi(k)$ to the real space $\chi^{FT}(R)$. The real space function $\chi^{FT}(R)$ has maxima in the distances of the neighbor atoms. The complete theory is rather complicated; we refer to the existing literature [73]. The most often used software package for data analysis is Demeter [74] and for simulation of EXAFS profile FEFF package [75, 76].

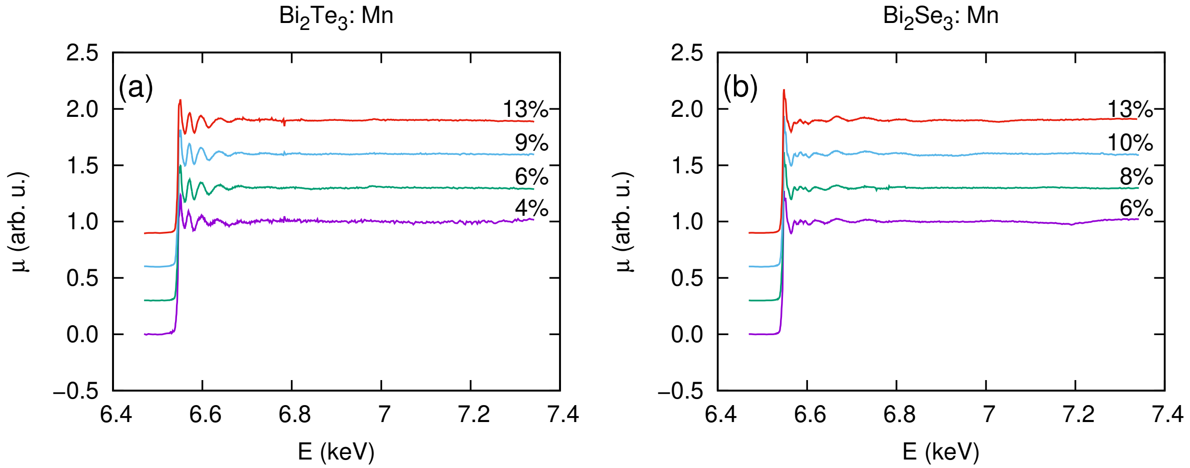

Figure 3.7: Experimental normalized XAFS spectra of various concentration of Mn-doped Bi_2Te_3 (a) and Bi_2Se_3 (b), respectively.

The experiment has to be carried out at synchrotron beamlines since no sufficient laboratory sources with tunable photon energy exist. There are several possibilities for the experimental setup. Bulk samples are most commonly measured in transmission regime using two detectors – most often ionization chambers. The first ionization chamber is positioned in front of the sample and measures the intensity of the incoming beam; the second chamber is behind the sample and measures transmitted intensity. The transmission of the chamber is optimally around 2/3; if the transmission is lower than 2/3, the absorption measurement statistic worsens. On the other hand, the measured signal is proportional to the absorption in the chamber, and too high transmission worsens the incoming beam measurement statistics. The sample transmission is an exponential function of its thickness; the best statistics one obtains with sample transmission of about 1/3 (1/e to be precise). Thus, the XAFS beamlines are usually equipped with ionization chambers, allowing them to fill with arbitrary pressure of selected noble gas to achieve optimal sensitivity for a wide range of chemical elements. The fluorescence of the particular element is proportional to the photoelectric component of total absorption corresponding to the particular edge. However, that is the only part important for XAFS analysis.

For thin films, the most common method is to measure fluorescence instead of a transmission. The incidence ionization chamber is still used similarly as in transmission mode, and the sample is irradiated at low angle incidence to maximize the signal from the film. The fluorescence signal is collected with an energy-dispersive x-ray detector.

In the following text, we show an example of XAFS used to characterize the positions of manganese atoms inside the topological insulator lattice of Bi_2Te_3 and Bi_2Se_3. The measurement was performed in the vicinity of Mn K edge at 6539 eV up to 7500 eV to cover sufficient EXAFS range. The experiment was carried out at synchrotron ESRF beamline BM23. Figure 3.7 shows normalized absorption spectra collected at samples with various Mn concentrations.

The spectra have similar features independent of manganese concentrations.

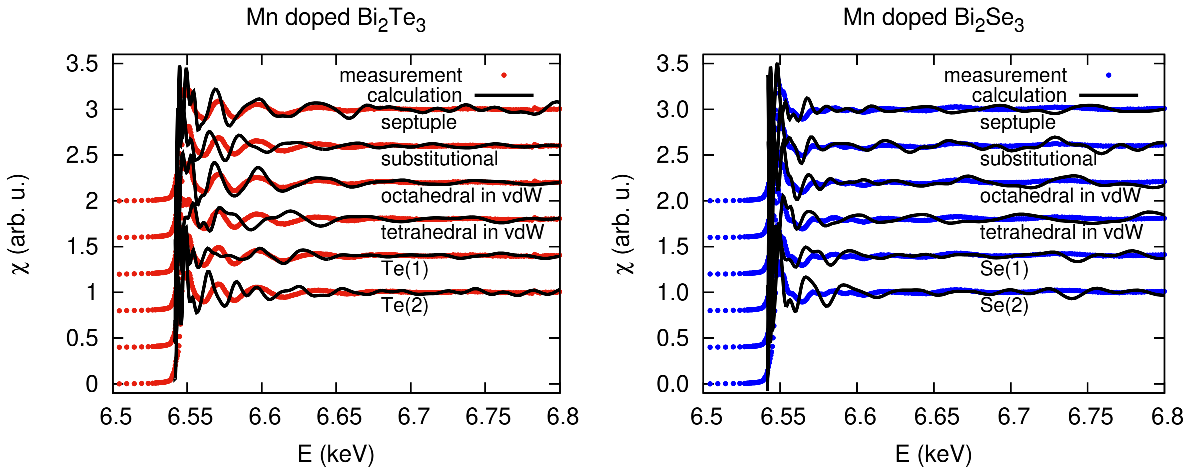

Figure 3.8: Experimental data and simulation of EXAFS part for various manganese positions in Bi_2Te_3 (a) and Bi_2Se_3 (b), respectively.

Mn doped Bi_2Se_3				
position	first shell	distance(Å)	second shell	distance (Å)
center of septuple layer	6 Se	2.719	6 Bi 6 Mn	3.977 4.12
substitutional Bi	3 Se(1) 3 Se(2)	2.972 3.041		
octahedral in vdW gap	6 Se	3.041		
tetrahedral in vdW gap	4 Se	2.394		
substitutional Se(1) close to vdW gap	3 Bi 3 Se(1)	2.972 3.284		
substitutional Se(2) central position in Bi_2Se_3 quintuple layer (QL)	6 Bi	3.041		
Mn doped Bi_2Te_3				
position	first shell	distance(Å)	second shell	distance (Å)
center of septuple layer	6 Te	2.909	6 Bi 6 Mn	4.293 4.385
substitutional Bi	3 Te(1) 3 Te(2)	3.073 3.246		
octahedral in vdW gap	6 Te	2.858		
tetrahedral in vdW gap	4 Te	2.533		
substitutional Te(1) close to vdW gap	3 Bi 3 Te(1)	3.073 3.637		
substitutional Te(2) in center of QL	6 Bi	3.246		

Table 3.1: Nominal distances of Mn neighbor atoms in various positions in Bi_2Se_3 and Bi_2Te_3 structures.

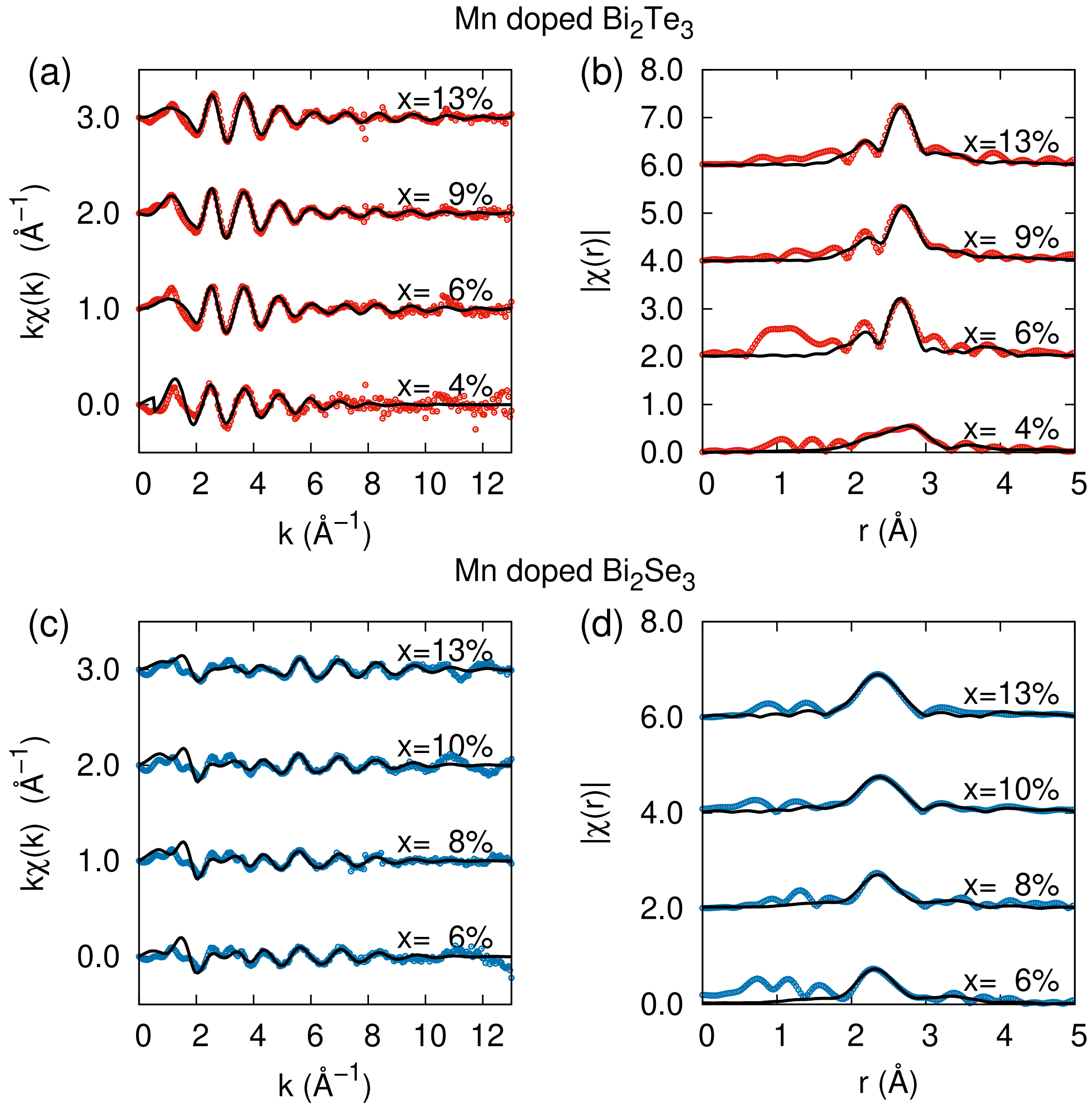

Figure 3.9: (a), (c) Extracted oscillatory part $\chi(k)$ of the absorption spectra above edge multiplied by wave vector k and its fit. (b), (d) Fit of the Fourier transform of the oscillatory part $\chi(r)$. Top row presents data of Mn doped Bi_2Te_3 samples, the bottom of Bi_2Se_3, respectively.

Mn doped Bi_2Se_3			
Mn concentration	6 Se (Å)	6 Bi (Å)	6 Mn (Å)
4	2.75±0.08	not fitted	not fitted
6	2.67±0.04	3.97±0.14	4.02±0.12
8	2.71±0.04	4.10±0.11	4.04±0.08
10	2.72±0.03	4.14±0.09	4.02±0.06
13	2.71±0.04	3.97±0.15	4.2±0.2
Mn doped Bi_2Te_3			
Mn concentration	6 Te (Å)	6 Bi (Å)	6 Mn (Å)
4	2.90±0.09	not fitted	not fitted
6	2.92±0.04	4.3±0.2	4.0±0.2
9	2.92±0.04	4.3±0.2	4.0±0.2
13	2.91±0.06	4.3±0.2	4.2±0.2

Table 3.2: Fitted distances of neighbor atoms in the first coordination (Se/Te) and second coordination shell (Bi and Mn) of Mn-doped Bi_2Se_3 and Bi_2Te_3.

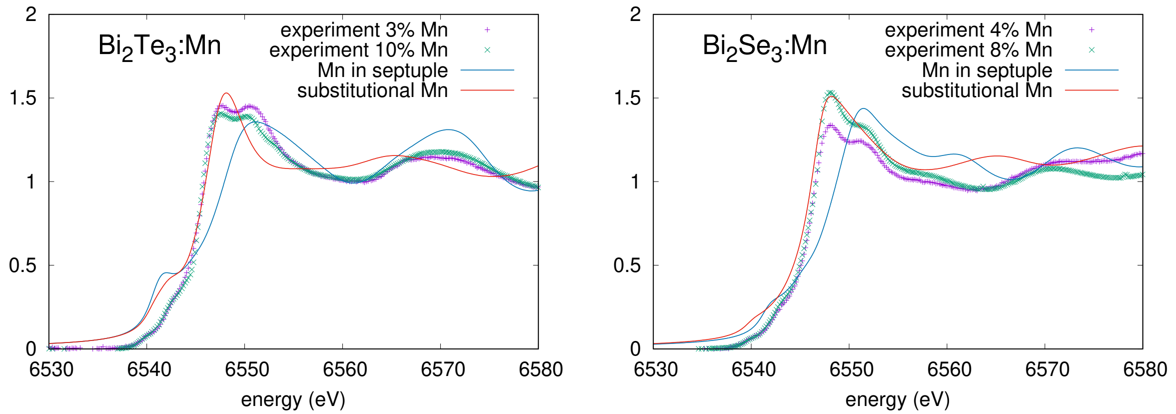

Figure 3.10: Near edge part of absorption spectra.

First, we will discuss the EXAFS part above the absorption edge. The absorption spectra are normalized to the height of the absorption edge (the height of the absorption edge is 1). The oscillatory part above the absorption edge was simulated using FEFF9 code [75] for various theoretical manganese positions in the structure of topological insulators, and comparison is shown in figure 3.8. Distances of the nearest neighbors are presented in table 3.2.1. The best fit to the experimental data has a central position in the septuple layer. However, in Bi_2Te_3 structure, the interstitial octahedral position inside the van der Waals gap has very similar distances to the nearest neighbor atoms as the central position of the septuple layer.

The fitting of the EXAFS oscillatory part is shown in figure 3.9, and the resulting distances are presented in table 3.2.1. The agreement of the fitted distances with nominal distance in the central position in the septuple layer is excellent. The agreement in the distances of the second coordination shell is acceptable within experimental error bars. The fitting of Mn atoms is difficult; the scattering power of Mn atoms is much weaker than bismuth, tellurium, or selenium. Their contribution to the experimental curve is small to heavier atoms.

The last analysis was done by calculating the shape of the edge using FDMNES code with a multiple scattering approach on a muffin-tin potential. The calculation of the exact energy of 3d-4f orbitals is incorrect, leading to incorrect pre-edge structure of the calculated spectra in figure 3.10. However, the main shape of the absorption edge structure is correct. Our calculations show that the most significant peak at the absorption edge is at higher energy for Mn in the central septuple position than for Mn in the substitutional position. The experimental spectra show a double peak structure indicating a specific manganese amount in the substitutional position. The substitutional peak is significantly higher in low manganese doped Bi_2Se_3 (4% Mn). This observation agrees with XRD analysis where Bi_2Se_3 samples with such Mn doping do not include sufficient septuples to accommodate all manganese atoms. Also, similar mixing was observed in $MnSb_2Te_4$ as discussed in section 3.1.3.

3.2.2 Transmission electron microscopy

The structural analysis by XRD was justified using transmission electron microscopy. The high-resolution transmission electron microscope FEI Titan Themis 60–300 is available in the CEITEC Nano core facility. The lamellae were prepared using a focused ion beam also in the CEITEC Nano core facility using FEI Helios dual beam scanning electron microscope. The lamellae thickness was in the range of 50–100 nm.

We have used chiefly a high-angle annular dark field (HAADF) detector and a high-resolution scanning transmission electron microscopy (STEM) regime. The focus of the incoming electron beam limits the spatial resolution. The STEM resolution of FEI Titan at 300 keV energy is about 1.4 Å allowing for resolution of individual atoms. The HAADF detector collects electrons scattered at higher angles. FEI Titan uses an angular range of 70–200 mrad. The theoretical interpretation of contrast in HAADF detector is relatively straightforward; heavier elements are stronger scatterers than light elements.

The example of analysis of $MnSb_2Te_4$ layer is presented in figure 3.11. The distribution of particular elements was further studied using energy dispersive x-ray spectroscopy (EDX). Panel 3.11(d) shows the spatial distribution of the HAADF signal, and panels 3.11(e-g) present the same area EDX signal of elements Mn, Sb, and Te, respectively. Extracted line profiles of HAADF and Mn EDX in the vertical direction are presented in panel 3.11(c). The EDX signal was collected for the lengthy exposition of about 30 minutes with higher flux than

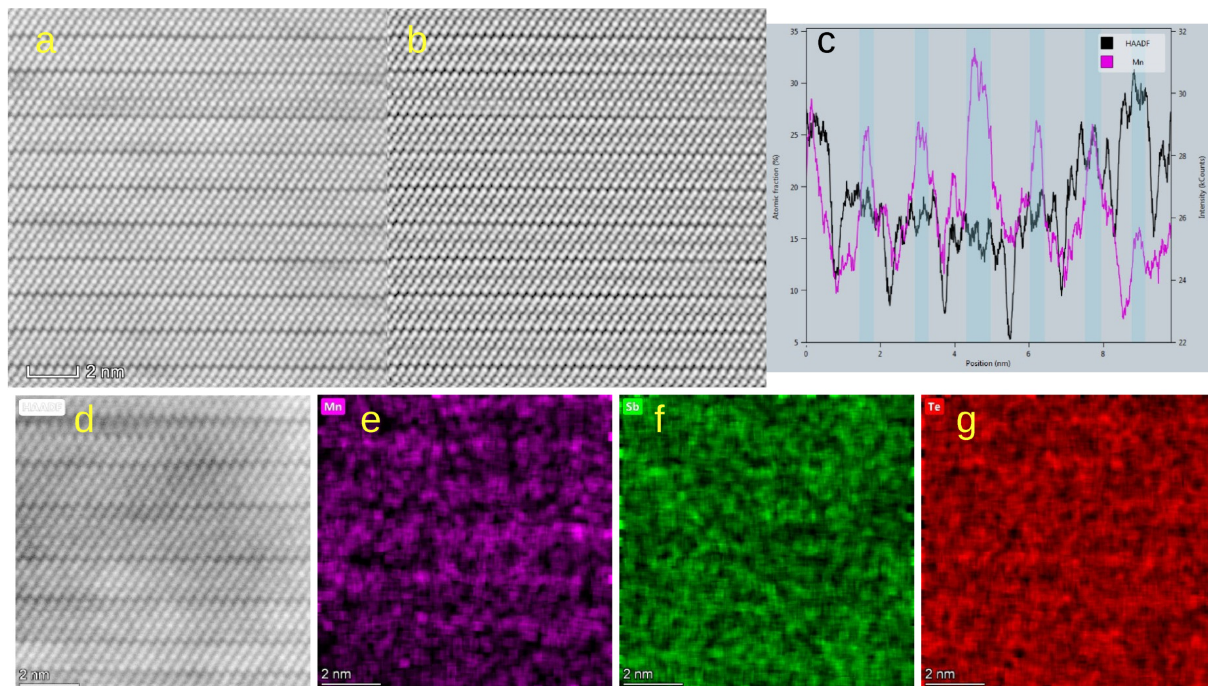

Figure 3.11: (a), (b), (d) HRSTEM of $MnSb_2Te_4$ sample with HAADF detector. (a), (b) Raw HAADF image and Fourier filtered HAADF image, respectively. (d) Smaller area HRSTEM and corresponding EDX elements map of Mn (e), Sb (f), and Te (g). (c) Extracted line profiles from panels (d) and (e) show the highest Mn concentration in the center of the septuple layer.

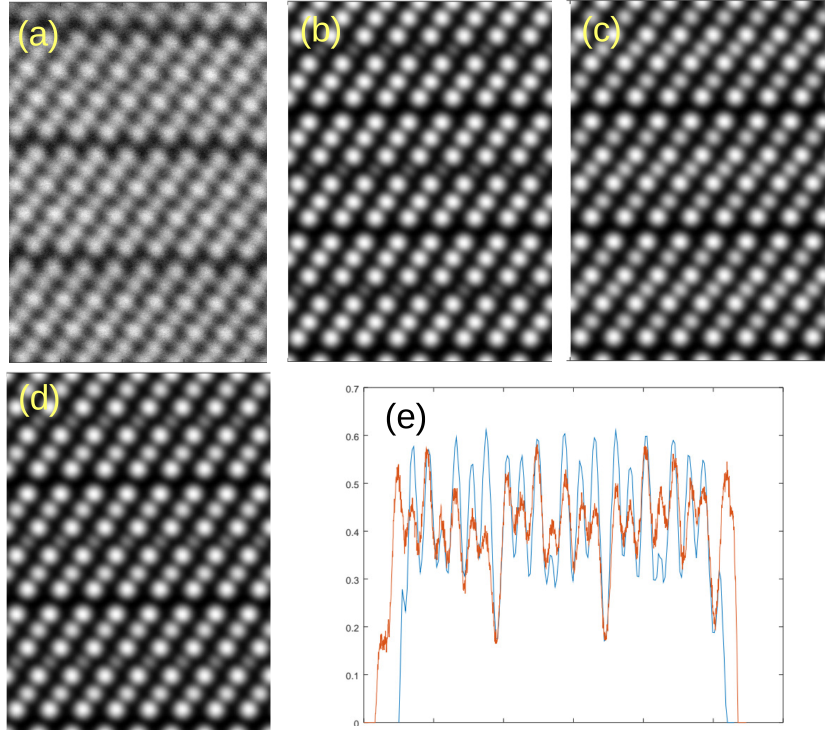

Figure 3.12: (a) HRSTEM experiment of $MnSb_2Te_4$ layer. (b), (c), (d) Panels show simulation with different concentrations of manganese in central and antimony positions. (b) Nominal $MnSb_2Te_4$ structure ($C_1 = 1, C_2 = 0$), (c) fully random occupation of Sb/Mn positions ($C_1 = C_2 = 1/3$). (d) partial intermixing of Mn/Sb ($C_1 = 0.8, C_2 = 0.15$). (e) comparison of extracted line profiles from the experiment (red) and simulation in panel (d) (blue), respectively.

usual HRTEM images. The resolution of EDX is thus about 0.5 nm. However, the Mn signal distribution suggests the manganese atoms concentrate in the septuple layer structure's central position in agreement with the XRD analysis presented in section 3.1.3.

Further quantitative analysis was done by simulating HAADF images in a specialized software μSTEM [77]. We have simulated several mixing conditions similar to the values obtained in section 3.1.3. The results compared to the experiment are shown in figure 3.12. Panel (a) shows the experimental image, and panels (b-d) show the simulated image with various Mn/Sb intermixing levels. Panel (b) shows the nominal structure of $MnSb_2Te_4$ with a central position occupied only by Mn atoms ($C_1 = 1, C_2 = 0$ in notation explained in section 3.1.3). The simulated HAADF signal in the central septuple layer position is too dark in simulation for the experiment. Simulated intensities of Sb and Te atoms are almost indistinguishable since Sb and Te differ just by one in atomic number. Panel (c) shows entirely random Sb/Mn intermixing ($C_1 = C_2 = 1/3$). The experimental intensity of the central septuple position is smaller than in Sb positions, indicating a not entirely random case. Panel (d) shows intermixing with $C_1 = 0.8, C_2 = 0.15$, which corresponds to a conclusion in section 3.1.3. The extracted intensity profile of the experimental and simulated HAADF intensity are shown in panel (e).

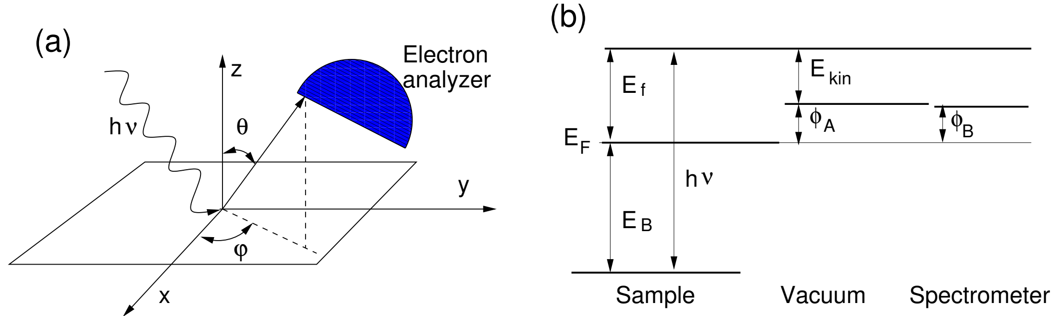

Figure 3.13: (a) schematic of the ARPES experiment. (b) Schematics of energy levels.

3.3 Angle-resolved photoemission spectroscopy

We have used angle-resolved photoemission spectroscopy (ARPES) to study the electronic band structure. The author participated in several ARPES experiments, but his scientific specialization is more focused on structural analysis. Therefore this chapter will be brief, covering only the basics of the ARPES method. For a more precise overview, we suggest further literature [78–81].

The principle of the method is to excite the electron system with the photon in ultraviolet to soft x-ray range (6–1000 eV). The excited electron can escape the sample; the electron optical system detects its momentum and kinetic energy. The schematics of the experimental setup are in figure 3.13. The simplest photoemission model is called the three-step model:

1. Excitation of the electron by photon absorption from the bound state to the excited state above the Fermi level.

2. Diffusion of the excited electron to the surface.

3. electron escapes from the material to the vacuum.

The three-step model is a significant simplification; we assume the initial and final states in the material are single particle states neglecting correlations with other electrons. The initial state has wave-vector $\boldsymbol{k}_i$ and final state $\boldsymbol{k}_f$. Let us assume the electron's initial state has binding energy E_B measured with respect to the Fermi level. The energy of the excited state is

$$E_f = h\nu - E_B, \tag{3.36}$$

where $h\nu$ is the energy of the incoming photon. The incoming photon's momentum is usually negligible concerning the size of the Brillouin zone. Momentum of photon with energy of 100 eV is 0.05 Å^{-1}, which approximately 2 % of the typical Brillouin zone. During the excitation process, the electron crystal momentum is conserved up to any reciprocal lattice vector $\boldsymbol{G}$

$$\boldsymbol{k}_f = \boldsymbol{k}_i + \boldsymbol{G}. \tag{3.37}$$

The probability per unit time of the transition from initial to final state w_{fi} can be calculated using Fermi's golden rule

$$w_{fi} = \frac{2\pi}{\hbar} \left| \langle \psi_f | \hat{H}_i | \psi_i \rangle \right|^2 \delta \left(E_f - E_B - h\nu \right), \tag{3.38}$$

where $\hat{H}_i$ is the photon interaction Hamiltonian. Usually, the dipole approximation is sufficient to describe the interaction

$$\hat{H}_i = \epsilon \cdot \boldsymbol{p}, \tag{3.39}$$

where ϵ is the polarization vector of incoming light.

The electron then diffuses towards the surface. The probability of reaching the surface exponentially decreases with the distance from the sample by an inelastic mean free path. A wave describes the electron state in a vacuum outside the sample with the kinetic energy of $E_{kin} = h\nu - E_B - \phi$, where ϕ is a work function. The components of electron wave vector $\boldsymbol{K}$ in a vacuum are described as

$$K_x = \frac{\sqrt{2mE_{kin}}}{\hbar}\sin\theta\cos\varphi,\ K_y = \frac{\sqrt{2mE_{kin}}}{\hbar}\sin\theta\sin\varphi,\ K_z = \frac{\sqrt{2mE_{kin}}}{\hbar}\cos\theta. \tag{3.40}$$

During the electron transition through the sample surface, the in-plane component of the electron momentum is conserved

$$\boldsymbol{K}_{\parallel} = \boldsymbol{k}_{\parallel}. \tag{3.41}$$

The out-of-plane component k_z can be determined by approximating the final state to be nearly free electron state. The wave vector of the final state is given by

$$E_f = E_0 + \frac{\hbar^2 k_f^2}{2m}, \tag{3.42}$$

where E_0 is the energy level corresponding state with zero wave vector. Usually, this level can be approximately assigned to the bottom of the valence band. Combining the above formulas, one can obtain the relation for the out-of-plane component of the wave vector

$$\frac{\hbar^2}{2m}(k_z^2 + \boldsymbol{k}_{\parallel}^2) = E_f - E_0, \tag{3.43}$$

$$k_z = \sqrt{\frac{2m}{\hbar^2}(E_f - E_0) - \boldsymbol{K}_{\parallel}^2} = \sqrt{\frac{2m}{\hbar^2}(E_{kin} + V_0)}, \tag{3.44}$$

where inner potential V_0 is the energy of the bottom of the valence band with respect to the vacuum level outside the sample $V_0 = |E_0| + \phi$.

We want to emphasize the following aspects of the ARPES technique:

- At a given photon energy, one measure only a particular two-dimensional cut through the complete band structure. The experiment will measure the photoelectron intensity as a function of electron kinetic energy and exit angles $I(E_{kin}, \theta, \varphi)$. Out-of-plane component of the wave vector k_z depends on kinetic energy and angle θ.
- The whole three-dimensional band structure has to be measured by changing photon energy in a range covering the whole Brillouin zone in k_z.
- bulk band states have energy dispersion with changing photon energy. The surface states are localized in z direction and do not disperse with k_z. This effect can be used to distinguish bulk and surface states.

Most of the above formulas were determined in the approximative three-step photoemission model. The better description of ARPES is a one-step model calculation whole transition process at once [82]. The final stage in the one-step model is a state combining free-electron wave in a vacuum with a damped state in the material.

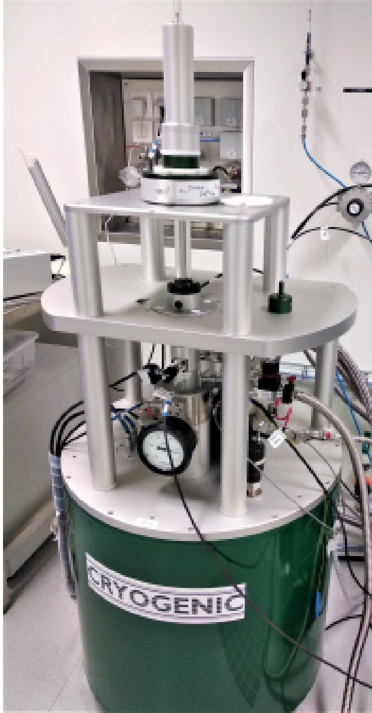

Figure 3.14: Superconducting magnet up to 9 T and cryostat down to 2 K made by Cryogenics company. The instrument is located in the CEITEC Nano core facility and can provide magnetic and transport measurements. The photo shows the setup with a vibrating sample magnetometer (VSM).

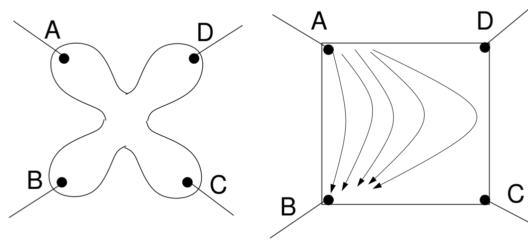

Figure 3.15: Schematics of four sample contacts in van der Pauw geometry. Left: ideal sample shape, Right: the real case for rectangular sample. The contacts have to be in corners, not inside the sample.

3.4 Electrical transport measurements

Transport measurements accompanied the structural analysis. In most cases, we have used van der Pauw geometry with four contacts in the corners of the thin rectangular sample. The sample resistivity and Hall conductivity are determined by measuring several current and voltage contact commutations [83].

Let's denote the resistance $R_{AB,DC} = V_{DC}/I_{AB}$ measured with current I_{AB} flowing between contacts A, B and voltage V_{DC} measured between contacts D and C. From the sym-

metry it follows $R_{AB,DC} = R_{BA,CD} = R_{DC,AB} = R_{CD,BA}$. The sample resistivity can be determined from two commutations using the van der Pauw formula

$$\exp\left(-\pi R_{AB,DC}/R_S\right) + \left(-\pi R_{BC,AD}/R_S\right) = 1, \qquad R_S = \frac{\rho}{t}, \tag{3.45}$$

where R_S is a sheet resistivity of the film, ρ resistivity of the sample and t sample (layer) thickness. The Hall coefficient R_H can be determined by measurement in the magnetic field B perpendicular to the sample plane

$$R_H = \frac{R_{AC,DB} + R_{BD,AC}}{2}\frac{t}{B}. \tag{3.46}$$

The average of two commutations will suppress the ohmic voltage contributions in case the contacts are not exactly symmetric. The concentration of majority charge carriers can be calculated as

$$n = \frac{r_H}{e_0 R_H}, \tag{3.47}$$

where we have neglected the contribution of minority carriers, e_0 is the elementary charge, and r_H is the Hall coefficient, usually close to 1.

The samples were measured in a Cryogenics device equipped with a closed-cycle helium cryostat, superconducting magnet up to 9 T magnetic field, and temperature down to 2 K, see figure 3.14. The contacts were made using conductive silver paste.

The ferromagnetic samples are known to have an anomalous Hall effect in addition to the ordinary Hall effect. The simple (naive and incorrect) theory would attribute the anomalous Hall effect to the magnetic field inside the sample as a sum of the external magnetic field and magnetization. The detailed theory is quite complicated [84]. In explaining the Hall effect in 3d metal, one has to consider the contribution of 3d and 4s electrons close to the Fermi level. Each of those bands has a different density of states and scattering rate, which also depends on the material's magnetic state, domain boundaries, and other properties. Thus, we did not analyze the anomalous Hall effect in detail, and we only used its presence as a measure of ferromagnetic order.

Chapter 4

Reprinted papers

The selected reprinted papers are divided into three groups: (i) papers describing properties of Bi_2Te_3, Bi_2Se_3 and $Bi_2(Se_xTe_{1-x})_3$ topological insulator films (1 – 3), (ii) papers dealing with magnetically doped topological insulators (4 – 7), and (iii) papers describing properties of Bi-doped topological crystalline insulators (Pb,Sn)Se and (Pb,Sn)Te.

1. *Growth, Structure, and Electronic Properties of Epitaxial Bismuth Telluride Topological Insulator Films on BaF2 (111) Substrates,*
   O. Caha, A. Dubroka, J. Humlíček, V. Holý, H. Steiner, M. Ul-Hassan, J. Sánchez-Barriga, O. Rader, T. N. Stanislavchuk, A. A. Sirenko, G. Bauer, and G. Springholz, Crystal Growth and Design **13**, 3365 (2013).

Share	40 %
author's contribution	XRD experiment and analysis, transport and thermoelectric experiment, manuscript writing

   The paper analyzes epitaxially grown bismuth telluride layers of stoichiometry Bi_2Te_3 and BiTe. The analysis is focused on structural analysis using the XRD technique. We have studied the size of the domains, strain lattice parameters, and twinning of the crystalline structure. Also, optical spectroscopy, Raman spectroscopy, transport, and ARPES results are included. The structure of the epitaxial layer can be controlled via the flux of particular compounds. The film grown using Bi_2Te_3 compound evaporation cell only tends to reach the stoichiometry of BiTe. To grow Bi_2Te_3, an additional Te flux is needed.

2. *Structure and composition of bismuth telluride topological insulators grown by molecular beam epitaxy,*
   H. Steiner, V. Volobuev, O. Caha, G. Bauer, G. Springholz, and V. Holý, J. Appl. Crystallography **47**, 1889 (2014).

Share	15 %
author's contribution	part of XRD experiment and analysis

   The non-stoichiometric alloy layers of $Bi_2Te_{3-\delta}$ were grown with varying tellurium flux. We have achieved stoichiometry within the range δ =0–1. The structure of thin films was analyzed using x-ray diffraction. The diffraction pattern was described by a model of random stacking of Bi_2Te_3 quintuple layer and Bi_2 bilayer. The non-linear stoichiometry dependence of the in-plane lattice parameter and average lattice spacing was determined.

3. *Interband absorption edge in the topological insulators $Bi_2(Te_{1-x}Se_x)_3$*,
A. Dubroka, O. Caha, M. Hronček, P. Friš, M. Orlita, V. Holý, H. Steiner, G. Bauer, G. Springholz, and J. Humlíček, Phys. Rev. B **96**, 235202 (2017).

Share	15 %
author's contribution	XRD experiment and analysis, contribution to manuscript writing

The $Bi_2(Se_xTe_{1-x})_3$ alloy layers were prepared using molecular beam epitaxy. The alloy layers were studied using ellipsometry and reflectivity in the far-infrared to near-UV range (0.06 eV to 6.5 eV) at low and room temperatures. The band gap of the layers was determined, considering the Burstein-Moss shift in highly doped semiconductors. The compositional of the band gap is non-linear with the maximum at about $x_{Se} = 30\,\%$. The alloy is a direct band gap semiconductor for higher selenium concentrations $x_{Se} > 30\,\%$. More tellurium-rich material $x_{Se} < 30\,\%$ has an indirect band gap with maxima of the valence band slightly off Γ-point.

4. *Non-magnetic band gap at the Dirac point of the magnetic topological insulator $(Bi_{1-x}Mn_x)_2Se_3$*,
J. Sánchez-Barriga, A. Varykhalov, G. Springholz, H. Steiner, R. Kirchschlager, G. Bauer, O. Caha, E. Schierle, E. Weschke, A. A. Uenal, S. Valencia, M. Dunst, J. Braun, H. Ebert, J. Minar, E. Golias, L. V. Yashina, A. Ney, V. Holý, and O. Rader, Nature Communications **7**, 10559 (2016).

Share	8 %
author's contribution	XRD experiment and analysis, contribution to ARPES and XMCD measurements, contribution to manuscript writing

The $(Bi,Mn)_2Se_3$ layers on BaF_2 were prepared and analyzed. The ARPES analysis has shown a band gap in Dirac point to be large ≈ 100 meV, and temperature independent. The ferromagnetic Curie temperature of about 10 K was determined by SQUID magnetometry and XMCD. The magnetic easy axis direction is in-plane. The band gap surviving up to room temperature is of non-magnetic origin.

5. *Structural and electronic properties of manganese-doped Bi_2Te_3 epitaxial layers*,
J. Růžička, O. Caha, V. Holý, H. Steiner, V. Volobuiev, A. Ney, G. Bauer, T. Duchoň, K. Veltruská, I. Khalakhan, V. Matolín, E. F. Schwier, H. Iwasawa, K. Shimada, and G. Springholz, New J. Phys. **17**, 013028 (2015).

Share	20 %
author's contribution	XRD, X-ray absorption spectroscopy manuscript writing

The magnetic alloy layers of $(Bi,Mn)_2Te_3$ were grown on BaF_2. The manganese positions were analyzed using x-ray absorption spectroscopy. The manganese positions were identified as an octahedral interstitial in the van der Waals gap. The crystalline structure is increasingly disordered with increasing manganese content. The ARPES measurements lack sufficient resolution and low enough temperature to observe magnetic band gap opening. However, we were unaware that Mn atoms occupy the septuple layers $MnBi_2Te_4$ at the time of publication. The structural analysis interpretation is not entirely correct.

6. *Large magnetic gap at the Dirac point in $Bi_2Te_3/MnBi_2Te_4$ heterostructures*,
E. D. L. Rienks, S. Wimmer, J. Sánchez-Barriga, O. Caha, P. S. Mandal, J. Růžička,

A. Ney, H. Steiner, V. V. Volobuev, H. Groiss, M. Albu, G. Kothleitner, J. Michalička, S. A. Khan, J. Minár, H. Ebert, G. Bauer, F. Freyse, A. Varykhalov, O. Rader, and G. Springholz, Nature **576**, 423 (2019).

Share	12 %
author's contribution	XRD experiment and analysis, x-ray absorption spectroscopy, transport measurement, preparation of some TEM samples, contribution to manuscript writing.

The Mn-doped samples were grown and analyzed using magnetic measurements, XRD, XAFS, HRTEM, and other methods. The structure was composed of random stacking of Bi_2Te_3 quintuple layers and $MnBi_2Te_4$ septuple layers. The concentration of septuple layers increases with manganese doping. The Curie temperature was found to be approximately 20 K, and the magnetization easy-axis is out-of-plane. The low-temperature ARPES and spin-resolved ARPES experiments have shown a band gap opening in the Dirac point with a size of 90 meV. The temperature dependence of the band gap size correlates with remanence magnetization. The paper presented the first direct observation of a magnetic band gap in the topological surface state. Bismuth selenide, on the contrary, does not show a magnetic band gap since its magnetization easy-axis is in-plane.

7. *Mn-Rich $MnSb_2Te_4$: A Topological Insulator with Magnetic Gap Closing at High Curie Temperatures of 45–50 K*,
S. Wimmer, J. Sánchez-Barriga, P. Kuppers, A. Ney, E. Schierle, F. Freyse, O. Caha, J. Michalička, M. Liebmann, D. Primetzhofer, M. Hoffman, A. Ernst, M. M. Otrokov, G. Bihlmayer, E. Weschke, B. Lake, E. V. Chulkov, M. Morgenstern, G. Bauer, G. Springholz, and O. Rader, Advanced Materials **2021**, 2102935 (2021).

Share	8 %
author's contribution	XRD experiment and analysis, x-ray absorption spectroscopy transport measurement, preparation of TEM samples, and contribution to TEM analysis and manuscript writing.

The layers of $MnSb_2Te_4$ with a slight excess of Mn were studied. We have found the concentration of Mn in the substitutional and central septuple layer positions. The magnetic Currie temperature is relatively high for a magnetic topological insulator, almost 50 K. Contrary to bismuth selenide and bismuth telluride, antimony telluride is p-doped. Thus photoemission study of the band gap. Instead, we have used scanning tunneling spectroscopy to show magnetic band gap opening correlating with magnetic order.

8. *Topological quantum phase transition from mirror to time reversal symmetry protected topological insulator*,
P. S. Mandal, G. Springholz, V. V. Volobuev, O. Caha, A. Varykhalov, E. Golias, G. Bauer, O. Rader, and J. Sánchez-Barriga, Nature Communications **8**, 968 (2017).

Share	10 %
author's contribution	XRD experiment and analysis contribution to ARPES experiments, contribution to manuscript writing.

This paper deals with (Pb,Sn)Se topological crystalline insulator. Topological crystalline insulators are merely protected by individual crystal symmetries and exist for an even number of Dirac cones. We demonstrated that Bi-doping of (Pb,Sn)Se (111) epilayers induces a quantum phase transition from a topological crystalline insulator to a $\mathbb{Z}_2$ topological insulator. The transition occurs because Bi-doping lifts the fourfold valley degeneracy and induces a gap at Γ, while the three Dirac cones at the $\bar{M}$ points of the surface Brillouin zone remain intact. We interpret this new phase transition as caused by a lattice distortion. Our findings extend the topological phase diagram enormously and make strong topological insulators switchable by distortions or electric fields.

9. *Giant Rashba Splitting in $Pb_{1-x}Sn_xTe$ (111) Topological Crystalline Insulator Films Controlled by Bi-Doping in the Bulk*,
V. V. Volobuev, P. S. Mandal, M. Galicka, O. Caha, J. Sánchez-Barriga, D. Di Sante, A. Varykhalov, A. Khiar, S. Picozzi, G. Bauer, P. Kacman, R. Buczko, O. Rader, and G. Springholz, Advanced Materials **29**, 1604185 (2017).

Share	10 %
author's contribution	XRD experiment and analysis, contribution to ARPES experiment, contribution to manuscript writing.

The topological properties of lead-tin chalcogenide topological crystalline insulators can be tuned by temperature and composition. We have shown that bulk Bi doping of epitaxial (Pb,Sn)Te (111) films induce a giant Rashba splitting at the surface that the doping level can tune. Tight binding calculations identify their origin as Fermi-level pinning by trap states at the surface.

4.1 Properties of thin films of topological insulators Bi_2Te_3 and BiTe

The paper analyzes epitaxially grown bismuth telluride layers of stoichiometry Bi_2Te_3 and BiTe. The analysis is focused on structural analysis using the XRD technique. We have studied the size of the domains, strain lattice parameters, and twinning of the crystalline structure. Also, optical spectroscopy, Raman spectroscopy, transport, and ARPES results are included. The structure of the epitaxial layer can be controlled via the flux of particular compounds. The film grown using Bi_2Te_3 compound evaporation cell only tends to reach the stoichiometry of BiTe. To grow Bi_2Te_3, an additional Te flux is needed.

CRYSTAL GROWTH & DESIGN

Article

pubs.acs.org/crystal

Growth, Structure, and Electronic Properties of Epitaxial Bismuth Telluride Topological Insulator Films on BaF_2 (111) Substrates

O. Caha,[†] A. Dubroka,[†] J. Humlíček,[†] V. Holý,[‡] H. Steiner,[§] M. Ul-Hassan,[§] J. Sánchez-Barriga,[∥] O. Rader,[∥] T. N. Stanislavchuk,[⊥] A. A. Sirenko,[⊥] G. Bauer,[§] and G. Springholz*[,§]

[†]Department of Condensed Matter Physics and CEITEC, Masaryk University, Kotlářská 2, 61137 Brno, Czech Republic

[‡]Department of Electronic Structures, Charles University, Praha, Czech Republic

[§]Institut für Halbleiter- und Festkörperphysik, Johannes Kepler Universität, Altenbergerstrasse 69, 4040 Linz, Austria

[∥]Helmholtz-Zentrum Berlin für Materialien und Energie, Elektronenspeicherring BESSY II, Albert-Einstein-Straße 15, 12489 Berlin, Germany

[⊥]Department of Physics, New Jersey Institute of Technology, Newark, New Jersey 07102, United States

Supporting Information

ABSTRACT: Epitaxial growth of topological insulator bismuth telluride by molecular beam epitaxy onto BaF_2 (111) substrates is studied using Bi_2Te_3 and Te as source materials. By changing the beam flux composition, different stoichiometric phases are obtained, resulting in high quality Bi_2Te_3 and Bi_1Te_1 epilayers as shown by Raman spectroscopy and high-resolution X-ray diffraction. From X-ray reciprocal space mapping, the residual strain, as well as size of coherently scattering domains are deduced. The Raman modes for the two different phases are identified and the dielectric functions derived from spectroscopic ellipsometry investigations. Angular resolved photoemission reveals topologically protected surface states of the Bi_2Te_3 epilayers. Thus, BaF_2 is a perfectly suited substrate material for the bismuth telluride compounds.

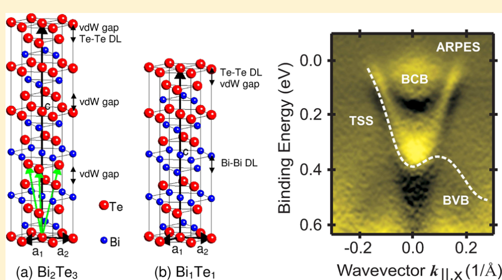

INTRODUCTION

Recent discovery of a new class of materials, called topological insulators, has opened up a whole new research arena.[1−5] Topological insulators behave in the bulk like ordinary insulators but support in addition a conducting two-dimensional topological surface state with linear energy-momentum dispersion shaped like a Dirac cone.[2,6,7] Because of strong spin−orbit coupling, the electron momentum in these surface states is locked to the spin orientation and spin-flip scattering is prohibited by time reversal symmetry.[1,8] As a result, spin polarized currents can be produced without the needs of external magnetic fields, which offers great advantages for spintronic or quantum computation applications.[1,5,9] The helical spin structure of the topological surface states also provides a basis for fundamental new physics such as magnetic monopoles and Majorana fermions.[1,2]

Among the new materials exhibiting three-dimensional topological insulating properties, the bismuth chalcogenides Bi_2Te_3 and Bi_2Se_3 have attracted most attention because a single Dirac cone is formed at the Γ-point of the Brillouin zone within the bulk band gap, as has been revealed by angular resolved photoemission[6,7] and scanning tunneling spectroscopy studies.[10,11] Bi_2Te_3 is also a superior thermoelectric material for energy harvesting applications, since it exhibits the highest thermoelectric figure of merit at room temperature among all bulk materials.[12,13] Up to now, most studies of the topological properties of Bi_2Te_3 have been performed on bulk single crystals cleaved under ultrahigh vacuum conditions.[3,7,14] For practical device applications, however, epitaxial layers are desired[15] for monolithic integration in multilayers and gated heterostructures that would allow tuning of the Fermi level to the Dirac point and control spin polarized currents in devices.[15,16] Considerable efforts have been made to grow Bi_2Te_3 epitaxially on substrates like Si[17−21] or GaAs,[22−26] which, however, exhibit a very large lattice mismatch of up to 14% to Bi_2Te_3.

Bismuth telluride can crystallize in several different crystal structures in dependence of its stoichiometric composition. The crystal structure of the most common Bi_2Te_3 phase consists of of three Te^1−Bi−Te^2−Bi−Te^1 quintuplet layers (QL) as fundamental building block (see Figure 1a). These are stacked on top of each other in an ABCABC stacking sequence. In addition, several alternative phases with lower Te concentration exist, including Bi_1Te_1 (called tsumoite), as well as Bi_3Te_4 and

Received: January 9, 2013
Revised: May 15, 2013
Published: July 12, 2013

 © 2013 American Chemical Society dx.doi.org/10.1021/cg400048g | *Cryst. Growth Des.* 2013, 13, 3365−3373

Reprinted page 1 of paper [46] "Structure and properties of Bi_2Te_3 and BiTe thin films".

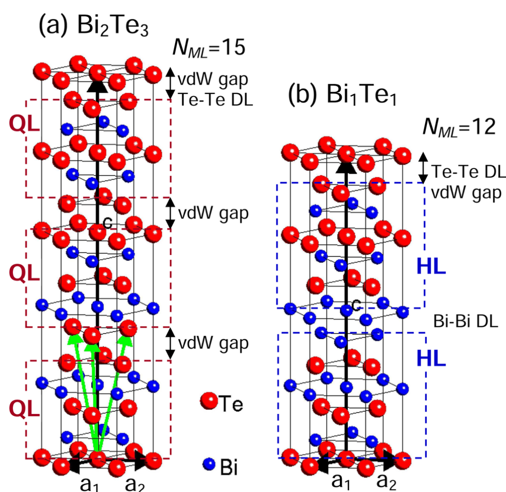

Figure 1. Hexagonal unit cell of (a) Bi_2Te_3 and (b) BiTe with the base vectors indicated by the black arrows. For Bi_2Te_3, the unit cell consist of 15 atomic lattice planes that are grouped in three quintuple layers (QL) with Te^1−Bi−Te^2−Bi−Te^1 stacking. The quintuple layers are van der Waals bonded to each other by a Te−Te double layer (van der Waals gap). For BiTe, the unit cell consists of 12 atomic lattice planes with Te^1−Bi^1−Te^2−Bi^2−Te^3−Bi^3−Bi^3−Te^3−Bi^2−Te^2−Bi^1−Te^1 stacking sequence that can be split in two hextuple layer (HL) blocks. The green arrows indicate an alternative definition of the crystal structure using rhombohedral base vectors. The lattice parameters of Bi_2Te_3 and BiTe are listed in Table 1.

Bi_4Te_3 (pilsenite) among others.[27] The different phases share the same hexagonal structure of $R\bar{3}m$ space group symmetry, but show a different stacking of the Bi and Te layers.[28,29] The Bi_1Te_1 structure, depicted in Figure 1b, consists of twelve atomic Te^1−Bi^1−Te^2−Bi^2−Te^3−Bi^3−Bi^3−Te^3−Bi^2−Te^2−Bi^1−Te^1 lattice planes[30] that can be split into two mirrored hextuple layers (HL). The unit cells of Bi_4Te_3 and Bi_3Te_4 consist even of 21 lattice planes grouped in three blocks of septuplet layers, comprising each of seven lattice planes. While Bi_2Te_3 has been intensely studied over the past few years, the properties of the other phases have remained rather unexplored. In particular, BiTe has been available only in the form of bulk crystals[30] or polycrystalline films,[31] that is, to the best of our knowledge no work on epitaxial BiTe layers has been published so far.

In the present work, we report on molecular beam epitaxy (MBE) of single phase Bi_2Te_3 and BiTe epilayers and we provide detailed insight in their structural and electronic properties. Contrary to most previous studies, epitaxial growth is carried out on BaF_2 (111) substrates,[32] which exhibit an almost perfect matching of the in-plane lattice constant to those of the bismuth telluride compounds (see Table 1). In fact, the lattice-misfit to Bi_2Te_3 of $\Delta a_{\|}/a$ = 0.04% is particularly small, that is, BaF_2 is practically lattice-matched. BaF_2 also features several additional advantages. First of all, BaF_2 is highly insulating and optically transparent, which is favorable for transport measurements and optical spectroscopy. Second, because of the perfect (111) orientation, cleaved BaF_2 substrates are virtually step free over tens of square micrometer surface areas, contrary to the usual miscut steps with spacing smaller than 100 nm present on standard Si or GaAs substrate surfaces. As the lattice plane stacking and the height of these steps differs from those of the bismuth tellurides, these steps act as sources for stacking faults and antiphase domain boundaries in epilayers. BaF_2 also shows a better matching of the in-plane thermal expansion coefficient of 18.7×10^{-6} K^{-1} to that of Bi_2Te_3 of 14×10^{-6} K^{-1} at 300 K[33] compared to Si (2.6×10^{-6} K^{-1}) or GaAs (5.73×10^{-6} K^{-1}). As shown in this work, this leads to rather low values of thermal stress within the epilayers. The thermal expansion coefficient of bulk BiTe has not been reported so far, but one can assume that it is similar to that of Bi_2Te_3.

In terms of growth, we show that by tuning of the beam flux composition, that is, the tellurium to bismuth flux ratio, single phase Bi_2Te_3 and BiTe epilayers are obtained. Their excellent structural perfection is demonstrated by high resolution X-ray diffraction and the optimum growth conditions for the different phases are derived. Quantitative evaluation of reciprocal space maps yields the strain as well as size of coherently scattering domains and by Raman scattering the active phonons in both compounds are identified. Raman experiments carried out in backscattering geometry from the surface as well as from the layer/substrate interface show that the entire epilayers are single phase even for thicknesses as large as 830 nm. By infrared and far-infrared spectroscopy we determine the plasma frequencies and thus, the free carrier concentrations of the

Table 1. Structural Properties of the BiTe and Bi_2Te_3 Epilayers Grown on BaF_2 (111) Substrates Determined by X-ray Reciprocal Space Mapping Compared to Results for Bulk Materials Reported in Literature[a]

composition	sample	d (nm)	a (Å)	c (Å)	R_L (nm)	R_V (nm)	$\Delta\phi$ (deg)
Bi_2Te_3-epilayers	M2780	830	4.3804	30.53	6000	200	0.08
	M2704	250	4.382	30.51	1300	80	0.05
Bi_2Te_3-bulk	ref 34		4.3835	30.487			
	ref 35		4.386	30.497			
	ref 36		4.3852	30.483			
BiTe-epilayers	M2777	400	4.402	24.202	200	40	0.18
	M2732	250	4.400	24.229	100	40	0.2
BiTe-bulk	ref 30		4.423	24.002			
	ref 37		4.422	24.052			
	ref 38		4.40	23.97			
BaF_2 (111)	ref 39		4.384	10.739			

[a]Also listed are the in- and out-of-plane lattice constant of the (111) BaF_2 substrates, with cubic lattice constants of a_0 = 6.200 Å. The average lateral and vertical mosaic block sizes $R_{L,V}$ and the root mean square angular lattice misorientation $\Delta\phi$ of the epilayers were obtained from Figure 4.

Reprinted page 2 of paper [46] "Structure and properties of Bi_2Te_3 and BiTe thin films".

layers. By angular resolved photoemission, the surface band structure of the Bi_2Te_3 epilayers is established, showing a well-resolved Dirac cone with pronounced hexagonal warping. Thus, these layers are very well suited for further studies of the topological properties of this material.

■ EXPERIMENTAL SECTION

Bismuth telluride epilayers were grown by molecular beam epitaxy in a Riber 1000 system under ultrahigh vacuum conditions at a background pressure of 5×10^{-10} mbar. The molecular beams were generated using a compound bismuth telluride effusion cell (nominal composition of Bi_2Te_3) operated at around 500 °C, and a separate tellurium cell operated at 280−330 °C for stoichiometry control. The flux rates were 1−2 Å/s for bismuth telluride and 0−2 Å/s for excess tellurium, which was controlled by a quartz crystal microbalance. The layers were deposited on cleaved BaF_2 (111) substrates at substrate temperatures between 300−400 °C measured with an infrared optical pyrometer. The surface structure of the films was monitored by in situ reflection high-energy electron diffraction as well as atomic force microscopy (AFM). X-ray diffraction experiments were performed using a high-resolution X-ray diffractometer equipped with a Cu tube, parabolic mirror and four-bounce Ge (220) Bartels monochromator on the primary side, and a channel-cut Ge (220) analyzer on the secondary side. Unpolarized Raman spectra were acquired with a Renishaw InVia spectrometer at room temperature in backscattering geometry. The exciting beam of a 632.8 nm HeNe laser was focused either on the front side surface or backside of the films through the transparent BaF_2 substrate. The spot size was about 2 μm and the laser power was low enough to avoid local heating.

The optical properties were determined by ellipsometric measurements using a home-built ellipsometer attached to a Bruker IFS55 EQUINOX mid-infrared Fourier spectrometer. In the near-infrared, visible, and ultraviolet range, ellipsometric spectra were acquired with a Woollam M-2000 and Jobin Yvon UVISEL ellipsometer. This was complemented by reflectance measurements in the 0.01−0.2 eV range using a Bruker IFS 66v/S spectrometer as well as far-infrared ellipsometric measurements at the NSLS synchrotron light source in Brookhaven. The Hall conductivity was determined by van der Pauw measurements. The electronic structure was determined by angle resolved photoemission spectroscopy (ARPES) at the UE112-PGM2a beamline of BESSY II, Berlin using a Scienta R8000 electron analyzer and linearly polarized light with 21 eV photon energy. For these measurements, the epilayers were protected after growth by a Te capping layer deposited in the MBE system. This layer was desorbed in the ultrahigh vacuum ARPES chamber just before the photoemission experiments.

■ RESULTS AND DISCUSSION

Molecular Beam Epitaxy. Epitaxial growth of bismuth telluride onto (111) BaF_2 substrates proceeds in a 2D growth mode at substrate temperatures above 300 °C independent of the beam flux composition, i.e., independent of the excess Te flux. This is evidenced by the streaked RHEED diffraction patterns observed during growth presented in Figure 2 for two samples grown with a Te flux of (a) 2 and (b) 0 Å/s, respectively. At substrate temperatures below 300 °C, a significant roughening of the surface due to limited surface diffusion occurs. For high excess Te flux greater than 2 Å/s, which is a factor of 2 larger compared to the bismuth telluride flux, the stoichiometric composition of the epilayers corresponds to Bi_2Te_3 as proven by the X-ray analysis described below. Without or with only very small excess Te flux, the Te content of the epilayers is reduced such that more Bi rich epilayers are formed with a stoichiometry close to the Bi_1Te_1 phase. For both types of samples, atomic force microscopy measurements reveal smooth, that is, atomically flat surfaces as

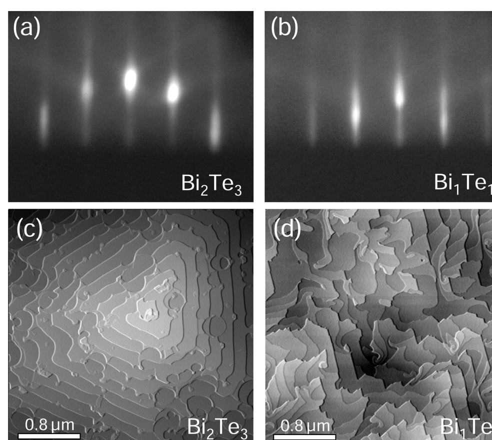

Figure 2. Reflection high-energy electron diffraction patterns observed in situ during molecular beam epitaxy of (a) Bi_2Te_3 and (b) Bi_1Te_1 along the $[1\bar{1}00]$ azimuth direction. Corresponding atomic force microscopy surface images of 400 nm thick epilayers are shown in panels c and d, respectively. The growth conditions differ only in the excess Te flux supplied during growth of 2 and 0 Å/s for panels a and c and panels b and d, respectively. The substrate temperature was 350 °C.

shown by Figure 2c and d, respectively. On the Bi_2Te_3 layers, surface steps of predominantly one quintuple unit thickness, that is, 10.1 Å height, are found, meaning that the surface is tellurium terminated at the van der Waals gaps, in agreement with previous studies.[40] For the BiTe layers, a broader variation of step heights from 4 Å corresponding to single BiTe bilayers, up to 24 Å equivalent to the 12 atomic layers of the hexagonal unit cell are observed. This arises from the fact that the unit cell of BiTe includes only one weakly bonded van der Waals Te−Te double layer (DL), that is repeated only every 12 atomic lattice planes (see Figure 1b). On a 10 μm length scale, the root-mean-square roughness of the epilayers is less than a few nm in both cases.

Apart from single phase Bi_2Te_3 and BiTe layers obtained with high, respectively, low excess Te flux, epilayers with mixed bismuth telluride phases are formed at intermediate Te flux rates. These layers show multiple X-ray diffraction peaks arising from several bismuth telluride phases and were not considered for further analysis. The RHEED patterns of these layers, however, are almost indistinguishable from those of the single phase layers as the different bismuth telluride phases differ only in their Bi−Te layer stacking sequence, whereas the overall hexagonal in-plane lattice structure and lattice constant is nearly preserved.[27]The AFM images of such layers exhibit a broader range of step heights because of the variation of the vertical lattice plane stacking of the different regions. This indicates that the coexistence of the different phases is mainly accommodated by stacking faults in the layers. In order to study and compare in detail the structural and electronic properties of the two main bismuth telluride phases, only single phase epilayers consisting of pure BiTe and Bi_2Te_3 were employed for further analysis. The corresponding sample parameters are indicated in Table 1 and the layer thicknesses ranged from 250 to 830 nm.

Structure Analysis. The crystal structures of the bismuth tellurides with the $R\bar{3}m$ space group can be described by two

Reprinted page 3 of paper [46] "Structure and properties of Bi_2Te_3 and BiTe thin films".

equivalent definitions of the base vectors in rhombohedral or hexagonal axes, as indicated by the black and green arrows in Figure 1, respectively. In this paper, we use the hexagonal definition of the base vectors *a* and *c* perpendicular, respectively, parallel to the hexagonally ordered atomic (Te,Bi) planes, where the *c*-axis is equivalent to the [0001] hexagonal or [111] rhombohedral direction. As illustrated by Figure 1, the structures of Bi_2Te_3 and BiTe mainly differ by their different stacking sequence. For Bi_2Te_3, the hexagonal unit cell consists of three quintuple layers, that is, five atomic Te^1−Bi−Te^2−Bi−Te^2 planes stacked on top of each other, corresponding in total to 15 lattice planes per unit cell. The quintuple layers are weakly bonded together by van der Waals forces between the Te−Te double layer, for which the lattice plane spacing is increased by ∼36% compared to the average value of 2.032 Å = $c/15$. The unit cell of BiTe consists of a single block of twelve atomic planes with Te^1−Bi^1−Te^2−Bi^2−Te^3−Bi^3−Bi^3−Te^3−Bi^2−Te^2−Bi^1−Te^1 stacking sequence.[30] As shown by Figure 1, it contains only one weakly bonded Te−Te van der Waals double layer, but an additional metallic Bi−Bi double layer in the middle of the cell that joins together two hextuplet layers with inverse stacking sequence. The nominal lattice parameters of Bi_2Te_3 are a = 4.384 Å and c = 30.487 Å,[34−36] and for BiTe, they are around 4.423 and 24.002 Å with some variation in literature[30,37,38] (see Table 1). Thus, the in-plane atomic distances in BiTe are slightly larger and the average vertical lattice-plane spacing slightly smaller compared to Bi_2Te_3. For both compounds, the in-plane hexagonal lattice parameter *a* fits well to the in-plane lattice constant $a_\parallel$ = 4.384 Å = $a_0/\sqrt{2}$ of (111) BaF_2 substrates. In fact, Bi_2Te_3 is practically lattice matched to BaF_2 with a lattice misfit $\Delta a_\parallel/a$ < 0.04%. For BiTe, the lattice-mismatch is somewhat larger, but it is still less than 0.9%, depending on the used bulk lattice parameter.

Phase analysis of the samples was assessed using X-ray diffraction along the symmetric truncation rod perpendicular to the epilayer surface. The resulting diffraction curves of Bi_2Te_3 and BiTe epilayers are presented in Figure 3 in red and blue color, respectively. Evidently, the layers show only the (000*l*) Bragg peaks of Bi_2Te_3 and BiTe as indicated by the vertical red and blue lines. Thus, the layers grow in *c*-axis orientation on the BaF_2 substrates for which the (111) and (222) peaks are indicated by the black dotted lines. For Bi_2Te_3, because of the 3-fold quintuple layer stacking, only the Bragg peaks with l = 3, 6, 9, 12, ... appear in the diffraction spectra, whereas no such simple selection rule exists for BiTe due to its twelve atomic layer stacking. As indicated by the crosses and triangles, for both samples the positions and intensities of the diffraction peaks correspond very well to the calculated values, and no other secondary phases are observed. This demonstrates that by appropriate choice of the MBE growth conditions single phase epilayers can be obtained.

Detailed structural information of the epilayers were derived by X-ray diffraction reciprocal-space mapping.[41] In this technique, the diffusely scattered intensity is measured as a function of the scattering vector $\boldsymbol{Q} = \boldsymbol{K}_{\text{final}} - \boldsymbol{K}_{\text{incident}}$ in the vicinity of various reciprocal-lattice vectors $\boldsymbol{h}$ (diffraction vector). For a structurally perfect layer, the reciprocal-space map (RSM) consists of a narrow vertical rod of lateral width ΔQ_x determined only by the experimental resolution. Its width along Q_z is inversely proportional to the layer thickness d according to $\Delta Q_z \approx 2\pi/d$. On the contrary, a layer with structural defects produces a broader RSM maximum, the shape of which depends on the nature and density of defects whereas its position depends on the composition and strain state of the layer.

For all samples, reciprocal space maps were recorded around the symmetric and asymmetric reciprocal lattice points (RLP) $\boldsymbol{h}_{\text{sym}}$ = (00012) and $\boldsymbol{h}_{\text{asym}}$ = (1$\bar{1}$016) for BiTe and $\boldsymbol{h}_{\text{sym}}$ = (00015) and $\boldsymbol{h}_{\text{asym}}$ = (1$\bar{1}$020) for Bi_2Te_3. The results are presented in Figure 4a−d, respectively. For the two phases, the chosen RLPs are approximately at the same positions in

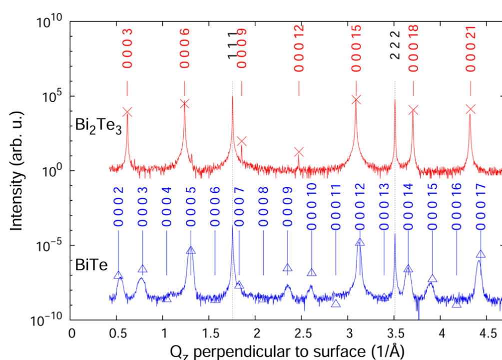

Figure 3. Symmetric X-ray diffraction scans along q_z perpendicular to the surface of Bi_2Te_3 (red line, sample M2780) and BiTe (blue line, sample M2777) epilayers grown on BaF_2 (111) substrates. The vertical lines denote the calculated (*hkl*) Bragg positions of the layer and substrate peaks, and the crosses and diamonds the intensity, that is, structure factors computed for the Bi_2Te_3, respectively, BiTe lattice structures shown in Figure 1. The sample parameters are listed in Table 1.

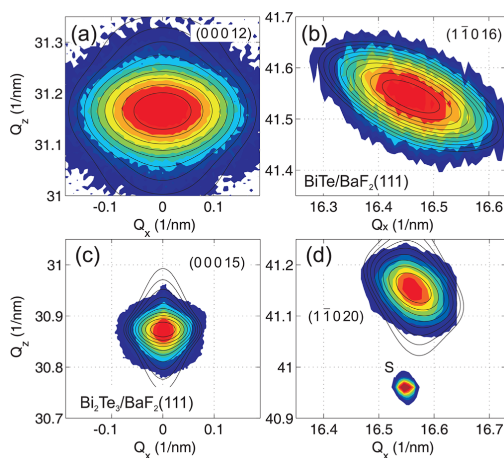

Figure 4. Reciprocal space maps of the 400 nm BiTe epilayer M2777 (top) and 800 nm Bi_2Te_3 epilayer M2780 (bottom) on BaF_2 (111), measured around the symmetric (00012) (a) and (00015) (c) as well as asymmetric (1$\bar{1}$016) (b) and (1$\bar{1}$020) (d) reciprocal lattice points. The simulation of the measured intensity distributions using a mosaic-block model is represented by the black contour lines and the resulting structure parameters are listed in Table 1.

Reprinted page 4 of paper [46] "Structure and properties of Bi_2Te_3 and BiTe thin films".

reciprocal space, which allows a direct comparison of the scattered intensity distributions. Evidently the intensity distribution is considerably broader for the BiTe compared to the Bi_2Te_3 epilayer, but in both cases the widths are larger than for a perfect epilayer. For the BiTe layer (upper part of Figure 4) the vertical and lateral full width at half-maximum (fwhm) is $\Delta Q_x = 0.1299\ nm^{-1}$ and $\Delta Q_z = 0.0823\ nm^{-1}$, respectively, and for the Bi_2Te_3 layer (lower part of Figure 4) $\Delta Q_x = 0.0328\ nm^{-1}$ and $\Delta Q_z = 0.0397\ nm^{-1}$. To account for this broadening, the defect structure was approximated by a mosaic model in which the layers consist of randomly placed and randomly rotated coherent domains (mosaic blocks).[41,42] For simulation of the reciprocal space maps, the coherent domains are assumed as uniaxial ellipsoids with mean lateral and vertical radii R_L and R_V, respectively, and root-mean square (rms) angular lattice misorientations $\Delta\phi$. The domain size is random and the radii are distributed according to the Gamma distribution with order m_R, so that the rms deviations of the radii are $\sigma_{L,R} = R_{L,V}/\sqrt{m_R}$.

The calculated reciprocal space maps for both samples are represented as solid iso-intensity contour lines in Figure 4 that are superimposed on the measured data and the best fit structure parameters are listed in Table 1. Evidently, the simulations are in nice agreement with both the symmetric and asymmetric RSMs for both phases. For the BiTe layer, the mosaic block parameters are derived as $R_L = (200 \pm 10)$ nm, $R_V = (40 \pm 5)$ nm, and $\Delta\phi = (0.18 \pm 0.02)°$. The simulations are not much sensitive to the order m_R in the range between 5 and 20. We have performed a similar analysis also on the thinner d = 250 nm BiTe layer and the resulting parameters are $R_L = (100 \pm 10)$ nm, $R_V = (40 \pm 5)$ nm, and $\Delta\phi = (0.20 \pm 0.02)°$ as listed in Table 1. The values are very similar for both samples except for the lateral size of coherent domains, which in both cases roughly equals half of the layer thickness, whereas the lattice misorientations $\Delta\phi$ and vertical coherent domain size R_V are independent of thickness. From the fit of the diffraction maxima, we obtain the BiTe lattice parameters as $a = (4.401 \pm 0.002)$ Å and $c = (24.21 \pm 0.01)$ Å, which are identical for both samples within the experimental precision. The lattice parameters differ somewhat from the bulk values listed in Table 1. This may arise from a residual epitaxial strain in the epilayers due to the nominal 0.9% mismatch to the BaF_2 substrate. However, given the uncertainty in the bulk lattice parameters, this could also be due to a deviation from the exact stoichiometric composition that also influences the lattice parameters.[29]

The same analysis was performed for the Bi_2Te_3 samples. The resulting fit of the symmetric and asymmetric RSMs are displayed in Figure 4c and d, which yields a mean vertical and lateral radius of coherent domains of $R_V = (100 \pm 30)$ nm and $R_L \approx (6000 \pm 200)$nm, where the latter exceeds the ~1 μm coherence width of the primary X-ray beam. The rms domain misorientation of $\Delta\phi = (0.08 \pm 0.02)°$ is significantly smaller than for the BiTe epilayers, and the same result was also found for the thinner 250 nm Bi_2Te_3 layer (see Table 1) with domain radii of $R_L = (130 \pm 50)$ nm and $R_V = (80 \pm 30)$ nm and an rms misorientation of $\Delta\phi = (0.05 \pm 0.03)°$. This evidences a higher structural perfection of the Bi_2Te_3 layers resulting from the almost perfect lattice matching to the BaF_2 substrates. Similar results were recently obtained for Bi_2Se_3,[43,44] where a significant improvement of the structural quality was found for growth on nearly lattice matched InP (111) substrates compared to Si (111).

From the fit of the RSMs, the lattice parameters of the Bi_2Te_3 epilayers were determined as $a = (4.380 \pm 0.001)$ Å and $c = (30.53 \pm 0.01)$ Å, which are identical to the bulk values (see Table 1) with a deviation of less than −0.08%, respectively, +0.14%. Essentially the same was also obtained for the thinner epilayer. Considering the bulk lattice constant of $a = 4.3835$ Å reported by Wyckoff,[34] a minute residual in-plane strain of −0.08% is inferred in the epilayers, corresponding to an in-plane stress of ~40 MPa using the elastic coefficients of Jenkins et al.[45] The ratio between the in-plane and out-of-plane strain values also agrees with the reported Poisson's ratio of Bi_2Te_3.[45] It is noted that the residual strain has actually the opposite sign of the +0.04% layer/substrate lattice mismatch. This can be explained by the thermal expansion coefficient mismatch between BaF_2 and Bi_2Te_3 of $18.7 \times 10^{-6}\ K^{-1}$ versus $14 \times 10^{-6}\ K^{-1}$, which induces a small compressive in-plane strain of −0.15% in the layers upon cooling from 350 °C to room temperature after growth. For thin Bi_2Te_3 epilayers on Si (111) a significantly larger out-of-plane strain value of −1% was recently reported.[21]

The epitaxial relationship of the samples was determined by azimuthal scans at the asymmetric $(1\bar{1}016)$ and $(1\bar{1}020)$ reciprocal lattice points of Bi_2Te_3, respectively, BiTe, where the samples were rotated around the surface normal vector at fixed X-ray incidence and exit angles. The results are displayed in Figure 5, where the azimuth angle ϕ is measured relative to the

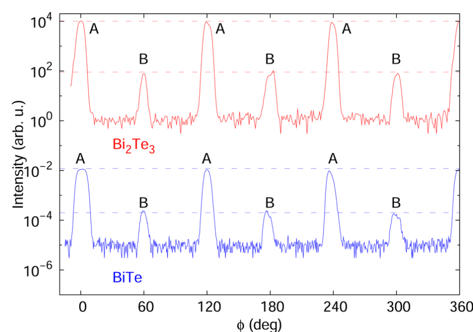

Figure 5. Azimuthal diffraction scans in the asymmetric diffraction maxima at $\boldsymbol{h} = (1\bar{1}020)$ for the Bi_2Te_3 epilayer (upper curve) and at $\boldsymbol{h} = (1\bar{1}016)$ for the BiTe layer (lower curve) on BaF_2 (111) substrates. The azimuthal angle φ is measured relative to the in-plane $[11\bar{2}]$ substrate direction. The major peaks in the positions ϕ = 0°, 120°, and 240° denoted by "A" correspond to the 3-fold symmetry along the c-axis with alignment of the $[1\bar{1}00]$ crystallographic direction of the layer to the $[11\bar{2}]$ direction of the BaF_2 substrate. The hundred times weaker secondary peaks at the intermediate azimuthal directions denoted by "B", correspond to twinned domains rotated by 180°.

$[11\bar{2}]$ surface direction of the (111) BaF_2 substrate. Evidently, for both samples the main layer peaks denoted by "A" appear at azimuths angles ϕ = 0°, 120°, 240°, and 360°, indicating that the $[1\bar{1}00]$ direction of the hexagonal layer lattice is parallel to the $[11\bar{2}]$ substrate direction. The appearance of equivalent peaks in azimuth directions differing by 120° is in agreement with the 3-fold $R\bar{3}m$ symmetry of the BiTe and Bi_2Te_3 lattice structures. However, the azimuthal scans also show weak additional secondary peaks denoted by "B" at azimuthal positions of 60°, 180° and 300°, indicating the presence of a small number of twinned domains for which the $[1\bar{1}00]$

Reprinted page 5 of paper [46] "Structure and properties of Bi_2Te_3 and BiTe thin films".

direction is antiparallel to the $[11\bar{2}]$ substrate direction, that is, the domain lattice is rotated by 180°. Reciprocal space maps measured in the vicinity of the secondary domain peaks show that the peak widths do not differ from those of the untwinned domains, i.e., the coherent size and rms misorientation is the same as that of the untwinned ones. Moreover, the intensity ratio of the twinned peaks does not show any dependence on the epilayer thickness. This indicates that the formation of the secondary twin domains occurs already in the early nucleation stage of growth. Since the intensity of the twinned domain peaks is only about 1/100 of the untwined ones, the probability of twin formation on BaF_2 (111) is very low for both Bi_2Te_3 and BiTe epilayers, which is contrary to the growth on Si (111) where a much higher twinning ratio was reported.[19] This is another indication for the superior quality of our layers.

Raman Scattering. For further assessment of the layer properties, Raman spectra were measured in the backscattering geometry both from the front side as well as back side of the layers through the transparent BaF_2 substrate. The penetration depth of the exciting 632.8 nm HeNe laser light was obtained from ellipsometric measurements and amounts to about 28 nm for Bi_2Te_3 and 25 nm for BiTe. The back side and front side Raman spectra of the 830 nm Bi_2Te_3 epilayer are shown in Figure 6a and b, respectively. Very similar spectra were measured at different spots of the sample as well as on the layer with smaller thickness. The Raman spectra show three strong bands, corresponding to the normal modes of A and E symmetry.[46] The peaks were fitted by convolution of Gaussian and Lorentzian lineshapes represented by the dashed lines in Figure 6a using an additional weak linear background. Evidently, the model spectra are in excellent agreement with the measured spectra, that is, the difference between the experimental and fitted spectra (open squares in Figure 6a) is very small and indicates only a slight asymmetry of the bands.

The frequencies and widths (fwhm) of the two A_g and one E_g vibrations of Bi_2Te_3 obtained from the fits of several independent measurements on different position and samples are listed in Table 2, together with literature values, correcting for the 1.5 cm^{-1}-wide Gaussian profile of our instrument. The small fwhm values confirm the excellent quality of our epilayers. Identical Raman spectra, i.e., peak positions and fwhm values were obtained from the front side and back side of the layers (see Table 2 and Figure 6b and a). This demonstrates that the epilayers are highly uniform in strain and composition both in the lateral as well as vertical direction and that the lattice perfection is already very high at the layer/substrate interface. This is a clear indication for pseudomorphic growth because of the near-perfect substrate lattice-matching. The only minor difference is the appearance of very weak additional bands in the front side Raman spectra, such as those labeled by arrows in Figure 6b, which we attribute to surface degradation in humid air and are not present in the Raman spectra collected from the backside from the layer/substrate interface. Detailed studies on the oxidation process of Bi_2Te_3 and Bi_2Se_3 have been presented elsewhere.[49]

Raman measurements were also performed for the BiTe epilayers and the result is shown in Figure 6b by the open circles. All BiTe samples exhibit six pronounced bands above 50 cm^{-1}, with slightly larger widths when excited through the substrate side. The latter is a signature of the less good lattice matching to the substrate in this case. Table 3 lists the frequencies and widths obtained from the fit of the Raman spectra, together with the only reported literature data obtained from a polycrystalline BiTe film grown by pulsed laser deposition (PLD) on silicon substrate.[31] Since 12 different Raman−active bands are expected for the rather complex BiTe structure[31] in a fairly narrow frequency interval, the relatively small widths of the Raman peaks of our samples (see Table 3) confirm the high quality of the layers found by our x−ray studies. The additional weak features at 72 and 75 cm^{-1} of variable strength in the spectrum from the film surface (arrows in Figure 6b) are again attributed to surface oxidization.

Table 2. Measured Raman Frequencies and Widths (fwhm) of the Bi_2Te_3 Epilayers in Units of cm^{-1} Derived from Figure 6 and Their Comparison with Literature Values from Epilayers,[26,25] Bulk Crystals,[46,47] as well as Microcrystals[48]

Bi_2Te_3	sample type	A^1_{1g}/fwhm	E^2_g/fwhm	A^2_{1g}/fwhm
front side	epilayers/BaF_2	60.9/3.0	101.2/3.7	133/9
back side	epilayers/BaF_2	60.6/3.1	100.8/4.0	133/10
ref 26	epilayer/GaAs	−/−	102/−	134/−
ref 25	epilayer/GaAs	−/−	99.8/−	132/−
ref 46	bulk	62.5/−	103/−	134/−
ref 47	bulk	62.0/5	102.3/6	134/10
ref 48	microcrystals	61/3.5	101/4.5	133/−

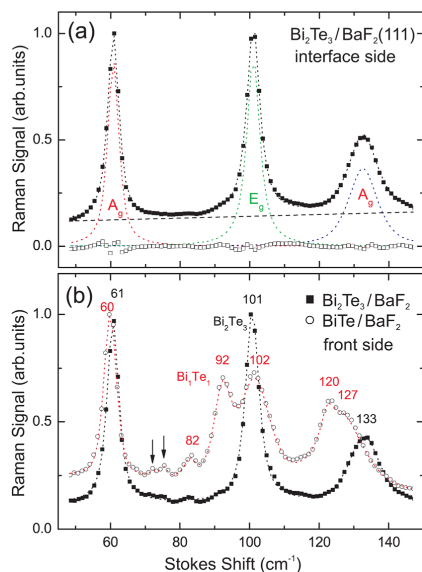

Figure 6. (a) Backside Raman spectrum (full squares) of the 830 nm Bi_2Te_3 epilayer measured through the transparent BaF_2 substrate from the Bi_2Te_3/BaF_2 interface. The dashed lines represent the deconvolution of the spectrum by the sum of three Gauss-Lorentzians and a linear background. The difference between measured and model spectra is represented by the open squares. (b)Front side Raman spectra of the Bi_2Te_3 (squares) and the 400 nm BiTe (open circles) epilayer. The dashed lines represent the model fits and the detected peak positions are labeled by the red and black numbers in units of cm^{-1}. The weak Raman bands highlighted by the arrows are attributed to surface oxidation.

Reprinted page 6 of paper [46] "Structure and properties of Bi_2Te_3 and BiTe thin films".

Table 3. Measured Raman Frequencies and Widths (fwhm) of the Bi_1Te_1 Epilayers in Units of cm^{-1} Derived from Figure 6b Compared to Literature Values Obtained for Polycrystalline Pulsed Laser Deposited (PLD) Films[31]

BiTe	sample type	ν/fwhm	ν/fwhm	ν/fwhm	ν/fwhm	ν/fwhm	ν/fwhm
front side	epilayers/BaF_2	60.0/3.3	83/2.8	92.3/4.7	101.6/9	122/6	128/7
back side	epilayers/BaF_2	59.0/4.5	83/10	90.8/6	101.9/11	120/7	126/17
ref 31	PLD films			88/−		117/−	

Optical and Electronic Properties. The optical constants of the Bi_2Te_3 and BiTe epilayers were determined over a wide spectral range from the far-infrared to the ultraviolet (UV), combining spectroscopic ellipsometry and reflectivity measurements including synchrotron data acquired at NSLS Brookhaven. The near-normal incidence infrared reflectivity was analyzed with the standard model of coherent interferences within a layer on a substrate,[50] assuming the dielectric function of the layer in the Drude-Lorentz form as described in detail in the Supporting Information.

Figures 7a and b show the real part of the optical conductivity $\sigma_1(\omega) = -i\omega\varepsilon_0(\varepsilon(\omega) - 1)$ derived for the BiTe

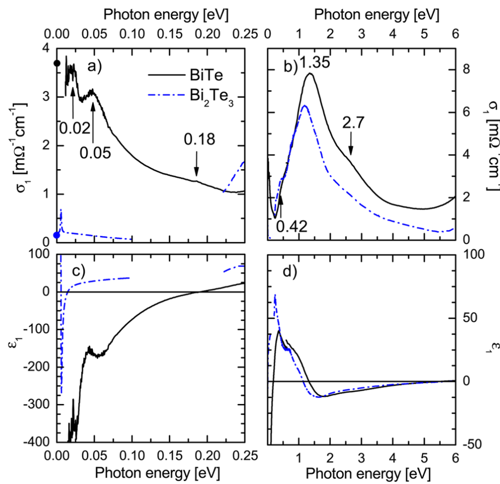

Figure 7. Real part of conductivity (top) and real part of the dielectric function (bottom) of BiTe (black solid lines) and of Bi_2Te_3 (blue dash-dotted lines) added for comparison. For clarity the spectra for the far-infrared (left) and near-infrared−ultraviolet ranges (right) are displayed on different scales. The dots in panel a correspond to the measured dc conductivity measured in van der Pauw geometry.

(black solid lines) and Bi_2Te_3 epilayers (blue dash-dotted lines), and Figure 7c and d the real part of the dielectric function $\varepsilon_1(\omega)$. The dispersion of the optical constants was obtained by the combination of reflectivity in the far-infrared, and ellipsometry at higher frequencies, using the variational dielectric function approach.[51] The Bi_2Te_3 sample is transparent in the energy range below about 0.2 eV and from the resulting interference fringes the layer thickness was determined as 830 nm. The BiTe epilayer is only slightly transparent below 0.2 eV because of much stronger free carrier absorption. The corresponding thickness was obtained as (390 ± 5) nm close to the nominal value of 400 nm. The derived pseudodielectric function of Bi_2Te_3 in the 0.6−6 eV range did not exhibit any detectable angular dependence. Consequently, it represents the in-plane response $\vec{E} \perp c$. At these photon energies the reported anisotropy of bulk Bi_2Te_3 is small.[52] The characteristic energies of the spectral features seen in Figure 7b are in good agreement with those of bulk Bi_2Te_3 reported in ref 52.

For BiTe, the absorption above 0.3 eV is due to interband transitions, dominated by the strong band at 1.35 eV, and side bands at 0.42 and 2.7 eV as indicated by the arrows in Figure 7b. This structure is similar to that of Bi_2Te_3, which is represented by the blue dash-dotted line for comparison. The interband transitions are likely related to the Bi−Te bilayer, which is the basic building block of both the Bi_2Te_3 and BiTe structure (see Figure 1). The weaker band at 0.18 eV in BiTe (see Figure 7a) is related to the 0.15 eV structure in Bi_2Te_3 reported in ref 52. At lower energies, the increase of the real part of conductivity and the decrease of the real part of the dielectric function with the decreasing photon frequency arises from the strong contribution of conducting electrons. The analysis of the spectra using the Drude model yields ω_{pl} = 1.58 ± 0.04 eV and γ = 0.09 ± 0.01 eV. Using

$$\omega_{pl}^2 = \frac{nq^2}{m^*\varepsilon_0} \tag{1}$$

where n is the carrier concentration and q and m^* the charge and effective mass, the free carrier concentration in BiTe is found to be about 20 times larger than in Bi_2Te_3, assuming the effective masses are roughly the same. Since our X-ray and Raman measurements have revealed a high crystalline perfection of the samples and no signatures of increased broadening is found in the optical spectra, this high carrier concentration in BiTe is probably not caused by extrinsic effects like vacancies but rather by a metal-like band structure, involving a band that crosses the Fermi level. This conclusion is supported by the analysis of the second BiTe sample that yielded also a large value of the plasma frequency (1.45 eV). To our knowledge, no calculations of the BiTe band structure have been available; however, calculations of the isostructural BiSe compound[53] show several bands crossing the Fermi level in the direction perpendicular to the c-axis, which supports our conclusion.

To confirm the large difference in the carrier concentration of the BiTe and Bi_2Te_3 layers, we have measured the DC electric and Hall conductivities by the Van der Pauw method. The DC conductivity of BiTe amounts to 3700 ± 200 ω^{-1} cm^{-1}. The Hall effect measurement revealed n-type conductivity with a carrier concentration of 7 ± 1 × 10^{20} cm^{-3} using a Hall factor of unity. From this carrier concentration and the measured plasma frequency, we derive the effective electron mass to be about 0.37 ± 0.05 m_e in BiTe. Since the Hall effect measurement on the Bi_2Te_3 samples were hampered by the Ettingshausen effect, we have measured the thermoelectric Seebeck coefficient instead, giving S = 170 ± 20 mV K^{-1} at 300 K, which yields a free electron concentration of 1.3 ± 0.3 × 10^{19} cm^{-3} (see ref 54), which is more than 1 order of magnitude lower than for the BiTe epilayer, in agreement with

Reprinted page 7 of paper [46] "Structure and properties of Bi_2Te_3 and BiTe thin films".

the optical data. The DC conductivity of Bi_2Te_3 amounts to $160 \pm 30\ \omega^{-1}\ cm^{-1}$. The DC conductivities derived from the electrical measurements are indicated in Figure 7a by the black, respectively, and blue dot on the ordinate axis. Clearly, the values agree well with the low-energy extrapolation of the infrared conductivity measurements, demonstrating a good consistency of our data.

To further assess the quality of the epilayers, we have performed angle resolved photoemission (ARPES) measurement of the electronic dispersion at the UE112-PGM2a beamline of BESSY II in Berlin under ultrahigh vacuum conditions at room temperature. For protection of the samples, the surface was capped in situ after by a 100 nm Te capping layer, which was desorbed in the photoemission chamber at BESSY just before the ARPES experiments. The resulting three-dimensional band dispersion is presented in Figure 8 for

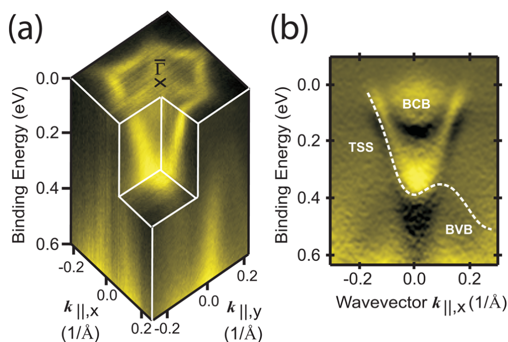

Figure 8. Band dispersion of the Bi_2Te_3 epilayers measured by angular resolved photoemission (ARPES). Panel (a) on the left shows the three-dimensional map of the photoemission intensity in the vicinity of the Γ point. The Fermi level is at 0 eV, and the k_x axis corresponds to the Γ−K direction in the hexagonal two-dimensional surface Brillouin zone and the k_y axis to Γ−M direction. Panel b shows the 2D dispersion (first derivative of the photoemission intensity with respect to energy) in the k_x direction. The dashed line indicates the topologically protected surface state (TSS). BCB denotes the bulk conduction band and BVB the bulk valence band. The measurements were performed using $\hbar\nu = 21$ eV photons for excitation.

Bi_2Te_3 grown under the same conditions as described above. Identical ARPES spectra were obtained from different places of the sample, indicating a high uniformity of the samples in the lateral direction. The topologically protected surface state (TSS) indicated by the dashed line in Figure 8b shows the expected linear dispersion with the Dirac point overlapping with the bulk valence band (BVB). The dispersion of the surface state deviates from the simple isotropic Dirac cone of Bi_2Se_3,[6] showing a significant hexagonal warping of the band dispersion at the Fermi level, as can be seen at the top of the ARPES map displayed in Figure 8a. According to the ARPES measurements, the bottom of the bulk conduction band (BCB) lies about ∼130 meV below the Fermi level (see Figure 8b), which compares very well to the value of 120 meV calculated from the bulk electron concentration $1.3 \times 10^{19}\ cm^{-3}$. This indicates that the free electron concentration at the surface assessed by ARPES does not differ significantly from the bulk concentration. Therefore, the Se capping and subsequent preparation of the clean surface for ARPES measurement by annealing does not produce a charge density on the surface. The ARPES results are in nice agreement with previous theoretical and experiments on the electronic band structure of Bi_2Te_3.[7] This demonstrates that the structural quality of the epitaxial bismuth telluride layers is very well suited for studies of the band structure of both bulk and topological surface states. Preliminary ARPES measurements on BiTe epilayers do not show a 2D surface state, which is an indication that BiTe is not a topological insulator.

■ CONCLUSION

In summary, we have demonstrated heteroepitaxial growth of different bismuth telluride phases onto BaF_2 (111) substrates using molecular beam epitaxy. The stoichiometric composition of the layers was adjusted by control of the Te flux provided during growth and single phase hexagonal BiTe and Bi_2Te_3 epilayers were obtained at low and high excess Te flux, respectively. The layers grow with their *c*-axis perpendicular to the surface and due to the good lattice matching to the BaF_2 substrate, a high structural perfection was obtained. The strain, size and tilts of the coherently scattering domains were determined by high resolution X-ray reciprocal space mapping, revealing a better structural perfection of Bi_2Te_3 compared to BiTe due to the almost perfect substrate lattice matching. This is supported by Raman measurements that show a low defect concentration and high crystalline quality present at the Bi_2Te_3/BaF_2 interface. This suggests that the layer/substrate lattice-mismatch is an important parameter for heteroepitaxial growth of bismuth telluride epilayers, in spite of the van der Waals bonding present in the crystal structure.

For both bismuth telluride phases, the Raman modes, electronic structure, and optical properties were derived from spectroscopic measurements and the plasma frequency of free electrons as well as the interband transitions were deduced. By angular resolved photoemission spectroscopy, the three-dimensional dispersion of the topologically protected surface state was measured for Bi_2Te_3 epilayers, revealing the Dirac point at the top of the bulk valence band and a strong hexagonal warping of the surface state at higher energies. The position of the Fermi level probed by photoelectron spectroscopy was found to be in good agreement with the carrier concentration in the bulk derived from transport measurements. Thus, the employed sample preparation produces very clean surfaces for photoemission studies. Infrared and transport measurements indicate a bulk metallic character of the BiTe material with a more than one order of magnitude higher carrier concentration as compared to Bi_2Te_3. To the best of our knowledge, the growth of epitaxial layers and infrared optical measurements of the BiTe phase was demonstrated for the first time. The small lattice mismatch between BiTe and Bi_2Te_3 provides good conditions for fabrication of heterostructures and superlattices of the two phases. This may open a new pathway for realization of topological insulator structures.

■ ASSOCIATED CONTENT

Ⓢ Supporting Information

Additional information and figures showing optical properties, This material is available free of charge via the Internet at http://pubs.acs.org.

■ AUTHOR INFORMATION

Corresponding Author

*E-mail: gunther.springholz@jku.at.

Reprinted page 8 of paper [46] "Structure and properties of Bi_2Te_3 and BiTe thin films".

Funding

The work was supported by the CSF grant P204/12/0595. Use of the National Synchrotron Light Source, Brookhaven National Laboratory, was supported by the U.S. Department of Energy, Office of Science, Office of Basic Energy Sciences, under Contract No. DE-AC02-98CH10886. Near-IR-VIS ellipsometry measurements at the Center for Functional Nanomaterials, Brookhaven National Laboratory, have been supported by DOE DE-AC02-98CH10886.

Notes

The authors declare no competing financial interest.

REFERENCES

(1) Hasan, M. Z.; Kane, C. L. *Rev. Mod. Phys.* **2010**, *82*, 3045.
(2) Zhang, H.; Liu, C.; Qi, X.; Dai, X.; Fang, Z.; Zhang, S. *Nat. Phys.* **2009**, *5*, 438.
(3) Hsieh, D.; Xia, Y.; Qian, D.; Wray, L.; Meier, F.; Dil, J.; Osterwalder, J.; Patthey, L.; Fedorov, A.; Lin, H.; et al. *Phys. Rev. Lett.* **2009**, *103*, 146401.
(4) Qu, D.; Hor, Y.; Xiong, J.; Cava, R.; Ong, N. *Science* **2010**, *329*, 821.
(5) Qi, X.-L.; Zhang, S.-C. *Rev. Mod. Phys.* **2011**, *83*, 1057.
(6) Xia, Y.; Wray, L.; Qian, D.; Hsieh, D.; Pal, A.; Lin, H.; Bansil, A.; Grauer, D.; Hor, Y.; Cava, R.; et al. *Nat. Phys.* **2009**, *5*, 398.
(7) Chen, Y. L.; Analytis, J. G.; Chu, J.-H.; Liu, Z. K.; Mo, S.-K.; Qi, X. L.; Zhang, H. J.; Lu, D. H.; Dai, X.; Fang, Z.; et al. *Science* **2009**, *325*, 178.
(8) Roushanm, P.; Seo, J.; Parker, C. V.; Hor, Y. S.; Hsieh, D.; Qian, D.; Richardella, A.; Hasan, M. Z.; Cava, R. J.; Yazdani, A. *Nature* **2009**, *460*, 1106.
(9) Moore, J. E. *Nature* **2010**, *464*, 194.
(10) Alpichshev, Z.; Analytis, J. G.; Chu, J. H.; Fisher, I. R.; Chen, Y. L.; Shen, Z. X.; Fang, A.; Kapitulnik, A. *Phys. Rev. Lett.* **2010**, *104*, 016401.
(11) Zhang, T.; Cheng, P.; Chen, X.; Jia, J.-F.; Ma, X.; He, K.; Wang, L.; Zhang, H.; Dai, X.; Xie, Z. F. X.; et al. *Phys. Rev. Lett.* **2009**, *103*, 266803.
(12) Tritt, T. *Science* **1999**, *283*, 804.
(13) Snyder, G. J.; Toberer, E. S. *Nat. Mater.* **2008**, *7*, 195.
(14) Hsieh, D.; Xia, Y.; Qian, D.; Wray, L.; Dil, J. H.; Meier, F.; Osterwalder, J.; Patthey, L.; Checkelsky, J. G.; Ong, N. P.; et al. *Nature* **2009**, *460*, 1101.
(15) He, L.; Kou, X.; Wang, K. L. *Phys. Status Solidi RRL* **2013**, *7*, 50.
(16) He, X.; Guan, T.; Wang, X.; Feng, B.; Cheng, P.; Chen, L.; Li, Y.; Wu, K. *Appl. Phys. Lett.* **2012**, *101*, 123111.
(17) Liu, H. W.; Yuan, H. T.; Fukui, N.; Zhang, L.; Jia, J. F.; Iwasa, Y.; Chen, M. W.; Hashizume, T.; Sakurai, T.; Xue, Q. K. *Cryst. Growth Design* **2010**, *10*, 4491.
(18) Chen, X.; Ma, X.-C.; Jia, J.-F.; Xue, Q.-K. *Adv. Mater.* **2011**, *23*, 1162.
(19) Krumrain, J.; Mussler, G.; Borisova, S.; Stoica, T.; Plucinski, L. *J. Cryst. Growth* **2011**, *324*, 115.
(20) Borisova, S.; Krumrain, J.; Luysberg, M.; Mussler, G.; Grutzmacher, D. *Cryst. Growth Design* **2012**, *12*, 6098.
(21) Fukui, N.; Hirahara, T.; Shirasawa, T.; Takahasi, T.; Kobayashi, K.; Hasegawa, S. *Phys. Rev. B* **2012**, *85*, 115426.
(22) Li, Y.-Y.; Wang, G.; Zhu, X.-G.; Liu, M.-H.; Ye, C.; Chen, X.; Wang, Y.-Y.; He, K.; Wang, L.-L.; Ma, X.-C.; et al. *Adv. Mater.* **2010**, *22*, 4002.
(23) Plucinski, L.; Mussler, G.; Krumrain, J.; Herdt, A.; Suga, S.; Grutzmacher, D.; Schneider, C. M. *Appl. Phys. Lett.* **2011**, *98*, 222503.
(24) Zhang, S. X.; Yan, L.; Qi, J.; Zhuo, M.; Wang, Y.-Q.; Prasankumar, R.; Jia, Q.; Picraux, S. *Thin Solid Films* **2012**, *21*, 6459.
(25) Cao, H.; Venkatasubramanian, R.; Liu, C.; Pierce, J.; Yang, H.; Hasan, M. Z.; Wu, Y.; Chen, Y. P. *Appl. Phys. Lett.* **2012**, *101*, 132104.
(26) Liu, X.; Smith, D. J.; Fan, J.; Zhang, Y.-H.; Cao, H.; Chen, Y. P.; Leiner, J.; Kirby, B. J.; Dobrowolska, M.; Furdyna, J. K. *Appl. Phys. Lett.* **2011**, *99*, 171903.
(27) Massalski, T. B.; Okamoto, H. *Binary Alloy Phase Diagrams*; ASM International: Materials Park, OH, 1996.
(28) Kim, Y.; Cho, S.; DiVenere, A.; Wong, G. K. L.; Ketterson, J. B. *Phys. Rev. B* **2001**, *63*, 155306.
(29) Bos, J. W. G.; Zandbergen, H. W.; Lee, M.-H.; Ong, N. P.; Cava, R. J. *Phys. Rev. B* **2007**, *75*, 195203.
(30) Yamana, K.; Kihara, K.; Matsumoto, T. *Acta Crystallogr. B* **1979**, *35*, 147.
(31) Russo, V.; Bailini, A.; Zamboni, M.; Passoni, M.; Conti, C.; Casari, C. S.; Bassi, A. L.; Bottani, C. E. *J. Raman Spectrosc.* **2008**, *39*, 205.
(32) Peranio, N.; Eibl, O.; Nurnus, J. *J. Appl. Phys.* **2006**, *100*, 114306.
(33) Madelung, O. *Semiconductors: Data Handbook*; Springer-Verlag: Berlin, 2004.
(34) Wyckoff, R. W. G. *Crystal Structures*, Vol. 2; Wiley, New York, 1964.
(35) Nakajima, S. *J. Phys. Chem. Sol.* **1963**, *24*, 479.
(36) *Natl. Bur. Stand. (U.S.) Monogr.* **1964**, *253*, 16.
(37) Shimazakí, H.; Ozawa, T. *Am. Mineral.* **1978**, *63*, 1162.
(38) Stasova, M. M.; Strukt., Zh. *Khim* **1967**, *8*, 655.
(39) Hayes, W. *Crystals with Fluoride Structure*; Clarendon: Oxford, U.K., 1974.
(40) Teweldebrhan, D.; Goyal, V.; Balandin, A. A. *Nano Lett.* **2010**, *10*, 1209.
(41) Pietsch, U.; Holý, V.; Baumbach, T. *High-Resolution X-Ray Scattering From Thin Films to Lateral Nanostructures*; Springer-Verlag: Berlin, 2004.
(42) Holý, V.; Kuběna, J.; Abramof, E.; Lischka, K.; Pesek, A.; Koppensteiner, E. *J. Appl. Phys.* **1993**, *74*, 1736.
(43) Tarakina, N. V.; Schreyeck, S.; Borzenko, T.; Schumacher, C.; Karczewski, G.; Brunner, K.; Gould, C.; Buhmann, H.; Molenkamp, L. W. *Cryst. Res. Design* **2012**, *12*, 1913.
(44) Schreyeck, S.; Tarakina, N. V.; Karczewski, G.; Schumacher, C.; Borzenko, T.; Brüne, C.; Buhmann, H.; Gould, C.; Brunner, K.; Molenkamp, L. W. *Appl. Phys. Lett.* **2013**, *102*, 041914.
(45) Jenkins, J. O.; Rayne, J. A.; Ure, J. R. W. *Phys. Rev. B* **1972**, *3*, 3171.
(46) Richter, W.; Kohler, H.; Becker, C. *Phys. Status Solidi B* **1977**, *84*, 619.
(47) Kullmann, W.; Geurts, J.; Richter, W.; Lehner, N.; Rauh, H.; Steigenberger, U.; Eichhorn, G.; Geick, R. *Phys. Status Solidi B* **1984**, *125*, 131.
(48) Atuchin, V.; Gavrilova, T.; Kokh, K.; Kuratieva, N.; Pervukhina, N.; Surovtsev, N. *Solid State Commun.* **2012**, *152*, 1119.
(49) Yashina, L. V.; Sánchez-Barriga, J.; Scholz, M. R.; Volykhov, A. A.; Sirotina, A. P.; Neudachina, V. S.; Tamm, M. E.; Varykhalov, A.; Marchenko, D.; Springholz, G.; Bauer, G.; Knop-Gericke, A.; Rader, O. *ACS Nano* **2013**, *7*, 5181.
(50) Azzam, R. M. A.; Bashara, N. M. *Ellipsometry and Polarized Light*; Elsevier Science Publisher: Amsterdam, 1987.
(51) Kuzmenko, A. B. *Rev. Sci. Instrum.* **2005**, *76*, 083108.
(52) Greenaway, D. L.; Harbeke, G. *J. Phys. Chem. Solids* **1965**, *26*, 1585.
(53) Gaudin, E.; Jobic, S.; Evain, M.; Brec, R.; Rouxel, J. *Mater. Res. Bull.* **1995**, *30*, 549.
(54) Mishra, S. K.; Satpathy, S.; Jepsen, O. *J. Phys.: Condens. Matter* **1997**, *9*, 461.

Reprinted page 9 of paper [46] "Structure and properties of Bi_2Te_3 and BiTe thin films".

Supplementary Material

Growth, Structure and Electronic Properties of Epitaxial Bismuth Telluride Topological Insulator Films on BaF_2 (111) Substrates

O. Caha, A. Dubroka, J. Humlíček, V. Holý, H. Steiner, M. Ul-Hassan, J. Sánchez-Barriga, O. Rader, T. N. Stanislavchuk, A. A. Sirenko, G. Bauer, and G. Springholz

(Dated: January 9, 2013)

PACS numbers:

OPTICAL PROPERTIES

The optical constants of the Bi_2Te_3 and BiTe epilayers were determined by combining spectroscopic ellipsometry and reflectivity measurements. For this purpose a mid-infrared ellipsometer attached to a Bruker IFS55 EQUINOX Fourier spectrometer as well as a Woollam M-2000 and Jobin Yvon UVISEL ellipsometer for the near-infrared, visible and ultraviolet range were employed. Reflectance measurements in the 0.01–0.2 eV range were done using a Bruker IFS 66v/S spectrometer and far-infrared ellipsometric measurements at the NSLS synchrotron in Brookhaven. Figure 1(a) presents the near-normal incidence infrared reflectivity of the Bi_2Te_3/BaF_2 sample (solid line). Since the layer is transparent in this energy range, the spectrum exhibits also features from the substrate – for example the structure near 0.02 eV is due to the substrate phonon. The sequence of minima and maxima at higher energies corresponds to the interference in the layer. We have analyzed the spectrum with the standard model of coherent interferences within a layer on a substrate [1] assuming the dielectric function of the layer in the Drude-Lorentz form

$$\epsilon(\omega) = \epsilon_\infty - \frac{\omega_{\rm pl}^2}{\omega(\omega + {\rm i}\omega\gamma)} + \sum_k \frac{\Omega_{{\rm pl},k}^2}{\Omega_{0,k}^2 - \omega^2 - {\rm i}\omega\Gamma_k} \quad (1)$$

where ϵ_∞ stands for the electronic interband contribution, $\omega_{\rm pl}$ and γ denotes the plasma frequency and broadening of the Drude term and $\Omega_{{\rm pl},k}$, $\Omega_{0,k}$ and Γ_k the plasma frequency, frequency and broadening of the Lorentz terms, respectively. The dielectric function of the BaF_2 was determined by fitting the reflectivity of a bare substrate in the far-infrared range assuming the 3–term Lorentz model similar to Eq. (1), from which we obtain in units of cm^{-1} except for ϵ_∞: $\epsilon_\infty = 2.16$, $\Omega_{0,1} = 186$, $\Omega_{{\rm pl},1} = 402$, $\Gamma_1 = 6.1$, $\Omega_{0,2} = 270$, $\Omega_{{\rm pl},2} = 57$, $\Gamma_2 = 51$, $\Omega_{0,3} = 330$, $\Omega_{{\rm pl},3} = 52$, $\Gamma_3 = 53$ at $T =$ at 300 K

The model spectrum of the whole layer–substrate structure presented as dashed line in Figure 1(a) fits very well to the measured data up to the energy of about 0.1 eV. At higher energies, the substrate is transparent and the quantitative analysis of the spectra is complicated due to the incoherent reflections from the backside of the sample. The model dielectric function involved also a Lorentz oscillator at $\Omega_0 = 5.6$ meV corresponding to the so-called alpha phonon [2], which lies outside the frequency range of our spectrometer. The resulting best–fit parameters for the epilayer are: $\epsilon_\infty = 45 \pm 2$, $\omega_{\rm pl} = (0.33 \pm 0.02)$ eV, $\gamma = (0.07 \pm 0.01)$ eV. In addition, we obtained the thickness of the layer as $d = (830 \pm 40)$ nm.

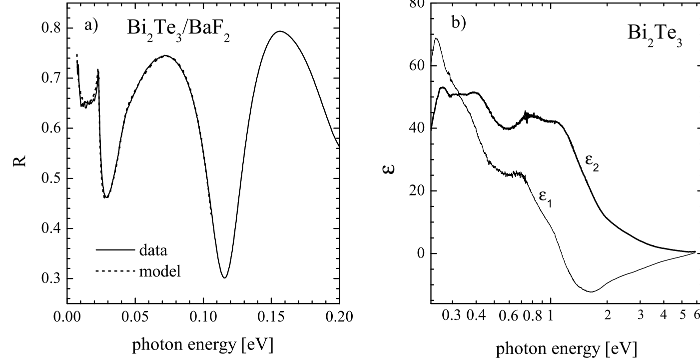

FIG. 1: (a) Far-infrared reflectivity of the Bi_2Te_3/BaF_2 epilayer (solid line) and a model spectrum (dashed line) for electric vector perpendicular to the c-axis, $E \perp c$. (b) Real and imaginary part of the dielectric function of Bi_2Te_3 obtained from ellipsometric measurements up to 5 eV.

Since the reflectivity was measured at near-normal incidence, the retrieved dielectric function corresponds to the in-plane direction, $\vec{E} \perp c$. The derived dielectric constants were included in the dielectric functions depicted in Fig. 7 of the manuscript.

Figure 1(b) displays the real and imaginary part of the dielectric function of the Bi_2Te_3 layer above 0.2 eV, where the layer is opaque. The spectra were obtained from the ellipsometric measurements at the angle of incidence of 70 degrees (0.6–6) eV, and at 75 degrees (0.2–0.6) eV. The displayed (pseudo)dielectric function was obtained assuming that the layer is isotropic. As usual, the pseudo-dielectric function very close to the in-plane contribution. This is particularly true for spectra acquired at low angles of incidence, and for large values of the index of refraction, with the in–plane orientation of the electric vector inside the layer. The pseudo-dielectric function measured in the 0.6–6 eV range did not exhibit any detectable angular dependence. Consequently, it represents the in-plane response, $\vec{E} \perp c$. At these photon energies the reported anisotropy of bulk Bi_2Te_3 is small [3]. The characteristic energies of the spectral features seen in Fig. 1(b) are in good agreement with those of bulk reported in Ref. [3]. However, the magnitude of our spectra is by a factor 1.5-2 smaller and our value $\epsilon_\infty = 45 \pm 2$ is smaller by a factor of ~ 2 than that obtained in Ref. [2]. The discrepancy is probably caused by errors in the absolute values of the measured reflectivity in the

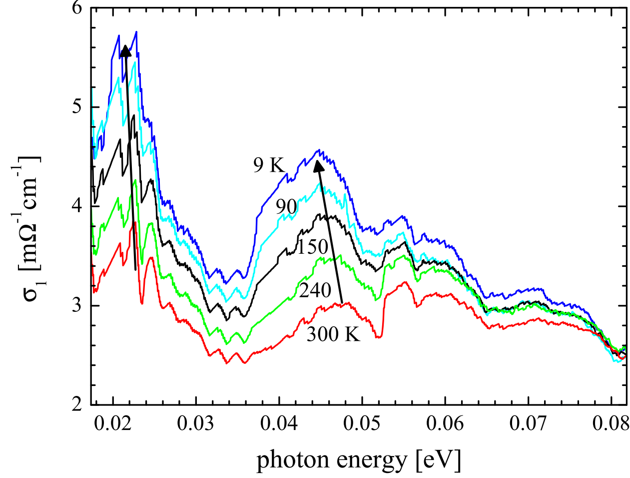

FIG. 2: Temperature dependence of the real part of conductivity of the BiTe epilayer in the far–infrared regime determined by ellipsometry at the NSLS synchrotron in Brookhaven.

cited works, or by the errors induced by extrapolations necessary for the Kramers-Kronig analysis.

As indicated in Fig.7 of the manuscript(a), the infrared conductivity of BiTe exhibits two bands near 0.02 and 0.05 eV that are superimposed on the Drude contribution. In order to inspect these bands in a greater detail, we have have performed low-temperature far-infrared ellipsometric measurements at the NSLS synchrotron in Brookhaven. Figure 2 displays the resulting real part of conductivity from 9 to 300 K. The sharper structures in the spectra are artefacts due to the inhomogeneity of the polarizer. Both bands at around 0.02 and 0.05 eV gradually sharpen and soften with decreasing temperature.

---

[1] R. M. A. Azzam and N. M. Bashara, *Ellipsometry and polarized light* (Elsevier Science Publisher B. B., 1987).

[2] W. Richter, H. Kohler, and C. Becker, Phys. Status Solidi B **84**, 619 (1977).

[3] D. L. Greenaway and G. Harbeke, J. Phys. Chem. Solids **26**, 1585 (1965).

4.2 Structure of Bi_xTe_y thin films with general stoichiometry

The non-stoichiometric alloy layers of $Bi_2Te_{3-\delta}$ were grown with varying tellurium flux. We have achieved stoichiometry within the range δ =0–1. The structure of thin films was analyzed using x-ray diffraction. The diffraction pattern was described by a model of random stacking of Bi_2Te_3 quintuple layer and Bi_2 bilayer. The non-linear stoichiometry dependence of the in-plane lattice parameter and average lattice spacing was determined.

CrossMark

research paper

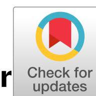

Journal of
Applied Crystallography
ISSN 1600-5767

Received 10 June 2014
Accepted 11 September 2014

Structure and composition of bismuth telluride topological insulators grown by molecular beam epitaxy

Hubert Steiner,[a] Valentine Volobuev,[a] Ondřej Caha,[b] Günther Bauer,[a] Gunther Springholz[a] and Václav Holý[c]*

[a]Institut für Halbleiter- und Festkörperphysik, Johannes Kepler Universität, Altenbergerstrasse 69, 4040 Linz, Austria, [b]Department of Condensed Matter Physics and CEITEC, Masaryk University, Kotlářská 2, 61137 Brno, Czech Republic, and [c]Department of Condensed Matter Physics, Charles University in Prague, Ke Karlovu 5, 121 16 Prague, Czech Republic. Correspondence e-mail: holy@mag.mff.cuni.cz

The structure and composition of $Bi_2Te_{3-\delta}$ topological insulator layers grown by molecular beam epitaxy is studied as a function of beam flux composition. It is demonstrated that, depending on the Te/Bi_2Te_3 flux ratio, different layer compositions are obtained corresponding to a Te deficit δ varying between 0 and 1. On the basis of X-ray diffraction analysis and a theoretical description using a random stacking model, it is shown that for $\delta \geq 0$ the structure of the epilayers is described well by a random stacking of Te–Bi–Te–Bi–Te quintuple layers and Bi–Bi bilayers sharing the same basic hexagonal lattice structure. The random stacking model accounts for the observed surface step structure of the layers and compares very well with the measured X-ray data, from which the lattice parameters *a* and *c* as a function of the chemical composition were deduced. In particular, the in-plane lattice parameter *a* is found to continuously increase and the average distance of the (0001) hexagonal lattice planes is found to decrease from the Bi_2Te_3 to the BiTe phase. Moreover, the lattice plane distances agree well with the linear interpolation between the Bi_2Te_3 and BiTe values taking the strain in the epilayers into account. Thus, the chemical composition $Bi_2Te_{3-\delta}$ can be directly determined by X-ray diffraction. From analysis of the X-ray diffraction data, quantitative information on the randomness of the stacking sequence of the Bi and Te layers is obtained. According to these findings, the layers represent random one-dimensional alloys of Te–Bi–Te–Bi–Te quintuple and Bi–Bi bilayers rather than a homologous series of ordered compounds.

© 2014 International Union of Crystallography

1. Introduction

Bismuth telluride has attracted tremendous interest in the past few years because it not only represents one of the best thermoelectric materials (Tritt, 1999; Snyder & Toberer, 2008) but is also an outstanding member of a new class of materials called topological insulators (Hasan & Kane, 2010; Zhang *et al.*, 2009; Hsieh *et al.*, 2009; Qu *et al.*, 2010; Qi & Zhang, 2011). These materials exhibit striking new physical properties owing to the existence of topologically protected two-dimensional surface states that display an energy momentum dispersion shaped like a Dirac cone (Zhang *et al.*, 2009; Xia *et al.*, 2009; Chen *et al.*, 2009). In these surface states, the electron momentum is locked to the spin direction (Hasan & Kane, 2010; Roushan *et al.*, 2009; Sanchez-Barriga *et al.*, 2014) and therefore, spin polarized currents can be induced without the needs of external magnetic fields. This offers interesting possibilities for novel spintronic devices (Hasan & Kane, 2010; Moore, 2010; Qi & Zhang, 2011) and may provide a basis for fundamentally new physics such as magnetic monopoles and Majorana fermions (Hasan & Kane, 2010; Zhang *et al.*, 2009).

In contrast to conventional III–V, II–VI or IV–VI compound semiconductors, bismuth telluride (as well as bismuth selenide) can exist in multiple phases with different chemical compositions, including Bi_2Te_3, Bi_3Te_4, Bi_5Te_6 and BiTe (Yamana *et al.*, 1979), among others (Massalski & Okamoto, 1996). These compounds constitute a homologous series of structures (Stasova, 1967; Kim *et al.*, 2001; Bos *et al.*, 2007) that share the same basic hexagonal lattice, formed by $ABCABC\ldots$ stacking of hexagonally ordered alternating Bi and Te layers, with additional Te–Te or Bi–Bi double layers inserted at certain distances to accommodate the differences in composition, *i.e.* the Te/Bi content. According to the Bi–Te phase diagram (Massalski & Okamoto, 1996), stoichiometric Bi_2Te_3 is the compound with the highest Te content, with a Te/Bi ratio of 1.5. For the other phases, this ratio is reduced as denoted by $Bi_2Te_{3-\delta}$, where $\delta > 0$ defines the Te deficit in the material compared with Bi_2Te_3.

Reprinted page 1 of paper [49] "Structure of Bi_2Te_{3-x} films".

For Bi_2Te_3, the basic building blocks of the lattice are Te–Bi–Te–Bi–Te quintuple layers (QLs) that are van der Waals bonded to each other through the facing Te–Te double layers (DLs). This gives rise to the well known threefold quintuple layer stacking described by a hexagonal unit cell containing three QLs (see Fig. 1*a*). As the Te content decreases (increasing the Te deficit δ), additional Bi–Bi double layers are inserted between the quintuple layers which, if inserted at regular distances, give rise to a homologous series of ordered compounds that can be regarded as adaptive natural superlattices (Stasova, 1967; Kim *et al.*, 2001; Bos *et al.*, 2007; Cava *et al.*, 2013). For example, for Bi_2Te_2 a Bi–Bi DL is inserted after every second QL, for Bi_5Te_6 after every fourth QL, for Bi_4Te_5 after every fifth QL and so forth. The corresponding stacking of the two-dimensional arrays in Bi_2Te_3, Bi_4Te_5, Bi_1Te_1 and Bi_4Te_3 is shown schematically in Fig. 1. A further overview of other ordered Bi_mTe_n phases [denoted (*mn*) in the following] can be found in papers by Kim *et al.* (2001), Bos *et al.* (2007) and Cava *et al.* (2013). It is noted that a similar homologous series also exists in the Bi–Se system, in which analogous phases occur (Lind & Lidin, 2003; Lind *et al.*, 2005; Valla *et al.*, 2012).

For practical applications of topological insulator materials, high-quality epitaxial layers with well controlled properties are of key importance (He *et al.*, 2013). Owing to the existence of different stoichiometric phases, however, the structure and composition of bismuth chalcogenide layers grown by molecular beam epitaxy (MBE) (Peranio *et al.*, 2006; Liu *et al.*, 2010; Chen *et al.*, 2011; Krumrain *et al.*, 2011; Borisova *et al.*, 2012; Fukui *et al.*, 2012; Li *et al.*, 2010; Plucinski *et al.*, 2011; Liu *et al.*, 2011; Zhang *et al.*, 2012; Cao *et al.*, 2012; Caha *et al.*, 2013) or other vapor phase methods are much less well defined than those of the usual binary semiconductors such as GaAs, InAs, ZnSe, PbTe *etc.*, where only one single well defined stoichiometric phase with 1:1 composition exists. As a result, the structure and composition of bismuth telluride epilayers are expected to strongly depend on the MBE growth conditions, but no detailed studies on this have been reported up to now.

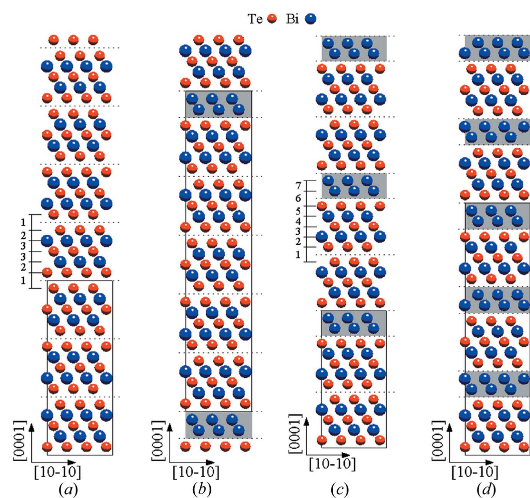

Figure 1
Stacking sequence of two-dimensional Bi and Te lattice planes in ordered homologous Bi_mTe_n ($Bi_2Te_{3-\delta}$) structures with different compositions: (*a*) Bi_2Te_3, (*b*) Bi_4Te_5, (*c*) Bi_1Te_1 and (*d*) Bi_4Te_3, with the corresponding Te deficits δ = 0, 0.5, 1 and 1.5, respectively. The black rectangles denote the crystallographic unit cells; the Bi–Bi DLs are emphasized by shaded areas. The numbers 1, ... , 7 in panels (*a*) and (*c*) refer to the distances of the (0001) lattice planes Δz_1 to Δz_7 as used for the model simulations (see the text).

To resolve this issue, we have investigated here the growth and structure of bismuth telluride layers as functions of the beam flux composition. We show that, although two-dimensional growth occurs for any composition, a continuous series of $Bi_2Te_{3-\delta}$ layers with arbitrary δ is obtained under conditions of reduced Te flux during growth. We developed a description of the structure of the $Bi_2Te_{3-\delta}$ layers based on the model of a stochastic sequence of QLs and DLs, which enables us to simulate the diffraction curves averaged over a statistical ensemble of all sequences. We demonstrate by the comparison of the measured and simulated diffraction curves that the resulting layer structure is formed by randomly incorporated Bi–Bi double layers after random numbers of quintuple layers rather than by ordered superstructures. Thus, only from the average distance of the Bi–Bi double layers is the actual stoichiometry δ defined. The average atomic layer spacing in the **c** direction is found to decrease with increasing δ value, roughly following the Vegard law connecting the limiting cases of Bi_2Te_3 and Bi_2Te_2 with δ = 0 and 1, respectively. As this average lattice plane spacing can be directly deduced from the position of selected Bragg diffraction maxima, the layer compositions can be unambiguously obtained. The composition has a profound influence not only on the step structure of the surface but also on the background carrier concentration and mobility, which is important for device applications. Similar effects are also expected for bismuth selenide layers.

2. Sample growth

Bismuth telluride layers were grown by molecular beam epitaxy using a compound bismuth telluride effusion source with nominal Bi_2Te_3 composition, yielding a beam flux with an overall Te/Bi flux ratio of approximately one. An additional tellurium source is used to tune the beam flux composition and to obtain a Te-rich beam flux composition, as needed to get the 2:3 stoichiometry in the growing layer or any other composition in between. To systematically study the effect of beam flux composition, a series of samples were grown in which the Te flux was varied between 0 and 2.4 Å s^{-1} ($\sim$1.25 monolayers per second), while keeping the bismuth telluride flux rate constant at $\sim$1 Å s^{-1} (0.1 QL s^{-1}). It is to be noted, however, that a large portion of the excess Te flux re-evaporates from the surface, and thus only a small fraction of Te atoms are actually incorporated, meaning that the composition of the layers differs from the impinging beam flux composition. The flux rates and beam flux ratios were determined by a quartz crystal microbalance moved into the substrate position. The

layer thickness was 350 nm and the growth temperature was 613 K for all samples, and a background pressure of $\sim 5 \times 10^{-10}$ mbar was maintained during growth. Cleaved $BaF_2(111)$ was used as substrate material. It is essentially lattice matched to Bi_2Te_3 (Caha *et al.*, 2013) because its in-plane lattice constant of $a_{\rm sub}^{(111)} = a_{\rm sub}(3)^{-1/2} = 0.4384$ nm is practically equal to the hexagonal lattice constant a = 0.4385 nm of Bi_2Te_3 (Nakajima, 1963; Wyckoff, 1964), *i.e.* the lattice mismatch $\Delta a/a$ is only 0.04%. For BiTe, a = 0.4423 nm (Yamana *et al.*, 1979; Shimazaki & Ozawa, 1978; Stasova, 1967) is slightly larger, but the lattice mismatch to BaF_2 is still below 1% (Caha *et al.*, 2013).

The surface evolution during growth was monitored using *in situ* reflection high-energy electron diffraction (RHEED). Figs. 2(*a*)–2(*d*) show representative RHEED patterns for four samples grown with different excess Te fluxes, $J_{\rm Te}$, increasing from 0 to 1.4 Å s^{-1}; there is no difference in the RHEED data for higher fluxes between 1.4 and 2.4 Å s^{-1}. The streaked RHEED patterns are practically indistinguishable, evidencing that two-dimensional growth occurs in all cases, resulting in a locally smooth terraced surface with atomic scale surface steps. For all layers, the resulting surface structure was determined by atomic force microscopy (AFM), and the results are presented in the middle panels of Fig. 2. All layers exhibit smooth surfaces, but the characteristic surface step structure drastically differs for the different samples. Whereas the sample grown with a high excess Te flux (Fig. 2*h*) shows a well defined terrace structure with rather smooth and straight step edges preferably aligned along three $\langle 1\bar{1}00 \rangle$ directions, for the other samples grown with lower excess Te flux (Figs. 2*e*–2*g*) much rougher step edges and a rather irregular step structure are formed.

A closer inspection of the AFM images reveals that a uniform, *i.e.* constant, step height h exists only for the high excess Te flux sample, where h = 1 nm is the height of one Te–Bi–Te–Bi–Te quintuple layer. In contrast, a variety of step heights is observed for the other samples, h ranging from ~0.4, 0.6, 1 and even 1.2 nm, corresponding to the height of one bilayer (BL), trilayer (TL), quintuple layer as well as a septuple (SL) layer. This is demonstrated by the surface profiles depicted in the bottom panel of Fig. 2, where the different step heights are labeled according to the corresponding number of atomic planes. This is clear evidence that the crystal structure, *i.e.* the layer stacking, strongly differs for the different samples. For the pure Bi_2Te_3 phase, the lattice is formed exclusively of QL blocks, which are weakly van der Waals bonded by the Te–Te layers of the adjacent QLs. Thus, there is a strong tendency to complete each QL before a new

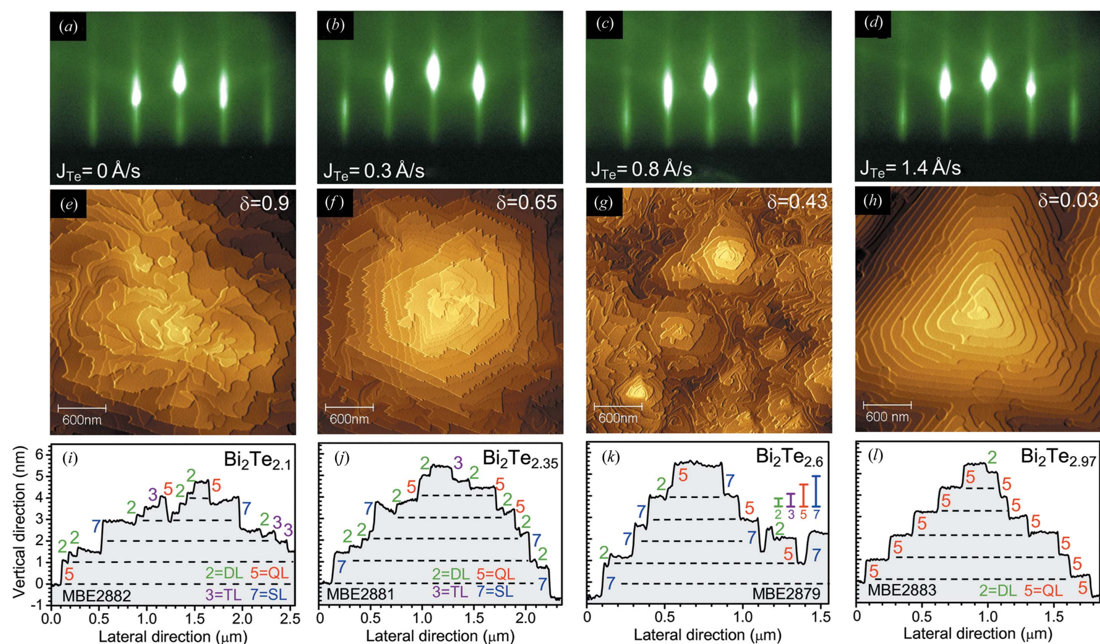

Figure 2
Top: RHEED patterns recorded during $Bi_2Te_{3-\delta}$ growth with different excess Te flux rates ($J_{\rm Te}$) from 0 to 1.4 Å s^{-1}, from (*a*) to (*d*), respectively, indicating two-dimensional growth in all cases. The main growth flux is provided from a compound Bi_2Te_3 effusion cell, giving a growth rate of 1 Å s^{-1}. Middle: AFM images of the resulting 350 nm-thick $Bi_2Te_{3-\delta}$ layers on $BaF_2(111)$ with the Te-deficit values δ indicated as determined by X-ray diffraction (image size 3 × 3 μm). Bottom: measured surface profiles for the different layers, with the different steps heights corresponding to double (2), triple (3), quintuple (5) and septuple (7) atomic lattice planes indicated by the numbers and by the vertical scale bars in view (*k*). The horizontal dashed lines represent the normal quintuple layer spacing of Δh = 1 nm expected for the pure Bi_2Te_3 phase.

Reprinted page 3 of paper [49] "Structure of Bi_2Te_{3-x} films".

QL nucleates on the surface, which results in a surface structure that exclusively features QL layer steps (Teweldebrhan *et al.*, 2010). This is a first indication that only the epitaxial layers grown with high excess Te flux, $J_{Te} \geq 1.4$ Å s^{-1}, grow in the pure Bi_2Te_3 phase. Further inspection also reveals that the QL layer steps tend to be straight and aligned along the $\langle 1\bar{1}10 \rangle$ surface directions, whereas the other types of steps observed for the samples grown with less excess Te flux do not show a clear preferred step direction, causing a much higher step-edge roughness as seen in Figs. 2(*f*)–2(*g*).

When reducing the Te flux during epitaxial growth, at some point there is not sufficient Te present on the surface to complete each quintuple layer and to maintain a fully Te-terminated surface state. As a result, with decreasing Te flux, more and more stacking faults are introduced in the QL layer stacking, leading to incomplete QL layers as well as to the introduction of additional Bi–Bi double layers into the Bi_2Te_3 lattice. This corresponds exactly to the structural motif of the $Bi_2Te_{3-\delta}$ phases with reduced Te content (Te deficit $\delta > 0$), in which such Bi–Bi double layers are introduced to decrease the overall Te/Bi ratio (see Fig. 1). As a result, surface steps with smaller as well as larger step heights are formed on the surface where, for example, an additional Bi–Bi–Te layer on top of a QL layer corresponds to a trilayer step height, whereas an additional Bi–Te layer leads to a DL surface step. Thus, the surface structure observed for the low Te flux samples is a clear indication that $Bi_2Te_{3-\delta}$ layers with significant Te deficit $\delta > 0$ are formed. However, it is evident that the addition of a Bi–Bi DL during growth does not occur synchronized over the whole layer surface but rather with considerable statistical variation at different locations. Therefore, disordered atomic layer stackings will be formed rather than well ordered superstructures. Under such conditions, domain boundaries between regions of different stackings are formed, resulting in a significantly increased defect density in the layers.

3. X-ray diffraction

To clarify in detail the structural properties of the samples with different compositions, X-ray diffraction measurements were performed using a Seifert diffractometer equipped with a primary Ge monochromator and parabolic mirror for Cu $K\alpha_1$ radiation and a pixel detector on the secondary side. Symmetric diffraction scans of various samples from the series are shown in Fig. 3, with the excess Te flux increasing from the top to the bottom. The diffraction curves were measured in the symmetric geometry, *i.e.* they represent the distributions of the diffracted intensity along the Q_z axis normal to the surface. All layers only show (000*L*) diffraction maxima, indicating growth with the hexagonal *c* axis perpendicular to the BaF_2 (111) surface independent of the beam flux composition.

For the layer grown with the highest excess Te flux ($\geq$1.4 Å s^{-1}) (lowest curve in Fig. 3), only diffraction peaks with *L* equal to a multiple of three, *i.e.* $L = 3, 6, 9, \ldots$, appear. This indicates that only the pure Bi_2Te_3 phase is formed, in which this selection rule arises from the fact that the unit cell is nonprimitive and it is composed of three quintuple layers stacked on top of each other and that these three QLs are identical in the symmetric diffraction geometry. As we discuss in detail below, the intensities of the (0009) and (00012) reflections are very low owing to the vanishingly small structure factor of a single QL.

With decreasing excess Te flux the diffraction peaks shift and broaden, and some even split into peak pairs as indicated by the short black arrows in Fig. 3. For the sample grown without excess Te flux (upmost curve in Fig. 3), the intensity and position of the diffraction peaks correspond to those expected for the Bi_1Te_1 phase (Caha *et al.*, 2013), exhibiting a unit cell composed of 12 atomic layers [two QLs plus one Bi–Bi DL, see Fig. 1(*c*)]. Thus, in contrast to Bi_2Te_3, the unit cell of Bi_1Te_1 is primitive. Therefore, all diffractions (000*L*) are allowed and more diffraction peaks appear for Bi_1Te_1 than for Bi_2Te_3, in spite of its smaller unit cell. For the samples with intermediate Te fluxes, *i.e.* intermediate compositions (middle curves in Fig. 3), there is no indication of the formation of

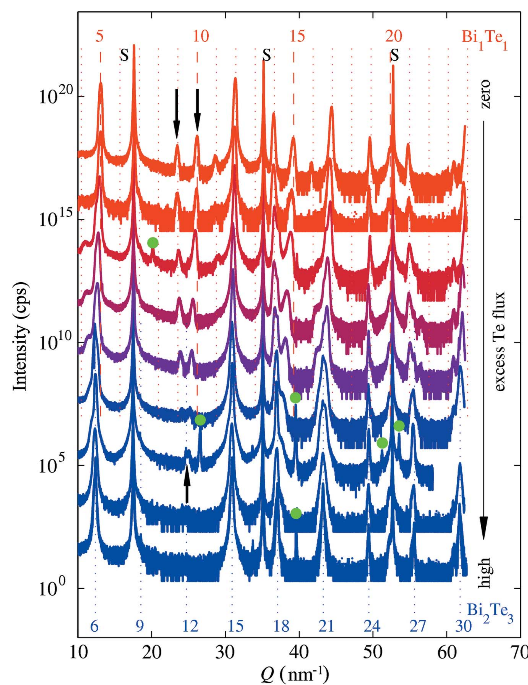

Figure 3
Symmetric diffraction curves for the $Bi_2Te_{3-\delta}$ sample series grown with different excess Te fluxes, increasing monotonically from zero for the topmost curve to $J_{Te} = 3$ Å s^{-1} for the lowest curve. The curves were measured in symmetric diffraction geometry along the (000*L*) rod perpendicular to the surface and for clarity are shifted vertically with respect to each other. The numbers in blue and red denote the *L* indexes of the diffraction maxima of the pure Bi_2Te_3 and Bi_1Te_1 phases, respectively; the color of the curves indicates a gradual change of the structure from Bi_2Te_3 (blue) to Bi_1Te_1 (red) with decreasing excess Te flux. The short vertical arrows indicate the splitting of the weak (00012) maximum of the (23) phase into two peaks with decreasing excess Te flux. The BaF_2 substrate diffraction peaks are labeled by S and the green circles mark the *Umweganregung* peaks (see text).

ordered superstructures as expected for the homologous series of ordered Bi_mTe_n phases, in which case additional peaks should appear. Instead, we only find a continuous shift of the diffraction peaks as a function of composition, *i.e.* the peaks of Bi_2Te_3 smoothly evolve into those of BiTe. Strikingly, with decreasing Te content, the diffraction peaks shift in various directions. For example, the (0006) peak of the Bi_2Te_3 phase shifts to the right, *i.e.* to higher Q_z, and seamlessly transforms into the (0005) peak of the Bi_1Te_1 phase, whereas in contrast the (00018) peak of Bi_2Te_3 shifts to the left to evolve into the (00014) diffraction maximum of Bi_1Te_1. Other peaks seem to stay nearly at a constant position [*e.g.* the (00015) peak of Bi_2Te_3] or split up or even disappear, as is seen, for example, for the (0009) and (00010) peaks of Bi_1Te_1 (denoted by the short black arrows in Fig. 3). With increasing Te content, these peaks move closer and closer to each other and eventually merge for the highest Te excess fluxes ($\delta < 0.2$), creating the (00012) diffraction peak of the Bi_2Te_3 phase. It is noted that several diffraction maxima denoted by S in Fig. 3 stem not from the layer but from the substrate or are created by the *Umweganregung* effect (denoted by green circles), *i.e.* the wave being previously diffracted by the substrate is diffracted by the layer, or the substrate diffracts the wave diffracted by the layer. These additional diffraction maxima are, therefore, ignored in the subsequent data analysis.

The diffraction data in Fig. 3 clearly demonstrate that there is a rather continuous evolution of the lattice structure as a function of composition, contrary to the picture of a discrete series of distinct homologous structures with different arrangements of unit cells. This means that the layer material resembles more a random one-dimensional alloy of Bi and Te lattice planes that can accommodate any arbitrary composition with a quasi-continuous adoption of the average lattice parameters. This assumption is also supported by the observation that the diffraction peaks for the intermediate compositions show a significant broadening as is common for disordered alloy materials.

To determine the lateral lattice parameter a of the hexagonal lattice of the samples, we have measured reciprocal-space maps of the diffracted intensity in the vicinity of the asymmetric reciprocal lattice point (313) of the substrate and of the $(1\bar{1}0\,20)$ one of Bi_2Te_3. As shown in Fig. 4, the two diffraction maxima occur close to each other in the same reciprocal plane perpendicular to the sample surface $(111)_{\rm cubic} \parallel (000\,1)_{\rm hexagonal}$, and their lateral reciprocal coordinates along $[1\bar{2}1]_{\rm cubic} \parallel [1\bar{1}00]_{\rm hexagonal}$ are given by

$$H_{\parallel}^{(\rm sub)} = \frac{2\pi}{a_{\rm sub}}(8/3)^{1/2}, \quad H_{\parallel}^{(mn)} = \frac{2\pi}{a_{mn}}(4/3)^{1/2}. \qquad (1)$$

As $a_{\rm sub} \simeq a_{mn}(2)^{1/2}$ [a_{mn} denotes the a parameter of the (mn) phase], the substrate and layer diffraction maxima have almost the same lateral positions. In Figs. 4(*a*) and 4(*b*), we show the reciprocal-space maps of the samples with the highest and lowest excess Te flux rates [(23)-like and (11)-like, respectively]. In the maps, the diffraction maxima of the substrate and the layer are denoted by S and L, respectively. The maxima occur at practically the same in-plane positions owing to the nearly identical in-plane lattice constants. For the samples with lower Te content grown under low excess Te conditions, the layer peak gradually moves to somewhat lower Q_x and higher Q_z values, indicating a continuous increase of the in-plane lattice parameter a and a concomitant decrease of the average distance of the hexagonal (0001) basal atomic planes (referred to here as inter-plane distances) as described in detail in §4.

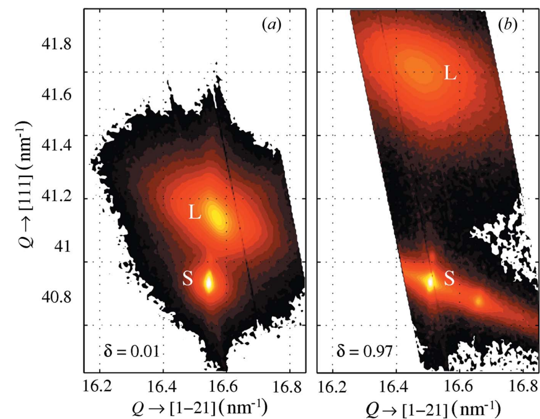

Figure 4
Asymmetric reciprocal-space maps of two $Bi_2Te_{3-\delta}$ layers grown with the highest (*a*) and lowest (*b*) excess Te flux rates and Te deficit $\delta \simeq 0$ and $\delta \simeq 1$, respectively, showing the (313) diffraction peaks of the substrate (denoted by S) and the $(1\bar{1}0\,20)$ maxima of the layer (L). The step of the iso-intensity contours is $10^{0.2}$.

4. Theory of X-ray diffraction from a random stack of layers

For the analysis of the measured diffraction data, we developed a theoretical description of X-ray diffraction from a random stack of layers based on the statistical theory of diffraction from randomly layered systems (Holstein, 1993). An elegant matrix formulation of this problem was proposed by Croset & de Beauvais (1997, 1998) and used for the description of X-ray diffraction from epitaxial layers with a random sequence of layers by Kopp *et al.* (2012). As we stated above, the structure of every trigonal (hexagonal) Bi_mTe_n phase can be described by the face-centered cubic like stacking of two-dimensional hexagonal (0001) arrays of Bi and Te atoms with different stacking sequence including Te–Bi–Te–Bi–Te quintuples as well as Bi–Bi double layers. Depending on the Te flux used during MBE deposition, the number of quintuplets n_j between the $(j-1)$th and jth Bi–Bi double layers can vary. In the following, we assume that n_j are random and the values n_j, n_k, $j \neq k$, are statistically independent. For the genuine (*i.e.* ideally periodic) Bi_2Te_3 and Bi_1Te_1 phases $n_j \to \infty$ and $n_j = 2$ hold, respectively (see Fig. 1). We assume that the measured intensity of diffracted X-rays is averaged over the statistical ensemble of all possible sequences of numbers n_j. This assumption is justified because

Reprinted page 5 of paper [49] "Structure of Bi_2Te_{3-x} films".

in our diffraction experiment the irradiated sample area is, by many orders of magnitude, larger than the coherence width of the primary X-ray beam (which lies below 1 μm). Using kinematical approximation of X-ray diffraction and restricting ourselves to symmetric diffraction only, the amplitude $E(Q)$ of the wave diffracted from a given sequence of two-dimensional arrays (characterized by the given sequence of n_j values) is given by

$$E(Q) = A \sum_{k=1}^{M} f_k(q) \exp(-iqz_k). \tag{2}$$

Here, A is the constant containing the primary intensity and polarization factor, $Q = 4\pi/\lambda \sin(\alpha_i)$ is the length of the scattering vector (α_i is the incidence angle), q is the complex length of the scattering vector corrected for refraction and absorption, m is the total number of two-dimensional atomic layers in the coherently irradiated volume, z_k is the coordinate of the kth layer along [0001], and f_k is the atomic scattering factor of the atoms in layer k consisting either of Bi or Te atoms (f_{Te} or f_{Bi}).

The sequence of the coordinates z_k is constructed from a given set of n_j values using the following rules:

(1) The inter-plane distances in the quintuplet not adjacent to a Bi–Bi doublet (*i.e.* in the layer sequence of ...Te‖Te–Bi–Te–Bi–Te‖Te...) are given by Δz_1, Δz_2, Δz_3, Δz_2, Δz_1, where Δz_1 is the distance of the van der Waals bonded Te–Te layers and $\Delta z_{2,3}$ are the Te–Bi distances with the QL.

(2) If a quintuplet adjoins a Bi–Bi doublet (*i.e.* for the layer sequence ...Te‖Bi–Bi‖Te–Bi–Te–Bi–Te‖Te...), the inter-plane distances are Δz_6, Δz_7, Δz_6, Δz_5, Δz_4, Δz_3, Δz_2, Δz_1, where the corresponding inter-plane distances are indicated in Fig. 1.

(3) If both ends of a quintuplet are attached to Bi–Bi doublets (sequence ...Te‖Bi–Bi‖Te–Bi–Te–Bi–Te‖Bi–Bi‖Te...), the inter-plane distances are Δz_6, Δz_7, Δz_6, Δz_5, Δz_4, Δz_4, Δz_5, Δz_6, Δz_7, Δz_6.

(4) A Bi–Bi doublet cannot adjoin another doublet; at least one quintuplet must occur between two doublets.

In this notation, $\Delta z_{2,3}$ correspond to the Te–Bi inter-plane spacings within a QL not adjacent to a Bi–Bi DL and Δz_1 is the inter-plane distance in the van der Waals bonded Te–Te double layer adjoining two QLs. If a QL adjoins a Bi–Bi DL, its inter-plane distances are modified from $\Delta z_{2,3,3,2}$ to $\Delta z_{2,3,4,5}$. Δz_6 is the inter-plane distances between the last Te layer of a QL and the first Bi layer in the DL, and Δz_7 is the distance between the Bi layers in the Bi–Bi DL. From our simulations it turned out, however, that the results are almost insensitive to the distances $\Delta z_{4,5}$. Therefore, we replaced these values by the corresponding distances $\Delta z_{3,2}$ within the quintuplets in the pure Bi_2Te_3 phase.

Using the rules listed above, we calculated directly the diffracted intensity averaged over the statistical ensemble of all random sequences $\{n_j,\ j = 1, \ldots, P,\ \langle n_j \rangle = N\}$ of the numbers of QLs between two Bi–Bi DLs; P is the total number of structure units in the layer stack (*i.e.* the total number of Bi–Bi DLs); the jth unit comprises n_j QLs and one Bi–Bi DL. The formula for the ensemble-averaged intensity is quite cumbersome and it is presented in Appendix *A*.

The diffracted intensity exhibits rapid oscillations caused by the fixed length of the layer stack; the period of the oscillations is roughly $2\pi/[(5N+2)\langle\Delta z\rangle]$, where $\langle\Delta z\rangle$ is the mean inter-plane distance and $N \equiv \langle n_j \rangle$ is the mean number of QLs between subsequent Bi–Bi DLs. In order to suppress these nonphysical oscillations we performed a numerical convolution of the calculated diffraction curve with a suitable peak function (we used a standard Gaussian function) corresponding to the limited coherence width L_{coh} of the incoming X-ray beam. The full width at half-maximum of this function is $2\pi/L_{coh}$. In the simulations we assumed L_{coh} = 0.2 μm (*i.e.* much longer than the QL length) and chose the number P of the structure units so large that the total thickness of the layer stack fairly exceeds L_{coh}. The value of L_{coh} affects only the widths of the diffraction peaks. The nominal layer thickness of 350 nm slightly exceeded L_{coh}; however, structure defects not included in the stacking model broadened the measured diffraction maxima.

The simulation model used here is similar to the statistical models of layered systems based on the Markow chain of the first order and published previously by Kopp *et al.* (2012). Both models can be directly compared, if we use n_j quintuple layers and one Bi–Bi double layer as the structure unit used in these works. As the number of n_j values could be large, our system is a 'many-state system' in the terminology used by Kopp *et al.* (2012). The matrix formalism used in the cited works is rather complicated for such many-state systems, and the direct averaging described in Appendix *A* can be used instead.

In Figs. 5, 6 and 7, we present illustrative results of the numerical simulations of the diffracted intensity along the (000L) direction for different lattice structures. First, let us consider ideally periodic Bi_mTe_n phases [denoted by (mn)] with various N. The corresponding diffraction curves are shown in Fig. 5, where the curve $N \to \infty$ corresponds to the ideal (23) phase, and N = 1, 2, 3, 5 refer to the (43), (11), (67) and (45) phases, respectively. As stated above, the diffraction maxima of Bi_2Te_3 along the (000L) rod appear only for $L = 3p$ (p is an integer), because the three quintuplets occurring in the unit cell are identical in symmetric (000L) diffraction, and therefore a three-times smaller structure unit (one QL) acts as the unit cell for symmetrical diffraction. We emphasize that the (00012) diffraction is almost forbidden in Bi_2Te_3, as its position nearly coincides with a sharp minimum of the structure factor of one QL, which is represented by the superimposed blue dashed curve in Fig. 5. Therefore, the intensity of the (00012) maximum is extremely sensitive to the inter-plane distances $\Delta z_{1,2,3}$ in the QL. Most notable, for $N \geq 2$, *i.e.* large distances of the Bi–Bi double layers, the diffraction curves of the ordered phases exhibit rather closely spaced diffraction peaks arising from the natural superlattice period produced by the periodically inserted Bi–Bi DLs, where the satellite spacing decreases inversely proportionally to N.

For the analysis of the positions of the diffraction peaks of the ideally ordered phases, let us assume for the moment that

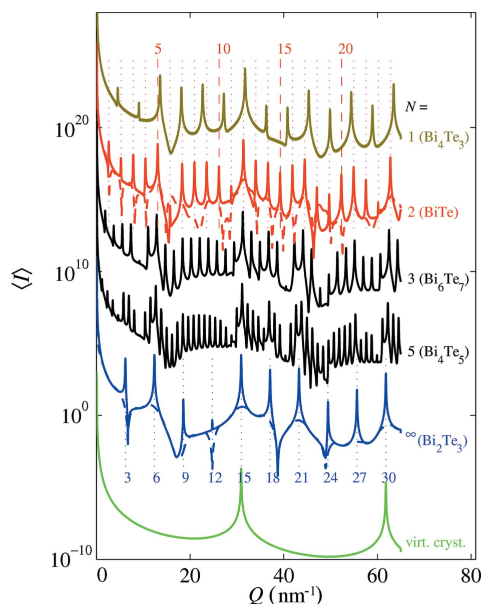

Figure 5
Diffraction curves calculated along the symmetric (000L) direction for ideally periodic, *i.e.* perfectly ordered, Bi_mTe_n phases with different (mn) numbers, corresponding to different numbers of quintuplets N = 1, 2, 3, 5 and $N \to \infty$ between two Bi–Bi doublets (see Fig. 1) from top to bottom. The blue and red numbers denote the diffraction indexes L of the (23) and (11) phases, respectively. The bottom green line represents the diffraction curve of a 'virtual' crystal having constant inter-plane distances and containing identical atoms. The blue and red dashed curves superimposed on the diffraction curves for the (11) and (23) phases are the structure factors of one QL and of one unit cell of the (11) phase, respectively. The curves are shifted vertically for clarity.

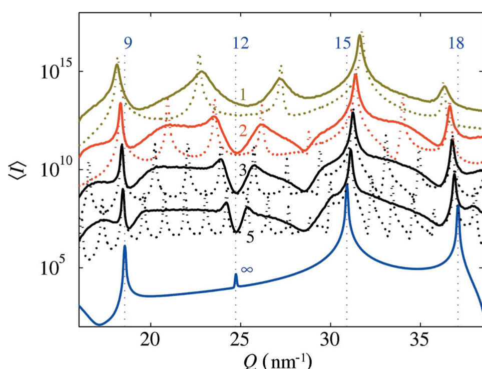

Figure 6
Details of the diffraction curves along the (000L) rod in the vicinity of the $(0\,0\,0\,12)^{(23)}$ maximum, calculated for various values of N of QLs between the Bi–Bi DLs for perfectly ordered phases, *i.e.* $m \to \infty$ (dotted lines), and for disordered phases with m = 10 (full lines). The values of N are indicated; the curves are shifted vertically for clarity. The vertical dotted lines and the blue numbers denote the theoretical positions and L values of the diffraction maxima of the (23) phase.

the inter-plane distances Δz_i are identical and equal to the mean inter-plane distance $\langle \Delta z \rangle$ of the actual structure. If the layers contain identical atoms (a virtual 'mixture' of Bi and Te atoms, for instance), the diffraction peaks of such a virtual crystal (VC) will appear at the following points on the (000L) rod,

$$Q_L^{(\mathrm{VC})} = \frac{2\pi}{\langle \Delta z \rangle} L, \qquad (3)$$

where L is an integer. The diffraction curve of such a virtual structure is plotted in Fig. 5 (bottom green line). Now, let us replace the virtual atoms in the layers by a sequence of Bi and Te atoms corresponding to an ideally ordered (mn) phase, keeping the same average inter-plane distance $\langle \Delta z \rangle$. This chemical modulation results in additional peaks that can be considered as modulation (superlattice) maxima accompanying the main mean maxima in equation (3). If the elementary unit cell of the ideally ordered (mn) phase consists of N_{Q} (Te–Bi–Te–Bi–Te) QLs and N_{D} (Bi–Bi) DLs, the maxima will appear at the points

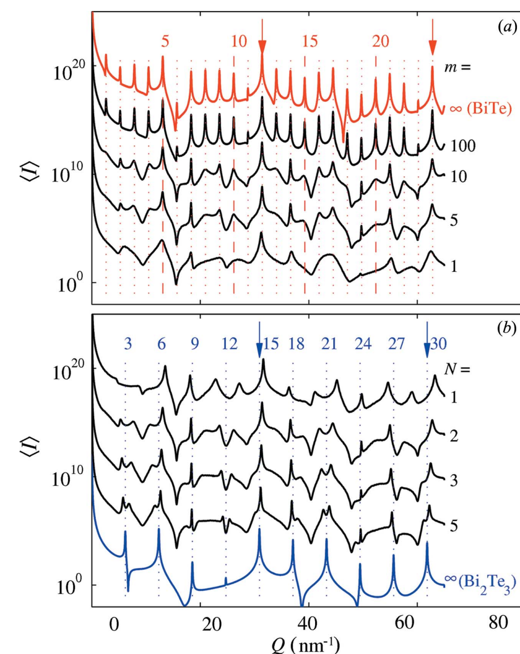

Figure 7
(000L) diffraction curves simulated for disordered Bi_nTe_m structures: (*a*) diffraction curves for Bi_1Te_1 with a constant number of QLs N = 2 but increasingly random positions of the Bi–Bi DLs in the crystal, as described by the different orders m of the γ distribution of the random numbers of QLs between two DLs; (*b*) shows the effect of disorder for different values of N from N = 1 [which corresponds to the disordered (11) phase] to $N \to \infty$ [(23) phase] and constant m = 10. The red numbers in (*a*) and the blue numbers in (*b*) denote the positions of the diffraction maxima and their indexes L of the (11) and (23) phases, respectively. The arrows denote the diffraction peaks of the virtual crystal (see text); the curves are shifted vertically for clarity.

Reprinted page 7 of paper [49] "Structure of Bi_2Te_{3-x} films".

$$Q_L^{(mn)} = \frac{2\pi}{(5N_Q + 2N_D)\langle\Delta z\rangle} L, \tag{4}$$

if we still assume constant inter-plane distances $\langle\Delta z\rangle$. Obviously $(m : n) = (2N_Q + 2N_D) : (3N_Q)$ must hold. For instance, in the (23) phase $N_Q = 3$ and $N_D = 0$ and, thus, the diffraction maxima appear at the points

$$Q_L^{(23)} = \frac{2\pi}{15\langle\Delta z\rangle} L \equiv \frac{2\pi}{5\langle\Delta z\rangle} p, \tag{5}$$

because only the maxima with $L = 3p$ (p is an integer) are allowed. In the (11) phase, $N_Q = 2$ and $N_D = 1$, *i.e.* the diffraction maxima are at

$$Q_L^{(11)} = \frac{2\pi}{12\langle\Delta z\rangle} L. \tag{6}$$

Let us now compare the positions of the diffraction maxima of different (mn) phases assuming the same value of $\langle\Delta z\rangle$ in all phases. From equations (3)–(6), it follows that only the maximum $(0\,0\,0\,15t)^{(23)}$ (t is an integer) of the (23) phase coincides with the maxima of other phases; these maxima correspond to the averaged structure used in equation (3) and their distance is $\Delta Q = 2\pi/\langle\Delta z\rangle$. If $t = 1$, for instance, the maximum $(0\,0\,0\,15)^{(23)}$ coincides with the maxima $(0007)^{(43)}$, $(0\,0\,0\,12)^{(11)}$, $(0\,0\,0\,17)^{(67)}$ and $(0\,0\,0\,27)^{(45)}$ of the phases (43), (11), (67) and (45), respectively; this maximum is equivalent to the first diffraction peak $(0001)^{(VC)}$ of the VC. Analogously, all maxima $(0\,0\,0\,15t)^{(23)}$ are equivalent to the VC diffraction maxima $(000t)^{(VC)}$. Because, as we show later, the average inter-plane distance $\langle\Delta z\rangle$ gradually decreases with decreasing N, these maxima move to larger Q with decreasing N, *i.e.* when moving from (23) towards the pure (11) phase. On the other hand, however, the positions of other maxima move in different ways with decreasing N. For instance, the maximum $(0\,0\,0\,18)^{(23)}$ does not correspond to any maximum of other (mn) phases, which is obvious from Fig. 5. In fact, with decreasing N, this maximum splits up into two maxima, with a separation that increases with decreasing N. In the case $N = 2$, however, only the left maximum from this pair appears [which corresponds to the $(0\,0\,0\,14)^{(11)}$ peak], as the right one coincides with a local minimum of the structure factor of the (11) phase (the red dashed curve in Fig. 5). Therefore, the maximum $(0\,0\,0\,18)^{(23)}$ seems to move to smaller Q with decreasing N. In the position of the almost forbidden maximum $(0\,0\,0\,12)^{(23)}$ a similar splitting occurs, converting to the diffraction maxima $(0009)^{(11)}$ and $(0\,0\,0\,10)^{(11)}$ of the (11) phase.

From this analysis it follows that only the diffraction maxima $(0001)^{(VC)} \equiv (0\,0\,0\,15)^{(23)} \to (0\,0\,0\,12)^{(11)} \to (0007)^{(43)}$ and $(0002)^{(VC)} \equiv (0\,0\,0\,30)^{(23)} \to (0\,0\,0\,24)^{(11)} \to (0\,0\,0\,14)^{(43)}$ can be used for the determination of the dependence of $\langle\Delta z\rangle$ on N. Fig. 6 demonstrates in detail the various types of the maxima described above. The VC maximum $(0\,0\,0\,15)^{(23)}$ moves to larger Q if we decrease N. This behavior corresponds to a decrease of $\langle\Delta z\rangle$ with decreasing N. On the other hand, the maximum $(0\,0\,0\,12)^{(23)}$ splits into a pair of maxima and, conversely, $(0009)^{(23)}$ and $(0\,0\,0\,18)^{(23)}$ move to smaller Q. As we explained above, this shift of the maxima does not correspond to an increase of $\langle\Delta z\rangle$.

A comparison of the measured diffraction curves of Fig. 3 with the curves simulated for perfectly periodic (mn) phases shown in Fig. 5 reveals that only the diffraction curve of the sample with the highest Te excess flux is similar to the calculated diffraction curve of the perfect (23) phase. The other experimental curves exhibit far fewer diffraction maxima than the simulated ones. Thus, the experimental results can only be explained if we assume a certain statistical disorder in the layer sequence. The strong effect of disorder on the simulated diffraction curves for the case of a constant mean number $\langle n\rangle \equiv N = 2$ of QLs between two Bi–Bi DLs, corresponding to an average composition equal to the (11) phase, with the different degrees of disorder accounted for by the order m of the γ distribution of the numbers n of QLs between two adjacent Bi–Bi DLs, is seen in Fig. 7(a). The curve $m = \infty$ corresponds to the ideally ordered (11) phase. When decreasing the order m, evidently the diffraction maxima become broadened and gradually disappear, except for the VC maxima $(0001)^{(VC)} \equiv (0\,0\,0\,12)^{(11)}$ and $(0002)^{(VC)} \equiv (0\,0\,0\,24)^{(11)}$ which correspond to the $(0\,0\,0\,15)^{(23)}$ and $(0\,0\,0\,30)^{(23)}$ peaks of the (23) phase. In Fig. 7(b) we demonstrate the dependence of the simulated diffraction curves on N, keeping the degree of disorder constant at $m = 10$. It is obvious that for small m (*i.e.* large σ_N) only a few modulation peaks persist: for instance, the pair of maxima that originates from the splitting of the $(0\,0\,0\,12)^{(23)}$ maximum is observed, whereas most other modulation peaks (*cf.* Fig. 5) disappear. This is also demonstrated by Fig. 6, where zoomed-in diffraction spectra are shown for the ordered (dotted curves) and disordered (solid curves) structures. However, the persisting splitting of the $(0\,0\,0\,12)^{(23)}$ maximum makes it possible to determine the mean number of QLs N also for disordered structures. The blue and red arrows in Figs. 7(a) and 7(b) denote the positions of the VC diffraction peaks $(0001)^{(VC)} \equiv (0\,0\,0\,15)^{(23)} \equiv (0\,0\,0\,12)^{(11)}$ and $(0002)^{(VC)} \equiv (0\,0\,0\,30)^{(23)} \equiv (0\,0\,0\,24)^{(11)}$. As the mean inter-plane distance $\langle\Delta z\rangle$ in the (23) phase is larger than that in the (11) phase, the VC maxima move to larger Q with decreasing N, *i.e.* when moving from the (23) phase towards (11). It is emphasized that this tendency is preserved also in disordered structures, meaning that the positions of the VC peaks can be used indeed for the determination of $\langle\Delta z\rangle$ in random structures.

5. Quantitative results

To determine the real structure of the $Bi_2Te_{3-\delta}$ epitaxial layers, the measured diffraction curves of all samples were fitted with the above described model, treating the inter-plane distances $\Delta z_{1,2,3,6,7}$ (assuming $\Delta z_4 = \Delta z_3$ and $\Delta z_5 = \Delta z_2$) as well as the mean number of quintuplets N between the Bi–Bi DLs and the order m of the γ distribution of the random numbers n as fit parameters. The fitted diffraction curves are presented as solid lines in Fig. 8, together with the experimental data (points).

Evidently, the fits of the measurements are satisfactory; the regions around the substrate and *Umweganregung* peaks were excluded from the fitting. The remaining discrepancies between the experimental data and the calculated diffraction curves may be caused by sample inhomogeneities both within the layers and on the surfaces.

As a result from the fits, we obtain for each sample the stacking sequences of Bi and Te layers as well as the inter-plane distances $\Delta z_{1,2,3,6,7}$ between the individual lattice planes, and by averaging over all Δz_k, the average inter-plane distance $\langle \Delta z \rangle$ is deduced. In addition, we obtain the overall Te deficit δ of the samples simply by summing up the total number of Te and Bi layers in a given stacking sequence. The composition is also directly related to the average number N of QLs between subsequent Bi–Bi DLs according to

$$\delta = 3/(N+1). \tag{7}$$

As expected, the mean inter-plane distances $\langle \Delta z \rangle$ obtained from the fit agree with the values directly derived from the $(0001)^{(VC)} \equiv (00015)^{(23)} \rightarrow (00012)^{(11)}$ and $(0002)^{(VC)} \equiv (00030)^{(23)} \rightarrow (00024)^{(11)}, \ldots$ peak positions in the diffraction curves. The latter method yields the $\langle \Delta z \rangle$ values with better accuracy because of the limited quality of the fit of the whole diffraction curves and because the former approach is independent of the model. Through the order parameter m, obtained from the fits, we also get information on the randomness of the stacking sequence, *i.e.* degree of deviation of the actual from the perfectly ordered structures.

In Fig. 9, all derived structure parameters of the samples are plotted as a function of the Te deficit δ calculated using the above equation. Fig. 9(*a*) shows the in-plane hexagonal lattice parameter a deduced from the reciprocal-space maps (*cf.* Fig. 4) and Fig. 9(*b*) shows the mean vertical inter-plane distance $\langle \Delta z \rangle$ (black filled circles) obtained from the simulations as functions of the Te deficit δ. Evidently, a gradually increases from a = 0.438 to ~0.44 nm when δ increases from 0 to 1, *i.e.* when the composition changes from (23) to (11). This can be described by a polynomial of $a(\delta)$ of the second order (see below). Conversely, the mean inter-plane distance decreases almost linearly from $\langle \Delta z \rangle$ = 0.2035 to 0.201 nm for the same change in composition. This means that with increasing Te deficit, *i.e.* an increasing number of inserted Bi–Bi DLs, the average inter-plane distance $\langle \Delta z \rangle$ shrinks and the lateral lattice parameter a expands.

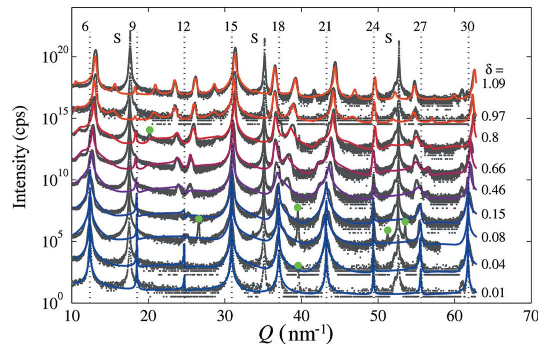

Figure 8
Measured (points) and simulated (lines) diffraction curves for the $Bi_2Te_{3-\delta}$ epitaxial layers grown using various excess Te flux rates, resulting in various Te deficits δ as obtained from the fitting procedure. The vertical dotted lines denote the positions of the diffraction peaks $(000L)^{(23)}$ of the (23) phase with corresponding L values indicated above. The colors of the lines denoting the fitted curves range from blue [(23) phase, δ = 0] to red [(11) phase, δ = 1]. The BaF_2 substrate peaks are marked by S; the curves are shifted vertically for clarity. The green circles mark the *Umweganregung* peaks.

According to literature data for bulk samples of various ordered (mn) phases, represented by the colored circles in Fig. 9(*a*) (Brebrick, 1968; Shimazaki & Ozawa, 1978; Yamana *et al.*, 1979; Korzhuev *et al.*, 1992; Feutelais *et al.*, 1993; Safarov, 1994; Bos *et al.*, 2007), the dependence of a_{bulk} of bulk Bi_mTe_n on δ can be expressed by a polynomial of the second order, too. On the basis of this observation, we interpolate the tabulated values of a_{bulk} to obtain the expected lateral lattice parameters a_{bulk} of the bulk materials having the same Te deficit δ as in our layers. These values, denoted by empty circles in Fig. 9(*a*), are assumed as relaxed lattice parameters of our $Bi_2Te_{3-\delta}$ layers ($a_{relaxed}$). The deviations between our values of a obtained for the epilayers [black circles in Fig. 9(*a*)] and those extrapolated from the bulk literature data are ascribed to a partial strain in the investigated samples due to the BaF_2 substrate, where with increasing Te deficit δ and a corresponding increase of in-plane lattice parameter a, a small but increasing lattice misfit develops.

In order to compare our values of the mean inter-plane distances $\langle \Delta z \rangle$ (black filled circles in Fig. 9*b*) with the published data for bulk material, we calculated the corresponding relaxed inter-plane distances $\langle \Delta z \rangle_{relaxed}$ using the elastic equilibrium formula

$$\langle \Delta z \rangle_{relaxed} = \langle \Delta z \rangle \left(1 + \frac{2C_{13}}{C_{33}} \frac{a - a_{relaxed}}{a_{relaxed}} \right), \tag{8}$$

where $C_{13,33}$ are the elastic constants of Bi_2Te_3 taken from the paper by Jenkins *et al.* (1972) (we neglected their dependence on δ). Fig. 9(*b*) shows the relaxed mean inter-plane distances of our layers (empty circles) in comparison with the distances reported for ideally ordered (mn) phases (Bos *et al.*, 2007) (colored circles). Clearly, after the strain correction the mean inter-plane distances agree very well with the published values for ideally ordered phases.

From this analysis, we obtain the following relations between the lattice parameters a and mean inter-plane distances $\langle \Delta z \rangle$ of the $Bi_2Te_{3-\delta}$ epitaxial layers as functions of the Te deficit δ:

$$\begin{aligned} a &= 0.0026\,(5)\,\delta^2 + 0.43764\,(8)\ (\text{nm}), \\ \langle \Delta z \rangle &= -0.0027\,(2)\,\delta + 0.2037\,(1)\ (\text{nm}). \end{aligned} \tag{9}$$

If we correct these values for the partial strain relaxation by equation (8), we obtain the values for the corresponding relaxed lattices

$$a_{\text{relaxed}} = -0.0023\,(1)\,\delta^2 + 0.0075\,(1)\,\delta + 0.43828\,(2)\ \text{(nm)},$$
$$\langle \Delta z \rangle_{\text{relaxed}} = 0.0019\,(1)\,\delta^2 - 0.0052\,(3)\,\delta + 0.2032\,(1)\ \text{(nm)}. \tag{10}$$

The numbers in the parentheses in equations (9) and (10) denote the statistical errors of the last digits. From these relations, the composition, *i.e.* Te/Bi content, in any $Bi_2Te_{3-\delta}$ samples can be deduced simply by measuring their in-plane lattice parameter a and/or the mean inter-plane distance $\langle \Delta z \rangle$ as described above. In particular, the inter-plane distances $\langle \Delta z \rangle$ (Fig. 9*b*) show a linear dependence on the Te deficit δ, nicely following the Vegard law in the range of δ from 0 to 1, *i.e.* between the pure Bi_2Te_3 and BiTe phases. This continuous dependence is an indication that the samples with intermediate compositions can be regarded as one-dimensional random alloys of these two phases. Furthermore, Figs. 9(*a*) and 9(*b*) indicate that the (43) phase deposited onto the $BaF_2(111)$ substrate should be stress-free, as both a, a_{relaxed} and $\langle \Delta z \rangle$, $\langle \Delta z \rangle_{\text{relaxed}}$ coincide if we extrapolate their values to $\delta \rightarrow 3/2$.

From the fits, we also obtain the δ dependences of the individual inter-plane distances $\Delta z_{1,2,3,6,7}$ between the lattice planes (see Fig. 1), and the results are presented in Fig. 9(*c*). Evidently, the inter-plane distances $\Delta z_{2,3}$ *within* the QLs and Δz_1 between *adjacent* quintuplets (black circles) are almost independent of the Te deficit δ, *i.e.* on the mean number N of QLs between the Bi–Bi DLs. In addition, the values agree well with the published ones for bulk Bi_2Te_3 (blue circles) (Safarov, 1994). This indicates that the QL building blocks of the $Bi_2Te_{3-\delta}$ compounds are practically unaffected by the insertion of additional Bi–Bi DLs. Conversely, the inter-plane distances *inside* the Bi–Bi DL (Δz_7) and *between* the DL and the first Te layer of the adjacent QL (Δz_6) (open symbols in Fig. 9*c*) strongly change on changing the Te deficit δ; namely Δz_7 inside the Bi–Bi DL decreases with increasing δ, and the separation between the DL and adjacent QL (Δz_6) increases. It is also noted that, while our values for Δz_j agree well with literature values for $\delta = 0$ (*i.e.* for Bi_2Te_3), a significant deviation is found when $\delta = 1$ (*i.e.* $Bi_2Te_2 \equiv Bi_1Te_1$ phase) (Yamana *et al.*, 1979), represented by the blue and red circles in Fig. 9(*c*), respectively. The latter observation may be explained by the fact that the lattice parameters a and $\langle \Delta z \rangle$ of our epitaxial layers have already deviated from the bulk literature values.

Fig. 9(*d*) shows the degree of stacking disorder as a function of the Te deficit δ, quantified in terms of the relative r.m.s. deviation σ_N/N of the number of QLs between two DLs. The r.m.s. deviations are very small for $\delta = 0$ and $\delta \rightarrow 1$, *i.e.* for composition close to the pure (23) and (11) phases, meaning that well ordered structures are formed in these cases. Between these limiting cases, however, the structures are highly disordered, and the maximum disorder is present for the sample with $\delta \simeq 0.15$, *i.e.* $N \simeq 19$. In this case, $\sigma_N \simeq N$ and therefore the random numbers n of the QLs between two Bi–Bi DLs are distributed according to a geometrical distribution. This distribution is 'memoryless', *i.e.* the sequence of doublets and quintuplets can be described by the Markow chain of the first order with one QL and one DL as two states. In such a chain, the probability that a quintuplet is followed by a doublet does not depend on the position of the previous doublet in the sequence. This is quite reasonable because, for very large average distances N between consecutive Bi–Bi doublets, it is rather unlikely that a sufficiently strong interaction exists that can mediate any ordering process.

Finally, we have also investigated the influence of the chemical composition on the carrier concentration and carrier mobilities of the layers. From Hall-effect measurements, we find for the samples with composition very close to Bi_2Te_3 ($\delta < 0.08$), an n-type conduction with an electron

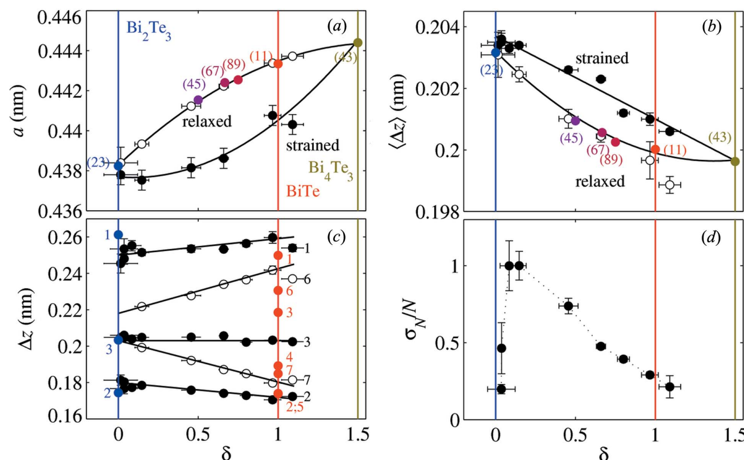

Figure 9
(*a*) Measured lateral lattice parameters a (black circles) of our $Bi_2Te_{3-\delta}$ epitaxial layers and calculated relaxed lateral lattice parameters (open circles) obtained by interpolation of the literature data plotted as a function of the Te deficit δ obtained from the fit. (*b*) Mean inter-plane distances $\langle \Delta z \rangle$ determined from the positions of the $(0\,0\,0\,15)^{(23)}$ and $(0\,0\,0\,30)^{(23)}$ diffraction maxima (black circles) as a function of δ. Open circles denote the relaxed values of $\langle \Delta z \rangle$ obtained after correction for the lateral strain using equation (8). Colored circles labeled with (mn) represent published lattice parameters a [in (*a*)] and inter-plane distances [in (*b*)] for ideally ordered bulk Bi_mTe_n phases (Bos *et al.*, 2007). (*c*) Inter-plane distances $\Delta z_{1,2,3,6,7}$ determined from the fit of the diffraction curves *versus* δ. The inter-plane distances for bulk Bi_2Te_3 and Bi_1Te_1 (Safarov, 1994; Yamana *et al.*, 1979) are denoted by blue and red circles, respectively. (*d*) The relative r.m.s. deviation σ_N/N of the numbers of QLs between two Bi–Bi DLs, quantifying the degree of disorder in the samples, plotted *versus* δ. In all panels, the vertical black, red and green lines denote the values for the (23), (11) and (43) phases with δ = 0, 1 and 1.5, respectively. The black lines in (*a*), (*b*) and (*c*) represent the linear and parabolic fits of the measured data.

concentration of about n = 2–10 × 10^{18} cm^{-3} and electron mobilities around 900 cm^2 V^{-1} s^{-1} at room temperature and of 1500 cm^2 V^{-1} s^{-1} at 77 K. For all other samples, the electron concentration is well above 10^{20} cm^{-3}, *i.e.* two orders of magnitude larger, and it tends to increase up to 10^{21} cm^{-3} with increasing Te deficit δ. This indicates that the Bi–Bi DLs act as electron donors. In fact, for Bi_2Te_3 epitaxial layers grown with very high excess Te flux containing exclusively QLs, we can also obtain *p*-doped layers. For the Te-deficit layers with high electron concentration and $\delta \geq 0.1$, the mobilities drop to around 30 cm^2 V^{-1} s^{-1}, practically independent of temperature and composition. This agrees well with the high degree of structural disorder in these samples, not only vertically but also laterally as shown in Fig. 2. The latter is due to the asynchronous incorporation of the Bi–Bi doublets across the surface during growth, which gives rise to a high density of domain boundaries in the lateral direction. Thus, the growth conditions and composition play a crucial role not only for the structure of the samples but also for the electronic transport properties, which are crucial for device applications.

6. Summary

In summary, we have determined the structural and growth properties of topological insulator $Bi_2Te_{3-\delta}$ layers grown by molecular beam epitaxy on $BaF_2(111)$ substrates. We have demonstrated that, depending on the excess Te flux employed during deposition, the actual chemical composition $Bi_2Te_{3-\delta}$ varies from δ = 1 with no excess Te flux up to δ = 0 for the highest excess flux. The Te content of the epilayers has a profound influence on their surface morphology as well as on the structural and transport properties. A detailed analysis of the X-ray diffraction curves using a statistical model of the layer stacking revealed that the actual stacking of the two-dimensional Bi and Te layers consists of a random sequence of Te–Bi–Te–Bi–Te quintuple layers and Bi–Bi double layers. From the fits of the diffraction data, we determined the δ dependencies of the in-plane lattice parameters and the mean inter-plane distances, revealing that these values continuously change as functions of composition, as expected for random alloys between Bi_2Te_3 ($\delta = 0$) and BiTe ($\delta = 1$). However, as the change in composition is accommodated by insertion of a larger or smaller number of two-dimensional Bi–Bi double layers in between the quintuple layers, exclusively absent only for Bi_2Te_3, these structures must be regarded as one-dimensional random alloys rather than as three-dimensional alloys with statistical occupancy of individual lattice sites by Te or Bi atoms. The relaxed lattice parameters determined by X-ray diffraction agree well with those of the homologous series of ordered Bi_mTe_n bulk crystals published in the literature. The individual inter-plane distances within and between the quintuple layers are found to be nearly independent of composition, whereas the distances in the Bi–Bi doublets and between the last Te layer in a quintuplet and the first Bi layer in the following doublet strongly depend on composition and are thus responsible for the change of the overall lattice constants. According to our simulations of the diffraction data, the Bi_2Te_3 and Bi_1Te_1 phases are quite well ordered, while the intermediate phases exhibit a high degree of disorder with a maximum disorder for $\delta \simeq 1$. In these structures, the statistical distribution of the number of quintuple layers between Bi–Bi double layers can be approximated by a Poisson distribution.

The composition and disorder strongly affect the electronic properties of the layers, and low carrier concentrations and high mobilities can only be achieved for $\delta \simeq 0$, corresponding to the Bi_2Te_3 phase without any Bi–Bi double layers. As shown previously (Caha *et al.*, 2013; Sanchez-Barriga *et al.*, 2014), these layers are well suited for investigations of their topological surface states and their spin polarization using angular-resolved photoemission spectroscopy.

APPENDIX *A*
Averaging of the diffracted intensity over random numbers of the quintuple layers

We define the *j*th structure unit containing n_j QLs and one Bi–Bi DL. From the rules for the construction of the layer sequence listed in §4, we derive the following formula for the unit thickness

$$D_j = (n_j - 1)(\Delta z_1 + 2\Delta z_2 + 2\Delta z_3) + 2(\Delta z_4 + \Delta z_5 + \Delta z_6) + \Delta z_7, \quad (11)$$

where Δz_j are the inter-plane distances defined in Fig. 1. The structure factor of the *j*th unit is calculated as a sum of the contributions of individual layers comprising one unit:

$$F_j(q) = \sum_{t=1}^{5n_j+2} f_t(q) \exp(-iqz'_t), \quad (12)$$

where z'_t is the vertical coordinate of the *t*th layer within the structure unit, starting from $z'_1 = 0$. The formula for the diffracted intensity can be reformulated using the structure factors of the units as follows,

$$E(Q) = A \sum_{j=1}^{P} F_j(q) \exp(-iqz_j), \;\; z_j = D_1 + \cdots + D_{j-1}, \quad (13)$$

and for the ensemble-averaged intensity we obtain

$$I(Q) = |A|^2 \Bigg(\sum_{j=1}^{P} \big\langle |F_j(q)|^2 \exp\left[2\mathrm{Im}(q) z_j\right] \big\rangle + 2\mathrm{Re}\Bigg\{ \sum_{j=2}^{P} \sum_{j'=1}^{j-1} \Big\langle F_j(q) F_{j'}(q)^* \exp\left[-i(qz_j - q^* z_{j'})\right] \Big\rangle \Bigg\} \Bigg). \quad (14)$$

Performing the ensemble averaging $\langle\ \rangle$ we assume that the random numbers n_j of of the QLs are statistically independent. Then, after some algebra we obtain the following final formula for the averaged intensity,

$$I(Q) = |A|^2 \left\{ \gamma \frac{\zeta^P - 1}{\zeta - 1} + 2\mathrm{Re}\left[\frac{\alpha\beta}{\zeta - \xi} \left(\frac{\zeta^P - 1}{\zeta - 1} - \frac{\xi^P - 1}{\xi - 1} \right) \right] \right\}, \quad (15)$$

where we used the following notation:

$$\xi = \langle \exp(iqD) \rangle, \ \zeta = \langle \exp[2\mathrm{Im}(q)D] \rangle, \\ \alpha = \langle F \rangle, \ \beta = \langle F^* \exp(-iqD) \rangle, \ \gamma = \langle |F|^2 \rangle. \tag{16}$$

These averages were calculated numerically assuming a γ distribution of the random numbers n_j with the averaged value N and order m. Neglecting the absorption [*i.e.* putting $\mathrm{Im}(q) = 0$] and assuming a very large number of structure units ($P \to \infty$), the resulting formula for the averaged intensity is rather simple:

$$I(Q) \to P|A|^2 \left[\gamma + 2\mathrm{Re}\left(\frac{\alpha\beta}{1-\xi} \right) \right]. \tag{17}$$

The work was supported by the Czech Science Foundation (project 14-08124S) and the Austrian Science Fund FWF (project IRON-SFB025).

References

Borisova, S., Krumrain, J., Luysberg, M., Mussler, G. & Grutzmacher, D. (2012). *Cryst. Growth Des.* **12**, 6098.

Bos, J. W. G., Zandbergen, H. W., Lee, M.-H., Ong, N. P. & Cava, R. J. (2007). *Phys. Rev. B*, **75**, 195203.

Brebrick, R. F. (1968). *J. Appl. Cryst.* **1**, 241–246.

Caha, O., Dubroka, A., Humlicek, J., Holy, V., Steiner, H., Ul-Hassan, M., Sanchez-Barriga, J., Rader, O., Stanislavchuk, T. N., Sirenko, A. A., Bauer, G. & Springholz, G. (2013). *Cryst. Growth Des.* **13**, 3365–3373.

Cao, H., Venkatasubramanian, R., Liu, C., Pierce, J., Yang, H., Hasan, M. Z., Wu, Y. & Chen, Y. P. (2012). *Appl. Phys. Lett.* **101**, 132104.

Cava, R. J., Ji, H., Fuccillo, M. K., Gibson, Q. D. & Hor, Y. S. (2013). *J. Mater. Chem. C*, **1**, 31763189.

Chen, X., Ma, X. C., He, K., Jia, J. F. & Xue, Q. K. (2011). *Adv. Mater.* **23**, 1162–1165.

Chen, Y. L., Analytis, J. G., Chu, J. H., Liu, Z. K., Mo, S. K., Qi, X. L., Zhang, H. J., Lu, D. H., Dai, X., Fang, Z., Zhang, S. C., Fisher, I. R., Hussain, Z. & Shen, Z. X. (2009). *Science*, **325**, 178–181.

Croset, B. & de Beauvais, C. (1997). *Surf. Sci.* **384**, 15–35.

Croset, B. & de Beauvais, C. (1998). *Surf. Sci.* **409**, 403–412.

Feutelais, Y., Legendre, B., Rodier, N. & Agafonov, V. N. (1993). *Mater. Res. Bull.* **28**, 591–596.

Fukui, N., Hirahara, T., Shirasawa, T., Takahasi, T., Kobayashi, K. & Hasegawa, S. (2012). *Phys. Rev. B*, **85**, 115426.

Hasan, M. Z. & Kane, C. L. (2010). *Rev. Mod. Phys.* **82**, 3045.

He, L., Kou, X. & Wang, K. L. (2013). *Phys. Status Solidi RRL*, **7**, 50.

Holstein, W. L. (1993). *J. Appl. Phys.* **74**, 4963–4971.

Hsieh, D., Xia, Y., Qian, D., Wray, L., Meier, F., Dil, J. H., Osterwalder, J., Patthey, L., Fedorov, A. V., Lin, H., Bansil, A., Grauer, D., Hor, Y. S., Cava, R. J. & Hasan, M. Z. (2009). *Phys. Rev. Lett.* **103**, 146401.

Jenkins, J. O., Ure, R. W. & Rayne, J. A. (1972). *Phys. Rev. B*, **5**, 3171–3184.

Kim, Y., Cho, S., DiVenere, A., Wong, G. K. L. & Ketterson, J. B. (2001). *Phys. Rev. B*, **63**, 155306.

Kopp, V. S., Kaganer, V. M., Schwarzkopf, J., Waidick, F., Remmele, T., Kwasniewski, A. & Schmidbauer, M. (2012). *Acta Cryst.* A**68**, 148–155.

Korzhuev, M. A., Chizhevskaya, S. N., Svechnikova, T. E., Karpinskii, O. G., Arakcheeva, A. V., Lubman, G. U. & Milykh, A. N. (1992). *Inorg. Mater.* **28**, 1093–1097.

Krumrain, J., Mussler, G., Borisova, S., Stoica, T., Plucinski, L., Schneider, C. M. & Grutzmacher, D. (2011). *J. Cryst. Growth*, **324**, 115.

Li, Y. Y. *et al.* (2010). *Adv. Mater.* **22**, 4002–4007.

Lind, H. & Lidin, S. (2003). *Solid State Sci.* **5**, 47–57.

Lind, H., Lidin, S. & Haussermann, U. (2005). *Phys. Rev. B*, **72**, 184101.

Liu, H. W., Yuan, H. T., Fukui, N., Zhang, L., Jia, J. F., Iwasa, Y., Chen, M. W., Hashizume, T., Sakurai, T. & Xue, Q. K. (2010). *Cryst. Growth Des.* **10**, 4491.

Liu, X., Smith, D. J., Fan, J., Zhang, Y.-H., Cao, H., Chen, Y. P., Leiner, J., Kirby, B. J., Dobrowolska, M. & Furdyna, J. K. (2011). *Appl. Phys. Lett.* **99**, 171903.

Massalski, T. B. & Okamoto, H. (1996). *Binary Alloy Phase Diagrams.* Materials Park: ASM International.

Moore, J. E. (2010). *Nature*, **464**, 194–198.

Nakajima, S. (1963). *J. Phys. Chem. Solids*, **24**, 479.

Peranio, N., Eibl, O. & Nurnus, J. (2006). *J. Appl. Phys.* **100**, 114306.

Plucinski, L., Mussler, G., Krumrain, J., Herdt, A., Suga, S., Grutzmacher, D. & Schneider, C. M. (2011). *Appl. Phys. Lett.* **98**, 222503.

Qi, X.-L. & Zhang, S.-C. (2011). *Rev. Mod. Phys.* **83**, 1057.

Qu, D. X., Hor, Y. S., Xiong, J., Cava, R. J. & Ong, N. P. (2010). *Science*, **329**, 821–824.

Roushan, P., Seo, J., Parker, C. V., Hor, Y. S., Hsieh, D., Qian, D., Richardella, A., Hasan, M. Z., Cava, R. J. & Yazdani, A. (2009). *Nature*, **460**, 1106–1109.

Safarov, M. G. (1994). *Russ. J. Inorg. Chem.* **39**, 1170–1172.

Sanchez-Barriga, J., Varykhalov, A., Braun, J., Xu, S.-Y., Alidoust, N., Kornilov, O., Minár, J., Hummer, K., Springholz, G., Bauer, G., Schumann, R., Yashina, L. V., Ebert, H., Hasan, M. Z. & Rader, O. (2014). *Phys. Rev. X*, **4**, 011046.

Shimazaki, H. & Ozawa, T. (1978). *Am. Mineral.* **63**, 1162–1165.

Snyder, G. J. & Toberer, E. S. (2008). *Nat. Mater.* **7**, 195.

Stasova, M. M. (1967). *Zh. Strukt. Khim.* **8**, 655.

Teweldebrhan, D., Goyal, V. & Balandin, A. A. (2010). *Nano Lett.* **10**, 1209–1218.

Tritt, T. (1999). *Science*, **283**, 804.

Valla, T., Ji, H., Schoop, L. M., Weber, A. P., Pan, Z.-H., Sadowski, J. T., Vescovo, E., Fedorov, A. V., Caruso, A. N., Gibson, Q. D., Muchler, L., Felser, C. & Cava, R. J. (2012). *Phys. Rev. B*, **86**, 241101(R).

Wyckoff, R. W. G. (1964). *Crystal Structures*, Vol. 2. New York: Wiley.

Xia, Y., Wray, L., Qian, D., Hsieh, D., Pal, A., Lin, H., Bansil, A., Grauer, D., Hor, Y., Cava, R. & Hasan, M. (2009). *Nat. Phys.* **5**, 398.

Yamana, K., Kihara, K. & Matsumoto, T. (1979). *Acta Cryst.* B**35**, 147–149.

Zhang, H., Liu, C., Qi, X., Dai, X., Fang, Z. & Zhang, S. (2009). *Nat. Phys.* **5**, 438.

Zhang, S. X., Yan, L., Qi, J., Zhuo, M., Wang, Y.-Q., Prasankumar, R., Jia, Q. & Picraux, S. (2012). *Thin Solid Films*, **21**, 6459.

Reprinted page 12 of paper [49] "Structure of Bi_2Te_{3-x} films".

4.3 Optical and structural properties of $Bi_2(Se_xTe_{1-x})_3$ alloy

The $Bi_2(Se_xTe_{1-x})_3$ alloy layers were prepared using molecular beam epitaxy. The alloy layers were studied using ellipsometry and reflectivity in the far-infrared to near-UV range (0.06 eV to 6.5 eV) at low and room temperatures. The band gap of the layers was determined, considering the Burstein-Moss shift in highly doped semiconductors. The compositional of the band gap is non-linear with the maximum at about $x_{Se} = 30\,\%$. The alloy is a direct band gap semiconductor for higher selenium concentrations $x_{Se} > 30\,\%$. More tellurium-rich material $x_{Se} < 30\,\%$ has an indirect band gap with maxima of the valence band slightly off Γ-point.

PHYSICAL REVIEW B **96**, 235202 (2017)

Interband absorption edge in the topological insulators $Bi_2(Te_{1-x}Se_x)_3$

A. Dubroka,[1,*] O. Caha,[1] M. Hronček,[1] P. Friš,[1] M. Orlita,[2,3] V. Holý,[1,4] H. Steiner,[5] G. Bauer,[5] G. Springholz,[5] and J. Humlíček[1]

[1]*Department of Condensed Matter Physics and Central European Institute of Technology, Masaryk University, Kotlářská 2, 611 37 Brno, Czech Republic*

[2]*Laboratoire National des Champs Magnetiques Intenses, CNRS-UGA-UPS-INSA-EMFL, 25, avenue des Martyrs, 38042 Grenoble, France*

[3]*Institute of Physics, Charles University in Prague, CZ-121 16 Prague, Czech Republic*

[4]*Department of Condensed Matter Physics, Charles University, Prague, Czech Republic*

[5]*Institut für Halbleiter- und Festkörperphysik, Johannes Kepler Universität, Altenbergerstrasse 69, 4040 Linz, Austria*

(Received 25 September 2017; published 12 December 2017)

We have investigated the optical properties of thin films of topological insulators Bi_2Te_3, Bi_2Se_3, and their alloys $Bi_2(Te_{1-x}Se_x)_3$ on BaF_2 substrates by a combination of infrared ellipsometry and reflectivity in the energy range from 0.06 to 6.5 eV. For the onset of interband absorption in Bi_2Se_3, after the correction for the Burstein-Moss effect, we find the value of the direct band gap of 215 ± 10 meV at 10 K. Our data support the picture that Bi_2Se_3 has a direct band gap located at the Γ point in the Brillouin zone and that the valence band reaches up to the Dirac point and has the shape of a downward-oriented paraboloid, i.e., without a camel-back structure. In Bi_2Te_3, the onset of strong direct interband absorption at 10 K is at a similar energy of about 200 meV, with a weaker additional feature at about 170 meV. Our data support the recent GW band-structure calculations suggesting that the direct interband transition does not occur at the Γ point but near the Z-F line of the Brillouin zone. In the $Bi_2(Te_{1-x}Se_x)_3$ alloy, the energy of the onset of direct interband transitions exhibits a maximum near $x = 0.3$ (i.e., the composition of Bi_2Te_2Se), suggesting that the crossover of the direct interband transitions between the two points in the Brillouin zone occurs close to this composition.

DOI: 10.1103/PhysRevB.96.235202

I. INTRODUCTION

Topological insulators belong to a class of materials that are insulating in the bulk, however on the surface they exhibit topological spin-polarized conducting states [1–4]. Since the spin polarization is potentially usable in spintronic devices, topological insulators have attracted a lot of attention in the past decade. $Bi_2(Te_{1-x}Se_x)_3$ compounds, originally employed for thermoelectric devices due to their large Seebeck constant, belong to this category thanks to the large spin-orbit coupling due to heavy bismuth atoms. The linearly dispersing surface states have been observed by angle-resolved photoemission spectroscopy (ARPES) [3,5–8]. Samples are usually of n-type with the Fermi level located in the conduction band because of the antisite doping related to Se vacancies [9].

The infrared and optical responses of $Bi_2(Te_{1-x}Se_x)_3$ compounds have been studied intensively in order to characterize their vibrational properties [10], interband absorption [11–16], and free charge-carrier properties [13,17–19]. Even the surface states [20–23] and strong Faraday rotation [24] have been observed by infrared spectroscopy. Despite the large experimental effort, several questions remain open. For example, controversial results on the values of the band gaps determined by optical spectroscopy and ARPES were reported [14,18], raising questions about the actual position of the direct interband transition onset in the Brillouin zone. Here we present an infrared spectroscopy study of $Bi_2(Te_{1-x}Se_x)_3$ thin films that focuses on the absorption edge of interband transitions. We discuss and account for the Burstein-Moss (BM) effect in order to obtain band-gap energies. We compare our results with ARPES data and band-structure calculations, and we discuss the location of the onset of direct interband transitions in the Brillouin zone.

The paper is organized as follows: In Sec. II we describe the sample growth, x-ray diffraction results, and details of the analysis of the optical data. The core of the paper is presented in Sec. III, where we discuss the results concerning the onset of interband absorption in Bi_2Se_3 (Sec. III B), Bi_2Te_3 (Sec. III C), and finally in $Bi_2(Te_{1-x}Se_x)_3$ alloys (Sec. III D).

II. EXPERIMENTAL TECHNIQUES

A. Sample preparation and x-ray diffraction

$Bi_2(Te_{1-x}Se_x)_3$ epilayers were grown by molecular beam epitaxy in a Riber 1000 system under ultrahigh-vacuum conditions at a background pressure smaller than 5×10^{-10} mbar. The molecular beams were generated using compound bismuth telluride or bismuth selenide effusion cells (nominal composition of Bi_2Te_3 and Bi_2Se_3, respectively) operated at around 400–500 °C, and separate tellurium or selenium cells operated at around 200–300 °C for stoichiometry control. The ternary alloys were grown combining Bi_2Se_3 and Te effusion cells (low Se content) or Bi_2Te_3 and Se effusion cells (high Se content), respectively. The particular flux rates of the compounds were around 1 Å/s for compound cells and 2–3 Å/s for tellurium or selenium, which were calibrated by a quartz crystal microbalance. The layers were deposited on 1-mm-thick cleaved BaF_2 (111) substrates at a temperature between 300 and 400 °C as measured with an infrared optical pyrometer. The surface structure of the films was monitored by *in situ* reflection high-energy electron diffraction evidencing two-dimensional (2D) growth for all samples under the given

*dubroka@physics.muni.cz

 ©2017 American Physical Society

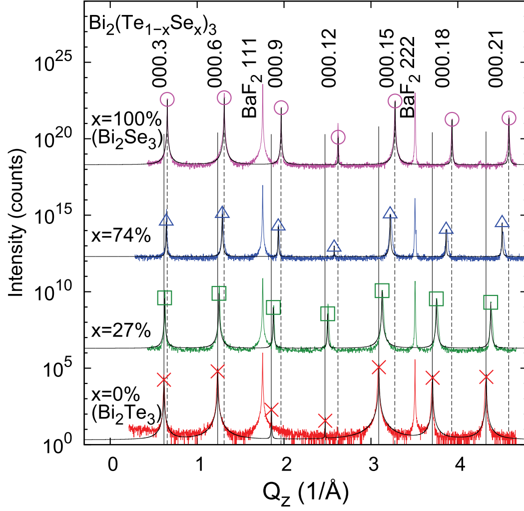

FIG. 1. Symmetric x-ray diffraction scans of our $Bi_2(Te_{1-x}Se_x)_3$ samples ordered from bottom to top with increasing selenium content recorded with Cu $K\alpha_1$ radiation. The spectra are shifted for clarity with respect to each other. The corresponding diffraction peaks shift to the higher Q_z values with increasing selenium content x and decreasing lattice constant c. Solid and dashed lines show the positions of the Bi_2Te_3 and Bi_2Se_3 diffraction peaks, respectively. The symbols denote calculated structure factors of the $Bi_2(Te_{1-x}Se_x)_3$ lattice assuming a random occupation of Te and Se atoms. Thin black lines represent simulated diffraction profiles corresponding to the calculated structure factors.

growth conditions. The Bi_2Te_3 and Bi_2Se_3 thin films from this growth series were recently characterized by x-ray and Raman spectroscopy [25,26].

The crystalline quality and the composition of our thin films were determined using x-ray diffraction. The symmetric scans along the (000l) reciprocal space direction are shown in Fig. 1 with respect to the scattering vector $Q_z = 4\pi/\lambda \sin\theta$, where $\lambda = 1.540\,56$ Å is the radiation wavelength and θ is the Bragg angle. The diffraction peaks of the $Bi_2(Te_{1-x}Se_x)_3$ alloy shift toward higher Q_z values with increasing selenium content and decreasing lattice parameter. The peaks are narrow in the whole composition range, indicating that no phase separation occurs in the studied samples. Since the structure factor of the 000.9 and 000.12 diffractions in Bi_2Te_3 is very small, the corresponding diffraction peaks are very weak. The chemical composition x of the $Bi_2(Te_{1-x}Se_x)_3$ alloy was determined from the c lattice parameter (see Table I) assuming a linear concentration dependence of the lattice parameter (Vegard's law). The intensities of the diffraction peaks in Fig. 1 correspond well to calculated structure factors of random $Bi_2(Te_{1-x}Se_x)_3$ alloys, i.e., with the same probability of Se and Te atoms occupying all of the anionic positions within the crystalline structure. The solid lines in Fig. 1 show simulations of the diffraction spectra with the corresponding structure factors and peak shape given by the Voigt profile with a constant width of 0.003 Å^{-1}, evidencing excellent agreement

TABLE I. Composition, x, lattice parameter along the c-axis, c, thickness, d, square of plasma frequency, ω_{pl}^2, and phonon frequency, ω_α and ω_β, of our $Bi_2(Te_{1-x}Se_x)_3$ thin films determined from 300 K data. The uncertainties of these values are typically 2% for x, 0.05 Å for c, 2% for d, 5% for ω_{pl}^2, and 2 cm^{-1} for ω_α and ω_β.

x (%)	c (Å)	d (nm)	ω_{pl}^2 (10^6 cm^{-2})	ω_α (cm^{-1})	ω_β (cm^{-1})
0	30.54	267	5.2	52	95
27	30.06	519	3.1	63	115
74	29.23	207	1.1	66	
100	28.75	458	3.0	68	129

with the measured data. The width corresponds to the mean size of 100 nm of the coherently diffracting domains. Sharp diffraction peaks indicate high crystalline quality of the layers and homogeneous chemical composition in the layer.

B. The optical spectroscopy and analysis of optical data

The optical properties were probed from the midinfrared to ultraviolet range using a combination of two commercial ellipsometers, Woollam IR-VASE (60–700 meV) and Woollam VASE (0.6–6.5 eV), equipped with variable retarders. In the ellipsometric experiments, the two ellipsometric angles Ψ,Δ and the depolarization are recorded [27]. The angles are linked to the Fresnel reflection coefficients for the p- and s-polarized waves, r_p and r_s, respectively, as $\tan\Psi e^{i\Delta} = r_p/r_s$. From the two angles, using a proper model for the layered structure, the real and imaginary parts of the dielectric function can be determined without the Kramers-Kronig relations. The room-temperature spectra of Ψ and Δ with respect to the photon energy E are shown in Fig. 2 (symbols) together with those of a model (solid lines) described below. The ellipsometric data were complemented in the far-infrared range (4–85 meV, 30–680 cm^{-1}) with near-normal incidence reflectance (see Fig. 3) measured with a Bruker Vertex 80v Fourier transform spectrometer. A gold mirror was used as a reference. The low-temperature data were acquired in the midinfrared range with the Woollam IR-VASE ellipsometer using a closed He-cycle cryostat. The cryostat was equipped with an ultralow vibration interface in order to decouple vibrations of the Gifford-McMahon refrigerator from the ellipsometer. The pressure in the cryostat chamber was 1×10^{-7} mbar at 300 K.

The data were analyzed with a model of coherent interferences in a thin film on a substrate. The dielectric function of BaF_2 was obtained from measurements on a bare substrate; e.g., for far-infrared data, see Fig. 3(a). In the model, we have taken into account also the incoherent reflections from the back side of the BaF_2 substrate that is cleaved and thus reflecting. The surface roughness was taken into account using an effective-medium approximation (Bruggeman model) [27]. The thickness of the surface roughness layer obtained from the fitting was between 5 and 11 nm, in good agreement with an rms roughness value between 4 and 9 nm obtained by atomic force microscopy. The surface roughness correction is increasingly important with a decreasing wavelength of light λ, e.g., it significantly influences the dielectric function above

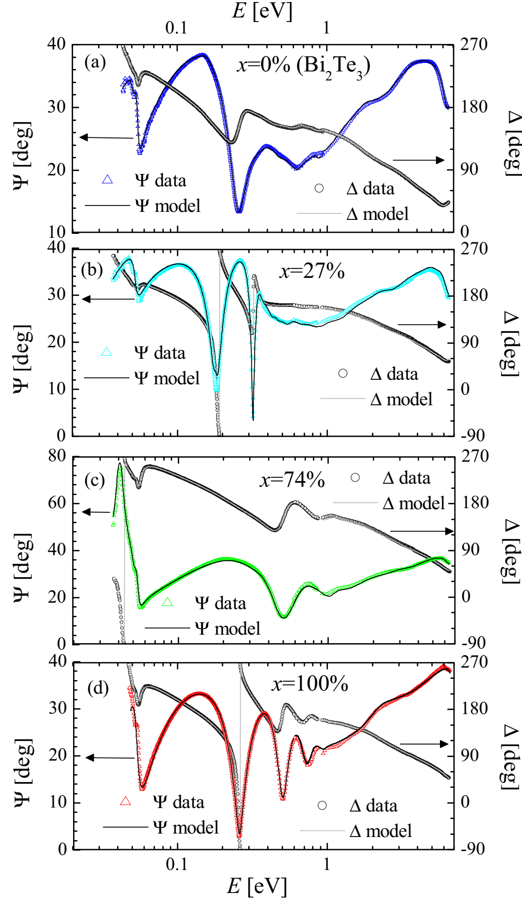

FIG. 2. Measured ellipsometric angles Ψ and Δ at 300 K (symbols) and model spectra (solid lines) of our $Bi_2(Te_{1-x}Se_x)_3$ samples with $x = 0\%$ (a), 27% (b), 74% (c), and 100% (d) as a function of photon energy E. The angle of incidence was 70°.

about 1 eV ($\lambda \approx 1\ \mu$m), however it has a negligible impact at lower energies. As the first step, we analyzed the response of the thin films in the whole measured frequency range. We have modeled the dielectric function of the layer as the sum

$$\hat{\varepsilon}(\omega) = 1 - \frac{\omega_{\rm pl}^2}{\omega(\omega + i\gamma)} + \sum_j \frac{\omega_{{\rm pl},j}^2}{\omega^2 - \omega_j^2 - i\gamma_j} + \sum_j \hat{G}_j(\omega), \qquad (1)$$

where the angular frequency, ω, relates to the photon energy, E, as $E = \hbar\omega$. The model consists of the Drude term for itinerant electrons (second term on the right-hand side), Lorentz oscillators for transverse optical phonons (third term on the right-hand side), and a set of Gaussian oscillators $\hat{G}_j(\omega)$ for interband transitions [27]. The fit of model spectra to the data was performed using the Woollam WVASE software.

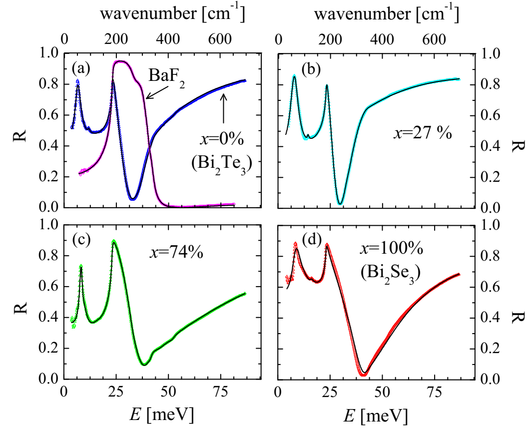

FIG. 3. Far-infrared reflectivity of our $Bi_2(Te_{1-x}Se_x)_3$ thin films on BaF_2 substrate at 300 K (symbols) together with model spectra (solid lines). Shown are results for samples with $x = 0\%$ (a), 27% (b), 74% (c), and 100% (d). In addition, the data (magenta circles) and the model spectrum (solid line) of the BaF_2 substrate are shown in panel (a).

The obtained best-fit model spectra, which are displayed in Figs. 2 and 3 as solid lines, are in very good agreement with the data (symbols). The main features in the raw spectra in the far-infrared frequency range are as follows (see Fig. 3): the strong (so-called α) phonon between 52 and 68 cm^{-1}, the much weaker (so-called β) phonon between 95 and 130 cm^{-1}, and the BaF_2 substrate phonon at 186 cm^{-1}. The frequencies of the α and β phonons (see Table I) compare well with reported values [10,14,18]. Between about 0.1 and 0.8 eV (see Fig. 2), the films are transparent and the raw ellipsometric data exhibit fringes due to interference in the layer. Above this range, the thin films are opaque and the features are solely due to the electronic interband transitions.

First we attempted to obtain the plasma frequency of the itinerant charge carriers, $\omega_{\rm pl}$, and the thickness of the layer, d. The results are summarized in Table I. The thickness values were consequently used in the point-by-point retrieval of the dielectric function in the frequency range of ellipsometric data. We have assumed that the response of the layer is isotropic. This is certainly an approximation for the anisotropic response of $Bi_2(Te_{1-x}Se_x)_3$ caused by the rhombohedral crystal structure. In general, in the oblique reflectance geometry of an ellipsometric measurement, the out-of-plane component of the dielectric function is probed as well, although the main contribution to the data usually corresponds to the in-plane component. However, if the value of the index of refraction is high, the wave refracts close to the sample normal, and the anisotropic corrections are quite small unless the out-of-plane dielectric function has strong resonances in the loss function [28,29]. These requirements are fulfilled between 0.1 and 0.7 eV, where the index of refraction is high (about 6–7).

Reprinted page 3 of paper [85] "Optical properties of $Bi_2(Se_xTe_{1-x})_3$ alloys".

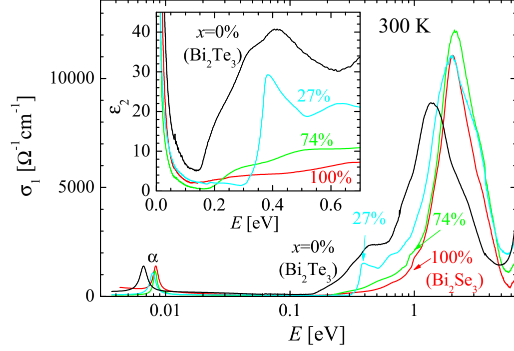

FIG. 4. The real part of the optical conductivity at 300 K of the $Bi_2(Te_{1-x}Se_x)_3$ samples in the whole measured frequency range. The inset displays the region of the onset of interband absorption in terms of ε_2.

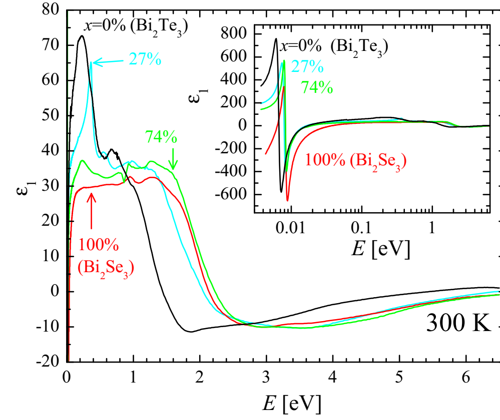

FIG. 5. The real part of the dielectric function, ε_1, at 300 K of the $Bi_2(Te_{1-x}Se_x)_3$ samples above the phonon energy range. The inset displays the data on a semilogarithmic scale including the large polarizability due to the α-phonon.

III. DISCUSSION

A. Overview of the absorption spectra

Figure 4 shows the spectra of our $Bi_2(Te_{1-x}Se_x)_3$ thin films at room temperature in the whole measured spectral range in terms of the real part of the optical conductivity $\sigma_1(\omega) = \omega\varepsilon_0\varepsilon_2(\omega)$, where ε_0 is the permittivity of vacuum and $\varepsilon_2(\omega)$ is the imaginary part of the dielectric function. The prominent absorption structures are due to the α phonon between 6 and 9 meV, a weak free charge-carrier response, and the interband transitions setting in above $\approx$0.1 eV. In the following, we focus on the region of interband absorption edge between 0.1 and 0.7 eV, displayed in the inset of Fig. 4 in terms of ε_2. Above the band gap, the maximum values of ε_2 range from about 5 for the least absorbing Bi_2Se_3 sample up to about 40 for the most absorbing Bi_2Te_3 sample. These high values are typical for direct interband transitions. Indirect transitions have values of ε_2 typically several orders of magnitude smaller [30]. Therefore, all the interband transitions discussed in this paper are direct, and we designate their onset energy as E_g^{direct}.

The real part of the dielectric function, ε_1, shown in Fig. 5, exhibits large values below the interband transitions ($\sim$0.2 eV) that range from 30 for Bi_2Se_3 up to more than 70 for Bi_2Te_3. The zero crossing of ε_1 above 5 eV indicates the renormalized plasma resonance of all valence electrons. The electronic polarizability is essentially due to the interband transitions below $\sim$4 eV; the contribution of the interband transitions above the measured frequency range to the low-energy value of ε_1 is relatively small (about 1). At the lowest measured energy ($\sim$5 meV; see the inset of Fig. 5), ε_1 reaches several hundred due to the low-lying α-phonon.

B. The absorption edge in Bi_2Se_3

Figure 6(a) shows the temperature dependence of ε_2 of the Bi_2Se_3 thin film in the midinfrared range. The onset of interband transitions with lowering temperature sharpens and shifts to higher energies similarly to previously published results [18]. The weak feature near 250 meV, which is most visible in the 80 K spectrum, is an artefact due to the sharp interference structure at this energy [see Fig. 2(d)]. Below the onset of interband transitions at low temperature, ε_2 is zero within the uncertainty of the analysis. This is consistent with the observed transmission values up to 14% measured on 225-μm-thick single crystal [24], which is possible only if $\varepsilon_2 \ll 0.1$.

Due to a significant concentration of free electrons, the Fermi level, E_F, lies in the conduction band. Consequently, the minimal energy necessary to excite the electrons from the valence to the conduction band, E_{min}, is larger than the band gap E_g^{direct} because of the Pauli blocking of the states below E_F. The latter effect is known as the Burstein-Moss (BM) effect or shift [31,32]. In such a case, a step in the absorption is expected. Indeed, it can be seen in Fig. 6(a) that at 10 K, $\varepsilon_2(E)$ has a steplike shape reaching a value of about 5 in a rather narrow interval 290–340 meV. The representative energy of such an onset can be estimated as the middle point of the step, $\approx$310 meV, as shown by the arrow. In a more sophisticated way, the onset can be determined with the help of the critical point model fitted to the second derivative of the dielectric function [33,34]. The contribution of a parabolic critical point (CP) located at an energy E_{CP} to the jth derivative of the dielectric function is

$$\frac{d^j\hat{\varepsilon}(E)}{dE^j} = Ae^{i\phi}(E - E_{\text{CP}} + i\Gamma)^{-n-j}, \qquad (2)$$

where A and ϕ are the amplitude and the phase factor, and n has the values $-1/2$, 0, and $1/2$ for a three-, two-, and one-dimensional CP, respectively. We have modeled the second derivative ($j = 2$) of the dielectric function shown in Fig. 6(b) with a sum of two CP functions of Eq. (2). The data below 280 meV were omitted because of spurious structures due to the interference mentioned above. The most pronounced structure centered at 312 meV was modeled with a two-dimensional CP ($n = 0$) that corresponds to the step in ε_2 [27]. Its center energy is very close to the middle

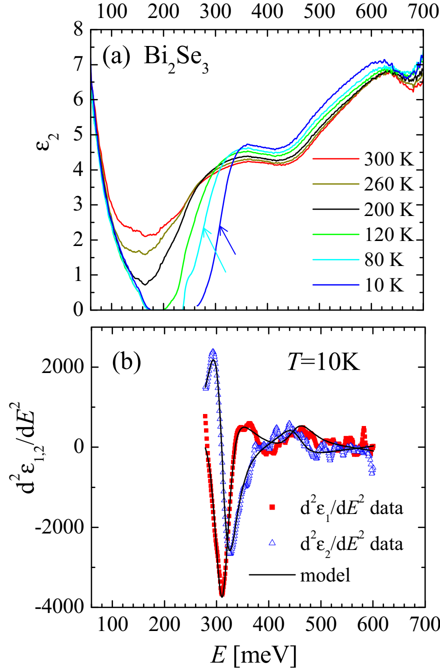

FIG. 6. (a) Temperature dependence of the imaginary part of the dielectric function, ε_2, of Bi_2Se_3. The arrows mark the energy of the lowest critical point at 10 and 80 K, respectively. (b) Second derivative of the real (red squares) and imaginary part (blue triangles) of the dielectric function at 10 K together with the spectrum of the critical point model (solid lines) specified in the text.

point estimated above. The weak structure near 450 meV was modeled with a three-dimensional CP.

Assuming for simplicity that the conduction and valence bands are parabolic, $E_{\min}$ and E_g^{direct} are related as

$$E_{\min} = E_g^{\text{direct}} + \frac{\hbar^2 k_{\text{F},a}^2}{2}\left(\frac{1}{m_\text{e}^a} + \frac{1}{m_\text{h}^a}\right), \tag{3}$$

where $k_{\text{F},a}$ is the in-plane Fermi wave vector, and m_e^a and m_h^a are the in-plane effective masses of the conduction and valence band, respectively [12]. With the help of the expression for the Fermi level with respect to the bottom of the conduction band, $E_\text{F} = \hbar^2 k_{\text{F},a}^2/(2m_\text{e}^a)$, Eq. (3) can be rewritten as

$$E_{\min} = E_g^{\text{direct}} + E_\text{F}\left(1 + \frac{m_\text{e}^a}{m_\text{h}^a}\right). \tag{4}$$

Since Bi_2Se_3 is anisotropic, the equienergy contour at the Fermi level has an ellipsoidal shape in k-space. For the case of biaxial anisotropy, the Fermi level can be calculated from the concentration of charge carriers n as

$$E_\text{F} = \frac{\hbar^2}{2(m_\text{e}^a m_\text{e}^b m_\text{e}^c)^{1/3}}\left(3\pi^2 n\right)^{2/3}, \tag{5}$$

where m_e^a, m_e^b, and m_e^c are the three effective masses. In the case of the uniaxial anisotropy of Bi_2Se_3, $m_\text{e}^a = m_\text{e}^b$. We have determined the concentration of charge carriers from their plasma frequency ω_{pl} (see Table I) as $n = \omega_{\text{pl}}^2 m_\text{e}^a \varepsilon_0/e^2$, where e is the elemental charge. For the evaluation of the BM shift, the following values of effective masses were used: $m_\text{e}^a = 0.14$ m [35] and $m_\text{h}^a = 0.24$ m [36], where m is the free-electron mass. The c-axis effective mass can be calculated from the effective-mass anisotropy $m_\text{e}^c/m_\text{e}^a = 1.6$ obtained for a Fermi energy ≈50 meV [37] above the conduction-band minimum, which is relevant for our sample. With these values, the BM shift amounts to 98 meV and the resulting band-gap value is $E_g^{\text{direct}} = 215 \pm 10$ meV at 10 K. The uncertainty is estimated from that of the effective masses. The calculation of the BM shift is based on the parabolic profile of the conduction and valence bands. The latter assumption is reasonably fulfilled for our relatively weakly doped sample with $n = 4.8 \times 10^{18}$ cm^{-3}, which is below the threshold of $\approx 10^{19}$ cm^{-3}, above which a significant nonparabolicity of the conduction band has been observed [37]. Similarly, the valence band was reported [36] to have a parabolic shape for the Fermi wave vector corresponding to our sample ($k_{\text{F},a} \approx 0.04$ Å^{-1}).

In the following, we compare the obtained value of E_g^{direct} with literature values for the band gap determined by optical spectroscopy and corrected for the BM shift. In their early study, Köhler and Hartman [12] reported on a BM shift in a series of single crystals with varying levels of doping, and they found $E_g^{\text{direct}} = 160$ meV ± 10% at 77 K. Based on an extrapolation, these authors estimated that the 0 K value would be 175 meV ± 10%. However, it seems that the temperature shift was underestimated. In our data, the shift of the absorption edge between 80 and 10 K is about 35 meV. When taking into account this value, we obtain $E_g^{\text{direct}} \approx 195$ meV at 10 K. In a recent study on thin films [18], Post *et al.* reported $E_g^{\text{direct}} = 190$ meV for a 99 quintuple-layer-thick film. The onset of absorption was obtained based on the extrapolation of ε_2^2 to zero. If this procedure is used for our data, we obtain $E_g^{\text{direct}} \approx 200$ meV, a value closer to the one obtained by Post *et al.* [18]. From a recent transmission experiment on single crystals, Ohnoutek *et al.* [24] reported $E_g^{\text{direct}} \approx 200$ meV. Notably, a very recent work [38] combining luminescence, transmission, and magnetotransport measurements estimated that the gap value is 220 ± 5 meV, which agrees within the error bars with our result. The values from all these reports fall into an interval 190–220 meV at 10 K and represent a fairly robust estimate for the value of the direct band gap. The differences between the results are presumably due to different ways in which the onset of absorption is defined and how the MB shift is calculated.

Post *et al.* [18] noted that these values are significantly smaller than the direct-band-gap value of 300 meV determined from some early ARPES data [3]. However, in later ARPES data with an improved signal-to-noise ratio, there is a noticeable intensity reaching up to the Dirac point located at about 0.2 eV below the bottom of the conduction band [6,39–43]. Explicitly, Chen *et al.* concluded that the valence band in Bi_2Se_3 extends up to the Dirac point from below [6]. In view of the more recent ARPES data, it becomes clear that the valence band is a downward-oriented paraboloid located at

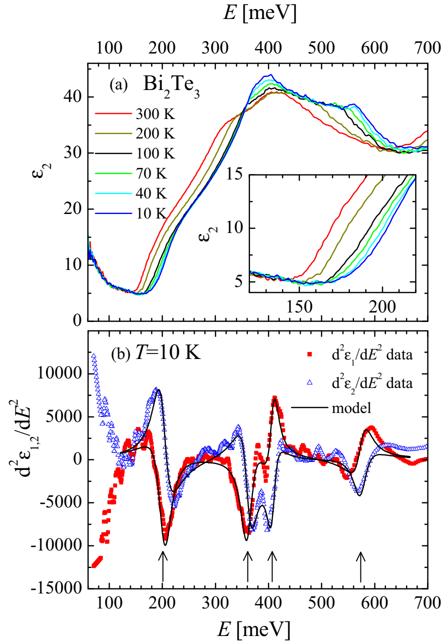

FIG. 7. (a) Temperature dependence of the imaginary part of the dielectric function, ε_2, of the Bi_2Te_3 sample. The inset shows the spectra on magnified scales. (b) Second derivative of the real (red squares) and imaginary part (blue triangles) of the dielectric function at 10 K together with critical point model spectra (solid lines). The arrows mark the positions of four critical points.

about 0.2 eV below the bottom of the conduction band and thus in accord with the ≈215 meV direct gap derived above. The M (or camelback) structure seen in ARPES data might be due to surface states or to a deeper-lying structure in the valence bands [40]. The latter scenario is confirmed by recent Shubnikov–de Haas (SdH) measurements [36] concluding that the top of the valence band is a downward-oriented paraboloid with no signatures of an M shape of the top of the valence band. Note that the M structure of the valence band seen in some LDA band-structure calculations [44] is absent in the more realistic results of *GW* calculations [43,45,46] that exhibit a paraboloidal shape of the valence band.

C. The absorption edge in Bi_2Te_3

Figure 7(a) displays the temperature dependence of ε_2 of our Bi_2Te_3 thin film. The absorption edge blueshifts with lower temperature similarly to Bi_2Se_3. To obtain the energy of the CPs, we have fitted the second derivative of the dielectric function with a set of three-dimensional CPs of Eq. (2). Figure 7(b) displays the second derivative at $T = 10$ K together with a model consisting of four CPs centered at 202, 362, 408, and 575 meV as marked by the arrows. At 300 K (not shown), the obtained energy of the lowest CP is 157 meV. If the extrapolation of $\varepsilon_2^2(E)$ toward zero is used to define $E_{\min}$, we obtain the values 190 and 152 meV at 10 and 300 K, respectively. Interestingly, the absorption onset is sharper at 300 K than at 10 K [see the inset of Fig. 7(a)], which is opposite to what is expected from thermal broadening effects. We have checked that this effect is not due to a freezing of the residual atmosphere on the sample at low temperature. Obviously below the main interband absorption that sets in near 200 meV at 10 K, an additional weaker interband absorption occurs with an onset at about 170 meV. Although it is weaker than the main interband transition, the magnitude of this absorption is still large (of the order of unity in ε_2), therefore it most likely corresponds to a direct interband transition. The energy of this onset is the same as that found in an earlier report by Sehr and Testardi [47].

Chapler *et al.* [14] reported the onset of interband absorption in Bi_2Te_3 thin films between 140 and 150 meV at 300 K, not too different from our value of 157 meV. Their onset value did not exhibit a significant blueshift with cooling to 10 K. A direct gap was observed in Ref. [48] at 220 meV with a weak onset at 150 meV on relatively highly doped Bi_2Te_3. The difference in the reported values is presumably caused by differences in the doping level and related MB shift and/or by a difference in the definition of the onset energy. Regardless of these relatively small differences, as noted by Chapler *et al.* [14], the onset of absorption at 10 K (≈200 meV in our data) is significantly smaller than the 290 meV value of the direct band gap at the Γ point observed in ARPES [5,49]. Note that in our data, the value of ε_2 at 290 meV is about 25, which corresponds to a very strong absorption due to direct interband transitions. Obviously, the onset occurs at a different point in the Brillouin zone. Band-structure calculations [44,50–52] indeed suggest that the direct gap should be close to the Z-F line in the Brillouin zone, where the interband transition energy is significantly smaller than that at the Γ point. The band-gap values have been treated theoretically in detail in Ref. [51] using the *GW* calculations. Direct interband transitions are predicted close to the Z-F line with an onset at 168 meV, in reasonably good agreement with our experimental value. In the calculations, it appears that their location is not exactly on the Z-F line but is close to about $1.3Z$; see Fig. 3(d) in Ref. [51]. An indirect fundamental band gap is predicted at a slightly lower energy of 156 meV.

ARPES results suggest that this interpretation is likely. The conduction band in Bi_2Te_3 has a strong hexagonal warping [5,49]. The ARPES intensity related to the conduction band is centered at the Γ point, however it has a snowflake-like shape with protrusions extending into the Γ-M direction. This direction of the projected surface Brillouin zone measured by ARPES involves the Z-F line of the bulk Brillouin zone. Since the valence band has an M shape, its energy increases from the Γ toward the M point and reaches a maximum at $k \approx 0.13$ Å^{-1}, where the difference between the valence and conduction band seems to be about 0.2 eV, a value compatible with our optical spectroscopy data.

According to the *GW* calculations [51,52], the structure of the calculated valence and conduction band along the Z-F line is rather complicated; it seems to have several extrema. It is possible that with changing temperature, the position of the lowest direct band gap changes, and at low temperature an interband transition with a smaller joint density of states

compared to the main one sets in and gives rise to the observed onset at 170 meV.

We estimate that the BM shift in Bi_2Te_3 is much smaller than in Bi_2Se_3. The main reason is that, as seen in the ARPES data [5,49], the electrons populate first the conduction-band states located at the Γ point or along the Γ-Z line [52] that lie at a smaller energy than those along the Z-F line. As a consequence, the minimum excitation energy is not increased for weakly doped samples. The BM shift likely occurs only for strongly doped samples where the Fermi level enters the conduction bands at the Z-F line. Secondly, the very steep increase of ε_2 above the band-gap edge is caused by a quite large joint density of states due to fairly flat bands where only a relatively small BM shift can be expected.

As a summary for Bi_2Te_3, at 10 K we observed a strong direct interband transition at about 200 meV accompanied with an onset of a weaker direct interband transition at about 170 meV. As suggested by band-structure calculations, the direct transition occurs near the Z-F line in the Brillouin zone. Since along the Γ-Z line the energy of the conduction band lies at a lower energy than along the Z-F line, as suggested by the band-structure calculations and ARPES [51,52], there should be an indirect band gap with an energy even lower than 170 meV, i.e., Bi_2Te_3 is an indirect semiconductor. However, these indirect transitions are masked in our data by the much stronger response of free charge carriers that yields a value of about 5 for ε_2 below E_g^{direct}. Since typically an indirect gap will not contribute to ε_2 with a value larger than about 0.1, consequently for our thin-film samples we cannot observe its contribution to the absorption.

D. The absorption edge in $Bi_2(Te_{1-x}Se_x)_3$

Figure 8(a) shows ε_2 spectra at 10 K of our alloy $x =$ 27% and 74% samples. For comparison, the spectra of Bi_2Se_3 and Bi_2Te_3 are shown as well. The spectrum of the $x = 27\%$ sample is qualitatively similar to that of Bi_2Te_3, i.e., it exhibits a very steep increase above the onset at 390 meV, reaching high values of ε_2 of about 25. On the contrary, the spectrum of the $x = 74\%$ sample is qualitatively similar to that of Bi_2Se_3, i.e., it displays a relatively gradual increase of absorption above the edge up to the values of $\varepsilon_2 \approx 10$. This suggests that the absorption edge occurs at the same point in the Brillouin zone, i.e., the Γ point for the $x = 74\%$ sample, whereas for the $x = 27\%$ sample it is rather at a point close to the Z-F line of the Brillouin zone, as for Bi_2Te_3.

We have analyzed the spectra in a similar way to that described above by fitting the second derivative of $\hat{\varepsilon}(E)$ with the CP model of Eq. (2). The second derivative of $\hat{\varepsilon}(E)$ for the $x = 74\%$ sample is shown in Fig. 8(b) together with the model consisting of two CP contributions marked by arrows. Similarly to Bi_2Se_3, the strong CP centered at 300 meV is modeled with a two-dimensional CP, and the weak one at 525 meV is modeled with a three-dimensional CP. Using the same formulas as for the Bi_2Se_3 sample, the BM shift amounts to 33 meV, and the band-gap value is 270 ± 10 meV.

The second derivative of $\hat{\varepsilon}(E)$ of the $x = 27\%$ sample is shown in Fig. 8(c). Unfortunately, here the spectra, similarly to our Bi_2Se_3 sample, exhibit near 180 and 330 meV artefacts that correspond to interference fringes [see Fig. 2(b)]. These

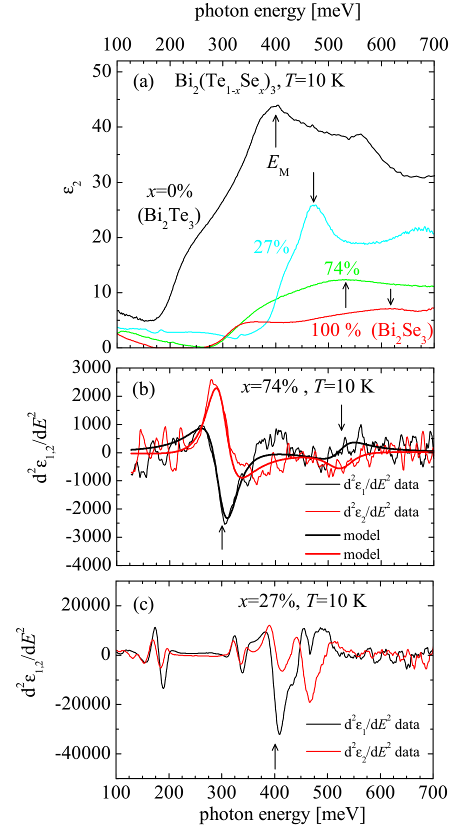

FIG. 8. (a) The imaginary part of the dielectric function of our $Bi_2(Te_{1-x}Se_x)_3$ samples at 10 K. The arrows mark the energy E_M of the maximum of ε_2. (b) The second derivative of the real (black thin line) and imaginary part (red thin line) of the dielectric function at 10 K of the $x = 74\%$ sample together with the critical point model spectra (thick lines). The arrows mark the position of two critical points. (c) The second derivative of the real (black line) and imaginary part (red line) of the dielectric function at 10 K of the $x = 27\%$ sample. The arrow marks the position of the main critical point. The structures near 180 and 330 meV are interference artefacts, as discussed in the text.

artefacts prevent us from fitting the data with the CP model; nevertheless, it is clear that the strongest feature centered at about 400 meV (marked by the arrow) corresponds to the strongest CP related to the onset of the direct interband transitions. Similarly to Bi_2Te_3, below this CP a weaker absorption occurs with the onset at about 340 meV; see Fig. 8(a). The plasma frequency of this sample is even smaller than that of the Bi_2Te_3 sample (see Table I), and thus, similarly to Bi_2Te_3, we estimate that the BM shift is either absent or negligibly small. Both the CP energy of 400 meV and the onset at 340 meV are significantly larger than the band-gap value of 290 meV reported [21] for a sample with similar Se content $x = 33\%$. However, the energy of the maximum of

Reprinted page 7 of paper [85] "Optical properties of $Bi_2(Se_xTe_{1-x})_3$ alloys".

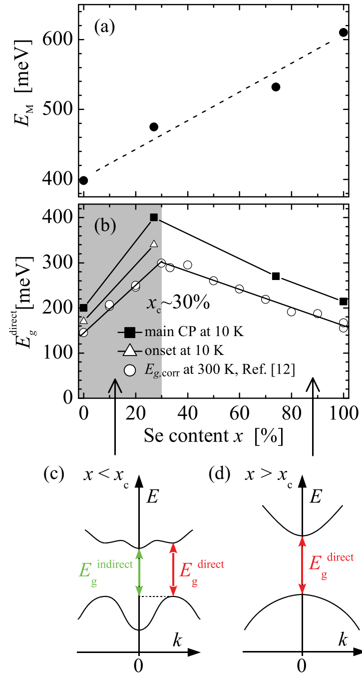

FIG. 9. (a) The energy E_M of the maximum of ε_2 of $Bi_2(Te_{1-x}Se_x)_3$ marked by the arrows in Fig. 8. The dashed line is a guide to the eye. (b) Extracted values of the onset of direct interband transitions, E_g^{direct}, at 10 K defined as the center position of the main lowest critical point (squares). The values for $x = 76\%$ and 100% were corrected for the Burstein-Moss shift as described in the text. The triangles represent the onset of a weaker direct interband absorption below the main critical point. The circles are previously reported [11] absorption edge energies at 300 K corrected for the Burstein-Moss effect. Parts (c) and (d) schematically represent the position of the direct interband transitions (red arrows) in the band structure for Se content $x < x_c$ (c) and $x > x_c$ (d), respectively, where $x_c \approx 30\%$. The green arrow in (c) depicts the indirect fundamental gap (see Refs. [51,52]).

ε_2 denoted here as E_M [see the arrows in Fig. 8(a)] occurs at different energy, namely at 520 meV at 10 K in the case of Ref. [21], whereas it is at 475 meV in our data. Since the energy of this maximum strongly increases with increasing x [see Fig. 9(a)], it is likely that the composition of the two samples is different, the one of Ref. [21] having a significantly larger value of x than our sample. We attribute the maximum E_M to a CP related to the Z-F line whose energy increases monotonically with Se content.

Figure 9(b) displays the extracted values of the onset of direct interband transitions, E_g^{direct}, at 10 K of all our samples. The squares correspond to the main CP energies. For the $x = 74\%$ and 100% samples, these were corrected for the BM shifts, while for the other two samples we expect that the BM shift is absent or small. The triangles correspond to a weaker absorption observed in the spectra of the $x = 0\%$ and 27% samples that is likely due to a weaker direct interband transition, as discussed above. In general, the dependence of the band-gap value on selenium content has a rooflike shape with a maximum for the $x = 27\%$ sample. This shape is very similar to the one reported for band-gap values at 300 K corrected for the Burstein-Moss effect in the early work of Greenaway and Harbecke [11], which are added for comparison to Fig. 9(b) as circles. The latter dependence exhibits a pronounced maximum of the direct gap near $x = 30\%$ content; our values are of course larger since they were obtained at 10 K. Similarly to their conclusion, we suggest that the direct interband transitions on the left and right side of the maximum corresponds to different points in the Brillouin zone. The position of the onset of direct interband transitions in the band structure for the two cases is schematically represented in Figs. 9(c) and 9(d) by red arrows. Figure 9(d) depicts a direct band gap in the center of the Brillouin zone between parabolic-like bands that occurs on the Bi_2Se_3 side of the $Bi_2(Te_{1-x}Se_x)_3$ alloy. On the Bi_2Te_3 side shown in Fig. 9(c), the direct band gap occurs off the Brillouin-zone center near the Z-F line, between the wing of the M-shaped valence band and a conduction band [51,52]. The green arrow depicts the indirect fundamental gap, which, however, has orders of magnitude lower absorption and therefore is masked in our data by the much stronger free charge-carrier response.

IV. CONCLUSION

We have examined the optical response of $Bi_2(Te_{1-x}Se_x)_3$ thin films, which reveal direct interband transitions. In Bi_2Se_3, after the correction for the Burstein-Moss effect, we find a band-gap value of 215 ± 10 meV at 10 K, in good agreement with the values from 190 to 220 meV reported in the literature [12,18,24,38]. Our result supports the conclusion of ARPES [6], GW calculations [45,46], and SdH measurements [36] that the direct band gap of Bi_2Se_3 is located at the Γ point in the Brillouin zone, and the valence band reaches up to the Dirac point and has a shape of a downward-oriented paraboloid.

In Bi_2Te_3, we observe a strong interband absorption that sets in at $\approx$200 meV at 10 K and a weaker albeit still direct interband transition with an onset at about 170 meV. These values support GW band-structure calculations that proposed that the direct interband transition occurs near the Z-F line. In the ternary $Bi_2(Te_{1-x}Se_x)_3$ alloys, the energy of the onset of the direct interband transition goes through a maximum for a Se content of about 30%. This behavior indicates that there is a crossover of the position of the direct interband transitions between the two different points in the Brillouin zone at this Se content.

ACKNOWLEDGMENTS

We acknowledge helpful discussions with I. Aguilera. This work was financially supported by the European Regional Development Fund Project CEITEC Nano+ (No. CZ.021.01/0.0/0.0/16_013/0001728), CEITEC Nano Research Infrastructure (ID LM2015041, MEYS CR, 2016–2019), CEITEC Brno University of Technology, and by EC via the TWINFUSYON project (No. 692034).

[1] D. Hsieh, D. Qian, L. Wray, Y. Xia, Y. S. Hor, R. J. Cava, and M. Z. Hasan, Nature (London) **452**, 970 (2008).
[2] A. A. Taskin and Y. Ando, Phys. Rev. B **80**, 085303 (2009).
[3] Y. Xia, D. Qian, D. Hsieh, L. Wray, A. Pal, H. Lin, A. Bansil, D. Grauer, Y. S. Hor, R. J. Cava, and M. Z. Hasan, Nat. Phys. **5**, 398 (2009).
[4] A. Nishide, A. A. Taskin, Y. Takeichi, T. Okuda, A. Kakizaki, T. Hirahara, K. Nakatsuji, F. Komori, Y. Ando, and I. Matsuda, Phys. Rev. B **81**, 041309 (2010).
[5] Y. L. Chen, J. G. Analytis, J. H. Chu, Z. K. Liu, S. K. Mo, X. L. Qi, H. J. Zhang, D. H. Lu, X. Dai, Z. Fang, S. C. Zhang, I. R. Fisher, Z. Hussain, and Z. X. Shen, Science **325**, 178 (2009).
[6] Y. L. Chen, J. H. Chu, J. G. Analytis, Z. K. Liu, K. Igarashi, H. H. Kuo, X. L. Qi, S. K. Mo, R. G. Moore, D. H. Lu, M. Hashimoto, T. Sasagawa, S. C. Zhang, I. R. Fisher, Z. Hussain, and Z. X. Shen, Science **329**, 659 (2010).
[7] K. Miyamoto, A. Kimura, T. Okuda, H. Miyahara, K. Kuroda, H. Namatame, M. Taniguchi, S. V. Eremeev, T. V. Menshchikova, E. V. Chulkov, K. A. Kokh, and O. E. Tereshchenko, Phys. Rev. Lett. **109**, 166802 (2012).
[8] M. Neupane, S.-Y. Xu, L. A. Wray, A. Petersen, R. Shankar, N. Alidoust, C. Liu, A. Fedorov, H. Ji, J. M. Allred, Y. S. Hor, T. R. Chang, H. T. Jeng, H. Lin, A. Bansil, R. J. Cava, and M. Z. Hasan, Phys. Rev. B **85**, 235406 (2012).
[9] J. Horák, Z. Starý, P. Lošťák, and J. Pancíř, J. Phys. Chem. Solids **51**, 1353 (1990).
[10] W. Richter, H. Köhler, and C. Becker, Phys. Status Solidi B **84**, 619 (1977).
[11] D. Greenaway and G. Harbeke, J. Phys. Chem. Solids **26**, 1585 (1965).
[12] H. Köhler and J. Hartmann, Phys. Status Solidi B **63**, 171 (1974).
[13] A. D. LaForge, A. Frenzel, B. C. Pursley, T. Lin, X. Liu, J. Shi, and D. N. Basov, Phys. Rev. B **81**, 125120 (2010).
[14] B. C. Chapler, K. W. Post, A. R. Richardella, J. S. Lee, J. Tao, N. Samarth, and D. N. Basov, Phys. Rev. B **89**, 235308 (2014).
[15] K. W. Post, Y. S. Lee, B. C. Chapler, A. A. Schafgans, M. Novak, A. A. Taskin, K. Segawa, M. D. Goldflam, H. T. Stinson, Y. Ando, and D. N. Basov, Phys. Rev. B **91**, 165202 (2015).
[16] A. Akrap, M. Tran, A. Ubaldini, J. Teyssier, E. Giannini, D. van der Marel, P. Lerch, and C. C. Homes, Phys. Rev. B **86**, 235207 (2012).
[17] M. Stordeur, K. K. Ketavong, A. Priemuth, H. Sobotta, and V. Riede, Phys. Status Solidi B **169**, 505 (1992).
[18] K. W. Post, B. C. Chapler, L. He, X. Kou, K. L. Wang, and D. N. Basov, Phys. Rev. B **88**, 075121 (2013).
[19] P. Di Pietro, F. M. Vitucci, D. Nicoletti, L. Baldassarre, P. Calvani, R. Cava, Y. S. Hor, U. Schade, and S. Lupi, Phys. Rev. B **86**, 045439 (2012).
[20] R. Valdés Aguilar, A. V. Stier, W. Liu, L. S. Bilbro, D. K. George, N. Bansal, L. Wu, J. Cerne, A. G. Markelz, S. Oh, and N. P. Armitage, Phys. Rev. Lett. **108**, 087403 (2012).
[21] A. A. Reijnders, Y. Tian, L. J. Sandilands, G. Pohl, I. D. Kivlichan, S. Y. Frank Zhao, S. Jia, M. E. Charles, R. J. Cava, N. Alidoust, S. Xu, M. Neupane, M. Z. Hasan, X. Wang, S. W. Cheong, and K. S. Burch, Phys. Rev. B **89**, 075138 (2014).
[22] K. W. Post, B. C. Chapler, M. K. Liu, J. S. Wu, H. T. Stinson, M. D. Goldflam, A. R. Richardella, J. S. Lee, A. A. Reijnders, K. S. Burch, M. M. Fogler, N. Samarth, and D. N. Basov, Phys. Rev. Lett. **115**, 116804 (2015).
[23] Y. Shao, K. W. Post, J.-S. Wu, S. Dai, A. J. Frenzel, A. R. Richardella, J. S. Lee, N. Sarnarth, M. M. Fogler, A. V. Balatsky, D. E. Kharzeev, and D. N. Basov, Nano Lett. **17**, 980 (2017).
[24] L. Ohnoutek, M. Hakl, M. Veis, B. A. Piot, C. Faugeras, G. Martinez, M. V. Yakushev, R. W. Martin, C. Drasar, A. Materna, G. Strzelecka, A. Hruban, M. Potemski, and M. Orlita, Sci. Rep. **6**, 19087 (2016).
[25] O. Caha, A. Dubroka, J. Humlíček, V. Holý, H. Steiner, M. Ul-Hassan, J. Sanchez-Barriga, O. Rader, T. N. Stanislavchuk, A. A. Sirenko, G. Bauer, and G. Springholz, Cryst. Growth Des. **13**, 3365 (2013).
[26] J. Humlíček, D. Hemzal, A. Dubroka, O. Caha, H. Steiner, G. Bauer, and G. Springholz, Phys. Scr. **T162**, 014007 (2014).
[27] *Handbook of Ellipsometry*, edited by G. Tompkins and E. A. Irene (William Andrew, Norwich, NY, 2005).
[28] C. Bernhard, J. Humlíček, and B. Keimer, Thin Solid Films **455–456**, 143 (2004).
[29] O. Foltin, K. Navrátil, P. Lošťák, and K. Vojtěchovský, Phys. Status Solidi A **132**, K97 (1992).
[30] P. Y. Yu and M. Cardona, *Fundamentals of Semiconductors*, 4th ed. (Springer, Berlin, 2010).
[31] E. Burstein, Phys. Rev. **93**, 632 (1954).
[32] T. S. Moss, Proc. Phys. Soc. (London), Ser. B **67**, 775 (1954).
[33] M. Cardona, Modulation spectroscopy, *Solid State Physics* (Academic, New York, 1969), Suppl. 11.
[34] J. Humlíček and M. Garriga, Temperature dependence of the optical spectra of $Si_{1-x}Ge_x$ alloys, *Silicon-germanium Carbon Alloys Growth, Properties and Applications* (Taylor&Francis, New York, 2002), p. 483.
[35] M. Orlita, B. A. Piot, G. Martinez, N. K. Sampath Kumar, C. Faugeras, M. Potemski, C. Michel, E. M. Hankiewicz, T. Brauner, Č. Drašar, S. Schreyeck, S. Grauer, K. Brunner, C. Gould, C. Brüne, and L. W. Molenkamp, Phys. Rev. Lett. **114**, 186401 (2015).
[36] B. A. Piot, W. Desrat, D. K. Maude, M. Orlita, M. Potemski, G. Martinez, and Y. S. Hor, Phys. Rev. B **93**, 155206 (2016).
[37] H. Köhler, Phys. Status Solidi B **58**, 91 (1973).
[38] G. Martinez, B. Piot, M. Hakl, M. Potemski, Y. S. Hor, A. Materna, S. G. Strzelecka, A. Hruban, O. Caha, J. Novák, A. Dubroka, C. Drašar, and M. Orlita, Sci. Rep. **7**, 6891 (2017).
[39] M. Bianchi, D. Guan, S. Bao, J. Mi, B. B. Iversen, P. D. C. King, and P. Hofmann, Nat. Commun. **1**, 128 (2010).
[40] M. Bianchi, R. C. Hatch, D. Guan, T. Planke, J. Mi, B. B. Iversen, and P. Hofmann, Semicond. Sci. Technol. **27**, 124001 (2012).
[41] K. Kuroda, M. Arita, K. Miyamoto, M. Ye, J. Jiang, A. Kimura, E. E. Krasovskii, E. V. Chulkov, H. Iwasawa, T. Okuda, K. Shimada, Y. Ueda, H. Namatame, and M. Taniguchi, Phys. Rev. Lett. **105**, 076802 (2010).
[42] C. Chen, S. He, H. Weng, W. Zhang, L. Zhao, H. Liu, X. Jia, D. Mou, S. Liu, J. He, Y. Peng, Y. Feng, Z. Xie, G. Liu, X. Dong, J. Zhang, X. Wang, Q. Peng, Z. Wang, S. Zhang, F. Yang, C. Chen, Z. Xu, X. Dai, Z. Fang, and X. J. Zhou, Proc. Natl. Acad. Sci. USA **109**, 3694 (2012).
[43] I. A. Nechaev, R. C. Hatch, M. Bianchi, D. Guan, C. Friedrich, I. Aguilera, J. L. Mi, B. B. Iversen, S. Blugel, P. Hofmann, and E. V. Chulkov, Phys. Rev. B **87**, 121111 (2013).

Reprinted page 9 of paper [85] "Optical properties of $Bi_2(Se_xTe_{1-x})_3$ alloys".

[44] W. Zhang, R. Yu, H.-J. Zhang, X. Dai, and Z. Fang, New J. Phys. **12**, 065013 (2010).
[45] O. V. Yazyev, E. Kioupakis, J. E. Moore, and S. G. Louie, Phys. Rev. B **85**, 161101 (2012).
[46] I. Aguilera, C. Friedrich, G. Bihlmayer, and S. Blugel, Phys. Rev. B **88**, 045206 (2013).
[47] R. Sehr and L. Testardi, J. Phys. Chem. Solids **23**, 1219 (1962).
[48] G. A. Thomas, D. H. Rapkine, R. B. vanDover, L. F. Mattheiss, W. A. Sunder, L. F. Schneemeyer, and J. V. Waszczak, Phys. Rev. B **46**, 1553 (1992).
[49] J. Sanchez-Barriga, M. R. Scholz, E. Golias, E. Rienks, D. Marchenko, A. Varykhalov, L. V. Yashina, and O. Rader, Phys. Rev. B. **90**, 195413 (2014).
[50] S. Mishra, S. Satpathy, and O. Jepsen, J. Phys. Condens. Matter **9**, 461 (1997).
[51] I. A. Nechaev and E. V. Chulkov, Phys. Rev. B **88**, 165135 (2013).
[52] M. Michiardi, I. Aguilera, M. Bianchi, V. E. de Carvalho, L. O. Ladeira, N. G. Teixeira, E. A. Soares, C. Friedrich, S. Blugel, and P. Hofmann, Phys. Rev. B **90**, 075105 (2014).

Reprinted page 10 of paper [85] "Optical properties of $Bi_2(Se_xTe_{1-x})_3$ alloys".

4.4 Manganese doping of Bi_2Se_3 topological insulator

The $(Bi,Mn)_2Se_3$ layers on BaF_2 were prepared and analyzed. The ARPES analysis has shown a band gap in Dirac point to be large $\approx 100\,meV$, and temperature independent. The ferromagnetic Curie temperature of about 10 K was determined by SQUID magnetometry and XMCD. The magnetic easy axis direction is in-plane. The band gap surviving up to room temperature is of non-magnetic origin.

nature COMMUNICATIONS

ARTICLE

Received 13 Jun 2015 | Accepted 26 Dec 2015 | Published 19 Feb 2016

DOI: 10.1038/ncomms10559 OPEN

Nonmagnetic band gap at the Dirac point of the magnetic topological insulator $(Bi_{1-x}Mn_x)_2Se_3$

J. Sánchez-Barriga[1], A. Varykhalov[1], G. Springholz[2], H. Steiner[2], R. Kirchschlager[2], G. Bauer[2], O. Caha[3], E. Schierle[1], E. Weschke[1], A.A. Ünal[1], S. Valencia[1], M. Dunst[4], J. Braun[4], H. Ebert[4], J. Minár[4,5], E. Golias[1], L.V. Yashina[6], A. Ney[2], V. Holý[7] & O. Rader[1]

Magnetic doping is expected to open a band gap at the Dirac point of topological insulators by breaking time-reversal symmetry and to enable novel topological phases. Epitaxial $(Bi_{1-x}Mn_x)_2Se_3$ is a prototypical magnetic topological insulator with a pronounced surface band gap of ~100 meV. We show that this gap is neither due to ferromagnetic order in the bulk or at the surface nor to the local magnetic moment of the Mn, making the system unsuitable for realizing the novel phases. We further show that Mn doping does not affect the inverted bulk band gap and the system remains topologically nontrivial. We suggest that strong resonant scattering processes cause the gap at the Dirac point and support this by the observation of in-gap states using resonant photoemission. Our findings establish a mechanism for gap opening in topological surface states which challenges the currently known conditions for topological protection.

[1] Helmholtz-Zentrum Berlin für Materialien und Energie, Elektronenspeicherring BESSY II, Albert-Einstein-Straße 15, 12489 Berlin, Germany. [2] Institut für Halbleiter und Festkörperphysik, Johannes Kepler Universität, Altenbergerstr. 69, 4040 Linz, Austria. [3] Department of Condensed Matter Physics, CEITEC, Masaryk University, Kotlarska 2, 61137 Brno, Czech Republic. [4] Department Chemie, Ludwig-Maximilians-Universität München, Butenandtstr. 5-13, 81377 München, Germany. [5] New Technologies Research Centre, University of West Bohemia, Univerzitni 8, 306 14 Pilsen, Czech Republic. [6] Department of Chemistry, Moscow State University, Leninskie Gory 1/3, 119991 Moscow, Russia. [7] Department of Condensed Matter Physics, Charles University, Ke Karlovu 5, 12116 Prague, Czech Republic. Correspondence and requests for materials should be addressed to J.S.-B. (email: jaime.sanchez-barriga@helmholtz-berlin.de) or to O.R. (email: rader@helmholtz-berlin.de).

Reprinted page 1 of paper [86] "Temperature independent gap in $(Bi,Mn)_2Se_3$ layers".

The topological surface state (TSS) of the three-dimensional topological insulator (3D TI) Bi_2Se_3 forms a Dirac cone in the band dispersion $E(k_{||})$ of electron energy E versus wave vector component $k_{||}$ parallel to the surface[1]. Differently from graphene, the electron spin is nondegenerate and locked to $k_{||}$, and the Dirac crossing point is protected by time-reversal symmetry (TRS) against distortions of the system[1,2]. This stability has been theoretically investigated demonstrating that nonmagnetic impurities at the surface and in the bulk can form a resonance in the surface-state density of states (DOS) without opening a band gap[3–5]. A magnetic field breaks TRS lifting the Kramers degeneracy $E(k_{||}, \uparrow) = E(-k_{||}, \downarrow)$ between up ($\uparrow$) and down ($\downarrow$) spins, and can open a band gap at the Dirac point[1]. For the two-dimensional quantum-spin-Hall system HgTe, the effect of a perpendicular magnetic field on the topologically protected edge state has been demonstrated successfully[6], and similar effects are expected from magnetic impurities in this system[7]. In subsequent studies on HgTe, the effect of the magnetic field was much smaller, and recently in an inverted electron-hole bilayer from InAs/GaSb, helical edge states proved robust in perpendicular magnetic fields of 8 T (ref. 8). At the surface of a 3D TI, calculations show that magnetic impurities can open a gap at the Dirac point and exhibit ferromagnetic order with perpendicular anisotropy mediated by the TSS through Ruderman–Kittel–Kasuya–Yosida (RKKY) exchange coupling[4,9,10].

3D TIs with magnetic impurities have been studied by angle-resolved photoelectron spectroscopy (ARPES). The magnetic impurities have been incorporated into the bulk[11] and at the surface of Bi_2Se_3 (ref. 10). For Fe impurities, the opening of large surface band gaps of $\sim$100 meV was reported in both cases[10,11]. In a previous work, however, we found that Fe deposited on Bi_2Se_3 does not open a gap for a wide range of preparation conditions, revealing a surprising robustness of the TSS towards magnetic moments[12]. This conclusion also extends to Gd/ Bi_2Se_3 (ref. 13) and Fe/Bi_2Te_3 (ref. 14).

The absence of a surface band gap is consistent with the recent finding that Fe on Bi_2Se_3 does not favour a magnetic anisotropy perpendicular to the surface, at least in the dilute limit[15]. In this respect, bulk impurities in TIs have an advantage over surface impurities in that ferromagnetic order and perpendicular magnetic anisotropies have been achieved in the bulk systems[11,16–21]. Fe incorporated in bulk Bi_2Te_3 is known to order ferromagnetically with a Curie temperature (T_C) of $\sim$12 K for concentrations of $x = 0.04$ showing an easy axis perpendicular to the base plane[16,17]. On the other hand, $(Bi_{1-x}Fe_x)_2Se_3$ has not been found to be ferromagnetic at temperatures above 2 K (ref. 17). For $x = 0.16$ and 0.25, ferromagnetic order was found at 2 K (ref. 11). By ARPES[22], surface-state band gaps in $(Bi_{1-x}Fe_x)_2Se_3$ were reported and assigned to a magnetic origin for Fe concentrations from $x = 0.05$ to 0.25 including nonferromagnetic concentrations such as $x = 0.12$ with a band gap of 45 meV (ref. 11). These band gaps have been attributed to short-range magnetic order. Concerning Mn incorporation, bulk $(Bi_{1-x}Mn_x)_2Se_3$ with $x = 0.02$ has been shown to exhibit a surface band gap with an occupied width of 7 meV (ref. 11), which was suggested as an indication of ferromagnetic order induced by the TSS[11]. However, much larger surface band gaps were observed for n-doped $(Bi_{1-x}Mn_x)_2Se_3$ films[20], where ferromagnetic order of Mn at the surface was found to be strongly enhanced with T_C up to $\sim$45 K. The ferromagnetic order resulted in an unusual spin texture of the TSS. The T_C at the surface was much higher than in the bulk[20], which was partially attributed to Mn surface accumulation. A strong enhancement of the surface T_C was also predicted by mean-field theory for this system (for example, from 73 K (bulk) to 103 K (surface))[23]. Magnetically doped TIs with ferromagnetic order are important as realizations of novel topological phases. When spin degeneracy is lifted by the exchange splitting, bulk band inversion can occur selectively for one spin. If also the Fermi level is in the band gap, as predicted for Cr and Fe in Bi_2Se_3 (ref. 24), this gives rise to an integer quantized Hall conductance σ_{xy} in thin films termed the quantized anomalous Hall effect[7,24]. This has recently been reported for Cr in $(Bi,Sb)_2Te_3$ (ref. 25). When a perpendicular magnetization breaks TRS at the surface of a bulk TI, the resulting mass and surface band gap give rise to quantized edge states. In this case σ_{xy} is half-integer quantized yielding a half quantum Hall effect[26] which can be probed at ferromagnetic domain boundaries at the surface[27] and leads to exotic topological magnetoelectric effects such as the point-charge-induced image magnetic monopole[28,29]. Another topological phase predicted for magnetically doped Bi_2Se_3 is the realization of a 3D Weyl fermion system in which the Dirac-like dispersions become a property of the bulk[30].

Here we present a detailed investigation on the correlation between the TSS and magnetic properties in the Bi-Mn-Se system, where the magnetic impurity Mn is introduced in the bulk of $\sim$0.4 μm thick $(Bi_{1-x}Mn_x)_2Se_3$ epilayers with concentrations up to $x = 0.08$. By ARPES we find remarkably large band gaps of $\sim$200 meV persisting up to temperatures of 300 K far above T_C, which is found to be $\sim$10 K at the surface showing only a limited enhancement by $\leq$4 K over the bulk T_C. We find that the magnitude of the band gaps by far exceeds that expected from TRS breaking due to magnetic order. By ARPES from quantum-well states we exclude that Mn changes the inverted bulk band gap. Using resonant photoemission and *ab initio* calculations we conclude that, instead, impurity-induced resonance states destroy the Dirac point of the TSS. We further support our conclusion by showing that extremely low-bulk concentrations of nonmagnetic In do also open a surface band gap in Bi_2Se_3. Our findings have profound implications for the understanding of the conditions for topological protection.

Results

Concentration and temperature dependence of surface band gap. Figure 1 shows Mn-concentration-dependent high-resolution ARPES dispersions of the TSS and bulk valence-band (BVB) states of $(Bi_{1-x}Mn_x)_2Se_3$ with x up to 0.08 measured at 12 K and 50 eV photon energy. At this energy, contributions from the bulk-conduction band (BCB) do not appear due to the dependence of the photoemission transitions on the component of the electron wave vector perpendicular to the surface $k_\perp$ (ref. 22), but the BCB is partially occupied as data at 21 eV photon energy reveal (Supplementary Fig. 1). The pure Bi_2Se_3 film (Fig. 1a) is n-doped and exhibits a well-resolved Dirac point with high photoemission intensity at a binding energy of $E_D \sim 0.4$ eV that is seen as an intense peak in the energy-distribution curve at zero momentum superimposed as red curve on the right-hand side of the panel. The intact and bright Dirac point marked by a horizontal dashed line in Fig. 1a demonstrates that the TSS is gapless in Bi_2Se_3. At larger binding energies, the lower half of the Dirac cone overlaps with the BVB, which is observed for all $(Bi_{1-x}Mn_x)_2Se_3$ samples (Figs 1b–d). Increasing Mn concentration, we find a gradual upward shift of the band edges in energy, revealing a progressive p-type doping (hole doping). Most notably, a surface band gap opens at the Dirac point with increasing Mn content. In each energy-distribution curve, the opening of the gap is also evident from the development of an intensity dip at the binding energy of the original Dirac point. Thus, the energy separation between the upper Dirac band minimum and the energy position of the intensity dip is about

Reprinted page 2 of paper [86] "Temperature independent gap in $(Bi,Mn)_2Se_3$ layers".

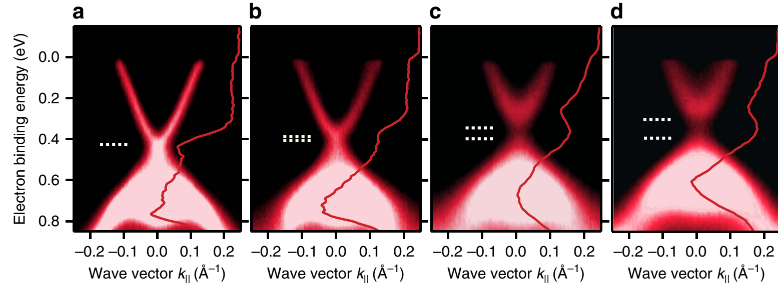

Figure 1 | Effect of Mn doping on the electronic band dispersions of $(Bi_{1-x}Mn_x)_2Se_3$. (**a**–**d**) Mn-concentration-dependent high-resolution ARPES dispersions measured at 50 eV photon energy and a temperature of 12 K for x values of (**a**) 0, (**b**) 0.02, (**c**) 0.04 and (**d**) 0.08. The red lines represent EDCs obtained in normal emission ($k_{||}=0$). A surface band gap opens at the Dirac point of the TSS which increases in size with increasing Mn content. The horizontal white-dashed lines highlight the minimum limit of the gap size after taking into account the contribution from the linewidth broadening. The opening of the gap leads to an intensity dip in the EDCs around the energy region of the original Dirac point. For $x=0.02$, the suppression of intensity at the Dirac point and the more parabolic surface-state dispersion are signatures of a small gap. Besides the increased linewidth broadening due to the Mn impurities, these effects become more pronounced with increasing Mn content.

half of the gap size. Note that the horizontal dashed lines in Figs 1b–d highlight the minimum limit of the gap size after taking into account the contribution from the linewidth broadening to the ARPES spectra (see Supplementary Note 1 and Supplementary Fig. 2). The surface band gap rapidly increases with Mn content and exceeds 200 meV for $x=0.08$. For $x=0.02$, the suppression of the Dirac point intensity as compared with the undoped Bi_2Se_3 film indicates the existence of a small gap. This is consistent with the fact that the TSS dispersion becomes slightly parabolic and is characterized by an increased effective mass of $m^* \approx 0.09m_e$ for $x=0.02$. This value increases further to $\approx 0.15m_e$ for $x=0.08$, where m_e is the free-electron mass.

The observed surface band gaps are similar to those previously reported[20], which have been attributed to long-range ferromagnetism and TRS breaking of the topologically protected surface state[20]. Figures 2a–d show high-resolution ARPES dispersions of the TSS, as well as the normal-emission spectra through the Dirac point at temperatures of 12 and 300 K for $x=0.08$ (see also Supplementary Fig. 3). Strikingly, there is no significant change as temperature is raised, and very clearly the band gap in the TSS persists up to room temperature. Moreover, we find a similar behaviour for the whole sample series independently of the Mn content, which challenges the dominant role of ferromagnetic order in inducing the band gap in the TSS, unless the surface T_C is above room temperature.

Bulk and surface magnetism. We begin in Fig. 3 with characterizing the bulk magnetic properties using superconducting quantum-interference device (SQUID) magnetometry. The comparison of measurements with in-plane and out-of-plane applied magnetic field in Fig. 3a shows that at a temperature of 2 K the bulk easy axis lies in the surface plane. This holds irrespective of the Mn concentration. Since the opening of a gap at the Dirac point requires a magnetization perpendicular to the surface[9], we concentrate in the following on the out-of-plane component of the magnetization. In the hysteresis loops displayed in Fig. 3b measured with an out-of-plane applied magnetic field at different temperatures, we observe a narrow magnetic hysteresis at 4.2 K, whereas paramagnetic behaviour emerges at 7 K once the ferromagnetic transition has been crossed (inset in Fig. 3b). For a better determination of T_C we present in Fig. 3c modified Arrott plots according to a 3D Heisenberg ferromagnet, normalized to the mass of the sample, with exponents $\beta=0.348$ and $\gamma=1.41$, from which we deduce

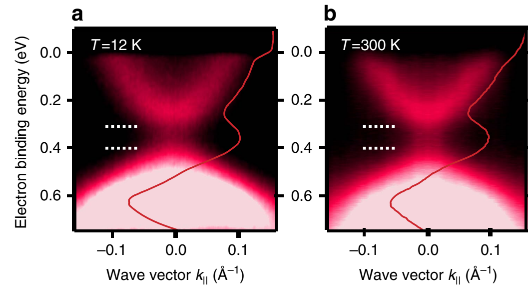

Figure 2 | Temperature dependence of the large energy scale surface band gap. (**a**,**b**) Energy-momentum ARPES dispersions obtained for Mn-doped Bi_2Se_3 epilayers with 8% Mn concentration. The red lines are the energy-distribution curves obtained in normal emission ($k_{||}=0$). The horizontal white-dashed lines highlight the surface gap. Measurements are taken at 50 eV photon energy and a temperature of (**a**) 12 K and (**b**) 300 K. The surface band gap does not show a remarkable temperature dependence.

$T_C=5.5$ K in the bulk (see also Supplementary Fig. 4). This is well below the temperature of our ARPES measurements shown in Figs 1 and 2.

The only remaining possibility that long-range ferromagnetism opens the gap at the Dirac point is an enhanced surface magnetism with magnetization perpendicular to the surface[9,20,23]. This cannot be verified directly by the bulk-sensitive SQUID magnetometry. Therefore, we perform X-ray magnetic circular dichroism (XMCD) measurements at the Mn $L_{2,3}$-edges to probe the near-surface ferromagnetic order. The detection by total electron yield leads to a probing depth in the nanometre range. Figure 4a shows for $x=0.04$ the normalized intensity of the Mn $L_{2,3}$ absorption edges obtained upon reversal of the photon helicity at a temperature of 5 K with an out-of-plane applied magnetic field of 3 T. The XMCD difference spectrum is shown in Fig. 4b, with the normalized XMCD difference signal following one part of the out-of-plane hysteresis as a function of the applied magnetic field as inset. The temperature dependence of the XMCD signal measured in remanence (0 T applied magnetic field) is presented in Fig. 4c for Mn concentrations of $x=0.04$ and 0.08. This signal is obtained after switching off an

Reprinted page 3 of paper [86] "Temperature independent gap in $(Bi,Mn)_2Se_3$ layers".

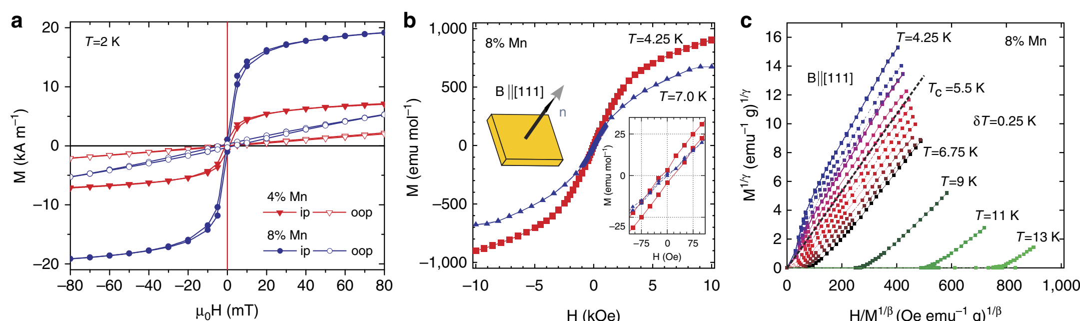

Figure 3 | Characterization of the bulk magnetic properties of Mn-doped Bi_2Se_3 films. (**a**) In-plane (ip) and out-of-plane (oop) magnetization curves for Mn concentrations of $x = 0.04$ and $x = 0.08$, measured at a temperature of 2 K using SQUID magnetometry. The magnetic anisotropy lies in the surface plane irrespective of the Mn concentration. (**b**) Corresponding hysteresis loops for $x = 0.08$ measured at a temperature of 4.25 K (squares) and 7 K (triangles), respectively. The applied magnetic field is perpendicular to the (111) sample surface (see sketch). Inset: a zoom-in around zero magnetic field showing hysteresis at 4.25 K and a paramagnetic state at 7 K. (**c**) Arrott plots at various temperatures from which a Curie temperature T_C of 5.5 K is deduced. Between 4.25 K and 6.75 K, data are shown for temperature increments of $\delta T = 0.25$ K.

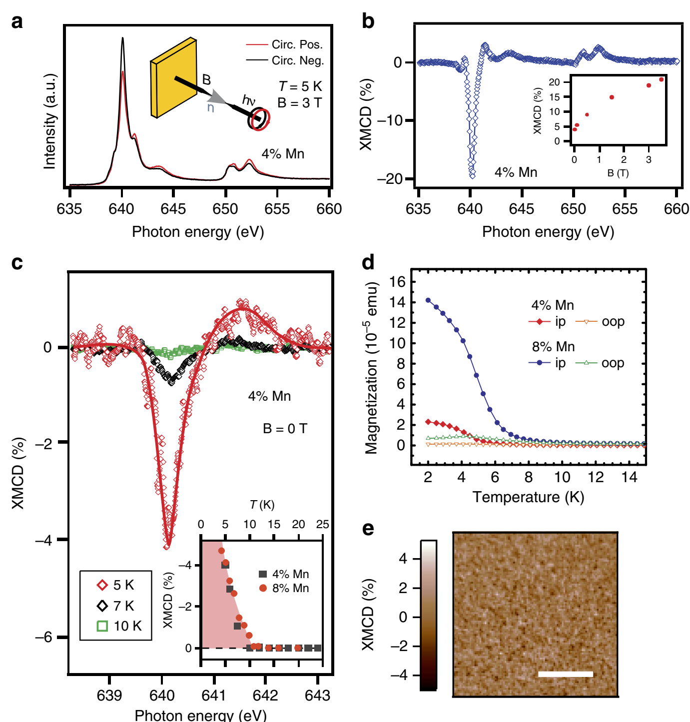

Figure 4 | XMCD in total electron yield at the Mn $L_{2,3}$-edges. (**a**) X-ray absorption spectra measured for opposite helicities of the circularly polarized incident light at 5 K with an out-of-plane applied magnetic field of 3 T. A sketch of the experimental geometry is also shown. (**b**) Corresponding XMCD difference spectrum. The inset shows XMCD measurements for different applied magnetic fields. (**c**) Temperature dependence of the remanent XMCD for a Mn concentration of $x = 0.04$. Inset: detailed temperature dependence for $x = 0.04$ and 0.08. (**d**) To re-examine the bulk magnetic properties, field-cooling measurements are obtained under an in-plane (ip) and out-of-plane (oop) applied magnetic field of 10 mT using SQUID magnetometry. The temperature dependence for $x = 0.04$ and 0.08 compares well with the surface-sensitive measurements shown in the inset of (**c**). (**e**) XMCD-PEEM image obtained using photoelectron microscopy for $x = 0.08$ at room temperature, revealing the absence of magnetic domains with partial or full out-of-plane magnetic order. Scale bar, 500 μm (horizontal white-solid line).

Reprinted page 4 of paper [86] "Temperature independent gap in (Bi,Mn)$_2$Se$_3$ layers".

applied magnetic field of 5 T perpendicular to the surface, and represents the remanent XMCD, which is proportional to the remanent magnetization of the film surface. We clearly observe a ferromagnetic Mn component in the remanent XMCD appearing around 640 eV which becomes increasingly more pronounced at lower temperatures. The lineshape of the XMCD spectrum is similar to that of Mn in GaAs[31], indicating a predominant d^5 configuration. More specifically, the lineshape compares rather well with Mn in Bi_2Te_3 for which the comparison with an Anderson impurity model recently gave a superposition of 16% d^4, 58% d^5 and 26% d^6 character[32]. The ferromagnetic Mn component shows surface ferromagnetic order in the remanent XMCD only below 10 K for Mn concentrations of $x = 0.04$ and 0.08 (inset in Fig. 4c). On one hand, this result is not inconsistent with the predicted strong-surface enhancement of T_C since the enhancement effect vanishes already when chemical potential and Dirac point differ by 0.2 eV (ref. 23). On the other hand, our XMCD result means that the magnetically induced gap would have to close above 10 K.

Having established that the bulk and surface magnetic properties of our samples are very similar, as a next step, we performed field-cooling experiments to re-examine the bulk magnetic properties. Figure 4d shows field-cooled SQUID data for an applied magnetic field of 10 mT parallel and perpendicular to the surface plane. Above T_C, there is no preferential orientation of the anisotropy axis perpendicular to the surface. Additional zero-field-cooled SQUID data compare rather well with these results (Supplementary Fig. 5). Further XMCD measurements under an in-plane and out-of-plane applied magnetic field are consistent with the SQUID data and are shown in Supplementary Fig. 6. These XMCD and SQUID results strongly suggest that above T_C also short-range static magnetic order does not play a role at the surface or in the bulk, respectively (see Supplementary Note 2), and that domains with partial or full out-of-plane magnetic order are absent. We further support this conclusion by additional XMCD measurements carried out by the means of X-ray photoelectron emission microscopy (XMCD-PEEM) at room temperature, with a lateral resolution of $\sim$20 nm. Figure 4e shows the XMCD image which due to the light incidence (16° grazing) is sensitve to both in- and out-of-plane components of the magnetization, with additional data given in Supplementary Figs 7,8. The XMCD image displays no magnetic domains at room temperature thus also excluding short-range static inhomogeneous magnetic order with magnetization partially or fully in or out of the surface plane, at least within our lateral resolution (see Supplementary Note 3 for details). A similar conclusion can be drawn regarding out-of-plane magnetic short-range fluctuations (see discussion in Supplementary Note 4 and Supplementary Fig. 9). All our observations taken together lead us to the important conclusion that the surface band gap is not due to magnetism and, thus, the novel topological phases cannot be realized with $(Bi_{1-x}Mn_x)_2Se_3$.

Absence of topological phase transition with concentration. There exists an alternative nonmagnetic explanation for the surface band gap. It is in principle possible that the incorporation of Mn changes the bulk band structure and even reverts the bulk band inversion, rendering Mn-doped Bi_2Se_3 topologically trivial. This topological phase transition with concentration is, for example, the basis for the HgTe quantum spin-Hall insulator[6]. Interestingly, it has been argued that a gap in the TSS can be a precursor of a reversed bulk band inversion, as discussed for $TlBi(S_{1-x}Se_x)_2$ (ref. 33). Indium substitution in Bi_2Se_3 behaves similarly, and leads to a topological-to-trivial quantum-phase transition with an inversion point between 3 and 7% In in thin films[34]. Figure 5 shows that the bulk band gap stays constant within 4% of its value for 8% Mn incorporation. This statement is possible because at low photon energies changes in the bulk band gap are traced most precisely from quantum-well states in normal emission ($k_{||} = 0$). The simultaneous quantization of BCB and BVB is created by surface band bending after adsorption of small amounts of residual gas[35]. This means that the scenario of reversed bulk band inversion does not hold here.

Another remarkable feature is the measured size of the surface band gap. A perpendicular magnetic anisotropy has recently been predicted by density-functional theory (DFT) for Co in Bi_2Se_3 (ref. 36) as well as for 0.25 monolayer Co adsorbed on the surface in substitutional sites, leading to a surface band gap of $\sim$9 meV (ref. 36), which, however, is one order of magnitude smaller than the gaps observed here. For $(Bi_{1-x}Mn_x)_2Te_3$, a surface band gap of 16 meV has been calculated under the condition of perpendicular magnetic anisotropy[37]. For Mn in Bi_2Se_3 at the energetically favoured Bi-substitutional sites, an in-plane magnetic anisotropy is predicted[38]. The size of the gap at the Dirac point is only 4 meV (ref. 38). Perpendicular anisotropy and ferromagnetic order are absent in our samples at the temperature of the ARPES measurements.

Role of the local magnetic moment and intercalation scenarios. If the large local magnetic moment of the Mn is responsible for the measured band gaps via TRS breaking, the effect should be equal or larger when Mn is deposited directly on the surface. Here we argue in the following way: If TRS is broken only due to the Mn magnetic moment, we do not require hybridization to open a gap. By depositing Mn we create a completely different environment for the Mn at the surface, allowing us to understand whether the Mn magnetic moment is solely responsible for the opening of large surface band gaps via TRS breaking and, ideally, without hybridization playing a role. Mn is very well suited for such comparison, as due to the high stability of its half-filled d^5 configuration, its high magnetic moment is to a large extent independent of the atomic environment and the resulting hybridization. DFT obtains 4.0 μ_B for most substitutional sites (except for the hypothetical Se-substitutional site with still 3.0 μ_B) and only for interstitial Mn the moment peaks with 5.0 μ_B (ref. 38). Mn deposition was performed at $\sim$30 K in order to keep the Mn atoms isolated from each other and on the surface. As the XMCD showed a predominant d^5 configuration for Mn bulk impurities, which is most stable, we can assume the same magnetic moment for Mn impurities deposited on the surface. Figure 6 shows that a similar *p*-doping occurs as with the Mn in the bulk. In another respect, the magnetic moments do not act in a similar way as in the bulk. Even 30% of a Mn monolayer on Bi_2Se_3 does not open a band gap at the Dirac point. This result is similar to what we have observed for Fe on Bi_2Se_3 (ref. 12) and Bi_2Te_3 (ref. 14).

Most recently, the appearance of surface band gaps in ARPES at the Dirac point of the TSS has been discussed based on different mechanisms. One is momentum fluctuations of the surface Dirac fermions in real space as observed by scanning tunnelling microscopy measurements of Mn-doped Bi_2Te_3 and Bi_2Se_3 bulk single crystals[39]. However, these fluctuations amount to 16 meV (ref. 39), much less than the present band gaps. Another mechanism is top-layer relaxation, that is, breaking of the van-der-Waals bond between quintuple layers during cleavage of bulk crystals as proposed in Xu *et al.*[20] This would open a gap due to hybridization of TSS's through the layer[40] but such an effect does not occur for epitaxial layers where no sample cleavage is used for surface preparation.

Reprinted page 5 of paper [86] "Temperature independent gap in $(Bi,Mn)_2Se_3$ layers".

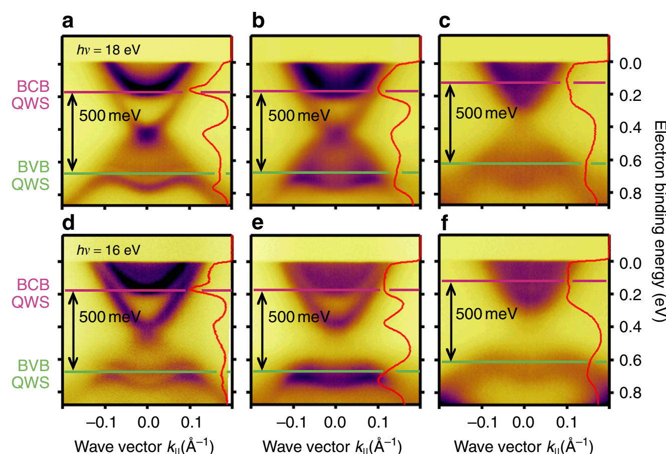

Figure 5 | Tracing changes in the bulk band gap of Mn-doped Bi_2Se_3 films. Changes in the bulk band gap are traced most precisely from quantum-well states (QWS) in normal emission (red curves on the right-hand side of each panel).(**a–c**) Energy-momentum dispersions acquired at a photon energy of $h\nu = 18$ eV for (**a**) Bi_2Se_3, (**b**) 2% and (**c**) 8% Mn doping. The simultaneous quantization of bulk-conduction band (BCB) and valence-band (BVB) is created by surface band bending after adsorption of small amounts of residual gas[35]. It is found that Mn doping does not change the bulk band gap of Bi_2Se_3. (**d–f**) Similar results as in **a–c**, respectively, but at a photon energy of $h\nu = 16$ eV, where large apparent surface band gaps are observed. This unexpected photon-energy dependence of a surface state is interpreted as coupling to bulk states mediated by the Mn impurities.

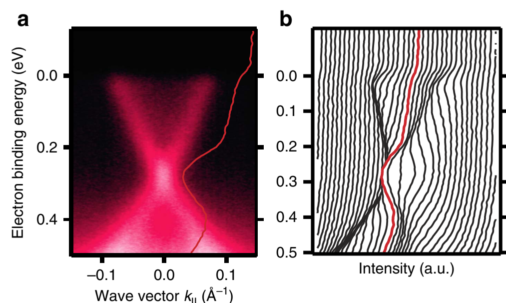

Figure 6 | Effect of Mn deposition on the surface of Bi_2Se_3 films. (**a**) Energy-momentum ARPES dispersion showing a gapless Dirac cone in pure Bi_2Se_3 films after deposition of 0.3 monolayer Mn at 30 K on the surface. Measurements are performed at the same temperature using 50 eV photon energy. (**b**) EDCs extracted from the measurements shown in **a**. The red curves in **a** and **b** emphasize the EDC in normal emission ($k_{||} = 0$).

If such a separation of quintuple layers occurs, it is more likely caused by the Mn. Principally, intercalated Mn in the van-der-Waals gaps could separate quintuple layers electronically, although such effect has not been seen in experiments yet. At these new interfaces TSS's could form and if they would behave like in ultra-thin Bi_2Se_3 films, they would hybridize and open a band gap[40]. However, band gaps of the order of ~100 meV would correspond to an unrealistic Mn intercalation pattern grouping three quintuple layers when compared with the films of Zhang *et al.*[40] In order to estimate the amount of Mn intercalation, we have analysed the change of the bulk lattice constant in our samples by X-ray diffraction (see Supplementary Note 5, Supplementary Figs 10–13 and Supplementary Tables 1,2). We find that the *c*-lattice constant increases by ~0.15% for 4% Mn and by ~0.45% for 8% Mn. If we would assume that this is completely due to an expansion of the van-der-Waals gaps, the interlayer distance would increase by only ~1.8% for 4% Mn and by less than ~5% for 8% Mn. According to DFT, intercalation of transition metals into the first van-der-Waals gap of Bi_2Se_3 leads to an expansion between 10 and 20% (ref. 41). New surface-state features can appear inside the bulk band gap but in order to be split remarkably off the BVB and BCB edges, expansions between 20 and 50% are required[41]. In addition, we point out that, despite our observation of a large surface band gap at room temperature, we observe a nearly zero spin polarization perpendicular to the surface (Supplementary Fig. 14). The absence of a hedgehog spin texture pinpoints a non-TRS breaking mechanism underlying the origin of the gap, a fact which is consistent with our conclusions derived from the magnetic properties. Moreover, it is understood that we cannot verify a small magnetic band gap opening of few meV as calculated in Schmidt *et al.*[36] and Henk *et al.*[37] because much larger gaps are present in the whole temperature range.

Topological protection beyond the continuum model. As we find that neither ferromagnetic order in the bulk or at the surface, nor the local magnetic moment of the Mn are causing the large band gaps that we observe, as we can exclude the nonmagnetic explanation of a reversal of the bulk band inversion and as we do not find sufficient indications for the nonmagnetic explanation of surface-state hybridization by van-der-Waals-gap expansion, we point out a different mechanism based on impurity-induced resonance states that locally destroy the Dirac point.

In fact, recently the treatment of the topological protection in the continuum model[3–5] has been extended for finite bulk band gaps[42,43]. As a result, surface[42] and bulk impurities[43] can mediate scattering processes via bulk states and the localized impurity-induced resonance states emerging at and around the Dirac point lead to a local destruction of the topological protection of the Dirac point. The resulting band gap opening depends on the resonance energy, impurity strength *U* as well as spatial location of the impurities[42,43]. A typical gap size is of the order of 100 meV

Reprinted page 6 of paper [86] "Temperature independent gap in $(Bi,Mn)_2Se_3$ layers".

(ref. 42). Moreover, the gap does not rely on a particular magnetic property of the impurity and, therefore, the mechanism should apply for magnetic impurities as well. The model can also explain the absence of the gap when Mn impurities are placed on the surface, since bulk-like resonance states do not form when Mn is placed only on the surface. A definite assignment, however, requires realistic electronic structure calculations since a simple atomic Mn d^5 configuration does not lead to states at the Dirac point.

To identify impurity resonances, we calculated for 8% Mn in Bi_2Se_3 at the Bi-substitutional sites the corresponding DOS by *ab initio* theory. The model structure used in the calculations is shown in Fig. 7a, where Bi atoms (yellow) acquire Mn character (blue wedges). The results of the calculation are shown in Fig. 7b, where it is seen that Mn impurity states (blue) strongly contribute to the total DOS (red) near the BVB maximum. The Mn impurity states in the gap are clearly identified by assuming ferromagnetic order and subtracting the minority from majority spin DOS. In experiment, impurity-band states are difficult to observe as the example of $Ga_{1-x}Mn_xAs$ shows[44], where—similarly to the present case—impurity states emerge near the BVB maximum. There are, in fact, indications for the impurity resonances in our data. If we look at the photon-energy dependence from 16 to 21 eV in the ARPES results shown in Supplementary Fig. 15, we see that the surface band gap is only well defined with respect to the minimum of the upper Dirac cone and consistent for 16–21 eV as well as 50 eV (for 50 eV see Figs 1,2, where the BCB does not appear). The lower Dirac cone exhibits despite its

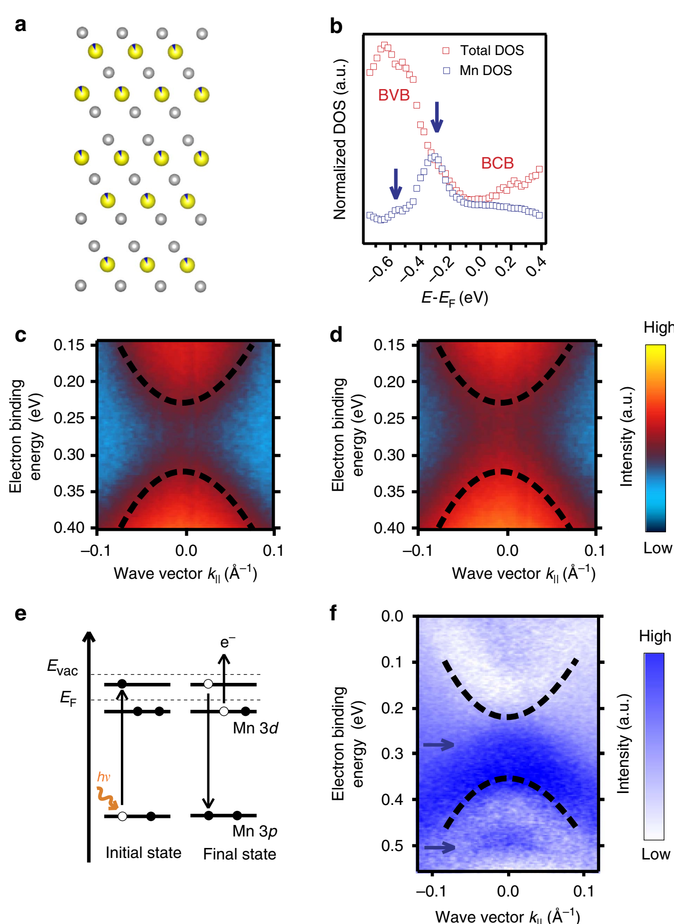

Figure 7 | Resonant photoemission and *ab initio* calculations. (**a**) The structure of Bi_2Se_3 doped with 8% Mn at the Bi-substitutional sites used in the calculations. Within the coherent-potential approximation, the Bi atoms (yellow) acquire Mn character (blue wedges). Se atoms are shown in grey colour. (**b**) Calculated density of states (DOS). The total DOS (red) contains contributions from impurity resonances (vertical blue arrows) of strong d-character, a seen in the partial Mn DOS (blue). For the purpose of the calculation, ferromagnetic order at $T=0$ K was assumed. (**c**,**d**) Resonant photoemission at the Mn *M*-edge, focusing on the region of the surface gap (8% Mn). (**c**) Off-resonant (48 eV photon energy) and (**d**) on-resonant data (50 eV). (**e**) Schematics of the resonant process. At the resonance energy, the excitation occurs via 3*p*–3*d* transitions. The exciting photon energy ($h\nu$) corresponds to a transition from an occupied core level to a valence-band empty state between the Fermi (E_F) and vacuum (E_{vac}) levels. The relaxation of excited electrons leads to enhanced photoemission from *d*-like Mn states. (**f**) Intensity difference obtained after subtracting off-resonant from on-resonant data. The resonances are seen in blue contrast and are marked with arrows, similar to the calculations shown in **b**.

Reprinted page 7 of paper [86] "Temperature independent gap in $(Bi,Mn)_2Se_3$ layers".

two-dimensional nature a photon-energy (wave vector perpendicular to the surface, $k_\perp$) dependence when Mn is incorporated. The reason for this difference is that the lower Dirac cone strongly overlaps with the BVB while the upper Dirac cone does not overlap with the BCB. This can also be seen in Fig. 5, where an apparent band gap of $\sim$200 meV occurs for 2% Mn at $h\nu = 16$ eV. At this small concentration, such an apparent gap seems to be nearly closed at 18 eV, where the suppression of the Dirac point intensity and the more parabolic TSS dispersion as compared with the undoped Bi_2Se_3 film indicates the existence of a small gap, in agreement with the results of Fig. 1. Note that the minimum band gap in the photon-energy dependence defines the gap size (see Supplementary Fig. 16). The minimum gap size observed at low photon energies agrees well with the one obtained at 50 eV. At 8% Mn, the surface band gap opens at all photon energies and reaches a minimum of $\sim$200 meV, that is, it is determined rather unambiguously, but some intensity appears in the surface band gap. Such intensity also appears in Xu *et al.*[20] The role of the impurity resonance is exactly to couple the TSS to bulk states. This 3D coupling is naturally different for the upper and lower Dirac cone due to the different bulk overlap and thus seen as the photon-energy dependence of the lower half of the Dirac cone.

We applied resonant photoemission which fortunately is comparatively strong for Mn due to its half-filled *d*-shell. Figures 7c and d show for 8% Mn off-resonant ($h\nu = 48$ eV) and on-resonant photoemission (50 eV) measurements via the Mn 3*p* core level, focusing on the region of the surface gap, respectively. The spectra were normalized to the photon flux after taking into account the photon-energy dependence of the photoionization cross sections of Bi 6*p* and Se 4*p*, respectively. Subtracting off-resonant from on-resonant data allows us to visualize directly the contribution from impurity resonances in the ARPES spectrum, as there is enhanced photoemission from *d*-like Mn states through decay of electrons that are excited via 3*p*–3*d* transitions (Fig. 7e). The difference spectrum shown in Fig. 7f reveals the existence of impurity resonances inside the surface band gap and near the valence-band maximum. The resonances are seen in blue contrast and are marked with arrows, similar to the calculations shown in Fig. 7b. The unexpectedly strong dispersion of the resonant states with wave vector $k_{||}$ is in qualitative agreement with our one-step model photoemission calculations (see Supplementary Fig. 17 and Supplementary Note 6), and additionally supports the physical picture of Mn-induced coupling to the bulk states. We should emphasize that the Mn d^5 configuration confirmed by our XMCD measurements offers much fewer states in the energy range of the Dirac cone than the other magnetic transition metals. The fact that already Mn breaks the Dirac cone indicates that the present result is of general importance for TIs doped with magnetic transition metals.

As nonmagnetic control experiment we have chosen thick In-doped Bi_2Se_3 bulk samples which give rise to a trivial phase close to $\sim$5% In concentration. Supplementary Fig. 18 shows that a large band gap of the order of $\sim$100 meV appears at the Dirac point already for a much smaller In concentration, namely 2%, far away from the inversion point of the topological quantum-phase transition (see Supplementary Note 7 and Supplementary Fig. 19 for more details). In addition, spin-resolved ARPES measurements around $k_{||} = 0$ for In-doped samples (Supplementary Fig. 14) reveal that the out-of-plane spin polarization is zero, similarly to the result for the gapped Dirac cone in Mn-doped samples. Interestingly, the size of the band gap for 2% In is of the same order as the one for 8% Mn whereas no gap appears for 4% Sn (Supplementary Fig. 18). This indicates that the concentration range at which the large surface gap develops varies from dopant to dopant. On the basis of ideas proposed recently[42,43], this might be associated with the impurity-dependent strength *U*, regardless whether the dopant is magnetic or not. Our control experiments demonstrate the existence of a mechanism for surface band gap opening which is not directly connected to long-range or local magnetic properties. Although it is not possible to directly search for In impurity resonances in the photoemission experiment as there is no resonant photoemission condition available, for completeness we point out that our conclusion on the nonmagnetic origin of the surface band gap in Mn-doped Bi_2Se_3 films would not have been possible unless several findings in our experiment differed from previous experiments[20]. This refers to the in-plane magnetic anisotropy, the absence of a temperature dependence of the gap, a much lower T_C, no out-of-plane spin polarization at the gapped Dirac point, no enhanced surface magnetism, a photon-energy dependence of the band gap, and an available resonant condition via the Mn 3*p* core level allowing us to directly observe the contribution from in-gap states.

To summarize, we revealed the opening of large surface band gaps in the TSS of Mn-doped Bi_2Se_3 epilayers that strongly increase with increasing Mn content. We find ferromagnetic hysteresis at low temperatures, with the magnetization oriented parallel to the film surface. Magnetic surface enhancement is absent. Even above the ferromagnetic transition, we observe surface band gaps which are one order of magnitude larger than the magnetic gaps theoretically predicted and, moreover, they do not show notable temperature dependence. No indication for a Mn-induced reversal of the bulk band inversion and no significant enhancement of the surface magnetic ordering transition with respect to the bulk are found. Control experiments with nonmagnetic bulk impurities, conducted in the topological phase, reveal that surface band gaps of the order of $\sim$100 meV can be created without magnetic moments. In line with recent theoretical predictions, we conclude that the band gap opening up to room temperature in Mn-doped films is not induced by ferromagnetic order and that even the presence of magnetic moments is not required. Our results are important in the context of topological protection and provide strong circumstantial evidence that Mn-doped Bi_2Se_3 is not suited for observing the quantized anomalous Hall effect or the half quantum Hall effect.

Methods

Sample growth and structural characterization. The samples were grown by molecular beam epitaxy on (111)-oriented BaF_2 substrates at a substrate temperature of 360 °C using Bi_2Se_3, Mn and Se effusion cells. The Mn concentration was varied between 0 and 8%, and a two-dimensional growth was observed by *in situ* reflection high-energy electron diffraction in all cases (see Supplementary Fig. 20 and Supplementary Note 8). All samples were single phase as indicated by X-ray diffraction. After growth and cooling to room temperature, the $\sim$0.4-μm-thick epilayers were *in situ* capped by an amorphous 50-nm thick Se layer, which was desorbed inside the ARPES and XMCD chambers by carefully annealing at $\sim$230 °C for $\sim$1 h. The Mn concentrations determined by core-level photoemission were in good agreement with those obtained from energy dispersive microanalysis, indicating no significant Mn accumulation at the surface of the samples (see Supplementary Fig. 21 and Supplementary Note 9).

High-resolution and spin-resolved ARPES. Temperature-dependent ARPES measurements were performed at the UE112-PGM2a beamline of BESSY II at pressures better than 1×10^{-10} mbar using p-polarized undulator radiation. Photoelectrons were detected with a Scienta R8000 electron energy analyser and the spin-resolved spectra were obtained with a Mott-type spin polarimeter coupled to the hemispherical analyser. For the spin-resolved measurements of Mn-doped Bi_2Se_3 samples, a magnetic field of $+0.3$ T was applied perpendicular to the surface plane at 20 K right before the acquisition of the spectra. Overall resolutions of ARPES measurements were 5 meV (energy) and 0.3° (angular). Resolutions for spin-resolved ARPES were 80 meV (energy) and 0.75° (angular).

Magnetic characterization. The characterization of the bulk magnetic properties was done by SQUID magnetometry. The bulk magnetization was recorded as a

Reprinted page 8 of paper [86] "Temperature independent gap in (Bi,Mn)$_2$Se$_3$ layers".

function of temperature and applied magnetic field applied either perpendicular (out-of-plane) or parallel (in-plane) to the surface of the films. The diamagnetic contribution of the BaF_2 substrate was derived from the field-dependent magnetization curves at room temperature and subtracted from all data. The characterization of the surface magnetic properties was done by XMCD and XMCD-PEEM measurements at the UE46-PGM1 and UE49-PGM1a beamlines of BESSY II, respectively. The experiments were performed using circularly polarized undulator radiation and under the same pressure conditions as the ARPES measurements. The XMCD spectra were taken using a high-field diffractometer as a function of temperature and applied magnetic field, and the XMCD-PEEM measurements were performed at room temperature and under grazing incidence (16°) with a lateral resolution of ~ 20 nm.

Theoretical calculations. The one-step model photoemission calculations were performed using the results of *ab initio* theory as an input, and taking into account wave vector and energy-dependent transition matrix elements. The *ab initio* calculations were performed within the coherent-potential approximation using the Munich SPR-KKR program package[45,46], with spin-orbit coupling included by solving the four-component Dirac equation.

References

1. Hasan, M. Z. & Kane, C. L. Topological insulators. *Rev. Mod. Phys.* **82,** 3045–3067 (2010).
2. Qi, X.-L. & Zhang, S.-C. Topological insulators and superconductors. *Rev. Mod. Phys.* **83,** 1057–1110 (2011).
3. Lee, W. C., Wu, C., Arovas, D. P. & Zhang, S. C. Quasiparticle interference on the surface of the topological insulator Bi_2Te_3. *Phys. Rev. B* **80,** 245439 (2009).
4. Biswas, R. R. & Balatsky, A. V. Impurity-induced states on the surface of three-dimensional topological insulators. *Phys. Rev. B* **81,** 233405 (2010).
5. Lu, J., Shan, W.-Y., Lu, H.-Z. & Shen, S.-Q. Non-magnetic impurities and in-gap bound states in topological insulators. *New J. Phys.* **13,** 103016 (2011).
6. König, M. *et al.* Quantum spin Hall insulator state in HgTe quantum wells. *Science* **318,** 766–770 (2007).
7. Liu, C.-X., Qi, X.-L., Dai, X., Fang, Z. & Zhang, S.-C. Quantum anomalous Hall effect in $Hg_{1-y}Mn_yTe$ quantum wells. *Phys. Rev. Lett.* **101,** 146802 (2008).
8. Du, L., Knez, I., Sullivan, G. & Du, R.-R. Robust helical edge transport in gated InAs/GaSb bilayers. *Phys. Rev. Lett.* **114,** 096802 (2015).
9. Liu, Q., Liu, C. X., Xu, C. K., Qi, X. L. & Zhang, S. C. Magnetic impurities on the surface of a topological insulator. *Phys. Rev. Lett.* **102,** 156603 (2009).
10. Wray, L. A. *et al.* A topological insulator surface under strong Coulomb, magnetic and disorder perturbations. *Nat. Phys.* **7,** 32–37 (2011).
11. Chen, Y. L. *et al.* Massive Dirac fermion on the surface of a magnetically doped topological insulator. *Science* **329,** 659–662 (2010).
12. Scholz, M. R. *et al.* Tolerance of topological surface states towards magnetic moments: Fe on Bi_2Se_3. *Phys. Rev. Lett.* **108,** 256810 (2012).
13. Valla, T., Pan, Z.-H., Gardner, D., Lee, Y. S. & Chu, S. Photoemission Spectroscopy of magnetic and nonmagnetic impurities on the surface of the Bi_2Se_3 topological insulator. *Phys. Rev. Lett.* **108,** 117601 (2012).
14. Scholz, M. R. *et al.* Intact Dirac cone of Bi_2Te_3 covered with a monolayer Fe. *Phys. Status Solidi RRL* **7,** 139–141 (2013).
15. Honolka, J. *et al.* In-plane magnetic anisotropy of Fe atoms on Bi_2Se_3 (111). *Phys. Rev. Lett.* **108,** 256811 (2012).
16. Kulbachinskii, V. A. *et al.* Ferromagnetic transition in the new diluted magnetic semiconductor p-$Bi_{2-x}Fe_xTe_3$. *Phys. Lett. A* **285,** 173–176 (2001).
17. Kulbachinskii, V. A. *et al.* Ferromagnetism in new diluted magnetic semiconductor $Bi_{2-x}Fe_xTe_3$. *Physica B* **311,** 292–297 (2002).
18. Hor, Y. S. *et al.* Development of ferromagnetism in the doped topological insulator $Bi_{2-x}Fe_xTe_3$. *Phys. Rev. B* **81,** 195203 (2010).
19. Dyck, J. S., Hájek, P., Lošťák, P. & Uher, C. Diluted magnetic semiconductors based on $Sb_{2-x}V_xTe_3$ ($0.01 < x < 0.03$). *Phys. Rev. B* **65,** 115212 (2002).
20. Xu, S.-Y. *et al.* Hedgehog spin texture and Berry's phase tuning in a magnetic topological insulator. *Nat. Phys.* **8,** 616–622 (2012).
21. Checkelsky, J. G., Ye, J., Onose, Y., Iwasa, Y. & Tokura, Y. Dirac-fermion-mediated ferromagnetism in a topological insulator. *Nat. Phys.* **8,** 729–733 (2012).
22. Hüfner, S. *Photoelectron Spectroscopy: Principles and Applications* (Springer, 1995).
23. Rosenberg, G. & Franz, M. Surface magnetic ordering in topological insulators with bulk magnetic dopants. *Phys. Rev. B* **85,** 195119 (2012).
24. Yu, R. *et al.* Quantized anomalous Hall effect in magnetic topological insulators. *Science* **329,** 61–64 (2010).
25. Chang, C.-Z. *et al.* Experimental observation of the quantum anomalous Hall effect in a magnetic topological insulator. *Science* **340,** 167–170 (2013).
26. Qi, X. L., Hughes, T. L. & Zhang, S. C. Topological field theory of time-reversal invariant insulators. *Phys. Rev. B* **78,** 195424 (2008).
27. Pankratov, O. A. Supersymmetric inhomogeneous semiconductor structures and the nature of a parity anomaly in $(2+1)$ electrodynamics. *Phys. Lett. A* **121,** 360–366 (1987).
28. Qi, X.-L., Li, R., Zang, J. & Zhang, S.-C. Inducing a magnetic monopole with topological surface states. *Science* **323,** 1184–1187 (2009).
29. Zang, J. & Nagaosa, N. Monopole current and unconventional Hall response on a topological insulator. *Phys. Rev. B* **81,** 245125 (2010).
30. Cho, G. Y. Possible topological phases of bulk magnetically doped Bi_2Se_3: turning a topological band insulator into the Weyl semimetal. Preprint at http://arxiv.org/abs/1110.1939 (2011).
31. Rader, O. *et al.* Identification of extrinsic Mn contributions in $Ga_{1-x}Mn_xAs$ by field-dependent magnetic circular x-ray dichroism. *J. Electron Spectr. Relat. Phenom.* **144,** 789–792 (2005).
32. Watson, M. D. *et al.* Study of the structural, electric and magnetic properties of Mn-doped Bi_2Te_3 single crystals. *New J. Phys.* **15,** 103016 (2013).
33. Sato, T. *et al.* Unexpected mass acquisition of Dirac fermions at the quantum phase transition of a topological insulator. *Nat. Phys.* **7,** 840–844 (2011).
34. Brahlek, M. *et al.* Topological-metal to band-insulator transition in $(Bi_{1-x}In_x)_2Se_3$ thin films. *Phys. Rev. Lett.* **109,** 186403 (2012).
35. Bianchi, M., Hatch, R. C., Mi, J., Iversen, B. B. & Hofmann, P. Simultaneous quantization of bulk conduction and valence states through adsorption of nonmagnetic impurities on Bi_2Se_3. *Phys. Rev. Lett.* **107,** 086802 (2011).
36. Schmidt, T. M., Miwa, R. H. & Fazzio, A. Spin texture and magnetic anisotropy of Co impurities in Bi_2Se_3 topological insulators. *Phys. Rev. B* **84,** 245418 (2011).
37. Henk, J. *et al.* Topological character and magnetism of the Dirac state in Mn-doped Bi_2Te_3. *Phys. Rev. Lett.* **109,** 076801 (2012).
38. Abdalla, L. B., Seixas, L., Schmidt, T. M., Miwa, R. H. & Fazzio, A. Topological insulator Bi_2Se_3(111) surface doped with transition metals: an ab-initio investigation. *Phys. Rev. B* **88,** 045312 (2013).
39. Beidenkopf, H. *et al.* Spatial fluctuations of helical Dirac fermions on the surface of topological insulators. *Nat. Phys.* **7,** 939–943 (2011).
40. Zhang, Y. *et al.* Crossover of the three-dimensional topological insulator Bi_2Se_3 to the two-dimensional limit. *Nat. Phys.* **6,** 584–588 (2010).
41. Eremeev, S. V., Vergniory, M. G., Menshchikova, T. V., Shaposhnikov, A. A. & Chulkov, E. V. The effect of van der Waal's gap expansions on the surface electronic structure of layered topological insulators. *New J. Phys.* **14,** 113030 (2012).
42. Black-Schaffer, A. M. & Balatsky, A. V. Strong potential impurities on the surface of a topological insulator. *Phys. Rev. B* **85,** 121103(R) (2012).
43. Black-Schaffer, A. M. & Balatsky, A. V. Subsurface impurities and vacancies in a three-dimensional topological insulator. *Phys. Rev. B* **86,** 115433 (2012).
44. Gray, A. X. *et al.* Bulk electronic structure of the dilute magnetic semiconductor $Ga_{1-x}Mn_xAs$ through hard x-ray angle-resolved photoemission. *Nat. Mater.* **11,** 957–962 (2012).
45. Ebert, H., Ködderitzsch, D. & Minár, J. Calculating condensed matter properties using the KKR–Green's function method–recent developments and applications. *Rep. Prog. Phys.* **74,** 096501 (2011).
46. Ebert, H. *et al.* The Munich SPR-KKR package, version 6.3. Available at http://ebert.cup.uni-muenchen.de/SPRKKR.

Acknowledgements

Financial support from the priority program SPP 1666 of the Deutsche Forschungsgemeinschaft (Grant No. EB154/26-1 and RA1041/7-1) and the Impuls-und Vernetzungsfonds der Helmholtz-Gemeinschaft (Grant No. HRJRG-408) is gratefully acknowledged. J.M. is supported by the CENTEM (CZ.1.05/2.1.00/03.0088) and CENTEM PLUS (LO1402) projects, co-funded by the ERDF as part of the Ministry of Education, Youth and Sports OP RDI programme. V.H. acknowledges the support of the Czech Science Foundation (project 14-08124S). G.S., H.S., R.K. and G.B. acknowledge support of the Austrian Science Funds (project SFB 025, IRON).

Author contributions

J.S.-B. and A.V. performed the photoemission experiments; G.S., G.B. and L.V.Y. provided samples and performed the growth and characterization; H.S., R.K. and A.N. performed the SQUID measurements; O.C. and V.H. performed X-ray diffraction measurements; J.S.-B., E.S. and E.W. performed the XMCD measurements; J.S.-B., A.A.Ü. and S.V. performed the XMCD-PEEM measurements; J.M., M.D., J.B. and H.E. carried out the calculations; J.S.-B. and E.G. performed the numerical simulations; J.S.-B. performed data analysis and figure planning; J.S.-B. and O.R. performed draft planning and wrote the manuscript with input from all the authors; J.S.-B. and O.R. were responsible for the conception and the overall direction of the study.

Additional information

Supplementary Information accompanies this paper at http://www.nature.com/naturecommunications

Competing financial interests: The authors declare no competing financial interests.

Reprinted page 9 of paper [86] "Temperature independent gap in $(Bi,Mn)_2Se_3$ layers".

Reprints and permission information is available online at http://npg.nature.com/reprintsandpermissions/

How to cite this article: Sánchez-Barriga, J. *et al.* Nonmagnetic band gap at the Dirac point of the magnetic topological insulator $(Bi_{1-x}Mn_x)_2Se_3$. *Nat. Commun.* 7:10559 doi: 10.1038/ncomms10559 (2016).

This work is licensed under a Creative Commons Attribution 4.0 International License. The images or other third party material in this article are included in the article's Creative Commons license, unless indicated otherwise in the credit line; if the material is not included under the Creative Commons license, users will need to obtain permission from the license holder to reproduce the material. To view a copy of this license, visit http://creativecommons.org/licenses/by/4.0/

Reprinted page 10 of paper [86] "Temperature independent gap in $(Bi,Mn)_2Se_3$ layers".

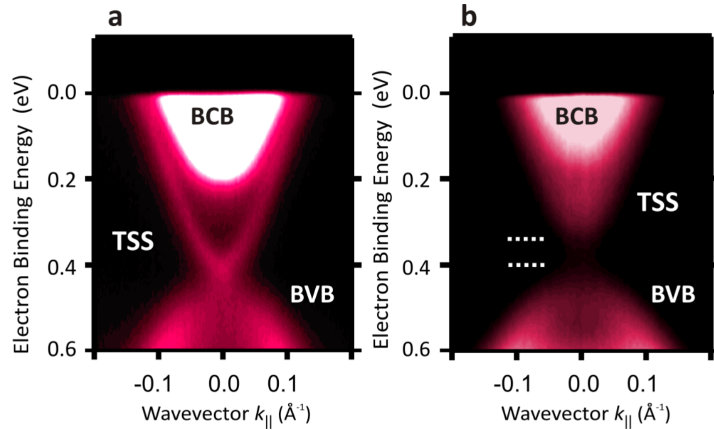

Supplementary Figure 1: **Probing the bulk-conduction band at low photon energy.** In contrast to Fig. 1 of the main text, the bulk-conduction band (BCB) is probed at 21 eV. (a, b) Energy-momentum ARPES dispersions of (a) undoped Bi_2Se_3 and (b) 8% Mn-doped Bi_2Se_3. The upward shift of the BCB in (b) is due to the p-type doping and not to a change in the bulk band gap or even a reversal of the bulk band inversion (see also Supplementary Fig. 15). The topological surface state (TSS) appears with weaker photoemission intensity which makes it difficult to observe when it approaches the BCB for 8% Mn in (b). The signal from the bulk-valence band (BVB) is also observed at higher binding energies. The TSS is better visible at 50 eV in Fig. 1 of the main text and in Supplementary Fig. 3. The horizontal white-dashed lines in (b) highlight the opening of the surface gap.

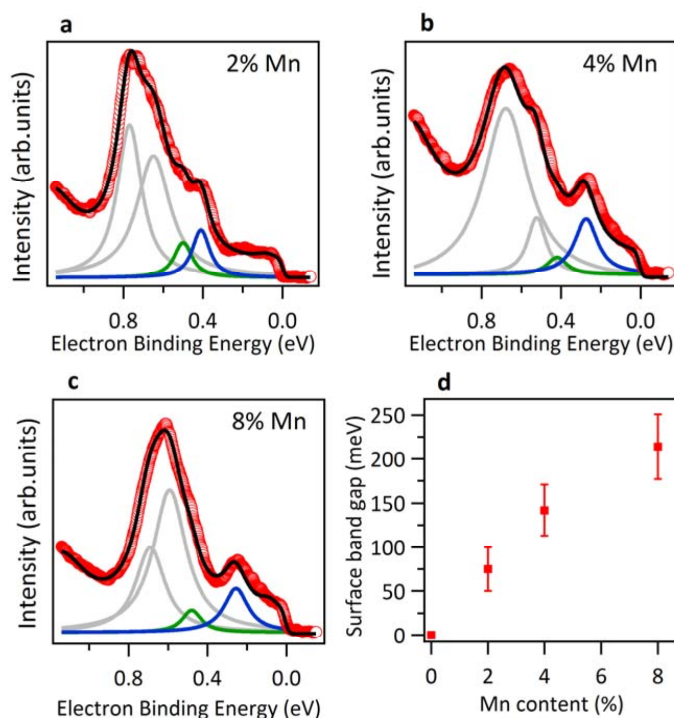

Supplementary Figure 2: **Surface band gap for different Mn concentrations.** (a-c) The experimental energy-distribution curves (EDCs) at zero momentum ($k_{\parallel}$=0, red circles), obtained from the ARPES spectra acquired at 50 eV photon energy and 12 K temperature, are fitted (solid black lines) considering a Shirley-like background [1]. The fitting procedure is explained in detail in Supplementary Note 1. The fit results for (a) 2%, (b) 4% and (c) 8% Mn-doped Bi_2Se_3 films are shown. (d) Size of the surface band gap obtained from the fits in (a-c). The surface band gap is determined from the energy separation between the fitted Lorentzian peaks shown in blue (green) color, which are located at the energy minimum (maximum) of the upper (lower) half of the Dirac cone. The Lorentzian peaks shown in gray color are contributions from the bulk-valence bands. Error bars in (d) correspond to the uncertainty of determining the energy position of the band dispersions. The error bars are estimated from the standard deviations of the peak positions over several fitting cycles.

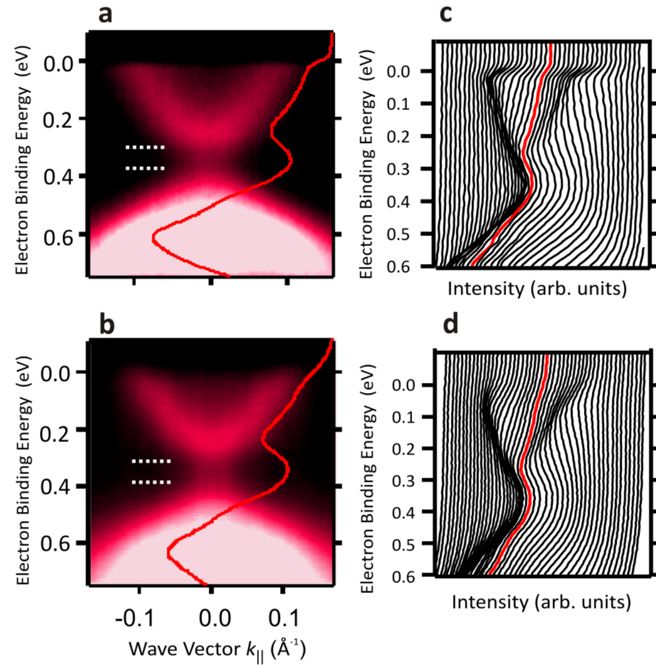

Supplementary Figure 3: **Temperature dependence of the surface band gap.** (a, b) Data as in Fig. 2 of the main text for 8% Mn-doped Bi_2Se_3 and (c, d) in a different representation as energy-distribution curves (EDCs), showing the absence of a temperature dependence of the surface band gap. Measurements were obtained at a temperature of (a, c) 12 K and (b, d) and 300 K. The red solid lines in (a-d) emphasize the EDCs in normal emission ($k_{||}$=0). The horizontal white-dashed lines in (a, b) highlight the surface band gap.

Reprinted supplement page 3 of paper [86] "Temperature independent gap in $(Bi,Mn)_2Se_3$ layers".

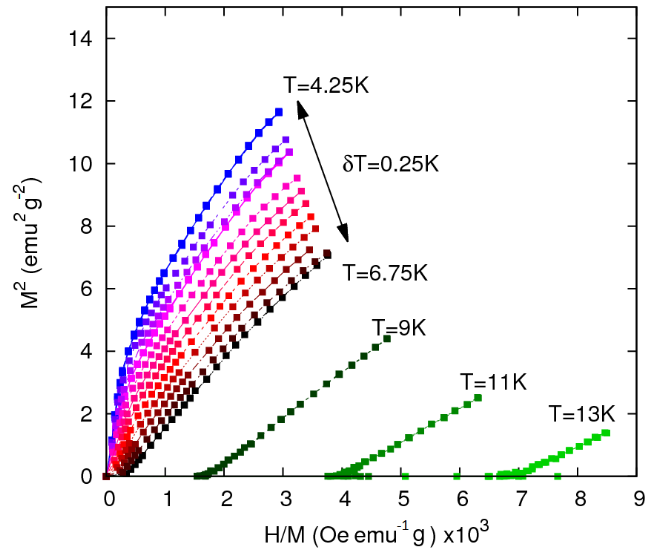

Supplementary Figure 4: **Conventional mass-normalized Arrott plot.** In Fig. 3c of the main text, we showed a modified Arrot plot according to a 3D Heisenberg ferromagnet [2, 3] normalized to the mass of the sample with the exponents β= 0.348 and γ = 1.41, from which we deduce a T_C of 5.5 K. Here we show for the same data a conventional mass-normalized Arrott plot. A similar presentation was used previously [4] for the determination of the ferromagnetic Curie temperature in $(Bi_{1-x}Mn_x)_2Te_3$. From the present plot, we deduce a by 2 K higher T_C.

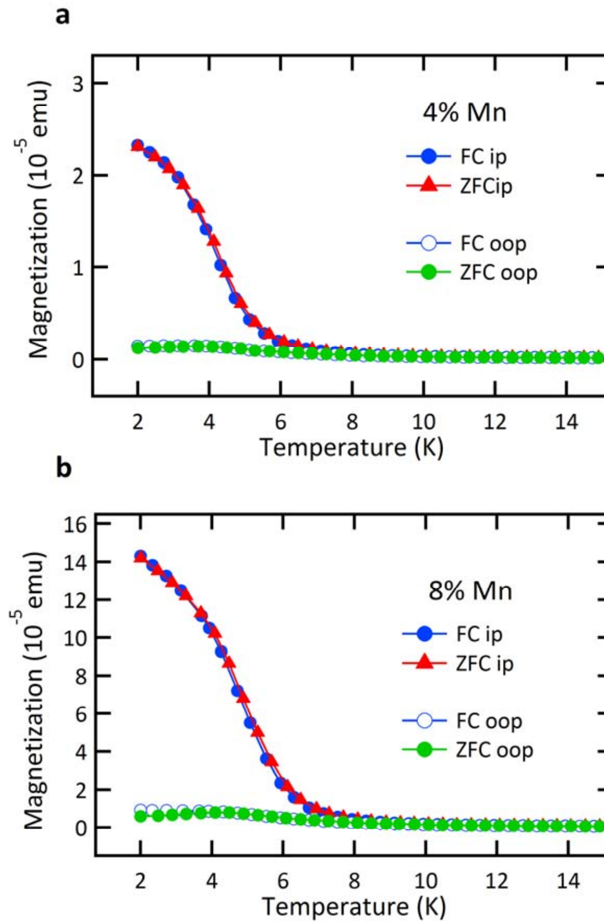

Supplementary Figure 5: **Temperature-dependence of the bulk magnetization.** Comparison between field-cooling (FC) and zero-field-cooling (ZFC) measurements obtained using SQUID magnetometry for (a) 4% and (b) 8% Mn doping. The temperature dependence of both the in-plane (ip) and out-of-plane (oop) components of the magnetization is shown. The FC measurements are performed under an applied magnetic field of 10 mT parallel and perpendicular to the surface. The ZFC and FC results are very similar for each composition, and compare well to the surface-sensitive XMCD measurements shown in the main text (see Supplementary Note 2 for details).

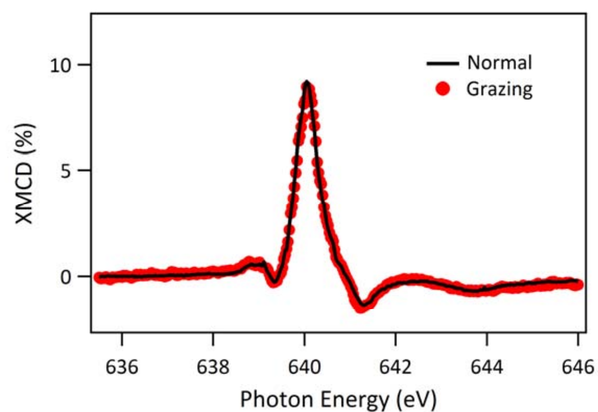

Supplementary Figure 6: **Surface-sensitive XMCD measurements for 8% Mn-doped Bi_2Se_3**. The spectra were obtained at the Mn L_3-edge and a temperature of 20 K under an applied magnetic field of -2T parallel (red circles) and perpendicular to the surface (black solid line). The x-ray beam impinged the sample in normal incidence (black solid line) and at a gracing incidence angle of 30° with respect to the surface plane (red circles); see Supplementary Notes 2 and 4 for details.

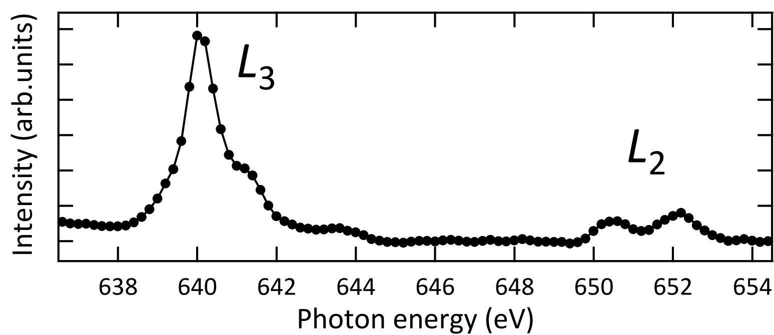

Supplementary Figure 7: **Absorption spectrum measured for the $(Bi_{1-x}Mn_x)_2Se_3$ sample doped with 8% Mn using X-PEEM.** The spectrum is obtained across the Mn $L_{2,3}$-edges from the same region of the sample shown in the XMCD images of Supplementary Fig. 8 below and plotted as the result of the sum of two absorption spectra recorded with opposite light helicity; see also Supplementary Note 3.

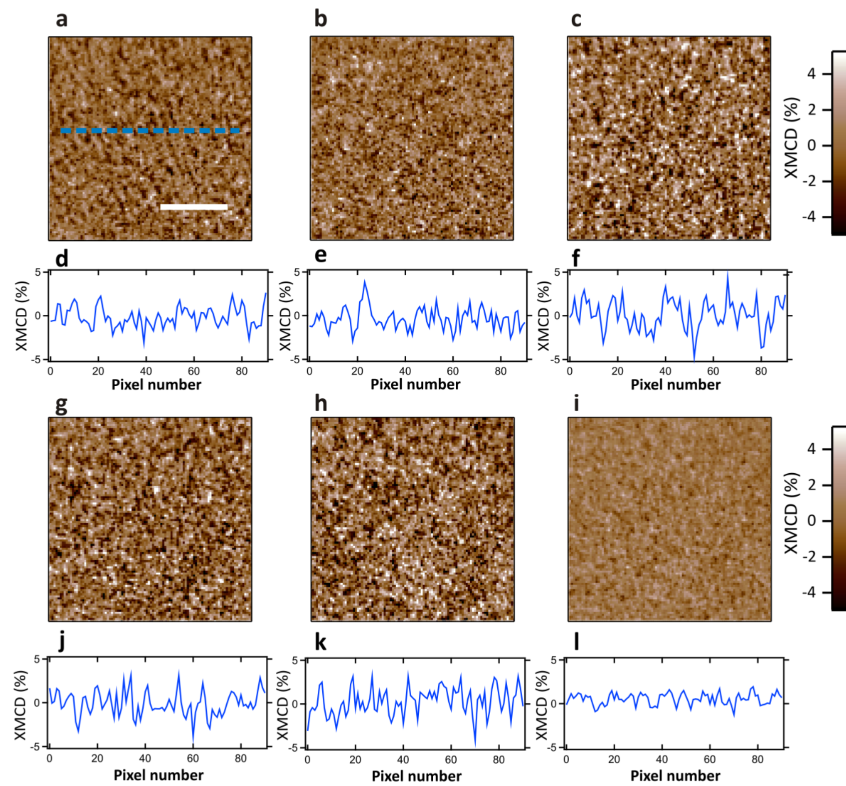

Supplementary Figure 8: **A sequence of XMCD-PEEM measurements.** (a-l) XMCD-PEEM measurements for the $(Bi_{1-x}Mn_x)_2Se_3$ sample doped with 8% Mn. (a, b, c, g, h) XMCD images obtained at the Mn L_3 -edge after pre-edge subtraction. Each XMCD consisted of 160 images (3 seconds integration time each). Panels (d, e, f, j, k) show the corresponding XMCD profiles across the same line [blue dotted line on panel (a)]. Panels (i) and (l) show the average XMCD and XMCD profile, respectively. The scale bar (horizontal white-solid line) shown in (a) is 500 μm and applies to all panels. Note the absence of correlation between the different individual measurements as well as the contrast decrease after averaging, indicating absence of ferromagnetic domains at room temperature; see Supplementary Note 3 for more details.

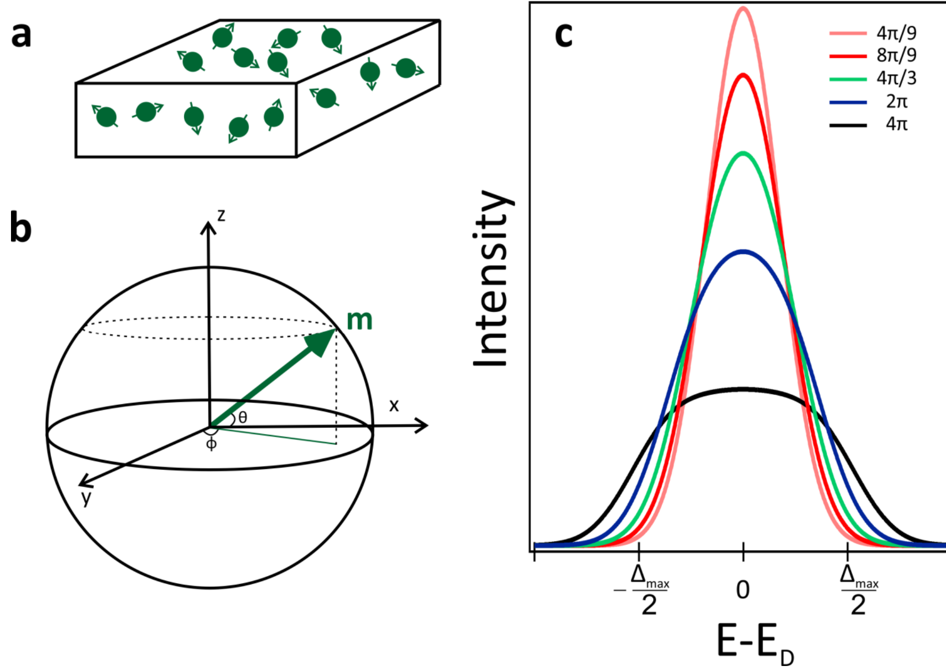

Supplementary Figure 9: **Simulations of spectral weight at the Dirac point.** (a) Schematic of a topological insulator hosting bulk magnetic impurities (green spheres) with random magnetic moments represented by green arrows. (b) A random magnetic moment in our simplified model is illustrated as a green arrow in the three-dimensional space. The in- and out-of-plane projection of the magnetic moment varies only with the polar angle θ and a randomized collection of magnetic impurities covers the whole polar and azimuthal (ϕ) range. The dashed line indicates the in-plane projection of the magnetic moment while the dashed circle encloses the full solid angle covered by a specific polar value. (c) Evaluation of the spectral weight using our model for different constraints in the magnetic moment orientation, plotted as a function of the energy away from the Dirac point (E-E_D). The constraints are chosen in accordance with the results of our magnetic characterization, which reveals either preferentially-oriented in-plane magnetic moments below T_c or random orientations of the Mn magnetic moments above T_c. The black curve corresponds to a fully randomized population after integration across all possible values of θ and ϕ. Blue, green, red and pink curves correspond to randomized magnetic moments constrained by symmetric polar angles with respect to the *x-y* plane which add up to the total solid angle indicated in the legend.

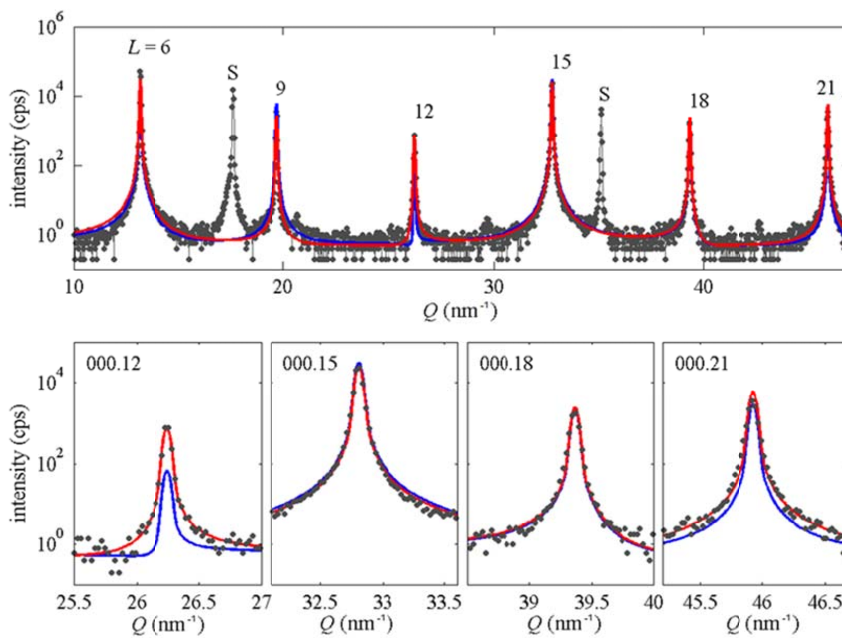

Supplementary Figure 10: **X-ray diffraction curves of the pure Bi_2Se_3 film.** The measured curves are shown as points and the simulations as lines. The upper panel shows the whole diffraction curve, the lower panels depict individual diffraction maxima. “S” in the upper panel denotes the substrate peaks, *L* are the orders of the diffraction peaks of Bi_2Se_3. The blue (red) curves depict the simulation results assuming nominal (changed) bilayer distances, respectively; see Supplementary Note 5 for details.

4.5 Manganese doping of Bi_2Te_3 topological insulator

The magnetic alloy layers of $(Bi,Mn)_2Te_3$ were grown on BaF_2. The manganese positions were analyzed using x-ray absorption spectroscopy. The manganese positions were identified as an octahedral interstitial in the van der Waals gap. The crystalline structure is increasingly disordered with increasing manganese content. The ARPES measurements lack sufficient resolution and low enough temperature to observe magnetic band gap opening. However, we were unaware that Mn atoms occupy the septuple layers $MnBi_2Te_4$ at the time of publication. The structural analysis interpretation is not entirely correct.

New Journal of Physics
The open access journal at the forefront of physics

Deutsche Physikalische Gesellschaft DPG
IOP Institute of Physics
Published in partnership with: Deutsche Physikalische Gesellschaft and the Institute of Physics

OPEN ACCESS

RECEIVED
2 October 2014

ACCEPTED FOR PUBLICATION
1 December 2014

PUBLISHED
15 January 2015

Content from this work may be used under the terms of the Creative Commons Attribution 3.0 licence.

Any further distribution of this work must maintain attribution to the author (s) and the title of the work, journal citation and DOI.

PAPER

Structural and electronic properties of manganese-doped Bi_2Te_3 epitaxial layers

J Růžička[1,2], O Caha[1,2], V Holý[3], H Steiner[5], V Volobuiev[5], A Ney[5], G Bauer[5], T Duchoň[4], K Veltruská[4], I Khalakhan[4], V Matolín[4], E F Schwier[6], H Iwasawa[6], K Shimada[6] and G Springholz[5]

[1] CEITEC, Masaryk University, Kotlářská 2, 61137 Brno, Czech Republic
[2] Department of Condensed Matter Physics, Faculty of Science, Masaryk University, Kotlářská 2, 61137 Brno, Czech Republic
[3] Department of Condensed Matter Physics, Faculty of Mathematics and Physics, Charles University in Prague, Ke Karlovu 5, 12116 Praha, Czech Republic
[4] Department of Surface and Plasma Science, Faculty of Mathematics and Physics, Charles University in Prague, V Holešovičkách 2, 18000 Praha, Czech Republic
[5] Institut für Halbleiter- und Festkörperphysik, Johannes Kepler Universität, Altenbergerstr. 69, 4040 Linz, Austria
[6] Hiroshima Synchrotron Radiation Center, Hiroshima University Kagamiyama 2-313, Higashi-Hiroshima, Hiroshima 739-0046, Japan

E-mail: holy@mag.mff.cuni.cz

Keywords: topological insulators, thin layers, EXAFS, ARPES

Abstract

We show that in manganese-doped topological insulator bismuth telluride layers, Mn atoms are incorporated predominantly as interstitials in the van der Waals gaps between the quintuple layers and not substitutionally on Bi sites within the quintuple layers. The structural properties of epitaxial layers with Mn concentration of up to 13% are studied by high-resolution x-ray diffraction, evidencing a shrinking of both the in-plane and out-of plane lattice parameters with increasing Mn content. Ferromagnetism sets in for Mn contents around 3% and the Curie temperatures rises up to 15 K for a Mn concentration of 9%. The easy magnetization axis is along the *c*-axis perpendicular to the (0001) epilayer plane. Angle-resolved photoemission spectroscopy reveals that the Fermi level is situated in the conduction band and no evidence for a gap opening at the topological surface state with the Dirac cone dispersion is found within the experimental resolution at temperatures close to the Curie temperature. From the detailed analysis of the extended x-ray absorption fine-structure experiments (EXAFS) performed at the Mn*K*-edge, we demonstrate that the Mn atoms occupy interstitial positions within the van der Waals gap and are surrounded octahedrally by Te atoms of the adjacent quintuple layers.

1. Introduction

Bismuth telluride (Bi_2Te_3) is a prototypical example for a three-dimensional (3D) topological insulator with a gapped bulk band structure and a topological two-dimensional (2D) surface state with Dirac-like energy–momentum dispersion and spin–momentum locking [1–3]. The surface states are protected by time-reversal symmetry and are immune to surface impurities and backscattering. When 3D transition metals such as Mn, Fe, Cr or V are incorporated as magnetic dopants [4], however, their local exchange fields can break time reversal symmetry and thus may lift the degeneracy of the Dirac points with a concomitant gap opening of the topological surface state [1–3, 5–8]. In addition, novel phenomena arising from the interaction between topologically protected states and ferromagnetic order have been theoretically predicted [1–3], including the topological magneto-electric effect, the quantum anomalous Hall effect, half-integer charges at magnetic domain boundaries [3]; some of these were already observed experimentally [9].

The solubility of magnetic ions in topological insulators is typically limited to a few percent and Mn-doped Bi_2Te_3 crystals and thin films with concentrations of up to 10% were found to be ferromagnetic with Curie temperatures around 10 K [10–16]. In some of these works, Mn-doped Bi_2Te_3 showed *p*-type conduction [10, 11] or at least a weak acceptor-like behavior of Mn [17] as evidenced by a downward shift of the Fermi level [10, 11, 17]. From this it was concluded that Mn ions preferentially occupy substitutional Bi lattice sites, forming

© 2015 IOP Publishing Ltd and Deutsche Physikalische Gesellschaft

$(Bi_{1-x}Mn_x)_2Te_3$ [11]. However, the downward shift of the Fermi level observed by angle-resolved photoelectron spectroscopy (ARPES) was rather small, i.e., much less than expected for purely substitutional Mn incorporation. In most other works, Mn-doped Bi_2Te_3 even retained its *n*-type character [14, 17], indicating a non-substitutional Mn incorporation. Indeed, recent compositional analysis of bulk crystals has revealed that Mn may also be incorporated interstitially as in $Mn_xBi_2Te_3$ [14], but no precise information on the actual incorporation sites was reported. It has also been suggested that Mn may incorporate in excess Bi–Bi double layers [12, 15] easily formed in bismuth telluride when grown under tellurium deficient conditions [12, 18, 19]. Thus, the mechanism of Mn incorporation has been rather unclear. Nevertheless, in all cases, Mn doping has resulted in ferromagnetic behavior, but without any remarkable dependence of the Curie temperatures on the carrier concentration [11, 14, 15, 20].

Due to the complex crystal structure of Bi_2Te_3 with its large hexagonal unit cell consisting of three Te–Bi–Te–Bi–Te quintuple layers (QLs) bonded together across a van der Waals (vdW) gap, several different possible lattice sites exist for the incorporation of magnetic dopants. These include substitutional incorporation for Bi atoms within the QLs as well as interstitial incorporation within the quintuple layers or within the van der Waals gap between the QLs in different local coordinations. Evidently, different lattice sites for Mn incorporation are expected to result in quite different electronic and magnetic properties of the material [16] and, thus, to a different influence on the topological surface states. Therefore, the determination of the actual position of Mn in the lattice of Bi_2Te_3 is of utmost importance for further studies on its striking topological properties and their interplay with ferromagnetism.

To resolve this issue, in this paper we report a detailed study on the lattice sites of Mn incorporation in Bi_2Te_3. For this purpose, we performed a systematic investigation on a series of Mn-doped epitaxial Bi_2Te_3 layers using high-resolution x-ray diffraction (XRD) and extended x-ray absorption fine-structure (EXAFS) measurements. These were complemented by magnetic characterization using a superconducting quantum interference magnetometer (SQUID), which revealed that the layers are ferromagnetic with Curie temperatures of up to 15 K. Angle-resolved photoelectron spectroscopy (ARPES) shows no opening of a gap of the topological surface state at temperatures down to 12 K. By detailed theoretical analysis of the XRD and EXAFS spectra, we show that Mn is incorporated predominantly as interstitial in octahedral positions within the vdW gaps of Bi_2Te_3, i.e., between two Te layers of adjacent QLs.

2. Growth

Mn-doped Bi_2Te_3 layers were grown by MBE on (111)-orientated BaF_2 substrates using a compound bismuth telluride effusion cell, a Mn cell, and an additional tellurium cell for stoichiometry control. The in-plane lattice-constant of BaF_2 (111) is almost exactly lattice-matched to the lattice constant *a* of the hexagonal basal planes of Bi_2Te_3 (lattice-mismatch less than 0.04 %) and, thus, growth proceeds with the *c*-axis orientation perpendicular to the surface [18]. A whole series of samples was grown where the Mn concentration was varied between 0 and 13%. For all samples, the substrate temperature was 330 °C and a background pressure of $\leqslant 5 \times 10^{-10}$ mbar was maintained during growth. The flux rates from the sources were measured using a cooled quartz crystal microbalance moved into the substrate deposition. The mass deposition rates were converted into the flux rate of atoms arriving at the surface using the density and molar mass of each component. The total growth rate of $(Bi,Mn)_2Te_3$ was $\sim$0.15 QL^{-1} or $\sim$1.5 Å s^{-1} and a high excess tellurium flux above 2.5 Å/s was provided during growth, corresponding to an overall Te-to-Bi(Mn) flux ratio of $\sim$5:1. Under these conditions, stoichiometric Bi_2Te_3 epilayers are obtained with no indication of formation of Bi–Bi double layers, as shown in detail by our previous work [18, 19]. The Mn concentration in the samples varied from $x_{Mn} = 0$ to 13% and was determined by the measured Mn-to-Bi flux ratios, where we defined x_{Mn} as the ratio of Mn atoms relative to the number of the sum of Bi and Mn atoms. Thus, the overall layer composition can be represented by $Mn_xBi_{1-x}Te_y$, where $y \leqslant 1.5$ depends on the type of Mn incorporation. For purely substitutional Mn, $y = 1.5$, whereas for purely interstitial Mn, $y = 1.5(1 - x)$, provided that the 2:3 ratio between Bi and Te is retained. Nice streaked reflection high-energy electron diffraction (RHEED) patterns were observed during growth for all samples irrespective of the Mn content, indicating 2D growth in all cases. All layers exhibit *n*-type conduction with an electron density of $\sim 10^{19}$ cm^{-3} that does not change significantly with Mn content.

3. Structural characterization by x-ray diffraction

The rhombohedral crystal structure of Bi_2Te_3 with $R\bar{3}m$ symmetry and the different possible incorporation sites of Mn are illustrated in figure 1. The unit cell with the *hexagonal* lattice parameters $a = 0.4385$ nm and $c = 3.051$ nm [18] consists of fifteen (0001) hexagonal lattice planes grouped in three $Te^{(1)}$–Bi-$Te^{(2)}$–Bi-$Te^{(1)}$ QLs stacked in ABCABC…sequence [see figure 1(a)]. The QLs are weakly bonded together by a double layer of

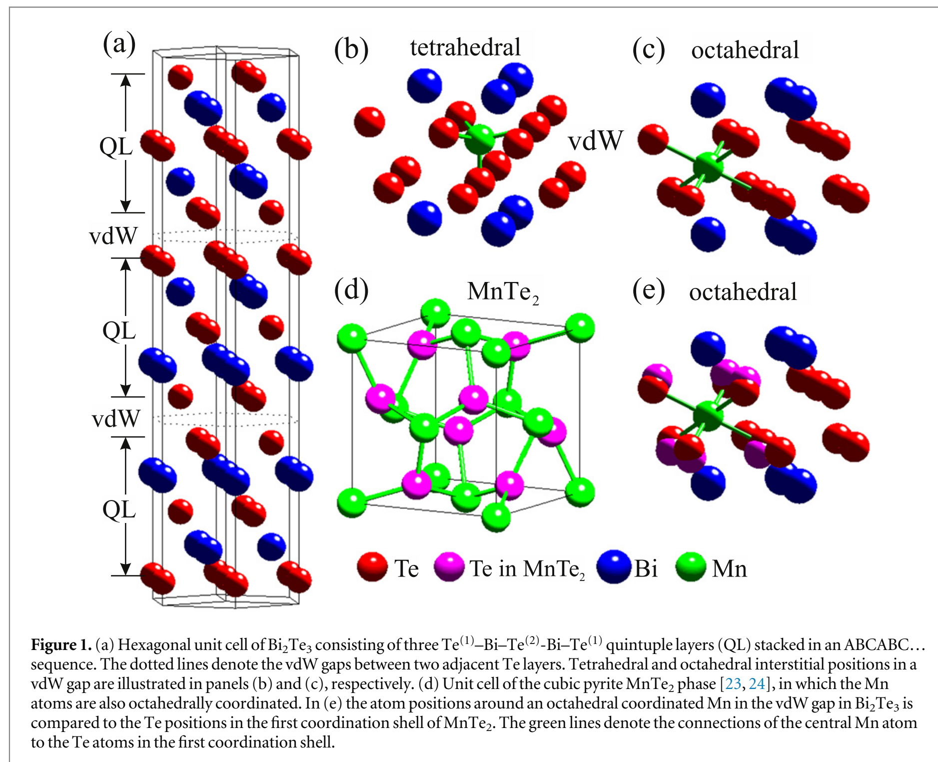

Figure 1. (a) Hexagonal unit cell of Bi_2Te_3 consisting of three $Te^{(1)}$–Bi–$Te^{(2)}$-Bi–$Te^{(1)}$ quintuple layers (QL) stacked in an ABCABC… sequence. The dotted lines denote the vdW gaps between two adjacent Te layers. Tetrahedral and octahedral interstitial positions in a vdW gap are illustrated in panels (b) and (c), respectively. (d) Unit cell of the cubic pyrite $MnTe_2$ phase [23, 24], in which the Mn atoms are also octahedrally coordinated. In (e) the atom positions around an octahedral coordinated Mn in the vdW gap in Bi_2Te_3 is compared to the Te positions in the first coordination shell of $MnTe_2$. The green lines denote the connections of the central Mn atom to the Te atoms in the first coordination shell.

Table 1. Nominal nearest-neighbor (NN) distances of Mn in the Bi_2Te_3 lattice for various possible positions of the Mn ions (see figure 1). For comparison, the NN Mn–Te distances in various other manganese telluride compounds [zinc blende (zb), wurzite (wz) and hexagonal MnTe (NiAs type) as well as cubic $MnTe_2$ (pyrite type)] are listed.

Mn position	NN distance (nm)
Substitutional Mn on Bi site in Bi_2Te_3	0.3032
Tetrahedral Mn as interstitial in vdW gap	0.2542
Octahedral Mn as interstitial in vdW gap	0.2885
Substitutional Mn in Bi-Bi DL in $Bi_2Te_{3-\delta}$	0.3268
Tetrahedral Mn in zb MnTe	0.2774
Tetrahedral Mn in wz MnTe	0.2513
Octahedral Mn in hexagonal MnTe (NiAs type)	0.2924
Octahedral Mn in $MnTe_2$ (pyrite type)	0.2904

Te atoms forming the vdW gaps of the structure. Because of the large inter-planar distance of the vdW gap, interstitial positions within the vdW gaps are expected to be favorable for Mn incorporation. Two possible interstitial positions in the vdW gaps exist, either tetrahedral or octahedral sites with 4, respectively, 6 nearest neighboring Te atoms, as illustrated in figures 1(b) and (c). Substitutional Mn is expected to reside on Bi atom positions within the QLs. The corresponding expected nominal nearest neighbor (NN) distances for these three different incorporation sites are listed in table 1, together with the NN distances of Mn in Bi–Bi DL in Te-deficit $Bi_2Te_{3-\delta}$, as proposed by [12, 15]. Also listed are the NN Mn–Te distances in several other manganese telluride compounds such as zinc blende (zb) MnTe ($a_0 = 6.338$ Å) [21], wurzite (wz) MnTe ($a = 6.49$ Å, $c = 6.701$ Å) [22], hexagonal, i.e., NiAs-type MnTe ($a = 4.148$ Å, $c = 6.710$ Å) [22] and cubic (pyrite) $MnTe_2$ ($a = 6.943$ Å) [23, 24]. In zb- and wz-MnTe, the Mn ions are tetrahedrally coordinated, whereas in the other two compounds Mn has an octahedral coordination. As illustrated by figures 1(d) and (e), in $MnTe_2$ the Mn ions are similarly coordinated as in the octahedral lattice sites in Bi_2Te_3.

In order to study the crystal structure of Mn-doped Bi_2Te_3, high resolution x-ray diffraction experiments were performed using CuK_α radiation and a diffractometer equipped with multilayer parabolic optics, a $4 \times (220)$ Ge Bartels monochromator and a $2 \times (220)$ Ge analyzer crystal. Symmetrical (000 L) scans of the

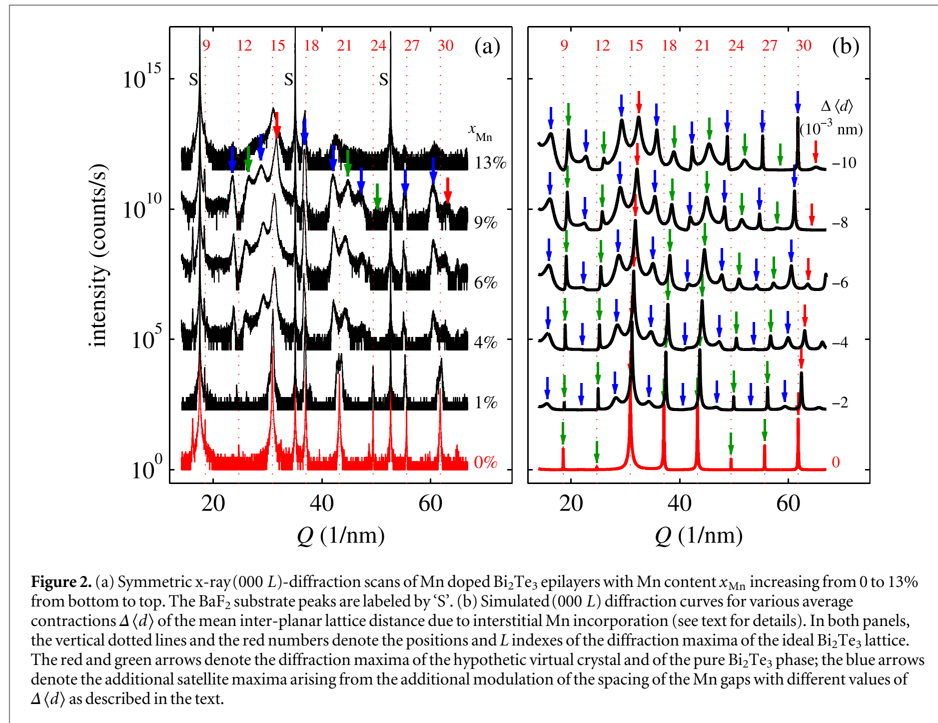

Figure 2. (a) Symmetric x-ray (000 L)-diffraction scans of Mn doped Bi_2Te_3 epilayers with Mn content x_{Mn} increasing from 0 to 13% from bottom to top. The BaF_2 substrate peaks are labeled by 'S'. (b) Simulated (000 L) diffraction curves for various average contractions $\Delta\langle d\rangle$ of the mean inter-planar lattice distance due to interstitial Mn incorporation (see text for details). In both panels, the vertical dotted lines and the red numbers denote the positions and L indexes of the diffraction maxima of the ideal Bi_2Te_3 lattice. The red and green arrows denote the diffraction maxima of the hypothetic virtual crystal and of the pure Bi_2Te_3 phase; the blue arrows denote the additional satellite maxima arising from the additional modulation of the spacing of the Mn gaps with different values of $\Delta\langle d\rangle$ as described in the text.

samples with different Mn content are presented in figure 2(a), where the scattered intensities are plotted as functions of the length Q of the scattering vector. The pure Bi_2Te_3 layer exclusively shows the diffraction maxima with $L = 9, 15, 18, 21, \ldots$ characteristic for the perfect Bi_2Te_3 phase (see [18, 19] for details), evidencing the absence of additional Bi–Bi double layers in the structure [19]. With increasing Mn content x_{Mn}, the diffraction maxima are shifted, and additional satellite maxima appear as indicated by the blue arrows in figure 2.

To analyze the diffraction data, we start with the diffraction data of the non-doped Bi_2Te_3 sample ($x_{Mn} = 0$). The unit cell of Bi_2Te_3 is non-primitive and consists of three identical QLs mutually shifted in a lateral direction [see figure 1(a)]. Therefore, in symmetric (000 L) diffraction [figure 2(a)], the structure factors of the quintuplets are identical and the effective structure unit of the crystal is one-third of the hexagonal unit cell c with a height $d_{QL} = c/3$. Thus, only diffraction maxima $L = 3, 6, 9, \ldots$ are allowed and the positions of these maxima are indicated by red dotted lines in figure 2. Ignoring the small differences in the inter-planar distances within the QLs and between them [19], Bi_2Te_3 can be considered as a periodic sequence of 2D hexagonal basal planes of atoms with *ABC*... stacking similar to a face-centered cubic lattice. In this layer sequence, the (Bi,Te) occupation of the lattice positions varies periodically along the [0001] growth direction. Replacing the true atoms in the lattice by a virtual 'mixture' of Bi and Te, the diffraction maxima of such a crystal will appear at $Q = 2\pi n/\langle d\rangle$, where n is an integer and $\langle d\rangle$ is the mean distance of the (0001)-planes of the virtual crystal, i.e., the average distance between the basal planes in the actual lattice. Since $\langle d\rangle = d_{QL}/5 = c/15$, the diffraction maxima of this virtual lattice appears at $L = 15, 30, 45, \ldots$ (red arrows in figure 2). As a result, these are the major diffraction maxima, whereas all other (000 L) maxima with $L = \ldots, 9, 12, 18, 21, 24, 27, 33, \ldots$) can be considered as modulation maxima caused by the periodic modulation of the occupation of the lattice planes either by Te or Bi atoms. Taking into account the modulation of the periodic sequence of QLs, we thus obtain the diffraction pattern of the Bi_2Te_3 phase, and the corresponding additional peaks are denoted by green arrows in figure 2. From this analysis, it follows that only the maxima $L = 15, 30$ (red arrows) can be used for determination of the average spacing $\langle d\rangle$ of the lattice planes, i.e., for derivation of the average lattice constant along the c-direction.

As shown in figure 2, with increasing Mn concentration, additional (satellite) maxima appear in the diffraction spectra (blue arrows). These satellites are caused by an additional modulation of the structure along the growth direction with a period $L_{mod} = 2\pi/\Delta Q$ that is given by the distance ΔQ between these satellite maxima. This is similar to the case of the tellurium deficit in the $Bi_2Te_{3-\delta}$ structures, where additional Bi–Bi double layers are randomly inserted between the quintuple layers [19]. In Mn-doped Bi_2Te_3, we assume that this

Reprinted page 4 of paper [87] "Properties of Manganese doped Bi_2Te_3".

Table 2. Lattice parameters a and c and additional structure modulation $\langle m \rangle$ and its rms fluctuation $\sigma_m/\langle m \rangle$ for Mn-doped bismuth telluride epilayers with different Mn concentrations x_{Mn} as determined by x-ray diffraction. Also listed are the Curie temperatures derived from SQUID data.

x_{Mn} (%)	a (nm)	c (nm)	$\langle m \rangle$	$\sigma_m/\langle m \rangle$	T_C (K)
0	0.4380 ± 0.0001	3.0508 ± 0.0015	—	—	0
1	0.4380 ± 0.0003	3.0399 ± 0.0045	13.8 ± 1.0	0.16 ± 0.02	0
3	0.4374 ± 0.0003	3.0101 ± 0.0075	2.6 ± 1.0	0.18 ± 0.02	7.5
6	0.4368 ± 0.0006	3.0098 ± 0.0105	2.2 ± 1.0	0.16 ± 0.02	10
9	0.4365 ± 0.0006	2.9850 ± 0.0150	2.0 ± 1.0	0.16 ± 0.02	15
13	0.4340 ± 0.0010	—	1.4 ± 2.0	0.25 ± 0.04	12

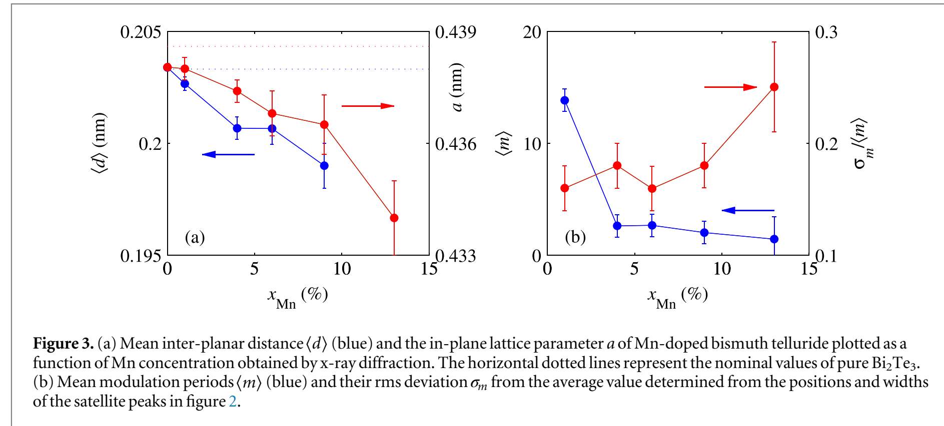

Figure 3. (a) Mean inter-planar distance $\langle d \rangle$ (blue) and the in-plane lattice parameter a of Mn-doped bismuth telluride plotted as a function of Mn concentration obtained by x-ray diffraction. The horizontal dotted lines represent the nominal values of pure Bi_2Te_3. (b) Mean modulation periods $\langle m \rangle$ (blue) and their rms deviation σ_m from the average value determined from the positions and widths of the satellite peaks in figure 2.

modulation comes from Mn incorporated in the vdW gaps between the QL layers, which changes the distance between the facing Te–Te layers in the gap in a modulated manner. To support this idea, a series of diffraction curves was simulated assuming that after every mth quintuple layer the distance of the Te–Te vdW gap and the distance between the first Te layer and the subsequent Bi layer is changed by Δd_{Te-Te} and Δd_{Te-Bi}, respectively. We averaged the diffracted intensity over random values of m with an average value of $\langle m \rangle$ and a root-mean square (rms) deviation σ_m with respect to this value. The such-created modulation period is related to m by $L_{mod} = 2d_{QL}/2\langle m \rangle$. The corresponding simulation results for different Δd and $\sigma_m = 0.8$ are presented in figure 2(b), where $\Delta \langle d \rangle$ denotes the deviation of the mean inter-planar distance from the value in the pure Bi_2Te_3 phase. From the structure of Bi_2Te_3, it follows that $\Delta \langle d \rangle = (\Delta d_{Te-Te} + 2\Delta d_{Te-Bi})/(5\langle m \rangle)$. The simulations reveal that the diffraction curves sensitively depend on $\Delta \langle d \rangle$; the dependence on the individual deviations $\Delta d_{Te-Te,Te-Bi}$ turned out to be negligible for $|\Delta d_{Te-Te,Te-Bi}| \leqslant 0.005$ nm.

As illustrated by figure 2(b), with this model, key features of the diffraction curves can be explained, such as the appearance of the additional modulation peaks (blue arrows in figure 2) with increasing Mn concentration, as well as the shifts of the diffraction peaks. Still, the model is too simple to exactly reproduce the shapes of the diffraction curves. From the simulations, it follows that with increasing negative values of $\Delta \langle d \rangle$, the lattice constants c decreases, and, consequently, the 'true' diffraction peaks (red and green arrows) move to larger Q. With increasing $\Delta \langle d \rangle$, the envelope curve of the diffraction maxima changes due to the change of the form factor within the structure period, similar to what is seen in the experiments. This is why, for instance, the maximum at $L = 30$ in the $\Delta \langle d \rangle = -0.006$ nm curve is smaller than its first satellite, whereas this maximum is completely suppressed for $\Delta \langle d \rangle = -0.01$ nm. This effect must be taken into account in the determination of $\Delta \langle d \rangle$ from the measured diffraction data.

For further evaluation of the experimental data, for each sample we have determined the mean inter-planar distances $\langle d \rangle$, the mean modulation period $\langle m \rangle$, as well as its rms deviation σ_m from the positions of the 'true', respectively, additional satellite peaks. In addition, the in-plane lattice parameter a of the layers was determined from the peak positions of the asymmetric $(10\bar{1}4)$ diffraction peaks measured by reciprocal space mapping [18]. The results are listed in table 2 and plotted in figure 3 as a function of the Mn concentration x_{Mn}. Clearly, the vertical average inter-planar distance $\langle d \rangle$ and thus, the lattice parameter c, as well as the in-plane lattice parameter a continuously decrease with increasing Mn content. This indicates that Mn is indeed incorporated in the bismuth telluride host lattice, and that Mn does not induce the formation of additional Bi–Bi double layers between the quintuplets as proposed by Lee et al [15]. As in the latter case, the in-plane lattice constant a should

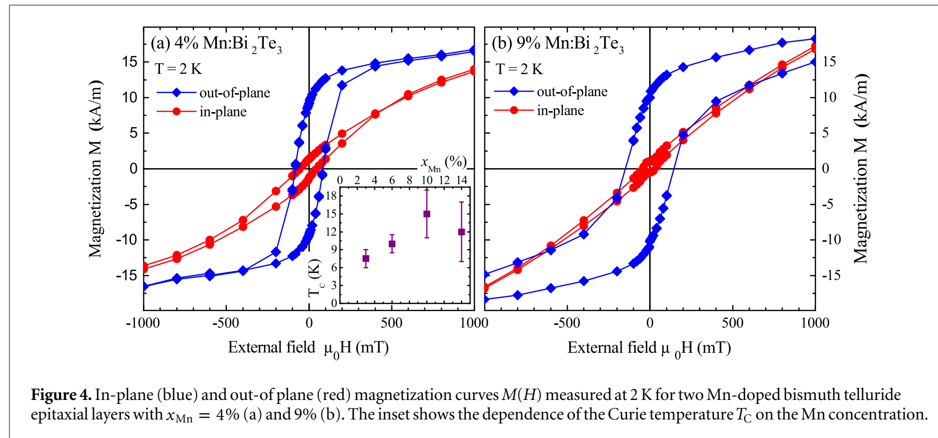

Figure 4. In-plane (blue) and out-of plane (red) magnetization curves $M(H)$ measured at 2 K for two Mn-doped bismuth telluride epitaxial layers with $x_{\mathrm{Mn}} = 4\%$ (a) and 9% (b). The inset shows the dependence of the Curie temperature T_C on the Mn concentration.

increase [19] rather than decrease with increasing alloy concentration. No additional modulation periodicity is found for $x_{\mathrm{Mn}} = 0$. For $x_{\mathrm{Mn}} = 1\%$, the modulation period $\langle m \rangle$ is about 14, i.e., very large, but it rapidly decreases for higher x_{Mn} to $\langle m \rangle \approx 2.5$ without significant further changes. For $x_{\mathrm{Mn}} = 13\%$, the value of $\langle d \rangle$ cannot be determined, since its diffraction curve does not exhibit the 'true' red- and green-arrow peaks and the diffraction maxima become very broad, so that the uncertainty in determining $\langle m \rangle$ is rather large. As in this case, the Mn concentration is close or even above the solubility limit, so it is likely that for this structure already some phase separation has occurred, with the formation of small amounts of secondary Mn–Te phases, leading to a structural degradation. However, the amount of secondary phases must still be small, as no extra diffraction peaks for secondary phases are observed in the diffraction data.

4. Magnetic and electronic properties

The magnetic properties of the Mn-doped Bi_2Te_3 epilayers were characterized by SQUID magnetization measurements, where the magnetization $M(H)$ and $M(T)$ were recorded as a function of temperature from 2 K to 300 K, and magnetic field H applied either perpendicular (out-of-plane) or parallel (in-plane) to the surface of the films. The diamagnetic contribution of the $BaF_2(111)$ substrate was derived from $M(H)$ curves at 300 K and was subtracted from all data. Note, that identical sample pieces were used for in-plane and out-of-plane measurements, as described in [25]. Figure 4 shows the in-plane and out-of-plane magnetization curves for the 4% and 9% Mn-doped Bi_2Te_3 samples at 2 K, representative for the entire sample series. For both samples, a clear hysteresis is observed, evidencing ferromagnetic properties, and in both cases, the *c* axis, i.e., the out-of-plane orientation, is clearly the easy axis of magnetization, similar to the findings of bulk samples [11, 14] and films grown on InP(111) [15]. The inset of figure 4(a) shows the dependence of the Curie temperature T_C on x_{Mn} estimated from the $M(T)$ measurements. T_C increases from 8.5 K for $x_{\mathrm{Mn}} = 3\%$ up to 15 K for $x_{\mathrm{Mn}} = 10\%$, consistent with previous findings [14, 15]. At high x_{Mn}, a slight decrease in T_C is observed, accompanied by a finite positive slope in the 2 K $M(H)$ curves at a high magnetic field above 1 T (not shown). We tentatively ascribe this observation to the onset of the formation of a secondary antiferromagnetic Mn-containing phase such as hexagonal MnTe or cubic $MnTe_2$, which reduces the effective concentration of ferromagnetic Mn incorporated in the bismuth telluride host. A detailed analysis of this secondary phase will be reported elsewhere.

To characterize the topological surface state and electronic band structure of the epitaxial layers, ARPES investigations were performed at the beamline BL-1 of the Hiroshima Synchrotron Radiation Center (HiSOR) at Hiroshima University, with a set-up described in detail elsewhere [26]. In order to avoid surface deterioration during air exposure of the samples during transportation, the samples were capped *in situ* in the MBE chamber by a Te/Se double layer after cooling to room temperature. This provides effective protection against surface oxidation. Prior to ARPES measurements, the samples were decapped in UHV by annealing at 130 °C and 250 °C for 15 minutes to completely desorb the Se and Te capping layers and regain a clean epilayer surface. This was checked and confirmed by low-energy electron diffraction. Low-temperature ARPES data recorded at 12 K for the series of samples with various x_{Mn} from 0 up to 13% are shown in figure 5.

For all Mn-doped bismuth telluride layers, the ARPES data shows a well-pronounced Dirac cone of their topological surface states up to highest x_{Mn} of 13%, i.e., no apparent gap opening at the Dirac point is observed within the experimental resolution of 30 meV. This is in contrast to previous results for $Bi_{2-x}Mn_xSe_3$ reported

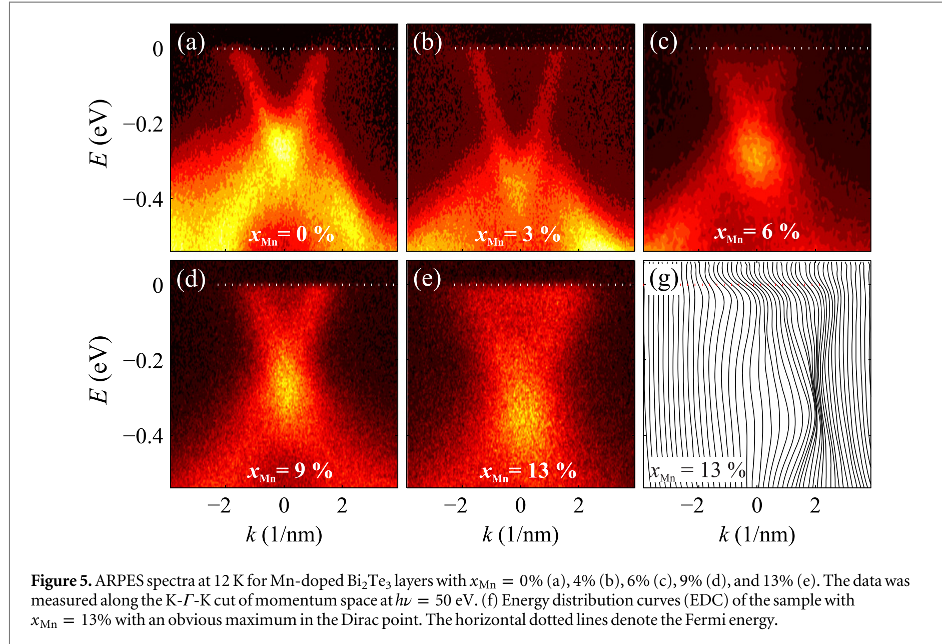

Figure 5. ARPES spectra at 12 K for Mn-doped Bi_2Te_3 layers with $x_{Mn} = 0\%$ (a), 4% (b), 6% (c), 9% (d), and 13% (e). The data was measured along the K-Γ-K cut of momentum space at $h\nu = 50$ eV. (f) Energy distribution curves (EDC) of the sample with $x_{Mn} = 13\%$ with an obvious maximum in the Dirac point. The horizontal dotted lines denote the Fermi energy.

by Xu *et al* [27], who have found a gap opening even above the bulk ferromagnetic Curie temperature, which was attributed to an enhanced ferromagnetic order at the surfaces. This is not found for our Mn-doped Bi_2Se_3 epilayers at $T = 12$ K. However, since the theoretically predicted gap opening is below 20 meV in the ferromagnetic phase for substitutional Mn incorporation [8], our observations do not completely rule out such an effect. It is noted that the absence of a gap opening as revealed by our experiments is in agreement with observations for bulk $Bi_{2-x}Mn_xTe_3$ [10, 11] and moreover, it has been theoretically predicted that under certain conditions, the topological surface states may survive upon moderate Mn doping [8]. For all our samples, the Fermi energy is within the conduction band (dashed horizontal lines in figure 5) irrespective of the Mn concentration. Thus, we do not observe a notable p-doping of bismuth telluride by Mn incorporation, i.e., Mn does not show an acceptor-like behavior. This is a first indication that Mn is not substitutionally incorporated on Bi lattice sites.

5. X-ray absorption spectroscopy

To gain further insights on the Mn incorporation, we have performed EXAFS experiments at the BM32 beamline of the European Synchrotron Radiation Facility in Grenoble. EXAFS measurements were performed at the MnK-edge (6.55 keV) at the incidence angle of 2.5° with respect to the sample surface. The MnKα fluorescence signal was detected using an energy dispersive detector placed nearly horizontally to the sample in order to suppress the elastic scattering signal of the horizontally polarized synchrotron x-ray beam. Several spectra were averaged, and the normalized EXAFS part $\chi(E)$ was extracted using the Athena software [28] as $\chi(E) = (\mu(E) - \mu_0(E))/\Delta\mu_0$, where $\mu(E)$ denotes the measured absorption spectrum, $\mu_0(E)$ is its smooth background corresponding to a absorption of an isolated ('bare') Mn atom and $\Delta\mu_0$ is the height of the absorption edge. The photon energy is transformed into wave vector k of the excited electron as $E = E_{edge} + \hbar^2k^2/(2m_e)$, where E_{edge} is the energy of the absorption edge and m_e is the electron mass. Normalized EXAFS spectra for the samples with different Mn concentration are presented in figure 6. Evidently, the spectra collected from various samples do not show significant differences, indicating that the Mn incorporation does not depend much on the Mn content of our samples. The signal from the sample with Mn content of $x_{Mn} = 1\%$ was too low compared to the background noise, so we did not include this sample in the data evaluation.

For the determination of the preferentially occupied Mn lattice sites, extensive *ab initio* simulations of the EXAFS spectra using the FEFF9 software [29] were carried out. In the simulations, octahedral and tetrahedral interstitial Mn positions within the vdW gaps, as well as substitutional Mn on Bi lattice sites, as well as

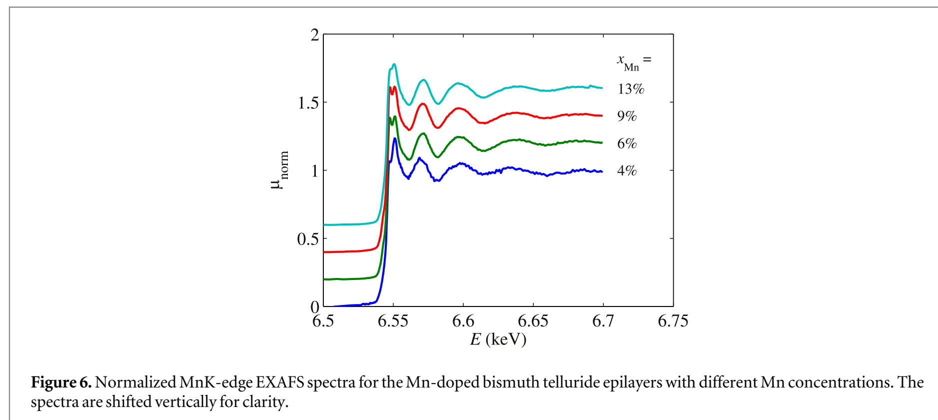

Figure 6. Normalized MnK-edge EXAFS spectra for the Mn-doped bismuth telluride epilayers with different Mn concentrations. The spectra are shifted vertically for clarity.

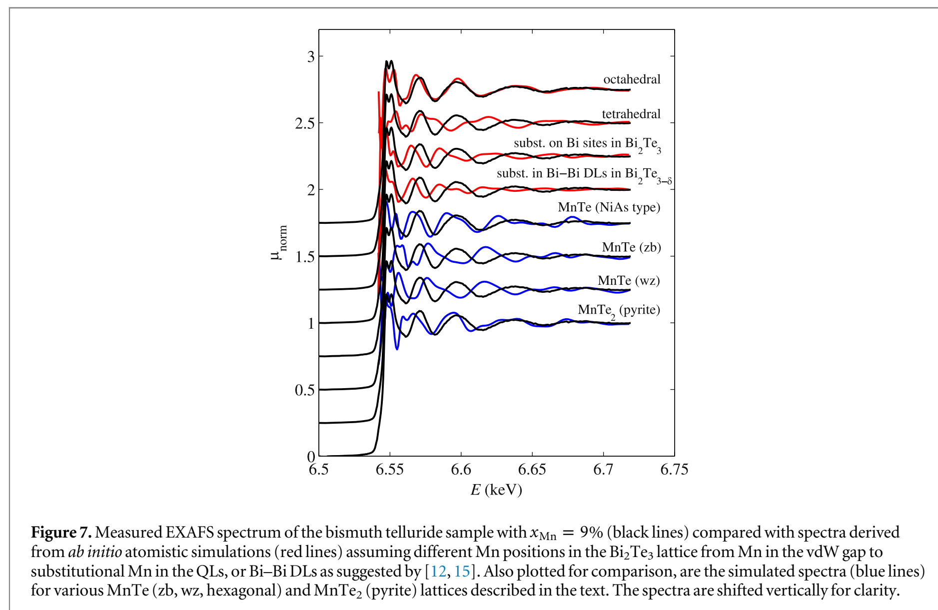

Figure 7. Measured EXAFS spectrum of the bismuth telluride sample with $x_{Mn} = 9\%$ (black lines) compared with spectra derived from *ab initio* atomistic simulations (red lines) assuming different Mn positions in the Bi_2Te_3 lattice from Mn in the vdW gap to substitutional Mn in the QLs, or Bi–Bi DLs as suggested by [12, 15]. Also plotted for comparison, are the simulated spectra (blue lines) for various MnTe (zb, wz, hexagonal) and $MnTe_2$ (pyrite) lattices described in the text. The spectra are shifted vertically for clarity.

substitutional Mn in extra Bi–Bi double layers between QL layers as suggested by [12, 15] were considered. For further comparison, simulations were also performed for various other manganese telluride phases, including zb, wz and hexagonal MnTe (NiAs-type) lattices, as well as cubic pyrite $MnTe_2$ (see figure 1) with the NN-distances listed in table 1. For all possible Mn sites, series of simulations were performed using variable cluster sizes up to 1.2 nm. The simulations showed that increasing the cluster radius beyond 0.9 nm did not cause any changes of the calculated results. Therefore, a cluster size of 0.9 nm was used for all simulations, which included 85 to 140 atoms, depending on the lattice structure assumed. This cluster size is typical for these types of simulations.

In figure 7, the experimental EXAFS spectrum for the sample with $x_{Mn} = 9\%$ is compared with the results of the FEFF9 simulations for the different Mn incorporation sites. It turns out that only for the octahedral interstitial Mn positions within the vdW gap (top curve in figure 7) the measured data is reproduced very well by the simulation, while for Mn incorporation at the other positions, the simulations strongly differ from the experimental spectra. The same result was also found for all other samples with different Mn concentrations. Thus, we conclude that Mn in Bi_2Te_3 is predominantly incorporated in the middle of the van der Waals gap between the QLs in octahedral coordination—at least under the given growth conditions. In the further data evaluation we therefore consider only the octahedral Mn interstitial position.

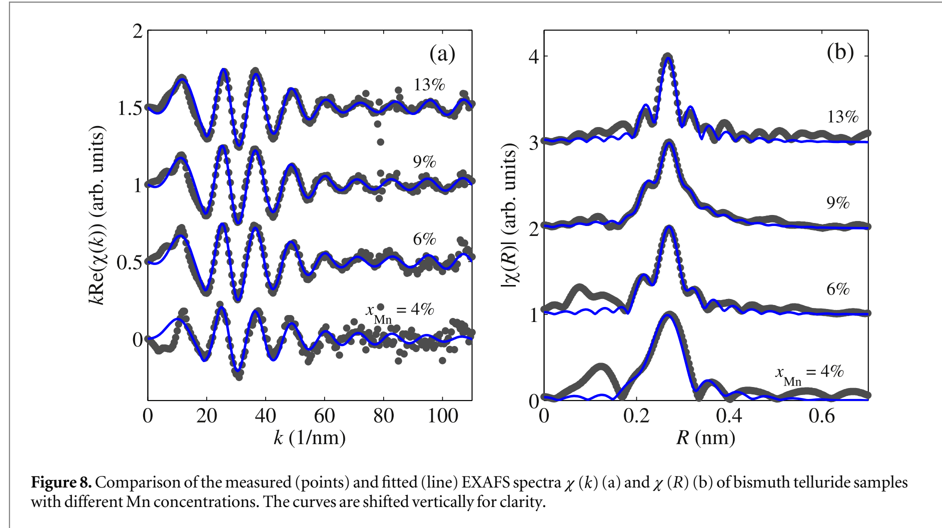

Figure 8. Comparison of the measured (points) and fitted (line) EXAFS spectra $\chi(k)$ (a) and $\chi(R)$ (b) of bismuth telluride samples with different Mn concentrations. The curves are shifted vertically for clarity.

Table 3. Distances of the six nearest tellurium atoms and two nearest bismuth atoms to the central Mn atom in octahedral configuration in Mn-doped bismuth telluride with different Mn concentrations x_{Mn} = 0 to 13% as determined from the fit of the $\chi(R)$ EXAFS data using the model of Mn incorporated interstitially in octahedral positions in the vdW Te–Te gap.

x_{Mn} (%)	d_{Mn-Te} (nm)	d_{Mn-Bi} (nm)
4	0.290 ± 0.009	—
6	0.292 ± 0.004	0.304 ± 0.010
9	0.292 ± 0.004	0.303 ± 0.010
13	0.291 ± 0.006	0.306 ± 0.014

For the refinement of the lattice structure around the Mn ion in the octahedral interstitial site, we have fitted the measured $\chi(k)$ EXAFS spectra, using the Artemis (IFEFFIT) software package [28]. In the fit we have included six Te atoms in the first coordination shell and two Bi atoms in the second coordination shell. The measured and fitted $\chi(k)$ and $\chi(R)$ curves of samples with $x_{Mn} = 4, 6, 9, 13\%$ are displayed in figures 8(a) and (b). From these fits, the NN and next-nearest neighbor (NNN) distances d_{Mn-Te} and d_{Mn-Bi} are obtained and the results are listed in table 3. We obtained $d_{Mn-Te} \approx 0.291$ nm and $d_{Mn-Bi} \approx 0.303$ nm for all samples, with an insignificant variation in dependence of the Mn content. This value is very close to the nominal value expected for undistorted pure Bi_2Te_3, whereas for the other possible incorporation sites, much different values would be expected (see table 1). The low Mn concentration for the $x_{Mn} = 4\%$ sample and the resulting comparatively high noise level in the data, did not allow us to fit the positions of the Bi atoms in the second coordination shell, i.e., only the Te positions in the first shell were refined for this sample.

We note that for the samples with low Mn contents of $x_{Mn} = 4$ and 6%, the theoretical $\chi(R)$ curves differ significantly in the range $R < 0.15$ nm. This region corresponds to long-range oscillations in energy dependence of the absorption spectrum $\mu(E)$, which is very sensitive to method used for the background subtraction. Since the measured fluorescence signal is proportional to the Mn content, the background and signal-to-noise is how it's usually stated ratio is higher for the samples with lower Mn content compared to those obtained for high x_{Mn}. The error limits in table 3 were determined as the reproducibility of the fitted distances with respect to various normalization methods of $\chi(R)$ obtained by the several data normalization methods available by the Athena software. The fitted d_{Mn-Te} values correspond within the error limits to the expected theoretical value of the ideal Bi_2Te_3 lattice listed in table 1. On the other hand, from the XRD data, we found that increasing the Mn concentration induces a contraction of the averaged lattice, both in lateral and vertical directions, which should affect the d_{Mn-Te} distances determined by EXAFS. However, the error limits of the EXAFS data are much larger than error limits of the XRD data, i.e., they are as large as the XRD observed-lattice contraction. Therefore, the sensitivity of EXAFS data does not allow us to see the effect of the small average lattice contraction to the first coordination around interstitial Mn atoms that was deduced by x-ray diffraction.

In [15], it has been suggested that Mn induces the creation of excess Bi–Bi double layers into which Mn atoms are substitutionally incorporated. According to this work, when increasing the Mn content, the structure

should change from pure Bi_2Te_3 phase towards the Bi_2Te_2 phase, in which a Bi–Bi DL occurs periodically after each pair of Te–Bi–Te–Bi–Te QLs. In our previous work [19], the structure of various $Bi_2Te_{3-\delta}$ phases was studied in detail, revealing that with increasing δ, i.e., when moving from Bi_2Te_3 towards Bi_2Te_2, the in-plane lattice parameter a increases, whereas the vertical lattice parameter c decreases. This is in contradiction to our results observed for Mn-doped Bi_2Te_2, where both lattice parameters a and c decrease with increasing x_{Mn} (see figure 3 and table 2). This fact supports our conclusion that the Mn atoms occupy interstitial places and do not evoke the creation of Bi–Bi DLs.

Finally, we compare the positions of the Te atoms in the first coordination shell around octahedral Mn interstitials in the vdW gaps with those of the Te atoms surrounding Mn in cubic $MnTe_2$ [24] [figures 1(d) and (e)]. We find that the structure of both first coordination shells, as well as the NN distances, is very similar indeed. Thus, the local lattice configuration around an occupied octahedral Mn interstitial can be considered as slightly deformed $MnTe_2$. This similarity is also obvious from the comparison of the measured and simulated EXAFS spectra in figure 7, where the spectrum simulated for the pyrite $MnTe_2$ is quite close to the experimental data for larger energies, i.e., for larger lengths of the photoelectron wave vector k. This coincidence implies the similarity of the first coordination shell around Mn in the investigated samples and in $MnTe_2$.

As the origin for the additional modulation of the lattice along the growth direction [0001] with the period of $L_{\mathrm{mod}} \approx 2D$, we propose that the Mn-occupation of the adjacent vdW gaps is not statistically independent, and a self-organized Mn modulation wave is created. This hypothesis needs further investigation. We note that if the Mn ions exclusively occupy octahedral positions and these sites occur on average only in every mth vdW Te–Te gap, the full occupation of these places corresponds to the phase $Mn_{1/m}Bi_2Te_3$. From this, it follows that in samples with $x_{\mathrm{Mn}} = 13\%$ and $m = 2$, every fourth of the possible octahedral sites within the vdW gaps is occupied.

6. Summary

Structural investigations of epitaxial ferromagnetic layers of the Mn-doped topological insulator Bi_2Te_3 reveal that the Mn dopant ions are incorporated mostly in octahedral interstitial positions in the middle of the van der Waals gaps between the adjacent Te layers of the quintuple layers. The local environment of the Mn ions corresponds to a distorted cubic $MnTe_2$ lattice with a nearest neighbor Mn–Te distance of 0.2901 Å. From the EXAFS data, we can rule out that Mn resides in sizable amounts on substitutional Bi sites or on tetrahedrally coordinated interstitial sites. This explains the rather small effect of Mn on the carrier type and concentration of the samples. These findings provide an important input for the ongoing experimental and theoretical investigations on the mechanisms that mediate ferromagnetism in n-type transition-metal-doped topological insulators in which charge carriers do not seem to play any dominant role, unlike in conventional Mn-doped ferromagnetic III–V semiconductors. Moreover, our findings are important for theoretical modeling of the effect of Mn incorporation on the topological surface state of bismuth telluride.

Acknowledgments

The assistance of Cornelius Strohm of BM23 beamline at ESRF is acknowledged. The work was supported by the Czech Science Foundation (projects P204/12/0595 and 14-08124S), by the Austrian Science Fund (project SFB-025 IRON), and by the Hiroshima Synchrotron Radiation Center (proposal 12-B-17).

References

[1] Hasan M Z and Kane C L 2010 *Mod. Phys. Rev.* **82** 3045
[2] Qi X L and Zhang S C 2010 *Phys. Today* **63** 33
[3] Qi X L and Zhang S C 2011 *Mod. Phys. Rev.* **83** 1057
[4] Zhang J M, Ming W, Huang Z, Liu G B, Kou X, Fan Y, Wang K L and Yao Y 2013 *Phys. Rev.* B **88** 235131
[5] Liu Q, Liu C X, Xu C, Qi X L and Zhang S C 2009 *Phys. Rev. Lett.* **102** 156603
[6] Chen Y L *et al* 2010 *Science* **329** 659–62
[7] Wray L A, Xu S Y, Xia Y, Hsieh D, Fedorov A V, Hor Y S, Cava R J, Bansil A, Lin H and Hasan M Z 2011 *Nat. Phys.* **7** 32–37
[8] Henk J, Flieger M, Maznichenko I V, Mertig I, Ernst A, Eremeev S V and Chulkov E V 2012 *Phys. Rev. Lett.* **109** 076801
[9] Chang C-Z *et al* 2013 *Science* **340** 167
[10] Hsieh D *et al* 2009 *Phys. Rev. Lett.* **103** 146401
[11] Hor Y S *et al* 2010 *Phys. Rev.* B **81** 195203
[12] Bos J W G, Lee M, Morosan E, Zandbergen H W, Lee W L, Ong N P and Cava R J 2006 *Phys. Rev.* B **74** 184429
[13] Choi J, Choia S, Choi J, Park Y, Park H M, Lee H W, Woo B C and Cho S 2004 *Phys. Status Solidi* B **241** 1541
[14] Watson M D *et al* 2013 *New J. Phys.* **15** 103016
[15] Lee J S, Richardella A, Rench D W, Fraleigh R D, Flanagan T C, Borchers J A, Tao J and Samarth N 2014 *Phys. Rev.* B **89** 174425
[16] Li Y, Zou X, Li J and Zhou G 2014 *J. Chem. Phys.* **140** 124704

[17] Vobornik I *et al* 2014 *J. Phys. Chem.* **118** 12333–9
[18] Caha O *et al* 2013 *Cryst. Growth Des.* **13** 3365–73
[19] Steiner H, Volobuev V, Caha O, Bauer G, Springholz G and Holy V 2014 *J. Appl. Cryst.* **47** 1889–900
[20] Chapler B C, Post K W, Richardella A R, Lee J S, Tao J, Samarth N and Basov D N 2014 *Phys. Rev* B **89** 235308
[21] Janik E, Dynowska E, Bak-Misiuk J, Leszczynski M, Szuszkiewicz W, Wojtowicz T, Karczewski G, Zakrzewski A K and Kossut J 1995 *Thin Solid Films* **267** 74–78
[22] Wyckoff R W G 1963 *Cryst. Struct.* **1** 85–237
[23] Elliott N 1937 *J. Am. Chem. Soc.* **59** 1958–62
[24] Johnston W D, Miller R C and Damon D H 1965 *J. Less Common Met.* **8** 272–87
[25] Ney A 2011 *Semicond. Sci. Technol.* **26** 064010
[26] Shimada K *et al* 2000 *Nucl. Instrum. Meth.* **467** 504–7
[27] Xu S Y *et al* 2012 *Nat. Phys.* **8** 616–22
[28] Ravel B and Newville M 2005 *J. Synchrotron Radiat.* **12** 537
[29] Rehr J J, Kas J J, Vila F D, Prange M P and Jorissen K 2010 *Phys. Chem. Chem. Phys.* **12** 5503

4.6 Band gap in manganese doped topological insulators Bi_2Te_3 and Bi_2Se_3

The Mn-doped samples were grown and analyzed using magnetic measurements, XRD, XAFS, HRTEM, and other methods. The structure was composed of random stacking of Bi_2Te_3 quintuple layers and $MnBi_2Te_4$ septuple layers. The concentration of septuple layers increases with manganese doping. The Curie temperature was found to be approximately 20 K, and the magnetization easy-axis is out-of-plane. The low-temperature ARPES and spin-resolved ARPES experiments have shown a band gap opening in the Dirac point with a size of 90 meV. The temperature dependence of the band gap size correlates with remanence magnetization. The paper presented the first direct observation of a magnetic band gap in the topological surface state. Bismuth selenide, on the contrary, does not show a magnetic band gap since its magnetization easy-axis is in-plane.

Article

Large magnetic gap at the Dirac point in $Bi_2Te_3/MnBi_2Te_4$ heterostructures

https://doi.org/10.1038/s41586-019-1826-7

Received: 10 May 2018

Accepted: 18 October 2019

Published online: 18 December 2019

E. D. L. Rienks[1,2,3,14], S. Wimmer[4,14], J. Sánchez-Barriga[1,14], O. Caha[5,14], P. S. Mandal[1,7], J. Růžička[5], A. Ney[4], H. Steiner[4], V. V. Volobuev[4,8,13], H. Groiss[9], M. Albu[10], G. Kothleitner[10], J. Michalička[6], S. A. Khan[11], J. Minár[11], H. Ebert[12], G. Bauer[4], F. Freyse[1,7], A. Varykhalov[1], O. Rader[1]* & G. Springholz[4]*

Magnetically doped topological insulators enable the quantum anomalous Hall effect (QAHE), which provides quantized edge states for lossless charge-transport applications[1–8]. The edge states are hosted by a magnetic energy gap at the Dirac point[2], but hitherto all attempts to observe this gap directly have been unsuccessful. Observing the gap is considered to be essential to overcoming the limitations of the QAHE, which so far occurs only at temperatures that are one to two orders of magnitude below the ferromagnetic Curie temperature, T_C (ref. [8]). Here we use low-temperature photoelectron spectroscopy to unambiguously reveal the magnetic gap of Mn-doped Bi_2Te_3, which displays ferromagnetic out-of-plane spin texture and opens up only below T_C. Surprisingly, our analysis reveals large gap sizes at 1 kelvin of up to 90 millielectronvolts, which is five times larger than theoretically predicted[9]. Using multiscale analysis we show that this enhancement is due to a remarkable structure modification induced by Mn doping: instead of a disordered impurity system, a self-organized alternating sequence of $MnBi_2Te_4$ septuple and Bi_2Te_3 quintuple layers is formed. This enhances the wavefunction overlap and size of the magnetic gap[10]. Mn-doped Bi_2Se_3 (ref. [11]) and Mn-doped Sb_2Te_3 form similar heterostructures, but for Bi_2Se_3 only a nonmagnetic gap is formed and the magnetization is in the surface plane. This is explained by the smaller spin–orbit interaction by comparison with Mn-doped Bi_2Te_3. Our findings provide insights that will be crucial in pushing lossless transport in topological insulators towards room-temperature applications.

The QAHE was first demonstrated in chromium-doped tetradymite topological insulators[2–5]. Subsequently, replacing chromium with vanadium was a successful strategy for achieving precise quantization with vanishing longitudinal resistance[6,7]. The effect occurs because of a modification of the band inversion in the ferromagnetic state. Exchange splitting and spin–orbit coupling lead to a release of the inversion of one of the spin sub-bands[2]. This should manifest itself as a magnetic gap that opens up at the Dirac point when the system is cooled below the Curie temperature. So far, however, direct observation of this gap has remained elusive and no clear correlation with ferromagnetism has been established.

Angle-resolved photoemission spectroscopy (ARPES) is the method of choice for the direct observation of the magnetic gap. Nevertheless, the situation has been confusing: large gaps of 0.05–0.2 eV were first reported for Mn-doped Bi_2Se_3 (refs. [12,13]), but were later shown not to be of magnetic origin[14]. Such gaps, however, did not appear when magnetic impurities were deposited on the surface of Bi_2Se_3 (refs. [14–16]). At low temperatures, a mobility gap of 32 meV was inferred from scanning tunnelling Landau level spectroscopy of V-doped Sb_2Te_3 (ref. [17]), but scanning tunnelling spectroscopy (STS) did not show a gap in this system[17]. STS did reveal gaps of 20–100 meV in Cr-doped $(Bi, Sb)_2Te_3$ (ref. [18]), but the temperature dependence was not investigated. In fact, a similar gap of around 75 meV was found for Cr-doped Bi_2Se_3 even at room temperature[19]. This suggests a nonmagnetic origin for these effects, because the ferromagnetic T_C is well below 50 K in all of these systems.

Interestingly, the configuration of the magnetic dopants is also contradictory. For isovalent magnetic doping, it has been predicted that

[1]Helmholtz-Zentrum Berlin für Materialien und Energie, Elektronenspeicherring BESSY II, Berlin, Germany. [2]Institut für Festkörperphysik, Technische Universität Dresden, Dresden, Germany. [3]Leibniz-Institut für Festkörper- und Werkstoffforschung Dresden, Dresden, Germany. [4]Institut für Halbleiter- und Festkörperphysik, Johannes Kepler Universität, Linz, Austria. [5]Department of Condensed Matter Physics, Masaryk University, Brno, Czech Republic. [6]Central European Institute of Technology, Brno University of Technology, Brno, Czech Republic. [7]Institut für Physik und Astronomie, Universität Potsdam, Potsdam, Germany. [8]National Technical University 'Kharkiv Polytechnic Institute', Kharkiv, Ukraine. [9]Christian Doppler Laboratory for Nanoscale Phase Transformations, Zentrum für Oberflächen- und Nanoanalytik, Johannes Kepler Universität, Linz, Austria. [10]Graz Center for Electron Microscopy, Institute of Electron Microscopy and Nanoanalysis, Graz University of Technology, Graz, Austria. [11]New Technologies Research Centre, University of West Bohemia, Pilsen, Czech Republic. [12]Department Chemie, Ludwig-Maximilians-Universität, München, Germany. [13]Present address: International Research Centre MagTop and Institute of Physics, Polish Academy of Sciences, Warsaw, Poland. [14]These authors contributed equally: E. D. L. Rienks, S. Wimmer, J. Sánchez-Barriga, O. Caha. *e-mail: rader@helmholtz-berlin.de; gunther.springholz@jku.at

Reprinted page 1 of paper [69] "Magnetic band gap in $MnBi_2Te_4$-Bi_2Te_3 heterostructures".

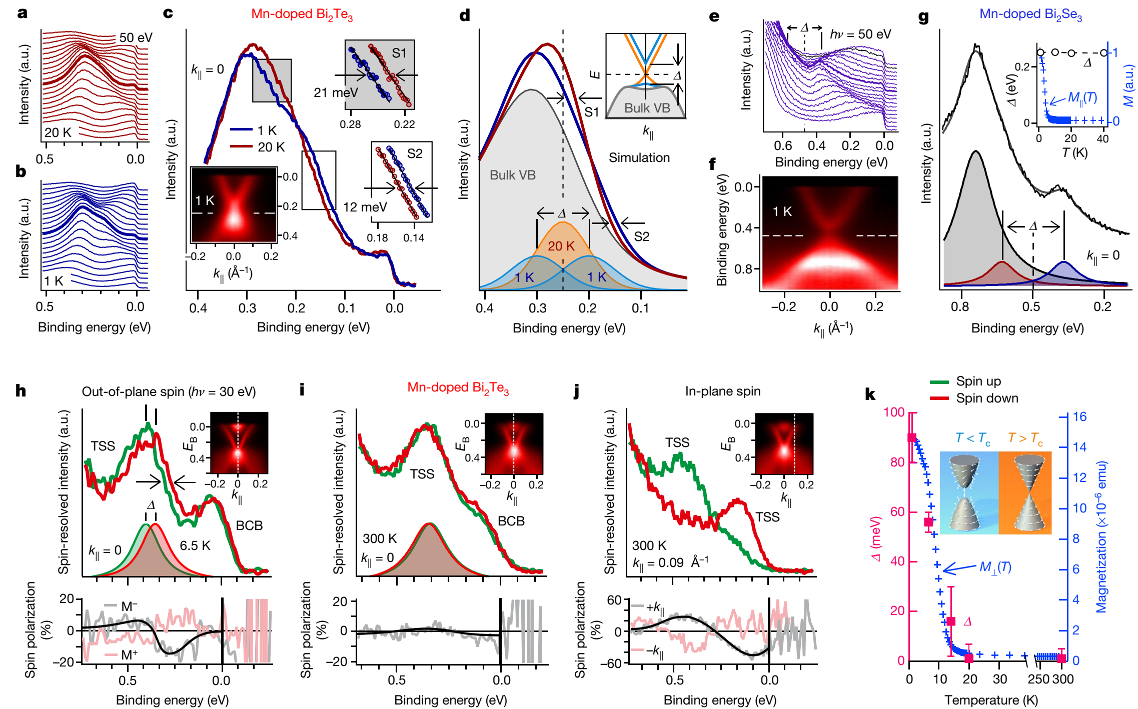

Fig. 1 | Magnetic gap of Mn-doped Bi_2Te_3. a–d, ARPES for Bi_2Te_3 with 6% Mn, above and below the Curie temperature (T_C) of around 10 K. The spectra in **c**, **d** and those marked by thick lines in **a**, **b** correspond to the centre of the surface Brillouin zone at $k_{\parallel} = 0$. Line fits in the regions S1 and S2 in **c** yield a splitting of more than 33 meV between 20 K and 1 K; according to the simulations shown in **d**, this splitting corresponds to a magnetic gap, Δ, of 90 ± 10 meV. The inset in **c** shows the energy, E, versus $k_{\parallel}$ momentum map at 1 K. a.u., arbitrary units. VB, valence band. **e–g**, Same analysis for Bi_2Se_3 with 6% Mn and a T_C of 6 K, revealing only a temperature-independent nonmagnetic gap, Δ, that does not correlate with magnetization (see inset). **h**, **i**, Spin-resolved ARPES of Bi_2Te_3 with 6% Mn at 6.5 K (**h**) and 300 K (**i**), showing that below T_C the gap at the Dirac point is ferromagnetically spin-split with out-of-plane spin orientation. At 6.5 K, the magnetic gap is $\Delta = 56 \pm 4$ meV. **j**, Away from the Dirac point, the conventional helical in-plane spin texture is measured. The out-of-plane component of the spin polarization reverses with the reversal in magnetization (M) (as shown in the lower part of **h**), and the in-plane spin component reverses with the in-plane wavevector $k_{\parallel}$ (lower part of **j**). **k**, The same temperature dependence is measured for $\Delta(T)$ and the magnetization $M(T)$. The inset shows a sketch of the measured spin textures below and above T_C.

Bi_2Se_3, Bi_2Te_3 and Sb_2Te_3 will form a QAHE state, which should thus occur when Bi or Sb are substituted by Cr or Fe, but not when the substituents are Ti or V, owing to their metallicity[2]. Moreover, nonisovalent magnetic dopants turn out to have surprisingly little effect on carrier concentration: that is, Mn-doped Bi_2Se_3 and Bi_2Te_3 always remain n-type[14,20], even though divalent Mn replacing trivalent Bi should act as a strong acceptor.

To resolve these issues, we present a comprehensive study of Mn-doped Bi_2Te_3 and Bi_2Se_3 that unequivocally reveals a large magnetic exchange splitting at the Dirac point of Bi_2Te_3. This splitting vanishes above the Curie temperature, which is clear-cut evidence for its magnetic origin. No increase in the gap size is observed for Mn-doped Bi_2Se_3 at temperatures down to 1 K. Through a multiscale structural analysis, we reveal that the actual lattice structure is very different to the anticipated random impurity system, as Mn doping induces the formation of self-organized heterostructures. This turns out to be crucial for obtaining large magnetic gaps[10].

Bandgap, spin texture and magnetism

Figure 1a–g shows the ARPES dispersions of Mn-doped Bi_2Te_3 and Bi_2Se_3 measured above and below the ferromagnetic phase transition (T_C = 10 K and 6 K, respectively). For Mn-doped Bi_2Te_3, the photoemission spectrum recorded at $h\nu = 50$ eV at the centre of the surface Brillouin zone shows an intensity maximum at a binding energy of 0.3 eV from the bulk valence band, while the Dirac point of the topological surface state (TSS) contributes a smaller peak at around 0.2 eV. On cooling from 20 K through T_C down to 1 K, the low energy flank of the peak develops a pronounced shoulder, forming a plateau at around 0.2 eV (Fig. 1a–c). Assuming that the single component for the topological surface state at 20 K becomes split into two equally intense components at 1 K (Fig. 1d), we arrive at a gap, Δ, of 90 ± 10 meV at low temperature (see Methods section 'ARPES' and Extended Data Fig. 1). Because T_C is 10 K in this sample, this proves the magnetic origin of this gap. This is the central result of our study.

To confirm the magnetic origin, we carried out spin-resolved ARPES. For the spectra shown in Fig. 1h–j, we chose a photon energy of $h\nu = 30$ eV at which bulk transitions are strong from the bulk conduction band (BCB) but overlap much less with the Dirac point of the TSS. At 6.5 K, the spectrum at the Dirac point—measured in remanence after field cooling (M^-)—is clearly spin-polarized, with spin orientation perpendicular to the surface and spin split by $\Delta = 56 \pm 4$ meV (Fig. 1h and Extended Data Fig. 2). Because the temperature is closer to T_C, this value is smaller than that derived at 1 K. Subsequent measurement at room temperature (Fig. 1i) shows that the spin polarization has completely disappeared, whereas subsequent cooling in an oppositely

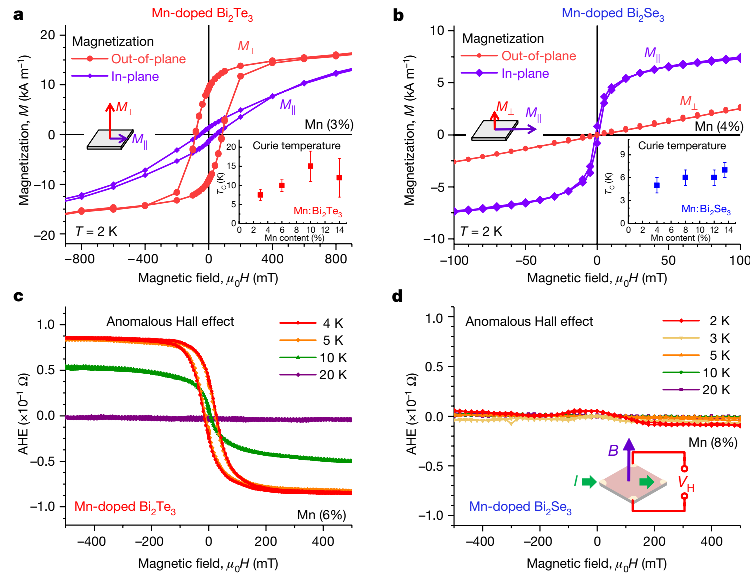

Fig. 2 | Magnetic properties. a, **b**, In-plane and out-of-plane magnetization $M(H)$ of Mn-doped Bi_2Te_3 (**a**) and Bi_2Se_3 (**b**) films with Mn concentrations of 3% and 4% at 2 K, measured with the magnetic field parallel, respectively, perpendicular to the surface, showing a perpendicular anisotropy (easy axis) for Bi_2Te_3 and an in-plane easy axis for Bi_2Se_3. The insets show the Curie temperature as a function of Mn concentration. **c**, **d**, Anomalous Hall effect (AHE) of Mn-doped Bi_2Te_3 (**c**) and Bi_2Se_3 (**d**) measured between 2 K and 20 K. The contribution of the ordinary Hall effect extracted from the high field data was subtracted (see Methods). Owing to the perpendicular magnetic anisotropy, only Mn-doped Bi_2Te_3 displays a pronounced anomalous Hall effect below T_C.

oriented field (M^+) leads to the opposite spin polarization (Fig. 1h, lower panel). This unambiguously proves that the out-of-plane spin polarization below T_C is due to ferromagnetic ordering of the system. Figure 1j shows that, away from the Dirac point, the characteristic helical in-plane spin texture of the parent Bi_2Te_3 is preserved, such that an overall spin texture as displayed in Fig. 1k is formed.

Our measurement of the gap probes the exchange splitting of p electrons of the host material, which ferromagnetically couple to the localized magnetic moments of the Mn ions[9]. The magnitude of the gap thus depends on the exchange coupling, J, and the magnetization, M, along the surface normal direction[21]. Indeed, the gap size nicely follows the temperature dependence of the perpendicular magnetization, $M_\perp$ (Fig. 1k, blue crosses). This clearly demonstrates the direct correlation between the gap and ferromagnetism in the system. In Fig. 1e–g we show that such temperature dependence is not observed for Bi_2Se_3 with a similar Mn concentration of 6%, where instead a large gap of roughly 200 meV exists at all temperatures from 1 K to 300 K (ref. [14]). In particular, the gap size does not increase when cooling down to 1 K, well below the T_C of about 6 K (Fig. 1g, inset). This rules out a substantial contribution of magnetism to the Dirac gap for Mn-doped Bi_2Se_3, in contrast to Bi_2Te_3, and serves as a cross-check for the magnetic gap opening.

Figure 2 shows the magnetization of Bi_2Te_3 and Bi_2Se_3 for comparable Mn concentrations. The Mn-doped Bi_2Te_3 film shows an easy-axis magnetization normal to the surface: that is, $M_\perp$ is greater than $M_\parallel$. This perpendicular anisotropy is robust because it does not depend on the Mn concentration (Extended Data Fig. 3) and also occurs for bulk single crystals[22]. By contrast, for Mn-doped Bi_2Se_3 the easy axis is parallel to the surface plane ($M_\perp$ is less than $M_\parallel$) for all investigated Mn concentrations. The coercive field is substantially larger for Mn-doped Bi_2Te_3 than for Mn-doped Bi_2Se_3, and the anisotropy field at which the in- and out-of-plane magnetizations are equal is two times higher for Mn-doped Bi_2Te_3 (Extended Data Fig. 3). Finally, the ferromagnetic T_C of Mn-doped Bi_2Te_3 is considerably higher (7–15 K) than for Mn-doped Bi_2Se_3 (5–7 K) (Fig. 2a, b, insets, and Supplementary Information on SQUID measurements). Altogether this shows that Mn-doped Bi_2Te_3 is the more robust and anisotropic ferromagnet. The opposite anisotropy is also revealed by the magnetotransport measurements shown in Fig. 2c, d, where, with magnetic fields applied perpendicular to the films, only Mn-doped Bi_2Te_3 displays a pronounced anomalous Hall effect below T_C, whereas it is negligible in Mn-doped Bi_2Se_3 (Fig. 2d). This perpendicular anisotropy in Mn-doped Bi_2Te_3 is precisely the precondition for the magnetic bandgap opening and the QAHE, whereas an in-plane magnetization as observed for Mn-doped Bi_2Se_3 merely shifts the Dirac cone in momentum parallel to the surface[9,23].

Multiscale structure analysis

To clarify how Mn is actually incorporated into Bi_2Te_3 and Bi_2Se_3, we carried out a multiscale structure analysis for both systems. Figure 3a shows Mn-doped Bi_2Te_3 in high-resolution scanning transmission electron microscopy (HRSTEM). Strikingly, we observe the emergence of a new structure composed of septuple and quintuple layers, instead of the expected periodic sequence of Te–Bi–Te–Bi–Te quintuple layers. The septuple layers consist of the sequence Te–Bi–Te–Mn–Te–Bi–Te, where the Mn atoms predominantly occupy the centre of the septuple[24]. This self-organized heterostructure formation does not exist for stoichiometric Bi_2Te_3 and Bi_2Se_3 (Extended Data Fig. 4a) and obviously disagrees with the commonly held notion of substitutional Mn incorporation[9,12,14,22,25]. Figure 3b and Extended Data Fig. 4b show that the same Mn-induced septuple/quintuple heterostructure formation also occurs in Bi_2Se_3, in agreement with recent observations[11,26]. Thus, it is a universal mechanism in both material systems. Moreover, we identify this structure as the explanation for the surprisingly small effect[14,20,27] of Mn doping on the carrier concentration and Fermi level of the system: Mn in $MnBi_2Te_4$ is electrically neutral because each septuple

Reprinted page 3 of paper [69] "Magnetic band gap in $MnBi_2Te_4$-Bi_2Te_3 heterostructures".

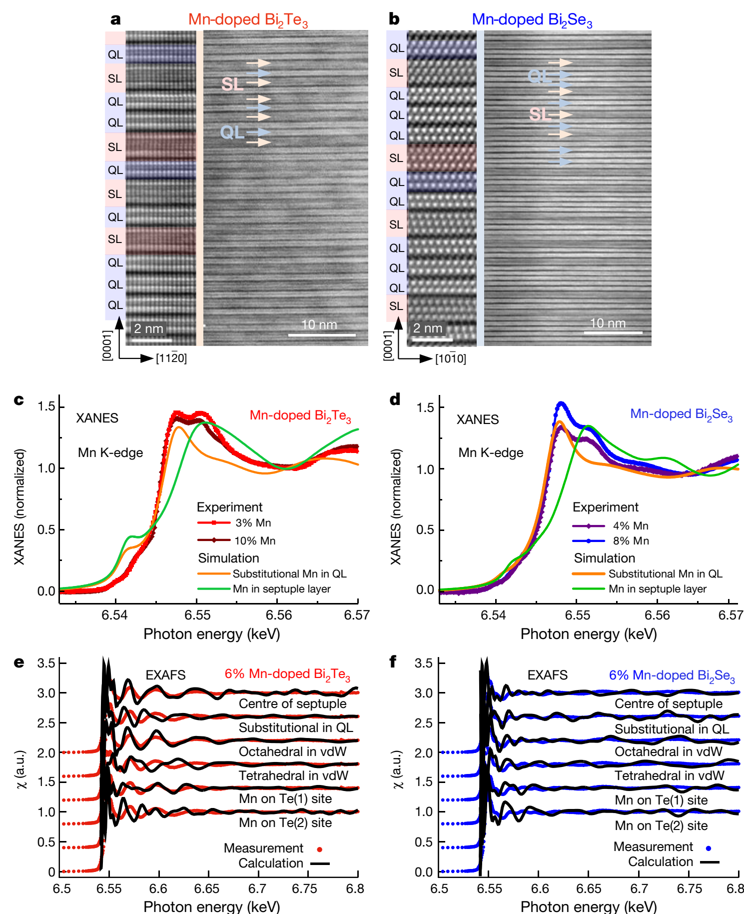

Fig. 3 | Structure analysis by STEM and X-ray absorption spectroscopy. **a**, **b**, STEM cross-sections of Mn-doped Bi_2Te_3 (**a**) and Bi_2Se_3 (**b**), revealing the formation of layered heterostructures consisting of $MnBi_2Te_4$ ($MnBi_2Se_4$) septuple layers (SLs) inserted between Bi_2Te_3 (Bi_2Se_3) quintuple layers (QLs). The images were recorded along the [$\bar{1}$100] (**a**) and [$\bar{1}2\bar{1}$0] zone axes (**b**). Owing to the atomic-number contrast, the heavy atoms (Bi) appear brighter in the high-angle annular dark field (HAADF) images. As a result, the septuple layers appear darker in the overview images because of incorporation of the lighter Mn atoms. The Mn concentration was 10% in **a**, and locally 9% and on average 6% in **b**, according to X-ray diffraction measurements (Fig. 4). **c**–**f**, Spectroscopic determination of the Mn-incorporation sites in Mn-doped Bi_2Te_3 (**c**, **e**) and Bi_2Se_3 (**d**, **f**) by X-ray absorption spectroscopy (XANES in **c**, **d** and EXAFS in **e**, **f**) at the Mn K-edge. Experimental data (symbols) are compared with simulations (solid lines) performed for different Mn-incorporation sites in the septuple and quintuple layers, in the van der Waals (vdW) gap or on Te (Se) antisites (see Extended Data Fig. 6).

is formed by insertion of a charge-compensated MnTe double layer into a quintuple layer.

To obtain element-specific information on the Mn-incorporation sites, we carried out X-ray absorption near-edge spectroscopy (XANES) and extended fine structure spectroscopy (EXAFS) at the Mn K-edge (Fig. 3c–f). We analysed the absorption spectra through simulations of all possible Mn-incorporation sites (see Methods section on 'XANES and EXAFS measurements and simulations' and Extended Data Figs. 6, 7), showing that Mn in Bi_2Te_3 indeed prefers to be incorporated into the newly formed septuple layers, and that only a minority is incorporated in the quintuple layers. Although the EXAFS data do not completely rule out the incorporation of Mn into octahedral sites in the van der Waals gap, the fact that septuples are never seen in undoped Bi_2Te_3 clearly suggests that the Mn sites are closely linked to the septuple layers. This is supported by high-resolution energy-dispersive X-ray (EDX) elemental maps of the Bi, Te and Mn atoms, in which Mn does not appear in the van der Waals gaps but mostly in the septuple layers (Extended Data Fig. 4c).

Turning to Mn-doped Bi_2Se_3 we do not observe as intense EXAFS oscillations as for Bi_2Te_3, indicating that Mn is distributed over different lattice sites, with a larger amount of substitutional Mn and a lesser fraction within the septuple layers. This is highlighted by the XANES spectra, which exhibit a characteristic double-peak structure, with the higher energy peak being attributed to Mn at the centre of the septuple and the lower energy peak to substitutional Mn. Again for Bi_2Se_3 the signal from Mn in the septuples is weaker compared with that in Bi_2Te_3. For tetrahedrally coordinated interstitial Mn and Mn on Te (Se) antisites, the simulations do not agree with the experiments, indicating that these are not favourable for Mn incorporation. Overall, we conclude that for Bi_2Te_3 the vast majority of Mn is incorporated within the septuple layers and that substitutional Mn is more readily formed in Bi_2Se_3, especially at lower Mn concentrations.

Reprinted page 4 of paper [69] "Magnetic band gap in $MnBi_2Te_4$-Bi_2Te_3 heterostructures".

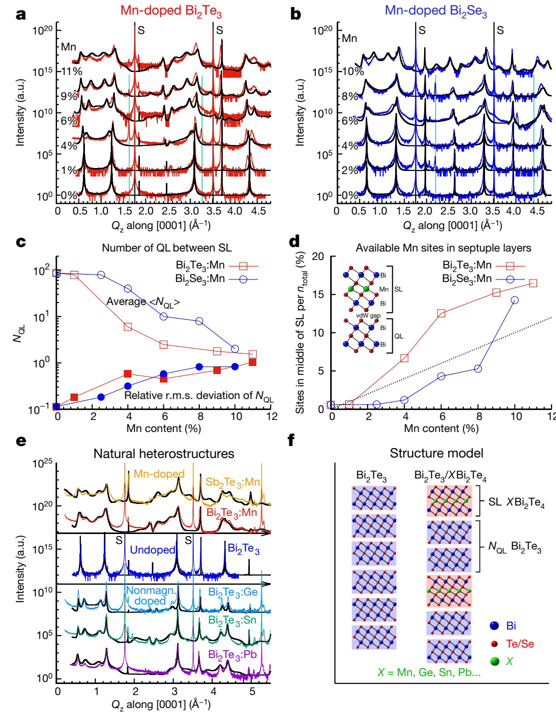

Fig. 4 | X-ray diffraction analysis of self-organized heterostructures in Mn-doped Bi_2Te_3 and Bi_2Se_3 as a function of Mn concentration. The Mn concentration varied from 0% to 11%. **a**, **b**, Measured diffraction spectra (red and blue lines) recorded along the vertical Q_z direction for Mn-doped Bi_2Te_3 (**a**) and Bi_2Se_3 (**b**) at different Mn concentrations. The diffraction peaks of the substrate are indicated by 'S'. The spectra were fitted using a paracrystal model of statistically varying alternations of Bi_2Y_3 quintuple (Y = Te, Se) and $MnBi_2Y_4$ septuple layers (see Methods). An excellent fit (black lines) is obtained for both systems. **c**, The derived average number of quintuples $\langle N_{QL}\rangle$ between the septuples (open symbols) and the r.m.s. width of the random distribution (filled symbols) are plotted against Mn concentration. A smaller average distance $\langle N_{QL}\rangle$—that is, a higher concentration of septuples—is found for Bi_2Te_3 than for Bi_2Se_3. **d**, The number of available Mn sites in the centre of the septuples relative to the total number, n_{tot}, of incorporated Mn atoms is plotted against the nominal Mn concentration. The number expected for unity occupancy is indicated by the dashed line. Experimental points below this line indicate a substantial fraction of Mn atoms residing in other lattice sites. This applies to Bi_2Se_3 but not to Bi_2Te_3. **e**, Structure analysis for Bi_2Te_3 doped with Ge, Sn or Pb and for Sb_2Te_3 doped with Mn. The good fit of the diffraction data with the paracrystal model (black lines) reveals that the same type of self-organized heterostructures (**f**) is formed in all cases.

To systematically map out the structure evolution on a larger length scale, we carried out X-ray diffraction investigations as summarized in Fig. 4a–d. For both systems we find a pronounced change with increasing Mn concentration, shown by the appearance of additional diffraction peaks that signify the emergence of septuple layers in the structure. The septuples are, however, not incorporated periodically at fixed distances, but rather stochastically after a varying number, N_{QL}, of quintuple layers. This is seen in the STEM cross-sections, where N_{QL} varies between one to seven. To evaluate the diffraction data, we have thus developed an one-dimensional paracrystal model, in which the overall structure is described as a statistically varying sequence of quintuple segments alternating with single septuple layers (see Methods section 'X-ray diffraction and simulation with random stacking model' and Extended Data Fig. 8). Each sequence is characterized by the average number, $\langle N_{QL}\rangle$, of quintuples between subsequent septuples and the randomness of the statistical N_{QL} distribution—that is, their root mean square (r.m.s.) deviation from the average value.

The model fits (black lines in Fig. 4a, b) show a remarkably good agreement with the diffraction spectra. This corroborates the formation of self-organized quintuple/septuple heterostructures in both systems. From the fits, we obtain the average $\langle N_{QL}\rangle$ between the septuple layers as well as the r.m.s. deviation as a function of Mn concentration. As shown in Fig. 4c, $\langle N_{QL}\rangle$ rapidly decreases and thus the density of septuples increases with increasing Mn concentration, underlining that the septuple formation is indeed driven by the Mn doping. This also explains why T_C varies so little with the Mn concentration in Fig. 2: the magnetic properties of the samples are largely those of the individual septuple layers. Apparently, in Bi_2Te_3 the formation of septuple layers starts at a lower Mn concentration than in Bi_2Se_3 and the average separation $\langle N_{QL}\rangle$ between the septuples is smaller. This difference is highlighted in Fig. 4d, where the number of available Mn sites in the septuples is plotted versus the actual Mn concentration, revealing that in Bi_2Te_3 all Mn atoms can be incorporated in the septuple layers, whereas in Bi_2Se_3 the density of septuples at low Mn concentrations is too small to accommodate all Mn atoms, which must thus be incorporated at other sites as well. We emphasize that our model of self-organized septuple/quintuple heterostructures applies not only to Mn, but also to other nonisovalent dopants such as Ge, Sn and Pb. As a result, very similar diffraction spectra that are well described by the same paracrystal model are obtained, as shown in Fig. 4e, f and Extended Data Fig. 9. This highlights that this new type of incorporation mechanism is completely generic in the tetradymite chalcogenide material systems.

Discussion

The electronic structure of transition-metal impurities in Bi_2Te_3 and Bi_2Se_3 has been studied extensively through density functional theory (DFT) calculations[9,25]. For Mn in Bi_2Se_3, a nonmagnetic bandgap of the measured size (200 meV) does not appear in any DFT calculation. Although in principle, depending on orbital symmetry, small gaps of around 4 meV might open even for an in-plane magnetization[25], this is obviously much less than what we observe experimentally. The only prediction of a nonmagnetic gap of the magnitude seen in our experiments is from calculations that assume an on-site Coulomb interaction, U, at the impurity site[28]. On the one hand, Mn forms more substitutional sites in Bi_2Se_3 than in Bi_2Te_3. They will lead to a larger Coulomb U than for Mn in the centre of the septuple layer, where Mn 3d levels can delocalize in the plane. The size of U, also termed the impurity strength[28], indeed affects the nonmagnetic gap: comparing Mn with In doping for Bi_2Se_3, we find that to reach the same gap size as for 8% Mn, only 2% In is required[29]. On the other hand, the effect of impurities on the nonmagnetic gap decreases with higher spin–orbit interaction in the host material[29], so that Bi_2Te_3 is less susceptible to a nonmagnetic gap opening than Bi_2Se_3.

To explain the marked difference in the magnetic anisotropy of Mn-doped Bi_2Te_3 and Bi_2Se_3, we calculated the magnetocrystalline anisotropy for the Bi_2Y_3/$MnBi_2Y_4$ (Y = Te, Se) heterostructures (see Methods section 'DFT calculation of magnetic anisotropy'). In agreement with recent model calculations[10], we find that the strong magnetocrystalline anisotropy favours out-of-plane magnetization in the telluride. In the selenide, however, because of the reduced spin–orbit interaction the magnetocrystalline anisotropy is 3.5 times smaller and practically cancelled by the shape anisotropy. Thus, the higher spin–orbit interaction in the telluride heterostructures turns the magnetization out of the plane and enables the magnetic gap to form at the Dirac point.

Reprinted page 5 of paper [69] "Magnetic band gap in $MnBi_2Te_4$-Bi_2Te_3 heterostructures".

Finally, our magnetic gap size of 90 meV for Mn-doped Bi_2Te_3 is five times larger than that predicted theoretically for substitutional Mn[9]. This huge enhancement arises from the naturally formed heterostructure and the enhanced wavefunction overlap of the TSS with the Mn atoms in the $MnBi_2Te_4$ septuple layer, which supports large magnetic gaps of 38–87 meV, as predicted[10]. Mn-doped Sb_2Te_3 displays the same heterostructure formation and out-of-plane magnetic anisotropy as Bi_2Te_3 (Extended Data Fig. 10), and because it is p-type, the Fermi level can be tuned into the magnetic gap by alloying of these systems. This demonstrates the great potential of such structures for stabilizing edge transport in QAHE devices. Theory also suggests that the nontrivial topology is retained in the heterostructures[10], in accordance with the persistence of the Dirac cone surface state and out-of-plane spin texture seen in our ARPES experiments. Therefore, Mn-based topological insulator heterostructures might not only boost edge transport in QAHE devices, but also facilitate the realization of new topological phases such as the axion insulator state[30,31] and the chiral Majorana fermion[32].

Online content

Any methods, additional references, Nature Research reporting summaries, source data, extended data, supplementary information, acknowledgements, peer review information; details of author contributions and competing interests; and statements of data and code availability are available at https://doi.org/10.1038/s41586-019-1826-7.

1. Onoda, M. & Nagaosa, N. Quantized anomalous Hall effect in two-dimensional ferromagnets: quantum Hall effect in metals. *Phys. Rev. Lett*. **90**, 206601 (2003).
2. Yu, R. et al. Quantized anomalous Hall effect in magnetic topological insulators. *Science* **329**, 61–64 (2010).
3. Chang, C.-Z. et al. Experimental observation of the quantum anomalous Hall effect in a magnetic topological insulator. *Science* **340**, 167–170 (2013).
4. Checkelsky, J. G. et al. Trajectory of the anomalous Hall effect toward the quantized state in a ferromagnetic topological insulator. *Nat. Phys*. **10**, 731–736 (2014).
5. Bestwick, A. J. et al. Precise quantization of the anomalous Hall effect near zero magnetic field. *Phys. Rev. Lett*. **114**, 187201 (2015).
6. Chang, C.-Z. et al. High-precision realization of robust quantum anomalous Hall state in a hard ferromagnetic topological insulator. *Nat. Mater*. **14**, 473–477 (2015).
7. Grauer, S., Schreyeck, S., Winnerlein, M., Brunner, K., Gould, C. & Molenkamp, L. W. Coincidence of superparamagnetism and perfect quantization in the quantum anomalous Hall state. *Phys. Rev. B* **92**, 201304(R) (2015).
8. Tokura, Y., Yasuda, K. & Tsukazaki, A. Magnetic topological insulators. *Nat. Rev. Phys*. **1**, 126–143 (2019).
9. Henk, J. et al. Topological character and magnetism of the Dirac state in Mn-doped Bi_2Te_3. *Phys. Rev. Lett*. **109**, 076801 (2012).
10. Otrokov, M. M. et al. Highly-ordered wide bandgap materials for quantized anomalous Hall and magnetoelectric effects. *2D Mater*. **4**, 025082 (2017).
11. Hagmann, J. A. et al. Molecular beam growth and structure of self-assembled Bi_2Se_3/$MnBi_2Se_4$ multilayer heterostructures. *New J. Phys*. **19**, 085002 (2017).
12. Xu, S.-Y. et al. Hedgehog spin texture and Berry's phase tuning in a magnetic topological insulator. *Nat. Phys*. **8**, 616–622 (2012).
13. Zhang, D. et al. Interplay between ferromagnetism, surface states, and quantum corrections in a magnetically doped topological insulator. *Phys. Rev. B* **86**, 205127 (2012).
14. Sánchez-Barriga, J. et al. Nonmagnetic band gap at the Dirac point of the magnetic topological insulator $(Bi_{1-x}Mn_x)_2Se_3$. *Nat. Commun*. **7**, 10559 (2016).
15. Scholz, M. R. et al. Tolerance of topological surface states towards magnetic moments: Fe on Bi_2Se_3. *Phys. Rev. Lett*. **108**, 256810 (2012).
16. Ye, M. et al. Quasiparticle interference on the surface of Bi_2Se_3 induced by cobalt adatom in the absence of ferromagnetic ordering. *Phys. Rev. B* **85**, 205317 (2012).
17. Sessi, P. et al. Dual nature of magnetic dopants and competing trends in topological insulators. *Nat. Commun*. **7**, 12027 (2016).
18. Lee, I. et al. Imaging Dirac-mass disorder from magnetic dopant atoms in the ferromagnetic topological insulator $Cr_x(Bi_{0.1}Sb_{0.9})_{2-x}Te_3$. *Proc. Natl Acad. Sci. USA* **112**, 1316–1321 (2015).
19. Chang, C.-Z. et al. Chemical-potential-dependent gap opening at the Dirac surface states of Bi_2Se_3 induced by aggregated substitutional Cr atoms. *Phys. Rev. Lett*. **112**, 056801 (2014).
20. Růžička, J. et al. Structural and electronic properties of manganese-doped Bi_2Te_3 epitaxial layers. *New J. Phys*. **17**, 013028 (2015).
21. Rosenberg, G. & Franz, M. Surface magnetic ordering in topological insulators with bulk magnetic dopants. *Phys. Rev. B* **85**, 195119 (2012).
22. Hor, Y. S. et al. Development of ferromagnetism in the doped topological insulator $Bi_{2-x}Mn_xTe_3$. *Phys. Rev. B* **81**, 195203 (2010).
23. Kharitonov, M. Interaction-enhanced magnetically ordered insulating state at the edge of a two-dimensional topological insulator. *Phys. Rev. B* **86**, 165121 (2012).
24. Lee, D. S. et al. Crystal structure, properties and nanostructuring of a new layered chalcogenide semiconductor, Bi_2MnTe_4. *CrystEngComm* **15**, 5532–5538 (2013).
25. Abdalla, L. B., Seixas, L., Schmidt, T. M., Miwa, R. H. & Fazzio, A. Topological insulator Bi_2Se_3 (111) surface doped with transition metals: an ab-initio investigation. *Phys. Rev. B* **88**, 045312 (2013).
26. Hirahara, T. et al. Large-gap magnetic topological heterostructure formed by subsurface incorporation of a ferromagnetic layer. *Nano Lett*. **17**, 3493–3500 (2017).
27. Lee, J. S. et al. Ferromagnetism and spin-dependent transport in n-type Mn-doped bismuth telluride thin films. *Phys. Rev. B* **89**, 174425 (2014).
28. Black-Schaffer, A. M. & Balatsky, A. V. Strong potential impurities on the surface of a topological insulator. *Phys. Rev. B* **85**, 121103(R) (2012).
29. Sánchez-Barriga, J. et al. Anomalous behavior of the electronic structure of $(Bi_{1-x}In_x)_2Se$ across the quantum phase transition from topological to trivial insulator. *Phys. Rev. B* **98**, 235110 (2018).
30. Mogi, M., Kawamura, M., Tsukazaki, A., Yoshimi, R., Takahashi, K. S., Kawasaki, M. & Tokura, Y. Tailoring tricolor structure of magnetic topological insulator for robust axion insulator., *Sci. Adv*. **10**, eaao1669 (2017).
31. Xiao, D. Realization of the axion insulator state in quantum anomalous Hall sandwich heterostructures. *Phys. Rev. Lett*. **120**, 056801 (2018).
32. He, Q. L., et al. Chiral Majorana fermion modes in a quantum anomalous Hall insulator-superconductor structure. *Science* **357**, 294–299 (2017).

© The Author(s), under exclusive licence to Springer Nature Limited 2019

Reprinted page 6 of paper [69] "Magnetic band gap in $MnBi_2Te_4$-Bi_2Te_3 heterostructures".

Methods

Sample growth

Mn-doped Bi_2Te_3, Bi_2Se_3, and Sb_2Te_3 layers were grown by molecular beam epitaxy (MBE) on $BaF_2(111)$ substrates using a Riber 1000 and a Varian GEN II MBE system. Compound Bi_2Te_3, Bi_2Se_3, and Sb_2Te_3 as well as elemental sources for Mn, Te and Se were used for control of stoichiometry and composition. For Pb-, Sn- and Ge-doped Bi_2Te_3, we used additional PbTe, SnTe and GeTe sources. Deposition was carried out at a growth temperature of 330 °C for Bi_2Te_3 and Sb_2Te_3 and 360 °C for Bi_2Se_3 to obtain perfect two-dimensional growth independently of dopant concentrations. This was verified by in situ reflection high-energy electron diffraction (RHEED; Extended Data Fig. 9). Details of growth procedures have been reported previously[14,20]. Our notation of x% Mn in Bi_2Te_3 refers to a nominal composition of $(Bi_{1-x}Mn_x)_2Te_{3+3x}$. All layers exhibited n-type conduction with electron concentrations of the order of a few times 10^{19} cm^{-3} (see Extended Data Fig. 5c), except for Mn-doped Sb_2Te_3 which is p-type with a hole concentration of a few times 10^{20} cm^{-3}. Immediately after growth, samples used for ARPES were capped in situ with amorphous Se and Te capping layers at room temperature to protect the surface against oxidation. This cap was removed just before the ARPES experiments by in situ sputtering and annealing.

ARPES

Photoemission experiments were performed with the ARPES-1[3] end station at the UE112-PGM2b undulator beam line of the BESSY II synchrotron radiation source. The lowest reachable temperature is 1 K. The experimental geometry has the following characteristics: with the central axis of the analyser lens and the polar rotation axis of the sample defined as the x and z axes of a spherical coordinate system, the photons impinge the sample under an azimuthal angle φ of 45° and a polar angle of 84°. The light polarization is horizontal (along the x axis). The entrance slit of the hemispherical analyser is placed parallel to the z axis. The measurements at $h\nu = 50$ eV were performed with an energy resolution of 10 meV. The temperature-dependent leading-edge shifts in Fig. 1c and Extended Data Fig. 1a are obtained by approximating the photoemission intensity in the indicated ranges with a line. The slope of this line is constrained to be identical for the low- and high-temperature spectra within the same section. Our notation Δ refers to the full gap.

The measurement of the magnetic exchange splitting at the Dirac point through the temperature dependence in ARPES is in a certain sense analogous to the case of gadolinium metal. In both cases the magnetic coupling of localized magnetic moments ($3d$ in Mn, $4f$ in Gd) is mediated by itinerant electrons ($5p$ in Te, $5d$ in Gd) which can be probed by ARPES. At the Dirac point, electronic states of the Te $5p$ character are probed. In Gd, the $5d$ band probed by ARPES splits by 0.85 eV when the temperature is lowered from 1.02 T_C to 0.27 T_C ($T_C = 293$ K for bulk Gd)[33].

Spin-resolved ARPES

Spin-resolved ARPES was measured at the RGBL2 end station at the U125/2 undulator beamline of BESSY II. It comprises a Scienta R4000 hemispherical analyser with two Mott-type spin polarimeters operated at 26 kV (ref. [34]). The lowest temperature is 6.5 K. Light is incident under an azimuthal angle of 45° and a polar angle of 90° (Extended Data Fig. 2a). The light polarization is horizontal (along the x axis). The spin polarimeter detects the out-of-plane and one in-plane component of the spin polarization. The measured in-plane projection is tangential to the Dirac cone and perpendicular to the analyser entrance slit and electron momentum. The out-of-plane component lies within the electron emission plane and is parallel to the sample normal along the z-direction. The angular resolution was 0.75° and the energy resolution of the measurement at a photon energy of 30 eV was set to 45 meV. We note that the measurement of the spin splitting is not limited by the energy resolution because the spin-up and spin-down channels count independently of each other. An example of this is the exchange splitting of a Ni(111) surface state, measured by spin-resolved inverse photoemission as 18 ± 3 meV at an energy resolution of 300–400 meV (ref. [35]).

Transport measurements

Temperature-dependent transport measurements were performed in van der Pauw geometry with out-of-plane magnetic fields ranging from 0 T to 2 T and temperatures down to 1 K using a Cryogenic mini cryogen-free system. Extended Data Fig. 5 shows the complete data set (Hall resistance plotted against magnetic field, as well as carrier concentration, n, and carrier mobility, μ, plotted against temperature) for the Mn-doped Bi_2Te_3 and Bi_2Se_3 films with respectively 6% and 8% Mn. Below the ferromagnetic transition T_C (10 K and 6 K, respectively), the Hall resistance comprises the contribution from the ordinary Hall effect (proportional to $1/ne$) and the anomalous Hall effect (proportional to the magnetization, M). Because the latter is proportional to the perpendicular magnetization, the anomalous Hall contribution is minute for Mn-doped Bi_2Se_3 films, for which the magnetization vector is nearly parallel to the film plane. Above T_C the anomalous Hall contribution is absent.

Magnetic characterization

The magnetic properties were determined by measuring magnetization, M, as a function of the applied external field, H, and as a function of temperature, T (ranging from 2 K to 300 K), using a superconducting quantum interference device (SQUID) magnetometer (Quantum Design MPMS-XL5). We determined the Curie temperature from the $M(T)$ curves as exemplified in Extended Data Fig. 3. Note that we do not observe an enhancement of T_C at the surface probed by XMCD[14]. The magnetic field was applied either parallel (out-of-plane) or perpendicular (in-plane) to the c axis of the films. The diamagnetic contribution of the $BaF_2(111)$ substrate was determined from the slope of the $M(H)$ curve recorded at 300 K in high magnetic fields, and was subtracted from the raw data. Identical sample pieces were used for in-plane and out-of-plane measurements. The sample size was 4 × 4 mm^2.

Scanning transmission electron microscopy

Atomic resolution HRSTEM images were obtained with a FEI Titan G2 60-300 STEM equipped with a Cs probe corrector and a FEI Titan 60-300 Themis equipped with a Cs image corrector, which were operated at 300 keV. The HRSTEM data were recorded with a HAADF detector and the images processed using a Wiener filter for noise minimization[36]. Thin cross-sectional lamellae from Mn-doped Bi_2Te_3 and Bi_2Se_3 films with Mn concentrations of 10% and 6%, respectively, were prepared by focused ion beam (FIB) milling (ZEISS Crossbeam XB 1540 and FEI Helios NanoLab 660) along two different crystallographic directions of the $BaF_2(111)$ substrate ($[\bar{2}11]$ and $[0\bar{1}1]$, respectively). Owing to the epitaxial relationship between the films and the $BaF_2(111)$ substrate, this yields $[\bar{1}100]$ and $[\bar{1}2\bar{1}0]$ zone axes with respect to the Bi_2Te_3 and Bi_2Se_3 layers. Pre-characterization of the lamellae and overview STEM images were obtained with a JEOL JEM-2200FS STEM operated at 200 keV. Shortly before the HRSTEM images were taken, the lamellae were additionally thinned to remove the amorphous surface layers and damaged regions caused by the initial FIB preparation using a Fischione 1040 NanoMill. To map the element distribution (Extended Data Fig. 4c), we carried out energy-dispersive X-ray analysis using a Bruker Super-X detector.

XANES and EXAFS measurements and simulations

The XANES and EXAFS spectra at the Mn K-edge were recorded at, respectively, the ID12 and BM23 beamlines of the European Synchrotron Radiation Facility in total fluorescence yield[37]. The isotropic XANES spectrum was derived from a weighted average of two XANES spectra recorded with two orthogonal linear polarizations parallel

and perpendicular to the *c* axis of the film. The resulting X-ray linear dichroism spectra corroborate the findings of XANES and EXAFS with regard to Mn incorporation.

For XANES simulations, we used the FDMNES code[38] with a multiple scattering approach on a muffin-tin potential, for a supercell comprising the nominal bulk Bi_2Te_3 or Bi_2Se_3 lattices with a Mn atom replacing one Bi atom within the quintuple layers (substitutional Mn), and with Mn incorporated in the central layers of the septuples (Extended Data Fig. 6). Note that placing Mn as an octahedral interstitial within the van der Waals (vdW) gap leads to somewhat similar results as with Mn in the central position of the septuple layer, while tetrahedral Mn interstitials were in lesser agreement with experiment (Fig. 3c–f). Concerning the pre-edge features in the XANES data, it is known that the FDMNES code using the multiple scattering formalism has difficulties in reproducing the 3*d*–4*p* hybridized states at the pre-edge feature well; nevertheless the main absorption features are well reproduced and we draw conclusions only from that spectral region.

We used identical input geometries for the EXAFS and XANES simulations. We measured EXAFS spectra for a series of Mn-doped Bi_2Te_3 and Bi_2Se_3 samples with Mn concentrations ranging from 4% to 13%. We fitted the EXAFS data at the Mn K-edge using the FEFF9 code, assuming Mn at different lattice sites. The spectra with a model of Mn atoms in the centre position of the septuple layer are shown in Extended Data Fig. 7. The first coordination shell includes six anion atoms in the octahedral environment. We note again that the substitutional position and the interstitial position in the van der Waals gap have octahedral coordination. The distances of the nearest neighbours in the first coordination shell derived from the fits are listed in Extended Data Fig. 7e. We note that Mn atoms substituting Bi, Te(1) or Se(1) atoms in the quintuple layers (using the notation of Extended Data Fig. 6) have two different neighbours with different distances.

X-ray diffraction and simulation with random stacking model

We determined the crystal structure using symmetric X-ray diffraction scans and reciprocal space maps in the vicinity of the $(10\bar{1}.20)$ reciprocal lattice point. The measurements were performed using a Rigaku SmartLab diffractometer with a copper X-ray tube and channel-cut Ge(220) monochromator. Symmetric scans along the [000.1] reciprocal space direction (*c* axis) were fitted with a modified one-dimensional paracrystal model[39], in which random sequences of Bi_2Te_3 (or Sb_2Te_3 or Bi_2Se_3) quintuple segments alternate with $MnBi_2Te_4$ (or $MnSb_2Te_4$ or $MnBi_2Se_4$) septuples along the *c* axis. For the samples doped with X = Pb, Sn or Ge (Fig. 4e), the septuples consist of XBi_2Te_4. For the quintuples, the spacings of atomic planes were set to the nominal values of Bi_2Te_3 and Bi_2Se_3, and for the septuples the distance of the Mn (or Pb, Sn or Ge) plane to the nearest neighbour Te (or Se) was set to correspond to the nearest-neighbour distances determined by EXAFS.

The random sequences of quintuple and septuple layers are generated using the following assumptions. First, the length of the individual quintuple segments, N_{QL}, is given by the gamma distribution with a certain mean value, $\langle N_{QL}\rangle$, and a r.m.s. deviation, σ (r.m.s.d.); we show its relative value, $\sigma/\langle N_{QL}\rangle$. The septuple segments always consist of only one single septuple layer—that is, septuple layers are not positioned next to each other. Note that we carried out additional test fits assuming a variable length of septuple segments, but the best fits tend to the result with just one septuple layer embedded in the blocks of quintuple layers. Thus, we fixed the length of the septuple segments to one, in order to keep the number of fitting parameters as small as possible.

Second, we set the distances of the individual atomic planes in the quintuples to the values of the pure Bi_2Y_3 phases (Y = Te, Se), as we described previously[39]. For the septuples we have set the distances of the next Te or Se anion sites to the Mn in the central planes to correspond to the distances determined by EXAFS. The total thickness of the septuple equals approximately 4/3 of d_{QL}: that is, $d_{SL} = 4/3d_{QL}$. This relation is almost exactly satisfied for Bi_2Te_3, whereas for Bi_2Se_3 $d_{SL} = 1.02 \times 4/3d_{QL}$.

For the random sequences generated in this way, we calculated the XRD diffraction spectra using the one-dimensional paracrystal model described before[39], and compared the spectra to the experimental data. Examples of simulated profiles with various parameter values are shown in Extended Data Fig. 8a–d. Extended Data Fig. 8a, b depict the influence of the average number of quintuples, $\langle N_{QL}\rangle$, between the septuples for a fixed disorder, that is, $\sigma/\langle N_{QL}\rangle = 0.5$. High values of $\langle N_{QL}\rangle$ correspond to an almost pure Bi_2Y_3 lattice with just few septuples present in the stack. Such a system corresponds to samples with low Mn doping. Smaller values of $\langle N_{QL}\rangle$ lead to a multilayer system, in which additional satellite diffraction peaks appear. The limiting case of $\langle N_{QL}\rangle = 1$, which is on average one quintuple alternating with one septuple, corresponds to the top blue line, with the peak positions corresponding to an average periodicity $P = d_{QL} + d_{SL}$ along the growth direction. Extended Data Fig. 8c, d show the influence of the randomness (r.m.s.) on the diffraction spectra for a constant $\langle N_{QL}\rangle$ of 5. A small r.m.s. corresponds to a periodic multilayer of quintuple and septuple segments, with corresponding sharp superlattice maxima, while large r.m.s. values correspond to a disordered system with accordingly smeared profiles. For the samples doped with X = Pb, Sn or Ge (Fig. 4e), the fitted paracrystal parameters are listed in Extended Data Fig. 9g.

We note that the relation $d_{SL} = 4/3d_{QL}$ has quite an important consequence for the diffraction spectra, because there is a single periodicity that is common to both quintuples and septuples. The simulated and experimental diffraction profiles shown in Fig. 4 have sharp peaks corresponding to such a periodicity independently of the statistical ordering of quintuple and septuple segments. The corresponding peaks appear at the positions (000.9) and (000.18) of the Bi_2Y_3 structure. The average interplanar distance in the septuples is smaller than in the quintuples, because the septuple has 7/5 = 1.4 more atomic planes but is only thicker by a factor of 4/3 = 1.33.

We have also determined the Mn-concentration dependence of the in-plane lattice parameter *a* of the Mn-doped Bi_2Y_3 layers from asymmetric reciprocal space maps recorded in the vicinity of the (101.20) reciprocal lattice point of the Bi_2Y_3 structure. These results, as well as those for the average interplanar distance in the *c* axis direction, $\langle d\rangle$, are plotted in Extended Data Fig. 8e, f. In Mn-doped Bi_2Te_3, we observe a decrease in both lattice parameters with increasing Mn content. This can be explained by the fact that a higher concentration of septuple layers leads to a smaller average interplanar distance, while for Mn-doped Bi_2Se_3 the Mn content has less influence on $\langle d\rangle$ owing to the smaller number of septuple layers formed. In fact, in Bi_2Se_3 we do not observe any concentration dependence of the interplanar distance $\langle d\rangle$ up to Mn concentrations of 8%. This is in agreement with the finding from X-ray diffraction that, for low Mn contents in Bi_2Se_3, only a very low number of septuples (Fig. 4) is present. Mn atoms also cause a small shrinking of the in-plane lattice parameter *a* for both Bi_2Te_3 and Bi_2Se_3 (Extended Data Fig. 8e, f).

DFT calculation of magnetic anisotropy

To get a reliable value for the magnetic anisotropy of Mn-doped Bi_2Y_3 (Y = Se, Te) with septuple/quintuple layer structure, we carry out ab initio calculations using the well established full-potential linearized augmented plane wave (FLAPW) method, as implemented in the WIEN2k code[40]. Our calculations are based on the local density approximation. Here we used experimental lattice parameters for the multilayer system with alternating septuple/quintuple layers, which corresponds to an Mn concentration of 8%. One part of the magnetic anisotropy energy, known as magnetocrystalline anisotropy (MCA), arises from spin–orbit coupling; the other part, the so-called shape anisotropy, E_{shape}, comes from the magnetic dipole–dipole interaction of the individual magnetic moments. It is well known that a sufficiently dense mesh in the Brillouin zone is important for *k*-space integration.

Reprinted page 8 of paper [69] "Magnetic band gap in $MnBi_2Te_4$-Bi_2Te_3 heterostructures".

On the basis of this insight, we used a 45 × 45 × 7 Monkhorst–Pack grid in the full Brillouin zone[41]. In our benchmark calculation for FePt[42] we showed that, in addition to the convergence of *k*-points, it is important to incorporate all FLAPW eigenfunctions when spin–orbit coupling is included as an additional term to the scalar-relativistic Hamiltonian, the so-called second variational step[43]. This basis set is controlled by energy parameters (E_{min} and E_{max}). To achieve a high accuracy, we set E_{min} to be −10 Ry and E_{max} to be 5 Ry. To obtain a stable value for the MCA, the energy parameters, E_ℓ, used for calculating radial wavefunctions, $u_\ell(r, E_\ell)$, are determined very precisely—that is, to better than 0.1 mRy.

As the WIEN2k code solves the Dirac equation in an approximate way, it is necessary to check the reliability of these sensitive calculations. For cross-checking we used the multiple-scattering KKR Green function method as implemented in the SPRKKR code[44,45]. This scheme solves the proper Dirac equation; hence the relativistic effects are fully included in SPRKKR, unlike with the second variational step.

Obtaining the MCA energy by subtracting the total energies is computationally very costly. The need for self-consistent calculations for two magnetization directions can be avoided if one relies on the magnetic force theorem. In this approach the MCA energy is calculated using a frozen spin-dependent potential[46]. The MCA energy is then obtained by subtracting the band energies. E_{shape} is calculated using classical electromagnetic theory. Good agreement has been found between WIEN2k and SPRKKR codes for the MCA energy calculation. For the sake of simplicity we present only the WIEN2k results (Extended Data Fig. 3g).

Ge-, Sn- and Pb-doped Bi_2Te_3 and Mn-doped Sb_2Te_3

Natural formation of quintuple/septuple layer heterostructures is a generic and universal feature in Bi- and Sb-based tetradymite chalcogenide topological insulators doped with elements that prefer a 2^+ state. This is demonstrated by a series of complementary thin film samples consisting of Bi_2Te_3 doped with Ge, Sn, and Pb, as well as of Sb_2Te_3 doped with Mn, using similar growth conditions to those described above. In all cases, two-dimensional growth was observed under the given growth conditions, as shown by the RHEED patterns recorded in situ during growth and depicted in Extended Data Fig. 9a–f. The structure of the films was analysed by X-ray diffraction, and the measured diffraction spectra were fitted with the same random stacking paracrystal model described in the section 'X-ray diffraction and simulation with random stacking', assuming that the additional doping element (X = Pb, Ge, Sn, Mn) induces the same type of septuple layer formation in which an additional XTe double layer is inserted . As shown in Fig. 4e, in all cases an excellent fit of the diffraction spectra is obtained with our paracrystal structure model. Moreover, for the same concentration of dopant elements, the average number of quintuple layers, $\langle N_{QL}\rangle$, between these additionally inserted septuple layers and its r.m.s. variation, σ_{QL}, derived from the model fits (see Extended Data Fig. 9g) turn out to be nearly the same for each dopant element.

Data availability

The data sets generated and analysed here are available from the corresponding authors on reasonable request.

Code availability

The code for the paracrystal model is available from the corresponding authors upon request. The electronic structure codes Wien2K and SPR-KKR and X-ray absorption fine structure codes FDMNES and FEFF9 can be downloaded after the corresponding licence requirements given on the respective webpages are fulfilled.

33. Kim, B., Andrews, A. B., Erskine, J. L., Kim, K. J. & Harmon, B. N. Temperature dependent conduction-band exchange splitting in ferromagnetic hcp gadolinium: theoretical predictions and photoemission experiments. *Phys. Rev. Lett*. **68**, 1931–1934 (1992).
34. Burnett, G. C., Monroe, T. J. & Dunning, F. B. High-efficiency retarding-potential Mott polarization analyzer. *Rev. Sci. Instrum*. **65**, 1893–1896 (1994).
35. Passek, F. & Donath, M. Spin-split image-potential-induced surface state on Ni(111). *Phys. Rev. Lett*. **69**, 1101–1104 (1992).
36. Mitchell, D. HRTEM Filter. *Austrian Centre for Electron Microscopy and Nanoanalysis* https://dm-script.tugraz.at/dm/source_codes/181 (2007).
37. Rogalev, A., Wilhelm, F., Goulon, J. & Goulon-Ginet, C. C. in *Magnetism and Synchrotron Radiation: Towards the Fourth Generation Light Sources* vol. 151 (eds Beaurepaire, E., Bulou, H., Joly, L. & Scheurer, F.) 289–314 (Springer, 2013).
38. Bunău, O. & Joly, Y. Self-consistent aspects of x-ray absorption calculations. *J. Phys. Condens. Matter* **21**, 345501 (2009).
39. Steiner, H. et al. Structure and composition of bismuth telluride topological insulators grown by molecular beam epitaxy. *J. Appl. Cryst*. **47**, 1889–1900 (2014).
40. Blaha, P., Schwarz, K., Madsen, G. K. H., Kvasnicka, D. & Luitz, J. *Wien2k, an augmented plane wave plus local orbital program for calculating the crystal properties*. http://www.wien2k.at (2001).
41. Monkhorst, H. J. & Pack, J. D. Special points for Brillouin-zone integrations. *Phys. Rev. B* **13**, 5188–5192 (1976).
42. Khan, S. A., Blaha, P., Ebert, H., Minár, J. & Sipr, O. Magnetocrystalline anisotropy of FePt: a detailed view. *Phys. Rev. B* **94**, 144436 (2016).
43. MacDonald, A. H. & Vosko, S. H. A relativistic density functional formalism. *J. Phys. C Solid State Phys*. **12**, 2977–2990 (1979).
44. Ebert, H., Ködderitzsch, D. & Minár, J. Calculating condensed matter properties using the KKR-Green's function method—recent developments and applications. *Rep. Prog. Phys*. **74**, 096501 (2011).
45. Ebert, H. The Munich SPRKKR package, version 7. http://olymp.cup.uni-muenchen.de (2012).
46. Mackintosh, R. & Andersen, O. K. in *Electrons at the Fermi surface* Vol. 3 (ed. Springford, M.) 149–222 (Cambridge Univ. Press, 1980).

Acknowledgements ARPES experiments were performed at BESSY II of Helmholtz-Zentrum Berlin and the EXAFS and XANES experiments at the European Synchrotron Radiation Facility. We thank B. Henne, F. Wilhelm and A. Rogalev for support with XANES and EXAFS measurements; W. Grafeneder and G. Hesser for TEM sample preparation; V. Holý for advice on the paracrystal model; and G. Bihlmayer and A. Ernst for helpful discussions. This project was supported by the Austrian Science Fund (FWF, project P30969-N27 and P28185-N27); the Austrian Federal Ministry for Digital and Economic Affairs, the National Foundation for Research, Technology and Development in the frame of the Christian Doppler Laboratory for Nanoscale Phase Transformations; the Deutsche Forschungsgemeinschaft (grants SPP 1666, SFB 1143 project C4, SFB 1277 project A2); the Central European Institute of Technology (CEITEC) Nano research infrastructure (ID LM2015041, MEYS CR, 2016-2019) and Computational and Experimental Design of Advanced Materials with New Functionalities (CEDAMNF; grant CZ.02.1.01/0.0/0.0/15_003/0000358) of the Czech Ministerstvo Školství Mládeže a Telovýchovy (MSMT); the Impuls- und Vernetzungsfonds der Helmholtz-Gemeinschaft (Virtual Institute New States of Matter and their Excitations and Helmholtz-Russia Joint Research Group no. HRSF-0067); and the European Union Horizon 2020 programme (grant 823717–ESTEEM3).

Author contributions Samples were grown by S.W., H.S., V.V.V. and G.S. X-ray analysis was carried out by S.W., H.S., G.S., J.R. and O.C. O.C. performed paracrystal modelling and magnetotransport measurements. XANES and EXAFS measurements were made by A.N., O.C., H.S. and G.S., and the simulations by O.C., A.N., J.R. and J. Minár. SQUID was carried out by A.N., and HR-STEM by M.A., H.G., S.W., G.K., O.C. and J. Michalička. DFT calculations were done by S.A.K., J. Minár and H.E. ARPES was carried out by E.D.L.R. and P.S.M., and spin-resolved ARPES by J.S.-B., F.F. and A.V. The work was coordinated by G.S., G.B. and O.R. The manuscript was written by O.R. and G.S. with input from all authors.

Competing interests The authors declare no competing interests.

Additional information
Supplementary information is available for this paper at https://doi.org/10.1038/s41586-019-1826-7.

Correspondence and requests for materials should be addressed to O.R. or G.S.

Peer review information *Nature* thanks Alexander Balatsky, Jacek Furdyna and the other, anonymous, reviewer(s) for their contribution to the peer review of this work.
Reprints and permissions information is available at http://www.nature.com/reprints.

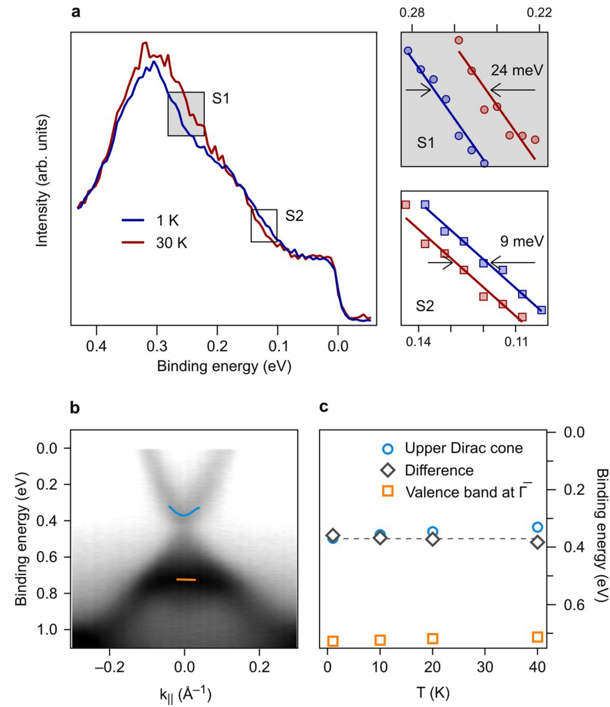

Extended Data Fig. 1 | ARPES measurements. a, Data for an additional Mn-doped Bi_2Te_3 film with Mn concentration of 10%. The normal emission spectra shown on the left, recorded at 1 K and 30 K, show a substantial redistribution of spectral weight around the binding energy of approximately 180 meV when crossing the ferromagnetic transition at T_C = 12 K. The shifts in the regions marked S1 and S2, shown on the right on a magnified scale, are of similar magnitude to that seen for the 6% Mn-doped case in Fig. 1. The shifts marked by arrows are compatible with a 100 meV gap opening at the Dirac point. ARPES was measured with p-polarized light and $h\nu$ = 50 eV. **b**, **c**, ARPES measurements, showing that the gap in 6%-Mn-doped Bi_2Se_3 is independent of temperature. **b**, ARPES $E(k)$ map recorded at 1 K, with the angle-dependent binding energies of the upper Dirac cone and bulk valence band indicated with blue and orange lines, obtained from Lorentzian fits to energy-distribution curves. **c**, Temperature dependence of the binding energies of the upper Dirac cone minimum (blue circles), the bulk valence band at $\bar{\Gamma}$ (orange squares) and their difference (black diamonds). The ferromagnetic Curie temperature is 6 K as obtained by SQUID. This analysis represents an alternative to that in Fig. 1g, which was based on fits of the upper and lower Dirac cones. In both cases, the data do not provide any indication of a relative or absolute shift of the band edges, or of a gap of the order seen in Mn-doped Bi_2Te_3 when crossing the ferromagnetic transition temperature.

Reprinted page 10 of paper [69] "Magnetic band gap in $MnBi_2Te_4$-Bi_2Te_3 heterostructures".

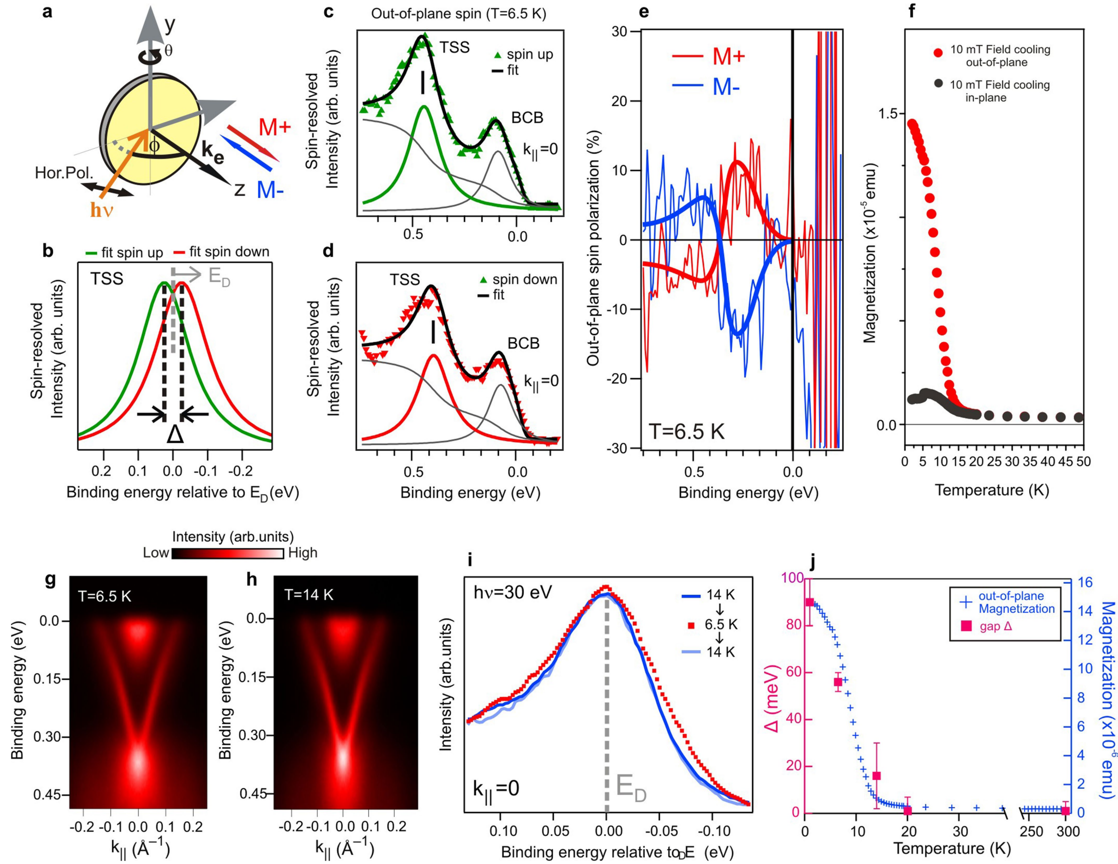

Extended Data Fig. 2 | Spin-resolved ARPES of Mn-doped Bi_2Te_3. **a**, Geometry of the spin-resolved ARPES experiments, including the magnetization directions indicated by M^+ and M^-. Hor. Pol., horizontal light polarization. **b**, Plot of the fit results from spin-up and spin-down spectra of the topological surface state (TSS) at the Dirac point (E_D), and determination of the magnetic exchange splitting, $\Delta = 56 \pm 4$ meV, at 6.5 K. **c**, **d**, Fit to the spin-resolved spectra at 6.5 K, including a transition from the bulk conduction band (BCB). **e**, Demonstration that the spin polarization reverses when the magnetization, *M*, is reversed. This reversal was achieved by field cooling in an applied field of 10 mT. **f**, Temperature-dependent magnetization, $M(T)$, measured by SQUID on a reference sample that was identical to that used to determine the magnetic field necessary for field cooling and magnetization reversal. **g**, **h**, Before the spin-resolved ARPES measurement, the reversible temperature-dependent broadening in ARPES was verified by cooling from 14 K to 6.5 K and warming up again to 14 K. At a photon energy of 30 eV, most of the intensity near the Fermi energy stems from the bulk conduction band. **i**, Reversible broadening of the energy-dispersion curves upon cooling from above to below T_C and warming up again. **j**, TSS gap at the Dirac point Δ derived by ARPES and spin-resolved ARPES (red squares), plotted against temperature, together with the temperature-dependent out-of-plane magnetization (blue crosses), showing that the magnetic exchange splitting at the Dirac point Δ faithfully follows the magnetization perpendicular to the sample surface. Data at 1 K and 20 K are from Fig. 1c, d. Data from spin-resolved photoemission (at 6.5 K and 300 K) have the smallest error. Data for 14 K were derived from **i**, taking the spin-resolved data from 6.5 K as a reference point.

Reprinted page 11 of paper [69] "Magnetic band gap in $MnBi_2Te_4$-Bi_2Te_3 heterostructures".

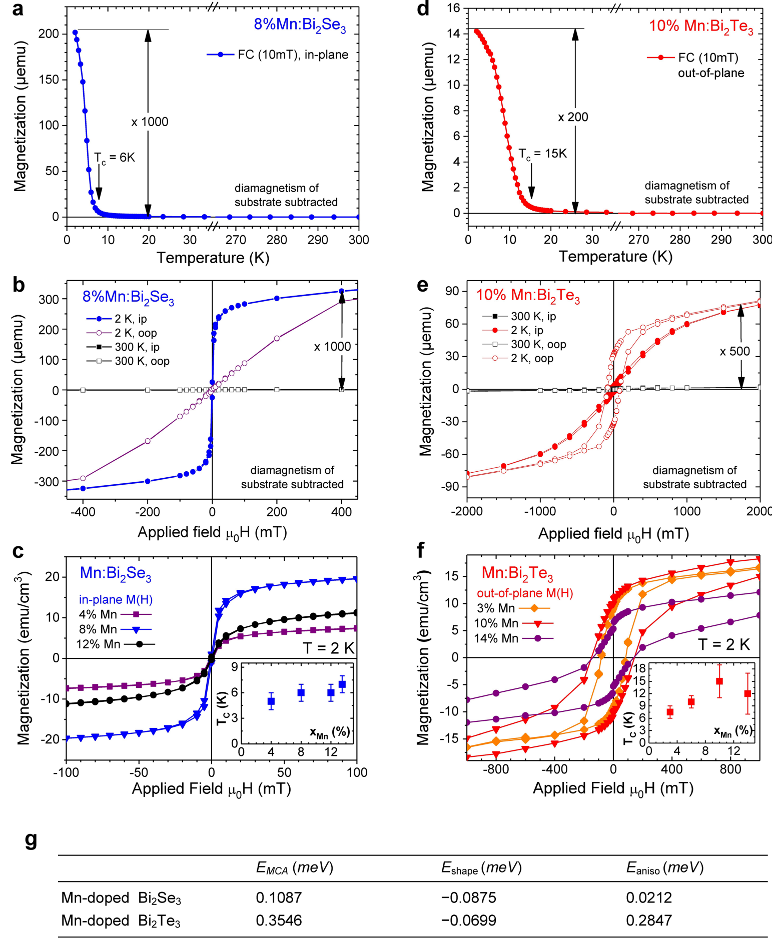

	E_{MCA} (meV)	E_{shape} (meV)	E_{aniso} (meV)
Mn-doped Bi_2Se_3	0.1087	−0.0875	0.0212
Mn-doped Bi_2Te_3	0.3546	−0.0699	0.2847

Extended Data Fig. 3 | Magnetic properties of Mn-doped Bi_2Se_3 and Bi_2Te3. **a**, **d**, Temperature-dependent magnetization, $M(T)$, used to determine the ferromagnetic Curie temperature, T_C, Mn-doped Bi_2Se_3 (**a**) and Bi_2Te_3 (**d**). The magnetization was measured after field cooling (FC) at 10 mT. As indicated, below T_C the magnetization of the samples rises steeply by more than two orders of magnitude. **b**, **e**, In-plane (ip) versus out-of-plane (oop) hysteresis loops at 300 K and 2 K, showing the absence of ferromagnetism at room temperature. **c**, **f**, Magnetization versus applied field, $M(H)$, for samples with different Mn concentrations, x_{Mn}, as indicated. For all Mn-doped Bi_2Se_3 films, the easy axis of magnetization is found to be in plane, whereas for all Mn-doped Bi_2Te_3 films it is perpendicular to the surface. The insets show the Curie temperature, T_C, plotted against Mn concentration. For all measurements, the diamagnetic contribution of the substrate measured at 300 K was subtracted. **g**, Magnetocrystalline anisotropy energy, E_{MCA}, obtained through DFT for $Bi_2Se_3/MnBi_2Se_4$ and $Bi_2Te_3/MnBi_2Te_4$ by subtracting band energies for two orientations of the magnetization. Shown are magnetocrystalline anisotropy $E_{MCA} = E^{(M\|x)} - E^{(M\|z)}$, shape anisotropy E_{shape} and total magnetic anisotropy $E_{aniso} = E_{MCA} + E_{shape}$.

Reprinted page 12 of paper [69] "Magnetic band gap in $MnBi_2Te_4$-Bi_2Te_3 heterostructures".

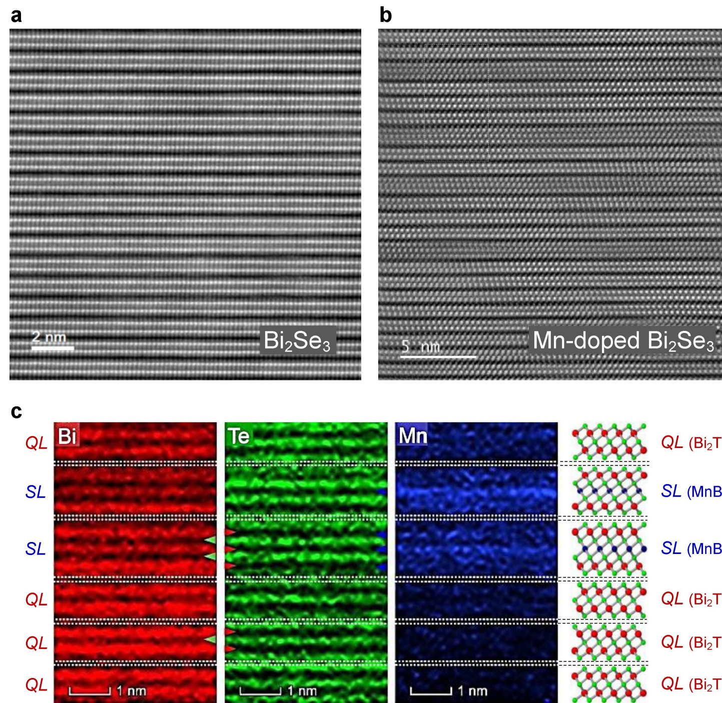

Extended Data Fig. 4 | STEM of pure and Mn-doped Bi_2Se_3 and EDX maps of Mn-doped Bi_2Te_3. a, b, Comparison of HR-STEM HAADF cross-sections of Bi_2Se_3 (**a**) and Mn-doped Bi_2Se_3 (x_{Mn} = 6%) (**b**) films grown under identical growth conditions, showing the high structural perfection and that additional septuple layers are formed only with Mn doping, whereas the pure Bi_2Se_3 film consists only of quintuple layers. These STEM cross-sections were recorded along two different zone axes. **c**, Atomic-layer-resolved distribution of the Bi, Te and Mn atoms of a Mn-doped Bi_2Te_3 film (x_{Mn} = 10%) obtained by STEM-EDX mapping. The Mn atoms are predominantly incorporated in the centre of the septuple layers and to a lesser extent in the outer layers of the septuple units. No Mn is seen in the van der Waals gaps. Note that in this sample, because of the higher Mn concentration, two subsequent septuples are observed in the STEM cross-section.

Reprinted page 13 of paper [69] "Magnetic band gap in $MnBi_2Te_4$-Bi_2Te_3 heterostructures".

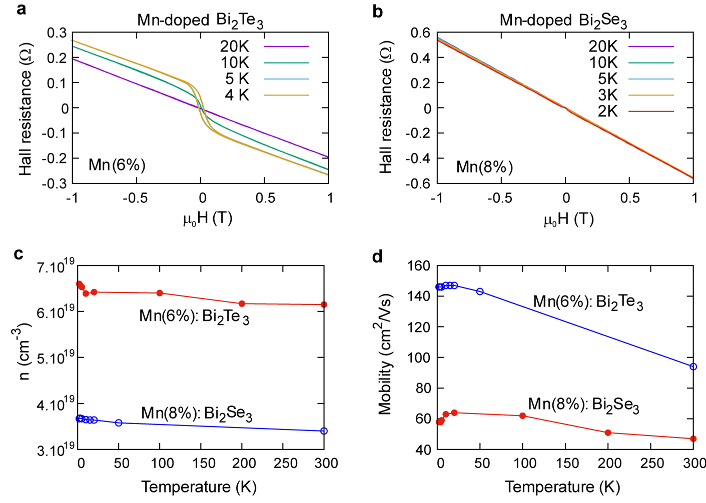

Extended Data Fig. 5 | Anomalous Hall effect. Data for Mn-doped Bi_2Te_3 and Bi_2Se_3 with respectively 6% and 8% Mn. **a**, **b**, Raw data for Hall resistance as a function of magnetic field applied perpendicularly to the surface, measured at different temperatures above and below T_C as indicated. **c**, **d**, Temperature dependence of the carrier concentration and Hall mobility. Note that above T_C the contribution of the anomalous Hall effect to the Hall voltage is negligible and therefore does not affect the carrier concentration and mobility measurements.

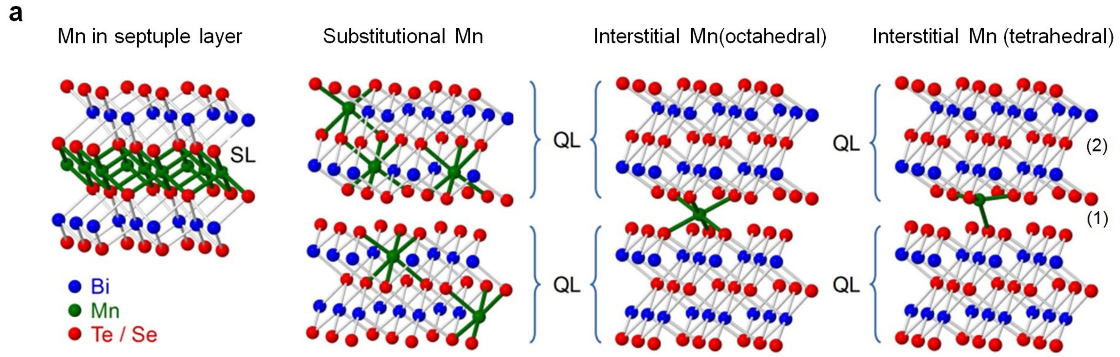

b

	Mn-doped Bi_2Te_3		Mn-doped Bi_2Se_3	
Mn Position	**NN atoms**	**Distance (Å)**	**NN atoms**	**Distance (Å)**
Center of septuple	6 Te	2.909	6 Se	2.719
Substitutional in QL (Bi)	3 Te(1) 3 Te(2)	3.073 3.246	3 Se(1) 3 Se(2)	2.972 3.041
Octahedral in vdW gap	6 Te	2.858	6 Se	3.041
Tetrahedral in vdW gap	4 Te	2.533	4 Se	2.394
Te(1)/Se(1) sites next to vdW gap	3 Bi 3 Te	3.073 3.673	3 Bi 3 Se	2.972 3.284
Te(2)/Se(2) sites at center of QL	6 Bi	3.246	6 Bi	3.041

Extended Data Fig. 6 | Possible Mn-incorporation sites in Bi_2Te_3 and Bi_2Se_3. **a**, Structure models for, left to right: Mn in the centre of septuple layers; Mn substituting for Bi in quintuple layers; and interstitial Mn in the van der Waals gaps on octrahedal sites and tetrahedral sites. **b**, Nominal nearest-neighbour (NN) distances of Mn atoms located in various positions as derived by EXAFS analysis, including also possible Mn on Te (Se) antisites in the quintuples. Index '1' refers to Te (Se) sites next to the van der Waals gaps, index '2' to those in the centre of the quintuple.

Reprinted page 15 of paper [69] "Magnetic band gap in $MnBi_2Te_4$-Bi_2Te_3 heterostructures".

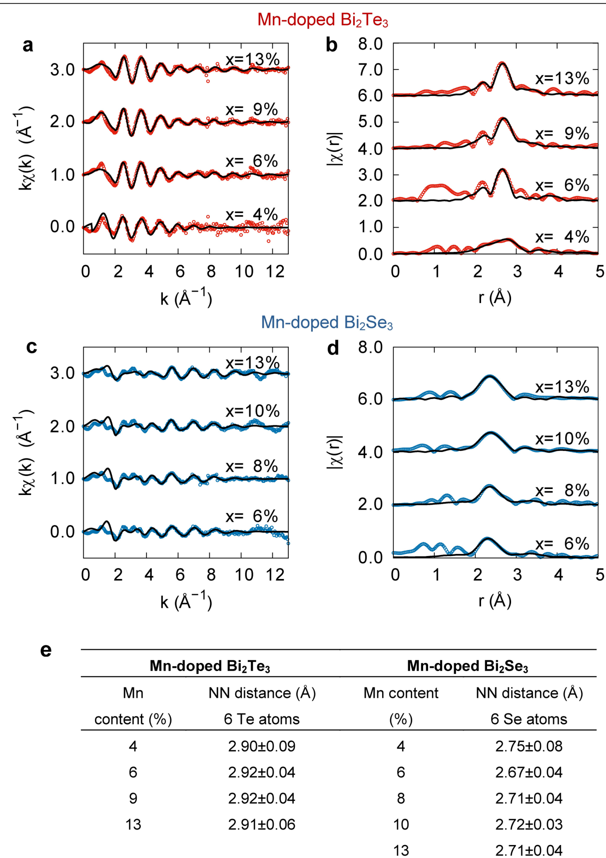

Mn-doped Bi_2Te_3		Mn-doped Bi_2Se_3	
Mn content (%)	NN distance (Å) 6 Te atoms	Mn content (%)	NN distance (Å) 6 Se atoms
4	2.90±0.09	4	2.75±0.08
6	2.92±0.04	6	2.67±0.04
9	2.92±0.04	8	2.71±0.04
13	2.91±0.06	10	2.72±0.03
		13	2.71±0.04

Extended Data Fig. 7 | Fits of EXAFS oscillations for different amounts of Mn doping. a, **b**, Bi_2Te_3; **c**, **d**, Bi_2Se_3. Experimental data points are represented by the red or blue circles; black lines denote fitted curves (unlike the simulations in Fig. 3). **a**, **c** are plotted with respect to the wavevector **k** and the background-subtracted EXAFS absorption $\chi(k)$ is **k**-weighted; **b**, **d** show the magnitude, that is, the absolute value of $\chi(R)$ after Fourier transformation. **e**, EXAFS-fitted nearest-neighbour distances of Mn atoms in Bi_2Te_3 and Bi_2Se_3 as a function of Mn concentration.

Reprinted page 16 of paper [69] "Magnetic band gap in $MnBi_2Te_4$-Bi_2Te_3 heterostructures".

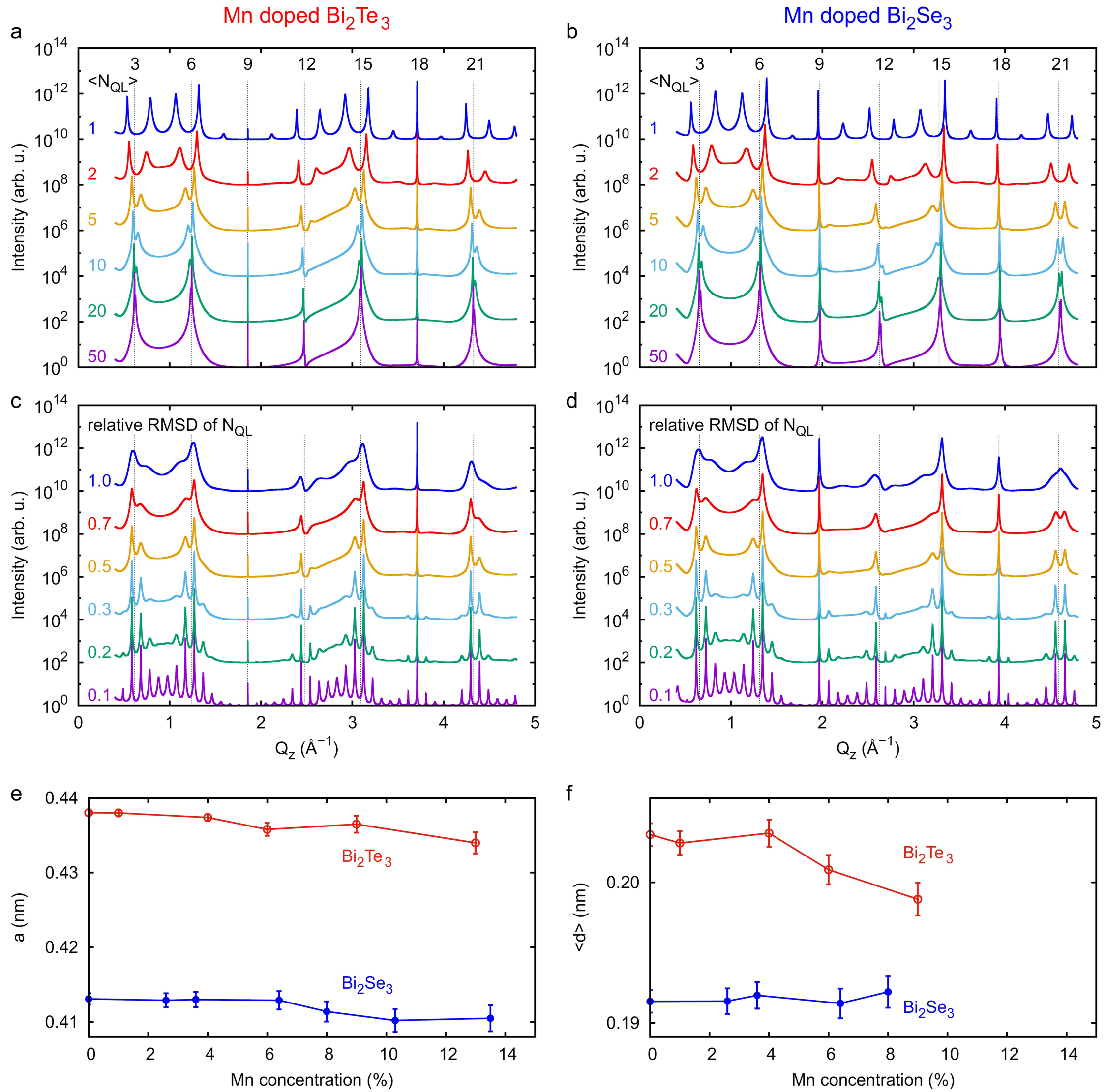

Extended Data Fig. 8 | Simulated diffraction patterns. a–d, Varying paracrystal parameters of the septuple/quintuple heterostructures of: **a**, **c**, Mn-doped Bi_2Te_3 and **b**, **d**, Mn-doped Bi_2Se_3. **a**, **b** depict the influence of different average numbers of quintuples, $\langle N_{QL} \rangle$, between the septuples with a fixed relative r.m.s. deviation (r.m.s.d.) of its distribution, set to 0.5. At high $\langle N_{QL} \rangle$, the system approaches the pure Bi_2Y_3 (Y = Te, Se) phase. **c**, **d** show simulations for different r.m.s.d. of the statistical distribution of the number of quintuples between the septuples but constant average separation, $\langle N_{QL} \rangle = 5$. The limit of r.m.s.d. = 0 corresponds to a perfectly periodic multilayer of five quintuples alternating with one septuple; the additional maxima are the resulting superlattice satellite peaks. A larger r.m.s.d. means a more disordered multilayer. Dashed lines are plotted at positions of the (000.ℓ) peaks of the pure Bi_2Y_3 structure. **e** shows the average vertical (0001) lattice plane spacing $\langle d \rangle$ as a function of Mn concentration determined by the fit of the experimental diffraction spectra presented in Fig. 4a,b, and panel **f** the corresponding in-plane lattice constants determined from reciprocal space maps around the (101.20) reciprocal lattice point.

Reprinted page 17 of paper [69] "Magnetic band gap in $MnBi_2Te_4$-Bi_2Te_3 heterostructures".

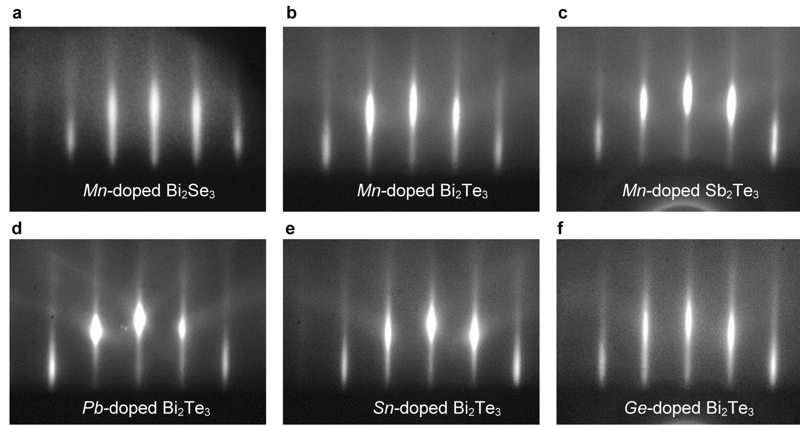

g

Material system	<N_{QL}>	σ_{QL}	%SL
Pb - doped Bi_2Te_3	2.1	1.3	14
Sn - doped Bi_2Te_3	2.6	1.5	12
Ge - doped Bi_2Te_3	3.0	1.5	10
Mn - doped Bi_2Te_3	2.3	1.8	14
Mn - doped Sb_2Te_3	3.5	1.7	11

Extended Data Fig. 9 | RHEED. a–f, Comparison of RHEED patterns for: **a** Mn-doped Bi_2Te_3; **b**, Mn-doped Bi_2Se_3; **c**, Mn-doped Sb_2Te_3; **d**, Pb-doped Bi_2Te_3; **e**, Sn-doped Bi_2Te_3; and **f**, Ge-doped Bi_2Te_3, recorded during epitaxial growth, showing perfect two-dimensional growth in all cases. The layer thickness was 200 nm and the dopant concentration was around 10% in all cases. The corresponding X-ray diffraction curves of the samples are shown in Fig. 4, and the values derived from the fits using the septuple/quintuple paracrystal stacking model are listed in **g**. $\langle N_{QL} \rangle$ is the average number of quintuples between consecutive XBi_2Te_4 septuple layers; σ_{QL} is the relative r.m.s.d. of the distribution; and %SL is the occupancy of Mn sites in the septuple layers.

Reprinted page 18 of paper [69] “Magnetic band gap in $MnBi_2Te_4$-Bi_2Te_3 heterostructures”.

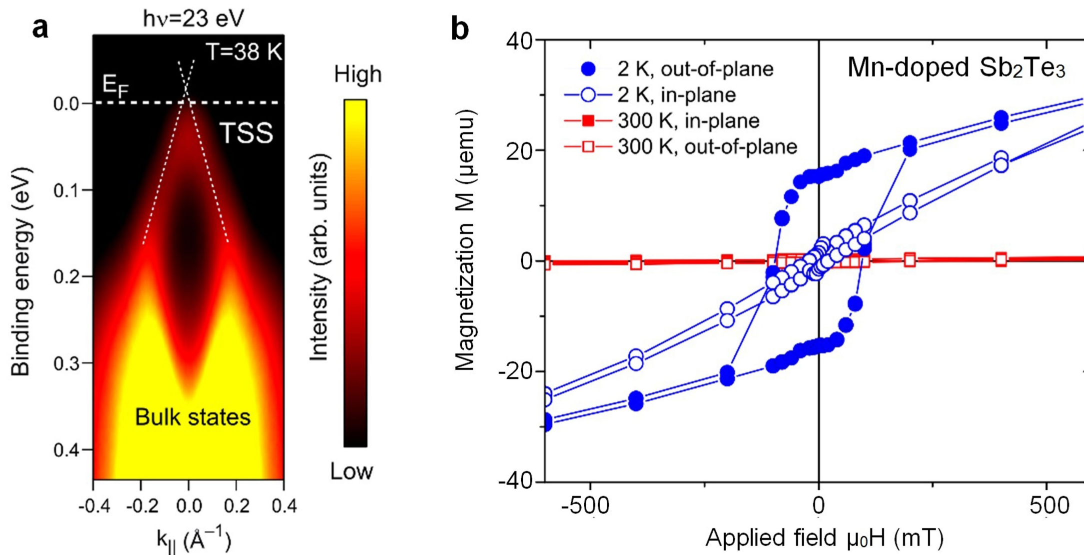

Extended Data Fig. 10 | Electronic and magnetic properties of Mn-doped Sb_2Te_3. a, Angle-resolved photoemission spectrum recorded at a temperature of 38 K and a photon energy of 23 eV photon energy, showing p-type behaviour and that the Fermi level, E_F, is close to the Dirac point, the latter being only slightly above the top of the valence band. **b**, In-plane and out-of-plane hysteresis curves, $M(H)$, recorded through SQUID at 2 K (blue) and 300 K (red), showing the same perpendicular magnetic anisotropy with easy axis normal to the surface as for Mn-doped Bi_2Te_3 (Fig. 2 and Extended Data Fig. 3).

Reprinted page 19 of paper [69] "Magnetic band gap in $MnBi_2Te_4$-Bi_2Te_3 heterostructures".

4.7 Ferromagnetic transition in magnetic topological insulators $MnSb_2Te_4$

The layers of $MnSb_2Te_4$ with a slight excess of Mn were studied. We have found the concentration of Mn in the substitutional and central septuple layer positions. The magnetic Currie temperature is relatively high for a magnetic topological insulator, almost 50 K. Contrary to bismuth selenide and bismuth telluride, antimony telluride is p-doped. Thus photoemission study of the band gap. Instead, we have used scanning tunneling spectroscopy to show magnetic band gap opening correlating with magnetic order.

Check for updates

ADVANCED MATERIALS
www.advmat.de

Mn-Rich $MnSb_2Te_4$: A Topological Insulator with Magnetic Gap Closing at High Curie Temperatures of 45–50 K

Stefan Wimmer, Jaime Sánchez-Barriga, Philipp Küppers, Andreas Ney, Enrico Schierle, Friedrich Freyse, Ondrej Caha, Jan Michalička, Marcus Liebmann, Daniel Primetzhofer, Martin Hoffman, Arthur Ernst, Mikhail M. Otrokov, Gustav Bihlmayer, Eugen Weschke, Bella Lake, Evgueni V. Chulkov, Markus Morgenstern, Günther Bauer, Gunther Springholz, and Oliver Rader**

Ferromagnetic topological insulators exhibit the quantum anomalous Hall effect, which is potentially useful for high-precision metrology, edge channel spintronics, and topological qubits. The stable 2+ state of Mn enables intrinsic magnetic topological insulators. $MnBi_2Te_4$ is, however, antiferromagnetic with 25 K Néel temperature and is strongly n-doped. In this work, p-type $MnSb_2Te_4$, previously considered topologically trivial, is shown to be a ferromagnetic topological insulator for a few percent Mn excess. i) Ferromagnetic hysteresis with record Curie temperature of 45–50 K, ii) out-of-plane magnetic anisotropy, iii) a 2D Dirac cone with the Dirac point close to the Fermi level, iv) out-of-plane spin polarization as revealed by photoelectron spectroscopy, and v) a magnetically induced bandgap closing at the Curie temperature, demonstrated by scanning tunneling spectroscopy (STS), are shown. Moreover, a critical exponent of the magnetization $\beta \approx 1$ is found, indicating the vicinity of a quantum critical point. Ab initio calculations reveal that Mn–Sb site exchange provides the ferromagnetic interlayer coupling and the slight excess of Mn nearly doubles the Curie temperature. Remaining deviations from the ferromagnetic order open the inverted bulk bandgap and render $MnSb_2Te_4$ a robust topological insulator and new benchmark for magnetic topological insulators.

1. Introduction

The quantum anomalous Hall effect (QAHE) offers quantized conductance and lossless transport without the need for an external magnetic field.[1] The idea to combine ferromagnetism with topological insulators for this purpose[2–4] has fuelled the materials science.[5,6] It led to the experimental discovery of the QAHE in Cr- and V-doped (Bi, $Sb)_2Te_3$[7–11] with precise quantized values of the Hall resistivity down to the sub-part-per-million level.[12–15] The stable 3+ configuration of V or Cr substitutes the isoelectronic Bi or Sb[3,16,17] enabling ferromagnetism by coupling the magnetic moments of the transition metal atoms. Hence, time-reversal symmetry is broken enabling - through perpendicular magnetization - a gap opening at the Dirac point of the topological surface state.[2–5] This gap hosts chiral edge states with precisely quantized conductivity. However, the

S. Wimmer, A. Ney, G. Bauer, G. Springholz
Institut für Halbleiter- und Festkörperphysik
Johannes Kepler Universität
Altenberger Straße 69, Linz 4040, Austria
E-mail: Gunther.Springholz@jku.at

J. Sánchez-Barriga, E. Schierle, F. Freyse, E. Weschke, B. Lake, O. Rader
Helmholtz-Zentrum Berlin für Materialien und Energie
Albert-Einstein-Straße 15, 12489 Berlin, Germany
E-mail: rader@helmholtz-berlin.de

P. Küppers, M. Liebmann, M. Morgenstern
II. Institute of Physics B and JARA-FIT
RWTH Aachen Unversity
52074 Aachen, Germany

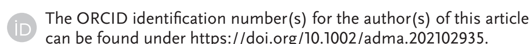
The ORCID identification number(s) for the author(s) of this article can be found under https://doi.org/10.1002/adma.202102935.

© 2021 The Authors. Advanced Materials published by Wiley-VCH GmbH. This is an open access article under the terms of the Creative Commons Attribution License, which permits use, distribution and reproduction in any medium, provided the original work is properly cited.

DOI: 10.1002/adma.202102935

F. Freyse
Institut für Physik und Astronomie
Universität Potsdam
Karl-Liebknecht-Straße 24/25, 14476 Potsdam, Germany

O. Caha
Department of Condensed Matter Physics
Masaryk University
Kotlářská 267/2, Brno 61137, Czech Republic

J. Michalička
Central European Institute of Technology
Brno University of Technology
Purkyňova 123, Brno 612 00, Czech Republic

D. Primetzhofer
Department of Physics and Astronomy
Universitet Uppsala
Lägerhyddsvägen 1, Uppsala 75120, Sweden

M. Hoffman, A. Ernst
Institute for Theoretical Physics
Johannes Kepler Universität
Altenberger Straße 69, Linz 4040, Austria

Reprinted page 1 of paper [70] "Magnetic order and band gap in $MnSb_2Te_4$".

experimental temperatures featuring the QAHE are between 30 mK[7,13] and a few K[18,19] only, significantly lower than the ferromagnetic transition temperatures T_C in these systems.[20] If the temperature of the QAHE could be raised, applications such as chiral interconnects,[21] edge state spintronics,[22,23] and metrological standards[14,15] become realistic.

One promising approach is the so-called modulation doping in which the magnetic dopants are located only in certain parts of the topological insulator. This implies strong coupling of the topological surface state to the magnetic moments at a reduced disorder level.[18,24] Most elegantly, this has been realized for Mn-doped Bi_2Te_3 and Bi_2Se_3. The tendency of Mn to substitute Bi is weak, such that Mn doping leads to the spontaneous formation of septuple layers with $MnBi_2Te_4$ stoichiometry. These septuple layers are statistically distributed among quintuple layers of pure Bi_2Te_3 or Bi_2Se_3 at low Mn concentration[25,26] and increase in number with increasing Mn concentration.[25] Eventually, only septuple layers remain when the overall stoichiometry of $MnBi_2Te_4$ or $MnBi_2Se_4$[26,27] is reached. Density functional theory (DFT) calculations found that $MnBi_2Te_4$ forms ferromagnetic layers with antiferromagnetic interlayer coupling[28,29] as confirmed by experiments at low temperatures.[29–32] As a result, $MnBi_2Te_4$ is an antiferromagnetic topological insulator[29,33–36] that can exhibit axion states.[5] The QAHE, however, has only been realized in a limited way: ultra thin flakes consisting of odd numbers of septuple layers exhibited an anomalous Hall effect (AHE) that is nearly quantized. This is caused by the uncompensated ferromagnetic septuple layer without partner. Nevertheless, exact quantization still required a magnetic field.[37] A ferromagnetic AHE has also been observed for systems with either a larger amount of quintuple layers[38–40] or via alloying of Sb and Bi in $MnBi_{2-x}Sb_xTe_4$ [31,32,41] or both.[42,43] Most notably, a nearly quantized AHE has been observed up to 7 K for a $MnBi_2Te_4/Bi_2Te_3$ heterostructure after unconventional counter doping inducing vacancies by electron bombardment.[19]

A central drawback of the Bi_2Te_3 and Bi_2Se_3 host materials is their strong n-type doping. In contrast, Sb_2Te_3 is p-doped and much closer to charge neutrality.[44] Indeed, mixtures of Bi_2Te_3 and Sb_2Te_3 with stoichiometries close to Sb_2Te_3 have been employed for the QAHE using Cr and V doping.[7–11] Magnetism of dilute Mn-doped Sb_2Te_3 has initially been studied by Dyck *et al.* obtaining $T_C \simeq 2$ K and perpendicular anisotropy.[45] Later, a higher $T_C = 17$ K was reported for 1.5% Mn doping.[46] Stoichiometric bulk $MnSb_2Te_4$ provided antiferromagnetism (Néel temperature $T_N = 20$ K)[31,32,47], ferromagnetism[48] as well as ferrimagnetism[47,49] (T_C = 25–34 K), depending on the composition and synthesis conditions. By comparison with scattering methods, it has been conjectured that this is related to Mn–Sb site exchange within the septuple layers[42,47,50] which could even lead to spin glass behaviour.[51] DFT calculations found that the perfectly ordered $MnSb_2Te_4$ is antiferromagnetic[28] but topologically trivial,[47,52–55] while Mn–Sb site exchange can render the interlayer coupling ferromagnetic.[47,50]

Here, epitaxial $MnSb_2Te_4$ is studied using spin- and angle-resolved photoemission spectroscopy (ARPES), scanning tunneling microscopy (STM) and STS, magnetometry, X-ray magnetic circular dichroism (XMCD) and DFT. All experiments were performed as a function of temperature to pin down the intricate correlation between magnetism and non-trivial band topology essential for the QAHE. It is revealed that the material unites the favorable properties of a topological insulator with its Dirac point close to the Fermi level E_F with that of a ferromagnetic hysteresis with out-of-plane anisotropy and record-high T_C, twice as high as the T_N previously reported for antiferromagnetic $MnBi_2Te_4$ and $MnSb_2Te_4$.[31,32] Moreover, temperature dependent STS finds a magnetic gap of 17 meV at E_F for 4.3 K that closes exactly at T_C as expected for a ferromagnetic topological insulator. Moreover, by combining DFT, STM, Rutherford backscattering, and X-ray diffraction (XRD) it is uncovered that a partial substitution of Sb atoms by Mn is decisive to render $MnSb_2Te_4$ both ferromagnetic and a topological insulator.

2. Structure

Epitaxial $MnSb_2Te_4$ films with 200 nm thickness were grown by molecular beam epitaxy (MBE) using an Mn:Sb_2Te_3 flux ratio of 1:1 in order to obtain the desired 1:2:4 stoichiometry of the $MnSb_2Te_4$ phase (Note S1, Supporting Information). **Figure 1**a shows the cross section of the $MnSb_2Te_4$ lattice structure revealed by high-resolution high-angle annular dark-field scanning transmission electron microscopy (HAADF-STEM). It consists of septuple layers (SL) with stacking sequence Te–Sb–Te–Mn–Te–Sb–Te, Figure 1c, that corresponds to the $MnSb_2Te_4$ stoichiometry. The composition was verified by Rutherford backscattering spectrometry (RBS), indicating a small excess of Mn of 6% in the layers (composition of $Mn_{1.06}Sb_{1.94}Te_4$, see Figure S1, Supporting Information), which is attributed to the fact that a small amount of Sb_2Te_3 desorbs from the surface during growth. Like with $MnBi_2Te_4/Bi_2Te_3$,[56] the exchange

A. Ernst
Max Planck Institute of Microstructure Physics
Weinberg 2, 06120 Halle, Germany
M. M. Otrokov
Centro de Física de Materiales (CFM-MPC)
Centro Mixto CSIC-UPV/EHU, San Sebastián/Donostia 20018, Spain
M. M. Otrokov
IKERBASQUE
Basque Foundation for Science
Bilbao 48011, Spain
G. Bihlmayer
Peter Grünberg Institut and Institute for Advanced Simulation
Forschungszentrum Jülich and JARA
52425 Jülich, Germany
E. V. Chulkov
Donostia International Physics Center (DIPC)
San Sebastián/Donostia 20018, Spain
E. V. Chulkov
Departamento de Polímeros y Materiales Avanzados: Física, Química y Tecnología, Facultad de Ciencias Químicas
Universidad del País Vasco UPV/EHU
San Sebastián/Donostia 20080, Spain
E. V. Chulkov
Saint Petersburg State University
Saint Petersburg 198504, Russia
E. V. Chulkov
Tomsk State University
Tomsk 634050, Russia

© 2021 The Authors. Advanced Materials published by Wiley-VCH GmbH

Reprinted page 2 of paper [70] "Magnetic order and band gap in $MnSb_2Te_4$".

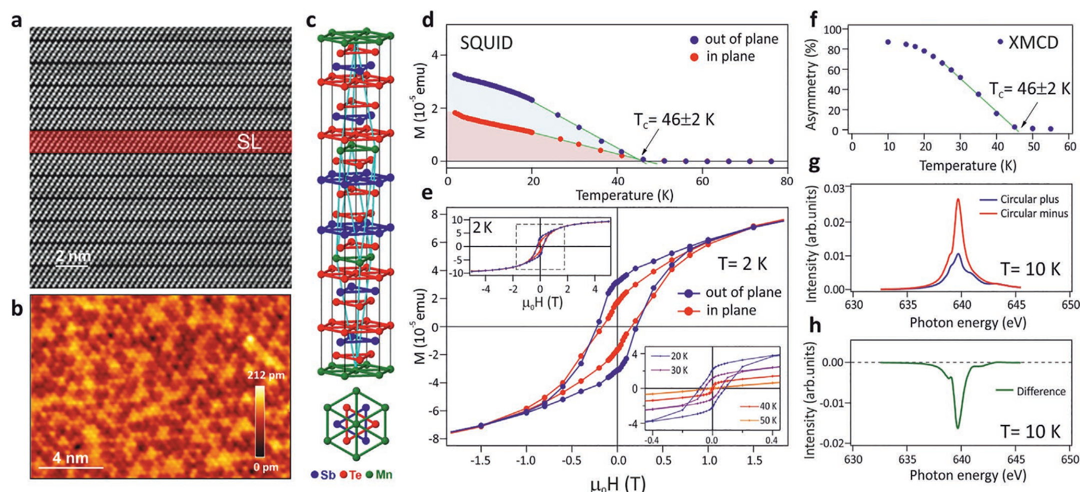

Figure 1. Structural and magnetic properties of epitaxial $MnSb_2Te_4$. a) Cross-sectional HAADF-STEM image of the septuple layer sequence formed in the $MnSb_2Te_4$ films on BaF_2 substrates. For clarity, one of the septuple layers is highlighted by red color and denoted as SL. The weak van-der-Waals-like bond between the Te-terminated septuple layers is the natural surface termination. b) STM image of the flat topography of this surface, recorded at $T =$ 4.3 K, sample voltage of 500 mV and current of 200 pA. c) Sketch of the ideal crystal structure as side view and top view. d) SQUID magnetometry as a function of temperature while cooling the sample in 10 mT from 300 K down to 2 K. e) Hysteresis loops probed by SQUID. The insets show a larger H range and the temperature dependence. Perpendicular anisotropy can be deduced from the larger out-of-plane signal. f) Temperature-dependent XMCD signal at the Mn L_3-edge and the (0001) Bragg peak position recorded in X-ray scattering geometry at 0 T after field cooling in 0.5 T. g) Corresponding full XMCD spectra recorded with opposite circular polarizations at 10 K. h) Difference of the spectra in (g). Linear extrapolation in (d,f) (green lines) reveals a ferromagnetic Curie temperature $T_C = 46 \pm 2$ K for both experimental probes.

coupling is strongly enhanced in these septuple layers relative to a disordered system where Mn substitutes Bi randomly.

The nearly exclusive formation of septuple layers in the entire $MnSb_2Te_4$ samples is confirmed by high-resolution XRD (Figure S2, Supporting Information), revealing only a minute number of residual quintuple layers. In contrast, STEM and XRD of V-doped $(Bi, Sb)_2Te_3$ shows quintuple layers only.[57] This highlights that septuple layers are unfavorable for V^{3+} incorporation but very favorable for Mn as this requires the addition of a charge neutral transition $metal^{2+}/Te^{2-}$ bilayer to each quintuple layer, which is possible for Mn^{2+} but not for V^{3+}. In addition, detailed XRD analysis reveals a 10% Mn–Sb site exchange within the septuple layers (see Figure S2, Supporting Information), meaning that Mn does not reside exclusively in the center of the septuple layers but also to a small extent on Sb sites in the adjacent cation layers. The amount of Mn–Sb site exchange is, however, significantly smaller as compared to single crystals reported to be of the order of 30–40%.[47,49] This is due to the much lower growth temperature of our epilayers of 290 °C compared to 600–650 °C for single crystals. Indeed, STM images of the atomically flat and Te-terminated surface of our $MnSb_2Te_4$ epilayers (Figure 1b) exhibit triangular features, pointing to defects in the cation layer beneath the surface.[58,59] These defects occur with an atomic density of 5–10%. Since this is larger than for undoped Sb_2Te_3 films,[58] the triangles are most likely caused by subsurface Mn atoms on Sb sites, in line with the XRD and RBS results. As shown by DFT below, these defects turn out to be decisive for the ferromagnetic interlayer coupling in $MnSb_2Te_4$. Similar conjectures have been raised previously.[42,47,50,51,60]

3. Magnetic Properties

Figure 1d displays the temperature-dependent magnetization $M(T)$ measured by superconducting quantum interference device (SQUID) magnetometry. The measurements were recorded while cooling the sample from 300 K to 2 K in a field of 10 mT perpendicular (blue) or parallel (red) to the film surface. Most strikingly, the $MnSb_2Te_4$ epilayers show pronounced ferromagnetic behavior by $M(H)$ hysteresis loops (Figure 1e) with record high T_C of 45–50 K (Figure 1d), revealed independently for several samples (Figure S3, Supporting Information). This is significantly higher than the antiferromagnetic or ferromagnetic transition temperatures of bulk crystals (Table I, Supporting Information). Moreover, it is twice as large as the $T_N \leq 25$ K of $MnBi_2Te_4$ films grown under the same conditions. It has been crosschecked that the displayed magnetization in $M(T)$ curves is identical to the corresponding hysteresis loops. In particular, the large remanent magnetization observed by the bulk sensitive SQUID measurements excludes that it is caused by uncompensated antiferromagnetically coupled septuple layers only.[37] However, the $M(H)$ hysteresis curve (Figure 1e) shows a rounded shape that persists up to fields much higher than those typical for domain reversals and it does not saturate up to ±5 T where the average magnetic moment per Mn atom is of the order of 1–1.5μ_B, similar to that of bulk $MnSb_2Te_4$ single crystals.[31,47,49] This is because very high fields of 60 T are required to fully polarize the system[61] and is in line with a similar rise of the Hall resistance with applied field in Figure S10, Supporting

© 2021 The Authors. Advanced Materials published by Wiley-VCH GmbH

Reprinted page 3 of paper [70] "Magnetic order and band gap in $MnSb_2Te_4$".

Information. This suggests additional types of competing magnetic orders. Indeed, a small kink in $M(T)$ is observed at 20–25 K (Figure S3, Supporting Information), close to the Néel temperature reported earlier for antiferromagnetic $MnSb_2Te_4$.[31] This implies that the high-temperature ferromagnetism is most likely accompanied by ferrimagnetism as also supported by the relatively large in-plane hysteresis and magnetization, Figure 1e, in line with observations of competing ferro- and antiferromagnetic order in bulk $MnSb_2Te_4$.[40,42,47,48,50,51,61]

Ferromagnetism is fully confirmed by element specific zero-field XMCD recorded in diffraction geometry (see Note S7, Supporting Information). For these measurements, the sample was remanently magnetized at ≈0.5 T and 10 K. From spectra recorded with oppositely circularly polarized light at the (0001) Bragg peak, the intensity difference $C_+ - C_-$ (Figure 1h) was deduced for 0 T with the photon energy tuned to the Mn-L_3 resonance (Figure 1g). The asymmetry $(C_+ - C_-)/(C_+ + C_-)$ directly yields the magnetization of the Mn atoms. Its temperature dependence (Figure 1f) impressively confirms the SQUID data with high $T_C \simeq 46$ K and unambiguously attributes the ferromagnetism to the Mn atoms. (For magnetotransport data, see Figure S10, Supporting Information.) The record-high T_C with magnetic easy axis perpendicular to the surface (crystallographic *c*-axis) as well as the large coercivity (≈0.2 T) render the samples very robust ferromagnets. Note that the spin-orbit interaction is crucial for both out-of-plane easy axis and large coercivity.[25] While it is sufficiently strong to turn the magnetization out of plane in Mn-doped Bi_2Te_3, the effect in Mn-doped Bi_2Te_3 is too weak.[25,62] The present data reveals that Sb_2Te_3 is sufficiently heavy, that is, spin-orbit coupling sufficiently large, to maintain the perpendicular anisotropy for high Mn content.

To elucidate the origin of the ferromagnetism, DFT calculations are employed (Section S11, Supporting Information). They firstly highlight the differences between $MnSb_2Te_4$ and $MnBi_2Te_4$. In both cases, the in-plane Mn coupling within each septuple layer is ferromagnetic. It is unlikely that the observed difference between antiferromagnetic interlayer coupling in $MnBi_2Te_4$ and ferromagnetic interlayer coupling in $MnSb_2Te_4$ is caused by the lowered spin-orbit interaction, since it obviously remains large enough to induce a strong out-of-plane anisotropy in both cases. However, the in-plane lattice constant a of $MnSb_2Te_4$ is ≈2% smaller than for $MnBi_2Te_4$. Hence, we calculated the exchange constants of $MnSb_2Te_4$ for a determined by XRD in comparison to those for a expanded to the value of $MnBi_2Te_4$ (see Table III, Supporting Information). Although the smaller in-plane lattice constant of $MnSb_2Te_4$ increases the in-plane exchange constant J between nearest neighbors by almost a factor of three, T_N remains barely changed because the enlarged in-plane overlap of the Mn d states concomitantly weakens the already small perpendicular interlayer coupling. However, the energy gain of antiferromagnetism against ferromagnetism becomes as low as 0.6 meV per Mn atom at the XRD lattice constant. This suggests that already small structural changes along the interlayer exchange path can easily induce the transition to ferromagnetic order.

Indeed, a small degree of Mn–Sb site exchange occurs in the setpuple layers, meaning that a small fraction of Mn actually resides on Sb sites. Including this site exchange, our DFT calculations reveal that already 2.5% of Mn on Sb sites and, in turn, 5% of Sb on Mn sites is sufficient to swap the sign of the interlayer exchange constant (see Table III, Supporting Information). This renders $MnSb_2Te_4$ ferromagnetic for a degree of site exchange that agrees well with our XRD analysis and the density of subsurface defects observed by STM (Figure 1b). An even stronger site exchange has been recently reported for bulk $MnSb_2Te_4$[47,49,51] and $MnSb_{1.8}Bi_{0.2}Te_4$ single crystals,[32] which corroborates that the Mn–Sb site exchange easily occurs. Thus, we conjecture that $MnSb_2Te_4$ single crystals remain antiferromagnetic[32] only for negligible Sb–Mn intermixing. It is noted that Mn on Sb sites tends to couple antiferromagnetically to the Mn in the central layer of the septuple layer, while the Mn moments in the center of the septuple layers always couple ferromagnetically to each other.

According to our DFT calculations, however, Mn–Sb site exchange barely increases the transition temperature ($T_N = 18$ K → $T_C = 25$ K, see Table III, Supporting Information). This can only be achieved by incorporation of excess Mn in the DFT calculations, while keeping the Mn concentration in the central layer constant. In fact it turns out that already a small Mn excess of 5% residing on the Sb sites strongly increases T_C to 44 K, which well reproduces the experimental $T_C = 45$–50 K values. The strong enhancement is caused by the simultaneous strengthening of the intra- and interlayer exchange constants (see Table III, Supporting Information). The conclusion is robust toward charge doping by up to 0.2% Te or Sb vacancies that negligibly changes T_C (Note S11, Supporting Information). Note that the excess Mn in the Sb layers is perfectly in line with our RBS results (Figure S1, Supporting Information) indicating a Mn excess of 6% in our samples.

4. Topology and Magnetic Gap

Next, we probe the topological properties of the epitaxial $MnSb_2Te_4$ layers, recalling that perfectly stoichiometric $MnSb_2Te_4$ has been predicted to be topologically trivial.[47,52–54] In particular, it could be turned into a topological insulator only by replacement of more than half of the Sb by Bi[53] or by compressing the lattice by as much as 3%.[52] However, as shown by **Figure 2**, our ARPES data from the $MnSb_2Te_4$ epilayers reveal the existence of a topological surface state with the dispersion of a Dirac cone along the wave vector parallel to the surface $\mathbf{k}_\parallel$. Varying the photon energy (Figure 2a,b and Figure S5, Supporting Information) to tune the electron wave number k_z perpendicular to the surface once through the whole bulk Brillouin zone (Table II, Supporting Information) reveals no dispersion, evidencing the 2D character of the Dirac cone, contrary to the lower-lying 3D bulk bands that strongly disperse with photon energy (Figure 2f, arrows). Moreover, spin-resolved ARPES of the 2D Dirac cone showcases a helical in-plane spin texture at $\mathbf{k}_\parallel$ away from the $\overline{\Gamma}$ zone center, that is, it exhibits the characteristic reversal of spin orientation with the sign of $\mathbf{k}_\parallel$ (Figure 2g,i, Figure S4, Supporting Information). This spin chirality is a key signature of a topological surface state. In addition, a pronounced out-of-plane spin polarization of about 25% occurs in the remanently magnetized sample at the $\overline{\Gamma}$ zone center in the vicinity of E_F, which reverses its sign when the sample is

© 2021 The Authors. Advanced Materials published by Wiley-VCH GmbH

Reprinted page 4 of paper [70] "Magnetic order and band gap in $MnSb_2Te_4$".

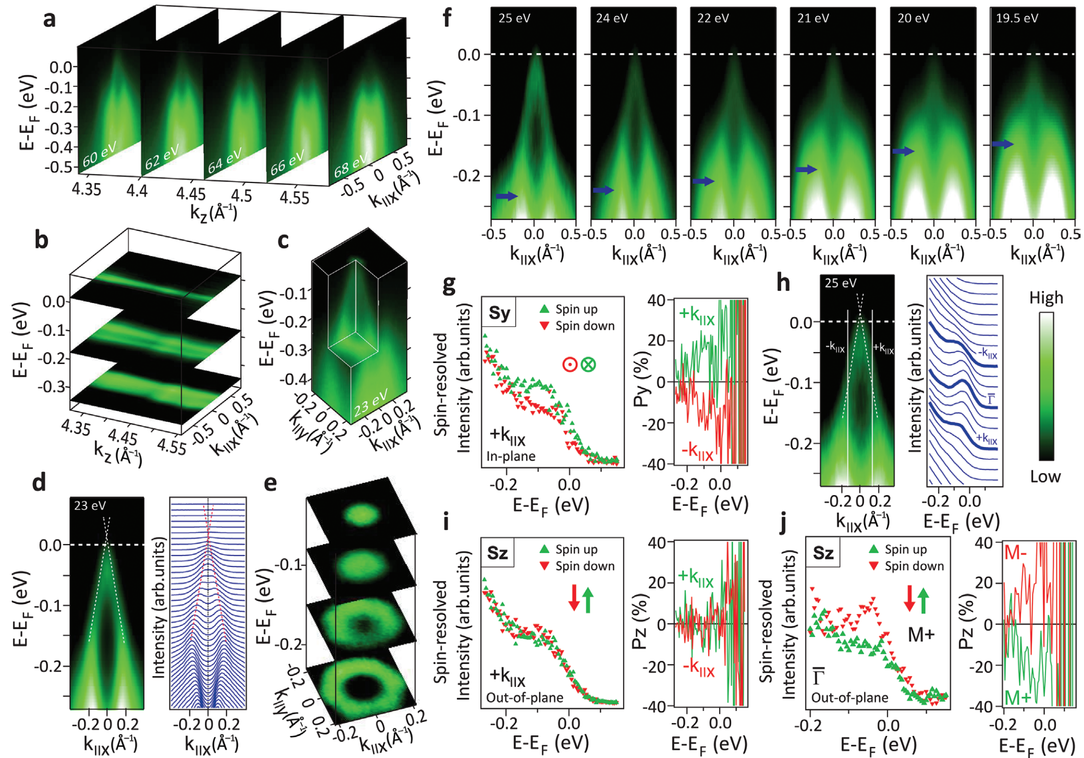

Figure 2. Topological properties of $MnSb_2Te_4$ revealed by ARPES. a) ARPES maps along $E(k_{\|x})$ for five different photon energies $h\nu$ displayed at the deduced k_z values. b) Same data as (a) displayed as $(k_{\|x}, k_z)$ maps via interpolation featuring negligible dispersion along k_z. The k_z range covers the whole Brillouin zone. c) Full 3D representation of the surface Dirac cone with $k_{\|x}$ pointing along the $\overline{\Gamma}-\overline{K}$ direction. d) Energy-momentum dispersion of the Dirac cone (left) and corresponding momentum-distribution curves (right) recorded at $h\nu = 23$ eV. The dashed, red lines along maxima result from fits to the data (Note S8, Supporting Information). They extrapolate to a Dirac point 20 meV above the Fermi level. e) Constant-energy cuts of the Dirac cone. f) ARPES maps along $E(k_{\|x})$ at different photon energies featuring a strong dispersion of a bulk valence band (blue arrows) with photon energy (i.e., k_z). g,i) Spin-resolved ARPES at $k_\|$ as marked in (h), hence, crossing the surface Dirac cone. Left: spectra for the two spin channels at one $k_{\|,x}$. Right: spin polarization for both $k_{\|,x}$, that is, $\pm k_{\|,x}$. g) In-plane spin direction S_y perpendicular to $k_\|$. i) Out-of-plane spin direction S_z. Data for S_x: Figure S4, Supporting Information. h) Left: surface Dirac cone with marked $k_\|$ of the spectra in (g,i) and dashed line along intensity maxima as deduced by fitting (Note S8, Supporting Information). Right: energy distribution curves showing where (g,i,j) were measured. j) Spin-resolved ARPES recorded at $\overline{\Gamma}$ and 30 K, and showcasing an out-of-plane spin polarization that reverses sign with reversal of the sample magnetization (M^+ and M^-, right).

magnetized in the opposite direction (Figure 2j). Such out-of-plane spin texture at $\overline{\Gamma}$ is evidence for a magnetic gap opening at the Dirac point.[63] Combined, the ARPES results demonstrate that $MnSb_2Te_4$ is a ferromagnetic topological insulator with clear fingerprints of a magnetic gap at $\overline{\Gamma}$. Favorably, the Dirac point of the topological surface state is rather close to E_F. Indeed, extrapolation of the observed linear bands, deduced by Lorentzian peak fitting (Figure 2d,h), yields a position of the Dirac point E_D of 20 ± 7 meV above E_F at 300 K (Note S8, Supporting Information).

Since a Dirac point above E_F is not accessible for ARPES, here we employ low temperature STS to directly probe the ferromagnetic gap expected to open up at $T < T_C$. **Figure 3**a shows a topography STM image of the $MnSb_2Te_4$ epilayer at 4.3 K together with six STS spectra recorded at different locations on the surface. All spectra consistently reveal a gap at E_F varying, however, significantly in size. Attributing the energy region where $dI/dV \approx 0$ as gap (Note S9, Supporting Information), a full map of the gap size Δ is obtained for a larger surface region (Figure 3b),[64,65] with the corresponding gap histogram displayed as inset. The gap size varies in the range 0–40 meV with a mean value of 17 meV and a spatial correlation length of 2 nm observed consistently in three distinct areas (Figure S7, Supporting Information). A corresponding set of dI/dV curves recorded along the dashed line in Figure 3b is depicted in Figure 3c and showcases the small-scale bandgap fluctuations. Likely, the spatial variation of Δ is caused by the spatially varying subsurface defect configurations, that is, by the Mn atoms on Sb lattice sites. Indeed, the gap fluctuations appear on the same length scale as the topographic features in Figure 1b. The average gap center position is only 0.6 meV above E_F (Figure S7, Supporting Information), which compares well to the value of

 © 2021 The Authors. Advanced Materials published by Wiley-VCH GmbH

Reprinted page 5 of paper [70] "Magnetic order and band gap in $MnSb_2Te_4$".

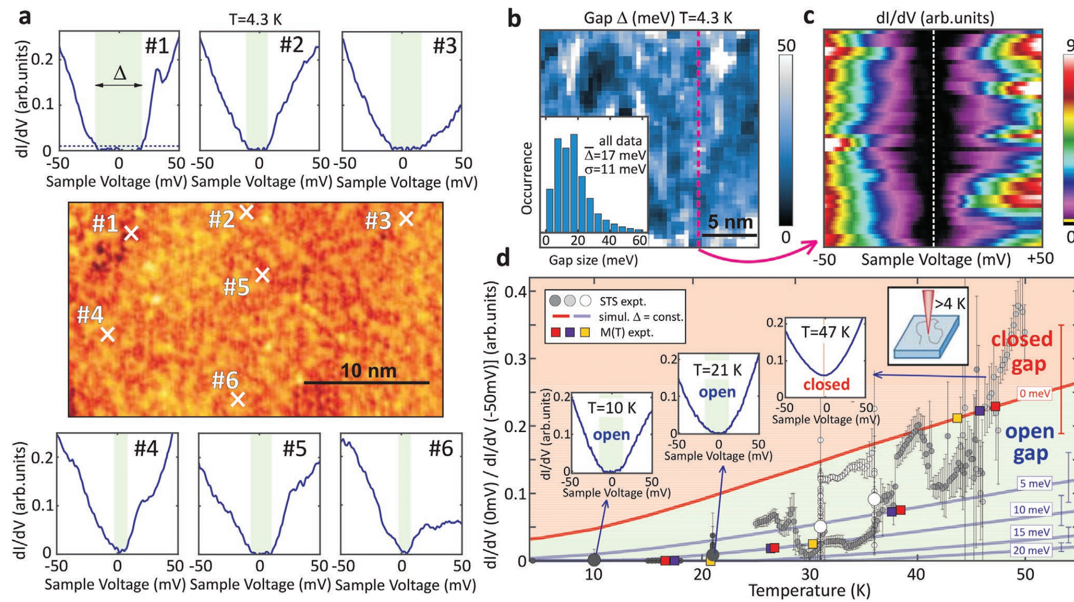

Figure 3. Spatial variation of the magnetic energy gap and its closing at T_C. a) Center: STM image of $MnSb_2Te_4$ recorded at T= 4.3 K after ultrahigh vacuum sample transfer from the MBE system, V = 0.5 V, I= 0.2 nA. Surrounding: dI/dV spectra recorded at the crosses as labelled. The dashed line in the upper left spectrum is the noise threshold used for determination of gap size Δ (Note S9, Supporting Information). b) Spatial map of gap size Δ. Inset: histogram of Δ resulting from three distinct areas, average gap size $\overline{\Delta}$ and standard deviation σ are marked. c) dI/dV spectra (color code) along the magenta dashed line in (b). The yellow line at the bottom of the color code bar marks the threshold for gap determination in (a,b). d) Small dots: Ratio $R = [dI/dV(V = 0\,\text{mV})]/[dI/dV(V = -50\,\text{mV})]$ deduced from $dI/dV(V)$ curves recorded at different T. The different gray shades correspond to different cooling cycles. Each point belongs to a single position on the sample surface within 1 nm. The error bars represent the standard deviation resulting from multiple curves measured at the same position. Large gray dots: average values of all data at corresponding T implying spatially averaged gap sizes $\overline{\Delta}$ (21 K) = 11 ± 5 meV, $\overline{\Delta}$ (31 K) = 6 ± 1 meV, and $\overline{\Delta}$ (36 K) = 4 ± 1 meV (Note S9, Supporting Information). Gray lines: T-dependence of the ratio R for the marked gap sizes $\overline{\Delta}$ as deduced by convolving the measured dI/dV data at 4.3 K with the Fermi distribution function (Figure S9b, Supporting Information). The area above Δ = 0 meV exhibits such a large R that the existence of a gap can be excluded. The error bars marked on the right result from the variation of the dI/dV curves at 4.3 K and represent a standard deviation (Figure S9b, Supporting Information). Colored squares: gap values deduced from XMCD (yellow, Figure 1f) and SQUID (red, violet, Figure S3, Supporting Information) via $\overline{\Delta}(T) \propto M(T)$.[70] Insets: selected dI/dV curves belonging to the points with blue arrows. For additional curves see Figure S8, Supporting Information.

$E_D - E_F$ = 20 meV determined by ARPES on another sample. The small difference most likely arises from small differences in the growth and surface conditions, but may also be caused by the different measurement temperatures (4.3 K vs 300 K) or larger-scale potential fluctuations.[66,67]

To prove that the energy gap is of magnetic origin,[25] the temperature dependence Δ(T) is probed by STS. This has not been accomplished yet for any magnetic topological insulator because at higher temperatures $k_B T \geq \Delta/5$ the STS gap Δ is smeared by the broadening of the Fermi–Dirac distribution, leading to a small non-zero tunneling current at voltages within the bandgap.[68] A direct deconvolution of the local density of states (LDOS) and the Fermi distribution function would require an assumption on the LDOS shape as function of energy. Such an assumption is impeded due to the significant spatial variation of the dI/dV curves at 4.3 K (Figure 3a–c), as also found consistently for other magnetic topological insulators.[64,69] Therefore, we developed a new method to derive Δ at elevated temperatures using the ratio between dI/dV at V = 0 mV and dI/dV at V well outside the region of the 4.3 K bandgap (Note S9, Supporting Information). Figure 3d displays the ratio $R = [dI/dV(0\,\text{mV})]/[dI/dV(-50\,\text{mV})]$ for a large number of dI/dV spectra recorded at temperatures varying between 4.3 K and 50 K (small dots). Selected dI/dV spectra at 10, 21 and 47 K are shown as insets (more dI/dV data in Figure S8, Supporting Information).

One can see that up to 20 K, the STS ratio R is zero and thus dI/dV = 0 nS at zero bias, directly evidencing the persistence of the gap. At higher temperatures the R values gradually increase, which is due to the convolution of the temperature broadening effect along with the decreasing magnetic gap size that goes to zero at $T = T_C$. To separate these two effects, we model the temperature dependence of the STS ratio for fixed gap sizes Δ(4.3K) = 0, 5, 10, 15 and 20 meV by convolving the dI/dV curves recorded at 4.3 K (Figure 3a–c) with the Fermi–Dirac distribution (Figure S9, Supporting Information). The corresponding model results are represented by solid gray lines in Figure 3d, where the red line marked with 0 meV indicates how the STS ratio R would evolve with temperature when the gap is zero. Clearly, up to T = 47 K, the experimental STS data points R are

© 2021 The Authors. Advanced Materials published by Wiley-VCH GmbH

Reprinted page 6 of paper [70] "Magnetic order and band gap in $MnSb_2Te_4$".

below this line. This evidences that the gap remains open up to T_C whereas for higher temperatures the gap is closed. This directly demonstrates the magnetic origin of the gap[25] due to the ferromagnetism of the $MnSb_2Te_4$ system.

Comparing the actual experimental data points with the calculated lines reveals that the gap size continuously decreases as the temperature increases and that it closes rather precisely at T_C = 45–50 K in line with the T_C obtained by XMCD and SQUID. As described above, the gap size varies spatially across the surface (Figure 3a–c) due to local disorder. Accordingly, at higher temperatures the STS ratios also exhibit a considerable variation depending on where the STS spectra were recorded. For this reason, larger ensembles of data points were recorded at four selected temperatures T = 10, 21, 31, and 36 K within an area of 400 nm^2. From this, the average gap sizes were deduced as $\bar{\Delta}$(21 K) = 11 ± 5 meV, $\bar{\Delta}$(31 K) = 6 ± 1 meV, and $\bar{\Delta}$(36 K) = 4 ± 1 meV, represented by the large gray and white dots in Figure 3d. Thus, the gap indeed gradually shrinks as the temperature approaches T_C and is closed above, fulfilling precisely the expectations for a ferromagnetic topological insulator.[25] Note that the different gray shades of the small data points mark different cooling runs starting from an initial elevated temperature. Hence, during cooling the tip slowly drifts across the sample surface while measuring at varying temperature, thus exploring the variations of Δ versus T and spatial position simultaneously. Accordingly, the visible trend of $\Delta(T)$ relies on the sufficient statistics of probed locations to obtain reliable spatially averaged $\bar{\Delta}$ (large dots).

The conclusion that the gap closes at T_C is corroborated by comparing the experimental $\bar{\Delta}(T)$ gap evolution with the $M(T)$ magnetization, based on the relation $\bar{\Delta}(T) \propto M(T)$ derived by theory[70] and previous experiments.[25] Combining the $M(T)$ data from SQUID and XMCD (Figure 1d,f and Figure S3, Supporting Information) and the low temperature gap $\bar{\Delta}$(4.3 K) = 17 meV from STS (Figure 3b), $\bar{\Delta}(T) = \bar{\Delta}(4.3\,\mathrm{K}) \cdot M(T)/M_0$ is obtained and, thus, straightforwardly $\bar{R}(T)$ from the magnetization data. The results are presented as yellow, blue, and red dots in Figure 3d, demonstrating nice agreement with the STS experiments. This further demonstrates the magnetic origin of the gap. Since the center of the gap (Figure S7, Supporting Information) is close to the Dirac point position observed by ARPES (Figure 2e,h), the gap is attributed to the topological surface state, consistent with the out-of-plane spin polarization near the Dirac point observed in Figure 2j. Such a magnetic gap of a topological surface state close to E_F is highly favorable for probing the resulting topological conductivity and its expected quantization.

5. DFT Calculations

To clarify the origin of the discovered ferromagnetic topological insulator, the electronic band structure of $MnSb_2Te_4$ was calculated by various DFT methods, considering different magnetic configurations, including chemical as well as magnetic disorder (Note S11, Supporting Information). As a general result, the ferromagnetic topological insulator phase is only formed by introducing magnetic disorder. Calculating the bulk band structure, the perfect ferromagnetic system without disorder emerges as a topological Weyl semimetal with a zero bulk bandgap and a Weyl crossing point located along ΓZ at about 5% of the Brillouin zone away from Γ (**Figure 4**f,g, Figures S11 and S12, Supporting Information). While this is in agreement with recent calculations,[49,54] it obviously disagrees with our STS and ARPES results. On the other hand, the disorder-free antiferromagnetic system is found to be a topological insulator with a bulk bandgap of 120 meV (Figure 4k). This is evidenced by the band inversion at Γ in Figure 4k indicated by the color coding of the spectral function difference between cationic and anionic sites [red (blue): dominating anion (cation) character, see Note S11, Supporting Information]. This color code is also used in Figure 4f–k. Slab calculations of the antiferromagnetic surface band structure (Figure 4d) indeed reveal the topological surface state with a gap at the Dirac point due to time reversal symmetry breaking. Discrepancies to earlier calculations[52,53] are discussed in Note S11, Supporting Information.

For a more realistic modelling, complex magnetic orders have to be taken into account, deviating from perfect ferromagnetic or antiferromagnetic order as implied by our magnetometry results (Figure 1e, Figure S3, Supporting Information). The extreme case of completely disordered local magnetic moments, without net magnetization, showcases a bulk bandgap of 135 meV with nontrivial topology (Figure 4j) as seen from the band inversion around the gap close to Γ. Varying the degrees of magnetic disorder (Figure 4g–i, Figure S12, Supporting Information) shows that already 20% of magnetic disorder breaks up the Weyl point of ferromagnetic $MnSb_2Te_4$ and opens an inverted bandgap. This topological insulator induced by magnetic disorder is robust against chemical disorder such as the Mn–Sb site exchange that proved to be essential for inducing ferromagnetic order in the system. While a Mn–Sb site exchange of 5% does not affect the band topology, 20% site exchange renders the system trivial (see Figure S11, Supporting Information). The reason is the lowered spin-orbit interaction in the Sb layers. We have also simulated 7–10% Mn–Sb site exchange plus Mn excess and find that the system is still topological. Our results imply that, contrary to previous conclusions,[47] defect engineering can accomplish simultaneously a nontrival band topology and ferromagnetism with high Curie temperature for the $MnSb_2Te_4$ system.

To further assess the robustness of the magnetic gap, slab calculations are employed for various magnetic disorder configurations. The simplest case of a purely ferromagnetic slab does not lead to a Dirac cone, since the bulk bandgap vanishes (Figure 4b). The pure antiferromagnetic order, on the other hand, creates a pronounced Dirac cone with magnetic gap of 16 meV, Figure 4d,e, matching the gap size found by STS (Figure 3b). The magnetic gap size turns out to be a rather local property caused by the exchange interaction in near-surface $MnSb_2Te_4$ septuple layers. As such, the gapped Dirac cone also forms when the surface of an antiferromagnet is terminated by a few ferromagnetic layers (see Figure S13d, Supporting Information). A relatively strong out-of-plane spin polarization at the gap edges (≈60%) is found in that case, matching the results of the spin-resolved ARPES measured at 30 K (≈25%) nicely, if one takes into account the temperature dependence of the magnetization (Figure 1d,f). For more random combinations of antiferromagnetic and ferromagnetic layers, the Dirac cone with magnetic gap persists,

© 2021 The Authors. Advanced Materials published by Wiley-VCH GmbH

Reprinted page 7 of paper [70] "Magnetic order and band gap in $MnSb_2Te_4$".

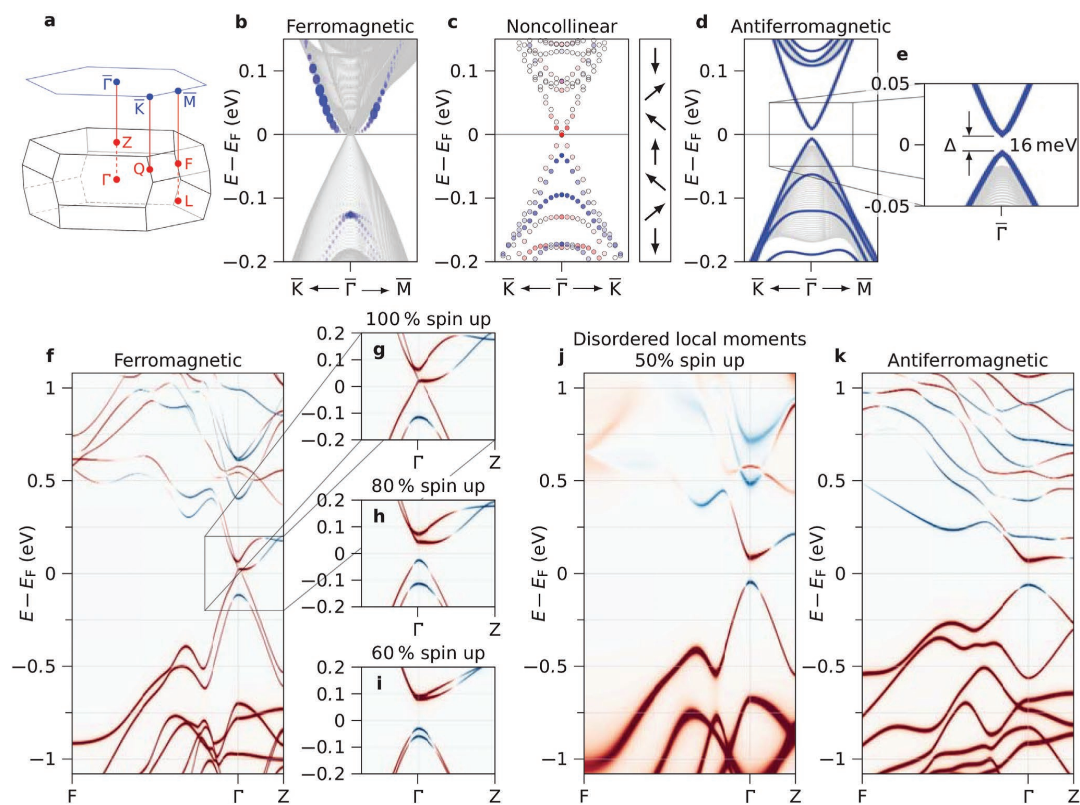

Figure 4. Theoretical predictions for $MnSb_2Te_4$. a) Brillouin zone of the bulk (bottom) and the surface (top) of $MnSb_2Te_4$ with high symmetry points marked. b–e) Band structure from DFT calculations of slab geometries for various magnetic configurations as marked on top. b) Ferromagnetic interlayer coupling calculated for a thick slab. Blue dots: surface states identified via their strength in the top septuple layer. c) Non-collinear interlayer coupling as sketched to the right by a vector model and calculated for a thin slab. The color code marks the out-of-plane spin polarization of the gapped surface-localized Dirac cone on the background of uncolored bulk-like states. d) Antiferromagentic interlayer coupling calculated for a slab (blue lines) on top of the projected bulk band structure (gray lines). A gapped Dirac cone appears at $\overline{\Gamma}$ in the slab calculation. e) Zoom into (d) with marked size of the magnetic gap in the Dirac cone (topological surface state). f–k) Band structures from DFT calculation of a bulk geometry for magnetic configurations as marked on top. Color represents the spectral function difference between anion and cation sites for each state with red (blue) representing dominating anion (cation) character (Note S11, Supporting Information). f) Ferromagnetic interlayer coupling exhibiting a topologically protected Weyl cone around Γ. g) Zoom into (f). h,i) same as (g) but with magnetic disorder modelled via overlap of collinear spin-up and spin-down states at each Mn site (Note S11, Supporting Information). j) Same as (f), but with full magnetic disorder. (k) Antiferromagnetic interlayer coupling. Note that (h–k) feature an inverted bandgap at Γ as visible by the exchanged colors of the two bands surrounding E_F rendering these structures topological insulators.

albeit the bulk bandgap vanishes due to the more extended ferromagnetic portions in the structure (see Figure S13a, Supporting Information). Finally, for a system where the magnetic moments of adjacent septuple layers are continuously tilted with respect to each other, a gapped Dirac cone was also observed (see Figure 4c). Likewise, alternate rotations of adjacent collinearly coupled Mn layers by relative angles ≥40° open a gap in the Weyl cone (Figure S12, Supporting Information). Hence, magnetic disorder turns out to be a decisive tool to accomplish topological insulator properties for $MnSb_2Te_4$.

Last but not least, it is noted that the slope of the temperature dependent $M(T)$ shows a remarkable linear behavior toward T_C, described by an effective critical exponent β = 0.7–1.2. This large β apparently persists for about half of the range between $T = 0$ K and T_C (Figure 1d,f). Such large β values do not exist in any classical model ranging from $\beta \simeq 0.125$ for the 2D Ising model to the mean-field value of 0.5. The behavior at the classical critical point may, however, strongly change due to quantum fluctuations, which can lead to $\beta = 1$ in the presence of disorder[71] as experimentally observed.[72,73] Note that such disorder is witnessed in our samples by the spatial gap size fluctuations (Figure 3). Moreover, the magnetic phases of $MnSb_2Te_4$ are energetically very close to each other (Table III, Supporting Information)[28] which may lead to changes as a function of temperature as suggested by the kink in the $M(T)$ curve (Figure S3, Supporting Information).

© 2021 The Authors. Advanced Materials published by Wiley-VCH GmbH

Reprinted page 8 of paper [70] "Magnetic order and band gap in $MnSb_2Te_4$".

6. Summary and Conclusion

Epitaxial $MnSb_2Te_4$ with regularly stacked septuple layers and a slight Mn excess features a robust nontrivial band topology at record-high Curie temperatures up to $T_C = 50$ K. DFT band structure calculations, ARPES and STS experiments showcase a 2D Dirac cone of a topological surface state with a magnetic gap of ≈17 meV close to the Fermi level. The gap disappears at T_C and above, signifying its magnetic origin. This is corroborated by the out-of-plane spin polarization at the Dirac point observed by spin-resolved ARPES. Ferromagnetism is triggered by the modifications of the exchange interactions induced by Mn–Sb site exchange in combination with a slight in-plane contraction. Most importantly, excess Mn on Sb sites significantly enforces the ferromagnetic interactions, leading to a factor of two increase of the Curie temperature. Last but not least, the spin-orbit interaction in $MnSb_2Te_4$ compared to $MnBi_2Te_4$ turns out to be still sufficiently large to maintain both the band inversion and the perpendicular magnetic anisotropy. This renders $MnSb_2Te_4$ highly favorable for the quantum anomalous Hall effect and other topology-based device applications as the critical temperature is twice as large as for $MnBi_2Te_4$ and the Dirac point is close to E_F with small spatial variations. Altogether, our results underline that the magnetic properties and interlayer couplings are highly sensitive to the structural disorder in the material and that magnetic disorder is essential to sustain the magnetic topological insulator phase. Indeed, the magnetization features an exotic critical exponent $\beta \approx 1$, which indicates the influence of a quantum critical point, likely merging ferromagnetic and antiferromagnetic order.

7. Experimental Section

Details on the sample growth, STEM, RBS, XRD, SQUID magnetometry, resonant scattering and XMCD, ARPES with spin polarimetry, STM and STS, electrical transport measurements, and DFT calculations are provided in the Supporting Information.

Supporting Information

Supporting Information is available from the Wiley Online Library or from the author.

Acknowledgements

The authors thank Ondrej Man for help with lamella preparation for STEM and gratefully acknowledge financial support from the Austrian Science Funds (FWF, I4493-N: P30960-N27), the Impuls- und Vernetzungsfonds der Helmholtz-Gemeinschaft (Grant No. HRSF-0067, Helmholtz-Russia Joint Research Group), the CzechNanoLab project LM2018110 funded by MEYS CR, the CEITEC Nano Research Infrastructure, the Swedish Research Council (Project No. 821-2012-5144), the Swedish Foundation for Strategic Research (Project No. RIF14-0053), the Spanish Ministerio de Ciencia e Innovación (Project No. PID2019-103910GB-I00), Tomsk State University (Project No. 8.1.01.2018), and Saint Petersburg State University (Project No. 73028629). The work was also funded by the Deutsche Forschungsgemeinschaft within SPP1666 Topological Insulators and Germany's Excellence Strategy—Cluster of Excellence Matter and Light for Quantum Computing (ML4Q) EXC 2004/1 — 390534769, and the Graphene Flagship Core 3. G.Bihlmayer gratefully acknowledges computing resources on the supercomputer JURECA at the Jülich Supercomputing Centre.

Open access funding enabled and organized by Projekt DEAL.

Conflict of Interest

The authors declare no conflict of interest.

Author Contributions

P.K., J.S.-B., and S.W. contributed equally to this work, which was coordinated by M.M., G.S., and O.R.

Data Availability Statement

The data that support the findings of this study are available from the corresponding author upon reasonable request.

Keywords

magnetic bandgap, magnetic topological insulators, magnetization, $MnSb_2Te_4$, Mn–Sb site exchange, molecular beam epitaxy

Received: April 18, 2021
Revised: June 29, 2021
Published online:

[1] M. Onoda, N. Nagaosa, *Phys. Rev. Lett.* **2003**, *90*, 206601.
[2] C.-X. Liu, X.-L. Qi, X. Dai, Z. Fang, S.-C. Zhang, *Phys. Rev. Lett.* **2008**, *101*, 146802.
[3] R. Yu, W. Zhang, H.-J. Zhang, S.-C. Zhang, X. Dai, Z. Fang, *Science* **2010**, *329*, 61.
[4] Z. Qiao, S. A. Yang, W. Feng, W.-K. Tse, J. Ding, Y. Yao, J. Wang, Q. Niu, *Phys. Rev. B* **2010**, *82*, 161414(R).
[5] Y. Tokura, K. Yasuda, A. Tsukazaki, *Nat. Rev. Phys.* **2019**, *1*, 126.
[6] M. Nadeem, A. R. Hamilton, M. S. Fuhrer, X. Wang, *Small* **2020**, *16*, 42.
[7] C.-Z. Chang, J. Zhang, X. Feng, J. Shen, Z. Zhang, M. Guo, K. Li, Y. Ou, P. Wei, L.-L. Wang, Z.-Q. Ji, Y. Feng, S. Ji, X. Chen, J. Jia, X. Dai, Z. Fang, S.-C. Zhang, K. He, Y. Wang, L. Lu, X.-C. Ma, Q.-K. Xue, *Science* **2013**, *340*, 167.
[8] J. G. Checkelsky, R. Yoshimi, A. Tsukazaki, K. S. Takahashi, Y. Kozuka, J. Falson, M. Kawasaki, Y. Tokura, *Nat. Phys.* **2014**, *10*, 731.
[9] X. Kou, S.-T. Guo, Y. Fan, L. Pan, M. Lang, Y. Jiang, Q. Shao, T. Nie, K. Murata, J. Tang, Y. Wang, L. He, T.-K. Lee, W.-L. Lee, K. L. Wang, *Phys. Rev. Lett.* **2014**, *113*, 137201.
[10] A. Bestwick, E. Fox, X. Kou, L. Pan, K. L. Wang, D. Goldhaber-Gordon, *Phys. Rev. Lett.* **2015**, *114*, 187201.
[11] A. Kandala, A. Richardella, S. Kempinger, C.-X. Liu, N. Samarth, *Nat. Commun.* **2015**, *6*, 7434.
[12] C.-Z. Chang, W. Zhao, D. Y. Kim, H. Zhang, B. A. Assaf, D. Heiman, S.-C. Zhang, C. Liu, M. H. W. Chan, J. S. Moodera, *Nat. Mater.* **2015**, *14*, 473.
[13] S. Grauer, S. Schreyeck, M. Winnerlein, K. Brunner, C. Gould, L. W. Molenkamp, *Phys. Rev. B* **2015**, *92*, 201304(R).

© 2021 The Authors. Advanced Materials published by Wiley-VCH GmbH

Reprinted page 9 of paper [70] "Magnetic order and band gap in $MnSb_2Te_4$".

[14] E. J. Fox, I. T. Rosen, Y. Yang, G. R. Jones, R. E. Elmquist, X. Kou, L. Pan, K. L. Wang, D. Goldhaber-Gordon, *Phys. Rev. B* **2018**, *98*, 075145.
[15] M. Götz, K. M. Fijalkowski, E. Pesel, M. Hartl, S. Schreyeck, M. Winnerlein, S. Grauer, H. Scherer, K. Brunner, C. Gould, F. J. Ahlers, L. W. Molenkamp, *Appl. Phys. Lett.* **2018**, *112*, 072102.
[16] M. Ye, W. Li, S. Zhu, Y. Takeda, Y. Saitoh, J. Wang, H. Pan, M. Nurmamat, K. Sumida, F. Ji, Z. Liu, H. Yang, Z. Liu, D. Shen, A. Kimura, S. Qiao, X. Xie, *Nat. Commun.* **2015**, *6*, 8913.
[17] M. Li, C.-Z. Chang, L. Wu, J. Tao, W. Zhao, M. H. Chan, J. S. Moodera, J. Li, Y. Zhu, *Phys. Rev. Lett.* **2015**, *114*, 146802.
[18] M. Mogi, R. Yoshimi, A. Tsukazaki, K. Yasuda, Y. Kozuka, K. S. Takahashi, M. Kawasaki, Y. Tokura, *Appl. Phys. Lett.* **2015**, *107*, 182401.
[19] H. Deng, Z. Chen, A. Wołoś, M. Konczykowski, K. Sobczak, J. Sitnicka, I. V. Fedorchenko, J. Borysiuk, T. Heider, Ł. Pluciński, K. Park, A. B. Georgescu, J. Cano, L. Krusin-Elbaum, *Nat. Phys.* **2020**, *17*, 36.
[20] Z. Zhou, Y.-J. Chien, C. Uher, *Appl. Phys. Lett.* **2005**, *87*, 112503.
[21] X. Zhang, S.-C. Zhang, *Proc. SPIE* **2012**, *8373*, 837309.
[22] K. Yasuda, M. Mogi, R. Yoshimi, A. Tsukazaki, K. S. Takahashi, M. Kawasaki, F. Kagawa, Y. Tokura, *Science* **2017**, *358*, 1311.
[23] A. C. Mahoney, J. I. Colless, L. Peeters, S. J. Pauka, E. J. Fox, X. Kou, L. Pan, K. L. Wang, D. Goldhaber-Gordon, D. J. Reilly, *Nat. Commun.* **2017**, *8*, 1836.
[24] D. Xiao, J. Jiang, J.-H. Shin, W. Wang, F. Wang, Y.-F. Zhao, C. Liu, W. Wu, M. H. Chan, N. Samarth, C.-Z. Chang, *Phys. Rev. Lett.* **2018**, *120*, 056801.
[25] E. D. L. Rienks, S. Wimmer, J. Sánchez-Barriga, O. Caha, P. S. Mandal, J. Růžička, A. Ney, H. Steiner, V. V. Volobuev, H. Groiss, M. Albu, G. Kothleitner, J. Michalička, S. A. Khan, J. Minár, H. Ebert, G. Bauer, F. Freyse, A. Varykhalov, O. Rader, G. Springholz, *Nature* **2019**, *576*, 423.
[26] J. A. Hagmann, X. Li, S. Chowdhury, S.-N. Dong, S. Rouvimov, S. J. Pookpanratana, K. M. Yu, T. A. Orlova, T. B. Bolin, C. U. Segre, D. G. Seiler, C. A. Richter, X. Liu, M. Dobrowolska, J. K. Furdyna, *New J. Phys.* **2017**, *19*, 085002.
[27] D. S. Lee, T.-H. Kim, C.-H. Park, C.-Y. Chung, Y. S. Lim, W.-S. Seo, H.-H. Park, *Cryst. Eng. Comm* **2013**, *15*, 5532.
[28] S. V. Eremeev, M. M. Otrokov, E. V. Chulkov, *J. Alloys Compd.* **2017**, *709*, 172.
[29] M. M. Otrokov, I. I. Klimovskikh, H. Bentmann, D. Estyunin, A. Zeugner, Z. S. Aliev, S. Gaß, A. U. B. Wolter, A. V. Koroleva, A. M. Shikin, M. Blanco-Rey, M. Hoffmann, I. P. Rusinov, A. Y. Vyazovskaya, S. V. Eremeev, Y. M. Koroteev, V. M. Kuznetsov, F. Freyse, J. Sánchez-Barriga, I. R. Amiraslanov, M. B. Babanly, N. T. Mamedov, N. A. Abdullayev, V. N. Zverev, A. Alfonsov, V. Kataev, B. Büchner, E. F. Schwier, S. Kumar, A. Kimura, L. Petaccia, G. Di Santo, R. C. Vidal, S. Schatz, K. Kißner, M. Ünzelmann, C. H. Min, S. Moser, T. R. F. Peixoto, F. Reinert, A. Ernst, P. M. Echenique, A. Isaeva, E. V. Chulkov, *Nature* **2019**, *576*, 416.
[30] J.-Q. Yan, Q. Zhang, T. Heitmann, Z. Huang, K. Y. Chen, J.-G. Cheng, W. Wu, D. Vaknin, B. C. Sales, R. J. McQueeney, *Phys. Rev. Mat.* **2019**, *3*, 064202.
[31] J.-Q. Yan, S. Okamoto, M. A. McGuire, A. F. May, R. J. McQueeney, B. C. Sales, *Phys. Rev. B* **2019**, *100*, 104409.
[32] Y. Chen, Y.-W. Chuang, S. H. Lee, Y. Zhu, K. Honz, Y. Guan, Y. Wang, K. Wang, Z. Mao, J. Zhu, C. Heikes, P. Quarterman, P. Zajdel, J. A. Borchers, W. Ratcliff, *Phys. Rev. Mat.* **2020**, *4*, 064411.
[33] M. M. Otrokov, I. P. Rusinov, M. Blanco-Rey, M. Hoffmann, A. Y. Vyazovskaya, S. V. Eremeev, A. Ernst, P. M. Echenique, A. Arnau, E. V. Chulkov, *Phys. Rev. Lett.* **2019**, *122*, 107202.
[34] Y.-J. Hao, P. Liu, Y. Feng, X.-M. Ma, E. F. Schwier, M. Arita, S. Kumar, C. Hu, R. Lu, M. Zeng, Y. Wang, Z. Hao, H.-Y. Sun, K. Zhang, J. Mei, N. Ni, L. Wu, K. Shimada, C. Chen, Q. Liu, C. Liu, *Phys. Rev. X* **2019**, *9*, 041038.
[35] H. Li, S.-Y. Gao, S.-F. Duan, Y.-F. Xu, K.-J. Zhu, S.-J. Tian, J.-C. Gao, W.-H. Fan, Z.-C. Rao, J.-R. Huang, J.-J. Li, D.-Y. Yan, Z.-T. Liu, W.-L. Liu, Y.-B. Huang, Y.-L. Li, Y. Liu, G.-B. Zhang, P. Zhang, T. Kondo, S. Shin, H.-C. Lei, Y.-G. Shi, W.-T. Zhang, H.-M. Weng, T. Qian, H. Ding, *Phys. Rev. X* **2019**, *9*, 041039.
[36] Y. J. Chen, L. X. Xu, J. H. Li, Y. W. Li, H. Y. Wang, C. F. Zhang, H. Li, Y. Wu, A. J. Liang, C. Chen, S. W. Jung, C. Cacho, Y. H. Mao, S. Liu, M. X. Wang, Y. F. Guo, Y. Xu, Z. K. Liu, L. X. Yang, Y. L. Chen, *Phys. Rev. X* **2019**, *9*, 041040.
[37] Y. Deng, Y. Yu, M. Z. Shi, Z. Guo, Z. Xu, J. Wang, X. H. Chen, Y. Zhang, *Science* **2020**, *367*, 895.
[38] R. C. Vidal, A. Zeugner, J. I. Facio, R. Ray, M. H. Haghighi, A. U. Wolter, L. T. C. Bohorquez, F. Caglieris, S. Moser, T. Figgemeier, T. R. Peixoto, H. B. Vasili, M. Valvidares, S. Jung, C. Cacho, A. Alfonsov, K. Mehlawat, V. Kataev, C. Hess, M. Richter, B. Büchner, J. van den Brink, M. Ruck, F. Reinert, H. Bentmann, A. Isaeva, *Phys. Rev. X* **2019**, *9*, 041065.
[39] C. Hu, L. Ding, K. N. Gordon, B. Ghosh, H.-J. Tien, H. Li, A. G. Linn, S.-W. Lien, C.-Y. Huang, S. Mackey, J. Liu, P. V. S. Reddy, B. Singh, A. Agarwal, A. Bansil, M. Song, D. Li, S.-Y. Xu, H. Lin, H. Cao, T.-R. Chang, D. Dessau, N. Ni, *Sci. Adv.* **2020**, *6*, eaba4275.
[40] B. Chen, F. Fei, D. Wang, Z. Jiang, B. Zhang, J. Guo, H. Xie, Y. Zhang, M. Naveed, Y. Du, Z. Sun, H. Zhang, D. Shen, F. Song, *arXiv* **2020**, *2009*, 00039.
[41] G. Shi, M. Zhang, D. Yan, H. Feng, M. Yang, Y. Shi, Y. Li, *Chin. Phys. Lett.* **2020**, *37*, 047301.
[42] C. Hu, S. Mackey, N. Ni, *arXiv 2008.09097*, **2020**.
[43] S. Huan, S. Zhang, Z. Jiang, H. Su, H. Wang, X. Zhang, Y. Yang, Z. Liu, X. Wang, N. Yu, Z. Zou, D. Shen, J. Liu, Y. Guo, *Phys. Rev. Lett.* **2021**, *126*, 246601.
[44] C. Pauly, G. Bihlmayer, M. Liebmann, M. Grob, A. Georgi, D. Subramaniam, M. R. Scholz, J. Sánchez-Barriga, A. Varykhalov, S. Blügel, O. Rader, M. Morgenstern, *Phys. Rev. B* **2012**, *86*, 235106.
[45] J. S. Dyck, P. Svanda, P. Lostak, J. Horak, W. Chen, C. Uher, *J. Appl. Phys.* **2003**, *94*, 7631.
[46] J. Choi, S. Choi, J. Choi, Y. Park, H.-M. Park, H.-W. Lee, B.-C. Woo, S. Cho, *Phys. Status Solidi B* **2004**, *241*, 1541.
[47] Y. Liu, L.-L. Wang, Q. Zheng, Z. Huang, X. Wang, M. Chi, Y. Wu, B. C. Chakoumakos, M. A. McGuire, B. C. Sales, W. Wu, J. Yan, *Phys. Rev. X* **2021**, *11*, 021033.
[48] W. Ge, P. M. Sass, J. Yan, S. H. Lee, Z. Mao, W. Wu, *Phys. Rev. B* **2021**, *103*, 134403.
[49] T. Murakami, Y. Nambu, T. Koretsune, G. Xiangyu, T. Yamamoto, C. M. Brown, H. Kageyama, *Phys. Rev. B* **2019**, *100*, 195103.
[50] S. X. M. Riberolles, Q. Zhang, E. Gordon, N. P. Butch, L. Ke, J. Q. Yan, R. J. McQueeney, *Phys. Rev. B* **2021**, *104*, 064401.
[51] H. Li, Y. Li, Y.-K. Lian, W. Xie, L. Chen, J. Zhang, Y. Wu, S. Fan, *arXiv:2104.00898*, **2021**.
[52] D. Zhang, M. Shi, T. Zhu, D. Xing, H. Zhang, J. Wang, *Phys. Rev. Lett.* **2019**, *122*, 206401.
[53] B. Chen, F. Fei, D. Zhang, B. Zhang, W. Liu, S. Zhang, P. Wang, B. Wei, Y. Zhang, Z. Zuo, J. Guo, Q. Liu, Z. Wang, X. Wu, J. Zong, X. Xie, W. Chen, Z. Sun, S. Wang, Y. Zhang, M. Zhang, X. Wang, F. Song, H. Zhang, D. Shen, B. Wang, *Nat. Commun.* **2019**, *10*, 4469.
[54] C. Lei, S. Chen, A. H. MacDonald, *Proc. Natl. Acad. Sci.* **2020**, *117*, 27224.
[55] L. Zhou, Z. Tan, D. Yan, Z. Fang, Y. Shi, H. Weng, *Phys. Rev. B* **2020**, *102*, 085114.
[56] M. M. Otrokov, T. V. Menshchikova, M. G. Vergniory, I. P. Rusinov, A. Y. Vyazovskaya, Y. M. Koroteev, G. Bihlmayer, A. Ernst, P. M. Echenique, A. Arnau, E. V. Chulkov, *2D Mater.* **2017**, *4*, 025082.

© 2021 The Authors. Advanced Materials published by Wiley-VCH GmbH

Reprinted page 10 of paper [70] "Magnetic order and band gap in $MnSb_2Te_4$".

[57] C. L. Richardson, J. M. Devine-Stoneman, G. Divitini, M. E. Vickers, C.-Z. Chang, M. Amado, J. S. Moodera, J. W. A. Robinson, *Sci. Rep.* **2017**, *7*, 12061.
[58] Y. Jiang, Y. Y. Sun, M. Chen, Y. Wang, Z. Li, C. Song, K. He, L. Wang, X. Chen, Q.-K. Xue, X. Ma, S. B. Zhang, *Phys. Rev. Lett.* **2012**, *108*, 066809.
[59] J. Kellner, G. Bihlmayer, V. L. Deringer, M. Liebmann, C. Pauly, A. Giussani, J. E. Boschker, R. Calarco, R. Dronskowski, M. Morgenstern, *Phys. Rev. B* **2017**, *96*, 245408.
[60] Y. Yuan, X. Wang, H. Li, J. Li, Y. Ji, Z. Hao, Y. Wu, K. He, Y. Wang, Y. Xu, W. Duan, W. Li, Q.-K. Xue, *Nano Lett.* **2020**, *20*, 3271.
[61] Y. Lai, L. Ke, J. Yan, R. D. McDonald, R. J. McQueeney, *Phys. Rev. B* **2021**, *103*, 184429.
[62] J. Sánchez-Barriga, A. Varykhalov, G. Springholz, H. Steiner, R. Kirchschlager, G. Bauer, O. Caha, E. Schierle, E. Weschke, A. A. Ünal, S. Valencia, M. Dunst, J. Braun, H. Ebert, J. Minár, E. Golias, L. V. Yashina, A. Ney, V. Holý, O. Rader, *Nat. Commun.* **2016**, *7*, 10559.
[63] J. Henk, M. Flieger, I. V. Maznichenko, I. Mertig, A. Ernst, S. V. Eremeev, E. V. Chulkov, *Phys. Rev. Lett.* **2012**, *109*, 076801.
[64] I. Lee, C. K. Kim, J. Lee, S. J. L. Billinge, R. Zhong, J. A. Schneeloch, T. Liu, T. Valla, J. M. Tranquada, G. Gu, J. C. S. Davis, *Proc. Natl. Acad. Sci.* **2015**, *112*, 1316.
[65] C.-C. Chen, M. L. Teague, L. He, X. Kou, M. Lang, W. Fan, N. Woodward, K.-L. Wang, N.-C. Yeh, *New J. Phys.* **2015**, *17*, 113042.
[66] H. Beidenkopf, P. Roushan, J. Seo, L. Gorman, I. Drozdov, Y. S. Hor, R. J. Cava, A. Yazdani, *Nat. Phys.* **2011**, *7*, 939.
[67] C. Pauly, C. Saunus, M. Liebmann, M. Morgenstern, *Phys. Rev. B* **2015**, *92*, 085140.
[68] M. Morgenstern, *Surf. Rev. Lett.* **2003**, *10*, 933.
[69] P. Sessi, R. R. Biswas, T. Bathon, O. Storz, S. Wilfert, A. Barla, K. A. Kokh, O. E. Tereshchenko, K. Fauth, M. Bode, A. V. Balatsky, *Nat. Commun.* **2016**, *7*, 12027.
[70] G. Rosenberg, M. Franz, *Phys. Rev. B* **2012**, *85*, 195119.
[71] T. R. Kirkpatrick, D. Belitz, *Phys. Rev. B* **2015**, *91*, 214407.
[72] D. Fuchs, M. Wissinger, J. Schmalian, C.-L. Huang, R. Fromknecht, R. Schneider, H. v. Löhneysen, *Phys. Rev. B* **2014**, *89*, 174405.
[73] B. C. Sales, K. Jin, H. Bei, J. Nichols, M. F. Chisholm, A. F. May, N. P. Butch, A. D. Christianson, M. A. McGuire, *npj Quant. Mater.* **2017**, *2*, 33.

© 2021 The Authors. Advanced Materials published by Wiley-VCH GmbH

Reprinted page 11 of paper [70] "Magnetic order and band gap in $MnSb_2Te_4$".

© 2021 Wiley-VCH GmbH

ADVANCED MATERIALS

Supporting Information

for *Adv. Mater.,* DOI: 10.1002/adma.202102935

Mn-Rich $MnSb_2Te_4$: A Topological Insulator with Magnetic Gap Closing at High Curie Temperatures of 45–50 K

Stefan Wimmer, Jaime Sánchez-Barriga, Philipp Küppers, Andreas Ney, Enrico Schierle, Friedrich Freyse, Ondrej Caha, Jan Michalička, Marcus Liebmann, Daniel Primetzhofer, Martin Hoffman, Arthur Ernst, Mikhail M. Otrokov, Gustav Bihlmayer, Eugen Weschke, Bella Lake, Evgueni V. Chulkov, Markus Morgenstern, Günther Bauer, Gunther Springholz, and Oliver Rader**

Supporting Information

Mn-rich $MnSb_2Te_4$: A topological insulator with magnetic gap closing at high Curie temperatures of 45–50 K

S. Wimmer,[1] J. Sánchez-Barriga,[2] P. Küppers,[3] A. Ney,[1] E. Schierle,[2] F. Freyse,[2,4] O. Caha,[5] J. Michalička,[6] M. Liebmann,[3] D. Primetzhofer,[7] M. Hoffmann,[8] A. Ernst,[9,10] M. M. Otrokov,[11,12] G. Bihlmayer,[13] E. Weschke,[2] B. Lake,[2] E. V. Chulkov,[14,15,16,17] M. Morgenstern,[3] G. Bauer,[1] G. Springholz,[1] and O. Rader[2]

[1]*Institut für Halbleiter- und Festkörperphysik, Johannes Kepler Universität, Altenberger Straße 69, 4040 Linz, Austria*

[2]*Helmholtz-Zentrum Berlin für Materialien und Energie, Albert-Einstein-Straße 15, 12489 Berlin, Germany**

[3]*II. Institute of Physics B and JARA-FIT, RWTH Aachen University, 52074 Aachen, Germany**

[4]*Institut für Physik und Astronomie, Universität Potsdam, Karl-Liebknecht-Straße 24/25, 14476 Potsdam, Germany*

[5]*Department of Condensed Matter Physics, Masaryk University, Kotlářská 267/2, 61137 Brno, Czech Republic*

[6]*Central European Institute of Technology, Brno University of Technology, Purkyňova 123, 612 00 Brno, Czech Republic*

[7]*Department of Physics and Astronomy, Universitet Uppsala, Lägerhyddsvägen 1, 75120 Uppsala, Sweden*

[8]*Institute for Theoretical Physics, Johannes Kepler Universität, Altenberger Straße 69, 4040 Linz, Austria*

[9]*Institute for Theoretical Physics, Johannes Kepler Universität, Altenberger Straße 69, 4040 Linz, Austria*

[10]*Max Planck Institute of Microstructure Physics, Weinberg 2, 06120 Halle, Germany*

[11]*Centro de Física de Materiales (CFM-MPC), Centro Mixto CSIC-UPV/EHU, 20018 San Sebastián/Donostia, Spain*

[12]*IKERBASQUE, Basque Foundation for Science, 48011 Bilbao, Spain*

Reprinted supplement page 2 of paper [70] "Magnetic order and band gap in $MnSb_2Te_4$".

[13]*Peter Grünberg Institute and Institute for Advanced Simulation,*
Forschungszentrum Jülich and JARA, 52425 Jülich, Germany
[14]*Donostia International Physics Center (DIPC),*
20018 San Sebastián/Donostia, Spain
[15]*Departamento de Física de Materiales,*
Facultad de Ciencias Químicas, Universidad del País Vasco,
Apdo. 1072, 20080 San Sebastián/Donostia, Spain
[16]*Saint Petersburg State University, 198504, Saint Petersburg, Russia*
[17]*Tomsk State University, Tomsk, 634050, Russia*

(Dated: June 29, 2021)

CONTENTS

S1. Sample Growth 4

S2. Electron Microscopy 5

S3. Rutherford Backscattering Spectrometry 5

S4. X-ray Diffraction 5

S5. Magnetometry by SQUID 8

S6. Comparison with Magnetic Properties of Other $MnSb_2Te_4$ Samples 9

S7. Resonant Scattering and X-ray Circular Dichroism 10

S8. ARPES and spin-resolved ARPES 11

S9. Scanning Tunneling Microscopy and Spectroscopy 15
- A. Measurement Details 15
- B. Band Gap Determination at 4.3 K 16
- C. $dI/dV(V)$ Curves at Different Temperatures 17
- D. Determination of Band Gaps at Elevated Temperature 19

S10. Electric Transport Measurements 22

S11. Density Functional Theory Calculations 22
- A. Details of the Calculations 22
- B. Magnetic Ground State for Different Disorder Configurations 25
- C. Topological Properties for Different Disorder Configurations 26
- D. Influence of Charge Doping on the Magnetic Interactions 29

References 32

* These authors contributed equally to this work

The following Supporting Notes are ordered according to the methods applied. Each Supporting Note describes both the details of the experiment or the calculations and additional data supporting the conclusions from the main text.

S1: SAMPLE GROWTH

$MnSb_2Te_4$ films were grown by molecular beam epitaxy (MBE) on $BaF_2(111)$ substrates using a Varian GEN II system. Compound Sb_2Te_3 and elemental Mn and Te sources were employed for control of stoichiometry and composition. The Mn:Sb_2Te_3 flux ratio was set to 1:1 in order to obtain the nominal 1:2:4 stoichiometry of the $MnSb_2Te_4$ phase. The corresponding Mn and Sb_2Te_3 flux rates were 0.1 monolayers (ML)/s and 0.1 quintuple layers/s, respectively, determined by the quartz microbalance method with precision of $\pm 5\%$. In addition, an excess Te flux of 1.5 ML/s was used. Typical sample thicknesses were 200 nm. Deposition was carried out at a sample temperature of 290°C at which perfect 2D growth is sustained independently of the Mn concentration, as verified by *in situ* reflection high energy electron diffraction and atomic force microscopy. At the given substrate temperature of 290°C, the incorporation coefficient is unity for Mn due to its very low vapour pressure, but for Sb_2Te_3 a small fraction desorbs during growth and is thus, not incorporated. This leads to a slightly Mn rich composition of the epilayers as revealed by Rutherford backscattering spectrometry (RBS) described in Supporting Note S3. The composition was further checked by x-ray diffraction analysis described in Supporting Note S4. Only samples exhibiting the diffraction spectra of the $MnSb_2Te_4$ phase were used for further investigations.

For angle-resolved photoelectron spectroscopy (ARPES) performed at BESSY II and scanning tunneling microscopy (STM) performed at RWTH Aachen University, samples were transferred from the MBE system using an ultrahigh vacuum (UHV) suitcase operated in the low 10^{-10} mbar pressure range that allowed transportation without breaking UHV conditions. Samples used for magnetometry and x-ray magnetic circular dichroism (XMCD) were capped *in situ* after MBE growth with amorphous Se and Te capping layers to protect the surface against oxidation.

S2: ELECTRON MICROSCOPY

High-resolution scanning transmission electron microscopy (TEM) was performed with a FEI Titan 60-300 Themis instrument equipped with a Cs image corrector. The TEM data were recorded with a high-angle annular dark field (HAADF) detector and the images processed using a fast Fourier transform and Fourier mask filtering technique for noise minimization. Thin cross-sectional lamellae from $MnSb_2Te_4$ films were prepared by focused ion beam milling (FEI Helios NanoLab 660).

S3: RUTHERFORD BACKSCATTERING SPECTROMETRY

The chemical composition of the samples was determined by Rutherford backscattering spectrometry (RBS) employing a primary beam of 2 MeV $^4He^+$ ions provided by the 5 MV 15SDH-2 Pelletron accelerator at Uppsala University. A solid-state detector was placed in backscattering geometry under an angle of 170° with respect to the primary beam. The beam incidence angle was randomized in a 3° angular interval around an equilibrium angle of 18° with respect to the surface normal to counteract potential channeling effects. The resulting spectra (Fig. S1) were fitted by the SIMNRA software package [1] to obtain the film composition and confirm its uniformity over the film cross section. Analysis of the RBS data as shown in Fig. S1 yields an excellent fit (blue line in Fig. S1) for atom concentrations of 57.0% Te, 27.7% Sb and 15.3% Mn with a high uniformity throughout the film cross section. The obtained composition of $Mn_{1.06}Sb_{1.94}Te_4$ is close to the nominal $MnSb_2Te_4$ stoichiometry, but features a slight Mn excess of $\sim 6\%$ and a slight Sb deficiency of $\sim 3\%$, indicating a small amount of substitution of Sb atoms by additional Mn atoms in addition to Mn-Sb site exchange, as corroborated by x-ray diffraction analysis shown in Supporting Note S4.

S4: X-RAY DIFFRACTION

The crystalline structure was determined by x-ray diffraction (XRD) scans and reciprocal space maps recorded in the vicinity of the $(10\bar{1}.20)$ reciprocal lattice point. The measurements were performed using a Rigaku SmartLab diffractometer with Cu x-ray tube and channel-cut Ge(220) monochromator. The results are shown as red lines in Fig. S2. The

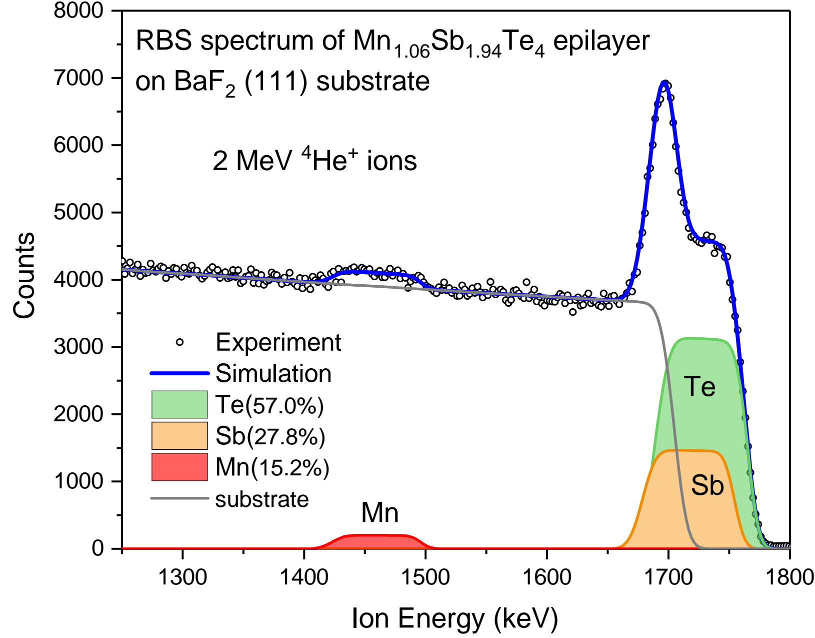

Figure S1. **Chemical composition and depth profile.** Rutherford backscattering spectrum measured in random geometry. The simulation of the total backscattering signal using SIMNRA (blue line) is in excellent agreement with the experimental data (open circles). The corresponding contributions of the film constituents (Te, Sb and Mn) are indicated by the green, orange and red lines and correspondingly shaded areas. The data reveal a slight Mn excess of $\sim 6\,\%$ and an Sb deficiency of $\sim 3\,\%$ with respect to the ideal $MnSb_2Te_4$ stoichiometry, suggesting a partial Mn replacement of Sb atoms in the Sb layer. This yields a composition of $Mn_{1.06}Sb_{1.94}Te_4$ of the films.

symmetric scans along the [000.1] reciprocal space direction (c-axis) were fitted with a modified one dimensional paracrystal model [2, 3] (black lines in Fig. S2). We have fitted the data of two samples and obtained consistent results of $a = 4.23$ Å and $c = 40.98$ Å.

The Mn-Sb site exchange was modelled by assuming various fractional occupancies of Mn on Mn sites $C_{Mn/Mn}$ in the central cation lattice plane of the septuples, ideally occupied by Mn only, the rest of these sites being occupied by Sb atoms. This accordingly leads to

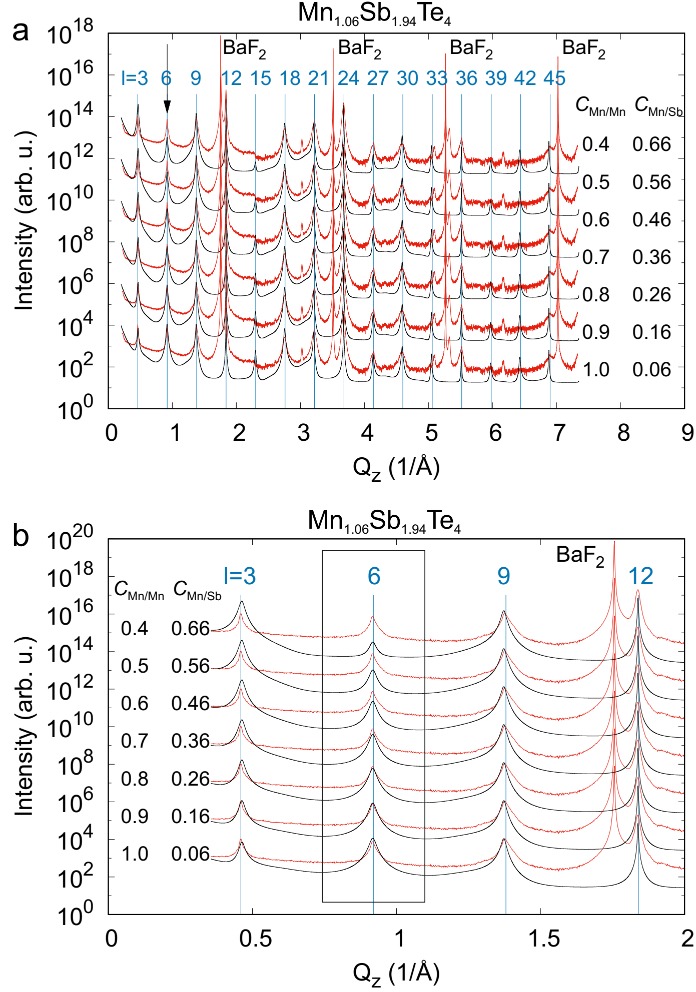

Figure S2. **X-ray diffraction spectra with fits.** (a) Experimental x-ray diffraction spectrum of the $MnSb_2Te_4$ epilayer (red lines) compared with simulations (black lines) using a one-dimensional paracrystal model [2, 3] while assuming different Mn occupation in the central layer ($C_{Mn/Mn}$) and in the adjacent nominal Sb layers ($C_{Mn/Sb}$) of the septuple. Blue lines denote positions of (0 0 0 l) reciprocal lattice points. (b) Zoom into (a) showcasing the strong sensitivity of the peak at $Q_z \approx 0.9$ Å^{-1} (black arrow in (a)) to the Mn-Sb site exchange. The concentration pairs $C_{Mn/Mn}$ and $C_{Mn/Sb}$ are chosen to correspond to the $Mn_{1.06}Sb_{1.94}Te_4$ stoichiometry determined by RBS. Peaks of the BaF_2 substrate are indicated.

a partial occupancy of the Sb sites in the outer cation lattice planes by Mn atoms with $C_{Mn/Sb} = (C_{tot} - C_{Mn/Mn})/2$ where C_{tot} is the total number of Mn atoms in each septuple. The factor 1/2 arises from the fact that the exchanged Mn from the center of the septuple is evenly distributed between the two outer Sb layers. In the case of excess Mn in the layers as seen by RBS, the sum $(C_{Mn/Mn} + C_{Mn/Sb}) > 1$.

With these definitions, the structure factor of $MnSb_2Te_4$ reads

$$F(Q_z) = \sum_n C_n f_n(Q_z) \exp(-iQ_z z_n), \tag{1}$$

where $f_n(Q_z)$ is the atomic form factor of the n-th atom in the unit cell, z_n its coordinate, C_n its occupancy, Q_z its position in reciprocal space and the summation runs over all atoms in the septuple layer. For Sb, Te, and Mn the atomic form factors at $Q_z = 0.9\,\text{Å}^{-1}$ are 48.9, 49.9 and 23.6, respectively.

The comparison of the measured diffraction spectrum with the simulation for different amounts of Mn-Sb site exchange are shown in Fig. S2, taking into account the small Mn excess in the layers ($C_{Mn/Mn} + C_{Mn/Sb} = 1.06$) as derived by RBS (Fig. S1). $C_{Mn/Mn} = 0.4$ and $C_{Mn/Sb} = 0.66$ at the top of the figure corresponds to 40% Mn atoms in the center and 66% in the outer two cation layers of the septuple. Figure S2(b) highlights the low Q_z region, evidencing the strong sensitivity of the [000.6] peak at $Q_z = 0.9\,\text{Å}^{-1}$ to the Mn and Sb exchange. For this peak, the two different cation layers contribute to the structure factor with almost exactly opposite phase, while the contribution of the Te layers almost cancels. Because of the different Mn and Sb atomic form factors, the intensity of this peak rapidly diminishes with increasing Mn-Sb exchange and completely vanishes for complete intermixing, i.e., $C_{Mn/Mn} \simeq C_{Mn/Sb}$. The best fit to the experiment is found for $C_{Mn/Mn}$ between 0.9 and 0.8 and $C_{Mn/Sb} \sim 0.2$, evidencing a non-ideal distribution of Mn and Sb in the respective layers.

S5: MAGNETOMETRY BY SQUID

The magnetic properties were determined by a superconducting quantum interference device (SQUID) magnetometer (Quantum Design MPMS-XL) as a function of temperature from 2 K to 300 K. The external field **H** was applied either parallel (in plane) or perpendicular (out of plane) to the epilayer surface, that itself is oriented perpendicular to the

crystallographic c axis. The diamagnetic contribution of the substrate was determined from the slope of the magnetization $M(H)$ recorded at high magnetic fields and 300 K well above the Curie temperature T_C of $MnSb_2Te_4$, where the magnetic contribution of the thin film is completely superseded by that of the thousand times thicker substrate. The derived substrate contribution was then subtracted from the raw data recorded at lower T. Identical sample pieces were used for in-plane and out-of-plane measurements.

Figure S3 shows out-of-plane $M(T)$ data while field cooling at 10 mT for three different samples. They reveal a quite similar T_C and consistently display a ferromagnetic behavior via its remanence. Data for sample 1 are also shown in Fig. 1 (main text) where they give a slightly smaller T_C within the error bars.

Figure S3 (top) features a small kink at 20–25 K that indicates deviations from pure ferromagnetic order possibly indicating a second phase transition that might contribute to the large critical exponent $\beta \simeq 1$ as discussed in the main text and attributed there to the vicinity to a quantum critical point.

S6: COMPARISON WITH MAGNETIC PROPERTIES OF OTHER $MNSB_2TE_4$ SAMPLES

Table I compares the results of our three $MnSb_2Te_4$ samples with data from the literature. The comparison highlights the exceptionally large Curie temperature of the Mn-rich epitaxial films.

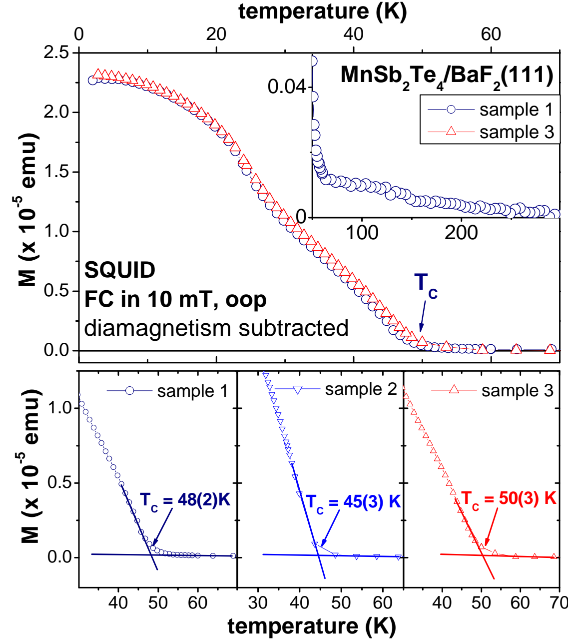

Figure S3. **Magnetometry by SQUID.** Magnetization $M(T)$ of three individual $MnSb_2Te_4$ epilayers measured by SQUID. $M(T)$ was measured in out-of-plane (oop) direction while field cooling (FC) in a field of 10 mT. Linear extrapolation to $M = 0\,\mathrm{emu}$ was used to estimate T_C as marked. Notice the small kink in $M(T)$ around 20 K in the top panel which indicates deviations from pure ferromagnetic order. Inset: Full temperature dependence of the magnetization $M(T)$ up to 300 K on a vertical scale enlarged by a factor of 40. From the SQUID raw data, the diamagnetic contribution from the BaF_2 substrate of 0.0205 μemu/Oe was substracted.

S7: RESONANT SCATTERING AND X-RAY CIRCULAR DICHROISM

Resonant scattering and XMCD were measured at the extreme ultraviolet (XUV) diffractometer of the UE46-PGM1 undulator beam line of BESSY II at Helmholtz-Zentrum Berlin. The XMCD signal was obtained by measuring the difference of the (0001) Bragg peak intensities for incident photons with opposite circular polarization and the photon energy tuned to the Mn-L_3 resonance. In this setup, the sample was field cooled down to 10 K in an external field of about 0.5 T provided by a removable permanent magnet. Subsequent po-

nominal stoichiometry	growth	magnetism	critical temperature	reference
$MnSb_2Te_4$	epitaxial film	FM	T_C=46-48 K	sample 1, this work
$MnSb_2Te_4$	epitaxial film	FM	T_C=45 K	sample 2, this work
$MnSb_2Te_4$	epitaxial film	FM	T_C=50 K	sample 3, this work
$MnSb_2Te_4$	single crystal	AFM	T_N= 19 K	J.-Q. Yan et al. [a])
$MnSb_2Te_4$	single crystal	AFM	T_N=19.5 K	Y. Chen et al. [b])
$MnSb_{1.8}Bi_{0.2}Te_4$	single crystal	FM	T_C=26 K	Y. Chen et al. [b])
$MnSb_2Te_4$	polycrystal	FM	T_C=25 K	Murakami et al. [c])

Table I. **Magnetic properties of $MnSb_2Te_4$** for epitaxial films, bulk crystals and polycrystals, comparing the ferromagnetic (FM) Curie temperatures T_C determined in the present work to T_C and antiferromagnetic (AFM) Néel temperatures T_N from the literature. [a]) J.-Q. Yan et al., Phys. Rev. B 100, 104409 (2019); [b]) Y. Chen et al., Phys. Rev. Mat. 4, 064411 (2020); [c]) T. Murakami et al., Phys. Rev. B 100, 195103 (2019).

larization dependent and wave-vector dependent measurements were performed in zero field at various temperatures. The recorded XMCD data are thus a direct measurement of the remanent ferromagnetic polarization of the Mn moments in $MnSb_2Te_4$.

S8: ARPES AND SPIN-RESOLVED ARPES

ARPES measurements were performed at 30 K with a Scienta R4000 hemispherical analyzer at the RGBL-2 end station of the U125/2 undulator beamline at BESSY II. Light is incident under an azimuthal angle of 45° and a polar angle of 90° with respect to the sample surface. The light polarization is linear and horizontal. Photon energies between 19 and 70 eV were employed. Spin-resolved ARPES spectra were acquired with a Mott-type spin polarimeter operated at 25 kV, capable of detecting both in-plane and out-of-plane spin components. Samples were transported to the RGBL-2 setup in a UHV suitcase to always maintain pressures below $1 \cdot 10^{-10}$ mbar. Overall resolution of ARPES measurements was 10 meV (energy) and 0.3 ° (angular). Resolutions for spin-resolved ARPES were 45 meV

(energy) and 0.75° (angular).

For the measurement in Fig. 2j, main text, the sample was magnetized in situ at 30 K by applying a pulsed magnetic field from a removable coil of $\sim \pm 0.5$ T in the direction perpendicular to the surface. As usual, the spin-resolved ARPES experiment is conducted in remanence. The movement between the ARPES chamber and the preparation chamber, where the coil is situated, is a vertical movement of the cryostat so that the sample is always at 30 K.

Figure S4 shows a complete set of spin-polarized ARPES data featuring all three orthogonal spin directions for a finite $k_{\|} = \pm 0.15\,\text{Å}^{-1}$. Only in-plane spin polarization perpendicular to the electron wave vector $k_{\|}$ appears and reverses sign with a sign change of $k_{\|}$. This evidences a spin texture that rotates anti-clockwise (right-handed) around the measured Dirac cone (Fig. 2g,i, main text) with the electron spin locked to the electron momentum. Such helical in-plane spin texture is a key signature of the topological character of the Dirac cone. Note that the ferromagnetism of $MnSb_2Te_4$ exhibits out-of-plane anisotropy such that bulk states cannot have in-plane spin polarization, which fully supports the assignment to the Dirac cone surface state. To deduce the Dirac point energy E_D, the peaks within momentum distribution curves are fitted by two Lorentzians (Fig. S4e) and the energy dependent peak maxima are connected via two fitted lines (Fig. S4d and Fig. 2d,h, main text) that cross at $E_D - E_F = 20 \pm 7$ meV. The binding energy range of the fit was determined by the possibility to fit separate Lorentzians, see Fig. S4d,e. Since we do not observe any surface band bending by residual gas adsorption (prominent for the n-doped systems such as Bi_2Se_3 and Bi_2Te_3), the Dirac point can be regarded as a rather good measure of the chemical potential.

Figure S5 shows that the Dirac cone surface state has no dispersion with the wave vector perpendicular to the surface plane, in contrast to the bulk valence band. Figure S5 is the input for Fig. 2b, main text, with linear interpolation between the 9 photon energies. Table II shows the momentum values in kinetic energy.

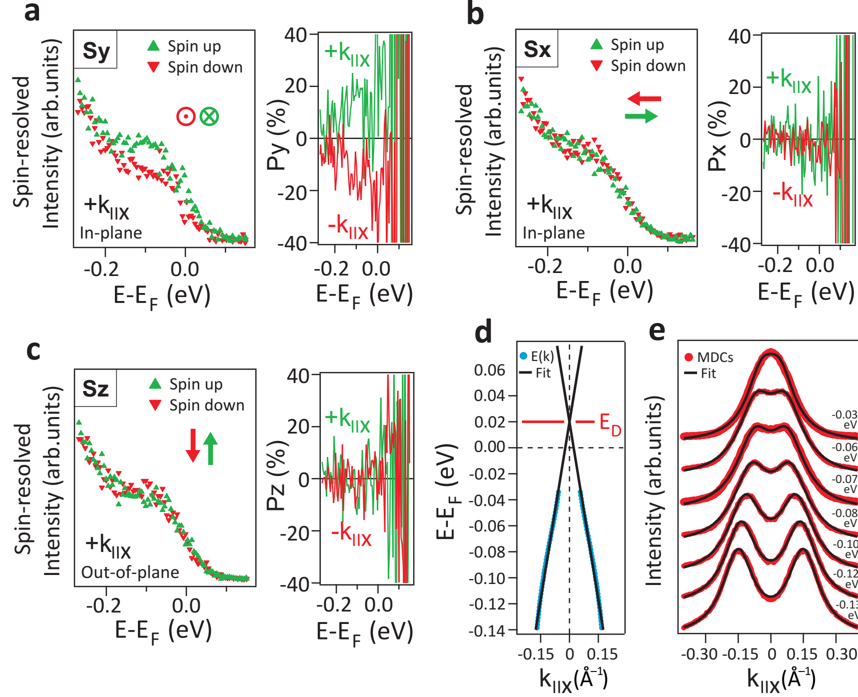

Figure S4. **Spin-resolved ARPES data and fit of Dirac cone.** All three spin polarization components are shown for $k_{\|,x} \simeq \pm 0.15\,\text{Å}^{-1}$ (indicated in Fig. 2h, main text). Left hand side of each subfigure shows the ARPES data for the two opposite spin channels at $k_{\|,x} \simeq +0.15\,\text{Å}^{-1}$, while the right hand side shows the resulting spin polarization P_i for both $k_{\|,x} \simeq \pm 0.15\,\text{Å}^{-1}$. (a) In-plane spin components perpendicular to $k_{\|,x}$ (same as Fig. 2g, main text). (b) In-plane spin components parallel/antiparallel to $k_{\|,x}$. (c) Out-of-plane spin components. The symbols for spin direction and orientation are relative to panel (d). (d) The Dirac energy E_D is determined by the crossing of two lines given by fits to experimental data points which, in turn, were determined by Lorentzians fitted to momentum distribution curves (MDC). These fits are shown in panel (e). $h\nu = 25$ eV.

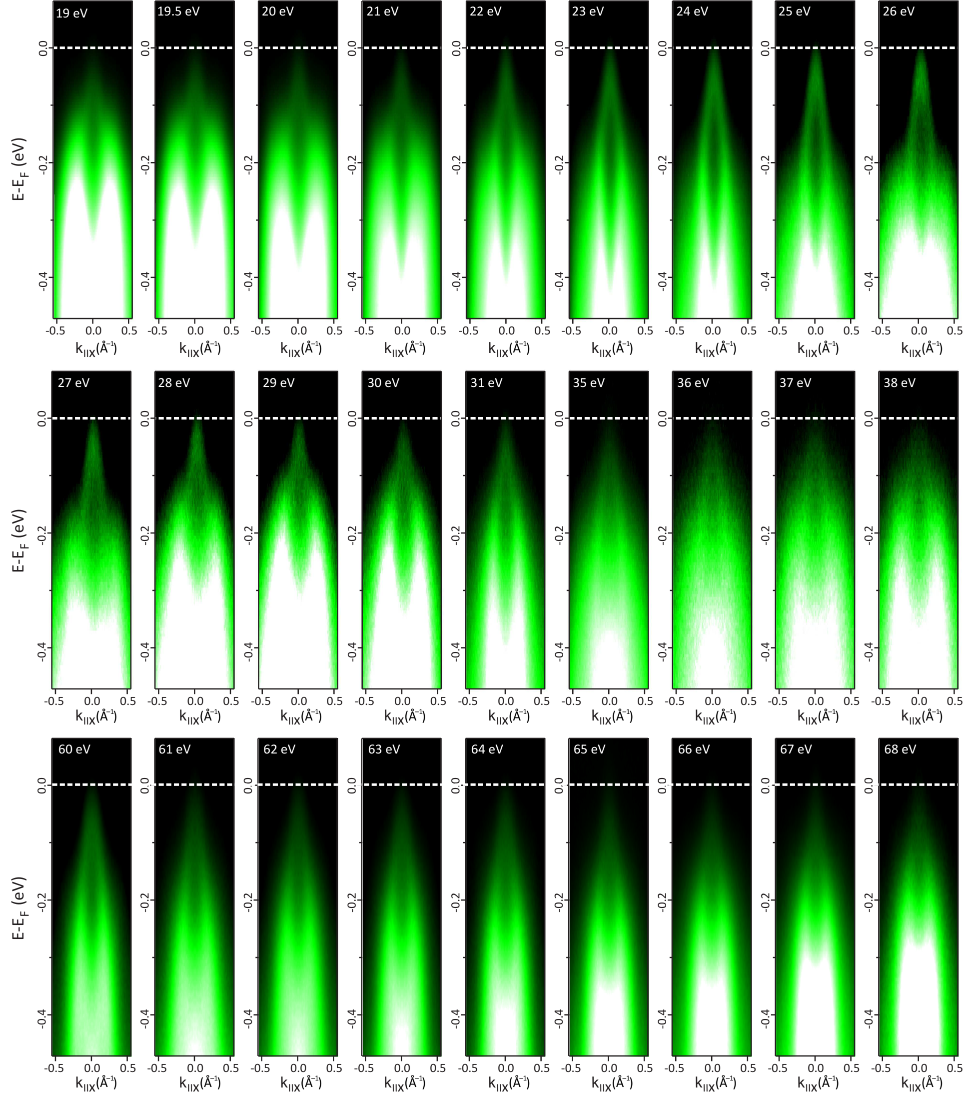

Figure S5. **Photon-energy-dependent ARPES data.** Energy-momentum dispersions for photon energies from 19 to 68 eV showing a 2D Dirac cone and the dispersion of 3D bulk states with photon energy. The periodicity in the bulk dispersion demonstrates that the bulk Brillouin zone is probed completely.

hν (eV)	k_z(Å^{-1})
60	4.341
61	4.371
62	4.401
63	4.431
64	4.460
65	4.490
66	4.519
67	4.548
68	4.576

Table II. **Perpendicular momentum.** Determination of the perpendicular momentum for the data shown in Fig. 2a,b, main text. Distance from Γ to Z corresponds to 0.1327 Å^{-1}. An inner potential of 11.8 eV was used.

S9: SCANNING TUNNELING MICROSCOPY AND SPECTROSCOPY

A: Measurement Details

STM measurements were conducted in a home built UHV-STM operating down to $T = 4.3\,\mathrm{K}$. Cr tips were firstly etched ex-situ and additionally prepared in UHV by field emission on clean W(110). Topography images were recorded in constant-current mode at a tunneling current I and bias voltage V applied to the sample. The $\mathrm{d}I/\mathrm{d}V(V)$ spectra for scanning tunneling spectroscopy (STS) were recorded after firstly stabilizing the tip-sample distance at voltage $V_{\mathrm{Stab}} = -0.1\,\mathrm{V}$ and current $I_{\mathrm{Stab}} = 0.1\,\mathrm{nA}$, if not mentioned differently in the captions. Afterwards, the feedback loop was opened and $\mathrm{d}I/\mathrm{d}V$ was recorded using standard lock-in technique with modulation frequency $f = 1219\,\mathrm{Hz}$ and amplitude $V_{\mathrm{mod}} = 1.4\,\mathrm{mV}$ while ramping V. The spectra were normalized to account for remaining vibrational noise during stabilization by equilibrating the integral between V_{Stab} and $V = 0\,\mathrm{mV}$. We crosschecked that dI/dV curves barely depend on the chosen I_{stab} and, hence, on the tip-surface distance (Fig. S6).

For measurements above the base temperature of 4.3 K, the STM body was exposed

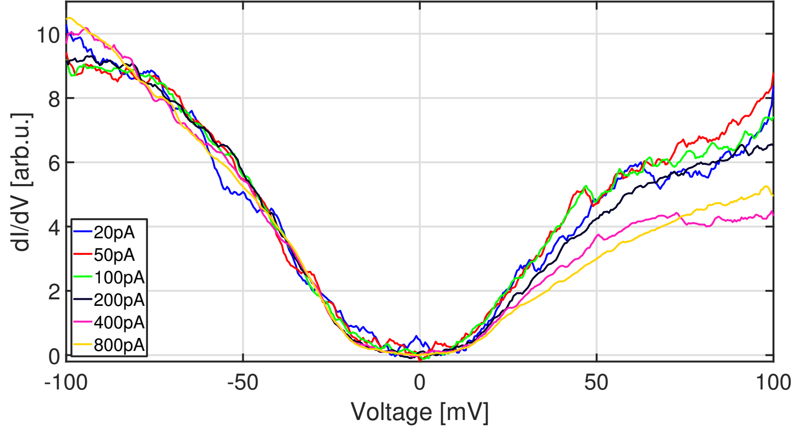

Figure S6. **STS curves recorded at different set points.** $dI/dV(V)$ curves recorded at the same position after stabilizing the tip at $V_{\text{stab}} = -100\,\text{mV}$ and various I_{stab} as marked, $T = 4.3\,\text{K}$.

to thermal radiation via opening of a radiation shield until a maximum $T \simeq 60\,\text{K}$ was achieved. Then, the shield was closed, and $\text{d}I/\text{d}V(V)$ curves were recorded while the sample temperature slowly decreased back to 4.3 K. Measurements at constant $T > 4.3\,\text{K}$ were performed with partly open shield. A more frequent stabilization between subsequent dI/dV curves was necessary due to the remaining thermal drift of the tip-sample distance during the cooling process. This implies shorter recording times that have been compensated by a more intense averaging of subsequently recorded curves.

B: Band Gap Determination at 4.3 K

The band gaps at $T = 4.3\,\text{K}$ were determined as follows. First, the noise level of the dI/dV curves was reduced by averaging 3×3 curves covering an area of $(1.2\,\text{nm})^2$. Subsequently, an averaging of $dI/dV(V)$ across $\pm 2\,\text{mV}$ in bias direction was employed. Then, we estimated the remaining dI/dV noise level as the maximum of $|dI/dV|$ that appears with similar strength positively and negatively. For that purpose, we employed about 50 randomly selected $dI/dV(V)$ curves. Afterwards, the threshold was chosen slightly above the determined noise level. This threshold is marked in Fig. 3a #1 as dashed line and in Fig. 3c as yellow line in the color code bar. The voltage width, where the $dI/dV(V)$ spectra stayed below this threshold, defines the measured gap Δ as used in Fig. 3a–c, main text.

We crosschecked that dI/dV values below the noise level appeared exclusively close to the determined band gap areas. The resulting gap size Δ turned out to barely depend on details of the chosen noise threshold.

Figure S7a and b display two additional $\Delta(x, y)$ maps like the ones in Fig. 3b, main text, but recorded on different areas of the sample surface. They exhibit a similar range of spatial fluctuations of Δ as shown in Fig. 3b, main text. Sometimes, Δ could not be determined from the $dI/dV(V)$ curves as, e.g., in the bright area marked by a black circle in Fig. S7a. There, the spectra stayed below the threshold on the positive $V > 0\,\mathrm{mV}$ side up to $100\,\mathrm{mV}$ while a gap edge is observed only on the negative side, for an unknown reason. These spectra ($\sim 5\,\%$ of all spectra) are discarded from further analysis including the histogram of Fig. 3b, main text. The correlation length ξ of $\Delta(x, y)$ is calculated as FWHM of the correlation function resulting in $\xi \simeq 2\,\mathrm{nm}$ as given in the main text.

The central energy within the gap, E_0, is deduced as the arithmetic mean of all voltages where the $\mathrm{d}I/\mathrm{d}V$ signal remains below the threshold. Figure S7c–f displays maps $E_0(x, y)$ for the three studied areas as well as a resulting E_0 histogram. Favorably, the average of E_0 is rather precisely at E_F showing only small spatial fluctuations in the meV range. The small discrepancy of the average $E_0 \simeq E_\mathrm{F}$ found by STS to the Dirac point determined by ARPES ($20\,\mathrm{meV}$ above E_F) might be due to the different recording temperatures ($4.3\,\mathrm{K}$ vs. $300\,\mathrm{K}$) or to sample to sample variations.

C: $dI/dV(V)$ Curves at Different Temperatures

Figure S8 displays $dI/dV(V)$ spectra recorded at various temperatures as used for the band gap evaluation displayed in Fig. 3d, main text. An obvious band gap with a voltage region of $dI/dV \simeq 0\,\mathrm{nS}$ is only found up to about $30\,\mathrm{K}$. At larger T, the curves partly stay close to $dI/dV = 0\,\mathrm{nS}$ around E_F, but partly strongly deviate from $dI/dV = 0\,\mathrm{nS}$. This varying behaviour requires a more detailed analysis to determine Δ, since a small deviation from $dI/dV = 0\,\mathrm{nS}$ might also be caused by Fermi level broadening of the tip that probes a local density of states (LDOS) of the sample with a small band gap.

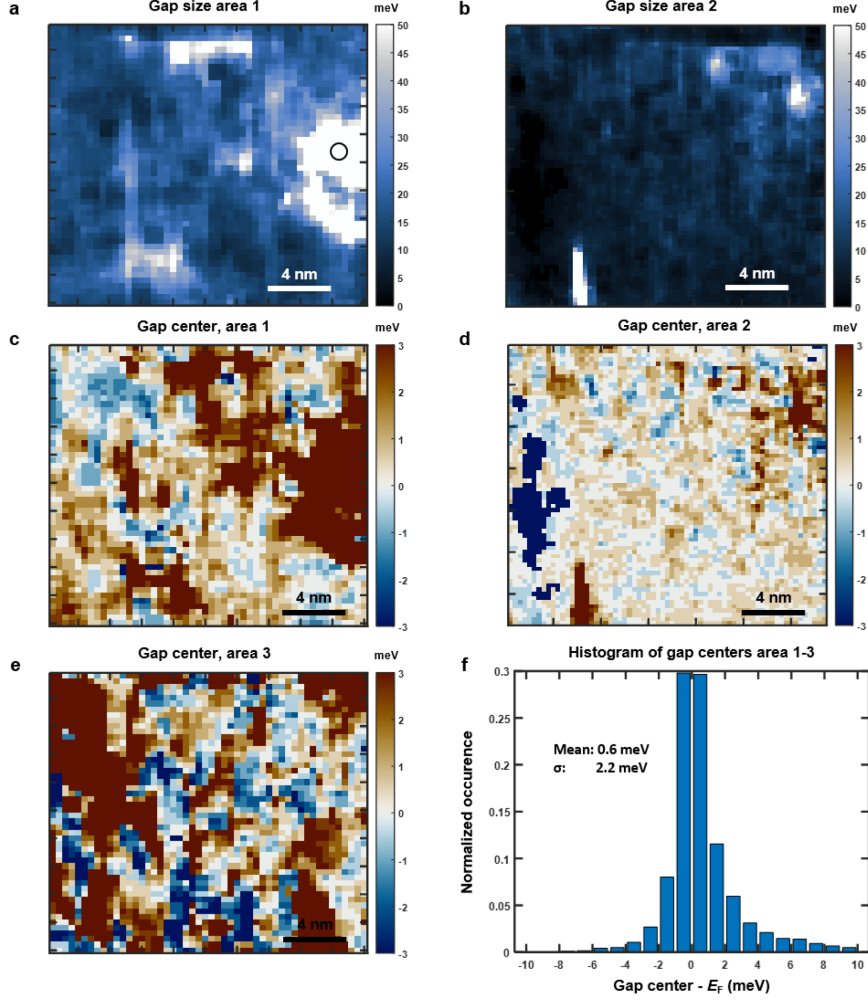

Figure S7. **Maps of gap size Δ and gap center E_0 at 4.3 K.** (a,b) Spatial maps of the gap size $\Delta(x, y)$ as obtained from $dI/dV(V)$ curves recorded at $T = 4.3$ K. Two additional surface areas named area 1 and area 2 are shown, while area 3 is displayed in Fig. 3b, main text. The black circle marks a region, where the determination of a band gap was not possible (see text). (c)-(e) Spatial maps of the center of the gap $E_0(x, y)$ with respect to the Fermi level E_F for the 3 different areas. (f) Histogram of E_0 for all three maps with marked mean and standard deviation σ.

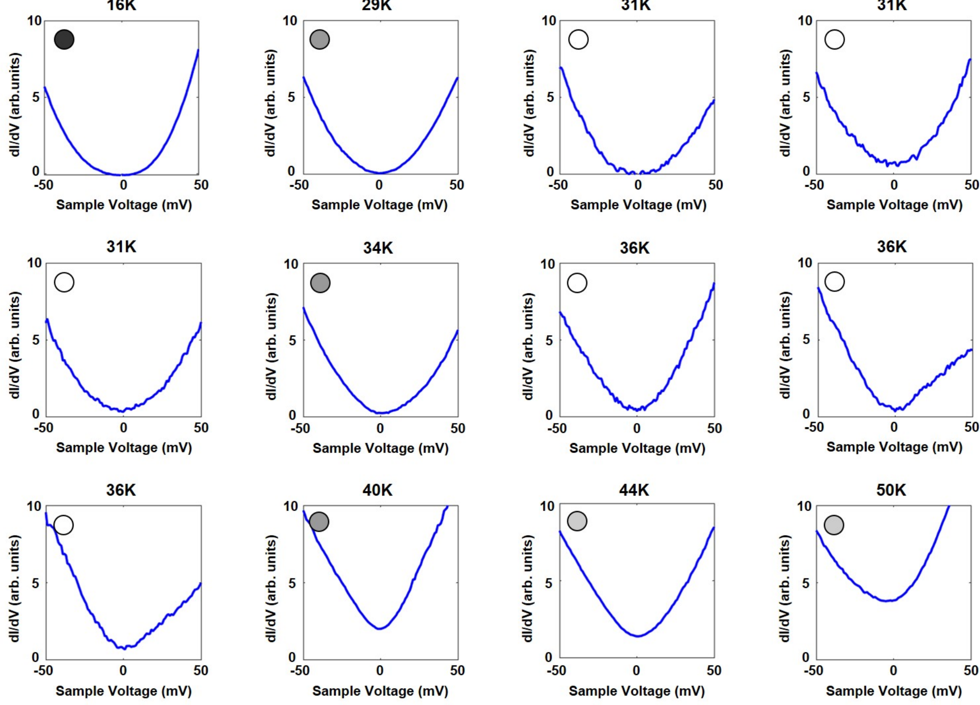

Figure S8. **STS spectra recorded at different temperatures.** Selected dI/dV(V) curves ordered with increasing T as marked on top. The dot in the upper left is colored identically to the extracted band gap from the same curve as displayed in Fig. 3d, main text.

D: Determination of Band Gaps at Elevated Temperature

The requirement of a more detailed analysis is demonstrated in Fig. S9a. A $dI/dV(V)$ spectrum exhibiting a gap size $\Delta = 17\,\mathrm{meV}$ is displayed (blue line) as recorded at 4.3 K. This spectrum is then convolved with the derivative of the Fermi-Dirac distribution function, proportional to $1/\cosh^2(eV/2k_\mathrm{B}T)$ [4] (other colored lines in Fig. S9a). By this convolution, we mimick the expected appearance of the same spectrum at elevated T. Obviously, the previously introduced method of gap determination would obtain $\Delta = 0\,\mathrm{meV}$ for all $T \geq$ 31 K, albeit the LDOS of the sample still exhibits $\Delta = 17\,\mathrm{meV}$.

In order to deduce the correct Δ from $dI/dV(V)$ curves recorded at such large T, we introduce the ratio $R = [\mathrm{d}I/\mathrm{d}V(0\,\mathrm{mV})]/[\mathrm{d}I/\mathrm{d}V(-50\,\mathrm{mV})]$ that turns out to be monotonously

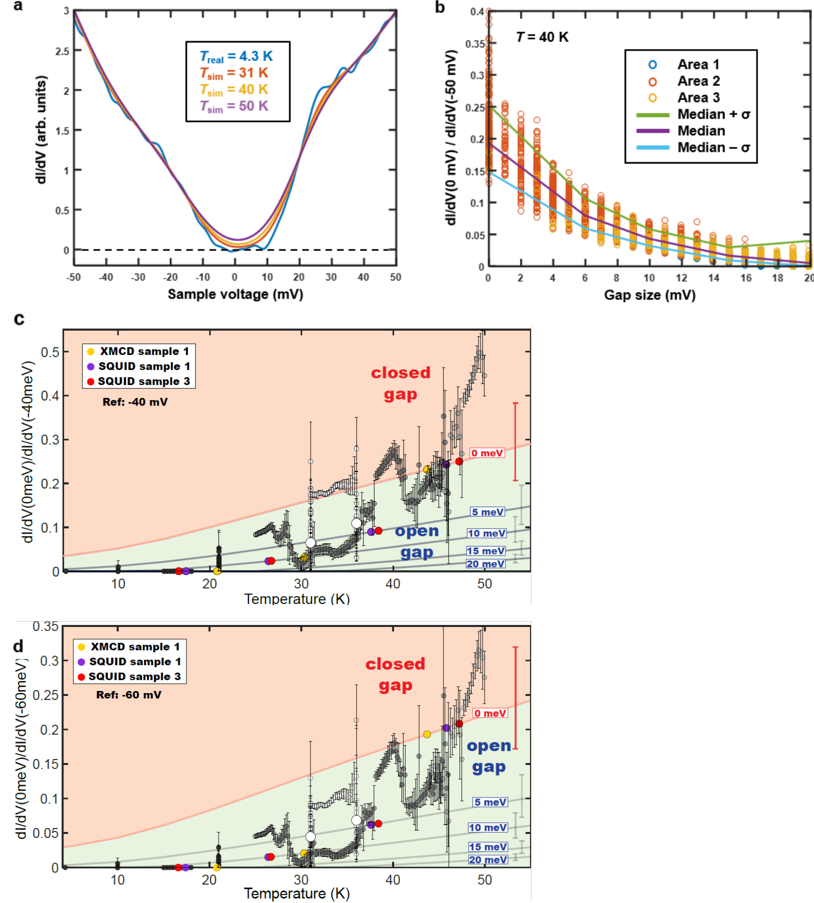

Figure S9. **Gap size determination at elevated T.** (a) $dI/dV(V)$ spectrum with gap $\Delta = 17\,\mathrm{meV}$ recorded at 4.3 K (blue) and the same spectrum after convolution with the derivative of the Fermi-Dirac distribution function for $T = 31\,\mathrm{K}$ (red), $T = 40\,\mathrm{K}$ (yellow) and $T = 50\,\mathrm{K}$ (violet). The Fermi level broadening leads to an apparently ungapped dI/dV curve, albeit the sample LDOS features a gap of 17 meV. (b) Relation between the measured gap size Δ of $dI/dV(V)$ curves recorded at 4.3 K and the ratio $R = [dI/dV(V = 0\,\mathrm{mV})]/[dI/dV(V = -50\,\mathrm{mV})]$ of the same $dI/dV(V)$ curves deduced after convolution with the derivative of the Fermi-Dirac distribution function at 40 K. Different circle colors: different areas (Fig. S7). Colored lines: median (violet) surrounded by the standard deviation $\pm\sigma$ (green, blue). (c,d) Same as Fig. 3d, main text, but using a different reference voltage V_{ref} to determine R. (c) $V_{\mathrm{ref}} = 40\,\mathrm{mV}$, (d) $V_{\mathrm{ref}} = 60\,\mathrm{mV}$.

anticorrelated with the gap size Δ. This is demonstrated in Fig. S9b for $T = 40\,\mathrm{K}$. All $dI/dV(V)$ curves recorded at 4.3 K (area 1–3, 8000 curves) are convoluted with the derivative of the Fermi-Dirac distribution of 40 K (as in Fig. S9a, yellow curve) before R is determined. Subsequently, each R is related to its corresponding Δ (same $dI/dV(V)$ curve) as deduced via the method described in subsection S9 B. The anticorrelation of R and Δ appears in Fig. S9b and is similarly found for all $T = 25-50\,\mathrm{K}$ (not shown). We used the resulting median of the simulated R values (violet line in Fig. S9b) to deduce Δ from a measured R for each $dI/dV(V)$ curve recorded at elevated T. The required simulated $R(T)$ curves for constant Δ are displayed as full lines in Fig. 3d, main text, for the sake of comparison with the R values of the measured $\mathrm{d}I/\mathrm{d}V$ curves. The error of $R(\Delta)$ at given T is taken as the 2σ width of the simulated $R(\Delta)$, marked by colored lines in Fig. S9b. For gap sizes below 10 meV, one observes an error of 2–4 meV only. Overall, the $R(\Delta)$ relation reaches a relative accuracy for Δ determination of $\pm 30\,\%$, as long as Δ remains below 20 meV. This error is displayed exemplarily on the very right of Fig. 3d, main text.

In addition, we determined errors for the measured R values. They are deduced as the standard deviation of subsequently recorded 25 $\mathrm{d}I/\mathrm{d}V(V)$ data sets (averaged from 10 subsequent $\mathrm{d}I/\mathrm{d}V$ curves each and smoothed by box averaging of width 3 mV). The measurement errors are displayed as error bars at the data points in Fig. 3d, main text (circles). Interestingly, these measurement errors increase significantly around $T \simeq 45\,\mathrm{K}$, i.e., close to T_{C}, where they get as large as 10 meV. Since the spatial drift during recording of the 25 data sets is below 1 nm, as deduced by comparing the long term development of $\mathrm{d}I/\mathrm{d}V$ data during cooling to the spatial fluctuations recorded at 4.3 K, these relatively large errors cannot be caused by a lateral drift of the tip with respect to the sample only. Likely, they are caused by enhanced temporal fluctuations of the gap close to T_{C} during recording of the 25 data sets. Thus, the increased error bars around T_{C} corroborate the relation of the band gap evolution to the magnetic properties additionally.

Error bars of the spatially averaged data points in Fig. 3d, main text, indicate the width of the R histograms obtained at the corresponding T.

The reference voltage $V_{\mathrm{ref}} = -50\,\mathrm{mV}$ used to determine R is chosen such that it is not influenced by temperature ($|eV_{\mathrm{ref}}| \gg 5k_{\mathrm{B}}T$) or gap size ($|eV_{\mathrm{ref}}| \gg \max(\Delta)/2$) and not influenced by spectroscopic features that might spatially vary due to disorder. We cross-checked that the exact value of V_{ref} barely influences the deduced Δ. This is demonstrated

in Fig. S9c–d displaying the same data set as Fig. 3d, main text, but using two different V_{ref}.

S10: ELECTRIC TRANSPORT MEASUREMENTS

Transport invstigations were performed in the van der Pauw geometry with applied magnetic fields ranging from -3 T to +3 T oriented parallel to the rhombohedral axis of the epilayers. A mini cryogen-free system was employed for the magnetotransport measurements at temperatures between 2 K and 300 K. The results are shown in Fig. S10, where the Hall and anomalous Hall effect as well as the magnetoresistance are shown as a function of applied field and temperature. Evidently, the anomalous Hall effect appears at temperatures below about 50 K where a pronounced hysteresis appears in the transport data at fields less than about 1 T. This perfectly agrees with the onset of ferromagnetism detected by SQUID and XMCD at temperatures of 45 – 50K. The carrier concentration in the films was determined from the Hall resistance above 1 T, i.e., well above the coercive field. The deduced hole concentrations of the $MnSb_2Te_4$ samples range from 1 to $3 \cdot 10^{20}\mathrm{cm}^{-3}$, similar to values reported in the literature [5, 6].

S11: DENSITY FUNCTIONAL THEORY CALCULATIONS

A: Details of the Calculations

The electronic and magnetic structures were calculated by two different methods based on density functional theory (DFT). Most of the bulk-type calculations (Figs. 4f–k, main text, Fig. S11, Fig. S12a,b) used a Green function method within the multiple scattering theory [7, 8]. To describe both localization and interaction of the Mn $3d$ orbitals appropriately, Coulomb U values of 3–5 eV were employed within a GGA+U approach [9]. During these calculations, we confirmed that different topological phases of $MnSb_2Te_4$ arise, if one uses either GGA+U or LDA+U, indicating that LDA+U is not sufficient. To account for antiferromagnetic configurations of $MnSb_2Te_4$, a double unit cell consisting of two septuple layers was used such as for Fig. 4k, main text, and Fig. S11a and c. In these structures, the Mn atoms couple ferromagnetically within the Mn planes and antiferromagnetically between neighboring Mn layers in adajacent septuple layers. For the determination of T_{N} and

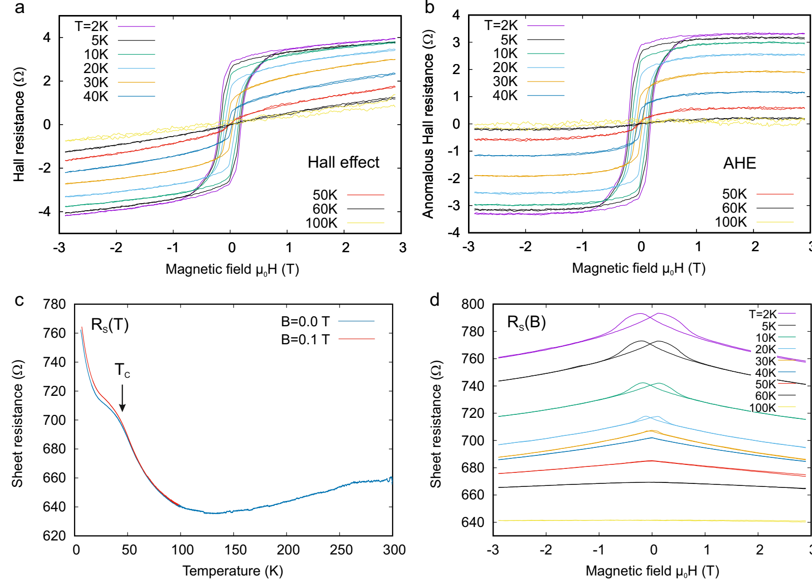

Figure S10. **Electrical transport of ferromangetic $MnSb_2Te_4$ films.** (a) Hall resistance, (b) anomalous Hall resistance and (d) magnetoresistance as a function of applied magnetic field recorded at various temperatures between 2 and 100 K, as indicated. Also shown in (c) is the sheet resistance as a function of temperature. All measurements clearly indicate ferromagnetic behavior with a T_C close to 50 K, in agreement with SQUID and XMCD measurements.

T_C, exchange constants J_{ij} were obtained by mapping the DFT calculations onto a classical Heisenberg model [10].

Different types of disorder were treated within a coherent potential approximation (CPA) [11, 12]. Chemical disorder is modelled by mixing various atomic species on the same atomic site (substitutional alloys). The elemental unit cell was used in this case such that only ferromagnetic order could be described. We simulated three types of chemical disorder, namely site exchange, i.e., placing as much Mn on Sb sites as Sb on Mn sites, Sb excess, i.e., additional, substitutional Sb in the Mn layers, and Mn excess, i.e., additional, substitutional Mn in the Sb layers. Electron (hole) doping was also modeled by CPA via mixing Te (Sb)

vacancies, that were simulated as empty spheres, with Te (Sb) atoms on the same site. Magnetic moment disorder was modeled by CPA via mixing two Mn atoms with opposite magnetic moment on the same atomic site. This approach has been proven to be very successful in mimicking spin moment fluctuations, e.g., to account for elevated temperatures. The 50 : 50 mixing represents the paramagnetic state, while smaller spin fluctuations are described by, e.g., 95 : 5 or 98 : 2 mixings.

The calculations in Fig. S12c–f were performed with the full-potential linearized augmented plane-wave method as implemented in the FLEUR code. Also here, GGA [13] with a Hubbard U correction using $U = 6$ eV and $J = 0.54$ eV was used and spin-orbit coupling was included self-consistently in the non-collinear calculations [14]. Thin film calculations were also performed with the FLEUR code (Fig. 4c, main text, and Fig. S13b–e). These calculations are restricted to relatively small and simple unit cells in order to retain high enough accuracy to derive the Dirac cone dispersion and the size of its magnetic gap by DFT. Instead, the surface band structure for the antiferromagnetic ground state in Fig. 4d–e, main text, for the ferromagnetic ground state in Fig. 4b, main text, and for the mixed state in Fig. S13a was calculated by the projector augmented-wave method [15] using the VASP code [16, 17]. The exchange-correlation energy was treated using the GGA [13]. The Hamiltonian contained scalar relativistic corrections and the spin-orbit coupling was taken into account by the second variation method [18]. In order to describe the van der Waals interactions, we made use of the DFT-D3 [19, 20] approach. The Mn $3d$ states were treated employing the GGA+U approximation [9] within the Dudarev scheme [21]. The $U_{\text{eff}} = U - J$ value for the Mn $3d$ states was chosen to 5.34 eV as in previous works [22–25].

For all three methods, the crystal structure of ideal $MnSb_2Te_4$ was fully optimized to obtain the equilibrium lattice parameters, namely cell volume, c/a ratio as well as atomic positions. Using this structure yields the antiferromagnetic topological insulator state for $MnSb_2Te_4$ within both the projector augmented-wave and full-potential linearized augmented plane-wave methods (VASP and FLEUR, respectively). For the Green function method both the experimental crystal structure as determined by XRD (Fig. S2) and the theoretically optimized one result in the antiferromagnetic topological insulator phase.

In order to visualize the topological character within bulk-type band structure calculations, we analyze the spectral function difference between anion and cation contributions of each state: $A^i_k(E) = A^{\text{anion}}_k(E) - A^{\text{cation}}_k(E)$. The resulting $A^i_k(E)$ are displayed as color

		$MnSb_2Te_4$				$MnSb_2Te_4$ with lattice
		0% disorder	5% disorder	5% extra Mn		constants of $MnBi_2Te_4$
		T_N=18 K	T_C=25 K	T_C=44 K		T_N=20 K
direction	r (Å)	J (meV)	J (meV)	J (meV)	r (Å)	J (meV)
||	4.23	0.519	0.458	0.674	4.34	0.180
||	7.36	-0.024	0.034	0.024	7.51	-0.007
||	8.52	0.016	0.025	0.033	8.68	0.025
⊥	16.8	-0.02	0.002	0.04	16.4	-0.035

Table III. **Magnetic structure, critical temperature, and Mn exchange integrals of $MnSb_2Te_4$ for four different crystal configurations (DFT).** The exchange integrals J for the four smallest distances r between the contributing Mn ions are additionally marked by $\|$ ($\perp$) for intralayer (interlayer) Mn pairs. The model with 0% disorder refers to ideal $MnSb_2Te_4$ with all Mn atoms in the central plane of the septuple layers at the experimental lattice constants $a = 4.23$ Å, $c = 40.98$ Å (XRD). In the second model (5% disorder), a Mn-Sb site exchange leads to an occupancy of 95% Mn and 5% Sb in the central lattice plane and 2.5% Mn and 97.5% Sb in each of the two outer cationic lattice planes of the septuple layer. In the third case, 2.5% extra Mn was substitutionally introduced in the Sb layers, such that the outer cationic planes contain 2.5% Mn and 97.5% Sb, while a 100% Mn occupancy appears in the central layer. The fourth model features ideal $MnSb_2Te_4$ with 0% disorder, but laterally expanded to the lattice constants of $MnBi_2Te_4$, i.e., $a = 4.34$ Å, $c = 40.89$ Å.

code in Fig. 4f–k, main text, Fig. S11, and Fig. S12a,b with red color for $A^i_k(E) > 0$ and blue color for $A^i_k(E) < 0$. Band inversion can, hence, be deduced from a mutually changing color within adjacent bands.

B: Magnetic Ground State for Different Disorder Configurations

Table III summarizes the magnetic properties for four different crystallographic configurations as obtained by bulk-type DFT calculations. The ideal $MnSb_2Te_4$ septuple layer configuration is antiferromagnetic with low $T_N = 18\,K$ (third row). To probe the role of the lattice constant for the magnetic properties, we slightly expanded the lattice within the

planes towards the lattice constant of $MnBi_2Te_4$ (last row). This led to a reduced nearest neighbor exchange constant J, but barely to a change in T_N. Introducing 5 % Mn-Sb site exchange, in line with the XRD and STM data, turned the interlayer coupling ferromagnetic, but still with a $T_C = 25$ K only, i.e., significantly lower than the experimental value (fourth row). However, adding 2.5 % Mn to each Sb layer in the septuple without removing Mn from the central layer of the septuple, i.e., incorporation of 5 % excess Mn, yields $T_C = 44$ K, very close to the experimental value (fifth row). Hence, we conclude, in line with RBS, STM and XRD data, that an excess Mn in combination with an Sb deficiency is responsible for the high ferromagnetic Curie temperature via Mn substitution in the Sb layers.

C: Topological Properties for Different Disorder Configurations

Figure S11 shows bulk band structure calculations for antiferromagnetic $MnSb_2Te_4$ with ideal stoichiometric order (a,c), ideal, ferromagnetic $MnSb_2Te_4$ (e) and ferromagnetic $MnSb_2Te_4$ with increasing Mn-Sb site exchange (b,d,f). Antiferromagnetic $MnSb_2Te_4$ is a topological insulator with inverted band gap at Γ, if spin-orbit coupling is considered (c). This is contrary to previous calculations that have suggested antiferromagnetic $MnSb_2Te_4$ to be trivial [26–29]. We assume that the topological insulator state of antiferromagnetic $MnSb_2Te_4$ was missed because structural optimization was either not performed in favor of experimental lattice constants [27, 29] or performed without van der Waals forces [26, 28] which both gave by $\sim 3\%$ larger c parameters than in the structurally optimized equilibrium lattice. Ferromagnetic $MnSb_2Te_4$ instead, is a Weyl semimetal without band gap that remains a Weyl semimetal for moderate Mn-Sb site exchange (Fig. S11b,d), but becomes topologically trivial at large site exchange (Fig. S11f). Hence, site exchange alone does not reveal the experimentally observed ferromagnetic topological insulator in contrast to the magnetic disorder as presented in Fig. 4g–j, main text.

Figure S12 corroborates the gap opening by magnetic disorder. Figure S12b displays the complete band structure at maximum spin mixture (50 % spin-up, 50 % spin down) for each Mn lattice site as partially presented in Fig. 4j, main text. An inverted band gap of about 100 meV is found at Γ. Note that the purely ferromagnetic phase in Fig. S12a is calculated for a unit cell of a single septuple layer only and, hence, differs from Fig. S11e employing a unit cell with two septuple layers, due to backfolding.

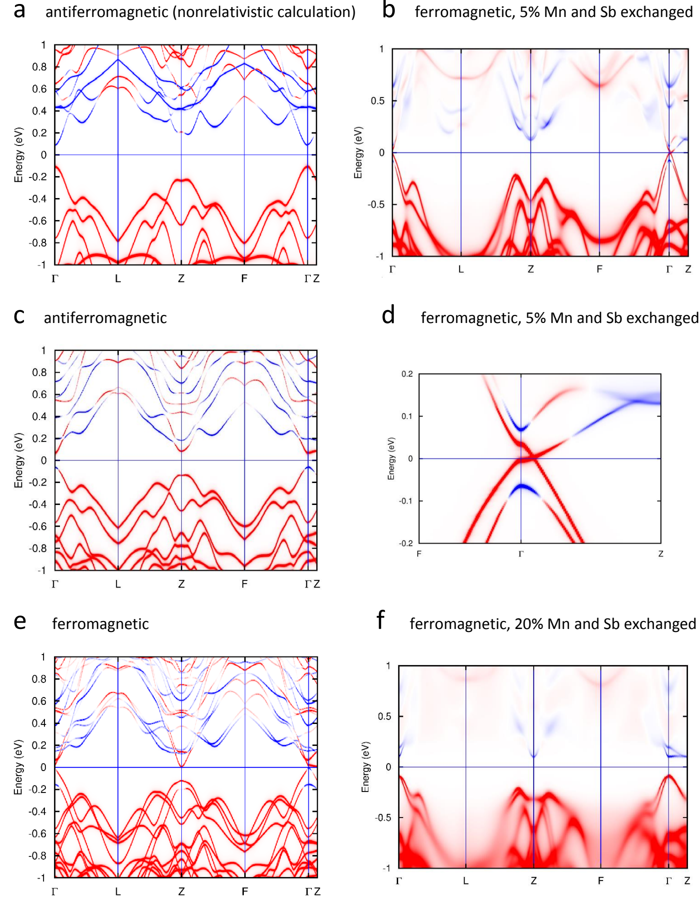

Figure S11. **Band Structure at Different Strength of Mn-Sb Site Exchange (DFT)**. Color represents the difference between anionic and cationic spectral function for each state, red: more anionic, blue: more cationic. (a) Antiferromagnetic, ideal $MnSb_2Te_4$ in a nonrelativistic (more precisely scalar relativistic) calculation. No band inversion occurs. (c) Antiferromagnetic, ideal $MnSb_2Te_4$ in a fully relativistic calculation yielding a band inversion. Only one inversion appears in the Brillouin zone (at Γ) evidencing a Z_2 topological insulator. (Also shown as Fig. 4k, main text, for the ferromagnetic unit cell.). (e) Same as (c) but for ferromagnetically ordered, ideal $MnSb_2Te_4$ with perfect out-of-plane alignment of Mn moments. A 3D Weyl semimetal occurs. The calculation used the antiferromagnetic unit cell for better comparison with (c). (b, d, f) Ferromagnetic $MnSb_2Te_4$ with different Mn-Sb site exchange as labeled (ferromagnetic unit cell). In (b) and (d), the Weyl point is preserved, while (f) shows a topologically trivial band gap.

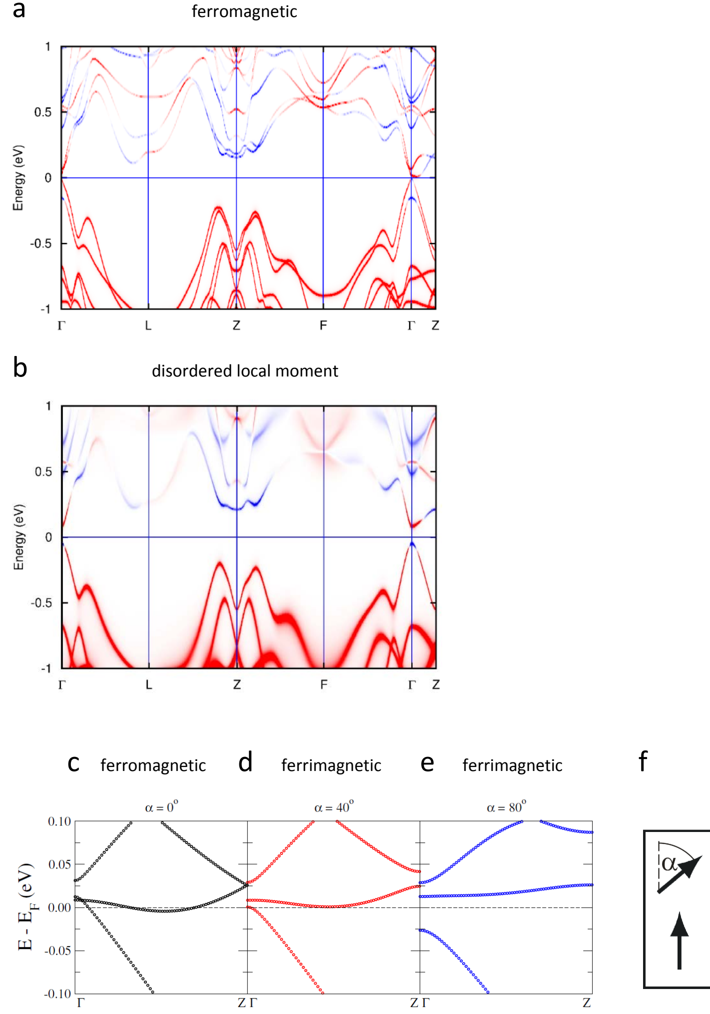

Figure S12. **Inverted band gap by magnetic disorder (DFT).** (a) Bulk band structure of ideal, ferromagnetic $MnSb_2Te_4$ with Mn moments perpendicular to the septuple layers (single layer unit cell). (Part of this figure is shown as Fig. 4f, main text.) (b) Same as (a), but with disordered local magnetic moments (50% spin up, 50% spin down). An inverted band gap appears at Γ. (Part of this figure is shown as Fig. 4j, main text.) (c–e) Alternative demonstration of gap opening at the Weyl point (two septuple layer unit cell): one layer exhibits a collinear out-of-plane ferromagnetic order, while the other is also collinear, but canted relative to the first one by an angle α as marked. (f) Vector model of the collinearly canted two septuple layers.

The Weyl point observed for the ferromagnetic $MnSb_2Te_4$ can also be opened by rotating the spins of adjacent Mn layers, while keeping a collinear spin order within each layer (Fig. S12c–f). Thus, magnetic disorder renders a dominantly ferromagnetic $MnSb_2Te_4$ a topological insulator as already discussed for Fig. 4g–j, main text.

Figure S13 shows the band structures of slab calculations for different magnetic disorder configurations, such that surface states are captured. They are performed, e.g., for a combination of ferromagnetic interior layers surrounded by a few antiferromagnetic layers on top and bottom (Fig. S13a). This configuration reveals a Dirac-type surface state with a gap around the Dirac point of 16 meV, very close to the average gap size observed by STS. The opposite configuration with antiferromagnetic interior surrounded by ferromagnetic surfaces also exhibits a gapped Dirac cone, here with 40 meV gap size, that might be enhanced by the thickness of this slab of only 7 septuple layers (Fig. S13d). Indeed, the spin-polarized states at the gap edge penetrate about 3 septuple layers into the bulk of the thin film (Fig. S13b). The out-of-plane spin polarization near the Dirac point amounts to $\sim 60\%$, nicely matching the experimentally found out-of-plane spin polarization in spin-resolved ARPES (Fig. 2j, main text). The latter amounts to $\sim 25\,\%$ at 30 K in line with the reduced magnetization at this elevated T (Fig. 1d,f, main text). Note that the band structure in Fig. S13d also features an exchange splitting of bulk bands as visible by the different colors around -0.2 eV.

The pure antiferromagnetic configuration (Fig. S13e) shows a small band gap of the topological surface state as well, while the pure ferromagnetic order leads to a gapped Weyl cone (Fig. S13c), likely being an artifact of the finite slab size of 7 septuple layers only.

D: Influence of Charge Doping on the Magnetic Interactions

Finally, the influence of charge doping on the magnetic properties of $MnSb_2Te_4$ was studied. For undoped, ideally stacked $MnSb_2Te_4$, the leading magnetic interaction between the septuple layers is of a superexchange type, which is responsible for the antiferromagnetic interlayer coupling. As shown above, chemical disorder by exchanging (replacing) Mn with (by) Sb changes the magnetic order to ferromagnetic. The presence of Mn defects could induce an additional Ruderman-Kittel-Kasuya-Yoshida (RKKY) interaction that might influence the magnetic order, if mobile charges are present. However, our calculations show only minor changes of exchange constants and the magnetic transition temperatures upon

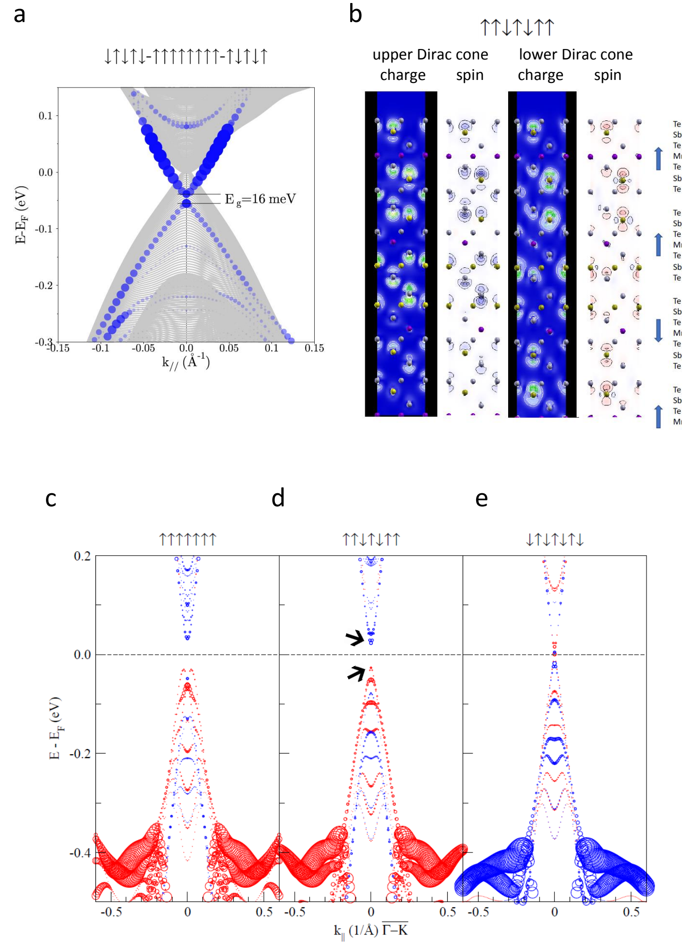

Figure S13. **Influence of magnetic structure on topological surface states (DFT).** (a) Band structure for a ferromagnetic bulk surrounded by antiferromagnetic surface layers as marked on top. Blue dots are surface states with dot diameter marking their strength at the surface septuple layer. A gap appears in the topological surface state. (b) Charge density and spin density of the states at the edges of the magnetically induced band gap in (d) displayed as thin film cross section. The magnetic configuration is marked on top. (c–e) Band structure for various magnetic configurations each marked on top. Colors denote the spin density in the out-of-plane direction. (c) Ferromagnetic order with out-of-plane anisotropy. (d) Two ferromagnetic septuple layers on both sides of three antiferromagnetic layers. Black arrows mark the states shown in (b). (e) Perfect antiferromagnetic order as in Fig. 4d,e, main text.

charge doping. For n-type doping by 0.2% Te vacancies, E_{F} shifts by 0.29 eV increasing T_{C} by 0.9 K only. For p-type doping by 0.2% Sb vacancies, E_{F} shifts by -0.08 eV increasing T_{C} by 1.6 K. This indicates that the RKKY interaction is negligible in $MnSb_2Te_4$.

[1] M. Mayer, *Nuclear Instrum. Methods B* **2014**, *332* 176.

[2] H. Steiner, V. Volobuev, O. Caha, G. Bauer, G. Springholz, V. Holý, *J. Appl. Cryst.* **2014**, *47*, 6 1889.

[3] E. D. L. Rienks, S. Wimmer, J. Sánchez-Barriga, O. Caha, P. S. Mandal, J. Růžička, A. Ney, H. Steiner, V. V. Volobuev, H. Groiss, M. Albu, G. Kothleitner, J. Michalička, S. A. Khan, J. Minár, H. Ebert, G. Bauer, F. Freyse, A. Varykhalov, O. Rader, G. Springholz, *Nature* **2019**, *576*, 7787 423.

[4] M. Morgenstern, *Surf. Rev. Lett.* **2003**, *10*, 06 933.

[5] J.-Q. Yan, S. Okamoto, M. A. McGuire, A. F. May, R. J. McQueeney, B. C. Sales, *Phys. Rev. B* **2019**, *100*, 10 104409.

[6] Y. Chen, Y.-W. Chuang, S. H. Lee, Y. Zhu, K. Honz, Y. Guan, Y. Wang, K. Wang, Z. Mao, J. Zhu, C. Heikes, P. Quarterman, P. Zajdel, J. A. Borchers, W. Ratcliff, *Phys. Rev. Mat.* **2020**, *4*, 6 064411.

[7] B. L. Gyorffy, M. J. Stott, In D. J. Fabian, L. M. Watson, editors, *Proc. of the Int. Conf. on Band Structure and Spectroscopy of Metals and Alloys.* Academic Press, **1973** 385.

[8] M. Geilhufe, S. Achilles, M. A. Köbis, M. Arnold, I. Mertig, W. Hergert, A. Ernst, *J. Phys.: Condens. Matter* **2015**, *27*, 43 435202.

[9] V. I. Anisimov, J. Zaanen, O. K. Andersen, *Phys. Rev. B* **1991**, *44*, 3 943.

[10] A. Liechtenstein, M. Katsnelson, V. Antropov, V. Gubanov, *J. Magn. Magn. Mat.* **1987**, *67*, 1 65.

[11] P. Soven, *Phys. Rev.* **1967**, *156*, 3 809.

[12] B. L. Gyorffy, *Phys. Rev. B* **1972**, *5*, 6 2382.

[13] J. P. Perdew, K. Burke, M. Ernzerhof, *Phys. Rev. Lett.* **1996**, *77*, 18 3865.

[14] P. Kurz, F. Förster, L. Nordström, G. Bihlmayer, S. Blügel, *Phys. Rev. B* **2004**, *69* 024415.

[15] P. E. Blöchl, *Phys. Rev. B* **1994**, *50*, 24 17953.

[16] G. Kresse, J. Furthmüller, *Phys. Rev. B* **1996**, *54*, 16 11169.

[17] G. Kresse, D. Joubert, *Phys. Rev. B* **1999**, *59*, 3 1758.

[18] D. D. Koelling, B. N. Harmon, *Journal of Physics C: Solid State Physics* **1977**, *10*, 16 3107.

[19] S. Grimme, J. Antony, S. Ehrlich, H. Krieg, *J. Chem. Phys.* **2010**, *132*, 15 154104.

4.8 Doping induced topological phase transition of (Pb,Sn)Se

This paper deals with (Pb,Sn)Se topological crystalline insulator. Topological crystalline insulators are merely protected by individual crystal symmetries and exist for an even number of Dirac cones. We demonstrated that Bi-doping of (Pb,Sn)Se (111) epilayers induces a quantum phase transition from a topological crystalline insulator to a $\mathbb{Z}_2$ topological insulator. The transition occurs because Bi-doping lifts the fourfold valley degeneracy and induces a gap at Γ, while the three Dirac cones at the $\bar{M}$ points of the surface Brillouin zone remain intact. We interpret this new phase transition as caused by a lattice distortion. Our findings extend the topological phase diagram enormously and make strong topological insulators switchable by distortions or electric fields.

nature COMMUNICATIONS

ARTICLE

DOI: 10.1038/s41467-017-01204-0 OPEN

Topological quantum phase transition from mirror to time reversal symmetry protected topological insulator

Partha S. Mandal[1,2], Gunther Springholz[3], Valentine V. Volobuev[3,4], Ondrej Caha[5], Andrei Varykhalov[1], Evangelos Golias[1], Günther Bauer[3], Oliver Rader[1] & Jaime Sánchez-Barriga[1]

Topological insulators constitute a new phase of matter protected by symmetries. Time-reversal symmetry protects strong topological insulators of the Z_2 class, which possess an odd number of metallic surface states with dispersion of a Dirac cone. Topological crystalline insulators are merely protected by individual crystal symmetries and exist for an even number of Dirac cones. Here, we demonstrate that Bi-doping of $Pb_{1-x}Sn_xSe$ (111) epilayers induces a quantum phase transition from a topological crystalline insulator to a Z_2 topological insulator. This occurs because Bi-doping lifts the fourfold valley degeneracy and induces a gap at $\overline{\Gamma}$, while the three Dirac cones at the $\overline{\mathrm{M}}$ points of the surface Brillouin zone remain intact. We interpret this new phase transition as caused by a lattice distortion. Our findings extend the topological phase diagram enormously and make strong topological insulators switchable by distortions or electric fields.

[1] Helmholtz-Zentrum Berlin für Materialien und Energie, Albert-Einstein Strasse 15, 12489 Berlin, Germany. [2] Institut für Physik und Astronomie, Universität Potsdam, Karl-Liebknecht Street 24/25, 14476 Potsdam, Germany. [3] Institute for Semiconductor and Solid State Physics, Johannes Kepler Universität, Altenberger Strasse 69, 4040 Linz, Austria. [4] National Technical University "Kharkiv Polytechnic Institute", Frunze Street 21, 61002 Kharkiv, Ukraine. [5] Department of Condensed Matter Physics, Masaryk University, Kotlářská 267/2, 61137 Brno, Czech Republic. Correspondence and requests for materials should be addressed to J.S-B. (email: jaime.sanchez-barriga@helmholtz-berlin.de)

Reprinted page 1 of paper [61] "Topological transition from TCI to TI via Bi doping".

Topological insulators are bulk insulators with a metallic surface state[1]. Provided that the system stays in the same symmetry class of the Hamiltonian[2], it is fundamentally impossible to follow a path from this topologically distinct phase of matter to a trivial phase without closing the insulating bulk band gap. For a strong topological insulator, metallic surface states are necessarily present at the boundary to a trivial insulator as, for example, air or vacuum. These topological surface states are protected by time-reversal symmetry and their energy vs. momentum dispersion mimics quasirelativistic, massless particles, with the shape of a Dirac cone and a peculiar helical spin texture[1–4]. The topological classification is given by the so-called Z_2 invariant ν_0, which for odd number of Dirac cones is $\nu_0 = 1$, giving rise to strong (Z_2) topological insulators, but for even number of cones is zero, characterizing weak topological or trivial insulators[5, 6].

It is possible to transform a strong (Z_2) topological insulator to a trivial insulator by alloying as has been shown for Bi_2Se_3:In[7, 8] and $BiTl(S_{1-x}Se_x)_2$[9]. The fundamental principle of bulk-boundary correspondence dictates again that this topological phase transition proceeds through a transition point where the bulk band gap closes. In this picture, it is supposed that the crystal symmetry is maintained through the phase transition. However, the crystal symmetry itself can protect topologically distinct phases as well, termed topological crystalline insulators (TCIs)[5, 10–14]. For TCIs, the decisive role of the crystal symmetry renders the topological protection dependent on the specific crystal face[10]. The topological invariants allow for an even number of Dirac cones, which are, however, not robust against disorder[5]. $Pb_{1-x}Sn_xSe$ and $Pb_{1-x}Sn_xTe$ represent such mirror-symmetry protected TCIs with fourfold valley degeneracy[5, 11] in which the trivial-to-TCI phase transition is reached for sufficiently large Sn contents[10, 15]. Upon cooling, the lattice contracts and the enhanced orbital overlap leads to an inverted (i.e., negative) bulk band gap, which, via bulk-boundary correspondence, gives rise to Dirac cone surface states. This has impressively been shown by temperature-dependent angle-resolved photoemission (ARPES)[15].

On the other hand, there are crystals that are not necessarily topological, but change their symmetry and their electronic properties with temperature. Such phase-change materials have been studied intensively for non-volatile data storage because their properties can be altered dramatically at the structural phase transition[16]. GeTe is such a prototypical material[16, 17] that transforms upon cooling from the cubic rock salt to a rhombohedral structure characterized by a large relative sublattice displacement. This gives rise to pronounced ferroelectricity of GeTe[18] and has recently been found to allow for an electrical switching of electronic properties[19]. Symmetry changes are potentially very interesting also for topological insulators. In fact, it has been shown for the TCI $Pb_{1-x}Sn_xSe$ that by breaking of mirror symmetries two out of the four Dirac cones at its (100) surface can be gapped[11, 20–22]. In that case, the topological phase remains, however, unchanged by the symmetry breaking and the

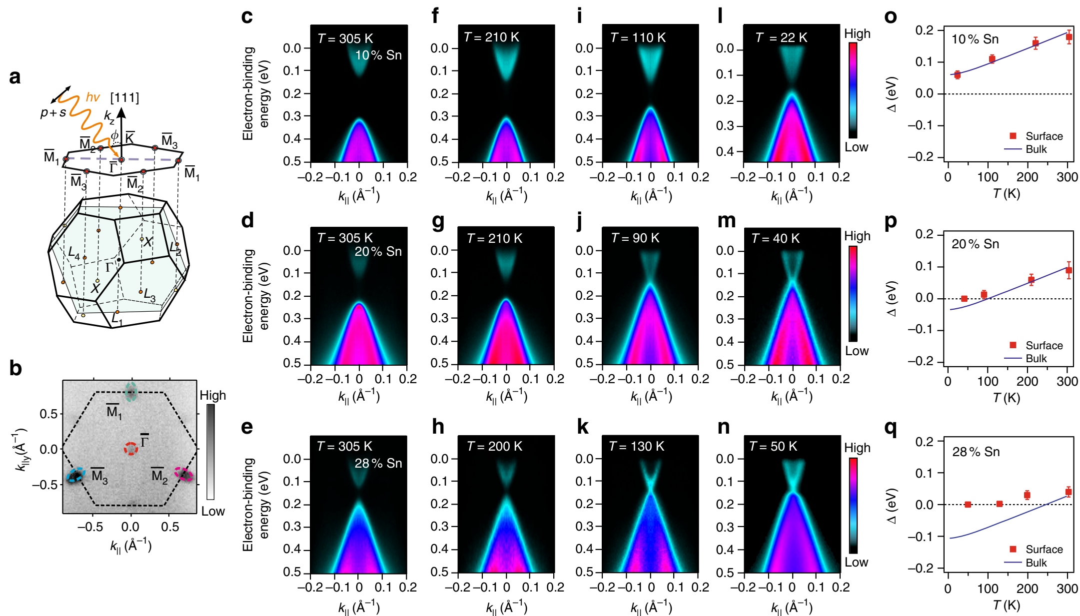

Fig. 1 Trivial to TCI phase transition induced by cooling. The phase transition into a topological crystalline insulator (TCI) is monitored for undoped $Pb_{1-x}Sn_xSe$ (111) films by ARPES around the $\overline{\Gamma}$ point. **a** For (111) films, the four bulk L-points of the bulk Brillouin zone project onto the surface $\overline{\Gamma}$-point for the longitudinal L-valley along [111], whereas the three oblique valleys project on the $\overline{M}$ points. **b** At these momenta, Dirac points appear in ARPES. **c–q** ARPES data measured at 18 eV photon energy as a function of temperature and Sn content. The $x_{Sn} = 10\%$ sample (**c**, **f**, **i**, and **l**) remains trivial down to low temperature as seen from the persistence of a band gap. For $x_{Sn} = 20\%$ (**d**, **g**, **j**, and **m**) and 28% (**e**, **h**, **k**, and **n**), gapless Dirac cones develop at low temperature due to the inversion of the bulk band gap. Panels **o–q** show the comparison of the measured surface (Dirac cone) band gap (red squares) with the bulk band gap (blue line) from optical data[27], evidencing that the surface gap closes when the bulk band gap changes sign. The error bars in the measured surface band gap correspond to the uncertainty in determining the energy position of the band dispersions at the $\overline{\Gamma}$-point (see Supplementary Note 6 for details). The ARPES dispersions were acquired using linearly polarized $p + s$ photons incident on the sample under an angle $\phi = 45°$ as shown in **a** (see also Supplementary Note 5)

Reprinted page 2 of paper [61] "Topological transition from TCI to TI via Bi doping".

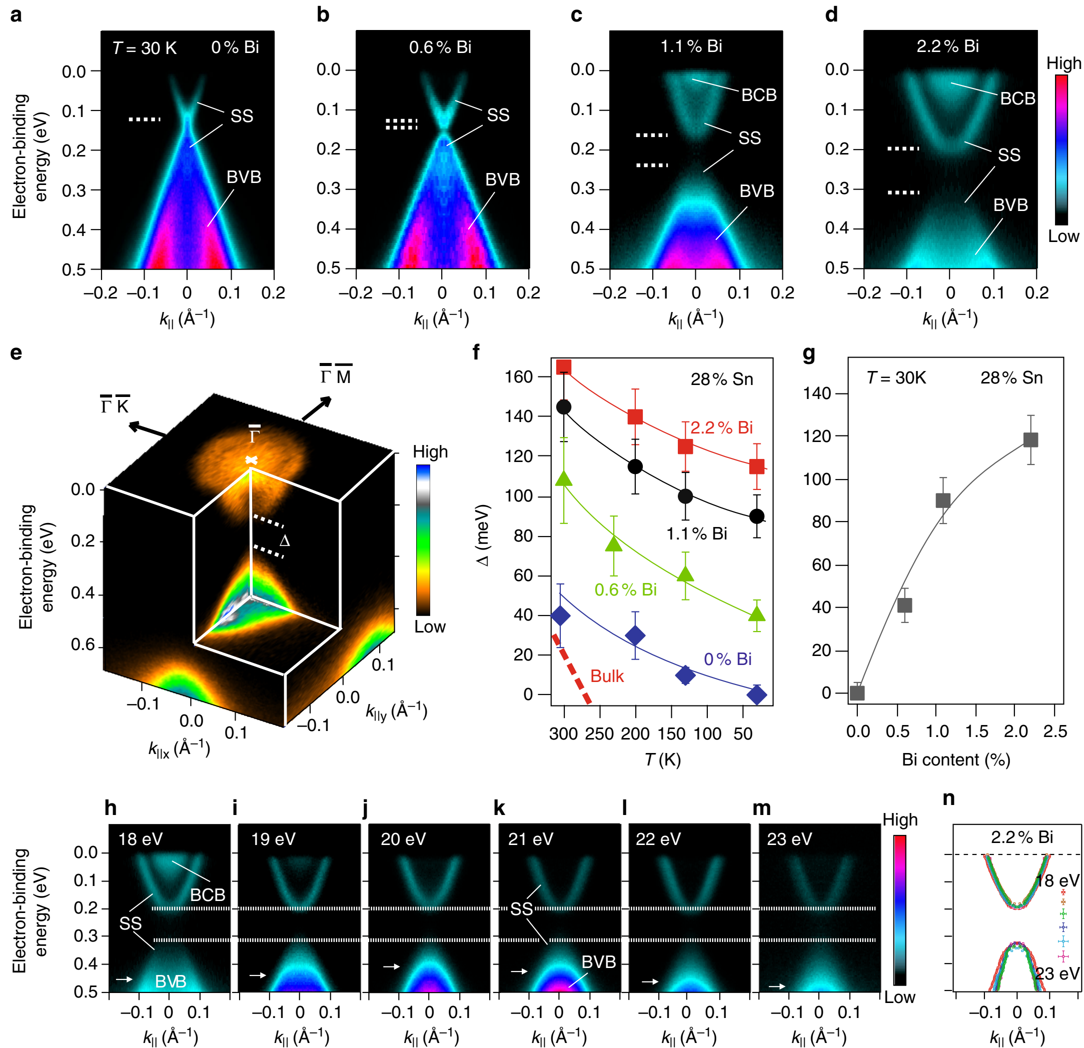

Fig. 2 Doping effect and gap opening at $\overline{\Gamma}$ induced by Bi. Incorporation of Bi in $Pb_{0.72}Sn_{0.28}Se$ (111) films leads to *n*-type doping and a gap opening at the $\overline{\Gamma}$ point as revealed by ARPES. **a**–**d** ARPES data measured at a temperature of 30 K and 18 eV photon energy. **e** Corresponding full ARPES map around the $\overline{\Gamma}$ point for $n_{Bi} = 2.2\%$. **f**, **g** Dependence of the surface band gap Δ on temperature and n_{Bi}. The error bars correspond to the uncertainty in determining the energy position of the band dispersions at the $\overline{\Gamma}$-point (Supplementary Note 6). **h**–**m** Photon energy dependence for $n_{Bi} = 2.2\%$, indicating that the gapped surface state (SS) is two-dimensional. At high binding energies, the dispersion of the bulk-valence band (BVB) with photon energy (marked with horizontal white arrows) can be distinguished from the lower half of the SS. The dispersion of the bulk-conduction band (BCB) can be observed between 18 and 20 eV, while the size of the surface gap remains qualitatively unchanged as indicated by horizontal dashed lines. **n** Energy-momentum dispersions of the upper and lower part of the SS as extracted from fits to results shown in **h**–**m** (see Supplementary Fig. 8 and Supplementary Note 7 for details). The error bars given in the legend represent the maximum uncertainty in determining the corresponding band dispersions

Z_2 invariant stays even. It is crucial for the present work to note that in principle the topological phase does not need to be preserved by a distortion. Indeed, topological phase transitions have recently been predicted for two-dimensional TlSe[23] and three-dimensional SnTe by distortions[24] and by finite-size effects[25].

Here, we investigate the band topology of the (111) surface of $Pb_{1-x}Sn_xSe$ by cooling through the complete trivial to topological phase transition. We demonstrate a new type of phase transition from crystal-symmetry-protected to time-reversal symmetry-protected topology controlled by Bi incorporation. We show that when Bi is introduced in the bulk making the system *n*-type, a gap is opened up at the one Dirac cone at the center of the surface Brillouin zone at $\overline{\Gamma}$, while the three Dirac cones located at the $\overline{M}$ points at the zone boundaries behave as in pure $Pb_{1-x}Sn_xSe$, that is, are gapless at low temperature. Our findings provide the first experimental evidence for a topological phase transition from a TCI with an even number of Dirac cones to a Z_2 time-reversal symmetry-protected strong topological insulator where the

Reprinted page 3 of paper [61] "Topological transition from TCI to TI via Bi doping".

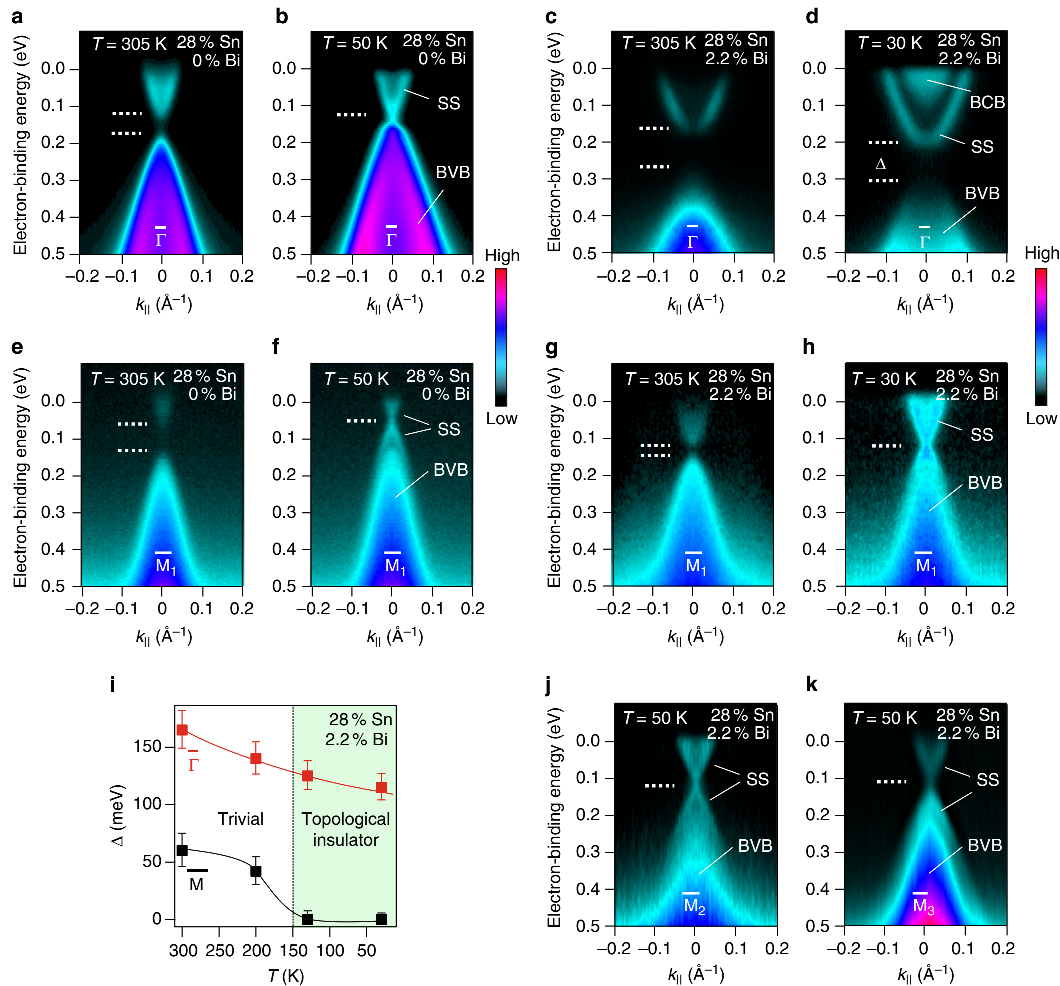

Fig. 3 TCI to Z_2 topological phase transition induced by Bi. **a**–**k** ARPES data of $Pb_{1-x}Sn_xSe$ (111) films recorded using 18 eV photon energy at $\overline{\Gamma}$ and $\overline{M}$ without (**a**, **b**, **e**, and **f**) and with high Bi doping (**c**, **d**, **g**, **h**, **j**, and **k**). Without Bi doping (**b**, **f**), the Dirac cones simultaneously close at $\overline{\Gamma}$ and $\overline{M}$ <150 K, whereas for high Bi concentration, the Dirac cone is gapped at $\overline{\Gamma}$ (**d**) and intact at all three $\overline{M}$ points at low temperatures (**h**, **j**, and **k**). **i** Temperature dependence of the gap Δ at $\overline{\Gamma}$ (red) and $\overline{M}$ (black). Solid lines are a guide to the eye, and the error bars correspond to the uncertainty in determining the energy position of the band dispersions at $\overline{\Gamma}$ and $\overline{M}$, respectively

number is odd (three). Following the recent prediction[24], the origin of the novel topological phase transition is interpreted as due to a sublattice shift and rhombohedral distortion along the [111] direction, which lifts the bulk band inversion only at the Z-point (L-point in the undistorted phase) projected onto $\overline{\Gamma}$. At the same time, we do not find any evidence for a bulk band gap closing across the phase transition, most likely, because the rhombohedral distortion does not leave the system in the same symmetry class where the TCI is defined.

Results

Effect of temperature and Sn concentration. We have grown both undoped and Bi-doped epitaxial (111) $Pb_{1-x}Sn_xSe$ films of high quality by molecular beam epitaxy (see Supplementary Fig. 1–6 and Supplementary Notes 1–4 for details). The samples were capped in-situ by a thin Se layer to protect the surface during transport to the ARPES setup, where the cap was desorbed by annealing (see also "Methods" section and Supplementary Note 5). ARPES measurements were performed using linearly polarized light incident on the sample under the geometry shown in Fig. 1a, which also depicts the bulk and (111) surface Brillouin zones of rock salt $Pb_{1-x}Sn_xSe$. In contrast to the natural (100) cleavage plane of bulk crystals previously studied[12, 13, 15, 26], for the (111) orientation, the four bulk L-points project on the following four time-reversal invariant surface momenta: $\overline{\Gamma}$ and three equivalent $\overline{M}$ points[27]. This is seen in the ARPES data shown in Fig. 1b, where the intensity from the Dirac cones at the three $\overline{M}$ points is enhanced by a photoemission final-state effect. Due to the sensitive dependence of the bulk band inversion on the lattice

Reprinted page 4 of paper [61] "Topological transition from TCI to TI via Bi doping".

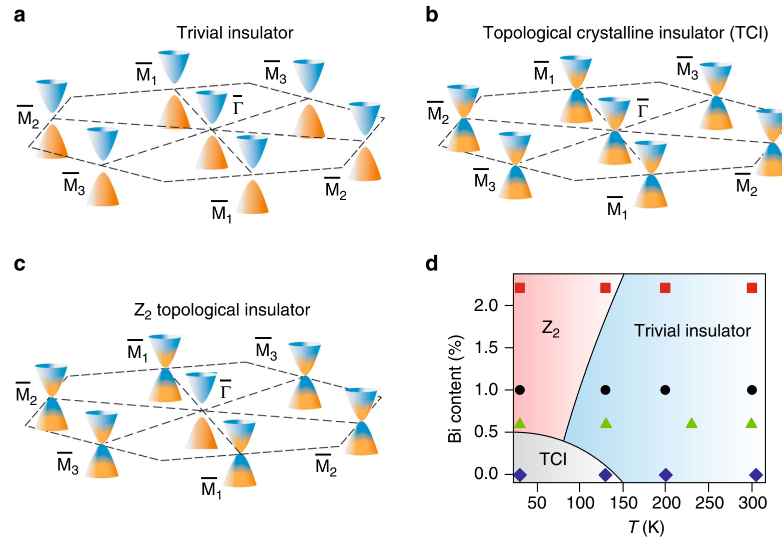

Fig. 4 Topological phase transition as a function of Bi doping and temperature. Schematic illustration of the transition from (**a**) trivial to (**b**) topological crystalline insulator (TCI) and eventually to (**c**) strong Z_2 topological insulator. **d** Topological phase diagram derived from our ARPES data for $x_{Sn} = 28\%$. The phase diagram contains a trivial phase at high temperature (positive gap Δ at all four *L*-points) with massive gapped cones at $\overline{\Gamma}$ and $\overline{M}$; a TCI phase at low temperature with even Z_2 invariant (all bulk *L*-points have negative, i.e., inverted gaps) and closed Dirac cones at $\overline{\Gamma}$ and all $\overline{M}$ points; a Z_2 topological insulator phase with odd Z_2 invariant due to a distortion along [111], giving three closed Dirac cones at the $\overline{M}$ points and an open gap at the $\overline{\Gamma}$ point

constant, the trivial to topological phase transition can be monitored during cooling by tracing the evolution of the bulk band gap[28] or by observation of the appearance of the Dirac cones in ARPES[15, 26]. Indeed, as seen in Fig. 1c–q, for our (111) films with low Sn concentrations and without Bi doping ($x_{Sn} = 10\%$, Fig. 1c, f, i, and l), the Dirac cone at the $\overline{\Gamma}$ point does not form down to 22 K, while for $x_{Sn} = 20\%$ (Fig. 1d, g, j, and m) and $x_{Sn} = 28\%$ (Fig. 1e, h, k, and n), the gapless Dirac cone appears at around 90 and 130 K, respectively.

Impact of Bi incorporation in the bulk. Figure 2 shows the effect of bulk Bi doping on the $\overline{\Gamma}$ Dirac cone of $Pb_{0.72}Sn_{0.28}Se$. When substitutionally incorporated at cation (Pb, Sn—group IV) lattice sites, the group V element Bi acts as electron donor due to its excess valence electron[29]. Increasing the Bi concentration n_{Bi} thus leads to a strong upward shift of the Fermi level by 200 meV for $n_{Bi} = 2.2\%$ (Fig. 2a–e). Remarkably, while for undoped $Pb_{0.72}Sn_{0.28}Se$, an intact Dirac cone is seen at 30 K, a surface gap as large as ~100 meV opens up at the $\overline{\Gamma}$ Dirac cone upon Bi doping and increases strongly with increasing Bi content (see Fig. 2f, g, Supplementary Fig. 7, and Supplementary Note 6). This leads to the general conclusion that for Bi concentrations >~0.6%, the gap at $\overline{\Gamma}$ does not close. Figure 2h–n demonstrates that within the experimental error bars, this gapped surface state does not disperse with the photon energy, i.e., momentum perpendicular to the surface plane, pinpointing its two-dimensional nature (see also Supplementary Fig. 8 and discussion in Supplementary Note 7). This observation is important to rule out that the probed state corresponds to the gapped bulk states.

The effect of Bi on the Dirac cones at the $\overline{\Gamma}$ and $\overline{M}$ points was evaluated in dependence of the Bi and Sn contents as well as of temperature. On the topologically trivial side ($x_{Sn} < 16\%$), for Bi doping $n_{Bi} < 0.6\%$, no difference in the gaps Δ at $\overline{\Gamma}$ and $\overline{M}$ is found, which remain open at all temperatures (Supplementary Figs. 9, 10, and Supplementary Note 8). On the topologically non-trivial side ($x_{Sn} > 16\%$), the Dirac cones at $\overline{\Gamma}$ (Fig. 3a–d) and $\overline{M}$ (Fig. 3e–h) close synchronously as a function of temperature for low Bi concentrations. This is shown by Fig. 3a, b, e, and f, where corresponding ARPES dispersions at 305 and 50 K are presented. In contrast, for high Bi concentrations (Fig. 3c, d, g, and h), the fourfold valley degeneracy is completely lifted such that the gap is closed to zero at all three $\overline{M}$ points (Fig. 3h–k), but opens as wide as 100 meV at the $\overline{\Gamma}$ point at 30 K (Fig. 3d). Thus, we conclude that of the even numbered Dirac cones per surface Brillouin zone, characteristic of a TCI, only three remain, qualifying $Pb_{1-x}Sn_xSe$:Bi as a strong Z_2 topological insulator already for moderate Bi doping. This is the central result of the present work. While a TCI is protected by mirror symmetry, the odd numbered Dirac cones of strong topological insulators are protected by time-reversal symmetry and robust against disorder. Figure 3i shows that the new Z_2 phase, which has never been observed before for this material class, exists in a wide temperature range from ~150 K down to the lowest temperature probed in our experiments.

Discussion

Due to the bulk-boundary correspondence, the formation of the Dirac cones at the surface indicates a bulk band inversion at the parent momenta in the Brillouin zone as indicated by Fig. 1a. The band structures and shape of the Dirac cones corresponding to the different topological phases are illustrated schematically in Fig. 4a–c, where the open and closed Dirac cones are colored such as to indicate the changes of the predominant charge density at the anion (orange) and cation sites (blue) occurring during the band inversion (see Supplementary Fig. 11 and Supplementary Note 9). The topological phase transition so far reported for $Pb_{1-x}Sn_xSe$[15, 26] occurs between trivial (Fig. 4a) and TCI phase (Fig. 4b) where all bulk band inversions behave equally. For the new topological phase transition into the Z_2 topological insulator phase (Fig. 4c), the bulk band inversion along the momenta

Reprinted page 5 of paper [61] "Topological transition from TCI to TI via Bi doping".

normal to the surface does not occur, triggered by the Bi doping. This means the discovery of two new topological phase transitions in $Pb_{1-x}Sn_xSe$: (i) from trivial to Z_2 topological by cooling and (ii) from topological crystalline to Z_2 topological by adding Bi. The resulting topological phase diagram (Fig. 4d) derived from our data shows the interdependence of these two pathways.

The observed behavior resembles the predictions by Plekhanov et al.[24] for SnTe. SnTe is known for its ferroelectric phase transition in which the anion and cation sublattices are shifted against each other along the [111] direction[17], connected to a transverse optical phonon softening[30]. Plekhanov et al.[24] tested small displacements and theoretically predicted that for a certain range of displacements a Z_2 topological insulator can exist.

In general, all IV–VI compounds are close to such a structural phase transition due to their mixed covalent-ionic bonding. They belong to the family of 10 electron systems and crystallize either in the cubic rock salt, rhombohedral, or orthorhombic structure. As calculated by Littlewood[31, 32], the type of structure in which a IV–VI compound crystallizes critically depends on the values of two bond orbital coordinates—one is a measure of the ionicity and the other of covalency or *s*–*p* hybridization, and based on these a phase diagram has been established[31, 32]. Due to the not fully saturated *p*-bonds, the rock salt structure is inherently unstable against rhombohedral distortions[31–33], which reduces the six nearest neighbors to three. The cubic/rhombohedral phase boundary is determined by the electronegativity difference between the constituting elements and as a physical explanation of the instability the resonating bond model was invoked[34]. For the six nearest neighbors, the number of available *p*-electrons (six per atom pair) is not sufficient to stabilize the cubic bonds[35]. Thus, SnTe and GeTe assume a rhombohedral structure and even for PbTe minute addition of <0.5% of Ge suffices to drive $Pb_{1-x}Ge_xTe$ into the rhombohedral phase, rendering it ferroelectric[36, 37]. Thus, very small changes on the group IV lattice sites give rise to structural phase transitions. Indeed, for our Bi-doped films, we find a small Bi-induced rhombohedral distortion along the [111] direction using x-ray diffraction (Supplementary Figs. 4–6 and Supplementary Note 4). This indicates a ferroelectric inversion symmetry breaking as the underlying physical mechanism, which has been suggested to be much enhanced at the surface[21, 38]. Because of the (111) orientation of our films, this symmetry breaking lifts the even number degeneracy of the Dirac cones such that a gap is opened only at the $\overline{\Gamma}$ point. This leaves an odd number of Dirac cones intact at the three $\overline{\mathrm{M}}$ points, causing the topological phase transition.

Finally, we would like to address the role of Bi as decisive ingredient for symmetry breaking even at small concentrations. Bi is another 10 electron system[33], covalently bonded and crystallizing in a rhombohedral structure. Accordingly, when incorporated at group IV lattice sites in $Pb_{1-x}Sn_xSe$, it shifts the alloy toward a more covalently bonded structure in the phase diagram[31, 32, 39]. Moreover, on such lattice sites, Bi also reduces the cation vacancy concentration and the latter strongly enhances the ferroelectric Curie temperature T_C of the cubic-to-rhombohedral phase transition[30, 35, 38, 40]. Indeed, in SnTe thin films with reduced vacancy concentration, ferroelectricity up to room temperature was recently reported[38]. Thus, both effects of the Bi, higher covalency, and lower vacancy concentration, contribute to structural symmetry breaking and trigger the novel TCI-to-Z_2 topological phase transition discovered in the present work.

Methods

Sample growth and characterization. Epitaxial growth of (111) $Pb_{1-x}Sn_xSe$ films on BaF_2 substrates was performed using molecular beam epitaxy (MBE) in ultra-high vacuum conditions better than 5×10^{-10} mbar at a substrate temperature of 380 °C. Effusion cells filled with stoichiometric PbSe and SnSe were used as source materials, as well as a ternary $Pb_{1-x}Sn_xSe$ source with $x_{Sn} = 25\%$. Bi-doping was realized using a Bi_2Se_3 effusion cell. The chemical composition of the layers was varied over a wide range from $x_{Sn} = 0$ to 40% by control of the SnSe/PbSe beam flux ratio, and a two-dimensional growth was observed by in situ reflection high-energy electron diffraction (Supplementary Fig. 1). The film thickness was in the range of 1–3 μm.

High-resolution ARPES. For the ARPES measurements, the films were capped in situ in the MBE chamber with a 200 nm thick amorphous Se layer at room temperature to protect the surface against oxidation during transport to the BESSY II synchrotron radiation source in Berlin, Germany. There the Se cap was completely desorbed in the ARPES preparation chamber by annealing at about 230 °C for 15 min in 3×10^{-10} mbar. ARPES measurements were performed at the UE112-PGM2a beamline of BESSY II at pressures better than 1×10^{-10} mbar using linearly polarized $p + s$ photons incident on the sample under an angle $\phi = 45°$. We used photon energies between 18 and 23 eV for the temperature-dependent ARPES measurements of the band dispersions, and a photon energy of 90 eV for the core levels (see Supplementary Fig. 12 and Supplementary Note 10). Emitted photoelectrons were detected with a Scienta R8000 electron energy analyzer at the ARPES 1^2 endstation. Overall resolutions of the ARPES measurements were 5 meV (energy) and 0.3° (angular).

Composition and structural characterization. The composition of the epilayers was determined using high-resolution x-ray diffraction and the Vegard's law (Supplementary Fig. 2 and Supplementary Note 2). We employed a Seifert diffractometer equipped with primary and secondary monochromator crystals. Upon Bi incorporation, the rhombohedral lattice distortion was determined from reciprocal space maps recorded around the (513) reflection (see Supplementary Figs. 4–6 and Supplementary Note 4).

Electrical characterization. The dopant concentration and transport properties were assessed by Hall effect measurements at 77 K (Supplementary Fig. 3 and Supplementary Note 3), evidencing carrier mobilities as high as $10^4\,\mathrm{cm^2\,V^{-1}\,s^{-1}}$ in dependence of the carrier concentration.

Data availability. The authors declare that all data supporting the findings of this study are available within the paper and its Supplementary Information files.

Received: 16 December 2016 Accepted: 24 August 2017
Published online: 17 October 2017

References

1. Hasan, M. Z. & Kane, C. L. Colloquium: topological insulators. *Rev. Mod. Phys.* **82**, 3045–3067 (2010).
2. Ezawa, M., Tanaka, Y. & Nagaosa, N. Topological phase transition without gap closing. *Sci. Rep.* **3**, 2790 (2013).
3. Qi, X.-L. & Zhang, S.-C. Topological insulators and superconductors. *Rev. Mod. Phys.* **83**, 1057–1110 (2011).
4. Bernevig, B. A. & Hughes, T. L. *Topological Insulators and Topological Superconductors* (Princeton University Press, Princeton, 2013).
5. Fu, L. & Kane, C. L. Topological insulators with inversion symmetry. *Phys. Rev. B* **76**, 045302 (2007).
6. Fu, L., Kane, C. L. & Mele, E. J. Topological insulators in three dimensions. *Phys. Rev. Lett.* **98**, 106803 (2007).
7. Brahlek, M. et al. Topological-metal to band-insulator transition in $(Bi_{1-x}In_x)_2Se_3$ thin Films. *Phys. Rev. Lett.* **109**, 186403 (2012).
8. Wu, L. et al. A sudden collapse in the transport lifetime across the topological phase transition in $(Bi_{1-x}In_x)_2Se_3$. *Nat. Phys.* **9**, 410–414 (2013).
9. Xu, S.-Y. et al. Topological phase transition and texture inversion in a tunable topological insulator. *Science* **332**, 560–564 (2011).
10. Fu, L. Topological crystalline insulators. *Phys. Rev. Lett.* **106**, 106802 (2011).
11. Hsieh, T. H. et al. Topological crystalline insulators in the SnTe material class. *Nat. Commun.* **3**, 982 (2012).
12. Tanaka, Y. et al. Experimental realization of a topological crystalline insulator in SnTe. *Nat. Phys.* **8**, 800–803 (2012).
13. Xu, S.-Y. et al. Observation of a topological crystalline insulator phase and topological phase transition in $Pb_{1-x}Sn_xTe$. *Nat. Commun.* **3**, 1192 (2012).
14. Ando, Y. & Fu, L. Topological crystalline insulators and topological superconductors: from concepts to materials. *Annu. Rev. Condens. Matter Phys.* **6**, 361–381 (2015).
15. Dziawa, P. et al. Topological crystalline insulator states in $Pb_{1-x}Sn_xSe$. *Nat. Mater.* **11**, 1023–1027 (2012).

Reprinted page 6 of paper [61] "Topological transition from TCI to TI via Bi doping".

16. Wuttig, M. & Yamada, N. Phase-change materials for rewriteable data storage. *Nat. Mater.* **6**, 824–832 (2007).
17. Schmitte, F. J. in *Physics of Non-Tetrahedrally Bonded Binary Compounds II* (ed. Madelung, O.) Landolt-Börnstein, New Series III/17F (Springer, Berlin, 1983).
18. Chattopadhyay, T., Boucherle, J. X. & von Schnering, H. G. Neutron diffraction study on the structural phase transition in GeTe. *J. Phys. C* **20**, 1431 (1987).
19. Di Sante, D., Barone, P., Bertacco, R. & Picozzi, S. Electric control of the giant Rashba effect in bulk GeTe. *Adv. Mater.* **25**, 509–513 (2013).
20. Okada, Y. et al. Observation of Dirac node formation and mass acquisition in a topological crystalline insulator. *Science* **341**, 1496–1499 (2013).
21. Zeljkovic, I. et al. Dirac mass generation from crystal symmetry breaking on the surfaces of topological crystalline insulators. *Nat. Mater.* **14**, 318–324 (2015).
22. Wojek, B. M. et al. Direct observation and temperature control of the surface Dirac gap in a topological crystalline insulator. *Nat. Commun.* **6**, 8463 (2015).
23. Niu, C. et al. Two-dimensional topological crystalline insulator and topological phase transition in TlSe and TlS monolayers. *Nano. Lett.* **15**, 6071–6075 (2015).
24. Plekhanov, E., Barone, P., Di Sante, D. & Picozzi, S. Engineering relativistic effects in ferroelectric SnTe. *Phys. Rev. B* **90**, 161108(R) (2014).
25. Safaei, S., Galicka, M., Kacman, P. & Buczko, R. Quantum spin hall effect in IV-VI topological crystalline insulators. *New J. Phys.* **17**, 063041 (2015).
26. Neupane, M. et al. Topological phase diagram and saddle point singularity in a tunable topological crystalline insulator. *Phys. Rev. B* **92**, 075131 (2015).
27. Polley, C. M. et al. Observation of topological crystalline insulator surface states on (111)-oriented $Pb_{1-x}Sn_xSe$ films. *Phys. Rev. B* **89**, 075317 (2014).
28. Strauss, A. J. Inversion of conduction and valence bands in $Pb_{1-x}Sn_xSe$ alloys. *Phys. Rev.* **157**, 608–611 (1967).
29. Zykov, V. A., Gavrikova, T. A., Il'in, V. I., Nemov, S. A. & Savintsev, P. V. Effect of bismuth impurity on carrier density in PbSe:Bi:Se epitaxial layers. *Semiconductors* **35**, 1254–1258 (2001).
30. Sugai, S. et al. Carrier density dependence of soft TO-phonon in SnTe by Raman scattering. *Solid State Commun.* **24**, 407–409 (1977).
31. Littlewood, P. B. The crystal structure of IV-VI compounds. I. Classification and description. *J. Phys. C Solid State Phys.* **13**, 4855–4873 (1980).
32. Littlewood, P. B. The crystal structure of IV-VI compounds. II. A microscopic model for cubic/rhombohedral materials. *J. Phys. C Solid State Phys.* **13**, 4875–4892 (1980).
33. Littlewood, P. B. Structure and bonding in narrow gap semiconductors. *Crit. Rev. Solid State Mater. Sci.* **11**, 229–285 (1983).
34. Nimtz, G. & Schlicht, B. in *Springer Tracts in Modern Physics* 1–117, Vol. 98, Narrow-gap semiconductors (Springer, Berlin, 1983).
35. Jantsch, W., Bussmann-Holder, A., Bilz, H. & Vogel, P. in *Springer Tracts in Modern Physics* 1-98, Vol. 99, Dynamical properties of IV-VI compounds (Springer, Berlin, 1983).
36. Bangert, E., Bauer, G., Fantner, E. J. & Pascher, H. Magneto-optical investigations of phase-transition-induced band-structure changes of $Pb_{1-x}Ge_xTe$. *Phys. Rev. B* **31**, 7958 (1985).
37. Lebedev, A. I. & Sluchinskaya, I. A. Influence of random fields on the ferroelectric phase transition in IV–VI semiconductors. *Ferroelectrics* **169**, 293–301 (1995).
38. Chang, K. et al. Discovery of robust in-plane ferroelectricity in atomic-thick SnTe. *Science* **353**, 274–278 (2016).
39. Kool, B. J. & Noheda, B. Ferroelectric chalcogenides–materials at the edge. *Science* **353**, 221–222 (2016).
40. Iizumi, M., Hamaguchi, Y., Komatsubara, K. F. & Kato, Y. Phase transition in SnTe with low carrier concentration. *J. Phys. Soc. Jpn.* **38**, 443–449 (1975).

Acknowledgements

This work was supported by SPP 1666 of DFG and the SFB-025 IRON of the Austrian Science Funds. P.S.M. is supported by Helmholtz Virtual Institute "New states of matter and their excitations." We thank Andrzej Szczerbakow for providing the MBE source material.

Author contributions

P.S.M., G.S., V.V.V., O.C., and J.S.-B. performed photoemission experiments with support from A.V. and E.G.; G.S. prepared and characterized the samples; G.S., V.V.V., and O.C. performed x-ray diffraction experiments; J.S.-B. and P.S.M. performed data analysis, figure and draft planning; J.S.-B., O.R., G.S., and G.B. coordinated the project and wrote the manuscript with input from all the co-authors.

Additional information

Supplementary Information accompanies this paper at doi:10.1038/s41467-017-01204-0.

Competing interests: The authors declare no competing financial interests.

Reprints and permission information is available online at http://npg.nature.com/reprintsandpermissions/

Publisher's note: Springer Nature remains neutral with regard to jurisdictional claims in published maps and institutional affiliations.

Open Access This article is licensed under a Creative Commons Attribution 4.0 International License, which permits use, sharing, adaptation, distribution and reproduction in any medium or format, as long as you give appropriate credit to the original author(s) and the source, provide a link to the Creative Commons license, and indicate if changes were made. The images or other third party material in this article are included in the article's Creative Commons license, unless indicated otherwise in a credit line to the material. If material is not included in the article's Creative Commons license and your intended use is not permitted by statutory regulation or exceeds the permitted use, you will need to obtain permission directly from the copyright holder. To view a copy of this license, visit http://creativecommons.org/licenses/by/4.0/.

© The Author(s) 2017

Reprinted page 7 of paper [61] "Topological transition from TCI to TI via Bi doping".

Supplementary Figures

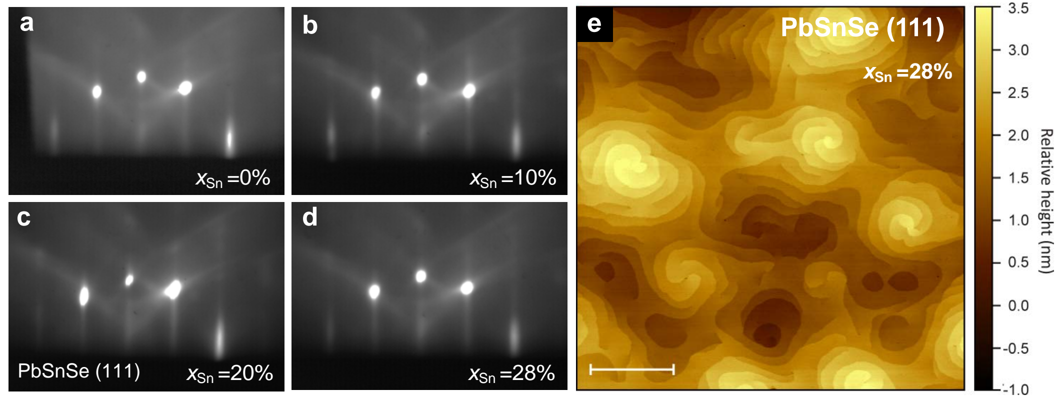

Supplementary Figure 1: **Growth and Surface Characterization.** Reflection high-energy electron diffraction of $Pb_{1-x}Sn_xSe$ epilayers on BaF_2 (111) substrates recorded during MBE growth for x_{sn} = 0, 10, 20 and 28% from (**a**) to (**d**), respectively. (**e**) Atomic force microscopy image of the x_{sn} = 28% epilayer with 1 µm thickness. Horizontal scale bar, 1 µm (white-solid line).

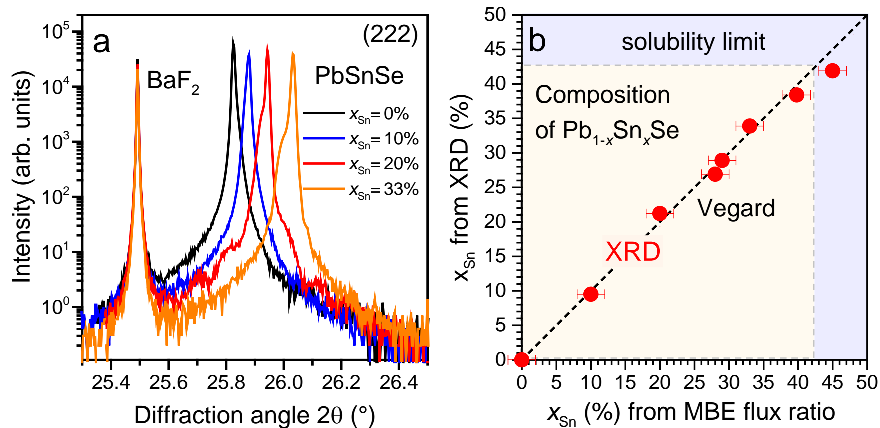

Supplementary Figure 2: **X-ray diffraction of $Pb_{1-x}Sn_xSe$ epilayers on BaF_2 (111).** (**a**) Radial (222) diffraction scans for selected compositions varying from x_{Sn} = 0 to 33%. (**b**) Sn content derived from Vegard's law (dashed line) plotted versus the beam flux ratio of SnSe/(PbSe+SnSe) used for molecular beam epitaxy (MBE). The boundary of the Sn solubility limit in single phase cubic $Pb_{1-x}Sn_xSe$ of about 42% is indicated. The error in x_{Sn} was derived from the 2% precision of the MBE flux measurements using the microbalance technique.

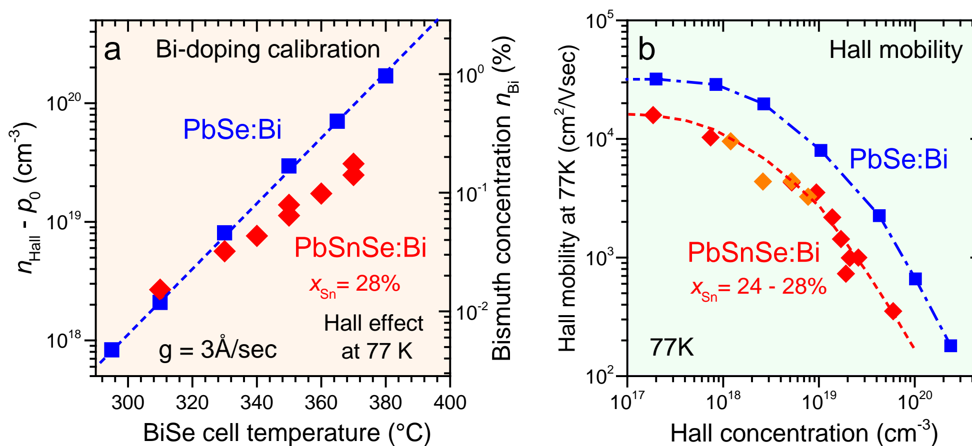

Supplementary Figure 3: **Bi doping and Hall effect transport measurements.** The measurements are obtained at 77 K for PbSe:Bi (■) and PbSnSe:Bi with x_{Sn} = 28% (◆). (**a**) Effective electron concentration ($n_{Hall} - p_0$) versus Bi_2Se_3 effusion cell temperature used during growth by molecular beam epitaxy for a constant film deposition rate of 3 $Ås^{-1}$. The background carrier concentration of undoped *p*-type reference layers due to cation vacancies was $p_0 = +2\times10^{17}$ for PbSe and $+8\times10^{17}$ cm^{-3} for $Pb_{0.72}Sn_{0.28}Se$. The dashed line represents the values expected for unity doping efficiency. The lower carrier concentration observed for $Pb_{0.72}Sn_{0.28}Se$ indicates a reduction of the doping efficiency with increasing Bi content, contrary to the behavior of PbSe. (**b**) Hall mobility of the epilayers versus carrier concentration. For low carrier concentrations, a saturation mobility of μ_{77K} = 32000 and 10500 $cm^2V^{-1}s^{-1}$ is obtained for PbSe and $Pb_{0.72}Sn_{0.28}Se$, respectively.

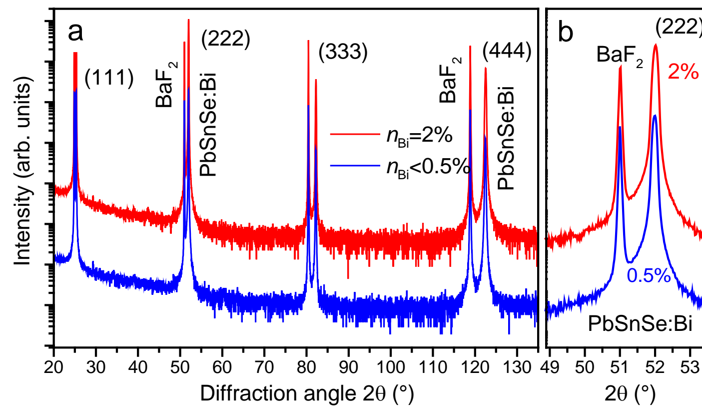

Supplementary Figure S4: **Structural effect of Bi-doping of $Pb_{1-x}Sn_xSe$.** (**a**) X-ray diffraction spectra of two $Pb_{0.72}Sn_{0.28}Se$ layers with high and low Bi dopant concentration (blue: n_{Bi} <0.5%, red: n_{Bi} = 2.2%), evidencing a single phase structure without any traces of secondary phases. (**b**) Zoom-in on the diffraction curves around the (222) Bragg reflection, evidencing no structural degradation due to Bi incorporation.

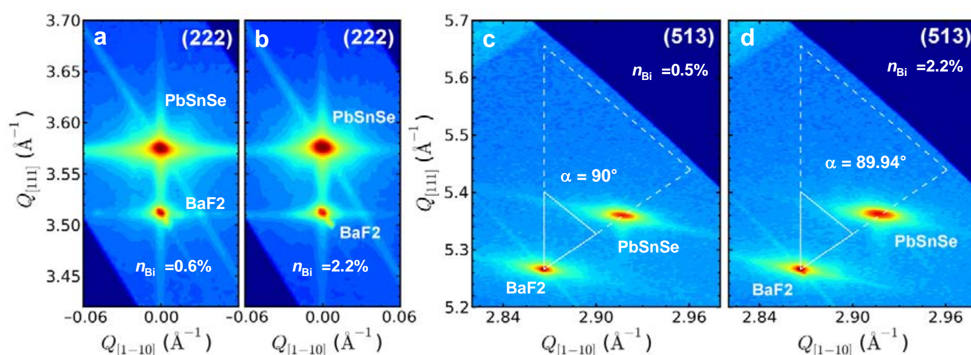

Supplementary Figure 5: **X-ray diffraction reciprocal space maps.** Results of two $Pb_{0.72}Sn_{0.28}Se$:Bi samples doped with n_{Bi} ~ 0.6% (**a, c**) and n_{Bi} = 2.2% (**b, d**), indicating a small rhombohedral lattice distortion for the latter with the distortion angle α = 89.94°. The reciprocal space maps were recorded around the symmetric (222) and asymmetric (513) reciprocal lattice points at room temperature.

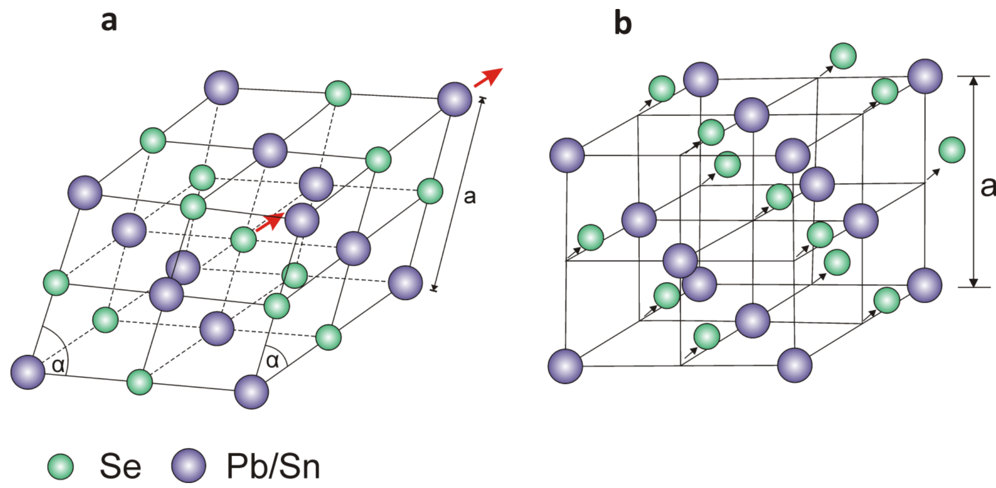

Supplementary Figure 6: **Rhombohedral distortion.** (**a**) Sketch of a rhombohedral distortion with rhombohedral angle $\alpha < 90°$. This angle corresponds to an elongation along [111] direction. (**b**) A sublattice shift (green atoms) is shown which is responsible for ferroelectricity. For simplicity, this is shown for a cubic structure. The sublattice shift typically also leads to a rhombohedral distortion.

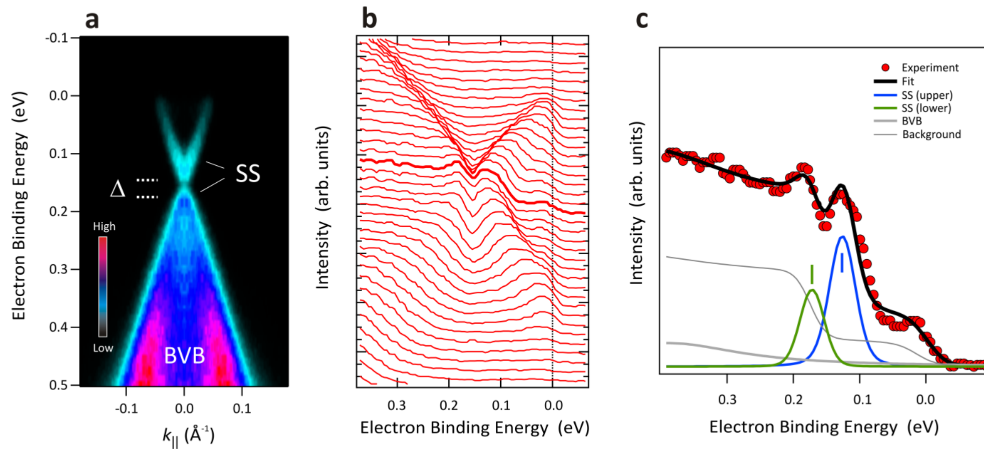

Supplementary Figure 7: **Determination of the surface band gap.** (**a**) Energy-momentum ARPES dispersion measured at 30 K and 18 eV photon energy for $Pb_{0.72}Sn_{0.28}Se$ doped with 0.6% Bi. (**b**) Corresponding energy-distribution curves (EDCs) extracted from **a**. The EDC at zero momentum is highlighted by a thick red solid line, and contains a double peak structure which is the signature of a ~45±10 meV gap. (**d**) Corresponding fit results (black solid lines) of the EDC at zero momentum (red circles) considering a Shirley-like background [4]. The size of the surface band gap is determined from the energy separation between the fitted Lorentzian peaks shown in blue (green) color, which are located at the energy minimum (maximum) of the upper (lower) part of the surface state (SS). The Lorentzian peaks shown in gray color as a thick solid line represent the contribution from the bulk-valence band (BVB).

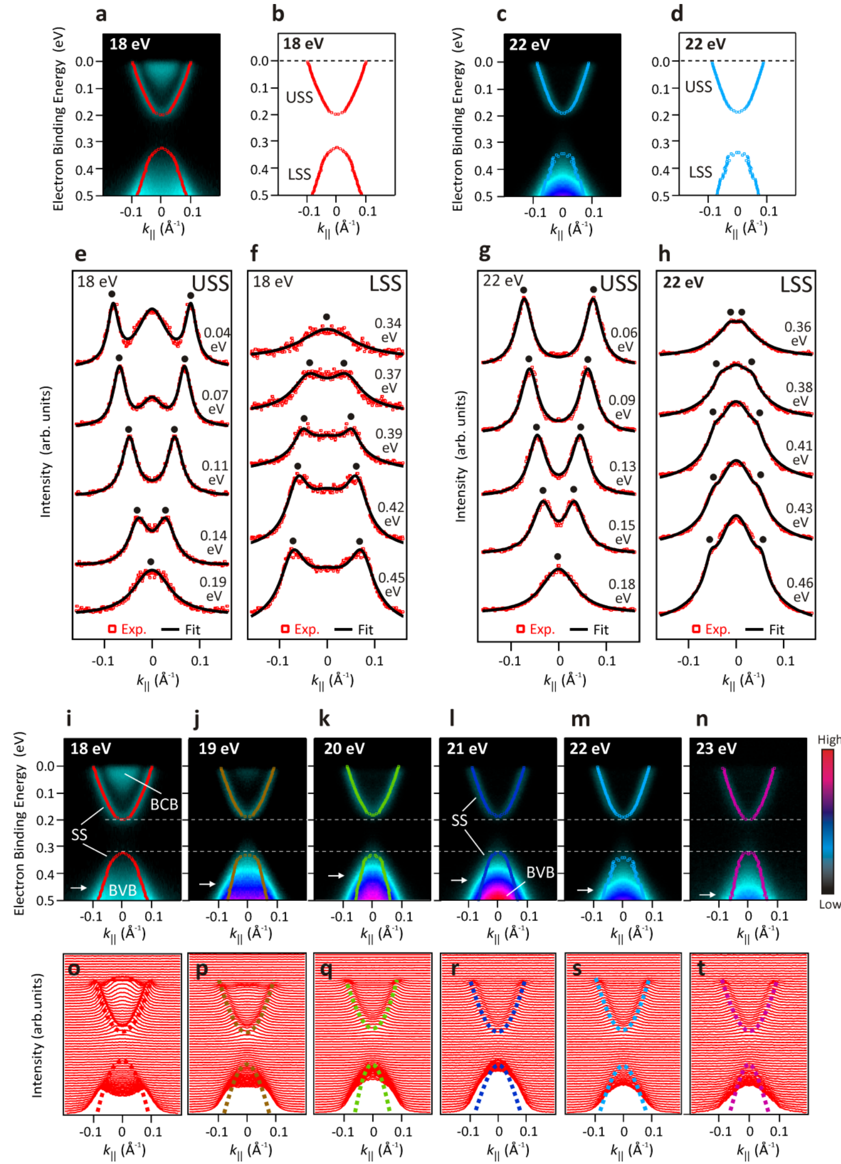

Supplementary Figure 8: **Photon energy dependence of $Pb_{0.72}Sn_{0.28}Se$ doped with 2.2% Bi.** (**a**) Band dispersion of the gapped surface state at 18 eV photon energy, with the peak positions extracted from fits to momentum-distribution curves (MDCs) superimposed. (**b**) Fit results as shown in (**a**), with the upper (USS) and lower (LSS) parts of the surface state indicated. (**c**) and (**d**): Analogous results for a photon energy of 22 eV as in (**a**) and (**b**), respectively. (**e-h**) Fits (black solid lines) to the experimental MDCs (red symbols) shown for selected binding energies across (**e**,**g**) the upper and (**f**,**h**) lower parts of the surface state at (**e**,**f**) 18 eV and (**g**,**h**) 22 eV photon energy. The intensity contributions from the surface state are marked with black filled circles on top of each fit. In (**h**), the intensity from the opposite branches of the surface state is clearly resolved as shoulders around the intensity of the bulk-valence band. (**i-n**) Photon-energy dependent ARPES spectra shown in Figs. 2h-m of the main text. For each photon energy, we have superimposed the fit results to MDCs shown in Fig. 2n of the main text. (**o-t**) MDCs extracted from the data shown in panels (**i-n**). Dashed lines are guides to the eye qualitatively following the fitted band dispersions.

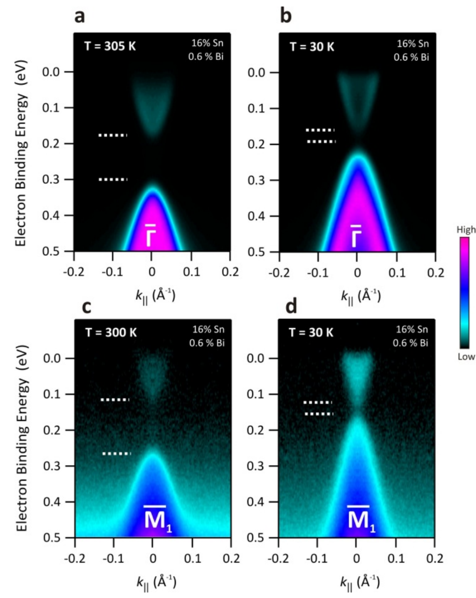

Supplementary Figure 9: **ARPES spectra of a control sample in the trivial state.** (**a-d**) Energy-momentum ARPES dispersions of a $Pb_{1-x}Sn_xSe$ (111) epilayer with 16% Sn and 0.6% Bi doping at (**a**,**b**) $\bar{\Gamma}$ and (**c**,**d**) $\bar{M}$, acquired at (**a**,**c**) room temperature and (**b**,**d**) 30 K. For this sample, the band gap becomes smaller but remains open at the lowest measured temperature. The data show that the band gaps at the $\bar{\Gamma}$ and $\bar{M}$ points exhibit similar behavior with decreasing temperature.

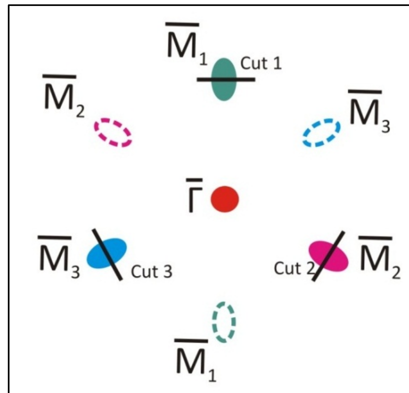

Supplementary Figure 10: **Schematic of the surface Brillouin zone of $Pb_{1-x}Sn_xSe$ (111).** The energy-momentum ARPES dispersions around the $\overline{M}$ points have been acquired with $k_{\|}$ running perpendicular to each individual $\overline{\Gamma}\overline{M}$ direction as indicated by the black solid lines.

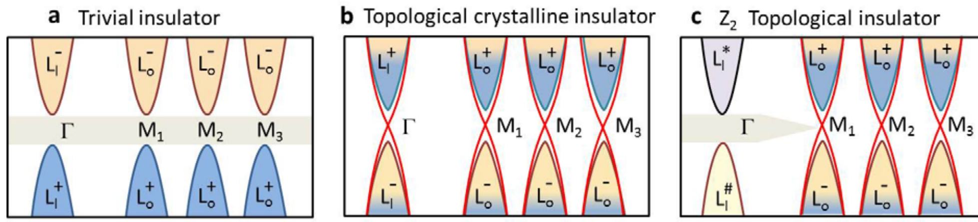

Supplementary Figure 11: **Sketch of the different topological phases.** (**a-c**) Relative position of the band extrema and Dirac cones at the $\overline{M}$ and $\overline{\Gamma}$ points of $Pb_{1-x}Sn_xSe$ (111) in the (**a**) trivial insulator, (**b**) topological crystalline insulator (TCI), and (**c**) Z_2 topological insulator phases. The surface state Dirac cones (red lines) together with the bulk conduction and valence bands are shown. In the trivial state, all gaps at $\overline{M}$ and $\overline{\Gamma}$ are equal. In the TCI state the bulk bands are inverted and a topological surface state is formed at all four symmetry points. In the Z_2 topological insulator state, the Dirac cones are closed at all three $\overline{M}$ points but open at $\overline{\Gamma}$. The reversal of the color of the bulk bands indicates the presence of the bulk band inversion.

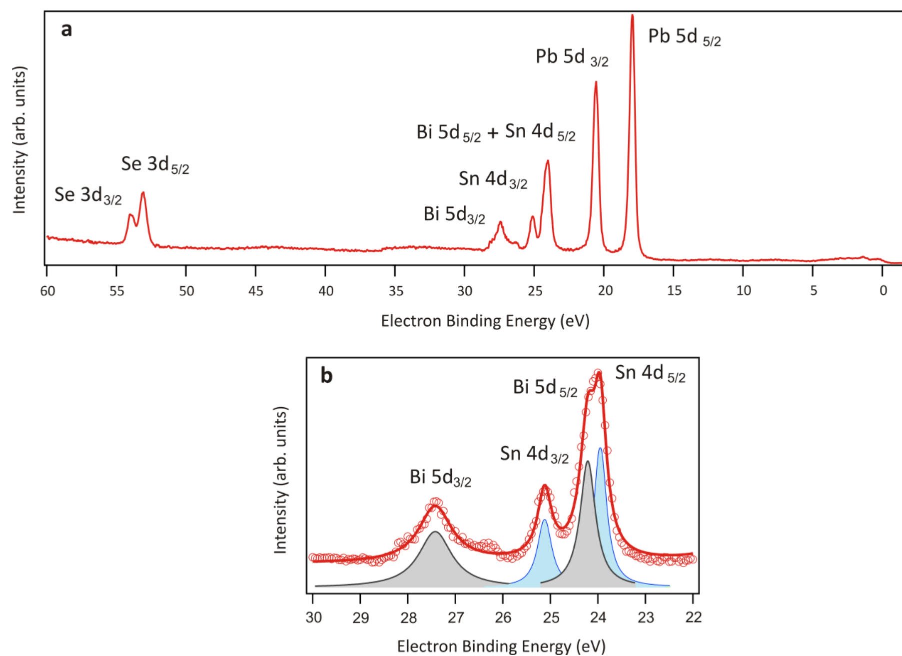

Supplementary Figure 12: **Core level spectra of $Pb_{0.72}Sn_{0.28}$Se:Bi film**. (**a**) 2.2% Bi doping measured after desorption of the Se cap at the ARPES setup. (**b**) Fitted spectra.

Supplementary Notes

Supplementary Note 1: Sample growth by molecular beam epitaxy

Epitaxial growth of (111) $Pb_{1-x}Sn_xSe$ films on BaF_2 substrates was performed in a Riber 1000 system for molecular beam epitaxy (MBE) in ultrahigh vacuum conditions better than 5×10^{-10} mbar. Effusion cells filled with stoichiometric PbSe and SnSe were used as beam flux sources. Alternatively, also a ternary $Pb_{0.75}Sn_{0.25}Se$ source was used. Bi-doping was realized using a compound Bi_2Se_3 effusion cell. The chemical composition of the layers was varied over a wide range from x_{Sn} = 0 to 40% by variation of the SnSe/PbSe beam flux ratio measured using a quartz microbalance moved into the substrate position. The composition of the layers determined from the beam flux ratio agrees within ±2% to the composition determined independently determined by x-ray diffraction as described below. The growth rates were around 1 µm h^{-1} (~1 monolayer s^{-1}) and the growth temperature was set to 380°C as checked by an IRCON infrared pyrometer. The film thickness was in the range of 1–3 µm.

For all layers smooth two-dimensional (2D) growth occurs after few nanometer deposition on BaF_2 (111) as evidenced by Supplementary Figs. 1a-d that present the reflection high-energy electron diffraction (RHEED) patterns recorded *in situ* during MBE growth for films with various Sn compositions. The high quality of the layers is evidenced by sharp diffraction spots on the Laue circle and intense Kikuchi lines arising from diffraction from subsurface bulk lattice planes. No surface reconstruction was observed during deposition. The surface of the films is atomically flat, exhibiting only single monolayer steps of 3.52 Å height as exemplified by the atomic force microscopy (AFM) image presented in Supplementary Fig. 1e for x_{sn} = 28%. At the given growth temperature, growth proceeds in a 2D step-flow mode. Due to pinning of surface steps at screw type threading dislocations originating from the $Pb_{1-x}Sn_xSe$ / BaF_2 (111) lattice-mismatch of $\Delta a/a$ ~ 1.6% a characteristic spiral step structure is formed (cf. Supplementary Fig. 1e) similar as described in Ref. [1].

Supplementary Note 2: X-Ray diffraction and composition

The structural properties and composition of the $Pb_{1-x}Sn_xSe$ epilayers were characterized in detail by high-resolution x-ray diffraction (XRD) using a Seifert diffractometer equipped with primary and secondary monochromator crystals. Films with thicknesses larger than 1 µm are generally fully relaxed as found by reciprocal space mapping of asymmetric Bragg reflections. With increasing Sn content, the diffraction peaks shift to larger diffraction angles as illustrated by Supplementary Fig. 2a for the (222) Bragg reflection, indicating a corresponding decrease of the lattice constant a_0. From the evaluation of the lattice parameter, we find that the lattice constant closely follows the Vegard's law given by:

$$a_0\,(x_{Sn}) = 6.124 - 0.123 \cdot x_{Sn}\ [\text{Å}] \qquad (1)$$

in agreement with previous works [2]. Here, a_0 = 6.124 Å is the lattice constant of pure PbSe. Due to the sharp diffraction peaks and the high-resolution x-ray diffraction set-up the precision of the lattice constant determination is ±0.001 Å, which translates into a precision for x_{Sn} of ±0.01, i.e., of ±1%. Supplementary Fig. 2b shows the resulting composition of the layers versus that obtained from *in situ* beam flux measurements using the quartz balance method, evidencing a very good agreement without adjustable parameters. Films with Sn content above 40% are found to be no longer single phase, resulting in a splitting of the diffraction peaks. This is due to the fact that SnSe exhibits an orthorhombic crystal structure, for which reason the solubility of Sn in cubic rock salt $Pb_{1-x}Sn_xSe$ is limited to about 42%.

Supplementary Note 3: Bi-doping and electrical characterization

Undoped $Pb_{1-x}Sn_xSe$ exhibits a *p*-type background carrier concentration due to cation (Pb/Sn) vacancies formed during growth. These cation vacancies form resonant acceptor like energy levels and thus induce a *p*-type hole conductivity. The *p*-type carrier concentration increases with increasing Sn content from around 10^{17} cm^{-3} for PbSe to above 10^{18} cm^{-3} for $x_{Sn} > 30\%$. Incorporating Bi makes the system *n*-type and allows tuning the Fermi level into the conduction band as required for studying the properties of the of the entire Dirac cones of the topological surface states by angle-resolved photoemission (ARPES). We use a Bi_2Se_3 effusion cell for doping, which promotes substitutional incorporation of Bi on cation lattice sites without the need of an additional Se flux. The solubility of Bi in PbSe and SnSe amounts to several percent according to the quasi binary phase diagrams [1], however, for *n*-doping only a small Bi_2Se_3 flux in the range of 10^{-5}-10^{-2} ML s^{-1} range is actually required, depending on the desired doping level. This doping flux was calibrated as described in detail in Ref. [3].

Doping action of Bi and the resulting electrical properties of the films were evaluated by Hall measurements of a large series of samples as shown in Supplementary Fig. 3. For Bi-doped PbSe the measured electron concentration n_H corrected for the background hole concentration p_0 increases linearly with Bi flux and therefore changes exponentially with Bi_2Se_3 effusion cell temperature (*cf*. Supplementary Fig. 3a, ■), indicating a unity doping efficiency in agreement with previous results for Bi-doped PbTe films [3]. This therefore provides a reliable calibration of Bi concentrations within a relative error of 10%.

For $Pb_{1-x}Sn_xSe$ films, the electron concentration n_H - p_0 (Supplementary Fig. 3b, ◆) is generally found to be lower for the same growth conditions. This indicates a reduced doping efficiency of Bi in PbSnSe compared to that in PbSe, in particular at higher doping concentrations. As shown in Supplementary Fig. 3b, for small electron densities in the 10^{17} cm^{-3} range, the mobility of the epilayers at 77K is as high as $\mu_{77K} = 32000$ cm^2 V^{-1}s^{-1} for PbSe and 10.500 cm^2 V^{-1}s^{-1} for $Pb_{0.72}Sn_{0.28}Se$. Due to the increased scattering the mobility rapidly decreases with increasing Bi-content in particular above the 10^{18} cm^{-3} level, as we have also previously reported for PbTe [3].

Supplementary Note 4: Structural effect of Bi-doping

The influence of Bi-doping on the structural properties of the epilayers was evaluated by high-resolution x-ray diffraction as shown by Supplementary Fig. 4. For Bi-concentrations as high as 2.2% (doping concentration of 3.5×10^{20} cm^{-3}) we do not find any indication of phase separation or secondary phase formation and no broadening of the diffraction peaks occurs (Supplementary Fig. 4b).

For further analysis of possible lattice deformations, reciprocal space maps were recorded around the (222) and (513) reciprocal lattice points as shown in Supplementary Fig. 5 for two $Pb_{0.72}Sn_{0.28}Se$ epilayers with high (2.2%) and low (<0.5%) Bi-doping. From the fit of the peak positions, the in-plane and out-of-plane lattice constants, as well as unit cell corner angle α (rhombohedral distortion) was derived using the relation:

$$\sin(\alpha/2) = a_{//}\sqrt{3}\,(2a_{\perp}^2 + 4\,a_{//}^2)^{-1/2} \qquad (2)$$

For low Bi-concentration the layers exhibit a cubic lattice structure with a corner angle α = 90°. The experimental error in α is of ±0.01°, as derived from the errors in the lattice parameter determination (±0.001 Å). For the high-Bi doped layers, however, a rhombohedral lattice distortion is found with α ~ 89.94° for $n_{Bi} = 2.2\%$ as shown by Supplementary Fig. 5d. This indicates that Bi-doping modifies the lattice structure and thus impacts the topological surface state in the presence of a rhombohedral distortion. The visualization of the rhombohedral angle α and the shift of anion and cation (111) planes that typically cause the

rhombohedral distortion is depicted in Supplementary Fig. 6. On the other hand, we point out that for the sample with $n_{\mathrm{Bi}} = 1\%$, since the distortion is still too weak, from the XRD data we cannot conclusively derive the exact point of the structural phase transition considering the error bars.

Supplementary Note 5: Angle-resolved photoemission spectroscopy

Photoemission experiments were performed at the undulator beamline UE112-PGM2a of the BESSY II synchrotron radiation source in Berlin, Germany. We used the endstation ARPES 1[2] which is equipped with a Scienta R8000 hemispherical analyzer allowing to detect emitted photoelectrons up to acceptance angles of 30°. The base pressure during experiments was better than 1×10^{-10} mbar. The epitaxial films were capped *in situ* after MBE growth with a 200 nm thick amorphous Se layer at room temperature to protect the surface against oxidation during transport to the ARPES setup, where the Se cap was completely desorbed in the preparation chamber by annealing at about 230°C for 15 min in 3×10^{-10} mbar. The corresponding valence band ARPES data were collected in a wide range of temperatures using linearly-polarized $p+s$ photons with energies ranging from 18 to 23 eV. The ARPES dispersions around the $\bar{\Gamma}$ and $\bar{\mathrm{M}}$ points were acquired using the photon beam geometry shown in Fig. 1a of the main text, where the light is incident on the sample under and angle of ϕ=45° with respect to the surface normal. The light incidence and electron detection planes were parallel to the $\bar{\mathrm{M}}$-$\bar{\Gamma}$-$\bar{\mathrm{M}}$ and $\bar{\mathrm{K}}$-$\bar{\Gamma}$-$\bar{\mathrm{K}}$ high symmetry directions of the surface Brillouin zone, respectively. The corresponding energy and angular resolutions were set to 5 meV and 0.1°, respectively.

Supplementary Note 6: Determination of the surface band gap

To determine the size of the surface band gaps as a function of Bi and Sn concentrations as well as of temperature, we have fitted the experimental energy-distributions curves (EDCs) at zero momentum extracted from the ARPES spectra shown in the main text. In Supplementary Fig. 7, we summarize the procedure used by taking a $\mathrm{Pb}_{0.72}\mathrm{Sn}_{0.28}\mathrm{Se}$ sample doped with 0.6% Bi as an example. Supplementary Fig. 7a displays the corresponding energy-momentum ARPES dispersion measured at 30 K and 18 eV photon energy. The intensity contributions from the bulk-valence band (BVB) states at high binding energies are clearly distinguishable from the dispersion of the upper and lower part of the surface state (SS) at lower binding energies. In particular, we observe that in contrast to the undoped $\mathrm{Pb}_{0.72}\mathrm{Sn}_{0.28}\mathrm{Se}$ sample measured under the same experimental conditions (see Fig. 2a of the main text), incorporating Bi leads to an intensity dip at the energy position of the original Dirac point which is the signature of a small gap. We also note that by increasing the Bi concentration, as also seen in Figs. 2c,d of the main text, the intensity dip becomes more and more pronounced which is related to the widening of the surface gap.

In Supplementary Fig. 7b we show the corresponding EDCs extracted from Supplementary Fig. 7a, where the EDC at normal emission is highlighted with a thick red line. The corresponding fit results (black solid lines) of the EDC (red circles) are shown in Supplementary Fig. 7c. The error bars in the determination of the surface gap shown in the main text correspond to the uncertainty of determining the energy position of the band dispersions, and are estimated from the standard deviations of the peak positions over several fitting cycles. Specifically, the size of the surface band gap is determined from the energy separation between the fitted Lorentzian peaks shown in blue (green) color, which are located at the energy minimum (maximum) of the upper (lower) part of the SS. We also point out that a lower limit of the surface band gap can be obtained from the ARPES spectra after considering the contribution from the linewidth broadening. The lower limit of the surface

band gap is approximately represented by horizontal dashed lines around the region of the gap in Figs. 2a-d and Fig. 3 of the main text. In Supplementary Figs. 7c, other Lorentzian peaks shown in gray color are contributions from the bulk-valence band (BVB). To extract the energy positions, the experimental ARPES spectra were fitted by a sum of Lorentzian functions plus a background. A typical spectrum containing N number of peaks was fitted by a function involving a convolution of the form:

$$\mathrm{I}(E,k) = \left[\mathrm{f}(E,T)\cdot\sum_{i=1}^{\mathrm{N}}\mathrm{M}_i^2\cdot\mathrm{A}_i(E_i,w_i)+\mathrm{B}(E)\right]\otimes\mathrm{G}(E) \qquad (3)$$

Where E_i, ω_i, and the matrix elements M_i are fitting parameters corresponding to the binding energy, width, and intensity of each Lorentzian peak, and f(E,T) is the Fermi function. The spectral function $A_i(E_i,\omega_i)$ is approximated by Lorentzian functions, and B(E) is assumed to be a Shirley-like background [4]. The full width at half maximum (FWHM) of the Gaussian slit function G(E) corresponds to the total energy resolution of the experiment, which is photon-energy dependent.

Supplementary Note 7: Photon energy dependence of $Pb_{0.72}Sn_{0.28}Se$ doped with 2.2% Bi

To analyze the energy-momentum band dispersions of the surface state as a function of photon energy, we have fitted the experimental momentum-distribution curves (MDCs) extracted from the ARPES measurements shown in Fig. 2h-m of the main text. In Supplementary Figs. 8a-h, we summarize the procedure used by taking representative results at 18 eV and 22 eV photon energy as an example. For the fitting procedure, we used a sum of Lorentzian peaks plus a constant background convoluted with a Gaussian function representing the momentum resolution, and thus a fit function which is similar to Supplementary Eq. (3) but with the electron momentum parallel to the surface as the main variable. Supplementary Fig. 8a shows the fit results of the upper and lower parts of the surface state superimposed on the corresponding ARPES dispersion measured at 18 eV. The fitted peak positions are also shown independently in Supplementary Fig. 8b. Analogous results for measurements at 22 eV photon energy are displayed in Supplementary Figs. 8c,d. From this comparison, we observe good agreement concerning both the energy positions of the upper and lower parts of the surface state as well as their overall dispersion with momentum parallel to the surface.

In Supplementary Figs. 8e-h, we show few-selected fits (black solid lines) to experimental MDCs (red symbols) obtained at various binding energies across the upper and lower parts of the surface state for photon energies of 18 eV (Supplementary Figs. 8e,f) and 22 eV (Supplementary Figs. 8g,h). The intensity contributions from the surface state are marked with black filled circles on top of each fit. Additional intensities from the bulk-conduction band (BCB) near the Fermi level and from the bulk-valence band (BVB) at high binding energies were fitted by extra Lorentzian peaks introduced into the analysis procedure. As seen in Supplementary Figs. 8e-h, the obtained fits are in remarkable agreement with the experimental MDCs. The intensity contributions from the upper part of the surface state (Supplementary Figs. 8e,g) appear as distinct peaks in the corresponding MDCs. This is also the case for the whole measured photon-energy range shown in Figs. 2h-m of the main text, even for photon energies where the dispersion of the BCB is clearly observed. Similarly, as seen in Supplementary Fig. 8f, the lower part of the surface state appears as pronounced peaks around the BVB intensity, which becomes progressively smaller with decreasing binding energy. This situation is more or less representative for fits to experimental MDCs up to photon energies of 21 eV. At higher photon energies, despite the dispersion of the BVB with momentum perpendicular to the surface k_z, we clearly resolve the opposite branches of the lower part of the surface state as pronounced shoulders around the BVB intensity (see

Supplementary Fig. 8h). This allows us to extract the energy positions of the lower surface state with relatively good accuracy, despite the partial overlap with the BVB which nevertheless introduces additional errors in the fitted band dispersions. The error bars in the MDC fits were estimated from the standard deviations of the peak positions over several fitting cycles. In particular, the error bars in $\Delta k_{\parallel}$ (ΔE) shown in Fig. 2n of the main text for each photon energy were taken as the maximum error obtained for the whole fitted range, and the corresponding error bars in energy were estimated from the obtained $\Delta k_{\parallel}$ values. These error bars represent the maximum uncertainty in determining the corresponding band dispersions as extracted from the MDC fits. Supplementary Figs. 8i-n display the photon-energy dependent ARPES spectra shown in Figs. 2h-m of the main text, where we have superimposed the corresponding results of the MDC fits for each photon energy. By comparing the maximum error bar obtained from the MDC fits to the maximum deviation between the fitted results for different photon energies shown in Fig. 2n of the main text, we derive a total accuracy representing the upper bound for the maximal k_z dispersion of the surface state of ±20 meV. This result strongly indicates that the gapped surface state is two dimensional, in contrast to the three-dimensional character of the BCB or the BVB which clearly disperse with photon energy as seen in Supplementary Figs. 8i-n.

Supplementary Note 8: ARPES of the surface state in the topologically trivial state

To determine whether in the topologically trivial phase the temperature dependence of the band gaps is similar at the $\bar{\Gamma}$ and at $\bar{\mathrm{M}}$ points, ARPES data were recorded for a ~0.6% Bi-doped $Pb_{1-x}Sn_xSe$ sample with a Sn content of 16% at temperatures ranging from 300 to 30 K. This particular Sn content was chosen to be close to the quantum critical point of the phase transition, but staying in the trivial phase for all investigated temperatures. The ARPES data shown in Supplementary Fig. 9 reveal both the valence and conduction band states with an open gap corresponding to the non-inverted band structure. At $\bar{\Gamma}$, we clearly observe the contribution from topologically trivial surface states forming as precursor states of the quantum-phase transition, which are also seen in Figs. 1-3 of the main text in agreement with previous observations on undoped topological crystalline insulators [5]. We also point out that the same precursor states have been observed in quantum-phase transitions between trivial and Z_2 topological insulators, which in addition preserve the helical spin texture despite their trivial origin [6]. Note that the intensity from the precursor states at the $\bar{\mathrm{M}}$ points is less resolved in our data most probably because of their tilted projection onto the (111) plane, which corresponds to an electron emission angle of about 21° in the particular geometry shown in Supplementary Fig. 10.

Supplementary Note 9: Band gaps and Dirac cones in the different topological phases

As described in the main text, $Pb_{1-x}Sn_xSe$ (111) exists in different topological states depending on temperature, Sn and Bi content. For low $x_{Sn} < 16\%$, $Pb_{1-x}Sn_xSe$ is topologically trivial with an open and equal band gap at the $\bar{\mathrm{M}}$ and $\bar{\Gamma}$ points of the surface Brillouin zone as shown schematically in Supplementary Fig. 11a. For higher x_{Sn}, a bulk band inversion occurs at low temperatures, which renders $Pb_{1-x}Sn_xSe$ as topological crystalline insulator, in which Dirac cones are formed at all four high symmetry points, i.e., all $\bar{\mathrm{M}}$ and $\bar{\Gamma}$ points. This is shown in Supplementary Fig. 11b. Upon Bi-doping, the valley degeneracy is lifted and a gap opens up at the $\bar{\Gamma}$ point, while the Dirac cones remain closed, i.e., ungapped at all three $\bar{\mathrm{M}}$-points (Supplementary Fig. 11c). This makes Bi-doped $Pb_{1-x}Sn_xSe$ a Z_2 topological insulator with odd number of band inversions.

Supplementary Note 10: Core-level photoemission

Core-level spectra measured with 90 eV photons for $Pb_{1-x}Sn_xSe$ with 28% Sn concentration and 2.2% Bi doping are shown in Supplementary Fig. 12a. The overlap of Bi $5d_{5/2}$ with Sn $4d_{5/2}$ emission is resolved by a fitting procedure, the results of which are shown in Supplementary Fig. 12b. To further evaluate the stoichiometry from the core-level spectra, in particular the Bi concentration, we analyzed the intensity ratios by taking into account the peak areas and the corresponding photoemission cross sections of the individual elements [7]. Specifically, we used a similar fitting procedure as the one described in Supplementary Note 6. After normalizing the peak areas of individual elements by their photoemission cross section, we derived the Bi concentration from the ratio $n_{Bi}=A_{Bi}/(A_{Bi}+B_{Pb}+C_{Sn})$, where A, B, C denote the corresponding peak areas normalized with respect to the area under the Se peak. For the core-levels shown in Supplementary Fig. 12, we derive $A_{Bi}=0.0973$, $B_{Pb}=2.04129$ and $C_{Sn}=0.84593$, which yields an absolute value of n_{Bi}~3.2 % that is in fair agreement with the more accurate result obtained using high resolution x-ray diffraction and the Vegard's law (see Supplementary Fig. 2 and Supplementary Note 2).

Supplementary References

1. Springholz, G., Ueta, A. Y., Frank, N. & Bauer, G. Spiral growth and threading dislocations for molecular beam epitaxy of PbTe on BaF_2 (111) studied by scanning tunneling microscopy. *Appl. Phys. Lett*. **69**, 2822-2824 (1996).

2. McCann, P. J., Fuchs, J., Feit, Z. & Fonstad, C. G. Phase equilibria and liquid-phase-epitaxy growth of PbSnSeTe lattice-matched to PbSe. *J. Appl. Phys.* **62**, 2994-3000 (1987).

3. Ueta, A. Y., Springholz, G., Schinagl, F., Marschner, G. & Bauer, G. Doping studies for molecular beam epitaxy of PbTe and $Pb_{1-x}Eu_xTe$. *Thin Solid Films* **306**, 320-325 (1997).

4. Shirley, D. A. High-resolution x-ray photoemission spectrum of the valence bands of gold. *Phys. Rev. B* **5**, 4709 (1972).

5. Wojek, B. *et al*. Spin-polarized (001) surface states of the topological crystalline insulator $Pb_{0.73}Sn_{0.27}Se$. *Phys. Rev. B* **87**, 115106 (2013).

6. Xu, S.-Y. *et al*. Unconventional transformation of spin Dirac phase across a topological quantum phase transition. *Nature Commun.* **6**, 6870 (2015).

7. Yeh, J. J. & Lindau, I. Atomic subshell photoionization cross sections and asymmetry parameters: $1 \leq Z \leq 103$, in *Atomic Data and Nuclear Data Tables*, **32**, 1-155 (1985).

4.9 Giant Rashba effect in (Pb,Sn)Te

The topological properties of lead-tin chalcogenide topological crystalline insulators can be tuned by temperature and composition. We have shown that bulk Bi doping of epitaxial (Pb,Sn)Te (111) films induce a giant Rashba splitting at the surface that the doping level can tune. Tight binding calculations identify their origin as Fermi-level pinning by trap states at the surface.

Giant Rashba Splitting in $Pb_{1-x}Sn_xTe$ (111) Topological Crystalline Insulator Films Controlled by Bi Doping in the Bulk

Valentine V. Volobuev, Partha S. Mandal, Marta Galicka, Ondřej Caha, Jaime Sánchez-Barriga, Domenico Di Sante, Andrei Varykhalov, Amir Khiar, Silvia Picozzi, Günther Bauer, Perla Kacman, Ryszard Buczko, Oliver Rader, and Gunther Springholz**

A novel class of topological insulators (TIs), called topological crystalline insulators (TCIs), has been recently predicted[1,2] and experimentally demonstrated for SnTe,[2,3] $Pb_{1-x}Sn_xTe$,[4,5] and $Pb_{1-x}Sn_xSe$.[6] In these IV–VI materials, an inversion of the L_{6+} and L_{6-} valence and conduction bands (CBs) occurs above a certain critical Sn content (see **Figure 1**a).[7–9] This induces a trivial to nontrivial topological phase transition that, due to the bulk-surface connectivity, gives rise to the formation of a 2D topological surface state (TSS) with linear dispersion of a Dirac cone and helical spin texture due to spin-momentum locking.[1,2,6,10–12] In TCIs, these TSSs are protected by crystal mirror symmetries[1,2] rather than by time-reversal symmetry as in conventional Z_2 topological insulators.[13,14] Thus, these surface states are formed on particular surfaces such as (001), (111), and (110), where the crystalline mirror symmetries are preserved.[1,2,12] Moreover, the band inversion is highly sensitive to external perturbations.[10,15,16] Therefore, the trivial to nontrivial topological phase transition can be controlled by many different means, such as by varying temperature,[1,6] pressure,[2] hybridization in ultrathin film geometries,[17–19] magnetic interactions,[20] or by breaking of mirror symmetries by strain,[16,21–23] electrostatic fields,[18] or ferroelectric (FE) lattice distortions.[24,25] This provides ample degrees of freedom for topology control not available in conventional Z_2 TIs. For this reason, TCIs offer an ideal template for observation of exotic phenomena such as partially flat band helical snake states and interfacial superconductivity,[16] large-Chern-number quantum anomalous Hall effect,[26] as well as for realization of novel topology-based devices such as topological photodetectors,[23] spin transistors,[18] and spin torque devices.[27]

For most of such applications, thin film structures with precisely controlled composition and Fermi level are required. Up to now, most work has been performed on highly p-type bulk crystals exploiting the natural (001) cleavage plane of the IV–VI compounds,[3,4,6] whereas for other surface orientations and practical devices epitaxial TCI film structures are required.[18,28–32] The (111) orientation is particularly interesting due to the polar nature of its surface[12] as well as the ease of lifting the fourfold valley degeneracy at the *L*-points of the Brillouin zone (BZ)[33] by opening a gap at particular Dirac points by strain[16] and quantum confinement[17–19] to induce a transition from a TCI to a normal Z_2-TI material.[25] Epitaxial growth strongly relies on lattice and thermal expansion matching between films and substrate material. Good results have been obtained, e.g., for PbSnTe on Bi_2Te_3 buffer layers,[31,34] but transport and photoemission investigations are offset by the intrinsic topological character of Bi_2Te_3,[31,35] as well as by PbSnTe/Bi_2Te_3 interdiffusion and intermixing. Most challenging, however, is the intrinsic p-type character of PbSnTe caused by the natural tendency of cation vacancy formation, creating resonant acceptor levels in the valence band (VB).[9] This tendency strongly increases with increasing Sn content and thus, SnTe always exhibits very high bulk hole concentrations of around 10^{20} cm^{-3}. This not only masks the topological surface state in transport and optical investigations but also impedes observing the Dirac point by angle-resolved photoemission (ARPES).

In the present work, we employ molecular beam epitaxy (MBE) to grow high-quality $Pb_{1-x}Sn_xTe$ films in which

Dr. V. V. Volobuev, Dr. A. Khiar, Prof. G. Bauer, Prof. G. Springholz
Institute for Semiconductor and Solid State Physics
Johannes Kepler Universität
Altenberger Str. 69, 4040 Linz, Austria
E-mail: valentyn.volobuiev@jku.at; gunther.springholz@jku.at
Dr. V. V. Volobuev
National Technical University "Kharkiv Polytechnic Institute"
Frunze Str. 21, 61002 Kharkiv, Ukraine
P. S. Mandal, Dr. J. Sánchez-Barriga, Dr. A. Varykhalov, Prof. O. Rader
Helmholtz-Zentrum Berlin für Materialien und Energie
Albert-Einstein Str. 15, 12489 Berlin, Germany
Dr. M. Galicka, Prof. P. Kacman, Prof. R. Buczko
Institute of Physics
Polish Academy of Sciences
Aleja Lotników 32/46, PL-02-668 Warszawa, Poland
Dr. O. Caha
Department of Condensed Matter Physics
Masaryk University
Kotlářská 2, 61137 Brno, Czech Republic
Dr. D. Di Sante, Dr. S. Picozzi
Consiglio Nazionale delle Ricerche CNR-SPIN
Via dei Vestini 31, 66100 Chieti, Italy
Dr. D. Di Sante
Institut für Physik und Astrophysik
Universität Würzburg
Am Hubland Campus Süd, Würzburg 97074, Germany

DOI: 10.1002/adma.201604185

© 2016 WILEY-VCH Verlag GmbH & Co. KGaA, Weinheim

Reprinted page 1 of paper [88] "Rashba splitting in (Pb,Sn)Te controlled by Bi doping".

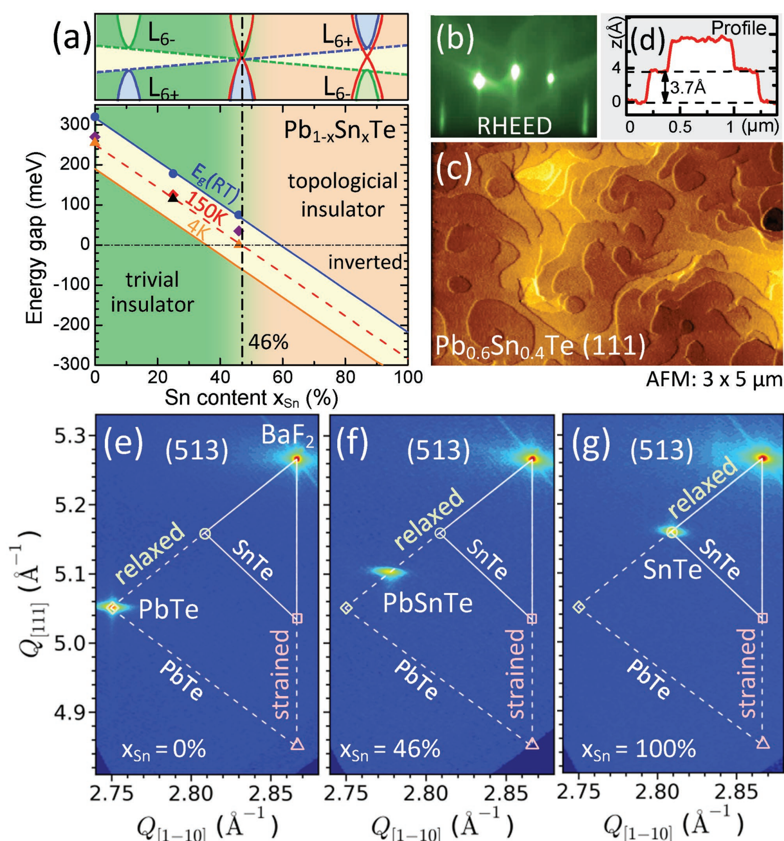

Figure 1. Basic properties of $Pb_{1-x}Sn_xTe$ (111) films. a) Band gap in dependence of Sn content x_{Sn} at $T = 300$, 150, and 4 K (solid/dashed lines) according to refs. [7] and [8]. Symbols: ARPES data for room temperature (●), 200 K (◆), 150 K (◆), and 100 K (▲). The band inversion and trivial to nontrivial topological phase transition occur at $x_{Sn} = 0.36$ and $= 0.6$ for 4 and 300 K, respectively. b,c) RHEED patterns and AFM image of a $Pb_{0.4x}Sn_{0.6}Te$ film grown by MBE on BaF_2 (111) substates. d) The extracted surface profile shows only single monolayer steps with a height of 3.7 Å. e–g) X-ray diffraction reciprocal space maps around the (513) Bragg reflection for three epilayers with $x_{Sn} = 0$, 0.46, and 1. As indicated, the layer peaks lie exactly on the line connecting the peak positions of bulk PbTe (◊) and SnTe (○), evidencing that all films are fully relaxed without residual lattice distortion. The expected peak positions of fully strained epilayers are indicated by (Δ, □).

"extrinsic" n-type doping is employed for compensation and control of carrier concentration. We show that Bi doping allows us to tune the Fermi level over a wide range from the valence to the conduction band and thus to observe the trivial to nontrivial topological phase transition under temperature and composition variation. By careful tuning of the doping level and growth conditions, low free carrier concentrations of about 10^{18} cm^{-3} and carrier mobilities as high as 10^4 cm^2 V^{-1} s^{-1} are achieved, providing excellent conditions for quantum transport and optical studies of nontrivial topology effects.[32] Most strikingly, we find that Bi doping induces a very large Rashba splitting of the valence band that is absent for undoped material and reaches values as high as 0.022 Å^{-1}. This yields a giant Rashba coupling constant of 3.8 eV Å^{-1} that is comparable to the record values recently reported for the BiTe–halide compounds.[36–38] By tight binding (TB) calculations we reveal that this Rashba splitting is caused by pinning of the Fermi level by acceptor-like trap states at the surface. The important outcome is that the Rashba effect can be tailored and tuned by bulk Bi doping. The coexistence and hybridization of TSS and Rashba-split surface states is unexpected due to the inversion symmetry of the rock salt structure and paves the way for novel topological spin–orbitronic devices.[39]

Epitaxial growth of $Pb_{1-x}Sn_xTe$ was performed by molecular beam epitaxy on BaF_2 (111) substrates using stoichiometric PbTe and SnTe beam flux sources.[40,41] The chemical composition of the layers was varied over a wide range from $x_{Sn} = 0$ to 1 by control of the SnTe/PbTe beam flux ratio, which was measured precisely using the quartz crystal microbalance method.[40] n-type doping was realized using a Bi_2Te_3 compound source to promote substitutional incorporation of bismuth into cation lattice sites,[42] where Bi acts as a donor because of its additional

© 2016 WILEY-VCH Verlag GmbH & Co. KGaA, Weinheim

Reprinted page 2 of paper [88] "Rashba splitting in (Pb,Sn)Te controlled by Bi doping".

valence electron compared to Pb or Sn.[42,43] The solubility of Bi_2Te_3 in SnTe and PbTe amounts to several percent according to the quasi binary phase diagrams.[44] For compensation of the native p-type carrier concentration, however, only small Bi concentrations well below 1% and Bi flux rates of 10^{-4}– 10^{-3} monolayer (ML) per second are required, compared to overall film growth rates of 1 ML s^{-1} (= 3.7 Å s^{-1}).

2D growth of $Pb_{1-x}Sn_xTe$ (111) films is observed for all compositions beyond a thickness of 100 nm as demonstrated by the reflection high-energy electron diffraction (RHEED) patterns and atomic force microscopy (AFM) image depicted in Figure 1b,c for $x_{Sn} = 0.4$. The high film quality is evidenced by sharp diffraction spots arranged on the Laue circle and the intense Kikuchi lines arising from scattering at subsurface lattice planes. No surface reconstruction is observed. The surface is atomically flat exhibiting about 200 nm wide terraces separated by single monolayer steps of 3.7 Å height (cf. Figure 1d). At the given substrate temperature of 350 °C, growth proceeds in a step-flow mode with the surface steps pinned by threading dislocations as described in detail in refs. [45] and [46]. Structural characterization by high-resolution X-ray reciprocal space mapping (see Figure 1e–g) demonstrates that the layers with 1–2 µm thickness are fully relaxed. Accordingly, their Bragg peaks lie exactly along the line connecting the bulk PbTe ($a_{PbTe} = 6.462$ Å) and SnTe ($a_{SnTe} = 6.323$ Å) reciprocal lattice points, as indicated by the dashed and solid lines, respectively. Thus, the epilayers are undistorted with equal in- and out-of-plane lattice constants. Systematic evaluation of the lattice parameter as a function of composition shows that it precisely follows Vegard's law.[47] In particular, for all samples the Sn content derived by X-ray diffraction perfectly agrees with the nominal growth values. Moreover, no traces of any secondary phases were detected.

The Bi doping action and transport properties were evaluated by Hall effect measurements, as summarized in **Figure 2**. Undoped PbTe layers are n-type in the low 10^{17} cm^{-3} range under stoichiometric MBE growth conditions.[40,42] On the contrary, the carrier type of $Pb_{1-x}Sn_xTe$ switches from n to p-type at $x_{Sn} > 15\%$ and thereafter the hole concentration rises exponentially with increasing Sn content, reaching hole densities as high as 2×10^{20} cm^{-3} for pure SnTe (see Figure 2a). This demonstrates an exceedingly low cation vacancy formation energy E_V of SnTe compared to PbTe.[48] For undoped $Pb_{1-x}Sn_xTe$ TCI films requiring x_{Sn} larger than 40%, the Fermi level is therefore always deep in the valence band.[3–5,33] We model the dependence of the cation vacancy formation energy on composition using $E_V(x_{Sn}) = E_{V,SnTe} + \Delta E_V\,(1 - x_{Sn})$, where ΔE_V is the vacancy energy difference between PbTe and SnTe. Assuming an Arrhenius-like behavior for the equilibrium vacancy concentration, the native free carrier concentration in $Pb_{1-x}Sn_xTe$ is predicted as

$$n_{n,p}\,(x_{Sn}) = -n_{n,PbTe} + n_{p,SnTe}\,e^{-\Delta E_V(1-x_{Sn})/kT} \tag{1}$$

where $n_{n,PbTe}$ and $n_{p,SnTe}$ are the intrinsic carrier concentrations of the parent binary materials for the given growth conditions.

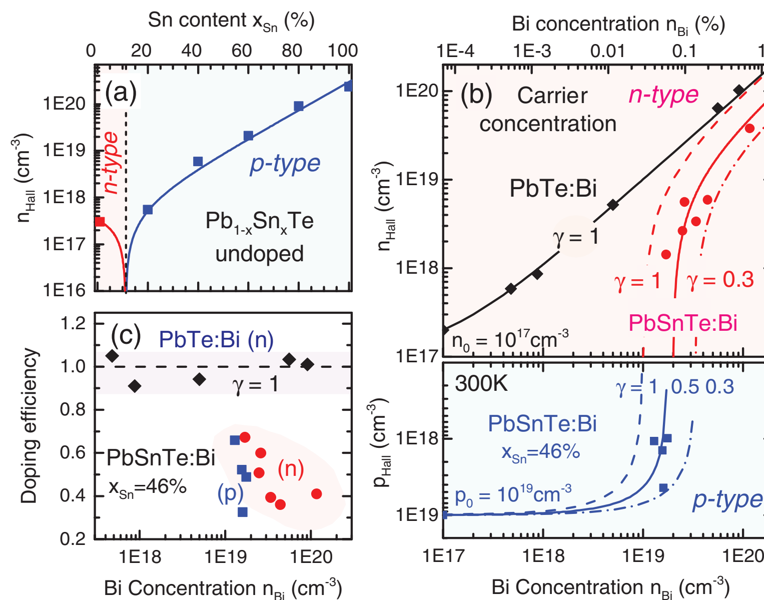

Figure 2. Effect of Bi doping of TCI films. a) Intrinsic carrier concentration of undoped $Pb_{1-x}Sn_xTe$ epilayers as a function of Sn content, revealing the high p-type character with increasing Sn content due to Sn vacancy formation. The solid line represents the fit of the experimental data assuming that the formation energy of vacancies decreases linearly with x_{Sn}. b) Hall concentrations n_{Hall} obtained for PbTe:Bi (◆) and $Pb_{0.54}Sn_{46}Te$:Bi (■: p-type; ●: n-type) as a function of Bi-dopant concentration. Solid lines: Expected n_{Hall} for different doping efficencies $\gamma = 1$ for PbTe (black line) and $\gamma = 1$, 0.5, and 0.3 for PbSnTe as indicated, based on the background carrier concentration measured for the undoped reference layers. c) Bi doping efficiency derived for PbTe (◆) and $Pb_{0.54}Sn_{46}Te$ (■: p-type; ●: n-type) versus Bi concentration.

© 2016 WILEY-VCH Verlag GmbH & Co. KGaA, Weinheim

Reprinted page 3 of paper [88] "Rashba splitting in (Pb,Sn)Te controlled by Bi doping".

As demonstrated by the solid line in Figure 2a, this model perfectly describes our experimental findings and from the fit of our data, a difference in the cation vacancy formation energy between PbTe and SnTe of $\Delta E_v = 360$ meV is derived.

Effective control of the carrier type and tuning of the carrier concentration by Bi doping is demonstrated in Figure 2b, where the Hall concentrations of Bi-doped PbTe (◆) and $Pb_{0.54}Sn_{0.46}Te$ (■,●) epilayers are plotted versus Bi concentration. For PbTe, the electron concentration rises perfectly linearly with Bi dopant concentration (solid line), evidencing a single ionized donor state and a unity doping efficiency $\gamma = (n - n_0)/n_{Bi}$ for Bi concentrations as high as 10^{20} cm^{-3}. This provides a precise calibration of the Bi flux for growth. For $Pb_{0.54}Sn_{0.46}Te$, Bi doping partially compensates the native hole concentration until for $n_{Bi} > 2 \times 10^{19}$ cm^{-3} the material switches from p to n-type with electron concentrations up to the mid-10^{19} cm^{-3} range (cf. Figure 2b). Thus, the carrier density can be tuned over a wide range. By precise control of the Bi flux, low carrier densities within the 10^{17} cm^{-3} range can be obtained, resulting in Hall mobilities as high as $\mu_H = 13\,000$ cm^2 V^{-1} s^{-1} at 77 K, comparable to or even exceeding the highest values reported for long-term annealed bulk PbSnTe single crystals with similar Sn content.[49] Inspection of Figure 2b reveals, however, that for highly doped $Pb_{0.54}Sn_{0.46}Te$ films the actual electron concentration is significantly below the expected values for $\gamma = 1$ (dashed line) and that the maximum electron concentration saturates in the mid-10^{19} cm^{-3} range even at high Bi concentrations. This means that the doping efficiency decreases with increasing Sn content to $\gamma < 0.4$ for $x_{Sn} = 46\%$ (Figure 2c), whereas for pure PbTe it is unity for all investigated Bi concentrations. This suggests that Bi develops an amphoteric character in the ternary materials and starts to occupy Te lattice sites as well, on which it acts like an acceptor. Thus, compensation of the native hole concentration becomes increasingly difficult at higher Sn contents.

The effect of Bi doping on the topological surface state and population of the electronic bands was studied in detail by ARPES as a function of temperature and composition in the 17–90 eV photon energy range. As shown by **Figure 3**, for n-doped $Pb_{0.54}Sn_{0.46}Te$:Bi films both conduction and valence bands are clearly visible in ARPES, whereas for undoped films only the lower branch of the valence band is seen because the Fermi level is well below the VB edge (see **Figure 4**a). For a Bi doping of $n_{Bi} = 4 \times 10^{19}$ cm^{-3} (= 0.3% Bi), the Fermi level E_F at room temperature is already by +100 meV above the CB edge and lowering the temperature induces a further upward shift to +160 meV at 110 K (cf. Figure 3a–c). At this temperature a well-resolved 2D TSS with linear dispersion appears, indicating the transition from the trivial to the nontrivial TCI state. Also, an increase in the Fermi velocity, i.e., slope of the $E(k)$ dispersion, occurs due to the decrease of the effective masses accompanying the closing of the gap.[8,9] This in turn leads to a decrease in the electronic density of states, which means that at lower temperatures the Fermi energy must shift upward to accommodate the nearly constant carrier concentration found by the Hall effect measurements.

The 2D nature of the observed surface state was verified by photon-energy-dependent ARPES investigations shown in Figure 3e–h. In spite of different admixtures of dispersive bulk and nondispersive surface signals at different photon energies, the absence of any photon energy dispersion corroborates that the observed bands are indeed surface states with 2D character. For the n-doped $Pb_{0.54}Sn_{0.46}Te$ films, linear extrapolation of the TSS from the CB yields a Dirac point position at 10–20 meV below the VB maximum at 110 K. This is revealed clearly by Figure 3j,k, where the ARPES intensity is depicted on a logarithmic scale. Also shown for comparison are the ARPES data of a film with $x_{Sn} = 26\%$, in which the gap remains fully open with $E_g \approx 120$ meV even at low temperatures, i.e., for low Sn contents $Pb_{1-x}Sn_xTe$ remains topologically trivial. Thus, the trivial to nontrivial topological phase transition is demonstrated for (111) epitaxial films both as a function of temperature and Sn content. It is noted that the topological phase transition was previously suggested to occur already at $x_{sn} \approx 0.25$ for cleaved (001) bulk $Pb_{1-x}Sn_xTe$ crystals.[5] However, this conclusion was based only on extrapolation of the dispersion of the VB of highly p-type material without directly observing the Dirac point and conduction band.

Remarkably, all n-doped films show a very large Rashba splitting of the valence band in the k_{II} direction. To map out its correlation with the doping level, ARPES was performed for a series of $Pb_{0.54}Sn_{0.46}Te$ layers with systematically increasing doping level. The results are presented in Figure 4 for Bi concentrations varying from 0% to 1%. Whereas for the undoped film the Fermi level is deep inside the VB, it strongly moves upward with increasing Bi content so that for $n_{Bi} > 0.2\%$ the full VB dispersion and CB appear. In fact, a total shift of E_F by as much as +280 meV is achieved by 1% Bi doping, evidencing the effective control of the Fermi level. Most importantly, we find that the Rashba splitting systematically increases with the Bi concentration. Thus, the Rashba effect is induced by the "bulk doping" of the material, which is in complete contrast to the Rashba effect in Z_2-TIs such as Bi_2Se_3, which is usually induced by alkaline[50,51] or transition metal deposition[52] or adsorption of water on the surface,[53,54] but not upon bulk doping.[52,55–58] Moreover, it is to be noted that in these Z_2-TIs the Rashba bands are completely separated in energy from the TSS, whereas in our TCI case the Dirac and Kramers point overlap (see Figure 3j). This suggests that a hybridization between the TSS and the Rashba bands may occur.

For quantitative evaluation, the Rashba bands were modeled using the effective mass approximation where the energy–momentum dispersion is given by

$$E(k_{\pm}) = \hbar^2k^2/2m^* + \alpha_R\left(\vec{\sigma}\times\hat{k}\right)\hat{z} = \hbar^2k^2/2m^* \pm \alpha_R k \quad (2)$$

where m^* is the effective carrier mass in the k_{II} direction, σ is the Pauli spin matrix, and α_R is the Rashba constant due to spin–orbit coupling and structural asymmetry at the surface. The Rashba effect causes the formation of two separate spin-polarized bands k_+ and k_- that are split by $2\Delta k_R$ in the k_{II} direction, as indicated schematically by the dashed lines in Figure 4d. This leads to a nested band structure with helical spin texture, forming concentric rings in the k_{xy} plane as corroborated by the constant energy ARPES maps depicted in Figure 4e–h. This is a key hallmark of the Rashba effect. From the data, we derive the momentum splitting Δk_R and Rashba energy E_R (= energy difference between the band maxima and the Kramers point) for each sample, which yields the Rashba

© 2016 WILEY-VCH Verlag GmbH & Co. KGaA, Weinheim

Reprinted page 4 of paper [88] "Rashba splitting in (Pb,Sn)Te controlled by Bi doping".

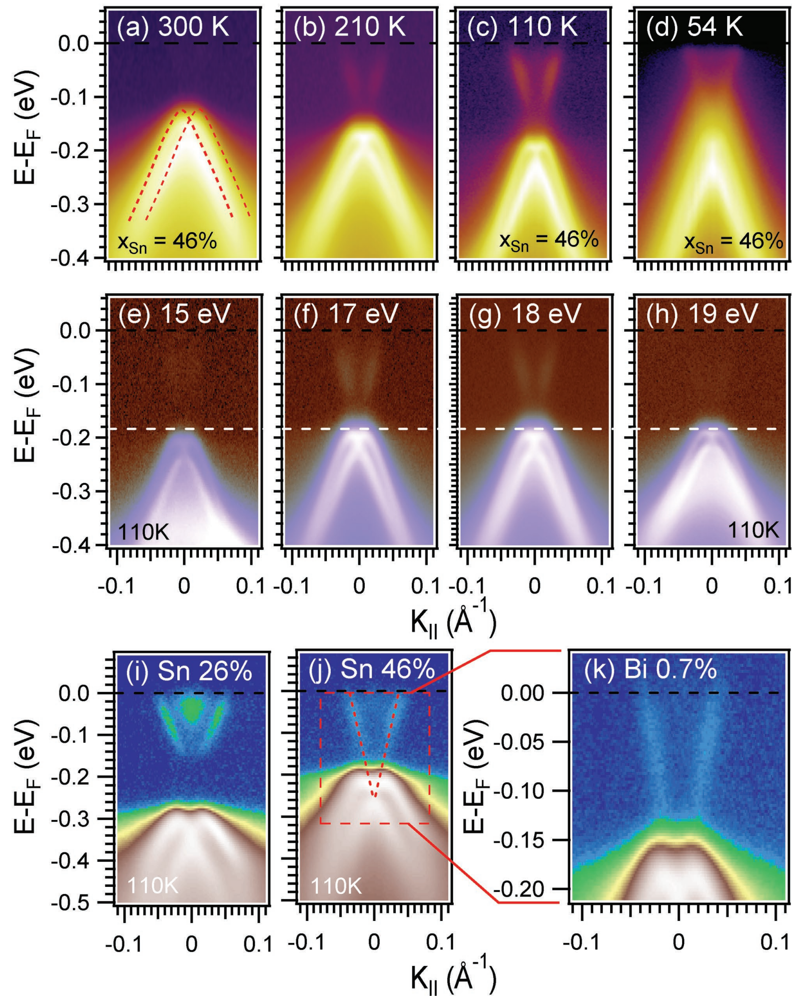

Figure 3. Topological phase transition characterized by ARPES. a–d) Temperature-dependent $E(k)$ maps of a $Pb_{0.54}Sn_{0.46}Te$ (111) epilayer with 0.25% Bi measured around $\overline{\Gamma}$ of the surface BZ using a photon energy of 18 eV. The topological transition occurs at about 110 K. Below 80 K photoemission becomes unstable due to photoninduced adsorption of residual gases and charging of the surface.[11] e–h) Photon energy dependence measured at 110 K. i–k) ARPES spectra of $Pb_{1-x}Sn_xTe$ epilayers with low (x_{Sn} = 26%) and high (46%) Sn content, demonstrating the trivial to nontrivial phase transition as a function of composition with an open gap for the former and with a closed gap for the latter at 110 K. The intensity is shown on a logarithmic scale to reveal the TSS in the CB.

coupling constant $\alpha_R = 2E_R/\Delta k_R$ as a function of the doping level. The results are summarized in **Table 1**, demonstrating a clear correlation between the Rashba parameters and Bi concentration. In particular, the Rashba constant assumes exceedingly large values of $\alpha_R = 3.8$ eV Å^{-1} for 1% Bi doping, which is comparable to the recently reported record values of the giant Rashba systems such as BiTeX (X = I, Br, and Cl) and α-GeTe where α_R is of the order of 2–4 eV Å^{-1}.[36–38,59–62]

The giant Rashba splitting is unexpected for materials possessing inversion symmetry as applies for the IV–VI compounds with cubic rock salt crystal structure. As recently suggested, FE lattice distortions can lead to a giant bulk Rashba splitting[59] in α-GeTe[61,62] and SnTe.[25] In our $Pb_{1-x}Sn_xTe$ films, however, we do not observe such distortions by X-ray diffraction down to 80 K, and even pure SnTe becomes ferroelectric only at low temperatures. Moreover, we do not observe any abrupt change of the Rashba effect with temperature (cf. Figure 3) as would be expected to occur at such an FE phase transition. Thus, we rule out bulk inversion symmetry breaking and the Dresselhaus mechanism as an origin for the observed Rashba effect.

© 2016 WILEY-VCH Verlag GmbH & Co. KGaA, Weinheim

Reprinted page 5 of paper [88] "Rashba splitting in (Pb,Sn)Te controlled by Bi doping".

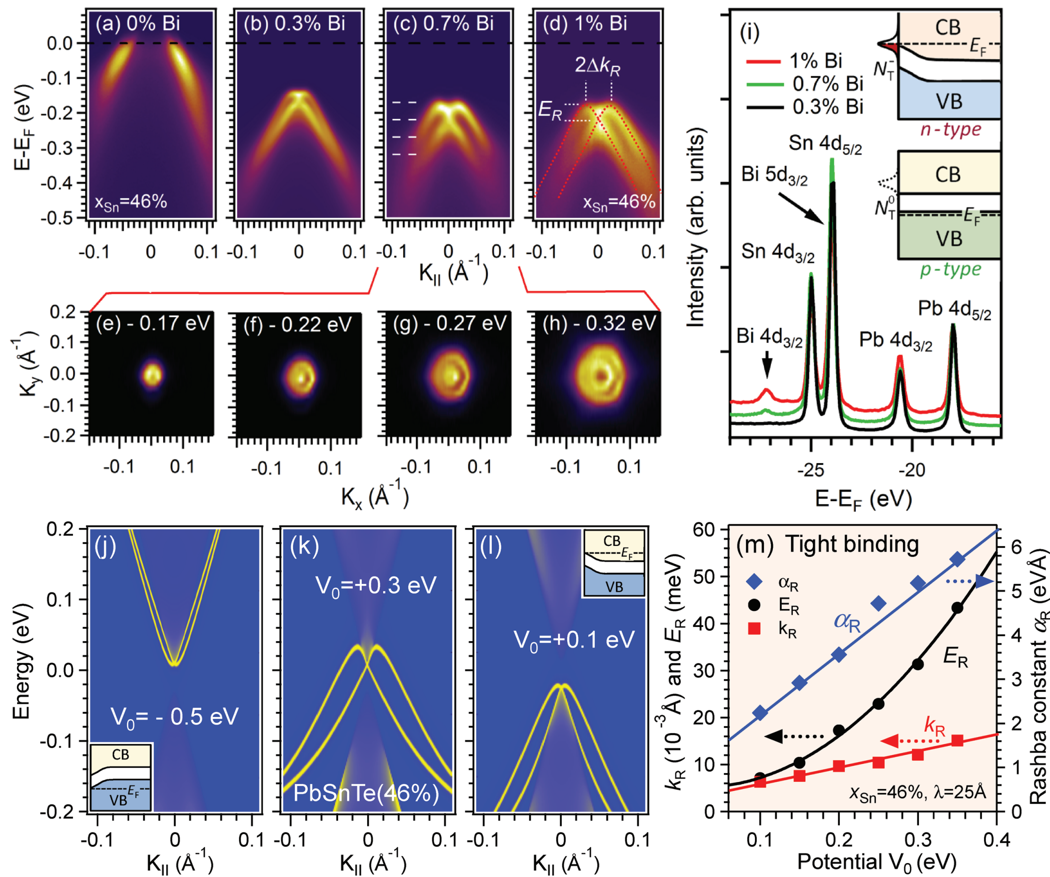

Figure 4. Effect of bulk Bi doping on the Rashba effect. a–d) ARPES spectra of $Pb_{0.54}Sn_{0.46}Te$ (111) with bulk Bi concentrations varying $n_{Bi} = 0$ to 1%, demonstrating effective tuning of the Fermi level and the strong increase of the Rashba splitting with Bi concentration. The ARPES maps were recorded around the $\bar{\Gamma}$-point at 100 K with a photon energy of 18 eV. The derivation of the Rashba constants α_R from the measured Δk_R and E_R is shown schematically in (d) and the results are listed in Table 1. e–h) Constant-energy contours at different binding energies for the sample with $n_{Bi} = 0.7\%$ showing the concentric rings of the Rashba bands and increasing hexagonal warping at lower energy. i) Core-level spectra excited with $h\nu = 90$ eV showing the Bi $4d_{3/2}$ peak for increasing doping level. The upper inset illustrates the surface band bending induced by localized electron traps N_T^- at the surface that become populated with increasing bulk doping, whereas without Bi doping (lower inset) the traps are not occupied and no band bending occurs. j–l) Tight binding supercell calculation of the Rashba effect in $Pb_{0.54}Sn_{0.46}Te$ (111) induced by j) an upward or k,l) a downward band bending toward the surface due to a negative and a positive surface potential V_0, respectively. The screening length was set to $\lambda = 25$Å and $T = 200$ K. The Rashba constants derived from calculations k_R, (■), E_R (●), and $\alpha_R = 2E_R/k_R$ (◆) are plotted in (m) as a function of surface potential.

Table 1. Rashba parameters of $Pb_{0.54}Sn_{0.46}Te$ (111) as a function of Bi concentration n_{Bi} measured by ARPES at 110 K (Figure 4), including Fermi energy E_F (relative to the top of the valence band), Rashba energy E_R, momentum splitting k_R, and Rashba coupling constant $\alpha_R = 2E_R/k_R$ of the Rashba bands.

n_{Bi} [%]	E_F [meV]	E_R [meV]	k_R [Å^{-1}]	α_R [eV Å^{-1}]
0	−80	–	–	–
0.3	+140	13	0.011	2.4
0.7	+170	30	0.017	3.5
0.9	+190	38	0.022	3.8

Instead, we invoke a symmetry breaking at the surface. In fact, the mere existence of the surface can produce spin-polarized surface states, as has been shown in the case of $Pb_{0.73}Sn_{0.27}Se$ in the normal insulator phase.[47] A surface band bending can tune these states to the band gap region, and/or produce new states localized at the surface and enhance the spin splitting. The pertaining Rashba effect will be thus confined to the surface, in agreement with the observed 2D nature of the Rashba bands revealed by the photon-energy dependence of Figure 3. We suggest that the surface band bending for PbSnTe (111) is caused by a pinning of the Fermi level by localized trap states at the surface due to dangling bonds. This results in the presence

 © 2016 WILEY-VCH Verlag GmbH & Co. KGaA, Weinheim

Reprinted page 6 of paper [88] "Rashba splitting in (Pb,Sn)Te controlled by Bi doping".

of a fixed surface charge σ_S that induces a depletion layer below the surface. For degenerately doped semiconductors this is described by the Thomas Fermi screening model with a screening potential of

$$V(z) = V_0 \exp(-z/\lambda) \tag{3}$$

where V_0 is the potential at the surface at $z = 0$ and $\lambda = \pi^{2/3}\,\hbar\sqrt{\varepsilon_0\varepsilon_s/e^2m^*(3n)^{1/3}}$ is the Thomas Fermi screening length,[63] which is of the order of few nanometers for highly doped semiconductors. The surface potential V_0 is related to the surface charge by $V_0 = -\sigma_S\lambda/\varepsilon_0\varepsilon_s$ through the Poisson's equation and the overall charge neutrality condition. For acceptor-like trap states, the trapped surface charge σ_S is negative so that the bands bend upward at the surface and V_0 assumes a positive value. Likewise, for donor-like surface states σ_S is positive, inducing a downward band bending corresponding to negative V_0 values.

The influence of the surface band bending on the surface spectral density of states was evaluated by tight binding calculations in which different surface potentials according to Equation (3) were superimposed on the atomic potentials of $Pb_{0.54}Sn_{0.46}Te$ obtained in refs. [6] and [12]. We assume an anion (Te) termination of the (111) surface as density functional theory (DFT) calculations[48] suggest that this surface exhibits a lower surface energy than the cation termination. The results are presented in Figure 4 for $\lambda = 2.5$ and V_0 varying from –0.5, +0.3, and +0.1 eV from (j) to (l), respectively, where the solid lines correspond to the 2D surface states and the shaded regions to the bulk bands. Evidently, surface band bending induces a strong Rashba splitting in either the CB or VB depending on the "sign" of V_0. Positive V_0 (i.e., upward band bending) leads to a Rashba splitting in the VB due to the confinement of the hole wave functions near the surface. Conversely, for negative V_0 the Rashba-split states appear in the CB. Comparison with our experiments reveals that only the upward band bending, i.e., $V_0 > 0$, is consistent with the ARPES data, which demonstrates the presence of a negative surface charge σ_S on the anion-terminated surface.

From our TB calculations, we derive the dependence of Rashba parameters as a function of surface potential as presented in Figure 4m. Evidently, the momentum splitting Δk_R and Rashba constant scale linearly, and E_R quadratically with the surface potential V_0, i.e., with increasing electric field strength $E \approx \mathrm{d}V/\mathrm{d}z$ at the surface. Comparison with the experimental values indicates a surface potential V_0 of around +0.1 to +0.3 eV for our samples, which for the given screening length and dielectric constant yields a surface charge of the order of 1/10 electron per surface atom. However, the observed increase of the Rashba splitting with increasing Bi doping dictates that this surface charge is not constant but varies with the bulk Fermi level. Thus, it cannot be simply due to the polar nature of the (111) surface as previously suggested,[64] but rather by localized surface trap states that are successively filled by electrons as the bulk Fermi level increases. For p-doped samples these trap states are unoccupied, corresponding to a flat band condition (cf. inset of Figure 4i) without a Rashba effect—as seen in our experiments. Comparing calculated and measured Rashba parameters, we find a good agreement for V_0 = +0.2 eV, where α_R is of the order of 3 eV Å^{-1} in both theory and experiment. The upward surface band bending also nicely explains the weak intensity of the CB band states in the ARPES measurements because it pushes the CB wave functions into the bulk away from the surface for which reason their spectral weight at the surface is strongly reduced. Also note that for a given α_R value, Δk_R and E_R of the TB calculations are somewhat smaller than the experimental values. Since both are proportional to the in-plane effective mass m^*, this is attributed to the fact that m^* is underestimated by a factor of 1.8 in the TB binding calculations as compared to the experiments. The effect of temperature and screening length variation is discussed in the Supporting Information.

To show that the Rashba effect is neither due to Bi accumulation at the surface nor due to specific properties of the Bi, additional experiments were performed. This is because it is well known that Bi on metal surfaces such as Ag(111) can induce a large Rashba splitting due to its large spin–orbit coupling.[65,66] To rule out such an effect, we have deposited 0.5–1 monolayer of Bi on top of undoped $Pb_{0.54}Sn_{0.46}Te$ (111) at a temperature of 200 K. The resulting ARPES data, shown in Supporting Information, Figure S1,[67] reveal that this does not cause any Rashba splitting of the PbSnTe bands, i.e., simple Bi accumulation on the surface by surface segregation cannot explain the observed Rashba effect. This is further underlined by the core level spectra of our films in Figure 4i that reveal that the surface concentration of Bi is very small in all samples, i.e., that no Bi accumulation actually occurs. To further demonstrate that the Rashba effect also does not rely on any specific property of the Bi dopant, we have prepared $Pb_{0.54}Sn_{0.46}Te$ films where Bi was replaced by Sb as group V n-type dopant. As shown in Supporting Information, Figure S1,[67] for such films a similar giant Rashba effect is observed. In fact, for a nominal Sb concentration of 3% we obtain an even larger Rashba splitting of Δk_R = 0.036 Å^{-1} and E_R = 56 meV as compared to the 1% Bi-doped sample. This clearly corroborates that the Rashba effect is solely controlled by the bulk Fermi level and thus it will occur for any other n-type dopant in this system.

In summary, we have shown that Bi and Sb-doped topological crystalline insulator $Pb_{1-x}Sn_xTe$ (111) films represent a giant Rashba system that features Rashba coupling constant as high as the record values reported in the literature. Contrary to most other systems, the strength of the Rashba effect is effectively controlled by the bulk doping. Our detailed analysis using tight binding calculations reveals that it originates from a large upward band bending at the surface due to electron surface traps whose occupancy is controlled by the bulk Fermi level. Since the Fermi level can also be tuned by electrostatic gates, this opens up a pathway for spintronic field effect device applications. Doping also allows compensating the intrinsic p-type character of TCI materials, resulting in high carrier mobilities that enable optical and topological quantum transport investigations otherwise screened by the bulk contribution. The magnitude of spin splitting is already sufficient for room temperature operation of spin-galvanic spintronic devices,[39,68–70] but beyond that the observed trend implies that the spin splitting can be even further enhanced by increased Bi or Sb doping levels. Thus, our findings open up new avenues for exploring exotic electrical and optical phenomena in topological systems, as well as novel spintronic devices driven by the Rashba effect.

© 2016 WILEY-VCH Verlag GmbH & Co. KGaA, Weinheim

Reprinted page 7 of paper [88] "Rashba splitting in (Pb,Sn)Te controlled by Bi doping".

Methods

Sample Preparation: Bi-doped $Pb_{1-x}Sn_xTe$ thin films were grown in a Varian Gen II MBE system on cleaved (111) BaF_2 substrates at 350 °C at a pressure below 10^{-9} mbar. The film growth was in situ monitored by RHEED. PbTe, SnTe, and Bi_2Te_3 were evaporated from compound effusion cells. In some cases, a $Pb_{0.44}Sn_{0.56}Te$ stoichiometric source was used. The PbTe/SnTe/Bi ratio was controlled and calibrated by a quartz crystal microbalance moved into the substrate position. The thickness of the films was in the range of 1—2 µm.

Sample Characterization: The surface of grown films was examined by AFM in contact mode. X-ray diffraction measurements and reciprocal space maps were performed using a double crystal Seifert 3003 diffractometer equipped with a channel cut Ge (200) monochromator. The composition was determined using the Vegard's law as well as energy dispersive X-ray microanalysis and photoelectron spectroscopy.

Transport Characterization: Hall measurements were carried out in Van der Pauw geometry with external magnetic fields up to 0.9 Tesla. Measurements were performed and room and liquid nitrogen temperature. Selected samples were also measured in high magnetic fields up to 7 T at 1.7 K. The obtained high field and low field carrier concentrations are consistent with each other within 20%.

ARPES Measurements: Angle-resolved photoemission was measured at UE112_PGM-2a-1^2 beamline at the Bessy II synchrotron (Berlin, Germany) with photon energies ranging from 15 to 90 eV and horizontally polarized light using a six-axes automated cryo-manipulator and a Scienta R8000 hemispherical analyzer with typical energy resolution better than 5 meV. For these investigations, the as-grown samples were transferred from the MBE to the synchrotron using a battery-operated ion getter pumped UHV suitcase (Ferrovac VSN40S) sustaining a base pressure better than 2×10^{-10} mbar. The ARPES experiments were carried out at pressures below 2×10^{-10} mbar.

Theoretical Calculations: The surface spectral density of states in the studied $Pb_{0.54}Sn_{0.46}Te$ films was obtained using the tight-binding approach within the virtual crystal approximation. The parameters for the constituent compounds, PbTe and SnTe, were taken from ref. [71], where they were obtained within a nearest-neighbor 18-orbital sp^3d^5 model with spin–orbit interactions included. To obtain a correct dependence of the band gap with temperature, an appropriate scaling of the hopping integrals with temperature had, however, to be found. The Bi incorporation was simulated by applying a surface potential described by Equation (3) within the Thomas Fermi screening model. The surface spectral functions were calculated using recursive Green's function method described in ref. [72].

Supporting Information

Supporting Information is available from the Wiley Online Library or from the author.

Acknowledgements

The authors acknowledge Helmholtz-Zentrum Berlin for provision of synchrotron radiation beam time at the UE112-PGM-2a beamline of BESSY II, and thank Prof. E. I. Rogacheva, National Technical University "KhPI" Kharkiv, Ukraine, and Dr. A. Szczerbakow, Institute of Physics of the Polish Academy of Sciences in Warszawa for providing the MBE source material. Tight binding calculations were partially carried out in the Academic Computer Center in Gdansk, Poland. This work was supported by the Austrian Science Funds (Grant SFB 025-IRON), the EU CALIPSO Program (Grant No. 312284), the Polish National Science Center (Grant Nos. 2013/11/B/ST3/03934 and 2014/15/B/ST3/03833), the Deutsche Forschingsgemeinschaft (Grant No. SPP 1666) and the Impuls-und Vernetzungsfonds der Helmholtz-Gemeinschaft (Grant No. HRJRG-408).

Note: The author list and article number in ref. 56 were corrected on January 12, 2017, after initial publication online.

Received: August 4, 2016
Revised: September 29, 2016
Published online: November 17, 2016

[1] L. Fu, *Phys. Rev. Lett.* **2011**, *106*, 106802.
[2] T. H. Hsieh, H. Lin, J. Liu, W. Duan, A. Bansi, L. Fu, *Nat. Commun.* **2012**, *3*, 982.
[3] Y. Tanaka, Z. Ren, T. Sato, K. Nakayama, S. Souma, T. Takahashi, K. Segawa, Y. Ando, *Nat. Phys.* **2012**, *8*, 800.
[4] S.-Y. Xu, C. Liu, N. Alidoust, M. Neupane, D. Qian, I. Belopolski, J. D. D. Denlinger, Y. J. J. Wang, H. Lin, L. A. a. Wray, G. Landolt, B. Slomski, J. H. H. Dil, A. Marcinkova, E. Morosan, Q. Gibson, R. Sankar, F. C. C. Chou, R. J. J. Cava, A. Bansil, M. Z. Z. Hasan, *Nat. Commun.* **2012**, *3*, 1192.
[5] Y. Tanaka, T. Sato, K. Nakayama, S. Souma, T. Takahashi, Z. Ren, M. Novak, K. Segawa, Y. Ando, *Phys. Rev. B: Condens. Matter Mater. Phys.* **2013**, *87*, 155105.
[6] P. Dziawa, B. J. Kowalski, K. Dybko, R. Buczko, A. Szczerbakow, M. Szot, E. Łusakowska, T. Balasubramanian, B. M. Wojek, M. H. Berntsen, O. Tjernberg, T. Story, *Nat. Mater.* **2012**, *11*, 1023.
[7] W. D. Johnston, J. G. King, R. Sci, I. Estermann, O. C. Simpson, O. Stern, H. S. W Massey, C. B. O. Mohr, P. Roy, J. O. Dimmock, I. Melngailis, A. J. Strauss, *Phys. Rev. Lett.* **1966**, *16*, 1193.
[8] H. Preier, *Appl. Phys.* **1979**, *20*, 189.
[9] G. Nimtz, B. Schlicht, in *Narrow-Gap Semiconductor*, Springer-Verlag, Berlin **1983**, pp. 1–117.
[10] Y. Ando, L. Fu, *Annu. Rev. Condens. Matter Phys.* **2015**, *6*, 361.
[11] B. M. Wojek, R. Buczko, S. Safaei, P. Dziawa, B. J. Kowalski, M. H. Berntsen, T. Balasubramanian, M. Leandersson, A. Szczerbakow, P. Kacman, T. Story, O. Tjernberg, *Phys. Rev. B* **2013**, *87*, 115106.
[12] S. Safaei, P. Kacman, R. Buczko, *Phys. Rev. B: Condens. Matter Mater. Phys.* **2013**, *88*, 045305.
[13] M. Z. Hasan, C. L. Kane, *Rev. Mod. Phys.* **2010**, *82*, 3045.
[14] X. L. Qi, S. C. Zhang, *Rev. Mod. Phys.* **2011**, *83*, 1057.
[15] T. H. Hsieh, H. Lin, J. Liu, W. Duan, A. Bansil, L. Fu, *Nat. Commun.* **2013**, *4*, 1901.
[16] E. Tang, L. Fu, *Nat. Phys.* **2014**, *10*, 964.
[17] M. Serbyn, L. Fu, *Phys. Rev. B: Condens. Matter Mater. Phys.* **2014**, *90*, 1.
[18] J. Liu, T. H. Hsieh, P. Wei, W. Duan, J. Moodera, L. Fu, *Nat. Mater.* **2013**, *13*, 178.
[19] S. Safaei, M. Galicka, P. Kacman, R. Buczko, *New J. Phys.* **2015**, *17*, 063041.
[20] B. A. Assaf, F. Katmis, P. Wei, C. Z. Chang, B. Satpati, J. S. Moodera, D. Heiman, *Phys. Rev. B: Condens. Matter Mater. Phys.* **2015**, *91*, 1.
[21] I. Zeljkovic, K. L. Scipioni, D. Walkup, Y. Okada, W. Zhou, R. Sankar, G. Chang, Y. J. Wang, H. Lin, A. Bansil, F. Chou, Z. Wang, V. Madhavan, *Nat. Commun.* **2015**, *6*, 6559.
[22] C. W. Niu, Y. Dai, Y. D. Ma, L. Yu, B. B. Huang, *Mater. Express* **2013**, *3*, 159.

 © 2016 WILEY-VCH Verlag GmbH & Co. KGaA, Weinheim

Reprinted page 8 of paper [88] "Rashba splitting in (Pb,Sn)Te controlled by Bi doping".

[23] X. Qian, L. Fu, J. Li, *Nano Res.* **2015**, *8*, 967.
[24] I. Zeljkovic, Y. Okada, M. Serbyn, R. Sankar, D. Walkup, W. Zhou, J. Liu, G. Chang, Y. J. Wang, M. Z. Hasan, F. Chou, H. Lin, A. Bansil, L. Fu, V. Madhavan, *Nat. Mater.* **2015**, *14*, 318.
[25] E. Plekhanov, P. Barone, D. Di Sante, S. Picozzi, *Phys. Rev. B: Condens. Matter Mater. Phys.* **2014**, *90*, 161108(R).
[26] C. Fang, M. J. Gilbert, B. A. Bernevig, *Phys. Rev. Lett.* **2014**, *112*, 046801.
[27] A. R. Mellnik, J. S. Lee, A. Richardella, J. L. Grab, P. J. Mintun, M. H. Fischer, A. Vaezi, A. Manchon, E. A. Kim, N. Samarth, D. C. Ralph, *Nature* **2014**, *511*, 449.
[28] H. Guo, C. H. Yan, J. W. Liu, Z. Y. Wang, R. Wu, Z. D. Zhang, L. L. Wang, K. He, X. C. Ma, S. H. Ji, W. H. Duan, X. Chen, Q. K. Xue, *APL Mater.* **2014**, *2*, 056106.
[29] C. Yan, J. Liu, Y. Zang, J. Wang, Z. Wang, P. Wang, Z.-D. Zhang, L. Wang, X. Ma, S. Ji, K. He, L. Fu, W. Duan, Q.-K. Xue, X. Chen, *Phys. Rev. Lett.* **2014**, *112*, 186801.
[30] C. M. Polley, P. Dziawa, A. Reszka, A. Szczerbakow, R. Minikayev, J. Z. Domagala, S. Safaei, P. Kacman, R. Buczko, J. Adell, M. H. Berntsen, B. M. Wojek, O. Tjernberg, B. J. Kowalski, T. Story, T. Balasubramanian, *Phys. Rev. B* **2014**, *89*, 075317.
[31] A. A. Taskin, F. Yang, S. Sasaki, K. Segawa, Y. Ando, *Phys. Rev. B: Condens. Matter Mater. Phys.* **2014**, *89*, 121302(R).
[32] B. A. Assaf, T. Phuphachong, V. V. Volobuev, A. Inhofer, G. Bauer, G. Springholz, L. A. de Vaulchier, Y. Guldner, *Sci. Rep.* **2016**, *6*, 20323.
[33] Y. Tanaka, T. Shoman, K. Nakayama, S. Souma, T. Sato, T. Takahashi, M. Novak, K. Segawa, Y. Ando, *Phys. Rev. B: Condens. Matter Mater. Phys.* **2013**, *88*, 235126.
[34] C.-H. Yan, H. Guo, J. Wen, Z.-D. Zhang, L.-L. Wang, K. He, X.-C. Ma, S.-H. Ji, X. Chen, Q.-K. Xue, *Surf. Sci.* **2014**, *621*, 104.
[35] T. Rauch, M. Flieger, J. Henk, I. Mertig, *Phys. Rev. B* **2013**, *88*, 245120.
[36] K. Ishizaka, M. S. Bahramy, H. Murakawa, M. Sakano, T. Shimojima, T. Sonobe, K. Koizumi, S. Shin, H. Miyahara, A. Kimura, K. Miyamoto, T. Okuda, H. Namatame, M. Taniguchi, R. Arita, N. Nagaosa, K. Kobayashi, Y. Murakami, R. Kumai, Y. Kaneko, Y. Onose, Y. Tokura, *Nat. Mater.* **2011**, *10*, 521.
[37] A. Crepaldi, L. Moreschini, G. Autes, C. Tournier-Colletta, S. Moser, N. Virk, H. Berger, P. Bugnon, Y. J. Chang, K. Kern, A. Bostwick, E. Rotenberg, O. V. Yazyev, M. Grioni, *Phys. Rev. Lett.* **2012**, *109*, 096803.
[38] M. Sakano, M. S. Bahramy, A. Katayama, T. Shimojima, H. Murakawa, Y. Kaneko, W. Malaeb, S. Shin, K. Ono, H. Kumigashira, R. Arita, N. Nagaosa, H. Y. Hwang, Y. Tokura, K. Ishizaka, *Phys. Rev. Lett.* **2013**, *110*, 107204.
[39] A. Manchon, H. C. Koo, J. Nitta, S. M. Frolov, R. A. Duine, *Nat. Mater.* **2015**, *14*, 871.
[40] G. Springholz, in *Lead Chalcogenides: Physics and Applications* (Ed: D. Khokhlov), Taylor & Francis, New York **2003**, pp. 123–207.
[41] P. H. O. Rappl, H. Closs, S. O. Ferreira, E. Abramof, C. Boschetti, P. Motisuke, A. Y. Ueta, I. N. Bandeira, *J. Cryst. Growth* **1998**, *191*, 466.
[42] A. Y. Ueta, G. Springholz, F. Schinagl, G. Marschner, G. Bauer, *Thin Solid Films* **1997**, *306*, 320.
[43] D. L. Partin, C. M. Thrush, S. J. Simko, S. W. Gaarenstroom, *J. Appl. Phys.* **1989**, *66*, 6115.
[44] T. Ikeda, M. B. Toussaint, K. Bergum, S. Iwanaga, G. Jeffrey Snyder, *J. Mater. Sci.* **2011**, *46*, 3846.
[45] G. Springholz, A. Y. Ueta, N. Frank, G. Bauer, *Appl. Phys. Lett.* **1996**, *69*, 2822.
[46] G. Springholz, G. Bauer, *J. Appl. Phys.* **1995**, *77*, 540.
[47] P. J. McCann, J. Fuchs, Z. Feit, C. G. Fonstad, *J. Appl. Phys.* **1987**, *62*, 2994.
[48] V. L. Deringer, R. Dronskowski, *ChemPhysChem* **2013**, *14*, 3108.
[49] C. R. Hewes, M. S. Adler, S. D. Senturia, *J. Appl. Phys.* **1973**, *44*, 1327.
[50] Z.-H. Zhu, G. Levy, B. Ludbrook, C. N. Veenstra, J. A. Rosen, R. Comin, D. Wong, P. Dosanjh, A. Ubaldini, P. Syers, N. P. Butch, J. Paglione, I. S. Elfimov, A. Damascelli, *Phys. Rev. Lett.* **2011**, *107*, 186405.
[51] T. Valla, Z.-H. Pan, D. Gardner, Y. S. Lee, S. Chu, *Phys. Rev. Lett.* **2012**, *108*, 117601.
[52] L. A. Wray, S.-Y. Xu, Y. Xia, D. Hsieh, A. V Fedorov, Y. S. Hor, R. J. Cava, A. Bansil, H. Lin, M. Z. Hasan, *Nat. Phys.* **2011**, *7*, 32.
[53] P. D. C. King, R. C. Hatch, M. Bianchi, R. Ovsyannikov, C. Lupulescu, G. Landolt, B. Slomski, J. H. Dil, D. Guan, J. L. Mi, E. D. L. Rienks, J. Fink, A. Lindblad, S. Svensson, S. Bao, G. Balakrishnan, B. B. Iversen, J. Osterwalder, W. Eberhardt, F. Baumberger, P. Hofmann, *Phys. Rev. Lett.* **2011**, *107*, 096802.
[54] H. M. Benia, C. Lin, K. Kern, C. R. Ast, *Phys. Rev. Lett.* **2011**, *107*, 177602.
[55] L. A. Wray, S.-Y. Xu, Y. Xia, D. Qian, A. V Fedorov, H. Lin, A. Bansil, Y. S. Hor, R. J. Cava, M. Z. Hasan, *Nat. Phys.* **2011**, *6*, 13.
[56] J. Sánchez-Barriga, A. Varykhalov, G. Springholz, H. Steiner, R. Kirchschlager, G. Bauer, O. Caha, E. Schierle, A. A. Ünal, S. Valencia, M. Dunst, J. Braun, H. Ebert, J. Minár, E. Golias, L. V. Yashina, A. Ney, E. Weschke, V. Holý, O. Rader, *Nat. Commun.* **2016**, *7*, 10559.
[57] T. Arakane, T. Sato, S. Souma, K. Kosaka, K. Nakayama, M. Komatsu, T. Takahashi, Z. Ren, K. Segawa, Y. Ando, *Nat. Commun.* **2012**, *3*, 636.
[58] D. Hsieh, Y. Xia, D. Qian, L. Wray, J. H. Dil, F. Meier, J. Osterwalder, L. Patthey, J. G. Checkelsky, N. P. Ong, A. V Fedorov, H. Lin, A. Bansil, D. Grauer, Y. S. Hor, R. J. Cava, M. Z. Hasan, *Nature* **2009**, *460*, 1101.
[59] S. Picozzi, *Front. Phys.* **2014**, *2*, 1.
[60] D. Di Sante, P. Barone, R. Bertacco, S. Picozzi, *Adv. Mater.* **2013**, *25*, 509.
[61] M. Liebmann, C. Rinaldi, D. Di Sante, J. Kellner, C. Pauly, R. N. Wang, J. E. Boschker, A. Giussani, S. Bertoli, M. Cantoni, L. Baldrati, M. Asa, I. Vobornik, G. Panaccione, D. Marchenko, J. Sánchez-Barriga, O. Rader, R. Calarco, S. Picozzi, R. Bertacco, M. Morgenstern, *Adv. Mater.* **2016**, *28*, 560.
[62] J. Krempaský, H. Volfová, S. Muff, N. Pilet, G. Landolt, M. Radović, M. Shi, D. Kriegner, V. Holý, J. Braun, H. Ebert, F. Bisti, V. A. Rogalev, V. N. Strocov, G. Springholz, J. Minár, J. H. Dil, **2015**, http://arxiv.org/abs/1503.05004.
[63] E. F. Schubert, *Doping in III–V Semiconductors*, Cambridge University Press, Cambridge, UK **1993**.
[64] C. Yan, J. Liu, Y. Zang, J. Wang, Z. Wang, P. Wang, Z.-D. Zhang, L. Wang, X. Ma, S. Ji, K. He, L. Fu, W. Duan, Q.-K. Xue, X. Chen, *Phys. Rev. Lett.* **2014**, *112*, 186801.
[65] C. R. Ast, J. Henk, A. Ernst, L. Moreschini, M. C. Falub, D. Pacile, P. Bruno, K. Kern, M. Grioni, *Phys. Rev. Lett.* **2007**, *98*, 186807.
[66] I. Gierz, F. Meier, J. H. Dil, K. Kern, C. R. Ast, *Phys. Rev. B* **1951**, *83*, 195122.
[67] See Supporting Information.
[68] S. D. Ganichev, E. L. Ivchenko, V. V. Bel'kov, S. A. Tarasenko, M. Sollinger, D. Weiss, W. Wegscheider, W. Prettl, *Nature* **2002**, *417*, 153.
[69] S. D. Ganichev, S. N. Danilov, P. Schneider, V. V. Bel'kov, L. E. Golub, W. Wegscheider, D. Weiss, W. Prettl, *J. Magn. Magn. Mater.* **2006**, *300*, 127.
[70] J. C. R. Sánchez, L. Vila, G. Desfonds, S. Gambarelli, J. P. Attané, J. M. De Teresa, C. Magén, A. Fert, *Nat. Commun.* **2013**, *4*, 2944.
[71] C. S. Lent, M. A. Bowen, J. D. Dow, R. S. Allgaier, O. F. Sankey, E. S. Ho, *Superlattices Microstruct.* **1986**, *2*, 491.
[72] M. P. Lopez Sancho, J. M. Lopez Sancho, J. Rubio, *J. Phys.* **1985**, *15*, 851.

© 2016 WILEY-VCH Verlag GmbH & Co. KGaA, Weinheim

Reprinted page 9 of paper [88] "Rashba splitting in (Pb,Sn)Te controlled by Bi doping".

Copyright WILEY-VCH Verlag GmbH & Co. KGaA, 69469 Weinheim, Germany, 2016.

ADVANCED MATERIALS

Supporting Information

for *Adv. Mater.,* DOI: 10.1002/adma.201604185

Giant Rashba Splitting in $Pb_{1-x}Sn_xTe$ (111) Topological Crystalline Insulator Films Controlled by Bi Doping in the Bulk

Valentine V. Volobuev, Partha S. Mandal, Marta Galicka, Ondřej Caha, Jaime Sánchez-Barriga, Domenico Di Sante, Andrei Varykhalov, Amir Khiar, Silvia Picozzi, Günther Bauer, Perla Kacman, Ryszard Buczko, Oliver Rader, and Gunther Springholz**

WILEY-VCH

Copyright WILEY-VCH Verlag GmbH & Co. KGaA, 69469 Weinheim, Germany, 2013.

Giant Rashba Splitting in $Pb_{1-x}Sn_xTe$ (111) Topological Crystalline Insulator Films Controlled by Bi-Doping in the Bulk

V. V. Volobuev[1,2]*, P.S. Mandal[3], M. Galicka[5], O. Caha[4], J. Sanchez-Barriga[3], D. Di Sante[6,7], A. Varykhalov[3], A. Khiar[1], S. Picozzi[6], G. Bauer[1], P. Kacman[5], R. Buczko[5], O. Rader[3], and G. Springholz[1]*

[1] Dr. V. V. Volobuev, Dr. A. Khiar, Prof. G. Bauer, Prof. G. Springholz, Institute for Semiconductor Physics, Johannes Kepler University, Altenberger Str. 69, 4040 Linz, Austria

[2] Dr. V. V. Volobuev, National Technical University "Kharkiv Polytechnic Institute", Frunze Str. 21, 61002 Kharkiv, Ukraine

[3] P.S. Mandal, Dr. J. Sanchez-Barriga, Dr. A. Varykhalov, Prof. O. Rader, Helmholtz-Zentrum Berlin, Elektronenspeichering BESSY II, Albert-Einstein Str. 15, 12489 Berlin, Germany

[4] Dr. O. Caha, Masaryk University, Kotlářská 2, 61137 Brno, Czech Republic

[5] Dr. M. Galicka, Prof. P. Kacman, Prof. R. Buczko, Institute of Physics, Polish Academy of Sciences, Aleja Lotników 32/46, PL-02-668 Warszawa, Poland

[6] Dr. D. Di Sante, Dr. S. Picozzi, Consiglio Nazionale delle Ricerche CNR-SPIN, Via dei Vestini 31, 66100 Chieti, Italy

[7] Dr. D. Di Sante, Institut für Physik und Astrophysik, Universität Würzburg, Am Hubland Campus Süd, Würzburg 97074, Germany

*) e-mail: valentyn.volobuiev@jku.at, gunther.springholz@jku.at

Synopsis: This supplemental information provides (i) results on additional investigations on the effect on the surface electronic band structure caused by bulk Sb-doping of PbSnTe epi-layers and of deposition of Bi on the top of the surface, (ii) tight binding calculations concerning the influence of the width of the depletion layer, i.e., Thomas Fermi screening length, as well as of temperature on the Rashba splitting of PbSnTe, including information of the spin polarization and (iii) magnetic field dependent Hall effect data.

1. Sb-Doping and the Effect of Bi Surface deposition

Additional control experiments were performed in order to demonstrate that the observed Rashba effect of PbSnTe is neither due to Bi accumulation at the surface nor due to specific properties of the Bi dopant. In the first set of experiments, we have deposited stepwise Bi on top of the $Pb_{0.54}Sn_{0.46}Te$ (111) surface at a temperature of 200K up to a coverage of 1 monolayer. The resulting ARPES data recorded after 1 ML deposition is shown in Figure S1c in comparison to the initial ARPES data recorded before Bi deposition. The result reveal that Bi on the surface alone does not cause *any* Rashba splitting of the PbSnTe bands. This unequivocally shows that the Rasbha effect we observed for our $Pb_{0.54}Sn_{0.46}Te$ films doped by Bi in the bulk cannot be caused by Bi surface segregation. This is further corroborated the comparison of the core level spectra of the bulk Bi-doped and the surface deposited Bi PbSnTe samples shown in Figure S1d and in the article Figure 4i, respectively. Whereas after 1ML surface deposition the characteristic Bi $5d_{3/2}$ core level peak is higher than the Sn 4d and Pb 5d core level peaks, for the bulk Bi-doped films with Bi concentration up to 1% the Bi core level peaks are very small and barely visible over the background. This evidences that no significant Bi accumulation occurs for the bulk-doped films.

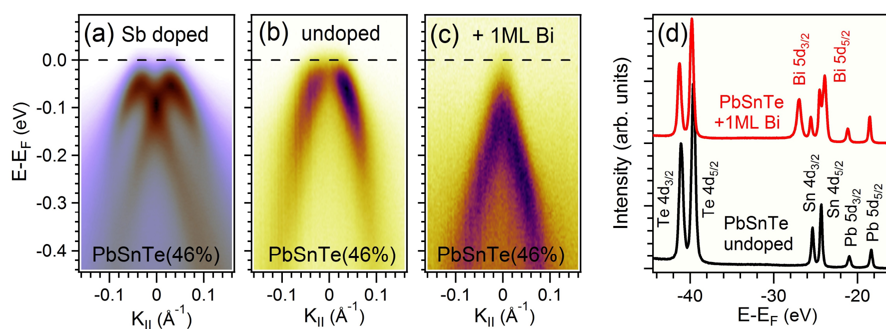

Figure S1: Effect of Sb-doping and Bi surface deposition. (a) ARPES map of a $Pb_{0.54}Sn_{0.46}Te$ (111) film with 3% Sb-doping in the bulk. A similar huge Rashba effect occurs as observed for the Bi-doped samples. (b,c) ARPES maps of an undoped $Pb_{0.54}Sn_{0.46}Te$ (111) layer before, respectively, after 1 monolayer Bi deposition on the surface at 200K. No Rashba effect is observed in this case. The maps were recorded around the $\bar{\Gamma}$-point at 100 K with a photon energy of $h\nu$ = 18 eV. (d) Core level spectra recorded before and after 1 ML Bi deposition using $h\nu$ = 90 eV.

To demonstrate that the Rashba effect does not rely on a specific property of the *n*-type dopant, we have also grown $Pb_{0.54}Sn_{0.46}Te$ films where Bi was replaced by Sb as group V *n*-type dopant. As shown by Figure S1a, for the Sb-doped film a similar huge Rashba effect is observed. In fact, for a nominal Sb concentration of 3% of this film, we obtain an even larger Rashba splitting of Δk_R = 0.036 $Å^{-1}$ and E_R = 56 meV than for the $Pb_{0.54}Sn_{0.46}Te$ doped with 1% of Bi. This corroborates that the Rashba effect is solely controlled by the bulk Fermi level and therefore occurs for any *n*-type dopant of the system.

2. Tight Binding Calculations

To find appropriate parameters for the Thomas Fermi screening potential, we have performed series of calculations, in which both the potential amplitude as well as the potential screening length have been changed (Equation 3 of main Article). For each pair of parameters the recursive, decimation method for finding the spectral density function for surface atoms [1] has been used. The method requires a finite range of the applied potential and therefore, the potential has been cut off at the range equal to λ and shifted in order to avoid a potential step. It has been checked that further increase of the range influences the obtained densities negligibly. The results have been compared with experiment. The most accurate agreement was achieved for λ=25 Å. To illustrate the dependence of the spectral density on the screening length λ we show in Figure S2 the results obtained for four different λ values and fixed V_0 = +0.3 eV. It can be seen that with increasing width λ of the depletion layer underneath the surface the position of the Kramers point shifts upwards and the number of localized bands increases. At λ = 50 Å the Kramers point of the surface state is shifted into the bulk CB and a second subband appears in the VB. At λ = 100 Å even a third subband appears. Since we do not see such additional subbands in the ARPES measurements, we conclude that the Thomas Fermi screening length must be well below 50 Å in our samples.

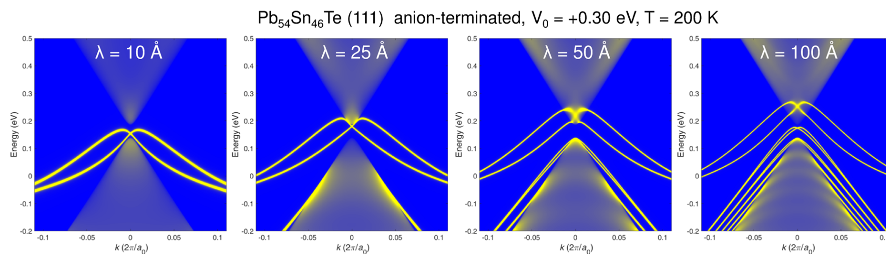

Figure S2: Tight binding calculation af the surface spectral density of states of $Pb_{0.54}Sn_{0.46}Te$ (111) as a function of screening length *λ* varying from 10 to 100Å, while the surface potential of V_0 = +0.3 eV and *T*=200K was kept constant. he solid lines correspond to the surface states and the shaded regions to the bulk bands.

Temperature dependence and spin polarization. In Figure S3 we present the temperature dependence of the TB calculations for the anion terminated (111) surface of $Pb_{0.54}Sn_{0.46}Te$ with applied surface potential V_0 = +0.2 eV and λ = 25 Å. Comparing Figure S3 with Figure 3a-d in the main article one can see that in both cases the gap closes at 110K. Below 110K the band gap opens and the electronic band structure is inverted. Together with reopening of the band gap also a gap in the Kramers point opens. The band above the Kramers point becomes now the lower part of the Dirac cone and the band below the Kramers point forms the upper band of the new Rashba pair. The lower part of Figure S3 shows the in-plane spin polarization of the bands where the green and red colors indicate opposite spin directions. Upon band inversion the spin chirality of the Rashba pair is opposite to the one in normal case. The Dirac cone is highly deformed by Thomas Fermi potential, which shifts the Dirac point to the position, where it appears to hybridize with the conduction band.

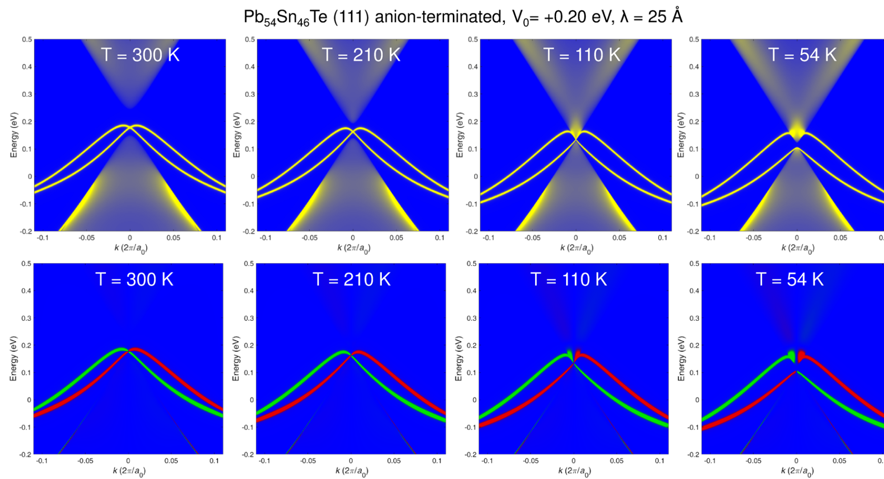

Figure S3: Tight binding surface spectral density (top) and in-plane spin polarization (bottom) of the spectral density of states in (111) $Pb_{0.54}Sn_{0.46}Te$ as a function of temperature with surface potential V_0 = +0.2 eV and λ = 25 Å. The solid lines correspond to the surface states and the shaded regions to the bulk bands and the red and green color to opposite in-plane spin polarization direction.

3. Magnetic Field Dependent Hall Measurements

Hall measurements were carried out in Van der Pauw geometry within variable external magnetic fields up to 0.9 Tesla. Measurements were performed and room temperature and liquid nitrogen. To verify that the obtained Hall concentrations and carrier mobilities do not depend on the applied magnetic field strength even for nearly compensated samples, we show in Fig. S4 the magnetic field dependence of the longitudinal and Hall resistance ρ_{xx} and ρ_{xy} of such a film with x_{Sn} = 46% and a Bi-doping level of 3.4 x 10^{19}cm^{-3}. From the linear fit of the Hall resistance a carrier concentration (n-type) of n = 1.43 x 10^{18} cm^{-3} at room temperature and of 1.02 x 10^{18} cm^{-3} at 77K is obtained. The corresponding carrier mobilities are μ = 600, respectively, 11000 cm^2/Vsec for this sample. Selected samples were also measured in high magnetic fields up to 7 T at 1.7K. The obtained high field carrier concentrations are consistent within 20% of the low field data.

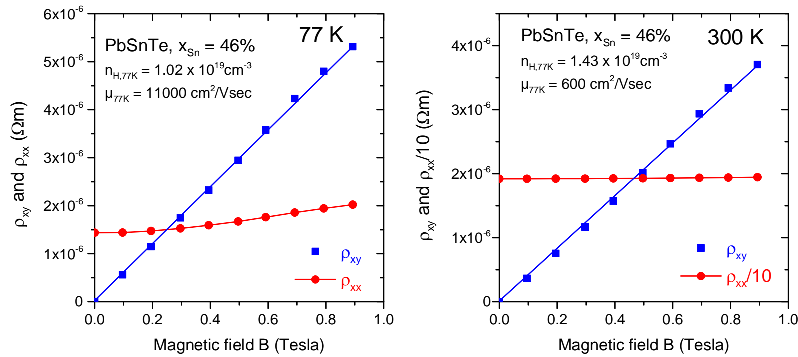

Figure S4: Magnetic field dependent longitudinal and Hall resistances ρ_{xx} and ρ_{xy} of a 1.9 µm thick $Pb_{0.54}Sn_{0.46}Te$ epilayer with Bi-doping level of 3.4 x 10^{19}cm^{-3} measured at 77 and 300 K. From the linear fit of the Hall resistance ρ_{xy} an n-type carrier concentration of n = 1.43 x 10^{18} cm^{-3} at room temperature and 1.02 x 10^{18} cm^{-3} at 77K were obtained, with corresponding carrier mobilities of μ = 600 and 11000 cm^2/Vsec, respectively.

References:

[1] M. P. Lopez Sancho, J. M. Lopez Sancho and J. Rubio, *J. Phys. F* **1985**, 15, 851.

Chapter 5

Conclusion and outlook

The topological insulators were intensively studied during the last one and a half decades since their prediction. We have focused on the experimental studies of chalcogenide topological insulators of Bi_2Te_3 and Bi_2Se_3 types. We have also studied manganese magnetically doped naturally grown heterostructures. We have experimentally supported theoretical predictions of a magnetic band gap opening in the Dirac point of the topological surface states. The magnetic order temperature below 20 K for bismuth telluride was later improved to almost 50 K in manganese antimony telluride.

We have also studied the properties of topological crystalline insulator films (Pb,Sn)Se and (Pb,Sn)Te. These materials can be n-doped by electrons with bismuth. The bulk doping of the materials can lead to a rhombohedral distortion of the crystal lattice and the appearance of the piezoelectric field. The electric field on the surface regions of the TCI film can lift up the degeneracy of one of four Dirac points and transform material from a topological crystalline insulator to a $\mathbb{Z}_2$ topological insulator.

Further research directions in the field will focus on preparing better-controlled systems. Instead of naturally grown random heterostructures, artificial heterostructures with periodically ordered magnetic and topological insulator layers promise possibilities of higher temperature ferromagnetic order. One of the possible outputs is to prepare a quantum anomalous Hall effect device working at a higher temperature than the achieved couple of Kelvin. However, since such a device needs suppressed charge carrier density in the bulk of the material, I wonder if such a device can work at room temperature in the foreseeable future or with current topological insulators.

The field of artificial heterostructures also can include normal insulator-topological insulator structures. Such structures can host topological states at each interface, enhancing their density for future applications. The telluride-based topological insulators and topological crystalline insulators can be combined with ferroelectric layers of GeTe-type ferroelectric. The inherent electric field can also change the topological properties of the material.

The topological insulators will be further studied for their possible applications in spintronics or quantum computing.

Bibliography

[1] F. Schindler, A. M. Cook, M. G. Vergniory, Z. Wang, S. S. P. Parkin, B. A. Bernevig, and T. Neupert, Science Advances **4**, eaat034 (2018).

[2] M. Z. Hasan and C. L. Kane, Rev. Mod. Phys. **82**, 3045 (2010).

[3] X.-L. Qi and S.-C. Zhang, Rev. Mod. Phys. (2011).

[4] Y. Ando, Journal of the Physical Society of Japan **82**, 102001 (2013).

[5] J. E. Moore, Nature **464**, 194 (2010).

[6] X.-L. Qi, T. L. Hughes, and S. C. Zhang, Phys. Rev. B **78**, 195424 (2008).

[7] L. Fu, C. L. Kane, and E. J. Mele, Phys. Rev. Lett. **98**, 106803 (2007).

[8] C. L. Kane and E. J. Mele, Phys. Rev. Lett. **95**, 226801 (2005).

[9] C. L. Kane and E. J. Mele, Phys. Rev. Lett. **95**, 146802 (2005).

[10] J. E. Moore and L. Balents, Phys. Rev. B **75**, 121306(R) (2007).

[11] R. Roy, Phys. Rev. B **79**, 195322 (2009).

[12] M. G. Vergniory, L. Elcoro, C. Felser, N. Ragnault, B. A. Barnevig, and Z. Wang, Nature **566**, 480 (2019).

[13] T. Zhang, Y. Jiang, Z. Song, H. Huang, Y. He, Z. Fang, H. Weng, and C. Fang, Nature **566**, 475 (2019).

[14] F. Tang, H. C. Po, A. Vishwanath, and X. Wan, Nature **566**, 486 (2019).

[15] K. von Klitzing, G. Dorda, and M. Pepper, Phys. Rev. Lett. **45**, 494 (1980).

[16] Quantum hall effect – https://en.wikipedia.org/wiki/quantum_hall_effect, 2017, Accessed = 2022-11-22.

[17] B. I. Halperin, Phys. Rev. B **25**, 2185 (1982).

[18] D. J. Thouless, M. Kohmoto, M. P. Nightingale, and M. den Nijs, Physical Review Letters **49**, 405 (1982).

[19] B. L. Halperin, Phys. Rev. B **61**, 2185 (1982).

[20] F. D. M. Haldane, Phys. Rev. Lett. **61**, 2015 (1988).

[21] R. Roy, Phys. Rev. B **79**, 195321 (2009).

[22] T. Fukui and Y. Hatsugai, J. Phys. Soc. Jpn. **76**, 053702 (2007).

[23] L. Fu and C. L. Kane, Phys. Rev. B **74**, 195312 (2006).

[24] B. A. Bernevig, T. L. Hughes, and S. C. Zhang, Science **314**, 1757 (2006).

[25] M. Konig, S. Wiedmann, C. Brune, A. Roth, H. Buhmann, L. W. Molenkamp, X.-L. Qi, and S.-C. Zhang, Science **318**, 766 (2007).

[26] O. A. Pankratov, S. V. Pakhomov, and B. A. Volkov, Solid State Communications **61**, 93 (1987).

[27] M. Fruchart and D. Carpentier, Comptes Rendus Physique **14**, 779 (2013).

[28] C. L. Kane and E. J. Mele, (2005), arXiv:cond-mat/0411737.

[29] L. Fu and C. L. Kane, Phys. Rev. B **76**, 045302 (2007).

[30] C.-X. Liu, X.-L. Qi, H. Zhang, X. Dai, Z. Fang, and S.-C. Zhang, Phys. Rev. B **82**, 045122 (2010).

[31] H. Zhang, C. Liu, X. Qi, X. Dai, Z. Fang, and S. Zhang, Nature Phys. **5**, 438 (2009).

[32] N. K.S., G. A.K., M. S.V., J. D., K. M.I., G. I.V., D. S.V., and F. A.A., Nature **438**, 197 (2005).

[33] J. W. McIver, D. Hsieh, H. Steinberg, P. Jarillo-Herrero, and N. Gedik, Nature Nanotechnology **7**, 96 (2012).

[34] A. M. Essin, J. E. Moore, and D. Vanderbilt, Phys. Rev. Lett. **102**, 146805 (2009).

[35] X.-L. Qi, R. Li, J. Zang, and S.-C. Zhang, Science **27**, 1184 (2009).

[36] A. Karch, Phys. Rev. Lett. **103**, 171601 (2009).

[37] J. Maciejko, X.-L. Qi, H. D. Drew, and S.-C. Zhang, Phys. Rev. Lett. **105**, 166803 (2010).

[38] R. Yu, W. Zhang, H.-J. Zhang, S.-C. Zhang, X. Dai, and Z. Fang, Science **329**, 61 (2010).

[39] C.-Z. Chang, W. Zhao, D. Y. Kim, H. Zhang, B. A. Assaf, D. Heiman, S.-C. Zhang, C. Liu, M. H. W. Chan, and J. S. Moodera, Nature Materials **14**, 473 (2015).

[40] L. Fu and C. L. Kane, Phys. Rev. Lett. **100**, 096407 (2008).

[41] Z.-Z. Li, F.-C. Zhang, and Q.-H. Wang, Scientific Reports **4**, 6363 (2014).

[42] D. S. Shapiro, A. Shnirman, and A. D. Mirlin, Phys. Rev. B **93**, 155411 (2015).

[43] T. W. Schmitt, M. R. Connolly, M. Schleenvoigt, C. Liu, O. Kennedy, J. M. Chávez-Garcia, A. R. Jalil, B. Bennemann, S. Trellenkamp, F. Lentz, E. Neumann, T. Lindström, S. E. de Graaf, E. Berenschot, N. Tas, G. Mussler, K. D. Petersson, D. Grützmacher, , and P. Schüffelgen, Nano Lett. **22**, 2595 (2022).

[44] I. T. Witting, T. C. Chasapis, F. Ricci, M. Peters, N. A. Heinz, G. Hautier, and G. J. Snyder, Advanced Electronic Materials **2019**, 1800904 (2019).

[45] J. Fikáček, P. Procházka, V. Stetsovych, S. Průša, M. Vondráček, L. Kormoš, T. Skála, P. Vlaic, O. Caha, K. Carva, J. Čechal, G. Springholz, and J. Honolka, New J. Phys. **22**, 073050 (2020).

[46] O. Caha, A. Dubroka, J. Humlíček, V. Holý, H. Steiner, M. Ul-Hassan, J. Sánchez-Barriga, O. Rader, T. N. Stanislavchuk, A. A. Sirenko, G. Bauer, and G. Springholz, Crystal Growth & Design **13**, 3365 (2013).

[47] J. W. G. Bos, H. W. Zandbergen, M.-H. Lee, N. P. Ong, and R. J. Cava, Phys. Rev. B **75**, 195203 (2007).

[48] Y. Kim, S. Cho, A. DiVenere, G. K. L. Wong, and J. B. Ketterson, Phys. Rev. B **63**, 155306 (2001).

[49] H. Steiner, V. Volobuev, O. Caha, G. Bauer, G. Springholz, and V. Holý, J. Appl. Crystallography **47**, 1889 (2014).

[50] Y. Xia, L. Wray, D. Qian, D. Hsieh, A. Pal, H. Lin, A. Bansil, D. Grauer, Y. Hor, R. Cava, and M. Hasan, Nature Phys. **5**, 398 (2009).

[51] J. C. Y. Teo, L. Fu, and C. L. Kane, Phys. Rev. B **78**, 045426 (2008).

[52] L. Fu, Phys. Rev. Lett. **106**, 106802 (2011).

[53] T. Neupert and F. Schindler, *Topological Matter*, Springer Series in Solid-State Sciences Vol. 190 (Springer, 2018), pp. 31–61, arxiv:1810.03484v1.

[54] F. Herman, R. Kortum, I. Ortenburger, and J. P. van Dyke, Journal de Physique Colloques **29**, C4 (1968).

[55] T. H. Hsieh, H. Lin, J. Liu, W. Duan, A. Bansil, and L. Fu, Nature Communications **3**, 982 (2012).

[56] Y. Shani, R. Rosman, A. Katzir, P. Norton, M. Tacke, and H. M. Preier, J. Appl. Phys. **63**, 5603 (1988).

[57] Y. Tanaka, Z. Ren, T. Sato, K. Nakayama, S. Souma, T. Takahashi, K. Segawa, and Y. Ando, Nature Physics **8**, 800 (2012).

[58] P. Dziawa, B. J. Kowalski, K. Dybko, R. Buczko, A. Szczerbakow, M. Szot, E. Łusakowska, T. Balasubramanian, B. M. Wojek, M. H. Berntsen, O. Tjernberg, and T. Story, Nature Materials **11**, 1023 (2012).

[59] S. Safaei, P. Kacman, and R. Buczko, Phys. Rev. B **88**, 045305 (2013).

[60] C. M. Polley, P. Dziawa, A. Reszka, A. Szczerbakow, R. Minikayev, J. Z. Domagala, S. Safaei, P. Kacman, R. Buczko, J. Adell, M. H. Berntsen, B. M. Wojek, O. Tjernberg, B. J. Kowalski, T. Story, and T. Balasubramanian, Phys. Rev. B **89**, 075317 (2013).

[61] P. S. Mandal, G. Springholz, V. V. Volobuev, O. Caha, A. Varykhalov, E. Golias, G. Bauer, O. Rader, and J. Sánchez-Barriga, Nature Communications **8**, 968 (2017).

[62] U. Pietsch, V. Holý, and T. Baumbach, *High-Resolution X-Ray Scattering From Thin Films to Lateral Nanostructures* (Springer-Verlag, Berlin, Heidelberg, New York, 2004).

[63] A. Authier, *Dynamical theory of x-ray diffraction* (Oxford University Press, 2001).

[64] W. L. Holstein, J. Appl. Phys. **74**, 4963 (1993).

[65] B. Croset and C. de Beauvais, Surf. Sci. **384**, 15 (1997).

[66] B. Croset and C. de Beauvais, Surf. Sci. **409**, 403 (1998).

[67] V. S. Kopp, V. M. Kaganer, J. Schwarzkopf, F. Waidick, T. Remmele, A. Kwasniewski, and M. Schmidbauer, Acta Cryst. A **68**, 148 (2012).

[68] P. R. Pukite, C. S. Lent, and P. I. Cohen, Surf. Sci. **161**, 39 (1985).

[69] E. D. L. Rienks, S. Wimmer, J. Sánchez-Barriga, O. Caha, P. S. Mandal, J. Růžička, A. Ney, H. Steiner, V. V. Volobuev, H. Groiss, M. Albu, G. Kothleitner, J. Michalička, S. A. Khan, J. Minar, H. Ebert, G. Bauer, F. Freyse, A. Varykhalov, O. Rader, and G. Springholz, Nature **576**, 423 (2019).

[70] S. Wimmer, J. Sánchez-Barriga, P. Kuppers, A. Ney, E. Schierle, F. Freyse, O. Caha, J. Michalička, M. Liebmann, D. Primetzhofer, M. Hoffman, A. Ernst, M. M. Otrokov, G. Bihlmayer, E. Weschke, B. Lake, E. V. Chulkov, M. Morgenstern, G. Bauer, G. Springholz, and O. Rader, Advanced Materials **33**, 2102935 (2021).

[71] V. Holý, J. Kuběna, E. Abramof, K. Lischka, A. Pesek, and E. Koppensteiner, J. Appl. Phys. **74**, 1736 (1993).

[72] O. Bunau and Y. Joly, J. Phys.: Condens. Matter **21**, 345501 (2009).

[73] J. J. Rehr and R. C. Albers, Rev. Mod. Phys. **72**, 621 (2000).

[74] B. Ravel and M. Newville, Journal of Synchrotron Radiation **12**, 537 (2005).

[75] J. Rehr, J. Kas, M. Prange, A.P.Sorini, Y. Takimoto, and F. Vila, Comptes Rendus Physique **10**, 548 (2009).

[76] J. J. Rehr, J. J. Kas, F. D. Vila, M. P. Prange, and K. Jorissen, Phys. Chem. Chem. Phys. **12**, 5503 (2010).

[77] L. J. Allen, A. J. D'Alfonso, and S. D. Findlay, Ultramicroscopy **151**, 11 (2015).

[78] S. Hüfner, editor, *Very High Resolution Photoelectron Spectroscopy* (Springer-Verlag, Berlin, Heidelberg, New York, 2007).

[79] H. Zhang, T. Pincelli, C. Jozwiak, T. Kondo, R. Ernstorfer, T. Sato, and S. Zhou, Nature Review Methods Primers **2**, 54 (2022).

[80] B. Q. Lv, T. Qian, and H. Ding, Rev. Mod. Phys. **93**, 025002 (2021).

[81] J. A. Sobota, Y. He, and Z.-X. Shen, Rev. Mod. Phys. **93**, 025006 (2021).

[82] J. Minár, J. Braun, S. Mankovsky, and H. Ebert, Journal of Electron Spectroscopy and Related Phenomena **184**, 91 (2011), Advances in Vacuum Ultraviolet and X-ray Physics.

[83] L. J. van der Pauw, Phillips resarch reports **13**, 1 (1958).

[84] N. Nagaosa, J. Sinova, S. Onoda, A. H. MacDonald, and N. P. Ong, Rev. Mod. Phys. **82**, 1539 (2010).

[85] A. Dubroka, O. Caha, M. Hronček, P. Friš, M. Orlita, V. Holý, H. Steiner, G. Bauer, G. Springholz, and J. Humlíček, Phys. Rev. B **96**, 235202 (2017).

[86] J. Sánchez-Barriga, A. Varykhalov, G. Springholz, H. Steiner, R. Kirchschlager, G. Bauer, O. Caha, E. Schierle, E. Weschke, A. A. Uenal, S. Valencia, M. Dunst, J. Braun, H. Ebert, J. Minar, E. Golias, L. V. Yashina, A. Ney, V. Holý, and O. Rader, Nature Communications **7**, 10559 (2016).

[87] J. Růžička, O. Caha, V. Holý, H. Steiner, V. Volobuiev, A. Ney, G. Bauer, T. Duchoň, K. Veltruská, I. Khalakhan, V. Matolín, E. F. Schwier, H. Iwasawa, K. Shimada, and G. Springholz, New J. Phys. **17**, 013028 (2015).

[88] V. V. Volobuev, P. S. Mandal, M. Galicka, O. Caha, J. Sánchez-Barriga, D. Di Sante, A. Varykhalov, A. Khiar, S. Picozzi, G. Bauer, P. Kacman, R. Buczko, O. Rader, and G. Springholz, Advanced Materials **29**, 1604185 (2017).

Chapter 6

List of publications

1. O. Caha, V. Křápek, V. Holý, S. Moss, J. Li, A. Norman, A. Mascarenhas, J. Reno, J. Stangl, and M. Meduňa, *X-ray diffraction on laterally modulated (InAs)(n)/(AlAs)(m) short-period superlattices*, J. Appl. Phys. **96**, 4833 (2004).

2. O. Caha, P. Mikulík, J. Novák, V. Holý, S. Moss, A. Norman, A. Mascarenhas, J. Reno, and B. Krause, *Spontaneous lateral modulation in short-period superlattices investigated by grazing-incidence X-ray diffraction*, Phys. Rev. B **72**, 035313 (2005).

3. J. Li, D. Stokes, O. Caha, S. L. Ammu, J. Bai, K. E. Bassler, and S. C. Moss, *Morphological instability in InAs/GaSb superlattices due to interfacial bonds*, Phys. Rev. Lett. **95**, 096104 (2005).

4. O. Caha, V. Holý, and K. E. Bassler, *Nonlinear evolution of Surface morphology in InAs/AlAs superlattices via Surface diffusion*, Phys. Rev. Lett. **96**, 136102 (2006).

5. O. Caha, V. Holý, and K. E. Bassler, *Growth evolution of superlattice morphology*, Acta Crystallograpica A-Foundation and Advances **63**, S254 (2007).

6. J. Kubena, A. Kubena, O. Caha, and P. Mikulik, *Development of oxide precipitates in silicon: calculation of the distribution function of the classical theory of nucleation by a nodal-points approximation*, J. Phys.-Condensed Matter **19**, 496202 (2007).

7. J. Kubena, A. Kubena, O. Caha, and M. Meduna, *Analysis of vacancy and interstitial nucleation kinetics in Si wafers during rapid thermal annealing*, J. Phys.-Condensed Matter **21**, 105402 (2009).

8. M. Meduna, O. Caha, M. Keplinger, J. Stangl, G. Bauer, G. Mussler, and D. Gruetzmacher, *Interdiffusion in Ge rich SiGe/Ge multilayers studied by in situ diffraction*, Physica Status Solidi A-Applications and Materials Science **206**, 1775 (2009).

9. M. Meduna, O. Caha, J. Kubena, A. Kubena, and J. Bursik, *Homogenization of CZ Si wafers by Tabula Rasa annealing*, Physica B-Condensed Matter **404**, 4637 (2009), 25th International Conference on Defects in Semiconductors, St Petersburg, Russia, JUL 20-24, 2009.

10. O. Caha and M. Meduna, *X-ray diffraction on precipitates in Czochralski-grown silicon*, Physica B-Condensed Matter **404**, 4626 (2009), 25th International Conference on Defects in Semiconductors, St Petersburg, Russia, JUL 20-24, 2009.

11. A. Hospodkova, E. Hulicius, J. Pangrac, J. Oswald, J. Vyskocil, K. Kuldova, T. Simecek, P. Hazdra, and O. Caha, *InGaAs and GaAsSb strain reducing layers covering InAs/GaAs quantum dots*, J. Crystal Growth **312**, 1383 (2010), 17th Amer Conference on Crystal Growth and Epitaxy/14th United States Biennial Workshop on Organometallic Vapor Phase Epitaxy/6th Inter Workshop on Modeling in Crystal Growth, Lake Geneva, WI, Aug 09-14, 2009.

12. J. H. Li, D. W. Stokes, J. C. Wickett, O. Caha, K. E. Bassler, and S. C. Moss, *Effect of strain on the growth of InAs/GaSb superlattices: An x-ray diffraction study*, J. Appl. Phys. **107**, 123504 (2010).

13. V. Holý, X. Marti, L. Horak, O. Caha, V. Novak, M. Cukr, and T. U. Schuelli, *Density of Mn interstitials in (Ga,Mn)As epitaxial layers determined by anomalous x-ray diffraction*, Appl. Phys. Lett. **97**, 181913 (2010).

14. V. Cech, S. Lichovnikova, R. Trivedi, V. Perina, J. Zemek, P. Mikulik, and O. Caha, *Plasma polymer films of tetravinylsilane modified by UV irradiation*, Surface & Coatings Technology **205**, S177 (2010), 7th Asian-European International Conference on Plasma Surface Engineering, Busan, South Korea, Sep 20-25, 2009.

15. M. Meduňa, O. Caha, J. Růžička, S. Bernatová, M. Svoboda, and J. Buršík, *Oxygen precipitation studied by x-ray diffraction techniques*, in *Gettering and Defect Engineering in Semiconductor Technology XIV*, edited by Jantsch, W and Schaffler, F, , Solid State Phenomena Vol. 178-179, p. 325, 2011, 14th International Biannual Meeting on Gettering and Defect Engineering in Semiconductor (GADEST2011), Loipersdorf Spa & Conf Ctr, Loipersdorf, Austria, Sep 25-30, 2011.

16. J. Kubena, A. Kubena, O. Caha, and M. Meduna, *Homogeneous and heterogeneous nucleation of oxygen in Si-CZ*, in *Gettering and Defect Engineering in Semiconductor Technology XIV*, edited by Jantsch, W and Schaffler, F, , Solid State Phenomena Vol. 178-179, p. 495, 2011, 14th International Biannual Meeting on Gettering and Defect Engineering in Semiconductor (GADEST2011), Loipersdorf Spa & Conf Ctr, Loipersdorf, Austria, Sep 25-30, 2011.

17. A. Hospodkova, J. Pangrac, J. Vyskocil, J. Oswald, A. Vetushka, O. Caha, P. Hazdra, K. Kuldova, and E. Hulicius, *InAs/GaAs quantum dot capping in kinetically limited MOVPE growth regime*, J. Cystal Growth **317**, 39 (2011).

18. S. Piano, X. Marti, A. W. Rushforth, K. W. Edmonds, R. P. Campion, M. Wang, O. Caha, T. U. Schuelli, V. Holý, and B. L. Gallagher, *Surface morphology and magnetic anisotropy in (Ga,Mn)As*, Appl. Phys. Lett. **98**, 152503 (2011).

19. D. Franta, I. Ohlidal, D. Necas, F. Vizda, O. Caha, M. Hason, and P. Pokorny, *Optical characterization of HfO2 thin films*, Thin Solid Films **519**, 6085 (2011).

20. O. Caha, S. Bernatova, M. Meduna, M. Svoboda, and J. Bursik, *Study of oxide precipitates in silicon using X-ray diffraction techniques*, Physica Status Solidi A-Applications and Materials Science **208**, 2587 (2011).

21. L. Zabransky, V. Bursikova, J. Bursik, P. Vasina, P. Soucek, O. Caha, M. Jilek, and V. Perina, *Study of the Indentation Response of Nanocomposite n-TiC/a-C:H Coatings*, Chemicke Listy **106**, S1508 (2012).

22. E. Mikmekova, M. Urbanek, T. Fort, R. Di Mundo, and O. Caha, *Effect of Hydrogen on the Properties of Amorphous Carbon Nitride Films*, in *Manufacturing Science and Technology, PTS 1-8*, edited by Fan, W, , Advanced Materials Research Vol. 383-390, p. 3298, 2012, International Conference on Manufacturing Science and Technology (ICMST 2011), Singapore, Singapore, SEP 16-18, 2011.

23. M. Meduna, O. Caha, M. Svoboda, and J. Bursik, *X-ray Laue and Bragg diffraction on oxygen precipitates in annealed CZ-Si wafers.*, Acta Crystallograpica A-Foundation and Advances **68**, S260 (2012).

24. M. Schmidbauer, A. Ugur, C. Wollstein, F. Hatami, F. Katmis, O. Caha, and W. T. Masselink, *Nucleation of lateral compositional modulation in InGaP epitaxial films grown on (001) GaAs*, J. Appl. Phys. **111**, 024306 (2012).

25. E. Piskorska-Hommel, V. Holý, O. Caha, A. Wolska, A. Gust, C. Kruse, H. Kroencke, J. Falta, and D. Hommel, *Complementary information on CdSe/ZnSe quantum dot local structure from extended X-ray absorption fine structure and diffraction anomalous fine structure measurements*, J. Alloys and Compounds **523**, 155 (2012).

26. M. Meduna, O. Caha, and J. Bursik, *Studies of influence of high temperature preannealing on oxygen precipitation in CZ Si wafers*, J. Crystal Growth **348**, 53 (2012).

27. M. Meduňa, J. Růžička, O. Caha, J. Buršík, and M. Svoboda, *Precipitation in silicon wafers after high temperature preanneal studied by X-ray diffraction methods*, Physica B-Condensed Matter **407**, 3002 (2012), 26th International Conference on Defects in Semiconductors (ICDS), Nelson, New Zealand, JUL 18-22, 2011.

28. P. Soucek, T. Schmidtova, L. Zabransky, V. Bursikova, P. Vasina, O. Caha, M. Jilek, A. El Mel, P.-Y. Tessier, J. Schaefer, J. Bursik, V. Perina, and R. Miksova, *Evaluation of composition, mechanical properties and structure of nc-TiC/a-C:H coatings prepared by balanced magnetron sputtering*, Surface & Coatings Technology **211**, 111 (2012), Symposium K on Protective Coatings and Thin Films held at the European-Materials-Research-Society Spring Meeting (E-MRS), Nice, France, May 09-13, 2011.

29. E. Mikmekova, J. Polcak, J. Sobota, I. Muellerova, V. Perina, and O. Caha, *Humidity resistant hydrogenated carbon nitride films*, Appl. Surface Science **275**, 7 (2013), 7th NANOSMAT, Prague, Czech Republic, Sep 18-21, 2012.

30. O. Caha, A. Dubroka, J. Humlíček, V. Holý, H. Steiner, M. Ul-Hassan, J. Sánchez-Barriga, O. Rader, T. N. Stanislavchuk, A. A. Sirenko, G. Bauer, and G. Springholz, *Growth, Structure, and Electronic Properties of Epitaxial Bismuth Telluride Topological Insulator Films on BaF2 (111) Substrates*, Crystal Growth & Design **13**, 3365 (2013).

31. O. Caha, P. Kostelník, J. Šik, Y. D. Kim, and J. Humlíček, *Lattice constants and optical response of pseudomorph Si-rich SiGe:B*, Appl. Phys. Lett. **103**, 202107 (2013).

32. P. Soucek, T. Schmidtova, V. Bursikova, P. Vasina, Y. T. Pei, J. T. M. De Hos, O. Caha, V. Perina, R. Miksova, and P. Malinsky, *Tribological properties of nc-TiC/a-C:H coatings prepared by magnetron sputtering at low and high ion bombardment of the growing film*, Surface & Coatings Technology **241**, 64 (2014), 56th Annual Technical Conference of the Society-of-Vacuum-Coaters, Providence, France, Apr 20-25, 2013.

33. L. Zabransky, V. Bursikova, P. Soucek, P. Vasina, T. Gardelka, P. St'ahel, O. Caha, V. Perina, and J. Bursik, *Study of the thermal dependence of mechanical properties, chemical composition and structure of nanocomposite TiC/a-C:H coatings*, Surface & Coatings Technology **242**, 62 (2014).

34. J. Humlíček, D. Hemzal, A. Dubroka, O. Caha, H. Steiner, G. Bauer, and G. Springholz, *Raman and interband optical spectra of epitaxial layers of the topological insulators Bi2Te3 and Bi2Se3 on BaF2 substrates*, Physica Scripta **T162**, 014007 (2014), 4th International School and Conference on Photonics, Belgrade, Serbia, Aug 26-30, 2013.

35. L. Zabransky, V. Bursikova, P. Soucek, P. Vasina, T. Gardelka, P. St'ahel, O. Caha, V. Perina, and J. Bursik, *Study of the thermal dependence of mechanical properties, chemical composition and structure of nanocomposite TiC/a-C:H coatings (Reprinted from Surface & Coatings Technology, vol 242, pg 62-67, 2014)*, Surface & Coatings Technology **255**, 158 (2014), Spring Meeting of the European-Materials-Research-Society (EMRS), Univ Poitiers, Strasbourg, France, May 27-31, 2013.

36. P. Souček, T. Schmidtová, L. Zabransky, V. Bursikova, P. Vasina, O. Caha, J. Bursik, V. Perina, R. Miksova, Y. T. Pei, and J. T. M. De Hosson, *On the control of deposition process for enhanced mechanical properties of nc-TiC/a-C:H coatings with DC magnetron sputtering at low or high ion flux*, Surface & Coatings Technology **255**, 8 (2014), Spring Meeting of the European-Materials-Research-Society (EMRS), Univ Poitiers, Strasbourg, France, May 27-31, 2013.

37. H. Steiner, V. Volobuev, O. Caha, G. Bauer, G. Springholz, and V. Holý, *Structure and composition of bismuth telluride topological insulators grown by molecular beam epitaxy*, J. Appl. Crystallography **47**, 1889 (2014).

38. J. Růžička, O. Caha, V. Holý, H. Steiner, V. Volobuiev, A. Ney, G. Bauer, T. Duchoň, K. Veltruská, I. Khalakhan, V. Matolín, E. F. Schwier, H. Iwasawa, K. Shimada, and G. Springholz, *Structural and electronic properties of manganese-doped Bi2Te3 epitaxial layers*, New J. Phys. **17**, 013028 (2015).

39. L. Zabransky, V. Bursikova, J. Daniel, P. Soucek, P. Vasina, J. Dugacek, P. St'ahel, O. Caha, J. Bursik, and V. Perina, *Comparative analysis of thermal stability of two different nc-TiC/a-C:H coatings*, Surface & Coatings Technology **267**, 32 (2015).

40. J. Sánchez-Barriga, A. Varykhalov, G. Springholz, H. Steiner, R. Kirchschlager, G. Bauer, O. Caha, E. Schierle, E. Weschke, A. A. Uenal, S. Valencia, M. Dunst, J. Braun, H. Ebert, J. Minar, E. Golias, L. V. Yashina, A. Ney, V. Holý, and O. Rader, *Nonmagnetic band gap at the Dirac point of the magnetic topological insulator (Bi1-xMnx)(2)Se-3*, Nature Communications **7**, 10559 (2016).

41. I. Gablech, V. Svatos, O. Caha, M. Hrabovsky, J. Prasek, J. Hubalek, and T. Sikola, *Preparation of (001) preferentially oriented titanium thin films by ion-beam sputtering deposition on thermal silicon dioxide*, J. Materials Science **51**, 3329 (2016).

42. A. Akrap, M. Hakl, S. Tchoumakov, I. Crassee, J. Kuba, M. O. Goerbig, C. C. Homes, O. Caha, J. Novak, F. Teppe, W. Desrat, S. Koohpayeh, L. Wu, N. P. Armitage, A. Nateprov, E. Arushanov, Q. D. Gibson, R. J. Cava, D. van der Marel, B. A. Piot, C. Faugeras, G. Martinez, M. Potemski, and M. Orlita, *Magneto-Optical Signature of Massless Kane Electrons in Cd3As2*, Phys. Rev. Lett. **117**, 136401 (2016).

43. M. Hakl, S. Tchoumakov, I. Crassee, A. Akrap, B. A. Piot, C. Faugeras, G. Martinez, O. Caha, J. Novak, A. Nateprov, E. Arushanov, W.-L. Lee, M. O. Goerbig, F. Teppe, M. Potemski, and M. Orlita, *Cyclotron resonance of Kane electrons observed in Cd3As2*, in *2017 42ND International Conference on Infrared, Millimeter, and Terahetrz Waves (IRMMW-THZ)*, International Conference on Infrared Millimeter and Terahertz Waves, 345 E 47TH ST, NEW YORK, NY 10017 USA, 2017, IEEE.

44. V. V. Volobuev, P. S. Mandal, M. Galicka, O. Caha, J. Sánchez-Barriga, D. Di Sante, A. Varykhalov, A. Khiar, S. Picozzi, G. Bauer, P. Kacman, R. Buczko, O. Rader, and G. Springholz, *Giant Rashba Splitting in Pb1-xSnxTe (111) Topological Crystalline Insulator Films Controlled by Bi Doping in the Bulk*, Advanced Materials **29**, 1604185 (2017).

45. V. Železný, O. Caha, A. Soukiassian, D. G. Schlom, and X. X. Xi, *Temperature-dependent far-infrared reflectance of an epitaxial (BaTiO3)(8)/(SrTiO3)(4) superlattice*, Phys. Rev. B **95**, 214110 (2017).

46. G. Martinez, B. A. Piot, M. Hakl, M. Potemski, Y. S. Hor, A. Materna, S. G. Strzelecka, A. Hruban, O. Caha, J. Novák, A. Dubroka, C. Drašar, and M. Orlita, *Determination of the energy band gap of Bi_2Se_3*, Scientific Reports **7**, 6891 (2017).

47. I. Gablech, O. Caha, V. Svatos, J. Pekarek, P. Neuzil, and T. Sikola, *Stress-free deposition of [001] preferentially oriented titanium thin film by Kaufman ion-beam source*, Thin Solid Films **638**, 57 (2017).

48. P. S. Mandal, G. Springholz, V. V. Volobuev, O. Caha, A. Varykhalov, E. Golias, G. Bauer, O. Rader, and J. Sánchez-Barriga, *Topological quantum phase transition from mirror to time reversal symmetry protected topological insulator*, Nature Communications **8**, 968 (2017).

49. C. Wang, O. Caha, F. Munz, P. Kostelnik, T. Novak, and J. Humlíček, *Mid-infrared ellipsometry, Raman and X-ray diffraction studies of AlxGa1-xN/AlN/Si structures*, Appl. Surface Science **421**, 859 (2017).

50. A. Dubroka, O. Caha, M. Hronček, P. Friš, M. Orlita, V. Holý, H. Steiner, G. Bauer, G. Springholz, and J. Humlíček, *Interband absorption edge in the topological insulators Bi-2(Te1-xSex)(3)*, Phys. Rev. B **96**, 235202 (2017).

51. I. Gablech, O. Caha, V. Svatos, J. Prasek, J. Pekarek, P. Neuzil, and T. Sikola, *Preparation of [001] Oriented Titanium Thin Film for MEMS Applications by Kaufman Ion-*

Beam Source, in *9th International Conference on Nanomaterials - Research and Application (NANOCON 2017)*, p. 117, 2018, 9th International Conference on Nanomaterials - Research and Application (NANOCON), Brno, Czech Republic, Oct 18-20, 2017.

52. P. Fris, D. Munzar, O. Caha, and A. Dubroka, *Direct observation of double exchange in ferromagnetic La0.7Sr0.3CoO3 by broadband ellipsometry*, Phys. Rev. B **97**, 045137 (2018).

53. P. Lepcio, F. Ondreáš, K. Zárybnická, M. Zbončák, O. Caha, and J. Jančář, *Bulk polymer nanocomposites with preparation protocol governed nanostructure: the origin and properties of aggregates and polymer bound clusters*, Soft Matter **14**, 2094 (2018).

54. I. Crassee, E. Martino, C. C. Homes, O. Caha, J. Novak, P. Tueckmantel, M. Hakl, A. Nateprov, E. Arushanov, Q. D. Gibson, R. J. Cava, S. M. Koohpayeh, K. E. Arpino, T. M. McQueen, M. Orlita, and A. Akrap, *Nonuniform carrier density in Cd3As2 evidenced by optical spectroscopy*, Phys. Rev. B **97**, 125204 (2018).

55. M. Hakl, S. Tchoumakov, I. Crassee, A. Akrap, B. A. Piot, C. Faugeras, G. Martinez, A. Nateprov, E. Arushanov, F. Teppe, R. Sankar, W.-l. Lee, J. Debray, O. Caha, J. Novak, M. O. Goerbig, M. Potemski, and M. Orlita, *Energy scale of Dirac electrons in Cd3As2*, Phys. Rev. B **97**, 115206 (2018).

56. G. Springholz, S. Wimmer, H. Groiss, M. Albu, F. Hofer, O. Caha, D. Kriegner, J. Stangl, G. Bauer, and V. Holý, *Structural disorder of natural BimSen superlattices grown by molecular beam epitaxy*, Phys. Rev. Materials **2**, 054202 (2018).

57. O. Sik, L. Skvarenina, O. Caha, P. M. Bullet, P. Skarvada, E. B. Bullet, and L. Grmela, *Determining the sub-Surface damage of CdTe single crystals after lapping*, J. Materials Science–Materials in Electronics **29**, 9652 (2018).

58. R. Krumpolec, T. Homola, D. C. Cameron, J. Humlíček, O. Caha, K. Kuldova, R. Zazpe, J. Prikryl, and J. M. Macak, *Structural and Optical Properties of Luminescent Copper(I) Chloride Thin Films Deposited by Sequentially Pulsed Chemical Vapour Deposition*, Coatings **8**, 369 (2018).

59. I. Gablech, V. Svatos, O. Caha, A. Dubroka, J. Pekarek, J. Klempa, P. Neuzil, M. Schneider, and T. Sikola, *Preparation of high-quality stress-free (001) aluminum nitride thin film using a dual Kaufman ion-beam source setup*, Thin Solid Films **670**, 105 (2019).

60. C. V. Falub, S. V. Pietambaram, O. Yildirim, M. Meduna, O. Caha, R. Hida, X. Zhao, J. Ambrosini, H. Rohrmann, and H. J. Hug, *Enhanced permeability dielectric FeCo/Al2O3 multilayer thin films with tailored properties deposited by magnetron sputtering on silicon*, AIP Advances **9**, 035243 (2019).

61. J. Rozbořil, K. Broch, R. Resel, O. Caha, F. Münz, P. Mikulík, J. E. Anthony, H. Sirringhaus, and J. Novák, *Annealing Behavior with Thickness Hindered Nucleation in Small-Molecule Organic Semiconductor Thin Films*, Crystal Growth & Design **19**, 3777 (2019).

62. E. D. L. Rienks, S. Wimmer, J. Sánchez-Barriga, O. Caha, P. S. Mandal, J. Růžička, A. Ney, H. Steiner, V. V. Volobuev, H. Groiss, M. Albu, G. Kothleitner, J. Michalička,

S. A. Khan, J. Minar, H. Ebert, G. Bauer, F. Freyse, A. Varykhalov, O. Rader, and G. Springholz, *Large magnetic gap at the Dirac point in Bi2Te3/MnBi2Te4 heterostructures*, Nature **576**, 423 (2019).

63. J. Krempasky, M. Fanciulli, L. Nicola, J. Minar, H. Volfova, O. Caha, V. V. Volobuev, J. Sanchez-Barriga, M. Gmitra, K. Yaji, K. Kuroda, S. Shin, F. Komori, G. Springholz, and J. H. Dil, *Fully spin-polarized bulk states in ferroelectric GeTe*, Phys. Rev. Research **2** (2020).

64. J. Seyd, I. Pilottek, N. Y. Schmidt, O. Caha, M. Urbanek, and M. Albrecht, *Mn3Ge-based tetragonal Heusler alloy thin films with addition of Ni, Pt, and Pd*, J. Phys.-Condensed Matter **32**, 145801 (2020).

65. J. A. Arregi, O. Caha, and V. Uhlir, *Evolution of strain across the magnetostructural phase transition in epitaxial FeRh films on different substrates*, Phys. Rev. B **101**, 174413 (2020).

66. J. Fikacek, P. Prochazka, V. Stetsovych, S. Prusa, M. Vondracek, L. Kormos, T. Skala, P. Vlaic, O. Caha, K. Carva, J. Cechal, G. Springholz, and J. Honolka, *Step-edge assisted large scale FeSe monolayer growth on epitaxial Bi(2)Se(3)thin films*, New Journal of Physics **22** (2020).

67. I. Mohelsky, A. Dubroka, J. Wyzula, A. Slobodeniuk, G. Martinez, Y. Krupko, B. A. Piot, O. Caha, G. Bauer, G. Springholz, M. Orlita, and J. Humlicek, *Landau level spectroscopy of Bi2Te3*, Phys. Rev. B **102** (2020).

68. J. Dvorak, O. Caha, and D. Hemzal, *Tuning of SPR for Colocalized Characterization of Biomolecules Using Nanoparticle-Containing Multilayers*, Plasmonics **16**, 1203 (2021).

69. R. Rechcinski, M. Galicka, M. Simma, V. V. Volobuev, O. Caha, J. Sanchez-Barriga, P. S. Mandal, E. Golias, A. Varykhalov, O. Rader, G. Bauer, P. Kacman, R. Buczko, and G. Springholz, *Structure Inversion Asymmetry and Rashba Effect in Quantum Confined Topological Crystalline Insulator Heterostructures*, Advanced Functional Materials **31** (2021).

70. J. Krempasky, L. Nicolai, M. Gmitra, H. Chen, M. Fanciulli, E. B. Guedes, M. Caputo, M. Radovic, V. V. Volobuev, O. Caha, G. Springholz, J. Minar, and J. H. Dil, *Triple-Point Fermions in Ferroelectric GeTe*, Phys. Rev. Lett. **126** (2021).

71. A. Kazakov, W. Brzezicki, T. Hyart, B. Turowski, J. Polaczynski, Z. Adamus, M. Aleszkiewicz, T. Wojciechowski, J. Z. Domagala, O. Caha, A. Varykhalov, G. Springholz, T. Wojtowicz, V. V. Volobuev, and T. Dietl, *Signatures of dephasing by mirror-symmetry breaking in weak-antilocalization magnetoresistance across the topological transition in Pb1-xSnxSe*, Phys. Rev. B **103** (2021).

72. P. Mikulik, O. Caha, and M. Meduna, *Laboratory and synchrotron rocking curve imaging for crystal lattice misorientation mapping*, Acta Crystallographica A-Foundation and Advances **77**, C837 (2021).

73. M. Meduna, O. Caha, E. Choumas, F. Bressan, and H. von Kanel, *X-ray rocking curve imaging on large arrays of extremely tall SiGe microcrystals epitaxial on Si*, J. Appl. Crystallography **54**, 1071 (2021).

74. S. Wimmer, J. Sanchez-Barriga, P. Kueppers, A. Ney, E. Schierle, F. Freyse, O. Caha, J. Michalicka, M. Liebmann, D. Primetzhofer, M. Hoffman, A. Ernst, M. M. Otrokov, G. Bihlmayer, E. Weschke, B. Lake, E. V. Chulkov, M. Morgenstern, G. Bauer, G. Springholz, and O. Rader, *Mn-Rich MnSb2Te4: A Topological Insulator with Magnetic Gap Closing at High Curie Temperatures of 45-50 K*, Advanced Materials **33** (2021).

75. M. Horky, J. A. Arregi, S. K. K. Patel, M. Stano, R. Medapalli, O. Caha, L. Vojacek, M. Horak, V. Uhlir, and E. E. Fullerton, *Controlling the Metamagnetic Phase Transition in FeRh/MnRh Superlattices and Thin-Film Fe50-xMnxRh50 Alloys*, ACS Applied Materials & Interfaces .

76. E. Gablech, Z. Fohlerova, K. Svec, F. Zales, O. Benada, O. Kofronova, J. Pekarkova, O. Caha, I. Gablech, J. Gabriel, and J. Drbohlavova, *Selenium nanoparticles with boron salt-based compound act synergistically against the brown-rot Serpula lacrymans*, International Biodeterioration & Biodegradation **169** (2022).

77. M. Zahradnik, M. Kiaba, S. Espinoza, M. Rebarz, J. Andreasson, O. Caha, F. Abadizaman, D. Munzar, and A. Dubroka, *Photoinduced insulator-to-metal transition and coherent acoustic phonon propagation in LaCoO3 thin films explored by femtosecond pump-probe ellipsometry*, Phys. Rev. B **105** (2022).

78. M. Kiaba, O. Caha, F. Abadizaman, and A. Dubroka, *Stabilization of the oxygen concentration in La0.3Sr0.7CoO3_delta thin films by 3 nm thin LaAlO3 capping layer*, Thin Solid Films **759** (2022).

79. N. Y. Schmidt, S. Abdulazhanov, J. Michalicka, J. Hintermayr, O. Man, O. Caha, M. Urbanek, and M. Albrecht, *Effect of Gd addition on the structural and magnetic properties of L1(0)-FePt alloy thin films*, J. Appl. Phys. **132** (2022).